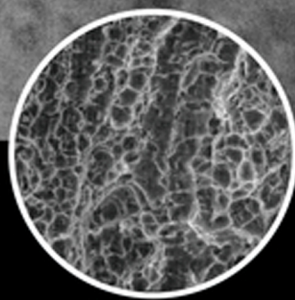
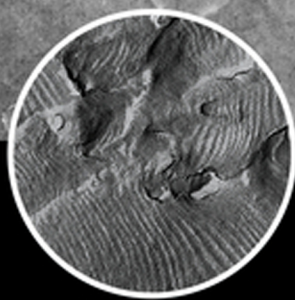


ARTHUR J. McEVILY



METAL FAILURES

MECHANISMS, ANALYSIS, PREVENTION

Second Edition

WILEY

Metal Failures

Metal Failures
Mechanisms, Analysis, Prevention

Second Edition

Arthur J. McEvily

WILEY

Cover image: background, © Michael Rutkowski; circle images, © courtesy of the author
Cover design: Michael Rutkowski

This book is printed on acid-free paper.

Copyright © 2013 by John Wiley & Sons, Inc. All rights reserved

Published by John Wiley & Sons, Inc., Hoboken, New Jersey
Published simultaneously in Canada

No part of this publication may be reproduced, stored in a retrieval system, or transmitted in any form or by any means, electronic, mechanical, photocopying, recording, scanning, or otherwise, except as permitted under Section 107 or 108 of the 1976 United States Copyright Act, without either the prior written permission of the Publisher, or authorization through payment of the appropriate per-copy fee to the Copyright Clearance Center, 222 Rosewood Drive, Danvers, MA 01923, (978) 750-8400, fax (978) 646-8600, or on the web at www.copyright.com. Requests to the Publisher for permission should be addressed to the Permissions Department, John Wiley & Sons, Inc., 111 River Street, Hoboken, NJ 07030, (201) 748-6011, fax (201) 748-6008, or online at www.wiley.com/go/permissions.

Limit of Liability/Disclaimer of Warranty: While the publisher and author have used their best efforts in preparing this book, they make no representations or warranties with the respect to the accuracy or completeness of the contents of this book and specifically disclaim any implied warranties of merchantability or fitness for a particular purpose. No warranty may be created or extended by sales representatives or written sales materials. The advice and strategies contained herein may not be suitable for your situation. You should consult with a professional where appropriate. Neither the publisher nor the author shall be liable for damages arising herefrom.

For general information about our other products and services, please contact our Customer Care Department within the United States at (800) 762-2974, outside the United States at (317) 572-3993 or fax (317) 572-4002.

Wiley publishes in a variety of print and electronic formats and by print-on-demand. Some material included with standard print versions of this book may not be included in e-books or in print-on-demand. If this book refers to media such as a CD or DVD that is not included in the version you purchased, you may download this material at <http://booksupport.wiley.com>. For more information about Wiley products, visit www.wiley.com.

Library of Congress Cataloging-in-Publication Data:

McEvily, A. J.

Metal failures : mechanisms, analysis, prevention / Arthur J. McEvily. -- 2nd edition.

p. cm

Includes bibliographical references and index.

ISBN 978-1-118-16396-2 (cloth); ISBN 978-1-118-41939-7 (ebk); ISBN 978-1-118-42116-1 (ebk)

1. Metals--Fracture. 2. Fracture mechanics. I. Title.

TA460.M382 2013

620.1'66--dc23

2012039445

Printed in the United States of America

10 9 8 7 6 5 4 3 2 1

To
Geof, Allysha, Keith, Joey, Ryan, Kyle, Courtney and Geneva Jane

Contents

Preface	xv
1. Failure Analysis	1
I. Introduction / 1	
II. Examples of Case Studies Involving Structural Failures / 6	
III. Summary / 25	
References / 25	
Problems / 26	
2. Elements of Elastic Deformation	27
I. Introduction / 27	
II. Stress / 27	
III. Strain / 32	
IV. Elastic Constitutive Relationships / 35	
V. State of Stress Ahead of a Notch / 44	
VI. Summary / 46	
References / 46	
Appendix 2-1: Mohr Circle Equations for a Plane Problem / 46	
Appendix 2-2: Three-Dimensional Stress Analysis / 49	
Appendix 2-3: Stress Formulas Under Simple Loading Conditions / 54	
Problems / 57	

3. Elements of Plastic Deformation **59**

- I. Introduction / 59
- II. Theoretical Shear Strength / 59
- III. Dislocations / 61
- IV. Yield Criteria for Multiaxial Stress / 68
- V. State of Stress in the Plastic Zone Ahead of a Notch in Plane-Strain Deformation / 70
- VI. Summary / 74
- For Further Reading / 75
- Appendix 3-1: The von Mises Yield Criterion / 75
- Problems / 76

4. Elements of Fracture Mechanics **80**

- I. Introduction / 80
- II. Griffith's Analysis of the Critical Stress for Brittle Fracture / 80
- III. Alternative Derivation of the Griffith Equation / 83
- IV. Orowan-Irwin Modification of the Griffith Equation / 84
- V. Stress Intensity Factors / 85
- VI. The Three Loading Modes / 88
- VII. Determination of the Plastic Zone Size / 88
- VIII. Effect of Thickness on Fracture Toughness / 89
- IX. The *R*-Curve / 91
- X. Short Crack Limitation / 92
- XI. Case Studies / 92
- XII. The Plane-Strain Crack Arrest Fracture Toughness, K_{Ia} , of Ferritic Steels / 95
- XIII. Elastic-plastic Fracture Mechanics / 96
- XIV. Failure Assessment Diagrams / 98
- XV. Summary / 101
- References / 101
- Problems / 102

5. Alloys and Coatings **105**

- I. Introduction / 105
- II. Alloying Elements / 106
- III. Periodic Table / 107

IV. Phase Diagrams / 108

V. Coatings / 126

VI. Summary / 130

References / 130

Problems / 130

6. Examination and Reporting Procedures 132

I. Introduction / 132

II. Tools for Examinations in the Field / 132

III. Preparation of Fracture Surfaces for Examination / 133

IV. Visual Examination / 133

V. Case Study: Failure of a Steering Column Component / 134

VI. Optical Examination / 135

VII. Case Study: Failure of a Helicopter Tail Rotor / 136

VIII. The Transmission Electron Microscope (TEM) / 136

IX. The Scanning Electron Microscope (SEM) / 138

X. Replicas / 142

XI. Spectrographic and Other Types of Chemical Analysis / 143

XII. Case Study: Failure of a Zinc Die Casting / 144

XIII. Specialized Analytical Techniques / 145

XIV. Stress Measurement by X-Rays / 146

XV. Case Study: Residual Stress in a Train Wheel / 149

XVI. The Technical Report / 150

XVII. Record Keeping and Testimony / 151

XVIII. Summary / 154

References / 155

Problem / 155

7. Brittle and Ductile Fractures 156

I. Introduction / 156

II. Brittle Fracture / 156

III. Some Examples of Brittle Fracture in Steel / 159

IV. Ductile-Brittle Behavior of Steel / 161

V. Case Study: The Nuclear Pressure Vessel Design Code / 168

VI. Case Study: Examination of Samples from the Royal Mail Ship (RMS)
Titanic / 172

VII. Ductile Fracture / 177	
VIII. Ductile Tensile Failure, Necking / 177	
IX. Fractographic Features Associated with Ductile Rupture / 183	
X. Failure in Torsion / 185	
XI. Case Study: Failure of a Helicopter Bolt / 185	
XII. Summary / 188	
References / 191	
Problems / 191	
8. Thermal and Residual Stresses	196
I. Introduction / 196	
II. Thermal Stresses, Thermal Strain, and Thermal Shock / 196	
III. Residual Stresses Caused by Nonuniform Plastic Deformation / 200	
IV. Residual Stresses Due to Quenching / 204	
V. Residual Stress Toughening / 207	
VI. Residual Stresses Resulting from Carburizing, Nitriding, and Induction Hardening / 207	
VII. Residual Stresses Developed in Welding / 209	
VIII. Measurement of Residual Stresses / 211	
IX. Summary / 211	
References / 211	
Appendix 8-1: Case Study of a Fracture Due to Thermal Stress / 212	
Problems / 213	
9. Creep	216
I. Introduction / 216	
II. Background / 216	
III. Characteristics of Creep / 217	
IV. Creep Parameters / 220	
V. Creep Fracture Mechanisms / 222	
VI. Fracture Mechanism Maps / 224	
VII. Case Studies / 225	
VIII. Residual Life Assessment / 230	
IX. Stress Relaxation / 232	
X. Elastic Follow-up / 233	

XI. Summary /	234
References /	234
Problems /	234

10. Fatigue 237

I. Introduction /	237
II. Background /	237
III. Design Considerations /	240
IV. Mechanisms of Fatigue /	246
V. Factors Affecting Fatigue Crack Initiation /	254
VI. Factors Affecting Fatigue Crack Growth /	257
VII. Analysis of the Rate of Fatigue Crack Propagation /	261
VIII. Fatigue Failure Analysis /	273
IX. Case Studies /	276
X. Thermal-Mechanical Fatigue /	285
XI. Cavitation /	285
XII. Composite Materials /	286
XIII. Summary /	287
References /	287
For Further Reading /	290
Problems /	290

11. Statistical Distributions 293

I. Introduction /	293
II. Distribution Functions /	293
III. The Normal Distribution /	294
IV. Statistics of Fatigue; Statistical Distributions /	296
V. The Weibull Distribution /	298
VI. The Gumbel Distribution /	302
VII. The Staircase Method /	307
VIII. Summary /	310
References /	310
Appendix 11-1: Method of Linear Least Squares (C. F. Gauss, 1794) /	311
Problems /	314

12. Defects **316**

- I. Introduction / 316
- II. Weld Defects / 316
- III. Case Study: Welding Defect / 321
- IV. Casting Defects / 328
- V. Case Study: Corner Cracking during Continuous Casting / 329
- VI. Forming Defects / 329
- VII. Case Studies: Forging Defects / 330
- VIII. Case Study: Counterfeit Part / 332
- IX. The Use of the Wrong Alloys; Errors in Heat Treatment, etc. / 333
- X. Summary / 334
- References / 334
- Problems / 334

13. Environmental Effects **336**

- I. Introduction / 336
- II. Definitions / 336
- III. Fundamentals of Corrosion Processes / 337
- IV. Environmentally Assisted Cracking Processes / 342
- V. Case Studies / 348
- VI. Cracking in Oil and Gas Pipelines / 350
- VII. Crack Arrestors and Pipeline Reinforcement / 352
- VIII. Plating Problems / 353
- IX. Case Studies / 353
- X. Pitting Corrosion of Household Copper Tubing / 356
- XI. Problems with Hydrogen at Elevated Temperatures / 356
- XII. Hot Corrosion (Sulfidation) / 358
- XIII. Summary / 358
- References / 358
- Problems / 359

14. Flaw Detection **360**

- I. Introduction / 360
- II. Inspectability / 360
- III. Visual Examination (VE) / 364

IV. Penetrant Testing (PT) / 364	
V. Case Study: Sioux City DC-10 Aircraft / 367	
VI. Case Study: MD-88 Engine Failure / 374	
VII. Magnetic Particle Testing (MT) / 375	
VIII. Case Study: Failure of an Aircraft Crankshaft / 378	
IX. Eddy Current Testing (ET) / 382	
X. Case Study: Aloha Airlines / 384	
XI. Ultrasonic Testing (UT) / 384	
XII. Case Study: B747 / 389	
XIII. Radiographic Testing (RT) / 389	
XIV. Acoustic Emission Testing (AET) / 391	
XV. Cost of Inspections / 393	
XVI. Summary / 393	
References / 394	
Problems / 394	
15. Wear	396
I. Wear / 396	
II. The Coefficient of Friction / 397	
III. The Archard Equation / 398	
IV. An Example of Adhesive Wear / 399	
V. Fretting Fatigue / 399	
VI. Case Study: Friction and Wear; Bushing Failure / 403	
VII. Roller Bearings / 404	
VIII. Case Study: Failure of a Railroad Car Axle / 410	
IX. Gear Failures / 410	
X. Summary / 414	
References / 414	
Problems / 415	
Concluding Remarks	417
Solutions to Problems	419
Name Index	469
Subject Index	473

Preface

As result of using the first edition in the teaching of courses on Failure Analysis in the United States, Europe, and Asia, it is clear that students need more background in fundamental areas such as elasticity and plasticity, phase diagrams, fatigue, and statistics in order to deal comfortably with the subject matter, and in this second edition, additional material has been presented to provide this background. In addition, new topics such as the staircase method in fatigue have been included and a few subjects, such as discussion of the stresses developed in crane hooks, have been omitted.

In addition, more homework problems have been included that are directly related to failure analysis so that the applicability of subjects such as fracture mechanics to real-world situations is more clearly understood. In this regard, Prof. Leon Shaw, formerly of the University of Connecticut and now with the Illinois Institute of Technology has been a valued contributor.

Further, as an aid to those readers who tackle the homework problems on their own, a section containing the solutions to these problems can be found at the end of the book.

One of the objectives of this second edition is to correct the typos and errata of the first edition. It is hoped that this objective has been met.

Finally, a special thank-you to Dr. Jirapong Kasivitamnuy of Chulalongkorn University for his input to this second edition. I would also like to thank Profs. Tul and Tawee of Chulalongkorn University, Prof. F. Kennedy of Dartmouth University, and Profs. S. Ishihara, M. Endo, A. Otuska, and Y. Mutoh of Japan for their assistance and encouragement.

A. J. McEvily
August 2013

Metal Failures

1

Failure Analysis

I. INTRODUCTION

Despite the great strides forward that have been made in technology, failures continue to occur, often accompanied by great human and economic loss. This text is intended to provide an introduction to the subject of failure analysis. It cannot deal specifically with each and every failure that may be encountered, as new situations are continually arising, but the general methodologies involved in carrying out an analysis are illustrated by a number of case studies. Failure analysis can be an absorbing subject to those involved in investigating the cause of an accident, but the capable investigator must have a thorough understanding of the mode of operation of the components of the system involved, as well as knowledge of the possible failure modes if a correct conclusion is to be reached. Since the investigator may be called upon to present and defend opinions before highly critical bodies, it is essential that opinions be based upon a sound factual basis and reflect a thorough grasp of the subject. A properly carried out investigation should lead to a rational scenario of the sequence of events involved in the failure as well as to an assignment of responsibility, either to the operator, the manufacturer, or the maintenance and inspection organization involved. A successful investigation may also result in improvements in design, manufacturing, and inspection procedures that preclude a recurrence of a particular type of failure.

The analysis of mechanical and structural failures might initially seem to be a relatively recent area of investigation, but upon reflection it is clear that the topic has been an active one for millennia. Since prehistoric times, failures have often resulted

in taking one step back and two steps forward, but often with severe consequences for the designers and builders. For example, according to the Code of Hammurabi, which was written in about 2250 BC (1):

If a builder build a house for a man and do not make its construction firm, and the house which he has built collapse and cause the death of the owner of the house, that builder shall be put to death. If it cause the death of a son of the owner of the house, they shall put to death a son of that builder. If it destroy property, he shall restore whatever it destroyed, and because he did not make the house which he built firm and it collapsed, he shall rebuild the house which collapsed at his own expense.

The failure of structures such as bridges, viaducts, and cathedrals resulted in better designs, better materials, and better construction procedures. Mechanical devices such as wheels and axles were improved through empirical insights gained by experience, and these improvements often worked out quite well. For example, a recent program in India was directed at improving the design of wheels for bullock-drawn carts. However, after much study, it was found that improvements in the design over those that had evolved over a long period of time were not economically feasible.

An example of an evolved design that did not work out well is related to the earthquake that struck Kobe, Japan, in 1995. That area of Japan had been free of damaging earthquakes for some time but had been visited frequently by typhoons. To stabilize homes against the ravages of typhoons, the local building practice was to use a rather heavy roof structure. Unfortunately, when the earthquake struck, the collapse of these heavy roofs caused considerable loss of life as well as property damage. The current design codes for this area have been revised to reflect a concern for both typhoons and earthquakes.

The designs of commonplace products have often evolved rapidly to make them safer. For example, consider the carbonated soft-drink bottle cap. At one time a metal cap was firmly crimped to a glass bottle, requiring a bottle opener for removal. Then came the easy-opening, twist-off metal cap. These caps were made of a thin, circular piece of aluminum that was shaped by a tool at the bottling plant to conform to the threads of the glass bottle. If the threads were worn, or if the shaping tool did not maintain proper alignment, then the connection between cap and bottle would be weak and the cap might spontaneously blow off the bottle while sitting on a shelf in a supermarket. Worse than that, there were a number of cases where, during the twisting-off process, the expanding gas suddenly propelled a weakly attached cap from the bottle and caused eye damage. To guard against this danger, the metal caps were redesigned to have a series of closely spaced perforations along the upper side of the cap so that as the seal between the cap and bottle was broken at the start of the twisting action, the gas pressure was vented and the possibility of causing an eye injury was minimized. The next stage in the evolution of bottle cap design has been to use plastic bottles and plastic caps. In a current design, the threads on the plastic bottle are slotted so that, as in the case of the perforated metal cap, as the cap is twisted the CO₂ gas is vented, and the danger of causing eye damage is reduced.

Stress analysis plays an important role both in design and in failure analysis. Ever since the advent of the Industrial Revolution, concern about the safety of structures has resulted in significant advances in stress analysis. The concepts of stress and strain developed from the work of Hooke in 1678 and were firmly established by Cauchy and Saint-Venant early in the nineteenth century. Since then, the field of stress analysis has grown to encompass the strength of materials and the theories of elasticity, viscoelasticity, and plasticity. The advent of the high-speed computer has led to further rapid advances in the use of numerical methods of stress analysis by means of the finite element method (FEM), and improved knowledge of material behavior has led to advances in development of constitutive relations based upon dislocation theory, plasticity, and mechanisms of fracture. Design philosophies such as safe-life and fail-safe have also been developed, particularly in the aerospace field.

In a *safe-life* design, a structure is designed as a statically determinate structure that is intended to last without failure for the design lifetime of the structure. To guard against premature failure, the component should be inspected at intervals during its in-service lifetime.

In the *fail-safe* approach, the structure is designed such that if one member of the structure were to fail, there would be enough redundancy built into the structure that an alternate load path would be available to support the loads (Fig. 1-1), at least until the time of the next inspection. (The use of both suspenders and a belt to support trousers is an example of a fail-safe, redundant approach.) Consideration must also be given to the spectrum of loading that a structure will be called upon to withstand in relation to the scatter in the ability of materials to sustain these loads. As indicated in, Fig. 1-2, danger of failure is present when these two distributions overlap.

In addition, new fields such as fracture mechanics, fatigue research, corrosion science, and nondestructive testing have emerged. Important advances have also been made in improving the resistance of materials to fracture. In the metallurgical field these advances have been brought about through improvements in alloy design, better control of alloy chemistry, and improvements in metal processing and heat treatment. The failure analyst often has to determine the nature of a failure; for example, was it due to fatigue or to an overload? In many cases, a simple visual examination may suffice to provide the answer. In other cases, however, the examination of a fracture surface (fractography) may be more involved and may require the use of laboratory

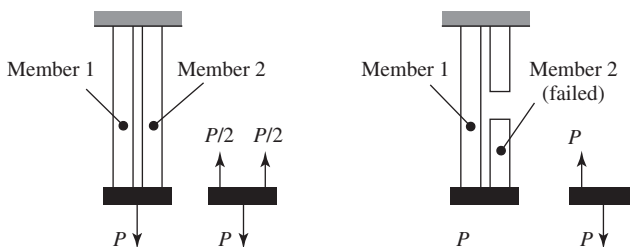


Fig. 1-1. Fail-safe load-carrying structure.

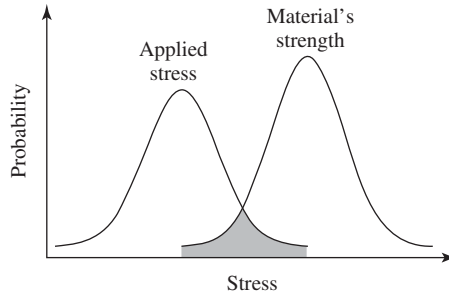


Fig. 1-2. Schematic frequency distributions showing the applied stresses and the resistance of the material.

instruments such as the light microscope, the transmission electron microscope, and the scanning electron microscope.

Many of today's investigations are quite costly and complex, and require a broad range of expertise as well as the use of sophisticated laboratory equipment. In some instances the investigations are carried out by federal investigators, as in the case of the TWA800 disaster (center fuel tank explosion), where both the Federal Bureau of Investigation (FBI) and the National Transportation Safety Board (NTSB) had to determine if the failure was due to a missile attack, sabotage, mechanical failure, or an electrical spark-ignited fuel tank explosion. The Three Mile Island accident (a faulty valve) involved the Nuclear Regulatory Commission (NRC), and the Challenger space shuttle disaster (O-ring) involved the National Aeronautics and Space Administration (NASA). Many investigations are also carried out by manufacturers to ensure that their products perform reliably. In addition, a number of companies now exist for the purpose of carrying out failure analyses to assist manufacturers and power plant owners, as well as to aid in litigation. The results of many of these investigations are made public, and thus provide useful information as to the nature and cause of failures. Unfortunately, the results of some investigations are sealed as part of a pretrial settlement to litigation, and the general public is deprived of an opportunity to learn that certain products may have dangers associated with them. A company may decide, on the basis of costs versus benefits, that it is cheaper to settle a number of claims rather than to issue a recall. This policy can sometimes be disastrous, as in the case of the recent rash of tire failures. Another example involved a brand of cigarette lighter that repeatedly malfunctioned and caused serious burn injuries. It was only after some 50 of these events had occurred and the cases had been settled that the dangers associated with this item were brought to light in a public trial.

An important outcome of failure analyses has been the development of building codes and specifications governing materials [the American Society for Testing and Materials (ASTM)], manufacturing procedures [the Occupational Safety and Health Administration (OSHA)], design [the American Society of Mechanical Engineers (ASME) Boiler and Pressure Vessel Codes, the Federal Aviation Administration

(FAA), NASA, the American Petroleum Institute (API)], construction (state and municipal codes), and operating codes (NASA, NRC, FAA). These codes and standards have often been developed to prevent a repetition of past failures, as well as to guard against potentially new types of failure, as in the case of nuclear reactors. Advances in steel making, nondestructive examination, and analytical procedures have led to a reduction of the material design factor (safety factor) for power boilers and pressure vessels from 4 to 3.5 (2). (Allowable stress values based upon the tensile strength are obtained by dividing the tensile strength by the material design factor.) Today the reliability of engineered products and structures is at an all-time high, but this reliability often comes with a high cost. In fact, in the nuclear industry, compliance with regulations intended to maximize safety may be so costly as to warrant the taking of a reactor out of service. It is also important for manufacturers to be aware of the state of the art as well as the latest standards. The number of manufacturers of small planes has dwindled because of product liability losses incurred when it was shown that their manufacturing procedures did not meet the current state-of-the-art safety standards. To guard against product failures, a number of firms now are organized in such a way that failure analysis is a line function rather than a staff function, and a member of the failure analysis group has to sign off on all new designs before they enter the manufacturing stage.

Please note that Standard International (SI) units as discussed in ASTM Standard E380 will be used in this text. Tables 1-1 to 1-4 provide the background on these SI units.

Table 1-1. Base SI Units

Quantity	Unit	Symbol
Length	meter	m
Mass	kilogram	kg
Time	second	s
electric current	ampere	A
Temperature	Kelvin	K
amount of substance	Mole	mol

Table 1-2. Derived SI Units with Special Names

Quantity	Unit	Symbol	Formula
Frequency	hertz	Hz	1/s
Force	Newton	N	kg.m/s ²
Pressure, Stress	pascal	Pa	N/m ²
Energy, work, quantity of heat	joule	J	N.m
power, radiant, flux	watt	Wb	J/s
Electric potential, potential difference, electromotive force	volt	V	W/A
electric capacitance	farad	F	C/V
electric resistance	ohm	Ω	V/A
electric conductance	siemens	S	A/V
magnetic flux	weber	Wb	V.s
magnetic flux density	tesla	T	Wb/m ²
inductance	henry	H	Wb/A

Table 1-3. Some Common Derived Units of SI

Quantity	Unit	Symbol
acceleration	meter per second squared	m/s ²
Area	square meter	m ²
current density	mole per cubic meter	A/m ²
density, mass	ampere per square meter	kg/m ³
electric charge density	kilogram per cubic meter	C/m ³
energy density	joule per cubic meter	J/m ³
Entropy	joule per kelvin	J/K
heat capacity	joule per kelvin	J/K
magnetic field strength	ampere per meter	A/m
molar energy	joule per mole	J/mol
molar entropy	joule per mole kelvin	J/mol
molar heat capacity	joule per mole kelvin	J/(mol.k)
power density	watt per square meter	W/m ²
Velocity	meter per second	m/s
viscosity, dynamic	pascal second	Pa-s
volume	cubic meter	m ³
wave number	1 per meter	1/m

Table 1-4. Selected Conversion Factors

To convert from multiply by	To	
atmosphere (760 mm Hg)	pascal (Pa)	1.013 25 × 10 ⁵
BTU	joule (J)	1.055 056 × 10 ³
BTU/h	watt (W)	2.930 711 × 10 ⁻⁴
Calorie	joule (J)	4.186 800
degree Fahrenheit	degree Celsius	t ⁰ C = (t ⁰ F – 32)/1.8
degree Celsius	degree kelvin (K)	tK = t ⁰ C – 273.2
inch	meter (m)	2.540 000 × 10 ⁻²
kgf/cm ²	pascal (Pa)	9.806 650 × 10 ⁴
kip (1000 lbf)	newton (N)	4.448 222 × 10 ³
kip/in ² (ksi)	pascal (Pa)	6.894 757 × 10 ⁶
ksi√/in	MPa√/m	1.097
pound-force (lbf)	newton (N)	4.448 222
pound (lb avoirdupois)	kilogram (kg)	4.535 924 × 10 ⁻¹
lbf/in ² (psi)	pascal (Pa)	6.894 757 × 10 ³
ton (short, 2000 lb)	kilogram (Kg)	9.071 847 × 10 ²
torr (mm Hg, 0 ⁰ C)	pascal (Pa)	1.333 22 × 10 ²
W h	joule (J)	3.600 000 × 10 ³
Yard	meter (M)	9.144 000 × 10 ⁻¹

II. EXAMPLES OF CASE STUDIES INVOLVING STRUCTURAL FAILURES

In order for a structure to reach the end of its design life safely, there has to be an interaction between design and testing, manufacturing, and inspection during

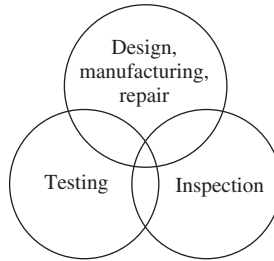


Fig. 1-3. Interaction between design and testing, manufacturing, and inspection.

its lifetime. These interactions are indicated in Fig. 1-3. If any one of the three is inadequate, failure may ensue, as discussed in the following examples.

A. Problems with Loads and Design

A.1. Problems with Wind Loadings (Design Problem) The Tay Bridge was a 3,140 m (10,300 ft) long single-track railroad bridge built in 1878 to span the Firth of Tay in Scotland (3). A portion of the bridge consisted of 13 wrought iron spans, each 73 m (240 ft) in length and 26.8 m (88 ft) above the water, which were supported by cast iron piers. On the fateful day of December 28, 1879, a gale developed with wind speeds of up to 120 km/h (75 mph). That evening a passenger train, while making a scheduled crossing, plunged into the Firth, together with the 13 center spans, and 75 passengers and crew members lost their lives.

The subsequent investigation revealed that a major cause of the disaster was that the gale-force winds produced lateral forces on the passenger cars that were transmitted to the bridge structure and led to its collapse. Such wind loading had not been properly taken into account in the design stage. In addition, the bridge was weakened by the poor quality of the construction materials and construction methods. This disaster underscored the obvious fact that all potential loading conditions must be considered in order to design safe and reliable structures.

Today we are much more aware of the importance of wind loading in structural design. Nevertheless, from time to time, problems still arise. For example, the Citicorp Tower in New York City was built in 1977 in accord with the building code, which required calculations for winds perpendicular to the building faces. However, this was a unique structure in that a church occupies one corner of the building site and the Citicorp Tower is built over and around it. In 1978 it was discovered that the building was unstable in the presence of gale-force quartering winds, that is, winds that come in at a 45° angle and hit two sides of the building simultaneously. The building was quickly reinforced to ensure its safety in the event of all types of wind loading, and a potential disaster was averted.

An instance where wind loading did result in a spectacular failure was that of the Tacoma Narrows suspension bridge, which failed in 1940 after only four months of service. The bridge, which connected the Olympic peninsula with the mainland

of Washington, had a narrow two-lane center span over a half mile in length. The design was unusual in that a stiffened girder, which caught the wind, was used, rather than a deep open truss, which would have allowed the wind to pass through. The design resulted in low torsional stiffness and so much flexibility in the wind that the bridge was known as “Galloping Gertie.” As the wind’s intensity increased to 67.2 km/h (42 mph), the bridge’s rolling, corkscrewing motion also increased until it finally tore the bridge apart. The ultimate cause of the failure was the violent oscillations, which were attributed to undamped torsional vibrations excited by the random action of turbulent winds as well as to the formation and shedding of vortices created as the wind passed by the bridge. As a result of this bridge failure, suspension bridges around the world were strengthened, and the aerodynamic characteristics of proposed bridges are checked in wind tunnels prior to construction.

A.2. Comet Aircraft Crashes (Design and Testing Problems) In the early 1950s the Comet aircraft was the first jet transport introduced into commercial passenger service. The plane was so superior to propeller-driven transports that it soon captured a large share of the market for future transport planes. However, not long after coming into service, two planes of the Comet fleet, on climbing to cruise altitude, underwent explosive decompression of the fuselage (as shown by subsequent investigation), which resulted in the loss of the planes as well as the lives of all aboard. Intensive investigation revealed that these crashes were due to fatigue cracking of the fuselage at regions of high stress adjacent to corners of more or less square (rather than round) windows, as shown in Fig. 1-4. The fatigue loading was due to the pressurization and depressurization of the cabin, which occurred in each takeoff and landing cycle. The presence of fatigue cracking was confirmed through study of the fracture surfaces of critical parts of the wreckage. These surfaces were found to contain fractographic markings, which are characteristic of fatigue crack growth (4).

In the course of the investigation, it was discovered that the same test fuselage had been used first in a static overpressurization test, to confirm that the fuselage could safely support the anticipated lower-level pressure loadings, and then in a fatigue test that, as a result of the overpressurization test, produced overly optimistic results. The results were overly optimistic because the overpressurization static test had caused the most highly stressed points to deform plastically in tension. Upon unloading, these plastically deformed regions went into a state of residual compressive stress, which significantly improved the fuselage’s resistance to fatigue crack initiation and growth in the fatigue test. A much better procedure would have been to use separate fuselages for each type of test.

The results of these crashes were significant. First of all, the Comet fleet was grounded and orders for new aircraft were canceled. Secondly, the crashes drew attention to the importance of fatigue crack growth in aircraft structures. Thirdly, it was realized that pressurized fuselages had to be designed so as to avoid catastrophic depressurization in the presence of damage such as fatigue cracking or penetration of debris should an engine explode. As a result of these crashes, significant steps to

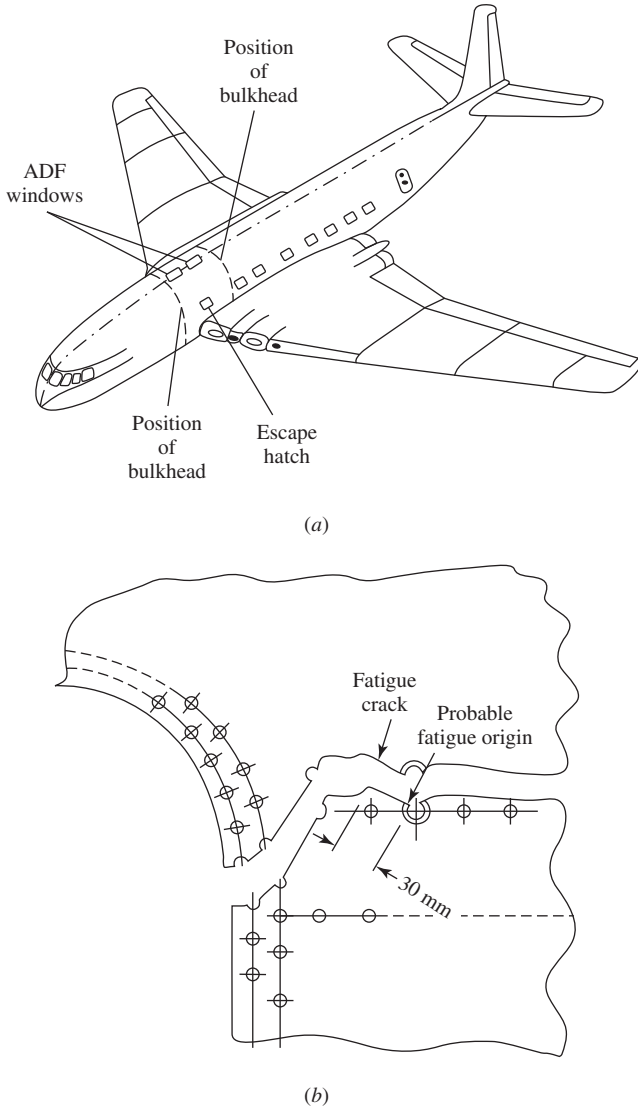


Fig. 1-4. (a) The Comet aircraft. (b) The location of fatigue cracking near an aft corner of the automatic direction finder (ADF) window. (After Jones, 3, with permission of Elsevier Science.)

improve the reliability of aircraft structures were taken in terms of design philosophy, consideration of the effects of fatigue crack growth, and inspection procedures.

As underscored by the Comet crashes, fatigue must be an important consideration in the design of aircraft. Certain components, such as turbine blades, which may experience 10^{10} stress cycles over their lifetimes, are designed such that the stresses

are well below the fatigue strengths of the materials. The design objective for such components is that fatigue cracks never develop within the design lifetime, for if a crack were to form in a turbine blade, it would rapidly grow to critical size, and hence periodic inspection would not detect it in time to avert blade failure. The situation with respect to the aircraft structure is different. Here cycles are accumulated at a slower rate than in engine components, and if a fatigue crack were to form, the critical size for fracture would be measured in terms of centimeters rather than millimeters, as in the case of a small turbine blade. This means that with proper inspection, it is possible to detect fatigue cracks in a structure before they have grown to critical size.

Aluminum alloys are widely used in the construction of aircraft structures. Their high strength-to-density ratio makes them attractive for this application. However, these alloys are characterized by relatively low fatigue strengths. If an aircraft structure were to be designed such that all repeated stresses were below the fatigue limit, the aircraft would be too heavy for economical flight. To reduce the weight of the structure, the design cyclic stresses are set at levels above the fatigue strength in what is referred to as the *finite life range*. This means that if the cyclic stresses are repeated often enough, fatigue cracks would eventually develop. Because of the statistical variation in fatigue lifetimes, as well as uncertainty with respect to the actual loading conditions, the designer must consider the possibility that fatigue cracks may appear within the lifetime of the structure. If cyclic tests are carried out on full-scale prototypes, the results will provide some knowledge of the fatigue strength of the structure as well as information about where fatigue cracks are likely to be located. However, actual structures in service may experience different cyclic loading conditions than the prototype; in addition, as in the case of aging aircraft, long-time effects associated with corrosion and fretting-corrosion may take place, effects that would not have been reflected in the prototype tests.

As mentioned earlier, two different design approaches have been developed in order to deal with the problem of fatigue cracking in aircraft structures. When the structure is designed to be statically determinant, a *safe-life* design approach is used. In this approach, the components of the structure are designed to have sufficient fatigue life to exceed the design lifetime of the aircraft, but inspections for fatigue cracks are required to ensure the safety of the aircraft structure. The other approach is known as *fail-safe*. In this approach, there is sufficient redundancy in the structure such that if a structural component failed, other structural members would have enough strength to carry the redistributed load. Further, these now more highly stressed surviving members should themselves not be in danger of failing prior to the next scheduled inspection. In principle, this approach is more reliable than safe life, but it entails a weight penalty.

A.3. Dan Air Boeing 707 Crash (5) (Design and Inspection Problems)

The following case study illustrates an instance where the fail-safe approach did not work out as planned. In 1977, a Boeing 707-300C aircraft on a scheduled cargo flight from London to Zambia was preparing to land when the right horizontal stabilizer and elevator separated in flight, causing the aircraft to pitch rapidly nose down and dive into the ground about 2 miles short of the runway. The pilot, copilot, and flight

engineer were killed. This plane was the first of the B-707-300C series convertible passenger/freighter production line, and had accumulated a total of 47,621 airframe hours and had made a total of 16,723 landings. It had made 50 landings since its last inspection. The horizontal stabilizer, as well as other components of this aircraft, had been designed using the fail-safe approach, but full-scale fatigue testing of the B-707-300C stabilizer had not been done.

However, a fail-safe design is only fail-safe if, after the failure of one component, the remaining components have sufficient residual strength to support the applied loads. A singly redundant structure (as in this case) is only fail-safe while the primary structure is intact. Once this structure has failed, the principle of safe-life obtains, and it becomes necessary to find the failure in the primary structure before the fail-safe members themselves can be weakened by fatigue, corrosion, or any other mechanism. Because the strength reserves in the fail-safe mode are usually well below those of the intact structure, this means that, in practice, the failure must be found and appropriate action taken within a short time compared with the normal life of the structure. In order to maintain the safety of a fail-safe structure, an adequate inspection program must be an integral part of the total design to ensure that a failure in any part of the primary structure is identified well before any catastrophic erosion of the strength of the fail-safe structure can occur.

Postaccident examination of the detached stabilizer revealed a failure of the top chord of the rear spar of the stabilizer due to the growth of a fatigue crack from a fastener hole. (The word *chord* has two different meanings in aircraft structural terminology. It is defined as the straight line joining the leading and trailing edges of an airfoil, and also as either of the two outside members of a truss connected and braced by web members. The latter definition is applicable here, that is, the chords of the stabilizer ran in the spanwise direction.) The rear spar consisted of a top chord, a middle chord, and a bottom chord, which were joined by an aluminum web. The purpose of the nominally unstressed middle chord was to act as a crack arrestor in the event that a fatigue crack propagated in the rear spar web from the top chord. There was evidence that the fracture of the web between the upper chord and the center chord had also failed prior to the crash. There was some fatigue cracking of the center chord, and both the center chord and lower chord had failed due to overload. This was not an isolated case, for a survey of 521 B-707 aircraft equipped with this type of horizontal stabilizer revealed that 7% had rear spar cracks of varying sizes.

The investigation was directed at the establishment of (a) the reason for and age of the fatigue failure and (b) the reason why the fail-safe structure in the rear spar had failed to carry the flight loads once the top chord had fractured as a result of fatigue.

The examination indicated that the total number of flights between the initiation of the fatigue crack and final failure of the upper chord was on the order of 7,200. The study concluded that additional fatigue crack growth had occurred after the top chord failure, and that there were probably up to 100 flights between top chord failure and stabilizer separation.

The recommended time to be spent in inspecting the horizontal stabilizer was of such duration, 24 minutes, as to suggest that a visual inspection rather than a more detailed examination was intended. The rear top and bottom spar chords had been

designed to permit them to be inspected externally, and the recommended inspection should have been adequate to detect a crack in the top chord provided that the crack was reasonably visible. It was known from those cracks detected as a result of the postaccident fleet inspection that partial cracks on the top chord, although visible to the naked eye when their precise location was known, were for all practical purposes undetectable visually. The recommended inspection could not therefore detect the crack in the spar chord unless the inspection occurred during the interval between top chord severance and total spar failure, which was not so in this case.

The investigators concluded that following the failure of the stabilizer rear spar top chord, the structure could not sustain the flight loads imposed upon it long enough to enable the failure to be detected by the then existing inspection schedule. Although the manufacturer had designed the horizontal stabilizer to be fail-safe, in practice it was not because of the inadequacy of the inspection procedure. The inspections were not adequate to detect partial cracks in the horizontal stabilizer rear spar top chord, but would have been adequate for the detection of a completely fractured top chord.

Horizontal stabilizers remain prone to fatigue. A British Concorde SST was grounded in 2000 when a growing fatigue crack in the left rear wing spar was found to have propagated a length of 76 mm (3 in.)(6).

A.4. Hartford Coliseum Roof Collapse (Design Problem) The roof of this three-year-old structure collapsed at 4:00 a.m. on January 18, 1978, during a freezing rainstorm after a period of snowfall. A triangular lattice steel space grid, 110 m (360 ft) by 91 m (300 ft), supported on four reinforced concrete pylons giving spans of 82 m (270 ft) and 64 m (210 ft), was used to support the roof. Smith and Epstein (7) concluded that the interaction of top chord compression members and their bracing played an important role in the redistribution of load and the eventual collapse. They noted that certain compression members were braced against buckling only in one plane. As loads increased, these members buckled out of plane and redistributed load to other members. Over a period of time, more chords buckled and fewer and fewer members carried the load. This situation worsened until the remaining members were unable to withstand the added stress due to the loads present that night, and the final sudden collapse took place.

This is an instance primarily of inadequate structural design.

A.5. Kansas City Hyatt Regency Walkways Collapse (8) (Construction Problem) On July 20, 1981, two suspended walkways within the atrium area of the Hyatt Regency Hotel in Kansas City, Missouri, collapsed, leaving 113 people dead and 186 people injured. In terms of loss of life and injuries, this was the most devastating structural collapse ever to take place in the United States. The second-floor walkway was suspended from the fourth-floor walkway, which was directly above it. In turn, the fourth-floor walkway was suspended from the atrium roof framing by three pairs of hanger rods. In the collapse, the second- and fourth-floor walkways fell to the atrium floor, with the fourth-floor walkway coming to rest on top of the lower walkway. Most of those killed or injured were either on the first-floor level of the atrium or on the second-floor walkway.

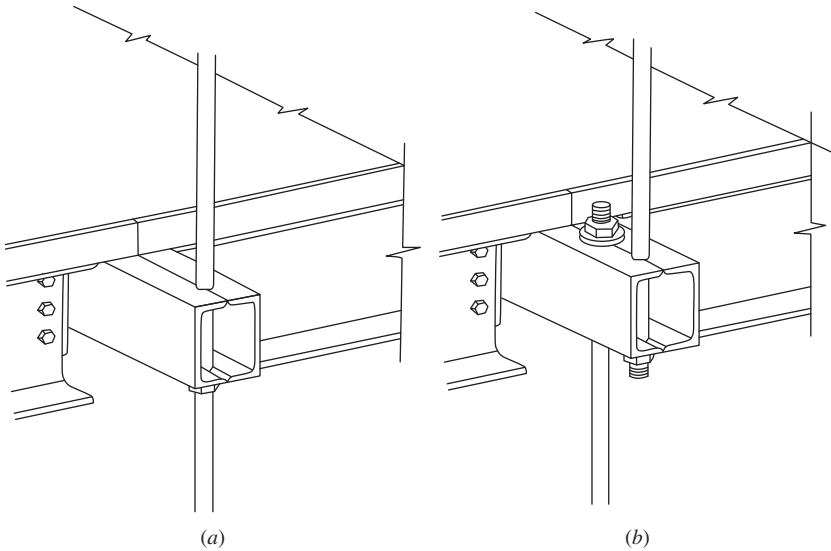


Fig. 1-5. A comparison of the Kansas City Hyatt walkway connectors. (a) As originally designed. (b) As built. (From National Bureau of Standards, 8.)

As they were originally approved for construction, the plans for the walkways called for the hanger rods to pass through the fourth-floor box beams and on through the second-floor box beams. The box beams were made up of a pair of 203 mm (8 in.) steel channels with the flanges welded toe-to-toe. The beams were to rest on hanger-rod washers and nuts below each set of beams, Fig. 1-5a. Under this arrangement, each box beam would separately transfer its load directly into the hanger rods.

However, during construction, drawings were prepared by the steel fabricator that called for discontinuous rather than continuous hanger rods, Fig. 1-5b. In this modified design, three pairs of hanger rods extended from the fourth-floor box beams to the roof framing, and three pairs of hanger rods extended from the second-floor box beams to the fourth-floor box beams. Under this arrangement, all of the second-floor walkway load was first transferred to the fourth-floor box beams, where both that load and the fourth-floor walkway load were transmitted through the box beam hanger rod connections to the ceiling hanger rods. This change essentially doubled the load to be transferred by the fourth-floor box beam–hanger rod assembly connections.

Postcollapse failure analysis indicated that the failure of the walkway system was initiated in one of the box beam–hanger rod connections. In this instance, the fabricator, the structural engineer, and the architect, each of whom had approved the design change, had not appreciated the consequences of that change.

B. Problems with Design, Inspection, Maintenance, and Repair

B.1. Collapse of the Mianus River Bridge in Connecticut (Inspection Problem) Demers and Fisher (9) provide a description of the collapse of a portion

of this bridge. A six-lane interstate highway supported by six sets of piers, which are skewed to run parallel to the river, spans the Mianus River in Greenwich, Connecticut. The bridge is composed of a number of individual spans, each supported on the outer edges by longitudinal girders. The bridge had been in service for 24 years when, on June 28, 1983, in the early hours of the morning—fortunately at a time when traffic was light—one of the eastbound spans completely separated from the bridge and fell to the river below, causing several fatalities. The span that failed had been suspended, as indicated in Fig. 1-6a, between adjacent spans that were cantilevered out from supporting piers. The failed span was a statically determinant structure, which meant that the failure of one main structural member of a span would lead to collapse of that span. Recall that a redundant structure is one in which failure of a structural component leads to a redistribution of loads to other members but not complete collapse. The span that failed employed pin-and-hanger assemblies at its eastern corners to connect the girders of adjacent components of the bridge. Collapse started at the southeast corner, as deduced from the position of the span after the failure. After the collapse, the southeast corner inside hanger was found to be straight and attached to the upper pin, whereas other connectors had been severely deformed. It was concluded that since the inside hanger was straight, the lower pin had separated from it prior to the collapse and had moved in the direction of the outer hanger. This unloading of the inner hanger doubled the load on the outer hanger. The resulting high bearing pressure at the upper surface of the upper pin led to the formation of a fatigue crack in the pin, which caused a portion of the upper pin to separate from the pin, thereby allowing the hanger to slip off the upper pin to bring about the final collapse of the span.

Postaccident inspection revealed that the bearing surface of the southeast corner inside hanger at the lower hole was severely corroded. The inside end of the lower pin was severely corroded and tapered, and the bottom edge had broken off. Movement of the lower pin required the failure of the restraining bolt through the pin. Extensive corrosion packout (compare Figs. 1-6b and 1-6c) between the outer washers was found on the outer side of both upper and lower assemblies, which resulted in plastic deformation of the retainer plate and high tensile stresses in the bolt, which led to its fracture. It was concluded that failure was the result of a progressive process that occurred over a period of time, and that corrosion packout was primarily responsible for the hanger displacement on the pin, which led to the collapse.

This failure underscored the importance of maintaining effective corrosion prevention and inspection programs to maintain the integrity of such structures.

B.2. The Mississippi River Bridge at Minneapolis (Design Problem) The I-35W Mississippi River bridge was an eight-lane, steel truss arch bridge across the Mississippi River in Minneapolis, Minnesota, built in 1964–1967. Forty years later, on August 1, 2007, it suddenly collapsed, killing 13 people and injuring 145. The bridge was Minnesota’s fifth busiest, carrying 140,000 vehicles daily. The NTSB found that the primary cause of failure was undersized gusset plates, which were 13 mm (0.5 in.) thick. Contributing to that design error was the fact that 51 mm (2 in.) of concrete had been added to the road surface over the years, increasing the

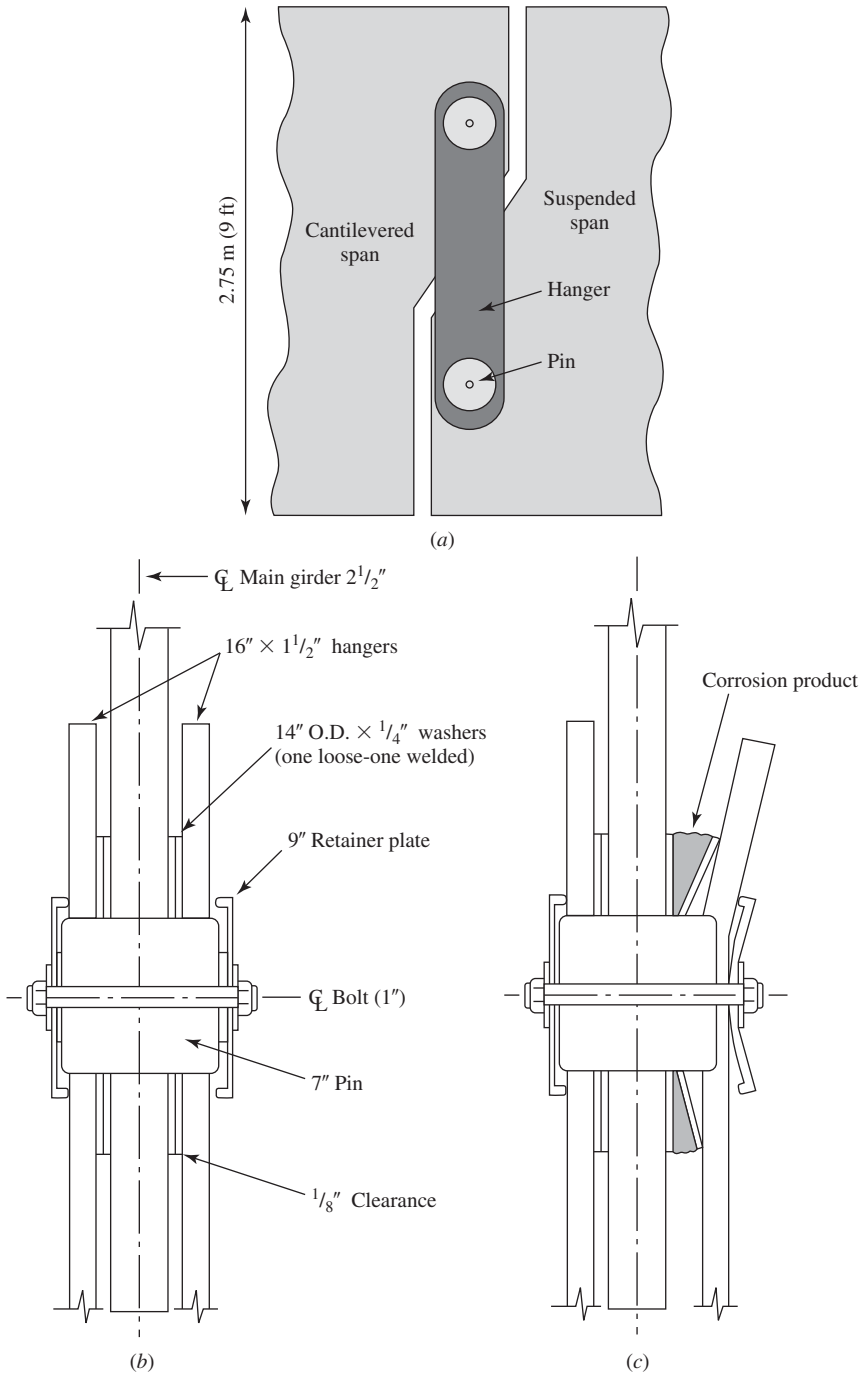


Fig. 1-6. The Mianus River bridge hangers. (a) Method of supporting the failed suspended span. (b) Pin-hanger assembly as built. (c) Pin-hanger assembly after 24 years of service. (Figs. 1.7b and 1.7c after Demers and Fisher, 9.)

dead load by 20%. Also contributing to the error was the extraordinary weight of construction equipment and material resting on the bridge just above its weakest point at the time of the collapse. That load was estimated at 262,000 kg (578,000 lb), consisting of sand, water, and vehicles. The NTSB determined that in contrast to the Mianus River Bridge collapse, corrosion was not a significant factor.

B.3. Aloha Airlines Boeing 737-200 (10) (Inspection Problem) In 1988, a Boeing 737-200 operated by Aloha Airlines, while en route from Hilo to Honolulu, Hawaii, experienced an explosive decompression and structural failure as the plane leveled off at 7,315 m (24,000 ft). Approximately 8.2 m (18 ft) of the cabin skin and structure aft of the cabin entrance door and above the passenger floor had separated from the airplane, Fig. 1-7. There were 89 passengers and 6 crew members on board. One flight attendant was swept overboard, and seven passengers and one flight attendant received serious injuries. An emergency landing was made on the island of Maui. As a result of the accident, the airplane was damaged beyond repair and was dismantled and sold for scrap.

The Boeing 737-200 involved had been manufactured in 1969. At the time of the accident it had acquired 35,496 flight hours and 89,680 flight cycles (landings), the second highest number of cycles in the worldwide 737 fleet. Due to the short distance between destinations on some Aloha Airline routes, the full pressurization of 52 kPa (7.5 psi) was not reached on every flight. Therefore, the number of full pressure cycles was significantly less than 89,680. The plane had also been exposed to warm, humid maritime air, which promoted corrosion.

Failure was found to have initiated along a fuselage skin longitudinal lap joint that had been “cold bonded.” The cold bonding process utilized an epoxy-impregnated woven “scrim” cloth to join the longitudinal edges of the single-thickness 0.91 mm (0.036 in.) skin panels together. In addition, the joint contained three rows of



Fig. 1-7. General view showing the damage sustained by the Aloha Airlines Flight 737. (From NTSB, 10.)

countersunk rivets. Fuselage hoop loads were intended to be transferred through the bonded joint rather than through the rivets, allowing for thinner skin with no degradation in fatigue life. However, early service history with production B-737 airplanes revealed that difficulties were encountered with the bonding process, and it was discontinued after 1972. In order to safeguard those B-737 planes that had been cold bonded, Boeing issued a number of service bulletins over a period of time directing the attention of operators to the problem of disbonding and provided information on how to check for disbonding using the eddy current nondestructive examination (NDE) method. In 1987 the FAA issued an airworthiness directive (AD) requiring that eddy current inspections of the bonds and repairs, if needed, be carried out in compliance with the Boeing service bulletins. Some of the bonds had low environmental durability, with susceptibility to corrosion. Some areas of the lap joints did not bond at all, and moisture and corrosion could contribute to further disbonding. When disbonding did occur, the hoop load transfer through the joint was borne by the three rows of countersunk rivets. However, the countersinking extended through the entire thickness of the 0.91 mm (0.036 in.) sheet, resulting in the creation of a knife edge at the bottom of the hole, which concentrated stress and promoted fatigue crack nucleation, Fig. 1-8. For this reason, fatigue cracking would be expected to begin in the outer layer of the skin along the lap joint along the upper, more highly stressed row of rivet holes.

The NTSB believed that the top rivet row was cracked at the critical lap joint before the accident flight takeoff, and determined that the probable cause of the accident was the failure of the Aloha Airlines maintenance program to detect the presence of the significant disbonding and fatigue damage that ultimately led to the failure of the lap joint and the separation of the fuselage upper lobe. This accident was significant in that it brought attention to some of the corrosion and fatigue problems that could develop in aging aircraft. It also focused attention on the problem of multiple-site damage (MSD), that is, the formation and possible linking up of fatigue cracks formed at adjacent rivet holes.

B.4. Chicago DC-10-10 Crash (11) (Maintenance Problem) On May 25, 1979, as American Airlines Flight 191, a McDonnell-Douglas DC 10-10 aircraft,

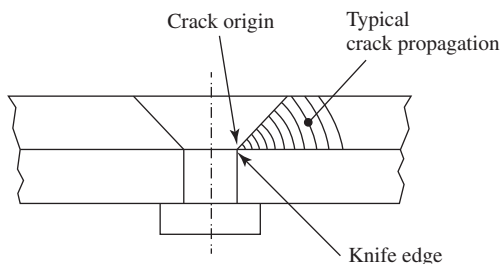


Fig. 1-8. A sketch of a countersunk rivet and an associated fatigue crack observed in Aloha Airlines 737.

was taking off from the Chicago-O'Hare International Airport, the left engine and pylon assembly separated from the aircraft, went over the top of the wing, and fell to the runway. The plane continued to climb to an altitude of 99 m (325 ft) and then rolled to the left and crashed. The aircraft was destroyed in the crash and subsequent fire, and the 271 persons on board were killed, as were 2 others on the ground, the worst loss of life in U.S. aviation history. The accident aircraft had entered service in 1972. It had accumulated a total of 19,871 flight hours, 341 of which had come since a maintenance procedure in Tulsa, Oklahoma.

The separation of the engine from the wing was found to be due to cracking of the aft bulkhead of the pylon, a problem created during the maintenance procedure in Tulsa. Figure 1-9a shows the pylon assembly. Note that the upper spar is attached to a flange on the forward side of the aft bulkhead, Fig. 1-9b. This flange turned out to be a critical element in the accident sequence. McDonnell-Douglas had issued a service bulletin calling for the replacement of the upper and lower spherical bearings that attached the pylon to the wing. In this procedure, McDonnell-Douglas indicated that the 6,126 kg (13,477 lb) engine was to be removed from the 847 kg (1,865 lb) pylon before the pylon was removed from the wing. Procedures for accomplishing this maintenance were also described. However, in contrast to the maintenance procedure advocated by McDonnell-Douglas, American Airlines decided to lower and raise the engine and pylon assembly using a forklift-type supporting device, since this procedure would save about 200 man-hours per aircraft and would reduce the number of disconnects from 79 to 27. An engineering change order (ECO) was issued by American Airlines in 1978 prescribing this maintenance procedure, and from March 29 to March 31, 1979, the accident aircraft underwent the spherical bearing modification using this procedure. It is noted that McDonnell-Douglas had discouraged the use of this procedure because of the risk involved in remating the engine-pylon assembly to the wing attach points, but it lacked the authority to either approve or disapprove the maintenance procedures of its customers. Also, members of the American Airlines engineering department did not witness the removal of the wing to pylon attachment assemblies, and consequently, they were not aware of difficulties such as controlling the forklift accurately.

Postaccident investigation revealed that a portion of the upper forward flange of the aft bulkhead had been fractured by overload in the inboard-outboard direction just forward of the radius between the flange and the bulkhead plane. The fracture had been initiated by a downward bending moment at the center section of the flange just forward of the fracture plane due to contact between the clevis and the flange. As a result of this contact, the aft fracture surface of the upper flange was deformed into a crescent shape that matched the shape of the lower end of the wing clevis. The length of this overload fracture was 254 mm (10 in.). Fatigue cracking was present at both ends of the overload fracture, and the total length of the crack due to both overload and fatigue was 330 mm (13 in.).

In postaccident inspections of the DC-10 fleet, four American Airlines planes and two Continental Airlines planes were found to have cracked upper flanges on the pylon aft bulkheads, with the longest of these cracks being 152 mm (6 in.). In addition, it was discovered that two Continental Airlines DC-10s, one in December

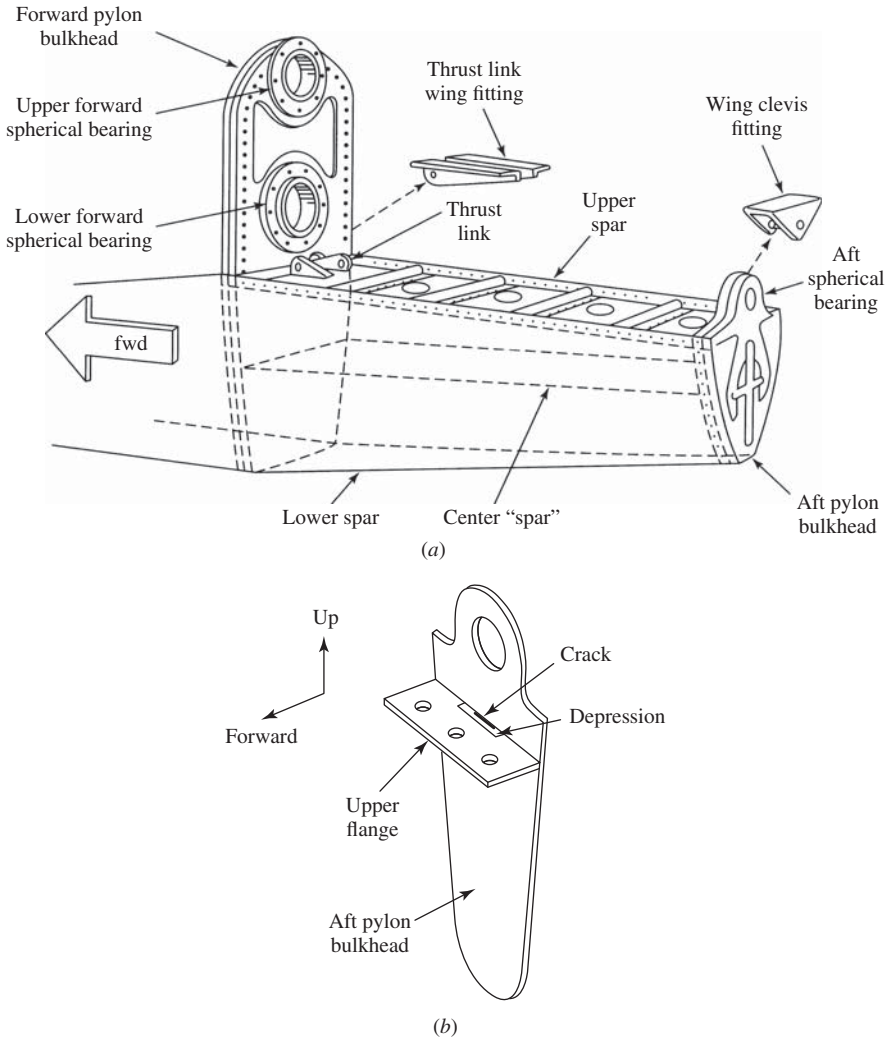


Fig. 1-9. (a) The pylon assembly of a DC-10. (b) Attachment of an upper spar to a flange on the forward side of the aft bulkhead. (Fig. 1-10a from NTSB, 11.)

1978 and the other in February 1979, had had fractures on their upper flanges. These two flanges had been damaged during this same maintenance operation, but they had been repaired and returned to service. McDonnell-Douglas had been informed of these problems, but neither the FAA nor other airlines had been informed because the events were considered to have been maintenance errors.

An examination of the maintenance procedure disclosed numerous possibilities for the upper flange of the aft bulkhead to be brought into contact with the wing-mounted clevis. A fracture-producing load could be applied during or after removal

of the attaching hardware in the aft bulkhead fitting. Because of the close fit between the pylon to wing attachments and the minimal clearance between the structural elements, maintenance personnel had to be extremely cautious when they detached or attached the pylon. A minor mistake by the forklift operator could easily damage the aft bulkhead and its upper flange.

The structural separation of the pylon was caused by a complete failure of the forward flange of the aft bulkhead after its residual strength had been reduced by the fracture induced during the maintenance operation as well as by additional fatigue crack growth in service. It is also clear that the poor communications between engineering and maintenance personnel and between the FAA, the manufacturer, and the airlines contributed to this accident.

B.5. JAL B-747SR, 1985 (12) (Repair Problem) In August 1985 a Japan Airlines Boeing 747SR (short-range) jet aircraft was on a flight from Tokyo to Osaka. On climbing through 7,315 m (24,000 ft) the rear pressure bulkhead failed, and as a result there was an explosive decompression, which led to loss of hydraulic power and of the pilot's ability to control the aircraft. Thirty minutes later the aircraft crashed into a mountain. This was the worst single-plane accident in aviation history, for of the 524 people on board, only 4 survived.

This aircraft had been in a takeoff mishap in June 1978, in which the tail section struck the runway, causing damage to the lower half of the rear pressure bulkhead. This bulkhead is in the shape of a hemisphere and is made of thin-gauge aluminum alloy sheets. At a joint between sheets the sheets overlap, and an additional piece of sheet material, known as a *doubler*, spans the riveted joint to provide extra strength. To repair the damage after the 1978 accident, a new lower-half bulkhead was riveted to the upper half. However, the two halves were not properly spliced together. On the upper side of the joint, there was a doubler and a stiffener on the inner side of the bulkhead, Fig.1-10. On the lower side of the joint, there was a doubler, but the doubler was not continuous with the upper doubler, so that a gap existed between the doublers, with only the sheet material carrying the load. In addition, the centroid of the load-bearing material was now on the inner side of the bulkhead. Therefore, the load on the sheet spanning the gap consisted not only of that due to the hoop tension, but also that due to bending because of the eccentric loading condition created by the doublers and the stiffener. Each time the cabin was pressurized, there was an increase in stress in the aluminum sheet spanning the gap over that expected. As a result of this stress increase, fatigue cracks were formed at each of the rivet holes on the lower half of the bulkhead just below the gap, another example of MSD. These fatigue cracks eventually linked up, and the resultant long crack led to the explosive decompression.

B.6. China Airlines B-747 (13) (Repair Problem) On May 25, 2002, China Airlines Flight 611, a B-747, on its last day of service with China Airlines was on a regularly scheduled flight from Taiwan to Hong Kong when it broke into pieces in midair and crashed, killing all 225 persons aboard.

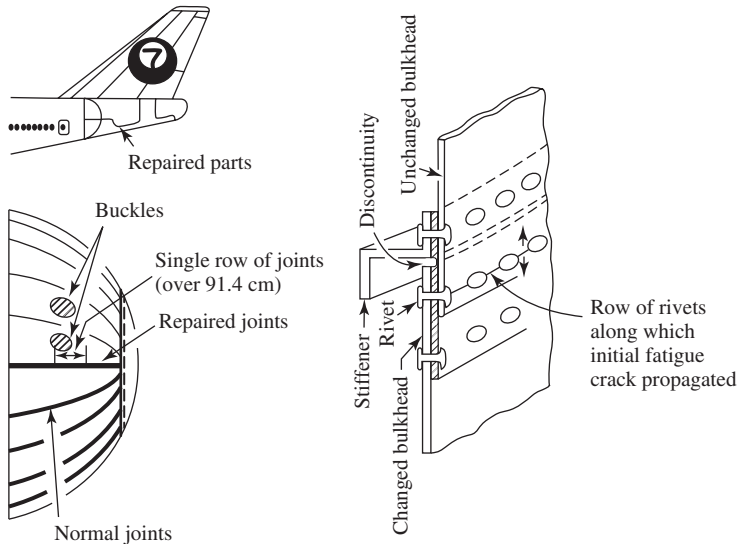


Fig. 1-10. The rear bulkhead of the JAL 747SR. (After Kobayashi, 12. *J. Japan Soc. Safety Eng.*)

It was found that the accident was the result of metal fatigue caused by inadequate maintenance after a previous incident that occurred on February 7, 1980, 22 years earlier, when, as in the case of the JAL 747SR, the accident aircraft suffered damage from a tail strike accident while landing in Hong Kong. A repair was conducted by a team from China Airlines in May 1980. However, the repair of the tail strike was not carried out in accordance with the Boeing *Structural Repair Manual*. The area of damaged skin was not removed (trimmed) and the repair doubler plate that was supposed to cover in excess of 30% of the damaged area did not extend enough beyond the entire damaged area to restore the overall structural strength. An explosive decompression of the aircraft occurred once the fatigue crack opened up, causing the complete disintegration of the aircraft in midair.

One piece of evidence of the metal fatigue is contained in pictures that were taken during an inspection of the plane years before the disaster. In the pictures, there are visible brown stains of nicotine around the doubler plate. This nicotine was deposited by smoke from the cigarettes of people who were smoking about seven years before the disaster (smoking was allowed in a pressurized plane at that time). The doubler plate had a brown nicotine stain all the way around it that could have been detected visually by any of the engineers when they inspected the plane. The stain suggested that there was a crack caused by metal fatigue behind the doubler plate, as the nicotine slowly seeped out due to pressure that built up when the plane reached its cruising altitude. The stains were apparently not noticed and no correction was made to the doubler plate, which eventually caused the plane to disintegrate in midair.

B.7. Air France Concorde Crash, July 25, 2000 (Design Problem) The crash of an Air France Flight 4590, a supersonic transport Concorde (SST), moments after takeoff from the Charles de Gaulle Airport near Paris, resulted in the deaths of 109 people aboard the jet and 5 people on the ground. The evidence gathered in this case, together with a past history of similar events that fortunately had not been catastrophic, indicated that the bursting of a tire on the left side of the plane while the plane was accelerating during its takeoff run was critical. A 406 mm (16 in.) piece of metal that fell to the runway from the engine of a plane that had taken off shortly before the Concorde may have caused the tire to burst. The metal strip matched a gash found in one of the Concorde's left tires, and it is probable that this piece caused the cut. There have been 57 cases of burst tires on Concorde, and in 7 instances these bursts have led to the rupture of fuel tanks, the severing of hydraulic lines, and the damaging of engines. French investigators believe that in the Paris crash, after the tire burst, a 3.6 kg (8 lb) piece of rubber penetrated the fuel tank, thereby releasing a plume of fuel that ignited (Fig. 1-11), since the plume was in close proximity to the two left side engines. Both British and French aviation authorities grounded the Concorde, and before they returned to service, fuel-tank liners were added to minimize potential damage related to tire bursts. However, in 2003 the Concorde was permanently grounded because of the Paris crash as well as other economic considerations.

B.8. Qantas Flight 32, A 380 Number 2 Engine Failure, November 4, 2010 (14) (Manufacturing Problem) This engine failure provides an example of the consequences of a manufacturing defect. A Qantas 380 four-engine jet with 469 passengers and crew aboard experienced a midair engine explosion minutes after takeoff from Singapore en route to Australia. The pilot shut down the damaged engine, and an hour and a half after the explosion, the plane landed back in Singapore. After the event, it was discovered that uneven boring inside an oil tube within a combustion chamber had caused thinning of the metal on one side of the tube, Fig. 1-12. It is believed that the fault led to a fatigue crack from which oil leaked



Fig. 1-11. Concorde on takeoff just prior to crash.

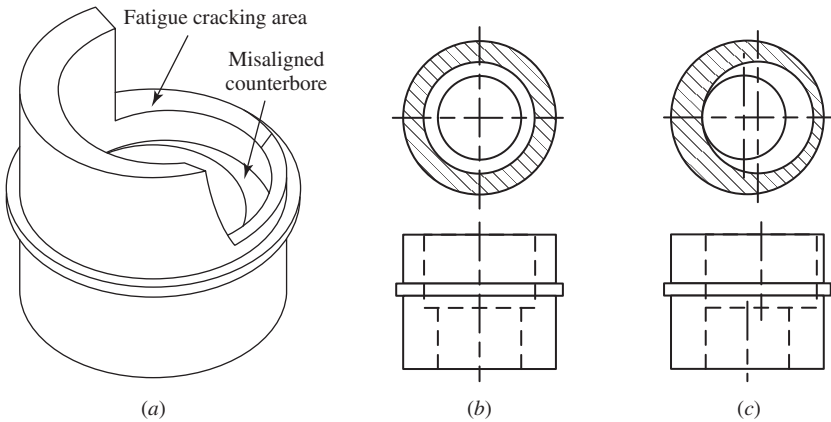


Fig. 1-12. Failure of an oil tube. (a) Failed part. (b) Concentric counterbore. (c) Misaligned counterbore.

into the superhot engine, creating an explosion that caused one of the turbine discs to shatter, thereby damaging the plane's left wing and fuselage. Similar tubes in other 380 aircraft were then checked by means of a highly specialized inspection procedure to be sure that a similar effect was not present in other 380 engines.

B.9. Southwest Airlines Boeing 737-300 Fuselage Failure, April 1, 2011 (15) (Manufacturing Problem)

The 737 was cruising at 10,360 m (34,000 ft) when a 1.5 m by 0.3 m (5 ft by 1 ft) crack suddenly opened in the roof of the fuselage, resulting in cabin decompression. The pilots landed the plane safely. It was subsequently found that the rivet holes at a seam between the upper and lower layers of the aluminum skin were not properly aligned due to a machining error, Fig. 1-13. This misalignment subsequently led to additional stress on the rivets and a reduction in fatigue life. The decompression resulted in a loss of cabin pressure, the driving force for crack propagation, and the crack was arrested before major damage could occur.

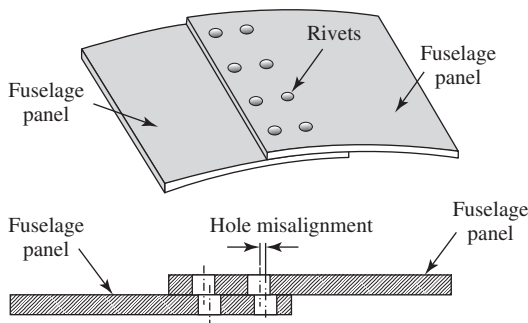


Fig. 1-13. Misaligned rivet holes.

B.10. Grumman Turbo Mallard G-73T (16) (Maintenance and Repair Problem) An in-flight breakup of a Grumman Turbo Mallard, a 47-year-old amphibious plane operated by Ocean Airways, occurred on December 19, 2005, as the plane took off from Miami bound for the Bahamas. Two crew members and 18 passengers were killed.

The NTSB investigation found that fatigue cracks in the rear stringer, lower skin, and rear spar cap (Fig. 1-14a) led to wing separation and the crash. An example of fatigue cracking emanating from holes drilled through the rear lower spar cap is given in Fig. 1-14b. In August 2005, the lower right wing skin and stringers had been replaced. At that time, a second hole may have been drilled. The combination of the two holes would have led to an increase in the local stress concentration factor and the promotion of fatigue cracking.

B.11. USS Thresher Submarine (16) (Maintenance and Repair Problem)

U.S. submarines have had a remarkably good safety record since the loss in 1963 of the nuclear-powered USS *Thresher*, which was operating at test depth when it sank with the loss of 129 lives. The test depth is the maximum depth at which a submarine is permitted to operate during sea trials. The test depth is set at two-thirds of the design depth for U.S. Navy submarines, while the British Royal Navy sets the test depth slightly deeper than half (4/7ths) of the design depth, and the German Navy sets it at exactly one-half of the design depth.

It is thought that the sinking of the *Thresher* was triggered by the failure of a brazed joint in a saltwater piping system in the engine room. Earlier tests using ultrasound equipment found potential problems with about 14% of the tested brazed joints, most of which were determined not to pose a risk significant enough to require a repair. The *Thresher* probably imploded at a depth of 400–610 m (1,300–2,000 ft). (The term *brazing* is used when the temperature in the brazing process exceeds some

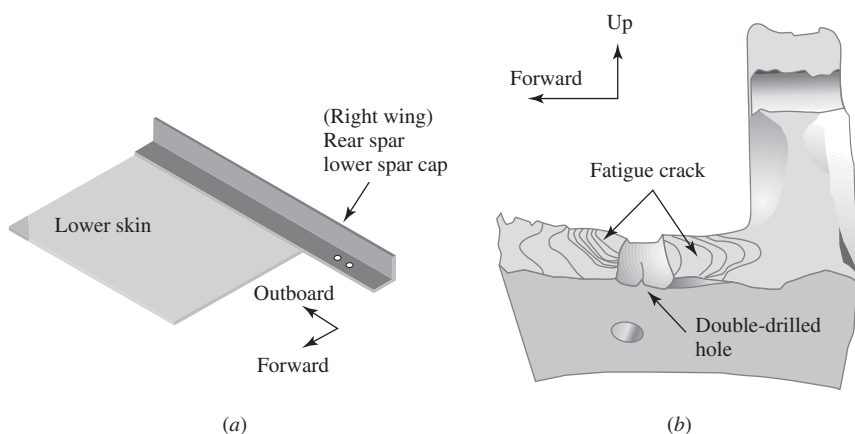


Fig. 1-14. (a) Rear spar cap and lower skin assembly. (b) Right wing rear spar lower spar cap fracture. Fatigue crack initiated from a double-drilled hole created during maintenance.

arbitrary value such as 425°C (800 F). Bonding results from the interdiffusion of base metal and filler metal without fusion of the base metal. The term *soldering* is used for temperatures below the arbitrary value.)

Since, in the case of a submerged submarine, the outside pressure is greater than the inside pressure, the situation with submarines is the reverse of that with jet aircraft. As a first order approximation, each 10 m (33 ft) of depth puts another atmosphere (1 bar, 14.7 psi, 100 kPa) of pressure on the hull, so that at 300 m (1,000 ft), the hull is supporting 30 atms. (30 bar, 441 psi, 3 MPa) of water pressure. If the hull consists of a high-strength steel, the operating depths are in the range of 250–400 m (80–1,300 ft). The corresponding pressures are 3.3–4.0 MPa (0.5–0.6 ksi) (if the hull were to be constructed of a high-strength titanium alloy, the operating depth increases to about 1,000 m and the pressure increases to 10 MPa [1.5 ksi]).

The crush depth is the submerged depth at which a submarine's hull will collapse due to pressure. The crush depth of an actual vessel should be slightly deeper than its design depth.

The maximum operating depth is the maximum depth at which a submarine is allowed to operate under any (e.g., battle) conditions.

In aircraft the skin is thin and the circumferential stress is given by $\sigma_h = pr_i/t$. In submarines the pressure hull thickness is much greater, and the circumferential stress on the inside surface of the hull is given by $\sigma_h = 2pr_o^2/(r_o^2 - r_i^2)$, where r_o is the outer radius of the hull and r_i is the inner radius.

III. SUMMARY

These examples indicate the range of design, maintenance, environmental, and inspection problems that can arise and endanger the integrity of structures. In many cases, structural failures occur because of design errors or because of unanticipated events not envisioned by the designer, such as in-field changes, poor inspection and maintenance procedures, and poor repair work. In the following chapters, failure mechanisms and investigative procedures will be discussed in greater detail, and additional case studies will be presented.

REFERENCES

- (1) R. F. Harper, *The Code of Hammurabi*, University of Chicago Press, 1904.
- (2) D. A. Canonico, Adjusting the Boiler Code, *Mech. Eng.*, vol. 122, no. 2, Feb. 2000, pp. 54–57.
- (3) D. R. H. Jones, *Engineering Material 3: Material Failure Analysis*, Pergamon Press, Oxford, 1993, pp. 291–314.
- (4) British Ministry of Transport and Civil Aviation, *Civil Aircraft Accident: Report of the Court of Inquiry into the Accidents to Comet G-ALYP on 10th January 1954 and Comet G-ALYY on 8th April 1954*, HMSO, London, 1955.
- (5) British cite causes of 707 Accident, *Aviation Week and Space Technology*, Sept. 24, 1979, vol. 111, p.189.

- (6) J. D. Morrocco, BA Keeps Its Fleet of Concorde Flying, *Aviation Week and Space Technology*, Aug. 7, 2000, p. 31.
- (7) E. A. Smith and H. I. Epstein, Hartford Coliseum Roof Collapse, *Civil Eng.-ASCE*, Apr. 1980, vol. 52, pp. 59–62.
- (8) *Investigation of the Kansas City Hyatt Regency Walkways Collapse*, National Bureau of Standards Building Science Series 143, NTSB, Washington, D.C., 1982.
- (9) C. E. Demers and J. W. Fisher, *A Survey of Localized Cracking in Steel Bridges, 1981 to 1988*, ATLSS Report No. 89-01, Lehigh University, Bethlehem, PA, 1989.
- (10) *Aloha Airlines, Flight 243, National Transportation Safety Board Aircraft Accident Report*, NTSB AAR-89/03, NTSB, Washington, D.C., 1989.
- (11) *American Airlines Flight 191, National Transportation Safety Board Aircraft Accident Report*, NTSB-AAR-79-17, 1979.
- (12) H. Kobayashi, On the Examination Report of the Crashed Japan Airlines Boeing 747 Plane; Failure Analysis of the Rear Pressure Bulkhead (in Japanese), *J. Japan Soc. Safety Eng.*, vol. 26, 1987, pp. 363–372.
- (13) http://en.wikipedia.org/wiki/China_Airlines_Flight_611. Anon., China Airlines Flight 611.
- (14) K. Drew and N. Clark, 3 Airlines Halt A380 Flights over Engine Explosion, *New York Times*, Nov. 4, 2010.
- (15) M. Wald, Board Blames F.A.A. and Airline for Crash, *New York Times*, May 31, 2007.
- (16) F. Fiorino, Aircraft Accidents, *Aviation Week and Space Technology*, June 4, 2007.

PROBLEMS

- 1-1.** This problem is related to the Comet (jet plane) disasters. The atmospheric air pressure in cm of Hg as a function of altitude in kilometers, h , can be expressed as:

$$p = 76 - 8.45h + 0.285h^2$$

The Comet's cruising altitude was 10 km, about twice the cruising altitude of commercial propeller-driven transport planes. Assume that the cabin in the Comet was maintained at a pressure equivalent to that at an altitude of 2.37 km. Determine the differential between the external pressure and the cabin pressure in MPa units. This differential is the pressure the fuselage must support.

- 1-2.** This problem is related to the Kansas City Hyatt Regency walkway collapse. If the vertical rod in Fig. 1-6 carried 10^5 Newtons, N , between the lower and upper balconies, and if an additional load of 5×10^4 N were to be carried by the rod between the upper balcony and the overhead support, determine the maximum bearing load at the upper balcony for each of the cases shown in Fig. 1-6.

2

Elements of Elastic Deformation

I. INTRODUCTION

In a failure analysis, the determination of the nature and magnitude of the stresses that had been developed in a failed component is often a significant aspect of the investigation. This chapter briefly reviews some basic definitions, constitutive relations, principal stresses, plane stress and plane strain Mohr circles, and the state of elastic stress ahead of a notch.

II. STRESS

A. Definitions

When a body is subjected to an external load, an internal load is built up throughout the body to maintain itself in equilibrium condition. On an arbitrarily oriented plane, as in Fig. 2-1a, there is a resultant internal force P acting on this plane. Stress is defined as the force per unit area. When the original area (or the area before deformation) A_0 is used, the stress is called the *engineering stress*. But if the current area A is used, the stress is called the *true stress*.

The internal force P makes an angle with a surface normal \bar{N} , as shown in Fig. 2-1a and can be decomposed into two components, one normal to the surface, P_n , and another one tangential to the surface, P_t (Fig. 2-1b). Therefore, there are two stress components: a normal stress and a shear stress, corresponding to a normal force P_n/A_0 and a tangential force P_t/A_0 , respectively.

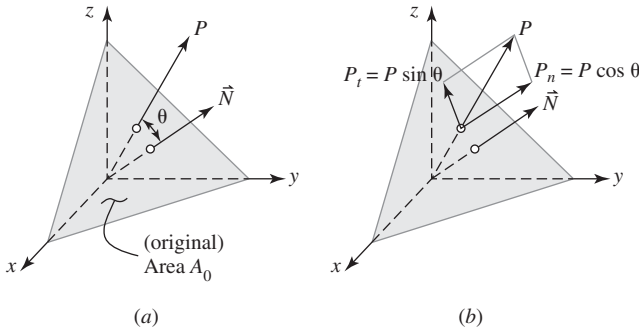


Fig. 2-1. Force P acting on a plane of area A_0 whose normal is in the direction N .

The engineering normal stress σ and the engineering shear stress τ are defined as

$$\sigma = \frac{P_n}{A_0} \quad (2-1)$$

and

$$\tau = \frac{P_t}{A_0} \quad (2-2)$$

respectively.

The true normal stress $\tilde{\sigma}$ and the true shear stress $\tilde{\tau}$ are defined as

$$\tilde{\sigma} = \frac{P_n}{A} \quad (2-3)$$

and

$$\tilde{\tau} = \frac{P_t}{A} \quad (2-4)$$

respectively.

For a strain of 10%, the true stress exceeds the engineering stress by about 5%; therefore, the difference between the two for strains less than 10% is not significant.

In a three-dimensional Cartesian coordinate system, there are three mutually perpendicular planes that pass through the same point of a body. Each plane has a positive and a negative face. The positive face is the one of a pair of parallel faces that intersects the axis at the more positive value. These six planes form a cube having an infinitesimal size, as shown in Fig. 2-2. Each face of a cube is subjected to an internal force that can be decomposed into three components along the coordinate axes. These force components produce one normal stress component and two shear stress components, as shown in Fig. 2-2. The stress components shown are all positive in the sense that they act parallel to the positive direction of an axis on a positive face of the cube and in the reverse direction on a negative face. The first subscript denotes the axis intersected by the face on which a stress acts, and the

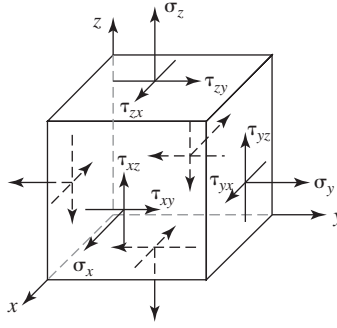


Fig. 2-2. Stress components acting on a cubic element.

second subscript denotes the direction in which the stress acts. The nine components of stress constitute a stress tensor, an example of which is shown in Eq. 2-5.

$$\sigma_{ij} = \begin{pmatrix} \sigma_x & \tau_{xy} & \tau_{xz} \\ \tau_{yx} & \sigma_y & \tau_{yz} \\ \tau_{zx} & \tau_{zy} & \sigma_z \end{pmatrix} \quad (2-5)$$

It is noted that stress is a second order tensor, involving a load and the area over which it acts.

In Fig. 2-2, there appear to be a total of nine different stresses. However, if the moment of forces is taken about the x -axis, for example, and the result is set equal to zero for equilibrium, it can be shown that $\tau_{yz} = \tau_{zy}$. Therefore, the order of the subscripts can be interchanged, the number of independent stress components is reduced to six, and the stress tensor becomes symmetric.

B. Decomposition of a Stress Tensor

The total stress tensor σ_{ij} can be separated into two component tensors; one is the *hydrostatic component* σ_{hyd} , which is related to the change in volume, and the other is the *distortional component*, also known as the *stress deviator tensor* σ_{dev} , which is related to the change in shape. The hydrostatic component of stress σ_{hyd} is given by

$$\sigma_{hyd} = \frac{\sigma_x + \sigma_y + \sigma_z}{3} \quad (2-6)$$

The hydrostatic stress σ_{hyd} is a scalar quantity whose numerical value is independent of the orientation of the x -, y -, and z -axes. As such, σ_{hyd} is an invariant quantity. The hydrostatic stress tensor is defined as

$$\sigma_{hyd} = \begin{pmatrix} \sigma_{hyd} & 0 & 0 \\ 0 & \sigma_{hyd} & 0 \\ 0 & 0 & \sigma_{hyd} \end{pmatrix} \quad (2-7)$$

The deviatoric stress tensor is defined as

$$\sigma_{dev} = \sigma_{ij} - \sigma_{hyd}$$

Thus,

$$\sigma_{dev} = \begin{pmatrix} \sigma_x - \sigma_{hyd} & \tau_{xy} & \tau_{xz} \\ \tau_{xy} & \sigma_y - \sigma_{hyd} & \tau_{yz} \\ \tau_{xz} & \tau_{yz} & \sigma_z - \sigma_{hyd} \end{pmatrix} \quad (2-8)$$

As an example, consider a body under simple tensile stress. For this stress state

$$\sigma_{hyd} = \frac{\sigma_x + 0 + 0}{3} = \frac{\sigma_x}{3}; \text{ then}$$

$$\sigma_{hyd} = \begin{pmatrix} \frac{\sigma_x}{3} & 0 & 0 \\ 0 & \frac{\sigma_x}{3} & 0 \\ 0 & 0 & \frac{\sigma_x}{3} \end{pmatrix}$$

and

$$\begin{aligned} \sigma_{dev} &= \begin{pmatrix} \sigma_x & 0 & 0 \\ 0 & 0 & 0 \\ 0 & 0 & 0 \end{pmatrix} - \begin{pmatrix} \frac{\sigma_x}{3} & 0 & 0 \\ 0 & \frac{\sigma_x}{3} & 0 \\ 0 & 0 & \frac{\sigma_x}{3} \end{pmatrix} \\ &= \begin{pmatrix} \frac{2\sigma_x}{3} & 0 & 0 \\ 0 & \frac{-\sigma_x}{3} & 0 \\ 0 & 0 & \frac{-\sigma_x}{3} \end{pmatrix} \end{aligned}$$

For a general stress state, see Appendix 2-2, section III.

C. Principal Stresses

There are three principal stresses, σ_1, σ_2 , and σ_3 , and they act on planes on which $\tau = 0$ (Fig. 2-3). In designating these stresses, the usual convention is to take $\sigma_1 > \sigma_2 > \sigma_3$ in the algebraic sense; that is, if the three principal stresses were of magnitude +10, +20, and -30, then σ_1 would equal +20, σ_2 would equal +10, and σ_3 would equal -30.

The maximum value of the shear stress acts on a plane whose normal is at 45° to the σ_1 and σ_3 principal stress directions (Fig. 2-4a). The magnitude of this shear stress is given by $\tau_1 = (\sigma_1 - \sigma_3)/2$. On the plane whose normal is at 45° to the σ_2 and σ_1 principal stress directions (Fig. 2-4b), the shear stress is given by $\tau_2 = (\sigma_1 - \sigma_2)/2$, and on the plane whose normal is at 45° to the σ_3 and σ_2 principal stress directions

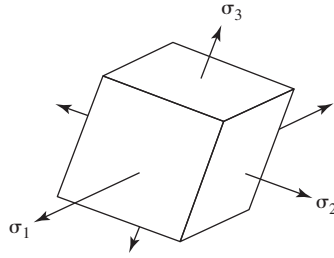


Fig. 2-3. Principal stresses.

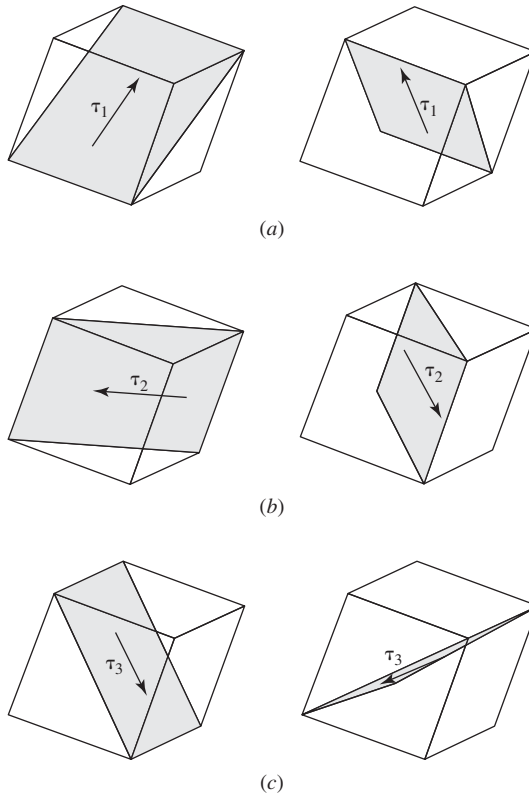


Fig. 2-4. Shear stress on a plane whose normal is at 45° to the principal stresses. (a) σ_1 and σ_3 ; (b) σ_2 and σ_1 ; and (c) σ_3 and σ_2 .

(Fig. 2-4c), the shear stress is given by $\tau_3 = (\sigma_2 - \sigma_3)/2$. Note also that to obtain the normal stresses acting on the 45° planes, simply replace the minus sign in the above relations with a plus sign. These relationships are easily visualized by means of Mohr circles, which are discussed in the next section. For the general case, see Appendix 2-2, sections I and II.

D. Mohr Circles

The state of stress at a point can be conveniently depicted by means of a Mohr circle (see Appendix 2-1 for a derivation). The axes for the Mohr circle plot are the shear stress τ (ordinate) and the normal stress σ (abscissa). Recall that the angle between two directions in the plot is twice the actual angle in the stressed body. Examples of Mohr circles for tension, compression, and pure shear (torsional loading) are given in Figs. 2-5a to Fig. 2-5c, respectively. The stresses acting on an element under pure shear (torsion) are shown in Fig. 2-6. The shear stresses shown are defined as positive when they act in a positive direction on a positive face and as negative when they act in a negative direction on a positive face (the face further along the positive direction of the x - or y -axis is the positive face). Since all the shear stresses shown are positive, a question arises as to how to plot them on the Mohr circle diagram. Note that the shear stress τ_{yx} acts on a plane whose normal is 45° counterclockwise from the first principal direction, σ_1 . On the Mohr circle this shear stress is therefore plotted at 90° counterclockwise from σ_1 , and the shear stress τ_{xy} is plotted at 90° clockwise from σ_1 .

III. STRAIN

The deformation of a body can result in a change in size (Fig. 2-7a) as well as a change in shape (Fig. 2-7b).

The engineering normal strain ε is defined as (see Fig. 2-8)

$$\varepsilon = \frac{\Delta l}{l_0} \quad (2-9)$$

where l_0 is the original length and Δl is the change in length.

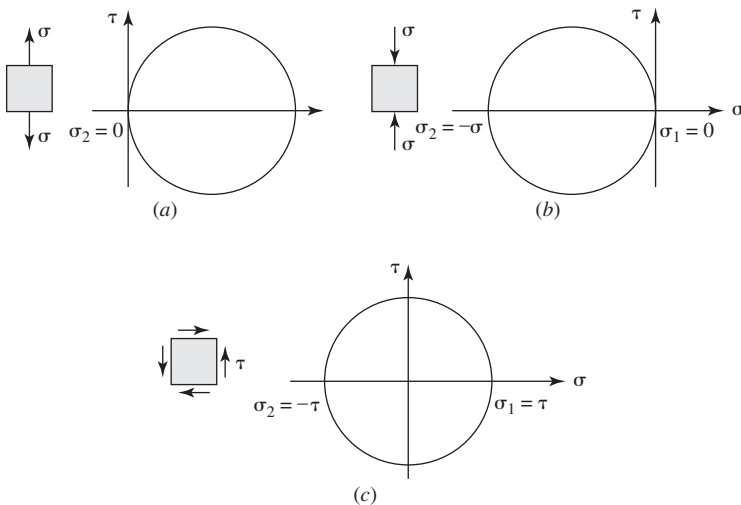


Fig. 2-5. Mohr circles. (a) Uniaxial tension. (b) Uniaxial compression. (c) Pure shear (torsion).

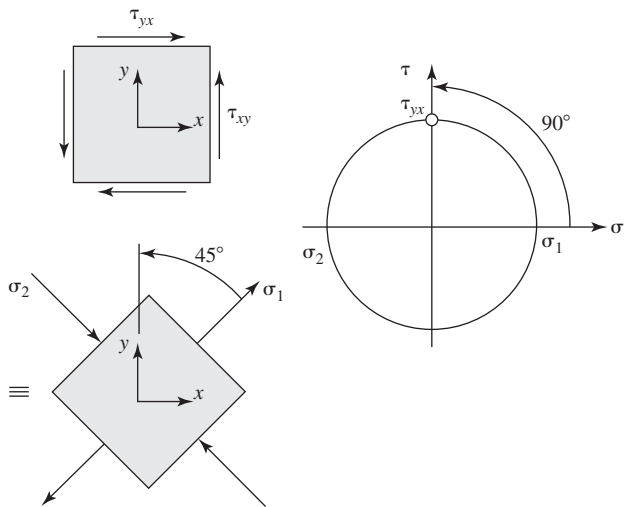


Fig. 2-6. Construction of a Mohr circle for a pure shear stress state.

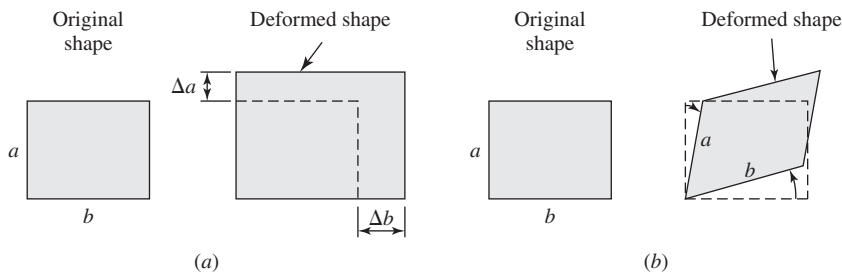


Fig. 2-7. Types of deformation. (a) Change in size. (b) Change in shape.

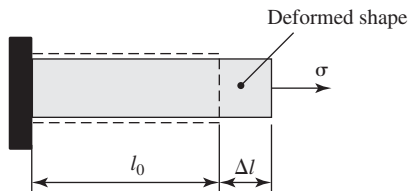


Fig. 2-8. Definition of normal strain.

The true normal strain $\tilde{\varepsilon}$ is defined as

$$\tilde{\varepsilon} = \ln \frac{l}{l_0} = \ln(1 + \varepsilon) \quad (2-10)$$

For $\varepsilon = 0.1$, $\varepsilon_t = 0.095$, and as with the definitions of stress, there is relatively little difference in the definitions of strain for strains of less than 10%.

The engineering shear strain γ describes a change in angle of lines that are originally perpendicular to each other. For the case of a simple shear, as shown in Fig. 2-9a, γ is defined as

$$\tan \gamma = \frac{\Delta}{h} \quad (2-11)$$

where Δ and h are defined in Fig. 2-9a. Since γ is a small angle, $\tan \gamma$ can be replaced by γ , where γ is in radians, that is,

$$\gamma = \frac{\Delta}{h} \quad (2-12)$$

The case of pure shear is shown in Fig. 2-9b. In this case, the total angle change on the xy -plane (or about the z -axis) is

$$\gamma = \frac{\gamma_{xy}}{2} + \frac{\gamma_{yx}}{2} \quad (2-13)$$

It can be shown that $\gamma_{xy} = \gamma_{yx}$.

In a three-dimensional Cartesian coordinate system, there are three mutually perpendicular lines that pass through the same point of a body, as shown in Fig. 2-10a. In Fig. 2-10b, an individual line along the coordinate axes monitors a change in size at that point of a body in the x -, y -, and z -directions and leads to

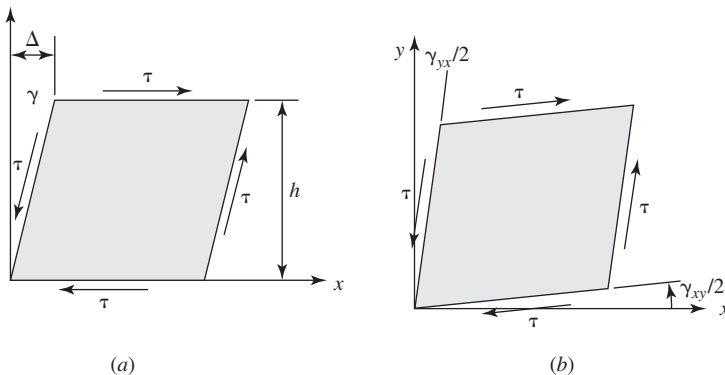


Fig. 2-9. Shear deformation. (a) Simple shear. (b) Pure shear.

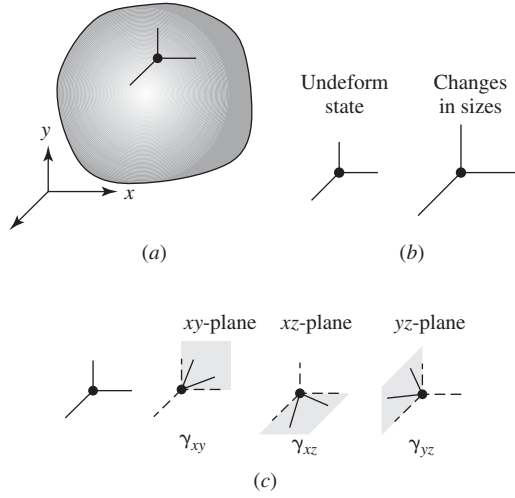


Fig. 2-10. (a) Monitoring a deformation at a point in a body. (b) Physical interpretation of a normal strain. (c) Physical interpretation of a shear strain.

three normal strain components defined as ε_x , ε_y , and ε_z , respectively. Any of two perpendicular lines monitor a change in angle on a plane parallel to these two lines and lead to three shear strain components defined as γ_{xy} , γ_{xz} , and γ_{yz} (also γ_{yx} , γ_{zx} , and γ_{zy}). Figure 2-10c demonstrates a physical interpretation of each shear strain component. These nine components of the strain form the following strain tensor ε_{ij} .

$$\varepsilon_{ij} = \begin{pmatrix} \varepsilon_x & \frac{\gamma_{xy}}{2} & \frac{\gamma_{xz}}{2} \\ \frac{\gamma_{yx}}{2} & \varepsilon_y & \frac{\gamma_{yz}}{2} \\ \frac{\gamma_{zx}}{2} & \frac{\gamma_{zy}}{2} & \varepsilon_z \end{pmatrix} \quad (2-14)$$

It should be noted again that there are only six independent strain components.

IV. ELASTIC CONSTITUTIVE RELATIONSHIPS

In this section the constitutive relationship for isotropic, homogeneous, and continuous media is presented.

A. Assumptions

(a) *Isotropy*: The properties are the same in all directions through a point in the material.

(b) *Anisotropy*: The properties are *not* the same in all directions through a point in the material (example: composite materials, single crystals). All metals and alloys are anisotropic to some degree as a result of processing.

(c) *Homogeneous*: The properties are the same at every point in the body, a difficult condition to achieve. For example, a casting may not be homogeneous, because faster cooling at the surface will result in a smaller grain size at the surface than in the interior of the casting.

(d) *Continuous*: No discontinuities such as holes are present in the body. The presence of casting porosity would violate this definition.

B. The Elastic Constants

(a) *Young's modulus*: Hooke's law is the earliest constitutive law in mechanics and dates back to 1670. It is basic to the field of stress analysis. In 1670, Hooke was involved in the design of a watch spring, and even in those days there was a patent law in England. To protect his patent rights while his developmental work was ongoing, he published the following anagram in Latin:

ceiiniosssttuv

Ten years later he revealed that the anagram was for the following relation:

Ut tensio sic vis, which translates roughly as "As I stretch, so the force." Later Young proposed a constant that linked stretch and force, and in 1825, Cauchy systematized the field of elasticity by providing our modern definitions of stress and strain. Hooke's law became the familiar expression $\sigma = E\varepsilon$, where E is known as Young's modulus.

(b) *Poisson's ratio*: Poisson's ratio ν is defined for unidirectional loading (Fig. 2-11) as minus the ratio of the transverse strain ε_{tran} to the longitudinal strain ε_{long} , that is,

$$\nu = -\frac{\varepsilon_{tran}}{\varepsilon_{long}} \quad (2-15)$$

(c) *Shear modulus*: The shear modulus G relates the elastic shear stress to the shear strain, that is, $\tau = G\gamma$. It can be shown that

$$G = \frac{E}{2(1 + \nu)} \quad (2-16)$$

(d) *Bulk modulus*: The bulk modulus K is defined as the ratio of the pressure p to the volumetric strain, Δ . Δ is known as the dilatation and is expressed as $\Delta = \Delta V/V$, where V is the volume and ΔV is the volume change. To determine the expression for the bulk modulus, consider a cube, each edge of which is equal to 1.0 units. Under a positive pressure p (Fig. 2-12), each edge will increase in length by an amount Δl , and the strain ε will be $\varepsilon = \Delta l/l$. Therefore, $\varepsilon = \Delta l$. The dilatation is therefore

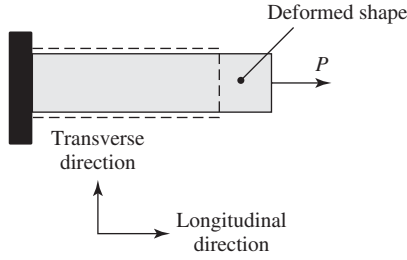


Fig. 2-11. A unidirectional loading.

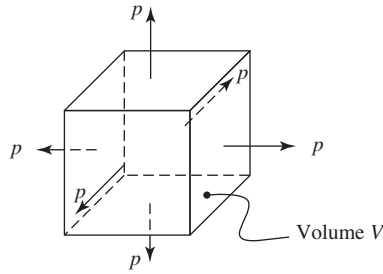


Fig. 2-12. A unit cube under pressure.

$$\Delta = \frac{\Delta V}{V}$$

$$\Delta = (1 + \varepsilon)^3 - 1 \approx \varepsilon_x + \varepsilon_y + \varepsilon_z = 3\varepsilon \quad (2-17)$$

so that

$$K = \frac{p}{3\varepsilon\varepsilon\varepsilon} \quad (2-18)$$

But

$$\varepsilon_x = p/E - \nu p/E - \nu p/E = \varepsilon,$$

hence $K = p/3(1 - 2\nu)$.

Engineering analyses often assume, as a reasonable approximation, that materials are isotropic, homogeneous, and continuous. When these approximations are adopted, these elastic constants are interrelated so that only two of them are independent. This means that only two material constants are needed in the analysis of elastic stress–strain behavior, for example, E and ν . However, in some very anisotropic crystals, as many as 21 constants may be needed in the analysis of stress–strain behavior. Cubic crystals such as nickel and copper have a high degree of symmetry, and for such crystals only three material constants are needed.

C. Elastic Stress–Strain Relations

C.1. Generalized Stress State The following expressions are used to determine the strains when the stresses are known (1):

$$\varepsilon_x = \frac{1}{E}[\sigma_x - \nu(\sigma_y + \sigma_z)] \quad (2-19a)$$

$$\varepsilon_y = \frac{1}{E}[\sigma_y - \nu(\sigma_z + \sigma_x)] \quad (2-19b)$$

$$\varepsilon_z = \frac{1}{E}[\sigma_z - \nu(\sigma_x + \sigma_y)] \quad (2-19c)$$

$$\gamma_{xy} = \frac{\tau_{xy}}{G} \quad (2-19d)$$

$$\gamma_{xz} = \frac{\tau_{xz}}{G} \quad (2-19e)$$

$$\gamma_{yz} = \frac{\tau_{yz}}{G} \quad (2-19f)$$

The following expressions are used to determine the stresses when the strains are known (1):

$$\sigma_x = \frac{\nu E}{(1 + \nu)(1 - 2\nu)}(\varepsilon_x + \varepsilon_y + \varepsilon_z) + \frac{E}{1 + \nu}\varepsilon_x \quad (2-20a)$$

$$\sigma_y = \frac{\nu E}{(1 + \nu)(1 - 2\nu)}(\varepsilon_x + \varepsilon_y + \varepsilon_z) + \frac{E}{1 + \nu}\varepsilon_y \quad (2-20b)$$

$$\sigma_z = \frac{\nu E}{(1 + \nu)(1 - 2\nu)}(\varepsilon_x + \varepsilon_y + \varepsilon_z) + \frac{E}{1 + \nu}\varepsilon_z \quad (2-20c)$$

$$\tau_{xy} = G\gamma_{xy} \quad (2-20d)$$

$$\tau_{xz} = G\gamma_{xz} \quad (2-20e)$$

$$\tau_{yz} = G\gamma_{yz} \quad (2-20f)$$

C.2. Plane-Stress State This is a special two-dimensional stress state with $\sigma_z = \tau_{xz} = \tau_{yz} = 0$; the stress–strain relationships in Eq. 2-19 become

$$\varepsilon_x = \frac{1}{E}(\sigma_x - \nu\sigma_y) \quad (2-21a)$$

$$\varepsilon_y = \frac{1}{E}(\sigma_y - \nu\sigma_x) \quad (2-21b)$$

$$\gamma_{xy} = \frac{\tau_{xy}}{G} \quad (2-21c)$$

However, there is a corresponding normal strain in the z -direction as

$$\varepsilon_z = -\frac{\nu}{E}(\sigma_x + \sigma_y) \quad (2-22)$$

Equation 2-21 can be rewritten in terms of strain as

$$\sigma_x = \frac{E}{1 - \nu^2} (\epsilon_x + \nu \epsilon_y) \quad (2-23a)$$

$$\sigma_y = \frac{E}{1 - \nu^2} (\epsilon_y + \nu \epsilon_x) \quad (2-23b)$$

$$\tau_{xy} = G\gamma_{xy} \quad (2-23c)$$

Example

The passenger cabin of a jet is pressurized at a level equal to the atmospheric pressure at an altitude of 2.4 km (8,000 ft). Note that 1 atm = 1.013×10^5 Pa = 76 cm Hg. From Fig. 2-13, at 2.4 km the atmospheric pressure p is 0.08 MPa. At an altitude of 10 km, $p = 0.027$ MPa; therefore, the cabin is subjected to an internal pressure, Δp , of $0.080 - 0.027 = 0.053$ MPa and the circumference of the fuselage increases by 0.2 m (7.9 in.). The fuselage can approximate to a thin-walled cylindrical vessel with an inside diameter $D = 16$ m. The fuselage is made of a high-strength aluminum alloy with Young's modulus $E = 70$ GPa, and Poisson's ratio $\nu = 0.3$. Determine the stress in the hoop direction (see Fig. 2-14).

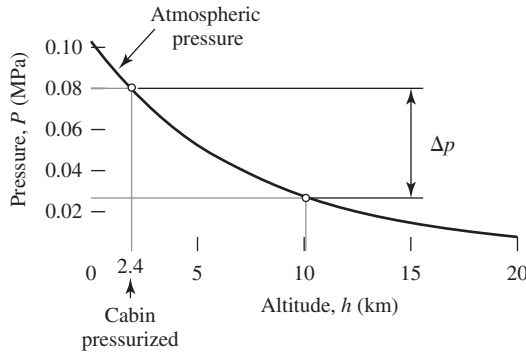


Fig. 2-13. Relationship between atmospheric pressure and altitude.

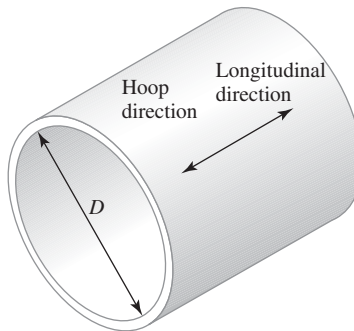


Fig. 2-14. Circumferential hoop and longitudinal directions.

Solution

The circumference of the fuselage at 2.4 km is $\pi D = 16\pi$; the corresponding normal strain in the hoop direction ε_{hoop} is $0.20/\pi D = 0.004$. The hoop stress, longitudinal stress, and radial (or thickness) stress components are (see Appendix 2-3, section III, for details)

$$\begin{aligned}\sigma_{hoop} &= \frac{\Delta p D}{2t} = \frac{0.053 \times 16}{2t} \\ \sigma_{long} &= \frac{\Delta p D}{4t} = \frac{\sigma_{hoop}}{2} \\ \sigma_{thick} &= 0\end{aligned}$$

From Eq. 2-21a, define the hoop and longitudinal directions as x - and y -directions, respectively. Therefore,

$$\begin{aligned}\varepsilon_{hoop} &= \frac{1}{E}[\sigma_{hoop} - \nu\sigma_{long}] \\ \varepsilon_{hoop} &= \frac{1}{E}\left[\sigma_{hoop} - \frac{\nu}{2}\sigma_{hoop}\right] = \frac{0.85}{E}\sigma_{hoop} \\ \sigma_{hoop} &= \frac{\varepsilon_{hoop}E}{0.85} = \frac{0.004 \times 70 \times 10^9}{0.85} = 330 \text{ MPa}\end{aligned}$$

The skin thickness t can be determined from

$$t = \frac{\Delta p D}{2\sigma_{hoop}} = \frac{0.053 \times 16}{2 \times 330} = 1.3 \text{ mm}$$

Note that at an altitude of 20 km, the hoop stress increases to 470 MPa.

C.3. Plane-Strain State This is a special two-dimensional stress state, with $\varepsilon_z = \gamma_{xz} = \gamma_{yz} = 0$; the stress-strain relationship in Eq. 2-19c becomes

$$0 = \frac{1}{E}[\sigma_z - \nu(\sigma_x + \sigma_y)]$$

Therefore, there is a corresponding normal stress in the z -direction given by

$$\sigma_z = \nu(\sigma_x + \sigma_y) \quad (2-24)$$

Substituting σ_z into Eq. 2-19a and Eq. 2-19b yields

$$\varepsilon_x = \frac{1+\nu}{E}[(1-\nu)\sigma_x - \nu\sigma_y] \quad (2-25a)$$

$$\varepsilon_y = \frac{1+\nu}{E}[(1-\nu)\sigma_y - \nu\sigma_x] \quad (2-25b)$$

and from Eq. 2-19d

$$\gamma_{xy} = \frac{\tau_{xy}}{G} \quad (2-25c)$$

Alternatively, Eq. 2-25 can be written as

$$\sigma_x = \frac{E}{(1-\nu)(1-2\nu)} [(1-\nu)\varepsilon_x + \nu\varepsilon_y] \quad (2-26a)$$

$$\sigma_y = \frac{E}{(1-\nu)(1-2\nu)} [(1-\nu)\varepsilon_y + \nu\varepsilon_x] \quad (2-26b)$$

$$\tau_{xy} = G\gamma_{xy} \quad (2-26c)$$

Example

Figure 2-15 shows a thin sheet of metal having a width more than 10 times its thickness. Bending of this thin sheet creates a stress gradient and lead to a plane-strain state of stress. Let the xyz axes be oriented such that the x -axis is in the direction of the strip, the y -axis is perpendicular to the strip ($\sigma_y = 0$), and the z -axis is in the width direction. Determine the apparent Young's modulus E_{apparent} defined as σ_x/ε_x .

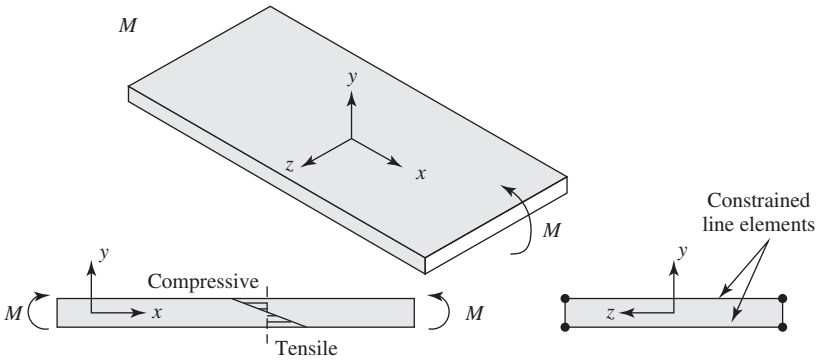


Fig. 2-15. Plane-strain bending of a thin sheet.

Solution

Because of the steep stress gradient in bending this thin strip, contraction in the z -direction is constrained and $\varepsilon_z = 0$.

$$\varepsilon_z = \frac{1}{E}(\sigma_z - \nu\sigma_x) = 0$$

Thus,

$$\begin{aligned}\sigma_z &= \nu\sigma_x \\ \varepsilon_x &= \frac{1}{E}(\sigma_x - \nu\sigma_z) \\ &= \frac{1}{E}(\sigma_x - \nu^2\sigma_x) = \frac{1}{E}\sigma_x(1 - \nu^2)\end{aligned}$$

where ε_x is the actual strain. Thus,

$$E_{\text{apparent}} = \frac{\sigma_x}{\varepsilon_x} = \frac{E}{(1 - \nu^2)}$$

That is, due to the plane-strain state, the apparent Young's modulus E_{apparent} is larger than the actual modulus E by approximately 10%.

D. Strain Energy Density

When an elastic body is subjected to gradually increasing external loads, work is done while deforming this body from its initial state to its final state. On the assumption that no energy is lost in the form of heat, the external work done by the loads will be converted into internal work called *strain energy*. The strain energy density U is defined as a strain energy per unit volume of a material that can be related to stress and strain components as

$$U = \int (\sigma_x d\varepsilon_x + \sigma_y d\varepsilon_y + \sigma_z d\varepsilon_z + \tau_{xy} d\gamma_{xy} + \tau_{xz} d\gamma_{xz} + \tau_{yz} d\gamma_{yz}) \quad (2-27)$$

E. Relationship between Elastic Constants

It was previously stated that for isotropic, homogeneous, and continuous materials, there are only two independent elastic constants. We now reach a state to prove it.

E.1. ε , ν , and G Consider a body subjected to torsion (Fig. 2-16a); the stress tensor under a pure shear is

$$\begin{pmatrix} 0 & \tau_{xy} & 0 \\ \tau_{yx} & 0 & 0 \\ 0 & 0 & 0 \end{pmatrix}$$

and a corresponding strain tensor is

$$\begin{pmatrix} 0 & \gamma_{xy}/2 & 0 \\ \gamma_{yx}/2 & 0 & 0 \\ 0 & 0 & 0 \end{pmatrix}$$

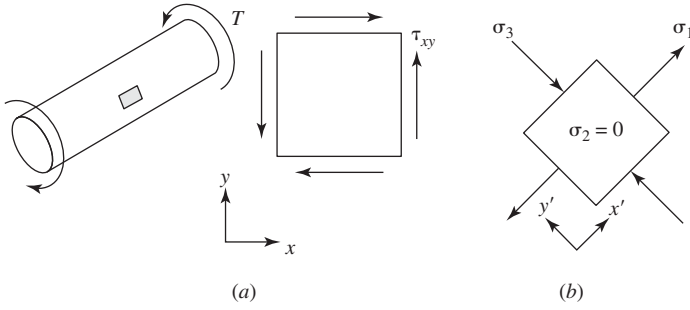


Fig. 2-16. State of stresses. (a) Pure shear. (b) Push-pull.

The strain energy density associated with the above *shear* stresses and strains is

$$U = \frac{1}{2} \tau_{xy} \frac{\gamma_{xy}}{2} + \frac{1}{2} \tau_{yx} \frac{\gamma_{yx}}{2} = \frac{1}{2} \tau_{yx} \gamma_{yx} = \frac{1}{2} \frac{\tau_{xy}^2}{G}$$

The state of stress under pure shear can be transformed into an equivalent system in a principal coordinate (Fig. 2-16b). The principal stresses are $\sigma_1 = \tau_{xy}$, $\sigma_2 = 0$, and $\sigma_3 = -\tau_{xy}$. Thus, the stress tensor is

$$\begin{pmatrix} \sigma_1 & 0 & 0 \\ 0 & 0 & 0 \\ 0 & 0 & \sigma_3 \end{pmatrix}$$

From Eq. 2-19a to Eq. 2-19c

$$\varepsilon_1 = \frac{\sigma_1}{E} - \nu \frac{\sigma_3}{E} = \frac{\sigma_1}{E} (1 + \nu)$$

$$\varepsilon_2 = 0$$

and

$$\varepsilon_3 = -\frac{\sigma_1}{E} (1 + \nu)$$

Therefore, a corresponding strain tensor (in a principal coordinate) is

$$\begin{pmatrix} \varepsilon_1 & 0 & 0 \\ 0 & 0 & 0 \\ 0 & 0 & \varepsilon_3 \end{pmatrix}$$

The strain energy density associated with the above *normal* stresses and strains is

$$U = \frac{1}{2} \sigma_1 \varepsilon_1 + \frac{1}{2} (-\sigma_1) (-\varepsilon_1) = \sigma_1 \varepsilon_1$$

$$U = \sigma_1 \left[\frac{\sigma_1}{E} (1 + \nu) \right] = \frac{\sigma_1^2}{E} (1 + \nu)$$

The pure shear and push-pull stress states are equivalent; therefore, the strain energy density associated with each state must be equal.

$$\frac{\sigma_1^2}{E}(1 + \nu) = \frac{1}{2} \frac{\tau_{xy}^2}{G}$$

since in torsion, σ_1 is numerically equal to τ_{xy} ; therefore,

$$G = \frac{E}{2(1 + \nu)}$$

E.2. E, ν , and K From Eq. 2-19a

$$\varepsilon = \frac{1}{E}[p - \nu(p + p)]$$

$$\varepsilon = \frac{p}{E}(1 - 2\nu)$$

Substituting into Eq. 2-18 yields

$$K = \frac{E}{3(1 - 2\nu)} \quad (2-28)$$

V. STATE OF STRESS AHEAD OF A NOTCH

Under tensile loading, the thickness of an unnotched or uncracked plate has no effect on the state of stress in the plate. However, when a notch or crack is present in the plate, the state of stress is affected by the thickness as well as by the notch, as will be discussed.

It is clear that if the number of independent stress components can be reduced from six to a smaller number, the analysis will be simpler. For example, if the independent components of stress lie only in one plane, there are only three independent stresses, that is, two normal stresses and one shear stress. There are two types of in-plane situations: one is known as *plane stress*, and the other is known as *plane strain*. In the analysis of these in-plane situations, the x - and y -axes will be taken in the plane, and the z -axis will therefore be perpendicular to the plane.

In plane stress, $\sigma_z = \tau_{xz} = \tau_{yz} = 0$, that is, the components of stress in the direction normal to the plane are zero. The three remaining components of stress are σ_x , σ_y , and τ_{xy} . In plane strain, $\varepsilon_z = \gamma_{xz} = \gamma_{yz} = 0$, that is, the components of strain in the z -direction are zero.

In plane strain, there are also three independent components of stress in the plane. However, a σ_z stress is also present because of a constraint on both elastic and plastic deformation in the z -direction. Consider a plate containing a hole of radius a , which is small compared to the width of the plate, Fig. 2-17a. The plate is elastically loaded in tension with the y -axis in the direction of loading and the x -axis transverse to

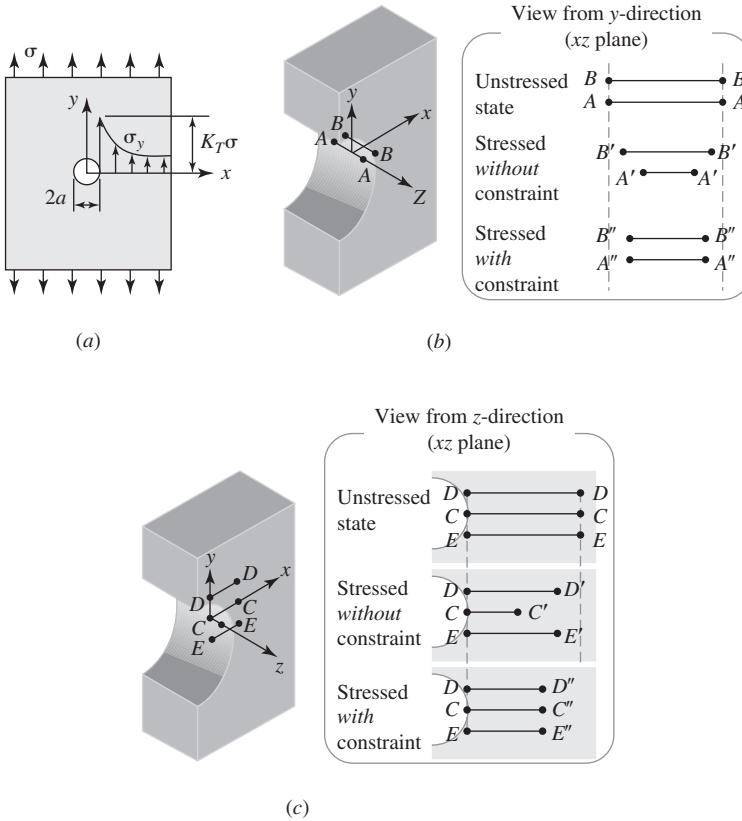


Fig. 2-17. (a) Normal stress distribution in the y -direction ahead of a notch root. (b) Constraint in the z -direction. (c) Constraint in the x -direction.

the direction of loading. At the notch root (coordinates $(0, a)$), σ_y is the principal stress σ_1 and is equal to $K_T \sigma$, where K_T is the stress concentration factor, and σ is the applied stress. Because of the Poisson effect, the material at the notch root will try to contract in the z - (thickness) direction, Fig. 2-17b. However, the adjacent, less heavily stressed material surrounding the root of the notch will not contract as much and will exercise a constraint on the ability of the most highly stressed material to contract. This constraint leads to a tensile stress σ_z being developed in the z -direction. This stress must be zero at the surface of the plate, but it quickly rises to a constant value.

Similarly, material in the x -direction at the root of the notch will try to contract, Fig. 2-17c, but again a constraint will be developed in the x -direction, which results in a tensile stress σ_x . In this case, the σ_x stress must be zero at the notch, but it rises to a maximum in the x -direction before falling off. In the case of a hole in a plate, the maximum value of this stress is 0.375 of the applied stress at a distance

measured from the center of the hole equal to $\sqrt{2}$ times the radius. It is noted that the solutions for in-plane stresses in plane-stress and plane-strain problems do not depend upon the material constants E and ν . The σ_x stress also leads to a constraint being developed in the z -direction, and the total resultant stress in the z -direction is given as $\sigma_z = \nu(\sigma_x + \sigma_y)$.

These z - and x -direction constraints transform the uniaxial tensile stress into a triaxial tensile stress state at the notch. It is important to note that the hydrostatic stress ahead of the notch is higher in plane strain than it is in plane stress, and for this reason it has a more deleterious effect on fracture resistance.

VI. SUMMARY

This chapter has reviewed the basic means for defining and analyzing elastic stresses and strains. Principal stresses and the use of Mohr circles were discussed, as was the distinction between plane stress and plane strain. A final topic was stress-strain relationships. The information in this chapter will be sufficient for many failure analyses, but in some cases, the use of more advanced techniques, such as finite element analysis (FEA) may be necessary.

REFERENCES

- (1) G. E. Dieter, Jr., *Mechanical Metallurgy*, 3rd ed., McGraw-Hill, New York, 1986.
- (2) I. Le May, *Principles of Mechanical Metallurgy*, Elsevier, Oxford, 1981.
- (3) P. C. Chou and N. J. Pagano, *Elasticity*, D. Van Nostrand Co., New York, 1967.

APPENDIX 2-1: MOHR CIRCLE EQUATIONS FOR A PLANE PROBLEM (1)

Given σ_x , σ_y , and τ_{xy} (Fig. 2.1-2a-1), find the stresses on a plane that makes an angle α with the y -axis; see Fig. 2.1-2b-1. In this figure, p_x and p_y denote the stress vector in the x - and y -directions acting on an inclined plane.

Equilibrium of force in the x -direction, that is, $\sum F_x = 0$, yields

$$p_x A - \sigma_x A \cos \alpha - \tau_{xy} A \sin \alpha = 0$$

or

$$p_x = \sigma_x \cos \alpha + \tau_{xy} \sin \alpha \quad (2A-1)$$

Similarly, in the y -direction

$$p_y = \sigma_y \sin \alpha + \tau_{xy} \cos \alpha \quad (2A-2)$$

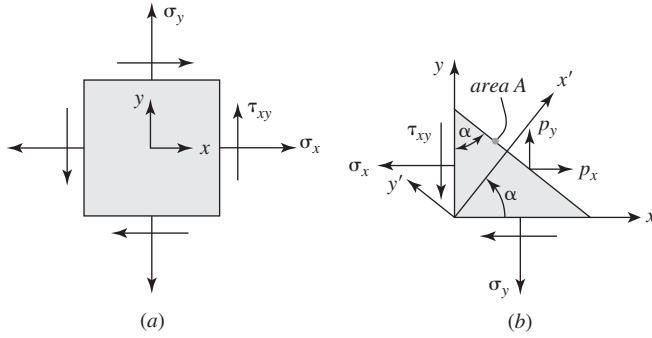


Fig. A2.1. (a) Two-dimensional stress state. (b) Stress vector on an inclined plane.

The normal stress on a x' -plane is obtained by projecting p_x and p_y in the x' direction. Thus,

$$\sigma_{x'} = p_x \cos \alpha + p_y \sin \alpha \quad (2A-3)$$

Substituting Eq. 2A-1,

$$\sigma_{x'} = \sigma_x \cos^2 \alpha + \sigma_y \sin^2 \alpha + 2\tau_{xy} \sin \alpha \cos \alpha \quad (2A-4)$$

Similarly,

$$\tau_{x'y'} = p_y \cos \alpha - p_x \sin \alpha$$

or

$$\tau_{x'y'} = (\sigma_y - \sigma_x) \sin \alpha \cos \alpha + \tau_{xy} (\cos^2 \alpha - \sin^2 \alpha) \quad (2A-5)$$

The stress $\sigma_{y'}$ may be found by substituting $(\alpha + \pi/2)$ for α in the equation for $\sigma_{x'}$

$$\sigma_{y'} = \sigma_x \cos^2(\alpha + \pi/2) + \sigma_y \sin^2(\alpha + \pi/2) + 2\tau_{xy} \sin(\alpha + \pi/2) \cos(\alpha + \pi/2)$$

And since

$$\sin(\alpha + \pi/2) = \cos \alpha \quad \text{and} \quad \cos(\alpha + \pi/2) = -\sin \alpha$$

we obtain

$$\sigma_{y'} = \sigma_x \sin^2 \alpha + \sigma_y \cos^2 \alpha - 2\tau_{xy} \sin \alpha \cos \alpha \quad (2A-6)$$

With the use of the following trigonometric identities,

$$\sin 2\alpha = 2 \sin \alpha \cos \alpha \quad (2A-7a)$$

$$\sin^2 \alpha = \frac{1}{2}(1 - \cos 2\alpha) \quad (2A-7b)$$

$$\cos^2 \alpha = \frac{1}{2}(1 + \cos 2\alpha) \quad (2A-7c)$$

we find that

$$\sigma_{x'} = \frac{\sigma_x + \sigma_y}{2} + \frac{\sigma_x - \sigma_y}{2} \cos 2\alpha + \tau_{xy} \sin 2\alpha \quad (2A-8a)$$

$$\sigma_{y'} = \frac{\sigma_x + \sigma_y}{2} + \frac{\sigma_x - \sigma_y}{2} \cos 2\alpha - \tau_{xy} \sin 2\alpha \quad (2A-8b)$$

$$\tau_{x'y'} = \frac{\sigma_y - \sigma_x}{2} \sin 2\alpha + \tau_{xy} \cos 2\alpha \quad (2A-9)$$

To determine the orientation of the planes of maximum and minimum normal stress, the expression for $\sigma_{x'}$ is differentiated with respect to α , and the derivative is set equal to zero:

$$\frac{d\sigma_{x'}}{d\alpha} = -(\sigma_x - \sigma_y) \sin 2\alpha + 2\tau_{xy} \cos 2\alpha \quad (2A-10)$$

or

$$\tan 2\alpha = \frac{2\tau_{xy}}{\sigma_x - \sigma_y} \quad (2A-11)$$

This equation has two roots that are 180° apart. Therefore, the two values of α differ by 90° .

Further, $\tau_{xy} \cos 2\alpha = -[(\sigma_y - \sigma_x)/2] \sin 2\alpha$, so that $\tau_{x'y'} = 0$ on these two planes. The planes on which the shear stress is zero are the principal planes; the normal stresses on these planes are the principal stresses.

Rewriting Eqs. 2A-8a and 2A-9, we obtain

$$\begin{aligned} \sigma_{x'} - \frac{\sigma_x + \sigma_y}{2} &= \frac{\sigma_x - \sigma_y}{2} \cos 2\alpha + \tau_{xy} \sin 2\alpha \\ \tau_{x'y'} &= \frac{\sigma_y - \sigma_x}{2} \sin 2\alpha + \tau_{xy} \cos 2\alpha \end{aligned}$$

Squaring both of these expressions and adding, we obtain

$$\left(\sigma - \frac{\sigma_x + \sigma_y}{2} \right)^2 + \tau^2 = \left(\frac{\sigma_x - \sigma_y}{2} \right)^2 + \tau_{xy}^2$$

where $\sigma = \sigma_{x'}$ and $\tau = \tau_{x'y'}$

This is the equation for a circle, that is, Mohr's circle for stress in the (σ, τ) coordinates with its center on the σ axis, translated $(\sigma_x + \sigma_y)/2$ units to the right of the origin, and with a radius of $\sqrt{[(\sigma_x - \sigma_y)/2]^2 + \tau_{xy}^2}$.

The Mohr circle for strain can be derived in a similar manner, and the axes are labeled ϵ and $\gamma/2$. $\gamma/2$ rather than γ is used, because the shear strain associated with each τ_{xy} in Fig. 2-9 is $\gamma/2$.

APPENDIX 2-2: THREE-DIMENSIONAL STRESS ANALYSIS

I. Principal Stresses and Stress Invariants

Consider the equilibrium of an infinitesimally small tetrahedron formed by a plane and the coordinate plane, as shown in Fig. A2.2.2a-1-a. The stresses acting on the coordinate planes are known. The stresses acting on plane ABC are not known. The normal to plane ABC is ON , and the direction cosines are l , m , and n with respect to the axes x , y , and z , respectively. The area of the triangle ABC is designated as dA . The areas of the faces AOB , COB , and AOC are equal to mdA , ldA , and ndA , respectively. Designate the stress vector acting on ABC as S , and its x , y , z components as S_x , S_y , and S_z , as in Fig. A2.2.2a-2-b. For equilibrium of forces in the x -direction,

$$S_x dA = \sigma_x l dA + \tau_{yx} m dA + \tau_{zx} n dA \quad (2A-12)$$

or

$$S_x = l\sigma_x + m\tau_{yx} + n\tau_{zx} \quad (2A-13a)$$

Similarly, equilibrium of forces in the y - and z -directions yields

$$S_y = l\tau_{xy} + m\sigma_y + n\tau_{zy} \quad (2A-13b)$$

$$S_z = l\tau_{xz} + m\tau_{yz} + n\sigma_z \quad (2A-13c)$$

If l , m , and n are replaced by l_1 , l_2 , and l_3 , and S_x , S_y , and S_z are replaced by S_1 , S_2 , and S_3 , Eq. 2A-13 can be rewritten in the index notation form as

$$S_j = \sigma_{ij} l_i \quad (2A-14)$$

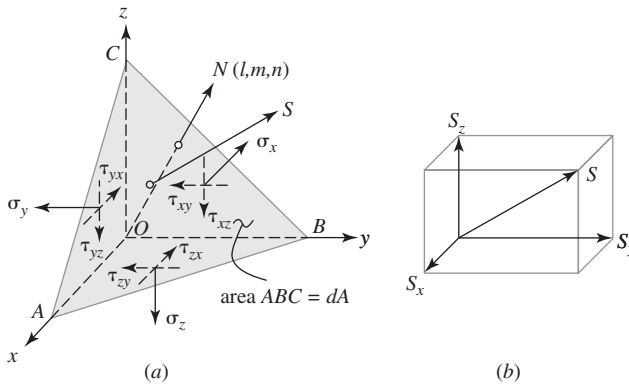


Fig. A2.2.2a-1. Stress vectors on an oblique plane.

To obtain the normal stress acting on dA , project the stresses S_x, S_y , and S_z onto the normal ON (see Fig. A2.2.2-a-1), to get

$$S_n = lS_x + mS_y + nS_z \quad (2A-15)$$

Substituting from Eq. 2A-13 results in

$$S_n = l^2\sigma_x + m^2\sigma_y + n^2\sigma_z + 2(lm\tau_{xy} + mn\tau_{yz} + nl\tau_{zx}) \quad (2A-16)$$

To obtain the resultant shear stress acting on this plane S_s ,

$$S_s^2 = S^2 - S_n^2 = S_x^2 + S_y^2 + S_z^2 - S_n^2 \quad (2A-17)$$

If $S = S_n$ then $S_s = 0$. The plane is then called a *principal plane*, and its normal is called a *principal direction* and S is called a *principal stress*. At every point on a body, there are three principal stresses, one or more of which may be equal to zero.

If ABC is a principal plane, then S has the same direction cosines as the normal. The components of stress are then

$$\begin{aligned} S_x &= lS, \\ S_y &= mS, \\ S_z &= nS \end{aligned} \quad (2A-18)$$

and Eq.2A-2 becomes

$$\begin{aligned} l(\sigma_x - S) + m\tau_{yx} + n\tau_{zx} &= 0, \\ l\tau_{xy} + m(\sigma_y - S) + n\tau_{zy} &= 0, \\ l\tau_{yx} + n\tau_{yz} + m(\sigma_z - S) &= 0 \end{aligned} \quad (2A-19)$$

or in tensor notation

$$l_i(\sigma_{ij} - \delta_{ij}S) = 0 \quad (2A-20)$$

where δ_{ij} is known as the *Kronecker delta*. δ_{ij} is equal to 1 for $i = j$ and is equal to 0 for $i \neq j$.

For Eq. 2A-20 to have a solution for l, m , and n , the determinant of the coefficients must vanish, resulting in

$$|\sigma_{ij} - \delta_{ij}S| = \begin{vmatrix} \sigma_x - S & \tau_{yx} & \tau_{zx} \\ \tau_{xy} & \sigma_y - S & \tau_{zy} \\ \tau_{xz} & \tau_{yz} & \sigma_z - S \end{vmatrix} = 0 \quad (2A-21)$$

Expanding the determinant results in a cubic equation for S :

$$S^3 - I_1S^2 - I_2S - I_3 = 0 \quad (2A-22)$$

where

$$\begin{aligned}
 I_1 &= \sigma_x + \sigma_y + \sigma_z \\
 I_2 &= \tau_{xy}^2 + \tau_{yz}^2 + \tau_{zx}^2 - (\sigma_x \sigma_y + \sigma_y \sigma_z + \sigma_z \sigma_x) \\
 I_3 &= \sigma_x \sigma_y \sigma_z + 2\tau_{xy} \tau_{yz} \tau_{zx} - (\sigma_x \tau_{yz}^2 + \sigma_y \tau_{zx}^2 + \sigma_z \tau_{xy}^2)
 \end{aligned} \tag{2A-23}$$

Equation 2A-22 has three real roots; consequently, there are three principal stresses that are designated σ_1 , σ_2 , and σ_3 . It is noted that the values in Eq. 2A-23 are independent of the coordinate axes.

To find the corresponding values of l , m , and n for a particular principal stress, substitute that principal stress into Eq. 2A-19 and use the relation $l^2 + m^2 + n^2 = 1$. If three principal stresses are distinct, the three corresponding directions will be unique and orthogonal. If two of the principal stresses are equal, one direction will be unique but the other two directions can be any two directions orthogonal to the first. If all of the principal stresses are equal, there are no unique principal directions, and any three directions can be chosen. This corresponds to a state of hydrostatic stress.

It is noted that the values of I_1 , I_2 , and I_3 in Eq. 2A-23 are independent of the orientation of the x -, y -, and z -axes. Therefore, I_1 , I_2 , and I_3 are known as the *first*, *second*, and *third invariants* of the stress tensor, respectively. If the coordinate axes are coincident with the directions of principal stress, then

$$\begin{aligned}
 I_1 &= \sigma_1 + \sigma_2 + \sigma_3 \\
 I_2 &= -(\sigma_1 \sigma_2 + \sigma_2 \sigma_3 + \sigma_3 \sigma_1) \\
 I_3 &= \sigma_1 \sigma_2 \sigma_3
 \end{aligned} \tag{2A-24}$$

II. Maximum and Octahedral Shear Stresses

From the Mohr circle (see Fig. A2.2.2a-2), the maximum in-plane shearing stresses are

$$\begin{aligned}
 \tau_1 &= \pm \frac{1}{2}(\sigma_1 - \sigma_3) \\
 \tau_2 &= \pm \frac{1}{2}(\sigma_1 - \sigma_2) \\
 \tau_3 &= \pm \frac{1}{2}(\sigma_2 - \sigma_3)
 \end{aligned} \tag{2A-25}$$

The associated normal stresses on planes of maximum shear stress are

$$\begin{aligned}
 \sigma_{n1} &= \frac{1}{2}(\sigma_1 + \sigma_3) \\
 \sigma_{n2} &= \frac{1}{2}(\sigma_1 + \sigma_2) \\
 \sigma_{n3} &= \frac{1}{2}(\sigma_2 + \sigma_3)
 \end{aligned} \tag{2A-26}$$

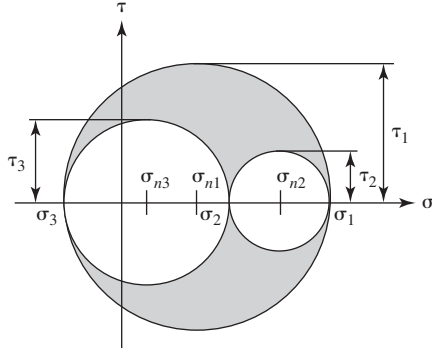


Fig. A2.2.2a-2. Mohr circle for the three-dimensional stress state.

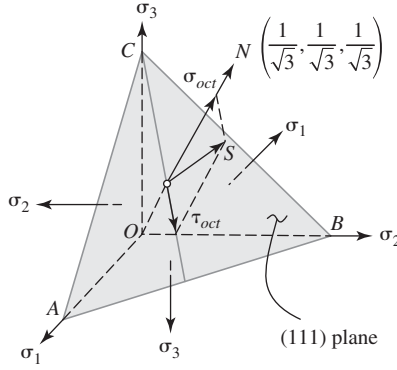


Fig. A2.2.2a-3. Stress vectors on the octahedral plane.

If the plane of interest is a (111) plane with respect to a principal coordinate, that is, an octahedral plane, then (see Fig. A2.2.2a-3)

$$l = m = n = \pm \frac{1}{\sqrt{3}} \quad (2A-27)$$

and the normal stress acting on this plane is

$$S_n = \frac{1}{3}(\sigma_1 + \sigma_2 + \sigma_3) = \sigma_m \equiv \sigma_{oct} \quad (2A-28)$$

The corresponding octahedral shear stress squared is

$$\begin{aligned} S_s^2 &= \frac{1}{3}(\sigma_1^2 + \sigma_2^2 + \sigma_3^2) - \frac{1}{9}(\sigma_1 + \sigma_2 + \sigma_3)^2 \\ &= \frac{1}{3}[(\sigma_1 - \sigma_m)^2 + (\sigma_2 - \sigma_m)^2 + (\sigma_3 - \sigma_m)^2] \\ &\equiv \tau_{oct}^2 \end{aligned} \quad (2A-29)$$

In terms of the stress invariants,

$$\tau_{oct} = \frac{\sqrt{2}}{3} \sqrt{I_1^2 + 3I_2} \quad (2A-30)$$

It should be no surprise that the octahedral shear stress is an invariant, since it is a function of the principal stresses at a point, each of which is itself an invariant, that is, it is independent of the orientation of the x -, y -, z -axes. However, the expression for the octahedral shear stress is of interest, as will be seen.

In terms of the principal stresses, the octahedral shear stress is

$$\tau_{oct} = \frac{1}{3} \sqrt{(\sigma_1 - \sigma_3)^2 + (\sigma_2 - \sigma_1)^2 + (\sigma_3 - \sigma_2)^2} \quad (2A-31)$$

In terms of the nonprincipal stresses, the octahedral shear stress is

$$\tau_{oct} = \frac{1}{3} \sqrt{(\sigma_x - \sigma_y)^2 + (\sigma_y - \sigma_z)^2 + (\sigma_z - \sigma_x)^2 + 6(\tau_{xy}^2 + \tau_{yz}^2 + \tau_{zx}^2)} \quad (2A-32)$$

III. Stress Deviator Tensor

In the analysis of elastic deformation, the stress tensor can be split into two parts, the *spherical* stress tensor and the stress *deviator* tensor. The spherical stress tensor is the stress tensor whose elements are

$$\sigma_m \delta_{ij} = \begin{bmatrix} \sigma_m & 0 & 0 \\ 0 & \sigma_m & 0 \\ 0 & 0 & \sigma_m \end{bmatrix} \quad (2A-33)$$

where $\sigma_m = \frac{1}{3}(\sigma_1 + \sigma_2 + \sigma_3) = \frac{1}{3}(\sigma_x + \sigma_y + \sigma_z) = \frac{1}{3}I_1$ is the hydrostatic stress σ_{hyd} . Define the stress deviator tensor as follows:

$$S'_{ij} = \sigma_{ij} - \sigma_m \delta_{ij} \quad (2A-34)$$

or

$$S'_{ij} = \begin{bmatrix} \sigma_x - \sigma_m & \tau_{xy} & \tau_{xz} \\ \tau_{xy} & \sigma_y - \sigma_m & \tau_{yz} \\ \tau_{xz} & \tau_{yz} & \sigma_z - \sigma_m \end{bmatrix}$$

$$S'_{ij} = \begin{bmatrix} \frac{2\sigma_x - \sigma_y - \sigma_z}{3} & \tau_{xy} & \tau_{xz} \\ \tau_{xy} & \frac{2\sigma_y - \sigma_z - \sigma_x}{3} & \tau_{yz} \\ \tau_{xz} & \tau_{yz} & \frac{2\sigma_z - \sigma_x - \sigma_y}{3} \end{bmatrix} \quad (2A-35)$$

In terms of the principal stresses, the stress deviator tensor is

$$S'_{ij} = \begin{bmatrix} \sigma_1 - \sigma_m & 0 & 0 \\ 0 & \sigma_2 - \sigma_m & 0 \\ 0 & 0 & \sigma_3 - \sigma_m \end{bmatrix}$$

$$S'_{ij} = \begin{bmatrix} \frac{2\sigma_1 - \sigma_2 - \sigma_3}{3} & 0 & 0 \\ 0 & \frac{2\sigma_2 - \sigma_3 - \sigma_1}{3} & 0 \\ 0 & 0 & \frac{2\sigma_3 - \sigma_1 - \sigma_2}{3} \end{bmatrix} \quad (2A-36)$$

To obtain the invariants of the stress deviator tensor, in Eq. 2A-22 replace S by $S' + (1/3)I_1$ to get

$$S'^3 - J_1 S'^2 - J_2 S' - J_3 = 0 \quad (2A-37)$$

where

$$J_1 = 0$$

$$J_2 = \frac{1}{3}(I_1^2 + 3I_2)$$

$$J_3 = \frac{1}{27}(2I_1^3 + 9I_1 I_2 + 27I_3) \quad (2A-38)$$

Of these J terms, J_2 is of particular interest. J_2 is expressed in terms of the stress components as

$$J_2 = \frac{1}{6}[(\sigma_x - \sigma_y)^2 + (\sigma_y - \sigma_z)^2 + (\sigma_z - \sigma_x)^2 + 6(\tau_{xy}^2 + \tau_{yz}^2 + \tau_{zx}^2)] \quad (2A-39)$$

or in terms of the principal stresses as

$$J_2 = \frac{1}{6}[(\sigma_1 - \sigma_2)^2 + (\sigma_2 - \sigma_3)^2 + (\sigma_3 - \sigma_1)^2] \quad (2A-40)$$

And comparing J_2 in Eq. 2A-38 with the expression for τ_{oct} in 2A-30, it is seen that

$$J_2 = \frac{3}{2}\tau_{oct}^2 \quad (2A-41)$$

APPENDIX 2-3: STRESS FORMULAS UNDER SIMPLE LOADING CONDITIONS

I. Bending of a Beam

Consider the beam of rectangular cross section in Fig. 2A-42. The depth of the beam is denoted as d . The width of the beam is denoted as b . An external moment M

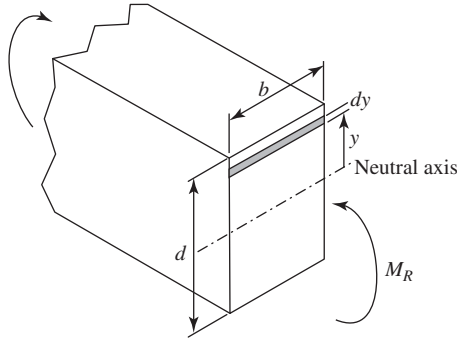


Fig. A2.3.2a-1. Free-body diagram of a beam under pure bending.

is applied to the beam. A resisting moment M_R must be developed to balance the external moment. It is assumed that the bending stress in the beam varies linearly from the neutral axis to the surface, being tensile at one surface and compressive at the other surface. The distance from the neutral axis parallel to d is denoted as y . The maximum value of y is $d/2$.

Consider a differential layer of material of height dy and width b . The resisting moment associated with this layer is dM_R . dM_R is given by the force dF acting on this layer $dF = [y/(d/2)]\sigma_{\max}b dy$ multiplied by the moment arm y , that is, $dM_R = (2y^2/d)\sigma_{\max}b dy$.

The total resisting moment is obtained by integrating the above expression between the limits of $-d/2$ and $d/2$:

$$\begin{aligned} M_R &= \int_{-d/2}^{d/2} dM_R = \int_{-d/2}^{d/2} \frac{2y^2}{d} \sigma_{\max} b dy \\ &= \frac{2y^3}{3d} \sigma_{\max} b \Big|_{-d/2}^{d/2} = 2 \times \frac{2(d/2)^3}{3d} \sigma_{\max} b = \frac{\sigma_{\max} b d^2}{6} \end{aligned}$$

or

$$\sigma_{\max} = \frac{6M}{bd^2} \quad (2A-42)$$

II. Torsion of a Circular Shaft

Consider a circular shaft of radius R ; an external torque T is applied to the shaft (Fig. A2.3.2a-2). A resisting torque T_R must be developed to balance the applied torque.

It is assumed that the shear stress developed in the shaft varies linearly from zero at the center of the shaft to a maximum at the surface of the shaft. The radial distance from the center of the shaft is r . The maximum value of r is R . Consider a differential

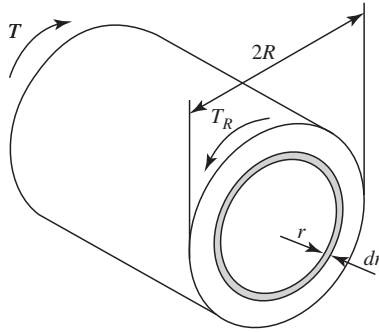


Fig. A2.3.2a-2. Free-body diagram of a circular shaft under torque.

area of radius r and thickness dr . The resisting torque associated with this area is dT_R .

$$\begin{aligned} dT_R &= (\tau_{\max} 2\pi r dr) r \left(\frac{r}{R} \right) \\ &= \frac{2\pi \tau_{\max}}{R} r^3 dr \\ T_R &= \int_0^R \frac{2\pi \tau_{\max}}{R} r^3 dr = \frac{2\pi \tau_{\max}}{R} \left[\frac{r^4}{4} \right]_0^R = \frac{1}{2} \pi \tau_{\max} R^3 \end{aligned}$$

or

$$\tau_{\max} = \frac{2T}{\pi R^3} \quad (2A-43)$$

III. Thin-Walled Cylinder

A thin-walled cylinder subjected to an internal pressure p is shown in Fig. A2.3.2a-3. The cylinder has an inner diameter of D and a wall thickness of t . The normal stress component on a transverse section is known as *longitudinal stress*, which is denoted

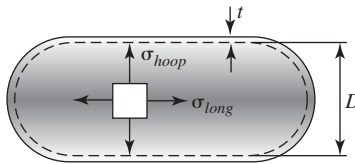


Fig. A2.3.2a-3. A thin-walled cylinder subjected to an internal pressure.

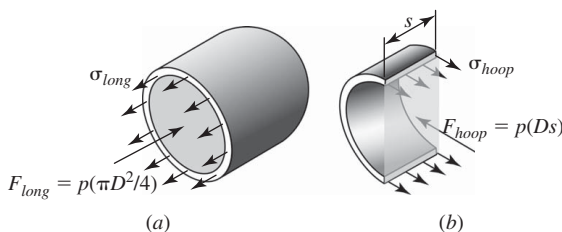


Fig. A2.3.2a-4. (a) Free-body diagram exposing longitudinal stress. (b) Free-body diagram exposing hoop stress.

as σ_{long} . The normal stress component on a longitudinal section is known as *hoop* or *circumferential stress* and is denoted as σ_{hoop} .

The free-body diagram used to determine the longitudinal stress is shown in Fig. A2.3.2a-4a. Consider an equilibrium condition of forces in the longitudinal direction:

$$\pi D t \sigma_{long} = \frac{\pi D^2}{4} p$$

or

$$\sigma_{long} = \frac{pD}{4t} \quad (2A-44)$$

The free-body diagram used to determine the hoop stress is shown in Fig. A2.3.2a-4b. Consider an equilibrium condition of forces in a transverse direction:

$$2st\sigma_{hoop} = pDs$$

or

$$\sigma_{hoop} = \frac{pD}{2t} \quad (2A-45)$$

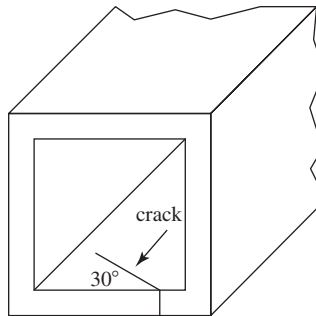
PROBLEMS

2-1. The circumferential (hoop) stress, σ_h , is given as $\sigma_h = \frac{pD}{2t}$. The fuselage skin of the Comet was a high-strength aluminum alloy, 0.91 mm thick. The fuselage was approximately 3.7 m in diameter and 33 m long. Standard atmospheric pressure is 1.013×10^5 Pa.

- At (a), determine the hoop stress in the fuselage in Prob. 1-1 at the cruising altitude of 10,000 m (32,800 ft).
- Assume that design details introduce a stress concentration of 3.0. Compute the maximum stress developed.

2-2. A thin-walled box beam was subjected to in-phase cyclic bending and torsional stresses in service. After a period of time, a crack at 30° to the transverse

direction was discovered in the lower wall of the box beam. Use the Mohr circle to determine the ratio of the bending stress to the shear stress.



2-3. Consider three flat, identical 2 mm (0.08 in.) thick steel ($E = 207 \text{ GPa}$ (30,000 ksi), $\nu = 0.25$) tensile specimens that contain a centrally located through-hole of radius a whose axis is in the thickness direction. The origin of the in-plane x, y coordinate system is at the center of the hole, with the y -direction being in the loading direction of the specimen. The specimens are each loaded in tension to a stress of 69 MPa (10 ksi). The stress developed at the point $\pm a, 0$ is 207 MPa (30 ksi), and the stress developed at $0, \pm a$ is -69 MPa (10 ksi). Consider the stress in the thickness direction to be zero when the specimens are independently loaded (plane stress).

- (a) What are the strains that develop at the coordinate positions given above?
- (b) Next, consider that the three specimens are firmly bonded together along their flat faces to form a single tensile specimen. This specimen is then loaded to 69 MPa (10 ksi), with the interfaces remaining plane. What are the stresses at mid-thickness at the coordinate positions given above?

2-4. Show that the dilatation, Δ , is equal to $\varepsilon_x + \varepsilon_y + \varepsilon_z$.

3

Elements of Plastic Deformation

I. INTRODUCTION

Plastic deformation in metals occurs as a result of the motion of line defects known as *dislocations*. These dislocations move at relatively low shear stresses compared to the theoretical shear strength. In this chapter the characteristics of dislocations are briefly described. Yield criteria for multiaxial stress states are discussed, as is the state of stress in the plastic zone ahead of a notch.

II. THEORETICAL SHEAR STRENGTH

The basic entity involved in plastic deformation is the dislocation, a line defect, which moves through a crystal (grain) on the shear plane in response to a shear stress, breaking bonds sequentially, line by line. Dislocation motion results in actual shear strengths which are much lower than the theoretical shear strength which is determined on the assumption that all bonds on the slip plane are broken simultaneously, not sequentially. The theoretical shear strength, as shown below,

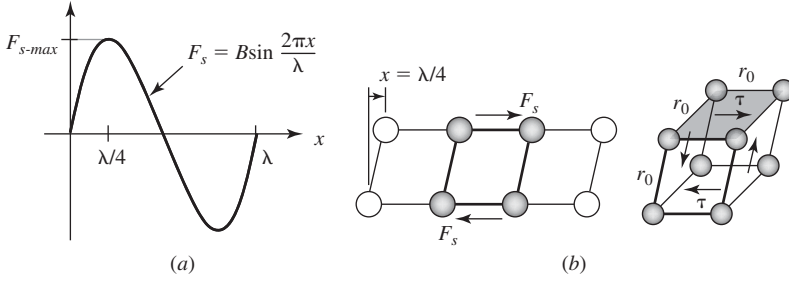


Fig. 3-1. Shear force development during slip.

is of the order of $G/10$, whereas the actual shear strength is more like $G/100$. The theoretical shear strength is estimated as follows.

Consider an approximate relationship between the shear force F_s and the shearing displacement of the adjacent crystallographic planes as in Fig. 3-1a,

$$F_s = B \sin \frac{2\pi x}{\lambda} \approx B \frac{2\pi x}{\lambda} \quad \text{for } x \ll \lambda \quad (3-1)$$

at

$$x = \lambda/4$$

$$F_s \equiv F_{s-\max} = B \quad (3-2)$$

Where $F_{s-\max}$ is the maximum value of F_s .

From Fig. 3-1b,

$$\tau_{\max} = \frac{B}{r_0^2} \quad (3-3)$$

From Eq. 3-1,

$$dF_s = B \frac{2\pi}{\lambda} dx \quad (3-4)$$

$$d\tau = \frac{B}{r_0^2} \frac{2\pi}{\lambda} dx \quad (3-5)$$

Using the definition of a shear strain γ ,

$$\gamma = \tan \frac{x}{r_0} \approx \frac{x}{r_0} \quad \text{for } x \ll r_0 \quad (3-6)$$

$$d\gamma = \frac{1}{r_0} dx \quad (3-7)$$

Using the definition of the shear modulus G ,

$$G = \frac{d\tau}{d\gamma} = \frac{\frac{B}{r_0^2} \frac{2\pi}{\lambda} dx}{\frac{1}{r_0} dx} = \frac{2\pi B}{r_0 \lambda} \quad (3-8)$$

For

$$\lambda = r_0, \quad G = 2\pi \tau_{\max} \quad (3-9)$$

$$\tau_{\max} = \frac{G}{2\pi} \approx \frac{G}{10} \quad (3-10)$$

III. DISLOCATIONS

If one were to apply the above expression for the theoretical shear strength to the case of a single crystal of a metal, it would be assumed that all of the atoms just above the plane of shearing move in one direction in unison and those atoms just below the plane of shearing move in the opposite direction, also in unison. If this were the case, the strengths of metals would be much higher than we know them to be. Why, then, are the shear strengths of metals more like $G/100$ rather than $G/10$? The answer to this question was provided in 1934 when three independent researchers, Orowan, Taylor, and Polyani, introduced the concept of the *edge dislocation*. In 1939 Burgers introduced the concept of the *screw dislocation*. Both edge and screw dislocations are line defects in the crystal and are the basic entities that allow, as we shall see, plastic deformation to occur at stress levels that are much lower than the theoretical strength due to the motion of these line defects.

Figure 3-2a shows a perfect crystal lattice that is free of defects.

Figure 3-2b shows a portion of a crystal that contains a line defect known as a *positive edge dislocation*. An extra half-plane of atoms, t shaded area in Fig. 3-2b, is associated with an edge dislocation. If the extra half-plane were below the slip plane, the line defect would be referred to as a *negative edge dislocation*.

Fig. 3-2c shows a portion of a crystal that contains a line defect known as a left-hand *screw dislocation*. The lower portion of this figure shows how the atoms are arranged around a screw dislocation.

A detailed view of the arrangement of atoms around a left-hand screw dislocation is shown in Fig. 3-3. Two planes of atoms are shown. In the upper plane, the atoms are represented by open circles. In the lower plane, the atoms are represented by filled circles. Away from the dislocation, the lattice is perfect, and filled circles are directly below open circles. However, in the vicinity of the screw dislocation, a perfect lattice does not exist.

In the lower portion of the figure, atom 1 is in the lower level, and atom 2 is just above. Suppose a circuit were to be made starting at atom 1, then moving up to

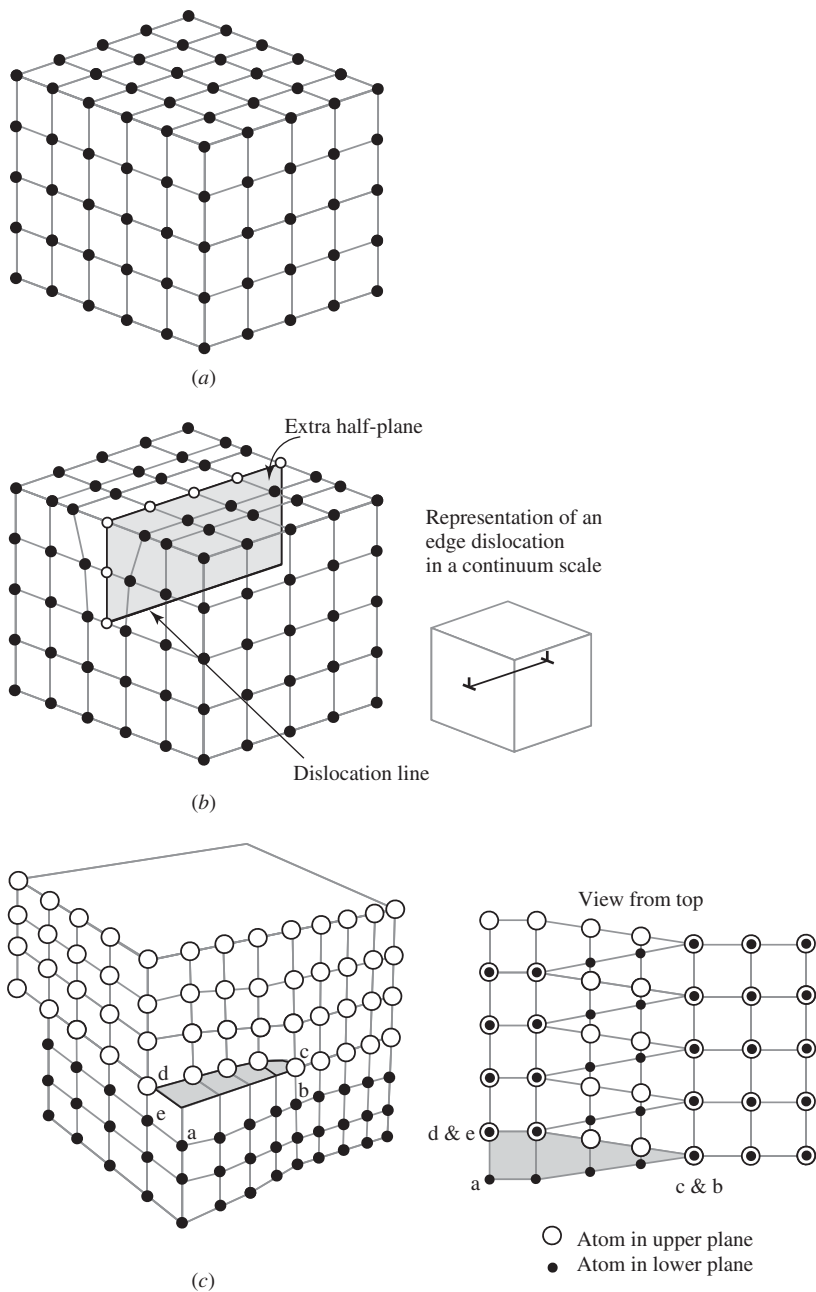


Fig. 3-2. Dislocation. (a) Perfect crystal. (b) Edge dislocation. (c) Screw dislocation.

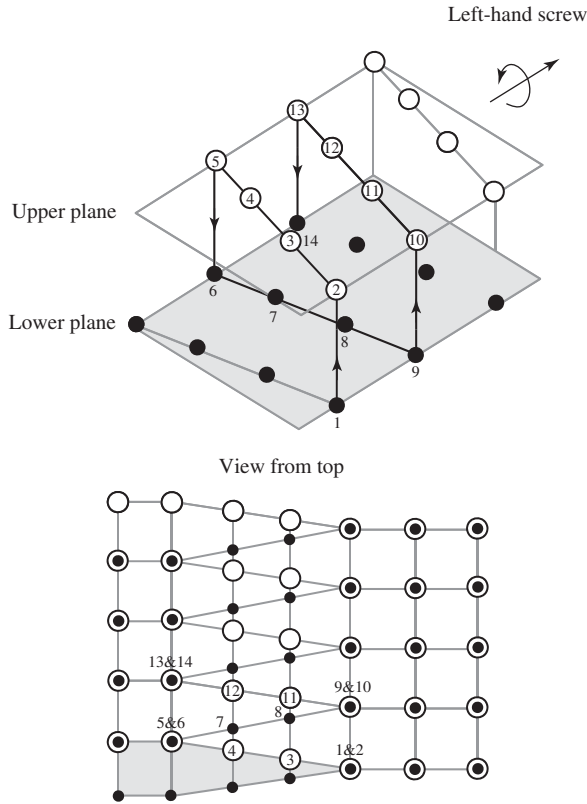


Fig. 3-3. Arrangement of atoms round a left-hand screw dislocation.

atom 2, then moving 4 atoms up the page, then dropping to the lower level, and then moving 4 atoms down the page. We would arrive back at the starting point, atom 1. However, if we again started at atom 1 in the lower level and moved to atom 2, and then moved three atom distances to atom 5, and then to atom 6 in the lower level, and then three atom distances to atom 9, we would find that we were not back at the starting point, atom 1. A vector from atom 9 to atom 1 would be needed to close the circuit. This vector is known as the *Burgers vector*, and it is always oriented in the slip direction.

Fig. 3-4 is similar to the lower portion of Fig. 3-3 and is a schematic drawing of two parallel planes of atoms. The open circles represent atoms in the plane just above the slip plane, and the solid circles represent atoms in the plane just below the slip plane. In this figure, a dislocation loop is shown. Note that dislocation loops consist of edge and screw components. In this figure, the edge components of the loop run horizontally near the top and bottom of the figure, and the screw components run vertically at the sides of the figure. Note that the sense of the upper edge dislocations is opposite to that of the lower and that the sense of one screw dislocation component

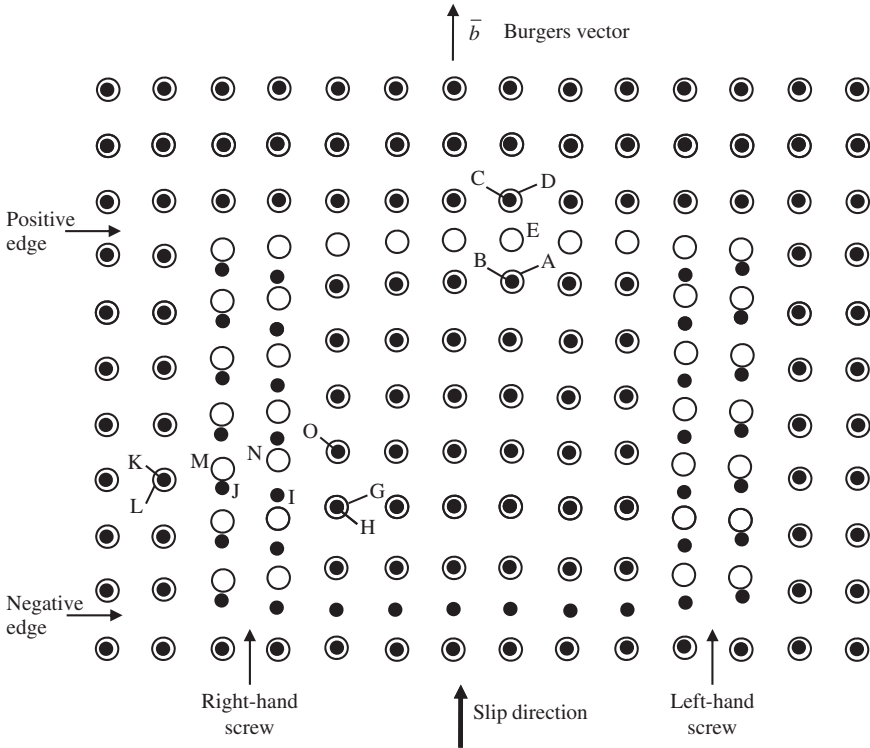


Fig. 3-4. A schematic of a dislocation loop. The right-hand screw (RHS) portion of the dislocation loop is on the left side of the figure and runs in the vertical direction. The left-hand screw (LHS) portion is on the right side of the figure and also runs in the vertical direction. A positive edge dislocation is near the top of the figure in the horizontal direction, and a negative edge dislocation is at the bottom.

of the loop is also opposite to that of the other. Under the action of a shear stress applied such that the upper plane is sheared upward on the page and the lower plane downward, the dislocation loop will expand. In this process, the atoms along the dislocation loop in the upper and lower planes change their positions slightly. If the direction of shearing were reversed, the dislocation loop would shrink and eventually annihilate itself.

A characteristic of a dislocation loop is that the Burgers vector is constant. Since the Burgers vector is perpendicular to the edge segment, a slip plane is defined and the edge segment is confined to move in this plane. However, the screw segments are parallel to the Burgers vector and therefore are not confined to move only in the slip plane. In fact, the screw segments may move onto slip planes that intersect the primary slip plane in a process known as *cross-slip*. This process is important in the widening of slip bands and in the nucleation of fatigue cracks. A dislocation in a slip plane is said to be *glissile*; a dislocation on a nonslip plane is said to be *sessile*.

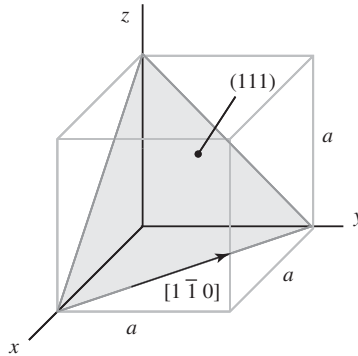


Fig. 3-5. Octahedral plane (shaded) and a slip direction.

The crystallographic planes and directions are identified by their Miller indices. The Miller index for a plane in the cubic system is given as the reciprocals of the intercepts of the plane with the crystallographic axes, reduced to the smallest integers and written in parentheses. $()$ are used in identifying a specific slip plane, $\{ \}$ are used in describing a class of similar slip planes, $[]$ are used in identifying a specific direction, and $\langle \rangle$ are used in describing a class of similar directions. A (111) plane is shown in Fig. 3-5. A direction is specified in terms of its components along the cube axes, again reduced to the smallest whole numbers and written in brackets. A $[1 \bar{1} 0]$ direction is also shown in Fig. 3-5. The combination of a slip plane and a slip direction is known as a *slip system*, and in face-centered cubic (fcc) crystals there are 12 of them, that is, four planes with three directions per plane, each of the (111) $[1 \bar{1} 0]$ type. The four planes comprise the faces of a regular tetrahedron, with the slip directions being the edges of the tetrahedron. It is generally considered that at least five independent slip systems must be available in order to carry out complex plastic deformation processes such as the formation of a neck during tensile straining. The fact that 12 independent systems are available in fcc crystals is in accord with the generally high ductility of such crystals, even at very low temperatures. However, ionic single crystals have only two independent slip systems. Such crystals may extend plastically by as much as 10%, but when failure occurs, it does so in a brittle manner by cleavage on (100) planes. The low-temperature brittle behavior of other materials, such as zinc crystals and beta-nickel-aluminides, is similarly related to the availability of less than five independent slip systems. However, at higher temperatures, slip in these materials can take place on additional crystallographic planes and the materials then behave in a ductile fashion, and a brittle-to-ductile transition temperature can be defined.

The resolved shear stress in a crystal is the shear stress acting on the slip plane in the slip direction of the crystal, as shown in Fig. 3-6. The onset of plastic deformation in a tensile test of a single crystal often occurs at a critical value of the shear stress that is independent of the orientation of the crystal with respect to the tensile axis. For a cylindrical single crystal of cross-sectional area A , if ϕ is the angle between

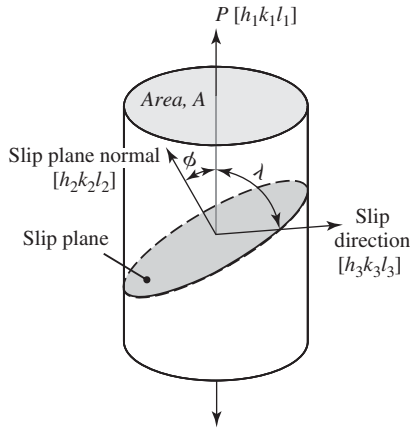


Fig. 3-6. Resolved shear stress.

the specimen axis and the slip-plane normal, then the area of the slip plane is given as $A / \cos \phi$. If λ is the angle between the specimen axis and the slip direction, then the component of axial load P acting in the slip direction is $P \cos \lambda$. The resolved shear stress, τ_{res} is given as

$$\tau_{res} = \frac{P \cos \lambda}{A / \cos \phi} = \sigma \cos \phi \cos \lambda \quad (3-11)$$

where σ is the tensile stress. In a tensile test of a single crystal, when plastic deformation occurs, slip steps are created on the surface due to the sliding action of adjacent parallel planes. Usually, a group of closely spaced, parallel planes are involved so that, instead of a single step, a group of steps, referred to as a *slip band*, is created. A number of these slip bands will be present on the surface of the crystal, with the number increasing with increase in strain.

Miller indices are not only useful in describing crystallographic planes and directions but also in carrying out calculations involving single crystals. For example, the spacing d between crystallographic planes in the cubic system is given as

$$d = \frac{a}{\sqrt{h^2 + k^2 + l^2}} \quad (3-12)$$

where a is the lattice parameter, that is, the length of the cube edge of the unit cell, and h , k , and l are the Miller indices of the plane. As another example, the cosine terms in Eq. 3-11 can be expressed in terms of Miller indices as follows: Let:

$[h_1 k_1 l_1]$ represent the Miller indices of the direction of loading,

$[h_2 k_2 l_2]$ represent the Miller indices of the direction of the slip plane normal, and

$[h_3 k_3 l_3]$ represent the Miller indices of the slip direction.

Then

$$\cos \phi = \frac{1}{\sqrt{h_1^2 + k_1^2 + l_1^2} \sqrt{h_2^2 + k_2^2 + l_2^2}} (h_1 h_2 + k_1 k_2 + l_1 l_2) \quad (3-13)$$

and

$$\cos \lambda = \frac{1}{\sqrt{h_1^2 + k_1^2 + l_1^2} \sqrt{h_3^2 + k_3^2 + l_3^2}} (h_1 h_3 + k_1 k_3 + l_1 l_3) \quad (3-14)$$

Such relationships are important in analyzing the behavior of single-crystal turbine blades, for example. However, in dealing with plastic deformation of polycrystalline alloys, a macroscopic, continuum approach is usually used in which the behavior of the many individual crystals involved is averaged out. The tensile test provides basic data for characterizing a material's mechanical behavior. The information to be obtained in such a test is the Young's modulus, the yield strength, the ultimate tensile strength, the percentage of elongation in a specified gauge length, and the percentage of reduction in area. In a test of a low-carbon steel, an upper and lower yield level will be evident, and it is usual to take the lower yield level in specifying the yield strength. The phenomenon of an upper and lower yield strength in low-carbon steel is due to the interaction of carbon with dislocations. This interaction prevents dislocation motion until the upper yield stress level is reached, whereupon the dislocations break away and new dislocations are created free of the restraint of the carbon atoms. In low-carbon steel, plastic deformation is usually initiated at a strain of the order of 0.001 at the shoulders of the specimen because of slightly higher stresses in this region due to stress concentrations. The plastic deformation then spreads at the lower yield level into the remainder of the test section in a series of parallel bands known as *Lüder's bands*. At a strain of the order of 0.01, the test section will be completely filled with these parallel bands, and the end of the lower yield level behavior is reached. Further straining results in the interaction of dislocations, and as a result, strain hardening develops. The strain hardening is manifested by an increase in the stress required for further deformation until the ultimate tensile stress is reached. Thereafter, the stress drops until the breaking stress is reached, and the specimen fractures. It is noted that three instabilities develop during the course of a tensile test of a low-carbon steel. One occurs at the transition from the upper to the lower yield point, the second occurs at the maximum stress, and the third occurs at the breaking stress. The breaking stress is not a true material property, but is a reflection of the testing machine stiffness that determines its ability to shed load in the latter part of a tensile test. Under dead weight loading, for example, a type of loading corresponding to zero stiffness, the breaking stress would coincide with the ultimate tensile stress. On the other hand, in a very stiff machine, it is possible to decrease the breaking stress to a very low value.

The upper and lower yield levels characteristic of low-carbon steel are not observed in most other alloys. In order to define a yield strength in such cases, an offset method is used in which a line is drawn parallel to the elastic loading line but offset from it by a specified amount of strain such as 0.002 (0.2%). The yield strength is defined as the point at which this line intersects the stress-strain curve.

In the mathematical treatment of plastic deformation, certain simplifications are made that reduce the complexity of the stress analysis. One basic assumption is that the volume remains constant, that is, $\Delta V = 0$. This is a reasonable assumption since the plastic deformation process is a shearing process involving the sliding of one element of material over another without a change in volume being involved. The dilatation Δ is given as

$$\Delta = \varepsilon_x + \varepsilon_y + \varepsilon_z \quad (3-15)$$

For plastic deformation, Δ is zero, since $\Delta V = 0$. In plane-strain with ε_z equal to zero, it follows that $\varepsilon_x = -\varepsilon_y$. There is only one independent component of strain in plane-strain plastic deformation, since the diameter of the Mohr circle is given as the difference between these two strains. Similarly, if work hardening is neglected, by setting the maximum shear stress in the plastic region equal to k , a material constant, there remains only one independent stress.

The value of Poisson's ratio for purely plastic deformation can also be evaluated, making use of the assumption that Δ is equal to zero. In a tensile test, the lateral strain $\varepsilon_y = \varepsilon_z = -\nu\varepsilon_x$; hence $\Delta V = \varepsilon_x - 2\nu\varepsilon_x$. For constancy of volume, $\Delta V = 0$, and therefore $\nu = 1/2$. (Note that in the elastic range where $\nu < 1/2$, there is a volume expansion in tension and a volume contraction in compression.)

Therefore, in plane-strain plastic deformation, Eq. 2-20c becomes

$$\sigma_z = \frac{1}{2}(\sigma_x + \sigma_y) \quad (3-16)$$

and Eq. 2-18 becomes

$$\sigma_{hyd} = \frac{1}{3} \left[\sigma_x + \sigma_y + \frac{1}{2} (\sigma_x + \sigma_y) \right] = \frac{1}{2} (\sigma_x + \sigma_y) = \sigma_z \quad (3-17)$$

IV. YIELD CRITERIA FOR MULTIAXIAL STRESS

An excessive amount of plastic deformation can itself be considered to be a type of failure. For simple tension loading, it is only necessary to keep the tensile stress below the yield stress to avoid problems associated with plastic deformation. However, many components are subjected to multiaxial stresses, and criteria for yielding under such stress states are needed for purposes of design and analysis. This section deals with the two most commonly used yield criteria.

A. Distortional (Shear) Energy Criterion

For a multiaxial stress state, the distortional energy criterion (or von Mises criterion) predicts that yielding will occur when the distortional energy of the combined stress state equals the distortional energy at yield in simple tension. As a result of this

assumption, the following criterion is derived. (Details of a derivation are shown in Appendix 3-1.)

$$\frac{1}{\sqrt{2}} \sqrt{(\sigma_1 - \sigma_3)^2 + (\sigma_2 - \sigma_1)^2 + (\sigma_3 - \sigma_2)^2} = \sigma_Y \quad (3-18)$$

The quantity on the left-hand side is designated as $\bar{\sigma}$; it is known as the *equivalent stress* for the combined stress state and is equal to the yield stress in simple tension. Note that since $\bar{\sigma}$ is based upon shear stresses, it has no hydrostatic component. A $\bar{\sigma}$ is also referred to as the *flow stress* in dealing with plastic deformation that exceeds the yield strain where strain hardening is important; that is, the yield strength is a function of the amount of plastic strain.

In pure shear $\sigma_1 = -\sigma_3 = k$, where k is the shear stress at yield in pure shear, and $\sigma_2 = 0$. Therefore, $\bar{\sigma} = \sqrt{3}k$, or $k = \bar{\sigma}/\sqrt{3}$. This leads to an expression for the equivalent shear stress:

$$\bar{\tau} = \sqrt{\frac{1}{6} [(\sigma_1 - \sigma_3)^2 + (\sigma_2 - \sigma_1)^2 + (\sigma_3 - \sigma_2)^2]} \quad (3-19)$$

An equivalent strain,

$$\bar{\varepsilon} = \sqrt{\frac{1}{2(1+\nu)^2} [(\varepsilon_1 - \varepsilon_3)^2 + (\varepsilon_2 - \varepsilon_1)^2 + (\varepsilon_3 - \varepsilon_2)^2]} \quad (3-20)$$

can also be defined. For plastic deformation where $\nu = 1/2$, the equivalent strain becomes

$$\bar{\varepsilon} = \sqrt{\frac{2}{9} [(\varepsilon_1 - \varepsilon_3)^2 + (\varepsilon_2 - \varepsilon_1)^2 + (\varepsilon_3 - \varepsilon_2)^2]} \quad (3-21)$$

For pure shear, $\varepsilon_1 = -\varepsilon_3 = \gamma/2$ and $\varepsilon_2 = 0$. Therefore, $\bar{\varepsilon} = (2/\sqrt{3})\varepsilon_1$, or $\varepsilon_1 = (\sqrt{3}/2)\bar{\varepsilon}$, or $\gamma = \sqrt{3}\bar{\varepsilon}$. This leads to the expression

$$\bar{\gamma} = \sqrt{\frac{2}{3} [(\varepsilon_1 - \varepsilon_3)^2 + (\varepsilon_2 - \varepsilon_1)^2 + (\varepsilon_3 - \varepsilon_2)^2]} \quad (3-22)$$

B. Maximum Shear Stress Criterion

The Tresca criterion,

$$\bar{\tau} = \frac{(\sigma_1 - \sigma_3)}{2} \quad (3-23)$$

is a maximum shear stress criterion and does not depend upon σ_2 . In general, the von Mises criterion is favored, but the Tresca criterion, because of its simple form in terms of principal stresses, is useful for purposes of illustration.

Figure 3-7 is a plot of the von Mises and Tresca yield criteria in two-dimensional stress space, that is, one of the three principal stresses is zero. For this diagram, the yield strength in tension is taken to be the common reference point.

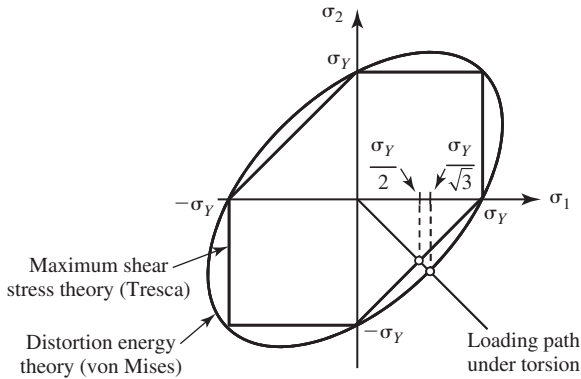


Fig. 3-7. The Tresca and von Mises yield criteria for plane stress.

V. STATE OF STRESS IN THE PLASTIC ZONE AHEAD OF A NOTCH IN PLANE-STRAIN DEFORMATION

In the elastic region, the determination of the state of stress ahead of notch is a relatively complex problem involving use of the theory of elasticity. In contrast, it is relatively simple to determine the state of stress in the plastic zone ahead of a notch under plane-strain loading conditions. The analysis of this state of stress provides insight as to why fracture processes are promoted by plane-strain loading conditions at notches and cracks.

Recall that for plastic deformation the volume is conserved and Poisson's ratio ν is equal to $1/2$. From the Mohr circle it can be seen that the normal stress acting on the plane of maximum shear stress is given as $\sigma_n = (\sigma_1 + \sigma_3)/2$. Under plane-strain conditions, this normal stress is also equal to σ_2 , which is the hydrostatic stress, σ_{hyd} (Eq. 3-17). In Fig. 3-8, this hydrostatic stress is shown acting in the radial and tangential directions of the curved element, that is, perpendicular to the planes

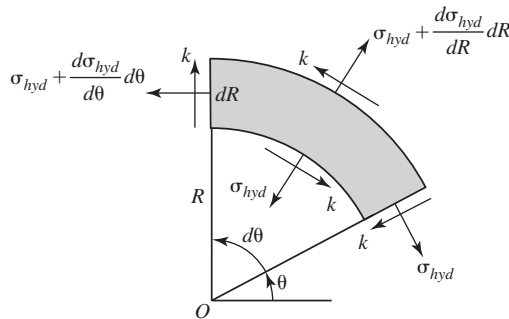


Fig. 3-8. The stress components acting on an element within the plastic range. The maximum shear stress required for plastic deformation is designated as k .

of maximum shear stress. The material is considered to be an ideally rigid plastic material, that is, elastic strains and strain hardening are neglected.

In the plastic regions, the traces of the planes of maximum shear stress are known as *slip lines*. In a plastic zone, the magnitude of the maximum shear stress is indicated by k , which is the yield stress in shear (torsion). The value of k depends upon the yield criterion when the tensile yield strength is taken as the standard of reference. When one of the three principal stresses is equal to zero, the yield surface for the von Mises criterion appears as an elongated ellipse, whereas the yield surface for the Tresca criterion appears as an elongated hexagon inscribed within the von Mises ellipse, as shown in Fig. 3-7. The value of σ_1 at the yield stress in torsion (pure shear) is designated as k . According to the von Mises criterion, $k = \sigma_Y/\sqrt{3}$. According to the Tresca criterion, $k = \sigma_Y/2$.

In Fig. 3-8, the value of θ is taken to be positive in the counterclockwise direction, and by taking moments about the origin, the following equation is obtained:

$$\Sigma M_O = 0$$

$$\frac{d\sigma_{hyd}}{d\theta}(d\theta)dR \left(R + \frac{dR}{2} \right) + k(R + dR)d\theta(R + dR) - kR d\theta R = 0 \quad (3-24)$$

which leads to

$$\frac{d\sigma_{hyd}}{d\theta} + 2k = 0 \quad (3-25)$$

or

$$d\sigma_{hyd} + 2k d\theta = 0 \quad (3-26)$$

which can be integrated to yield

$$\sigma_{hyd} + 2k\theta = \text{constant} \quad (3-27)$$

on a curved plane of maximum shear stress. Note that hydrostatic stress is independent of R and depends only on θ , the amount of rotation of the tangent to a slip line on going from one position to another. If the slip line were straight, there would be no change in θ and hence no change in the hydrostatic stress.

As can be seen from the Mohr circle for plane-strain conditions (Fig. 3-9a), σ_{hyd} is at the center of the circle, $\sigma_1 = \sigma_{hyd} + k$, and $\sigma_3 = \sigma_{hyd} - k$.

From Eq. 3-27, we have $\sigma_{hyd} + 2k\theta = \text{constant}$. The constant can be evaluated by noting that, at the free surface of the notch, Fig. 3-10, $\sigma_3 = 0$. If we set $\theta = 0$ along a slip line at this point, as in Fig. 3-10, then the unknown constant is equal to σ_{hyd} , which in turn is equal to k at this point; see Fig. 3.9b. We can then write

$$\sigma_{hyd} = k - 2k\theta \quad (3-28)$$

Note that the hydrostatic component of stress changes with change in θ . Therefore, both σ_1 and σ_3 must also change with θ to maintain the state of stress at the yield level. Any slip line must intersect the x -axis at an angle of $\pi/4$ radians since the

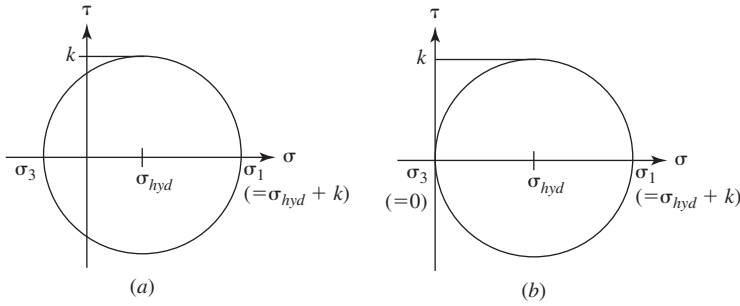


Fig. 3-9. (a) Mohr circle for arbitrary plane-strain plastic deformation. (b) Mohr circle for plane-strain deformation at a free surface.

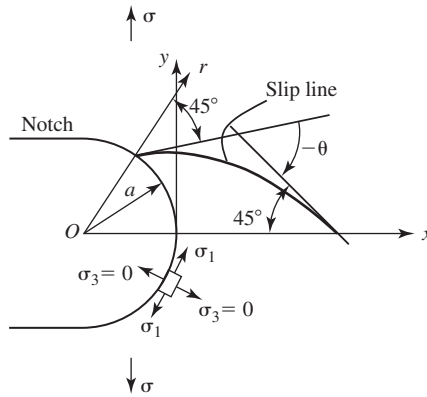


Fig. 3-10. The principal stresses acting at the free surface of a notch subjected to tensile loading.

x -direction is the direction of maximum principal stress. The maximum change in θ (radian) in going from notch to the center line along a slip plane in Fig. 3-10 is $\pi/2$. Therefore, the maximum value for the hydrostatic stress in this case (θ is negative) is

$$\sigma_{hyd} = k + 2k \frac{\pi}{2} = k(1 + \pi) \quad (3-29)$$

and

$$\sigma_1 = k + \sigma_{hyd} = 2k \left(1 + \frac{\pi}{2} \right) \quad (3-30a)$$

and

$$\sigma_3 = \sigma_1 - 2k = 2k \left(1 + \frac{\pi}{2} \right) - 2k = k\pi \quad (3-30b)$$

As mentioned above, the value of k depends upon the yield criterion in plane strain. For the Tresca criterion, $k = \sigma_Y/2$, where σ_Y is the yield strength in simple tension and $2k(1 + \pi/2) = 2.57\sigma_Y$. That is, triaxiality has raised the local stress for yield at a point ahead of the notch by a factor of 2.57!

For the von Mises criterion, $k = \sigma_Y/\sqrt{3}$. Therefore, $2k(1 + \pi/2) = 2.96\sigma_Y$, so that the local stress for yield has been raised by a factor of almost 3! For this reason, the local yield stress in a bar containing a U-shaped notch ($\pi/2$ radians) can be considered to be increased by a factor of 3 in a low-temperature, brittle fracture of steel. If the notch angle is less than $\pi/2$, there will be a corresponding reduction in the maximum stress ahead of the notch since the maximum value of θ is less than $\pi/2$ in assessing the role of a notch in a low-temperature, brittle fracture of steel.

Next, we derive a general expression for the value of σ_1 along the x -axis ahead of a notch. Let x be the distance along the x -axis measured from the tip of a notch of radius a . To develop an expression for the maximum stress acting in the y -direction as a function of the distance from the notch, use is made of the mathematical expression for the log spiral.

The distance r is the radial distance measured from the center of curvature of a notch radius a . The trajectories of σ_1 , the first principal stress, lie along arcs of circles that are concentric with the notch. The trajectories of σ_3 must be at right angles to these circular arcs, that is, they are radial lines. The maximum shear stress trajectories must cross both sets of lines at 45° . The logarithmic or equiangular spiral is a curve that makes a constant angle with the radius vectors (Fig. 3-11a), and hence also with the trajectories of σ_1 .

The curved elements in Fig. 3-8 are taken to be portions of logarithmic spirals that can be mathematically expressed as

$$\frac{r}{a} = e^{-(\cot \phi)\theta} \quad (3-31)$$

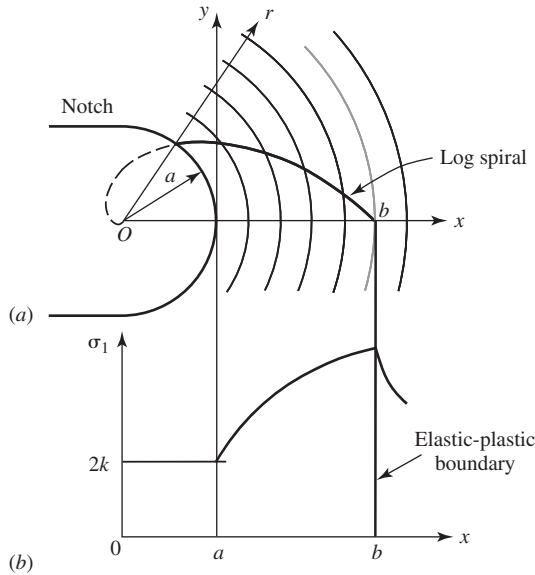


Fig. 3-11. (a) A logarithmic spiral and the principal stress trajectories at a notch subjected to tensile loading. (b) The principal stress perpendicular to the x -axis in the elastic-plastic region ahead of a notch loaded in tension.

and since in this case $\cot 45^\circ = 1$,

$$\frac{r}{a} = e^{-\theta} \quad (3-32)$$

(For a spiral in the opposite sense, $r/a = e^\theta$.)

Where a spiral intersects the notch, $r = a$. Since we are only interested in the change in θ in going from one point along a curved slip line to another, we can set the value of θ at the edge of the notch equal to zero. The angular rotation the spiral makes in going from the intersection point on the notch surface to the x -axis, point b , is θ_b , with the counterclockwise direction taken as positive. The distance Ob to a point where the spiral intersects the x -axis is given as $b = ae^{-\theta_b}$. The distance Ob can be set equal to $a + x$, where x is the distance along the x -axis measured from the notch, so that $a + x = ae^{-\theta_b}$. Therefore,

$$1 + \frac{x}{a} = e^{-\theta_b}$$

or

$$\ln \left(1 + \frac{x}{a} \right) = -\theta_b \quad (3-33)$$

To obtain an expression for σ_1 along the x -axis, this expression for θ_b is substituted into Eq. 3-30a to yield

$$\sigma_1 = 2k + 2k \ln \left(1 + \frac{x}{a} \right) = 2k \left[1 + \ln \left(1 + \frac{x}{a} \right) \right] \quad (3-34)$$

A plot of this relation is shown in Fig. 3-11*b*. It is noted that the value of σ_1 increases from $2k$ up to its maximum value as the distance ahead of the notch increases. Once this maximum value is attained at $\theta_b = -\pi/2$ for a parallel-sided notch, the stress remains constant with further increase in x until the elastic-plastic boundary is reached, whereupon the stress then decreases with a further increase in x . This stress distribution within the plastic zone ahead of a notch is in marked contrast to the elastic behavior where σ_1 is maximum at the notch root. The increase in peak stress within the plastic zone ahead of the notch has clear implications with respect to the site of the origin of fracture in notched components.

Note that under plane stress loading, plastic deformation is through-thickness rather than in-plane and occurs on planes at 45° to the y - z plane. Since the slip lines are straight, the level of the hydrostatic stress is constant throughout the plastic zone. As a result, the peak stress in the plastic zone is also constant and equal to σ_Y .

VI. SUMMARY

In this chapter, the importance of dislocations as the basic elements of plastic deformation has been discussed, and the concept of a critical resolved shear stress for yielding has been introduced. The von Mises and Tresca criteria for yield under

multiaxial states of stress have been discussed, and more detailed information is available in the appendix to this chapter. The final topic considered in this chapter is the state of stress ahead of a notch that is loaded under a condition of plane plastic strain.

FOR FURTHER READING

- (1) G. E. Dieter, Jr., *Mechanical Metallurgy*, 3rd ed., McGraw-Hill, New York, 1986.
- (2) A. Mendelson, *Plasticity: Theory and Application*, Macmillan, New York, 1968.
- (3) I. Le May, *Principles of Mechanical Metallurgy*, Elsevier, Oxford, 1981.
- (4) V. Dias da Silva, *Mechanics and Strength of Materials*, Springer, Berlin, 2006.

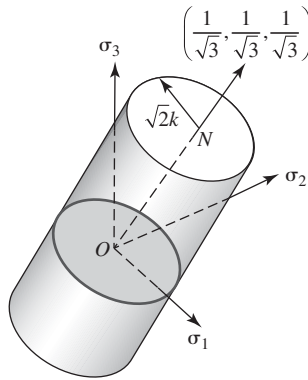
APPENDIX 3-1: THE VON MISES YIELD CRITERION

In three-dimensional stress space, with the coordinate axes aligned with the principal stress directions, a yield surface can be defined that is consistent with the von Mises criterion for yielding. Consider a line passing through the origin and making equal angles with the coordinate axes. Such a line is in the [111] direction, and the stress in this direction is the sum of the components of the three principal stresses resolved in the [111] direction. That is,

$$l_{11}l_{11}\sigma_1 + l_{21}l_{21}\sigma_2 + l_{31}l_{31}\sigma_3 = (\sigma_1 + \sigma_2 + \sigma_3)/3 = \sigma_{hyd} \quad (A3-1)$$

where l_{11} , l_{22} , and l_{33} are the direction cosines between the stress axes and the [111] direction. Therefore, as the distance along [111] increases, so does the magnitude of the corresponding hydrostatic stress.

The deviatoric stresses are in plane that is perpendicular to the [111] direction. The magnitude of the deviatoric stress increases with distance in this plane from the



The von Mises yield surface is the surface of a right circular cylinder of radius

Fig. A3-1. Schematic of the von Mises yield surface.

[111]. Yielding will occur when the radial vector in this plane reaches the critical von Mises value and is independent of the orientation of the radial vector in this plane. The overall yield surface is therefore in the form of a right-circular cylinder whose axis is in the [111] direction, Fig. A3-1.

The cross-sectional plane through the von Mises yield cylinder that passes through the origin and whose normal is in the [11] direction is known as the π plane, Fig. A3-2. On this plane, the hydrostatic stress is zero. If the π plane is rotated about the $[1\bar{1}0]$, until the σ_3 direction becomes normal to the plane of the page, and the with the circumference of the rotated plane retaining contact with the yield cylinder, then the elliptical two-dimensional yield surface shown in Fig. 3-7 is obtained. Fig. 3-7 is useful in dealing with plane stress problems involving σ_1 and σ_2 . Note that σ_3 is zero only in the case of pure shear where $\sigma_1 = -\sigma_2$. For other cases, $\sigma_3 = \sigma_1 + \sigma_2$, since the hydrostatic stress is zero on the π plane. The length of the $[1\bar{1}0]$ line in the rotated plane is seen to be $\sqrt{2}k$. Therefore, the radius of the yield circle in the π plane is also $\sqrt{2}k$, since the length of the $[1\bar{1}0]$ line was unchanged during rotation.

PROBLEMS

3-1. The von Mises criterion can be express in terms of nonprincipal stresses as

$$\frac{1}{\sqrt{2}} \left[(\sigma_x - \sigma_y)^2 + (\sigma_y - \sigma_z)^2 + (\sigma_z - \sigma_x)^2 + 6(\tau_{xy}^2 + \tau_{yz}^2 + \tau_{zx}^2) \right]^{1/2} = \sigma_o$$

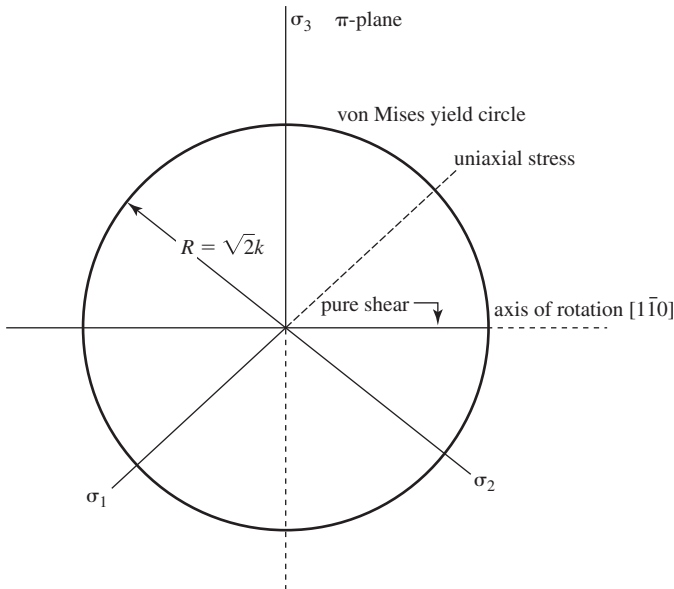


Fig. A3-2. The π plane.

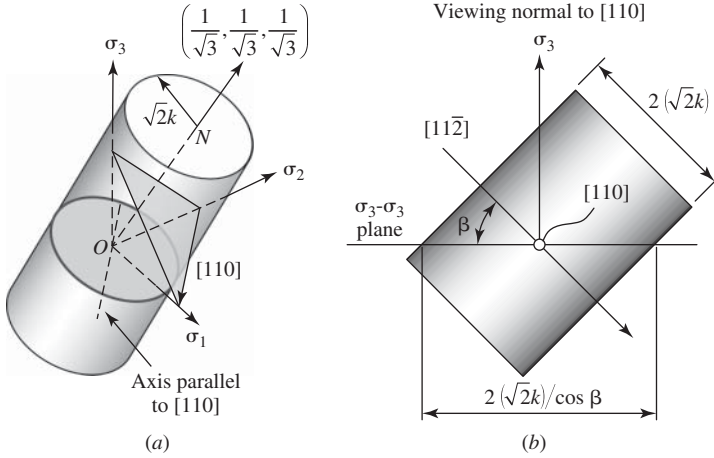


Fig. A3-3.

where σ_o is the yield stress in simple tension.

In the case of a thin-walled cylinder that is subjected to both tension and torsion, this expression reduces to

$$[\sigma_x^2 + 3\tau_{xy}^2]^{1/2} = \sigma_o$$

where the x -direction is taken along the axis of the cylinder.

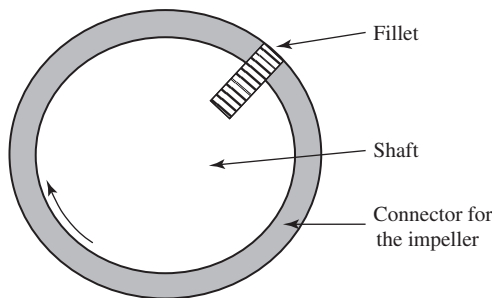
- (a) Plot the first quadrant of the von Mises relationship using σ_x/σ_o and τ_{xy}/σ_o as axes.
- (b) Determine the Tresca equivalent to the von Mises expression

$$[\sigma_x^2 + 3\tau_{xy}^2]^{1/2} = \sigma_o.$$

Plot as in part (a) above and compare with the von Mises predictions.

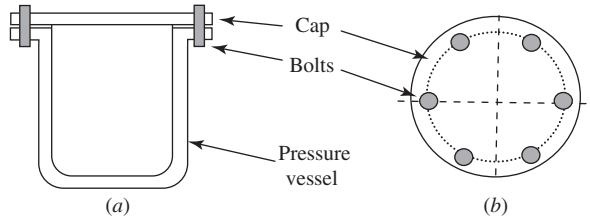
- 3-2. The included angle of the notch in the standard Charpy V-notched specimen is 45° , and the radius of the notch tip is 0.25 mm (0.01 in.).
 - (a) Assume that the material of the Charpy bar is elastic-plastic (no strain hardening). Determine the maximum stress that can exist in a plastic zone ahead of the notch as a function of the uniaxial yield stress, σ_Y , according to the von Mises criterion and also according to the Tresca criterion.
 - (b) At what distance ahead of the notch does this stress first exist?
- 3-3. The hydrostatic stress in plane strain at initial yielding is numerically equal to k , the yield stress in shear. Draw the Mohr circles at yield in tension based upon
 - (a) the Tresca criterion and
 - (b) the von Mises criterion.

- 3-4.** A sheet of material whose yield strength is 275 MPa (39.8 ksi) is biaxially loaded, with one principal stress being 300 MPa (43.5 ksi) and the other 150 MPa (21.7 ksi). According to the Tresca criterion, the material will yield. Will the material yield according to the von Mises criterion? Draw the Mohr circle at yield for each of these criteria.
- 3-5.** A thin-walled spherical shell of diameter 2.5 m (8.2 ft) and thickness 5 mm (0.2 in.) is made of an alloy steel with a yield strength of 1,000 MPa (145 ksi), an elastic modulus of 200 GPa (29,000 ksi), and a Poisson's ratio of 0.33. This container will be used to hold nitrogen gas with a pressure of 5 MPa (0.72 ksi).
- (a) Use the von Mises criterion to determine whether or not the thin-walled container will yield.
- (b) If a safety factor of 4.0 is used to guard against yielding, will the yield strength of the container be high enough?
- 3-6.** A shaft driven by an electrical motor is used to rotate an impeller. The connection between the shaft and the impeller involves a keyway and a fillet, as shown in the figure. Assume that the total force needed to rotate the impeller is 5,000 N (11.1 kips) and the shear strength of the cylindrical fillet is 400 MPa (58.0 ksi). Will a fillet with a diameter of 10 mm (0.4 in.) be sufficient to prevent shear yielding? If a safety factor of 4.0 is used to guard against yielding, is the size of the fillet still sufficient? Finally, what else must we consider in order to prevent failure of the fillet, shaft, and impeller? If you were allowed to modify the design, what would you do?



- 3-7.** A cylindrical pressure vessel was built to study the hydrogen storage properties of hydrogen storage materials. Each experiment for such studies calls for pressurization of the vessel with a hydrogen pressure of 20 MPa (2.9 ksi), then evacuation (down to 0.13×10^2 Pa [0.1 torr]), and repetition of the pressurization and evacuation 1,000 times. The pressure vessel is intended to be used for

at least 1,000 runs of this type of experiments. The sketch of the pressure vessel is shown. The cap is designed to seal the vessel by six bolts. The inner diameter of the cylindrical vessel is 25 mm (1 in.).



(a) Cross-sectional view of the pressure vessel. (b) Top view of the pressure vessel.

- (a) Calculate the total force on the cap when the hydrogen pressure in the vessel is 20 MPa (2.9 ksi).
- (b) Calculate the tensile force in each bolt when the hydrogen pressure is 20 MPa (2.9 ksi).
- (c) If the nominal area of the bolt is 50 mm^2 (4 in^2), what is the tensile stress in each bolt?
- (d) If the yield strength of the bolt is 400 MPa (58 ksi), will six bolts plastically deform when the vessel has a hydrogen pressure of 20 MPa (2.9 ksi)?
- (e) If a safety factor of 4.0 is used to guard against yielding, will six bolts still be enough?
- (f) Students in the lab have been told to tighten six bolts with a pretension that is equal to the tensile stress calculated in (c). What benefit will we get by doing this?

4

Elements of Fracture Mechanics

I. INTRODUCTION

The relatively new field known as *fracture mechanics*, based upon the work of Griffith and Irwin, is used to treat fracture problems involving cracks in a quantitative manner. This chapter presents the fundamentals of this field and discusses a number of conditions that must be met in order to make valid use of fracture mechanics in a failure analysis.

II. GRIFFITH'S ANALYSIS OF THE CRITICAL STRESS FOR BRITTLE FRACTURE

Griffith (1) studied the fracture behavior of silica glass, a very brittle material. At room temperature, the stress-strain curve for this type of glass is linear up to fracture. The theoretical strength of this glass is approximately $E/10$, but in the presence of small cracks, the fracture stress is orders of magnitude below the theoretical strength of the glass. Griffith's analysis succeeded in explaining why this was so and also provided the basis for the field of fracture mechanics.

The Griffith analysis is based upon the first law of thermodynamics, which states that in a closed system energy is conserved. Two types of energy are considered, strain energy and surface energy. Consider the two thin sheet specimens shown in

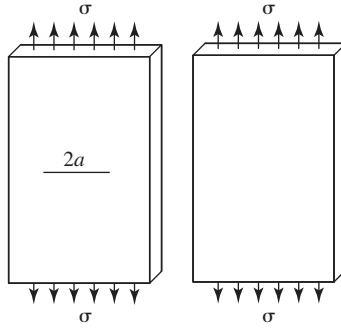


Fig. 4-1. Cracked and uncracked panels subjected to tensile loading.

Fig. 4-1 subjected to a tensile stress σ . One specimen has a crack, which is very small in length with respect to the width of the sheet; the other does not. If each of these specimens is loaded in tension to the same displacement, there will be a small difference in the load-extension plots, for it would take less of a load to extend the cracked specimen a given amount than the uncracked specimen. These plots are shown in Fig. 4-2, where the difference between the two cases has been exaggerated for clarity. The elastic energy stored in each specimen at a given extension Δ is given by the area under the corresponding curve and is equal to $\frac{1}{2} P \Delta$, where P for the cracked specimen is less than that for the uncracked specimen. Griffith used this difference in stored elastic energy to develop a theory for brittle fracture. He reasoned that on going from the uncracked to the cracked state, there is not only a decrease in elastic energy, but also an increase in surface energy, due to the creation of the new crack surfaces. He calculated that if a crack of length $2a$ were to develop in the uncracked body, ΔW_e , the total decrease in elastic stored energy per unit of thickness, would be given by

$$\Delta W_e = -\frac{\pi a^2 \sigma^2}{E} \quad (4-1)$$

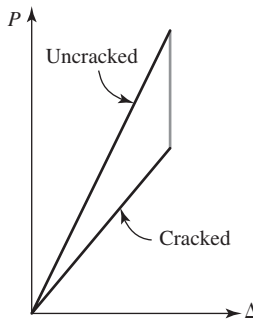


Fig. 4-2. Load deflection plots for the cracked and uncracked panels shown in Fig. 4-1.

where a is the half-crack length and E is Young's modulus. However, there is also an increase of energy in the system due to the creation of new surface areas of energy γ_s per unit of area. The total increase of surface energy ΔW_s is given by

$$\Delta W_s = 4a\gamma_s \quad (4-2)$$

where γ_s is the surface energy per unit area, a material constant. (The number 4 appears since the crack is of length $2a$, and it has an upper and a lower surface.)

Now comes the next step in the Griffith analysis. Suppose the specimen is already cracked; what condition must be met for the crack to propagate? Griffith reasoned that propagation would occur when the rate of strain energy release just equaled the rate at which energy was being absorbed through the creation of additional crack surface. This condition can be expressed as

$$\frac{d}{da} \left(-\frac{\pi a^2 \sigma^2}{E} + 4a\gamma_s \right) = 0 \quad (4-3)$$

or

$$-\frac{2\pi a \sigma_c^2}{E} + 4\gamma_s = 0 \quad (4-4)$$

which leads to

$$\sigma_c = \sqrt{\frac{2E\gamma_s}{\pi a}} \quad (4-5)$$

where σ_c is the critical stress required for propagation of a brittle crack. Note that, for stresses less than the critical value, the crack will not propagate because the strain energy that would be released in a virtual crack advance would be less than that needed to form new surface.

Griffith tested a brittle glass and found the results to be in agreement with predictions based upon Eq. 4-5.

Equation 4-5 can also be written as

$$\sigma_c \sqrt{\pi a} = \sqrt{2E\gamma_s} \quad (4-6)$$

where the extrinsic quantities σ_c and a are on the left-hand side of the equation and the intrinsic quantities E and γ_s are on the right-hand side. $\sigma_c \sqrt{\pi a}$ is a common combination of terms encountered in fracture mechanics and is designated as K_c . K in general is known as a *stress intensity factor*, and it depends upon component geometry, stress level, and crack length. For the Griffith geometry,

$$K = \sigma \sqrt{\pi a} \quad (4-7)$$

The subscript c in Eq. 4-6 is used to indicate that the value of K is at the critical level for fracture, that is,

$$K_c = \sqrt{2E\gamma_s} \quad (4-8)$$

K_c is often referred to as the *fracture toughness*.

In the linear-elastic range, the stress ahead of a crack under tension is governed by the stress intensity factor and is expressed as

$$\sigma_y = \frac{K}{\sqrt{2\pi r}} \quad (4-9)$$

where r is the distance measured from the crack tip.

III. ALTERNATIVE DERIVATION OF THE GRIFFITH EQUATION

Consider a plane specimen under a tensile stress σ that contains a through-thickness crack perpendicular to the direction of loading of length $2a$.

The increment of surface energy per unit of thickness involved in advancing the crack by an amount da , Fig. 4-3, is $4\gamma_s da$.

The corresponding change in the elastic strain energy is

$$\begin{aligned} \frac{d}{da}(\Delta W_E) &= -\frac{d}{da} \left[\frac{\pi \sigma^2 (a + da)^2}{E} - \frac{\pi \sigma^2 a^2}{E} \right] \\ \frac{d}{da}(\Delta W_E) &= -\frac{2\pi \sigma^2 a da}{E}. \end{aligned}$$

The crack will advance when the energy required to form a new element of surface, $4\gamma_s da$, is supplied by the released increment of strain energy, $-2\pi \sigma^2 a da/E$, that is, when

$$4\gamma_s da + \left(-\frac{2\pi \sigma^2 a da}{E} \right) = 0$$

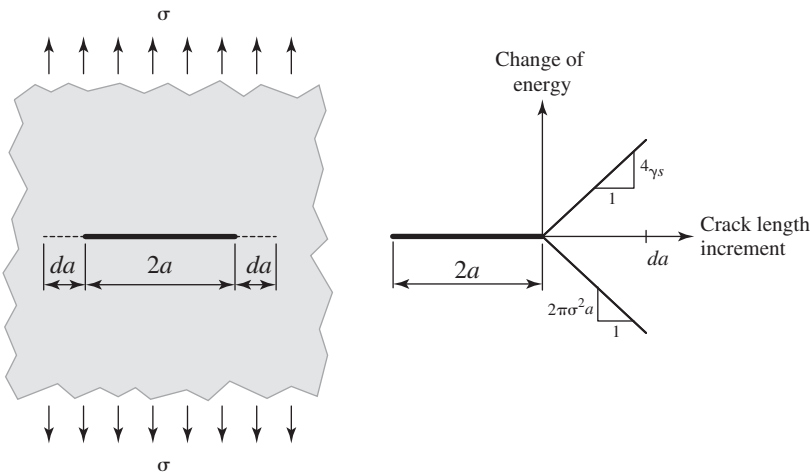


Fig. 4-3. Alternate view of energy balance in deriving a Griffith equation.

so that, as above,

$$\sigma_{cr} = \sqrt{\frac{2E\gamma_s}{\pi a}}$$

IV. OROWAN-IRWIN MODIFICATION OF THE GRIFFITH EQUATION

In later studies of the fracture of brittle steel carried out by Orowan (2) and by Irwin (3), it was found that the experimental values for γ_s were orders of magnitude higher than expected. These investigators reasoned that plastic deformation occurred during nominally brittle fracture of steel and that the plastic work involved greatly exceeded the surface energy γ_s . In order to preserve the linear-elastic Griffith formalism, $\sqrt{2E\gamma_s}$ was therefore written as $\sqrt{2E\gamma_p}$, where γ_p is the plastic work done per unit of area during fracture.

Equation 4-4 can be written as

$$2\gamma_p = G_c = \frac{\sigma_c^2 \pi a}{E} \quad (4-10)$$

where G_c is referred to as the *critical strain energy release rate* at a crack tip. (In the treatment of the fracture of polymers, G_c rather than K_{Ic} is considered to be the fracture toughness.)

In general, G can also be expressed as

$$G = \frac{\Delta W - \Delta U}{Bda} \quad (4-11)$$

where W is the external work, U is the internal (strain) energy, and B is the thickness. For fixed displacement conditions, $\Delta W = 0$, so G can be written as

$$G = - \left(\frac{dU}{Bda} \right) \quad (4-12)$$

Under plane-stress conditions, K_{Ic} and G_c are interrelated through

$$K_{Ic} = \sqrt{EG_c} \quad (4-13)$$

and

$$G_c = \frac{K_{Ic}^2}{E} \quad (4-14)$$

The stress intensity factors for plane stress and plane strain are the same and are independent of Poisson's ratio, ν . However, K_{Ic} , the plane-strain value of the fracture toughness under Mode I loading, does depend upon Poisson's ratio and is given as

$$K_{Ic} = \sqrt{\frac{EG_{Ic}}{(1 - \nu^2)}} \quad (4-15)$$

This is because the effective Young's modulus under plane-strain conditions is equal to $E/(1 - \nu^2)$.

V. STRESS INTENSITY FACTORS

Thus far, the only type of specimen geometry that has been discussed is the wide sheet containing a small crack. When the crack length is appreciable with respect to the width, a finite width correction of the stress intensity factor has to be made. Figure 4-4 is a plot of the correction factor for the center-cracked panel (CCP). For this case the stress intensity factor can be expressed as (4)

$$K = \sigma \sqrt{\pi a} \sqrt{\sec \frac{\pi a}{W}} \quad (4-16)$$

Figure 4-5 shows a semicircular surface crack, an important type of flaw when dealing with pressure vessels. The stress intensity factor for this flaw varies with its position along the flaw. The stress intensity factor at the corner, where the flaw meets the surface, is given as

$$K = 1.12 \left(\frac{2}{\pi} \right) \sigma \sqrt{\pi a} \quad (4-17)$$

At the point of maximum depth of the flaw, the stress intensity factor is slightly less, that is,

$$K = \left(\frac{2}{\pi} \right) \sigma \sqrt{\pi a} \quad (4-18)$$

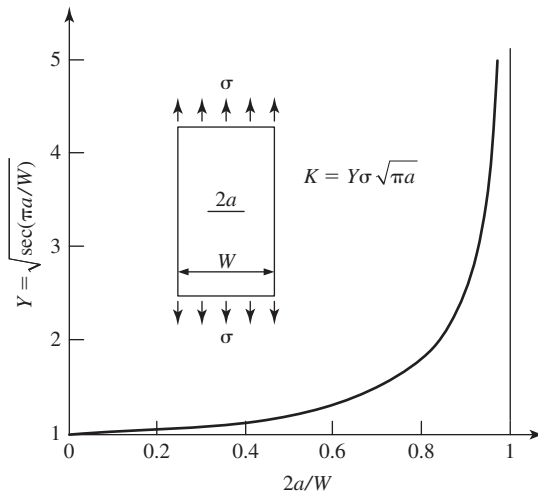


Fig. 4-4. Finite width correction of the stress intensity factor for a center cracked panel [4, 15].

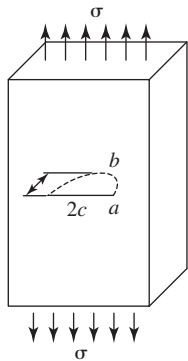


Fig. 4-5. A semicircular surface crack in an infinite plate, an important type of flaw when dealing with pressure vessels.

If the surface flaw is semielliptical in shape rather than semicircular, then the stress intensity factor at the surface is

$$K = \frac{1.12}{I_2} \sigma \sqrt{\pi a} \sqrt{\frac{a}{c}} \tag{4-19}$$

Where *a* is the maximum crack depth and *c* is the half-length of the crack along the surface, the stress intensity factor at the maximum depth is given as

$$K = \frac{1.12}{I_2} \sigma \sqrt{\pi a} \tag{4-20}$$

where *I*₂ is the elliptical integral of the second kind and is dependent upon the ratio of *a* to *c*, where *c* is the half-length of the crack along the surface and *a* is the maximum crack depth. For A tabulation of *I*₂ values as a function of *a/c* is given below.

<i>a/c</i>	0.0	0.1	0.2	0.3	0.4	0.5	0.6	0.7	0.8	0.9	1.0
<i>I</i> ₂	1.000	1.016	1.1051	1.097	1.151	1.211	1.277	1.345	1.418	1.493	π/2

For a wide panel containing a small, through-thickness edge crack as shown in Fig. 4-6, the stress intensity factor is

$$K = 1.12 \sigma \sqrt{\pi a}$$

The stress intensity factor for a three-point bend specimen with a support span equal to *S*, as shown in Fig. 4-7, is given in ASTM Designation E 399 as

$$K = \frac{PS}{BW^{3/2}} f(a/W) \tag{4-19a}$$

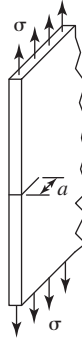


Fig. 4-6. A small through-thickness edge crack in a wide panel.

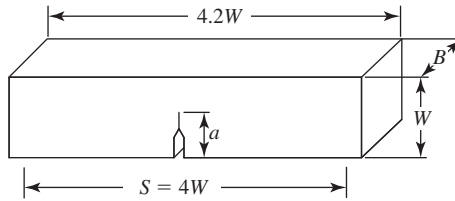


Fig. 4-7. A three-point bend specimen.

where P is the applied load and $f(a/W)$ is given as

$$f(a/W) = \frac{3(a/W)^{1/2} \{1.99 - (a/W)(1 - a/W)[2.15 - 3.93a/W + 2.7(a/W)^2]\}}{2[1 + 2(a/W)](1 - a/W)^{3/2}} \quad (4-19b)$$

The stress intensity factor for the compact tension (CT) specimen shown in Fig. 4-8 is given by ASTM Designation E 399 as

$$K = \frac{PS}{BW^{1/2}}f(a/W) \quad (4-20a)$$

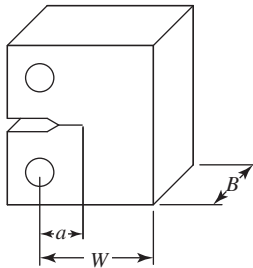


Fig. 4-8. A compact tension (CT) specimen.

where P is the applied load and $f(a/W)$ is given as

$$f(a/W) = \frac{(2 + a/W)[0.886 + 4.64(a/W) - 13.32(a/W)^2 + 14.72(a/W)^3 - 5.6(a/W)^4]}{(1 - a/W)^{3/2}} \quad (4-20b)$$

Further information on stress intensity factors can be found in a number of handbooks (5–8), which give them for a range of geometries and loading conditions.

VI. THE THREE LOADING MODES

A component containing a crack can be loaded in three different modes. These modes are illustrated in Fig. 4-9. Mode I is the tensile opening mode, and the stress intensity factor associated with this mode is designated as K_I . Mode II is the in-plane shearing mode, and the stress intensity factor associated with this mode is designated as K_{II} . Mode III is the out-of-plane tearing mode, sometimes referred to as the *anti-plane-strain mode*. The stress intensity factor associated with Mode III is designated as K_{III} .

VII. DETERMINATION OF THE PLASTIC ZONE SIZE

Irwin has shown that the linear-elastic fracture mechanics (LEFM) approach, which was initiated by Griffith, can be used even in the presence of plastic deformation. However, limits are imposed on the extent of plastic deformation for the LEFM approach to remain valid. It is required that the size of the plastic zone that develops in a metal at a crack tip be small with respect to the crack length. The first estimate of the size of the plane-stress plastic zone at a crack tip can be obtained by rearranging Eq. 4-9 to read

$$r = \frac{K^2}{2\pi\sigma_y^2} \quad (4-21)$$

Then, with σ_y set equal to σ_Y , the yield stress, the size of the plastic zone $r_{pzs,P\sigma}$, is

$$r_{pzs,P\sigma} = \frac{K^2}{2\pi\sigma_Y^2} \quad (4-22)$$

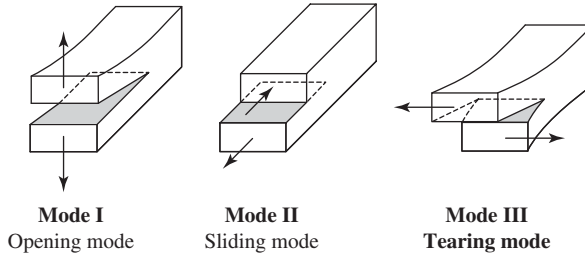


Fig. 4-9. The three loading modes. (a) Mode I, opening mode. (b) Mode II, sliding mode. (c) Mode III, tearing mode.

In a more detailed analysis, Dugdale (9) derived the following expression for the plane-stress plastic zone size for a centrally cracked sheet under tension:

$$r_{pzs,P\sigma} = a \left[\sec \left(\frac{\pi}{2} \frac{\sigma}{\sigma_Y} \right) - 1 \right] \quad (4-23)$$

For values of σ much less than σ_Y , Eq. 4-23 can be written as

$$r_{pzs,P\sigma} = \frac{\pi^2}{4} \left(\frac{K^2}{2\pi\sigma_Y^2} \right) \quad (4-24)$$

about two and one-half times larger than the first estimate given by Eq. 4-22.

ASTM Designation E 399 requires that the crack length be 16 times greater than $r_{pzs,P\sigma}$ to meet the conditions for a linear-elastic analysis. If it is not, then elastic-plastic fracture mechanics or some modification should be used in the analysis. Irwin (10) proposed that, in order to keep a linear-elastic framework for analysis when the crack length was small with respect to the plastic zone size, the crack length should be increased by one-half of the plastic zone size. If the Dugdale value for the plastic zone size is used, then the effective crack length, a_{eff} , according to the Irwin proposal, becomes

$$a_{eff} = a + \frac{1}{2}a \left[\sec \left(\frac{\pi}{2} \frac{\sigma}{\sigma_Y} \right) - 1 \right] = \frac{a}{2} \left[\sec \left(\frac{\pi}{2} \frac{\sigma}{\sigma_Y} \right) + 1 \right] \quad (4-25)$$

Equation 4-25 is useful in dealing with short cracks at stress levels that are high relative to the yield strength. For situations where the plastic zone is large with respect to the crack length, the stress intensity factor can be expressed as

$$K = Y\sigma\sqrt{\pi a_{eff}} \quad (4-26)$$

where Y is determined by the particular geometry under consideration. With the use of Eq. 4-23, Eq. 4-26 can be written as

$$K = Y\sigma\sqrt{\frac{\pi}{2}a \left[\sec \left(\frac{\pi}{2} \frac{\sigma}{\sigma_Y} \right) + 1 \right]} \quad (4-27)$$

Irwin (10) has estimated the plane-strain plastic zone size $r_{pzs,P\epsilon}$ to be one-third that of the plane-stress plastic zone size $r_{pzs,P\sigma}$. This is consistent with the higher degree of plastic constraint in plane strain as compared to plane stress.

VIII. EFFECT OF THICKNESS ON FRACTURE TOUGHNESS

The fracture toughness of a material is usually determined using a pre-fatigue-cracked plane specimen of the type shown in Fig. 4-8 (ASTM Designation E 399). An important factor affecting the magnitude of the fracture toughness is the thickness

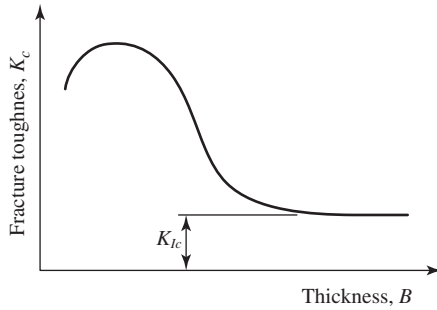


Fig. 4-10. Fracture toughness as a function of thickness.

of the specimen. Figure 4-10 shows the typical variation of the fracture toughness of a steel as a function of thickness. For thicknesses greater than 16 times the plane-stress plastic zone size, that is, $16(K^2/2\pi\sigma_Y^2) = 2.5(K^2/\sigma_Y^2)$, the specimen is in a condition of plane strain, and the fracture toughness is constant independent of thickness but at a minimum value. It is also required that the crack length a be greater than this value to ensure that the crack length is long with respect to the plastic zone size to ensure that an LEFM analysis is applicable. In addition, the length of the starter notch plus the fatigue crack is specified to be between 0.45 and 0.55 of the width W , which also fixes the size of the ligament ahead of the crack. The Mode I, plain-strain fracture toughness is designated as K_{lc} . For lesser thickness, the fracture toughness rises due to the loss of constraint and the development of plane-stress conditions. In this range, the fracture toughness is designated as K_c .

Another method for determining the fracture toughness involves evaluation of the crack tip opening displacement (CTOD) of notched and fatigue precracked specimens (ASTM Designation E 1290). An objective of the method is to determine the CTOD corresponding to the onset of unstable brittle crack extension. A clip gauge is mounted at the mouth of the notch, Fig. 4-11, and a load-crack mouth displacement record

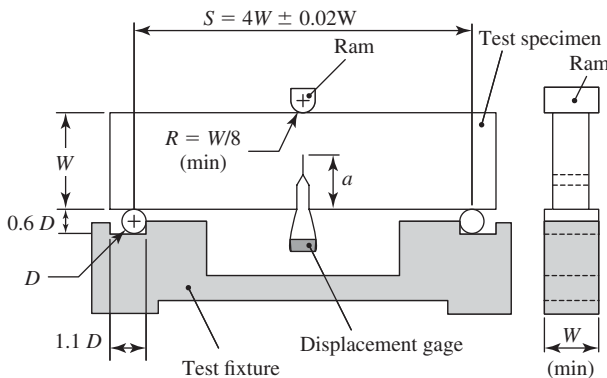


Fig. 4-11. Setup for the measurement of the crack mouth displacement by a clip gauge in a bend test.

is obtained. The crack mouth displacement is then converted into a corresponding CTOD value, and in the case of brittle fracture, the value of the CTOD at the onset of brittle fracture can be related to the fracture toughness by means of the relation

$$\text{CTOD}_c = \frac{4}{\pi} \frac{K_{Ic}^2}{\sigma_Y E} \quad (4-28)$$

This procedure is useful when materials are too ductile or lack sufficient size to be tested in accordance with the requirements of ASTM Designation E 399.

IX. THE R-CURVE

In ductile materials, particularly under plane-stress conditions, the onset of crack extension under rising-load test conditions occurs at a load level below the maximum load. There is a load range wherein a crack extends in a stable manner, that is, the resistance to unstable crack propagation increases with crack extension in the stable crack growth range. Even under plane-strain conditions of loading, there may be a small increment of stable crack growth before unstable crack growth occurs. This increased resistance is related to the increase of the plastic zone at the tip of the crack as well as to the blunting of the crack tip as it advances. This type of behavior is dependent upon specimen thickness, temperature, and strain rate. The *R*-curve is a plot of the applied stress intensity factor *K* versus the crack length, and the standard practice for the *R*-curve determination is given in ASTM E 561[17]. The *R*-curve can be matched with the applied *K*-curves to estimate the load necessary to cause unstable crack propagation at K_c , as shown in Fig. 4-12. In making this estimate, *R*-curves are regarded as though they are independent of the starting crack length a_0 and the specimen configuration in which they are developed. For a given material, specimen thickness, and test temperature, the *R*-curves appear to be a function of crack extension Δa only. To predict instability, the *R*-curves may be positioned as

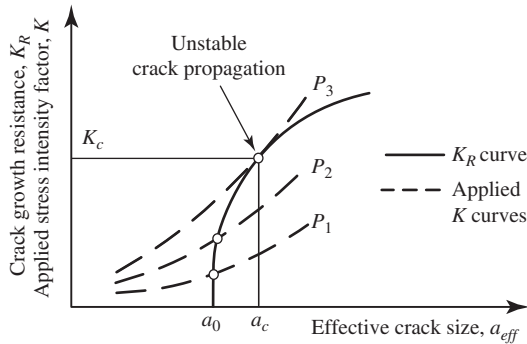


Fig. 4-12. Schematic representation of an *R*-curve and applied *K*-curves to predict instability at K_c under a load P_3 , and a critical crack length a_c , for an initial crack length a_0 .

in Fig. 4-12 so that the origin coincides with the initial crack length a_0 . Applied K -curves can be generated by assuming applied loads or stresses and calculating applied K as a function of crack length. The curve that develops tangency with the R -curve defines the critical load or stress that will cause the onset of unstable fracturing.

The unloading compliance characteristics, together with a compliance calibration curve, which is a curve that gives the compliance of the specimen as a function of crack length, can be used to determine the crack length and the corresponding K -level.

X. SHORT CRACK LIMITATION

The stress intensity factor is a product of stress and the square root of the crack length. Suppose one wanted to maintain K at a constant value while decreasing the crack length. This would require that the stress be increased accordingly. However, if we make the crack size short enough, the value of the stress would reach levels in excess of the tensile strength of the material. Therefore, straightforward linear-elastic fracture mechanics cannot be used when dealing with cracks of lengths less than 1 mm, (0.04 in.) and some modification is needed. This is a particularly important consideration in analyzing the behavior of short cracks in fatigue.

XI. CASE STUDIES

A. Failure of Cannon Barrels

When a shell is fired out of a cannon, some wear of the inner surface of the cannon takes place. During World War II, when the accumulated wear after the firing of a number of rounds became excessive, the barrel was removed from service. Much of this wear was associated with the type of propellant that was used at that time, but by the time of the Vietnam War, improvements in the propellants had been made, and the rate of wear was greatly reduced. However, a serious new problem arose, for the barrel could now experience many more firings in its lifetime, with each of these firings being another severe fatigue cycle. As a result, fatigue cracks formed on the inside of the barrel, and when they propagated to critical size, the gun would explode, often killing the gun crew. These explosions occurred because the critical crack length for fracture of the barrel was less than the wall thickness of the barrel because of the relatively low plane-strain fracture toughness of the steel used for the barrels. To deal with this problem, steels of higher fracture toughness were developed, so that if a fatigue crack were to propagate, it would not reach critical length while still within the wall of the barrel. It would instead penetrate to the outer side of the barrel, and any pressure buildup would be vented rather than cause an explosion. In all pressure vessels, it is desired to have the fracture toughness sufficiently high so that penetration of the pressure vessel wall occurs before fracture. Pressure vessels that meet this criterion will “leak before burst.”

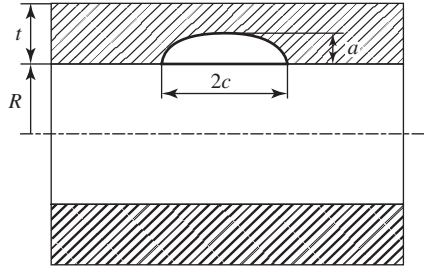


Fig. 4-13. Thick-walled cylinder with an internal semielliptical surface crack.

The following equations review some of the relationships used in the analysis of pressure vessels.

In a thin-walled tube, the hoop stress σ_h is given by

$$\sigma_h = \frac{p_i D}{2t} \quad (4-29)$$

where p_i is the internal pressure, D is the diameter, and t is the wall thickness.

The gun barrel is a thick-walled tube. In a thick-walled tube, the circumferential stress is given by

$$\sigma_h = \frac{D_o^2 p_i}{D_o^2 - D_i^2} \left(1 + \frac{D_o^2}{4r^2} \right) \quad (4-30)$$

The stress intensity factor at the deepest point for an internal, part-through, semielliptical, longitudinal crack of depth a and length $2c$ in a thick-walled pressure vessel of thickness t (Fig. 4-13) is given as (5)

$$K_I = \frac{p_i R}{t} \sqrt{\frac{\pi a}{Q}} F \left(\frac{a}{t}, \frac{a}{2c}, \frac{R}{t} \right) \quad (4-31)$$

where

$$F = 1.12 + 0.053\xi + 0.0055\xi^2 + (1 + 0.02\xi + 0.0191\xi^2) \frac{(20 - R/t)^2}{1400}, \quad (4-32)$$

and $\xi = (a/t)(a/2c)$, $Q = 1 + 1.464(a/c)^{1.65}$, a is the depth of the flaw, and $2c$ is the length of the flaw. This expression is valid for $5 \leq R/t \leq 20$ and $2c/a \leq 12$, and $a/t \leq 0.80$.

B. Failure of a Post-tensioned Steel Bar

This case study demonstrates how fracture mechanics can be used as analytical tool to support a failure investigation and to suggest design improvements based on a damage tolerance philosophy (19). Steel bars were used to prestress a steel frame, as shown in Fig. 4-14. These high-strength steel bars, 36 mm in diameter,

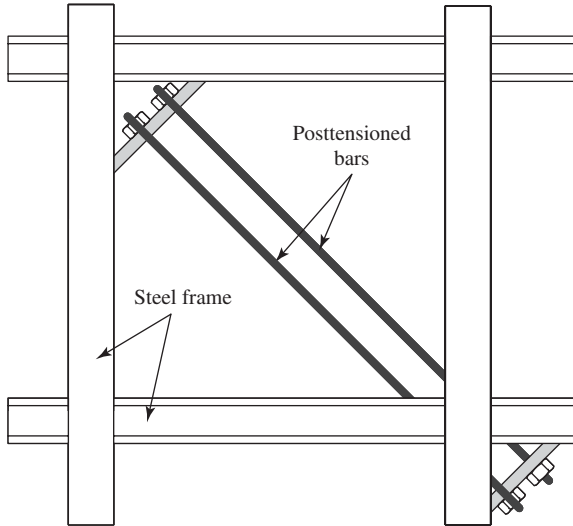


Fig. 4-14. Posttensioned bar in service.

were intended to be loaded to 60% of their ultimate tensile strength, 1,300 MPa. However, one of the bars failed at 30% (390 kN) of the expected rupture load, and the other at 46% (598 kN) of the rupture load.

Examination of the fracture surfaces revealed that in both cases small, semielliptical surface cracks of the type shown in Fig. 4-15, which were in the range of 1.0 mm (0.04 in.) in depth, triggered the fractures. Fracture toughness tests are conducted in accord with ASTM Designation E 399 [16], and a K_{Ic} value of $33 \text{ MPa}\sqrt{\text{m}}$ was obtained. This K_{Ic} value is quite low and explains why the bars were susceptible to unstable fracture even though they contained very small defects. The stress intensity

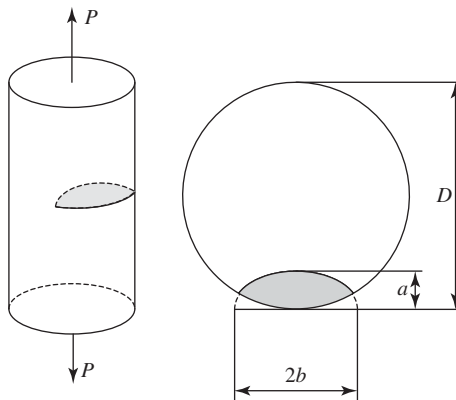


Fig. 4-15. Geometry and notation for a bar containing a surface crack.

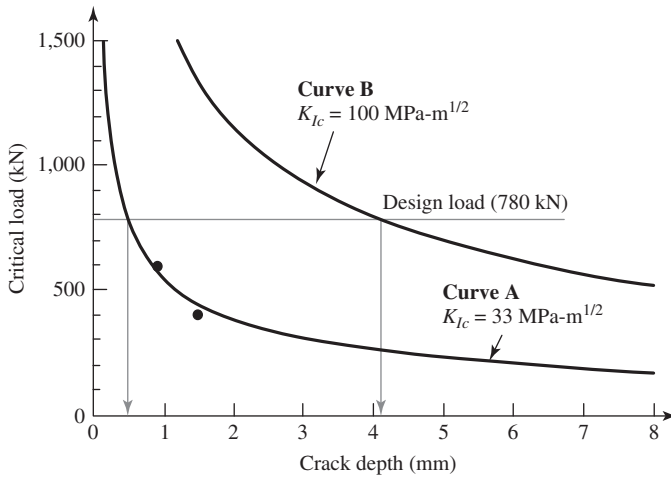


Fig. 4-16. Rupture load as a function of crack depth.

factor for a cylindrical bar containing a semielliptical surface crack under tensile load for small values of a/b is given as

$$K = \frac{4P}{D\sqrt{\pi D}} \left\{ \sqrt{\frac{a}{D}} \left[1.0806 + 0.6386 \left(\frac{a}{D} \right) - 2.444 \left(\frac{a}{D} \right)^2 + 13.463 \left(\frac{a}{D} \right)^3 \right] \right\} \quad (4-33)$$

where P is the applied (axial) force, D is a diameter of the bar, and a is a crack depth.

The critical load as a function of crack depth for $K_{Ic} = 33 \text{ MPa}\sqrt{\text{m}}$ is shown as curve A of Fig. 4-16. In this figure, the observed critical crack depth and load at fracture of the two broken bars are also plotted, and they conform well to the fracture mechanics predictions. The critical crack depth for the design load of 780 kN is only 0.5 mm (0.02 in.), a flaw size that is difficult to detect. To improve the design of the bar, fracture mechanics approach suggests the use of a steel with higher fracture toughness. For example, if K_{Ic} is set at $100 \text{ MPa}\sqrt{\text{m}}$, curve B in Fig. 4-16 is obtained and the critical crack depth is increased to a more easily detected size of 4.1 mm (0.16 in.).

XII. THE PLANE-STRAIN CRACK ARREST FRACTURE TOUGHNESS, K_{Ia} , OF FERRITIC STEELS

As will be discussed more fully in Chapter 7, ferritic steels at low temperature fracture in a low-toughness, brittle manner, whereas at a higher temperature they fracture in a high-toughness, ductile manner. In one type of crack-arrest test, a temperature gradient is established in a plane-strain specimen under stress, and a running crack is propagated from the low-temperature region toward the high-temperature region. The running crack will be arrested because of the increase in fracture toughness with

an increase in temperature. The value of the stress intensity factor at the point of arrest is designated K_{Ia} , and the temperature at the point of arrest is referred to as the *crack arrest temperature* for that loading condition. By changing the loading conditions, a plot of K_{Ia} versus temperature can be developed. The test is of significance in the design of safe structures, since above the arrest temperature, a crack whose stress intensity factor is equal to or less than K_{Ia} is not able to propagate.

The crack arrest toughness can also be obtained at constant temperature. The procedure for this test is given in ASTM Designation E 1221. In carrying out the requirements of this specification, a compact specimen is wedge loaded at a selected temperature, and a fast-running crack is created. This crack is arrested because, under the constant displacement loading conditions imposed, the stress intensity factor falls off as the crack advances.

XIII. ELASTIC-PLASTIC FRACTURE MECHANICS

The above LEFM procedures are applicable only when the plastic deformation is limited to a small zone at the tip of the crack. One of the requirements for a valid K_{Ic} determination (ASTM Designation E 399) is that the thickness of specimen B and crack length a satisfy the condition

$$B, a \geq 2.5 \frac{K_{Ic}^2}{\sigma_Y^2} \quad (4-34)$$

B and a will be given in inches when English units are used and in meters when SI units are used.

For the steels used in the nuclear reactor pressure field, K_{Ic} may have a value of $220 \text{ MPa}\sqrt{\text{m}}$ ($200 \text{ ksi}\sqrt{\text{in.}}$), and σ_Y may be 345 MPa (50 ksi).

The requirement on B for linear-elastic plane-strain conditions would be 1.02 m (40 in.), which is much too large. In order to obtain a valid estimate of K_{Ic} , an elastic-plastic procedure is used to determine a quantity J_{Ic} , a measure of the elastic-plastic fracture toughness, with specimens perhaps only 0.025 m (1 in.) or so in thickness. However, even in this type of test, there is a requirement that to maintain plane-strain conditions

$$B \geq 25 \frac{J_{Ic}}{\sigma_Y} \quad (4-35)$$

J_{Ic} has been shown to be experimentally the equivalent of G_{Ic} . In a J_{Ic} test, there will be large amounts of plastic deformation at the crack tip, and a plot of load versus displacement will no longer be linear. As shown below, there are procedures for relating J_{Ic} to K_{Ic} ; however, modification of the LEFM approach to the determination of fracture toughness is needed. In the modified approach, it is assumed that linear elastic-plastic behavior can be equivalent to nonlinear-elastic behavior. Figure 4-17 compares the load displacement curves for both linear- and nonlinear-elastic behavior for two different crack sizes, a and $a + da$. The strain energy release rate G at a fixed displacement is the area between the straight lines in Fig. 4-17a. The equivalent

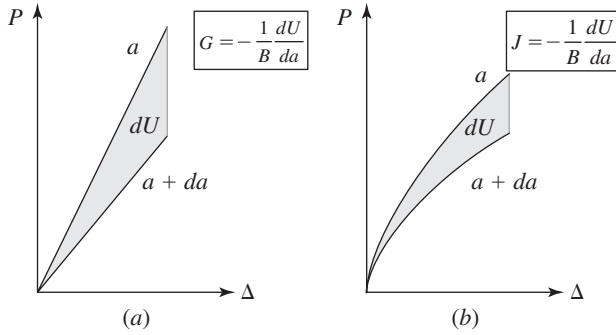


Fig. 4-17. Strain energy released due to crack advance at a fixed displacement. (a) In a linear-elastic material. (b) In a nonlinear-elastic material.

strain energy release rate per unit of thickness B for nonlinear behavior in Fig. 4-17b is designated as J , where J is given as

$$J = -\frac{dU}{B da} \quad (4-36)$$

where U is the strain energy. It has been shown that J can also be mathematically expressed as a path-independent integral around the crack tip (11).

ASTM Designation E 813 (18) discusses the procedures involved in the experimental determination of J_{Ic} , the value of J near the initiation of crack growth. One procedure involves the determination of the load versus load line displacement behavior of a fatigue precracked compact specimen. The expression for J consists of its elastic and plastic components, that is,

$$J = J_{el} + J_{pl} \quad (4-37)$$

where

$$J_{el} = \frac{K^2(1 - \nu^2)}{E} = \frac{K^2}{E'} \quad (4-38)$$

and

$$J_{pl} = \frac{\eta A_{pl}}{B_N b_o} \quad (4-39)$$

The constant η depends on the specimen type. For the compact specimen $\eta = 2 + 0.522b_o/W$, where B_N is the net specimen thickness, W is the width of the specimen measured from the load line, and b_o is the length of the uncracked ligament ahead of the fatigue crack. A_{pl} is the area shown in Fig. 4-18.

In the case of ductile metals, unstable crack growth does not occur at J_{Ic} . As in the case of the K - R curve discussed above, a J - R curve can be constructed for elastic-plastic behavior. ASTM Designation E 1152 describes the procedures involved in establishing this type of curve. The point of unstable crack growth is reached when the crack-driving force J equals the crack-resisting force J_R .

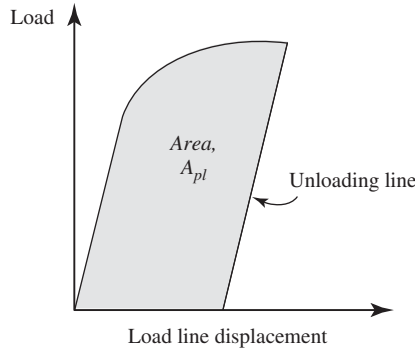


Fig. 4-18. A_{pl} in the determination of J .

The rate of creep crack growth has also been studied using fracture mechanics. By analogy with Eq. 4-12, J can be expressed as

$$J = -\frac{1}{B} \left(\frac{dU}{da} \right)_{\Delta} \quad (4-40)$$

The derivative of this expression with respect to time is known as C^* , that is,

$$C^* = -\frac{1}{B} \left(\frac{d\dot{U}}{da} \right)_{\Delta} \quad (4-41)$$

C^* has been found to be one of the more successful parameters for correlating steady-state creep crack growth data.

XIV. FAILURE ASSESSMENT DIAGRAMS

Failure assessment diagrams are plots that indicate safe and unsafe operating conditions in the presence of flaws (cracks). In these diagrams, failure is considered to occur either by general yield (collapse) or by fast fracture. From Eq. 4-26, the elastic-plastic stress intensity $K_{EP-P\sigma}$ under plane-stress conditions can be expressed as

$$K_{EP-P\sigma} = Y\sigma \sqrt{\frac{\pi}{2}a \left[\sec \left(\frac{\pi}{2} \frac{\sigma}{\sigma_Y} \right) + 1 \right]} \quad (4-42)$$

Under plane-strain conditions, with the size of the plastic zone taken to be one-third that of the plane-stress plastic zone, $K_{EP-P\epsilon}$ for plane-strain conditions can be written as

$$K_{EP-P\epsilon} = Y\sigma \sqrt{\frac{\pi}{3}a \left[\sec \left(\frac{\pi}{2} \frac{\sigma}{\sigma_Y} \right) + 2 \right]} \quad (4-43)$$

If $K_{EP-P\epsilon}$ is set equal to K_{Ic} , the value of the critical crack length, a_c , is given as

$$a_c = \frac{C_I^2}{\frac{\pi}{3} \left(\frac{\sigma}{\sigma_Y} \right)^2 \left[\sec \left(\frac{\pi}{2} \frac{\sigma}{\sigma_Y} \right) + 2 \right]} \quad (4-44)$$

where C_I is equal to $K_{Ic}/Y\sigma_Y$. Equation 4-43 can be used to construct a plot of σ/σ_Y versus a_c/C_I^2 , that is, the failure assessment curve, as shown in Fig. 4-19. A comparison with predictions based upon a linear-elastic analysis with $K_{LE} = Y\sigma\sqrt{\pi a}$ is also shown. At large values of a_c , the linear-elastic predictions are close to the elastic-plastic predictions, but at short crack lengths, the safe region is reduced in the elastic-plastic case.

Another form of failure assessment diagram can be constructed where the coordinates are $K_{LE}/K_{EP-P\epsilon}$ and σ/σ_Y . If $K_{EP-P\epsilon}$ is set equal to K_{Ic} , the value of the critical crack length, a_c then

$$\begin{aligned} \frac{K_{LE}}{K_{EP-P\epsilon}} &= \frac{K_{LE}}{K_{Ic}} = \frac{Y\sigma\sqrt{\pi a_c}}{Y\sigma\sqrt{\frac{\pi}{3} a_c \left[\sec \left(\frac{\pi}{2} \frac{\sigma}{\sigma_Y} \right) + 2 \right]}} \\ \frac{K_{LE}}{K_{Ic}} &= \frac{\sqrt{3}}{\sqrt{\left[\sec \left(\frac{\pi}{2} \frac{\sigma}{\sigma_Y} \right) + 2 \right]}} \end{aligned} \quad (4-45)$$

Figure 4-20 shows the plot of the failure assessment curve given by the above equation.

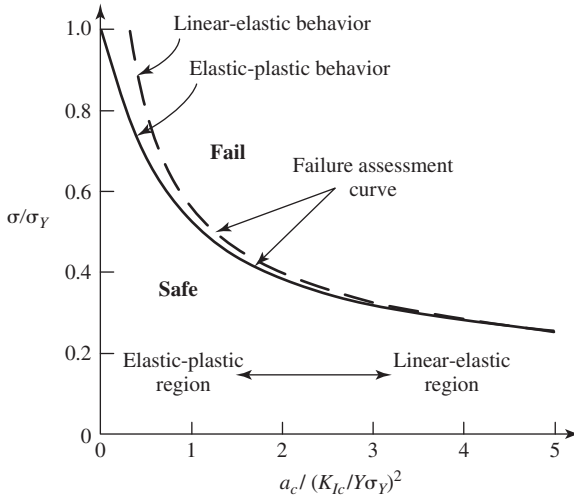


Fig. 4-19. Failure assessment diagram.

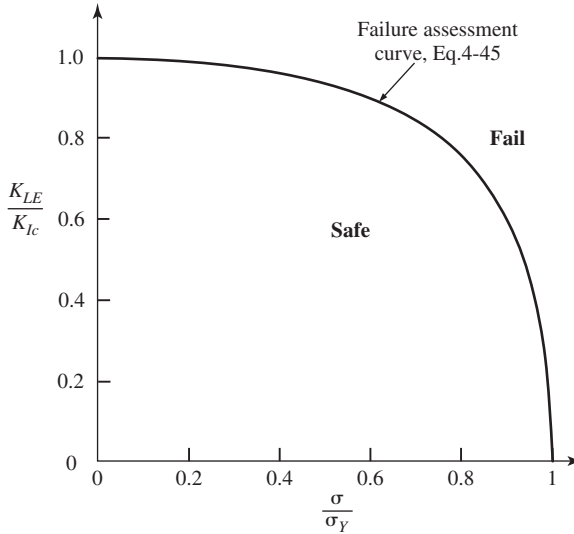


Fig. 4-20. Plane-strain failure assessment diagram.

A somewhat similar method of analysis known as the *R6 method* has been developed in England for use in assessing the safety of nuclear power plants (12). In the R6 procedure, the ratio K_{LE}/K_{Ic} (or K_c if the stress state is not plane strain) is called the *normalized stress intensity factor* and is denoted as K_r ; and the ratio σ/σ_Y is called the *normalized load* and is denoted as L_r . Therefore, a failure assessment curve has a functional form of $K_r = f(L_r)$. In this procedure, the failure assessment curve is divided into three options. For the option 3 curve, K_r is derived based on the J -integral parameter and J_{Ic} (or J_c if the stress state is not plane strain) as follows. From Eq. 4-38

$$K = \sqrt{J_{el}E'}$$

The fracture toughness K_c can be calculated from

$$K_c = \sqrt{J_c E'}$$

Therefore,

$$K_r = \sqrt{\frac{J_{el}}{J_c}} \quad (4-46)$$

For the option 2 curve, the expression $\sqrt{J_{el}/J_c}$ is approximate using a reference stress method that is required for a detailed stress-strain curve of the material considered. The option 1 curve is empirically fit to be a lower bound curve of an option 2 curve and is written in the following form:

$$K_r = (1 - 0.14L_r^2) [0.3 + 0.7 \exp(-0.65L_r^6)] \quad (4-47)$$

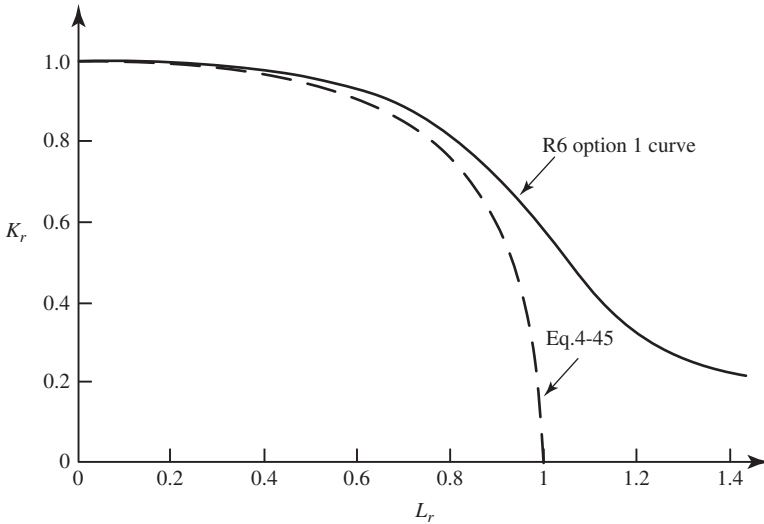


Fig. 4-21. R6 option 1 failure assessment curve.

It is a universal (general) curve in the same sense as the curve of Eq. 4-45 in that it is independent of material, component geometry, type of loading, and crack information. Figure 4-21 shows a plot of the option 1 curve in comparison with the curve given by Eq. 4-45.

XV. SUMMARY

This chapter has provided the elementary background in fracture mechanics which will be needed in subsequent chapters. References 13–15 provide more in-depth information concerning fracture mechanics.

REFERENCES

- (1) A. A. Griffith, The Phenomena of Rupture in Solids, *Phil. Trans. Royal Soc. London*, vol. A221, 1921, pp. 163–197; The Theory of Rupture, *Proc. 1st Int. Congress Appl. Mech.*, 1924, pp. 55–63.
- (2) E. Orowan, Energy Criteria for Fracture, *Welding J.*, vol. 34, 1955, pp. 157s–160s.
- (3) G. R. Irwin, Fracture Dynamics, in *Fracturing of Metals*, ASM, Material Park, OH, 1948, pp. 147–166.
- (4) C. E. Feddersen, Discussion, in Plane Strain Crack Toughness Testing, *ASTM STP 410*, 1967, pp. 77–79.
- (5) H. Tada, P. C. Paris, and G. R. Irwin, *The Stress Analysis of Cracks Handbook*, 2nd ed., Paris Productions, Inc., St. Louis, 1985.
- (6) G. C. Sih, *Handbook of Stress Intensity Factors*, Institute of Fracture and Solid Mechanics, Lehigh University, Bethlehem, PA, 1973.

- (7) D. P. Rooke and D. J. Cartwright, *Stress Intensity Factors*, HMSO, London, 1976.
- (8) *Stress Intensity Factors Handbook*, ed. by Y. Murakami, S. Aoki, N. Hasebe, Y. Itoh, H. Miyata, H. Terada, K. Tohgo, M. Toya, and R. Yuuki, Society of Materials Science, Kyoto, Japan, 1987.
- (9) D. S. Dugdale, Yielding of Steel Sheets Containing Slits, *J. Mech. Phys. Solids*, vol. 8, 1960, pp. 100–108.
- (10) G. R. Irwin, Plastic Zone Near a Crack and Fracture Toughness, *Proceedings of the 7th Sagamore Conference*, Syracuse University Press, Syracuse, NY, 1960, p. IV-63.
- (11) J. R. Rice, A Path Independent Integral and the Approximate Analysis of Strain Concentrations by Notches and Cracks, *J. Appl. Mech.*, vol. 35, 1968, pp. 379–386.
- (12) I. Milne, R. A. Ainsworth, A. R. Dowling, and A. T. Stewart, *Assessment of the Integrity of Structures Containing Defects*, Central Electricity Generating Board Report R/H/R6-Rev 3, London, UK, May 1986.
- (13) T. L. Anderson, *Fracture Mechanics*, CRC Press, Boca Raton, FL, 1991.
- (14) M. F. Kanninen and C. H. Popelar, *Advanced Fracture Mechanics*, Oxford University Press, Oxford, 1985.
- (15) D. Broek, *The Practical Use of Fracture Mechanics*, Kluwer Academic Publishers, Boston, 1988.
- (16) ASTM, *1990 Annual Book of ASTM Standards*, ASTM E399-83, ASTM, West Conshohocken, PA.
- (17) ASTM, *1990 Annual Book of ASTM Standards*, ASTM E561-86, ASTM, West Conshohocken, PA.
- (18) ASTM, *1990 Annual Book of ASTM Standards*, ASTM E813-89, ASTM, West Conshohocken, PA.
- (19) A. Valiente and M. Elices, Premature Failure of Prestressed Steel Bars, *Eng. Failure Anal.*, vol. 5, no. 3, 1998, pp. 219–227.

PROBLEMS

- 4-1.** Based upon ASTM E399, Standard Test Method for Plane-Strain Fracture Toughness of Metallic Materials, the stress intensity factor, K_I , for the widely used compact specimen (the depth of the notch is $0.2W$) is

$$K_I = \left(\frac{P}{BW^{1/2}} \right) f(a/W)$$

where $f(a/W)$ is given as

$$f(a/W) = \frac{(2 + a/W)(0.866 + 4.64a/W) - 13.32a^2/W^2 + 14.72a^3/W^3 - 5.6a^4/W^4}{(1 - a/W)^{3/2}}$$

Plot the ratio of $K_I/(P/BW^{1/2})$ for values of a/W between 0.25 and 0.75.

- 4-2.** K_I for a center-cracked panel is given as

$$K_I = \sigma \sqrt{\pi a} \sqrt{\sec \pi a/W}$$

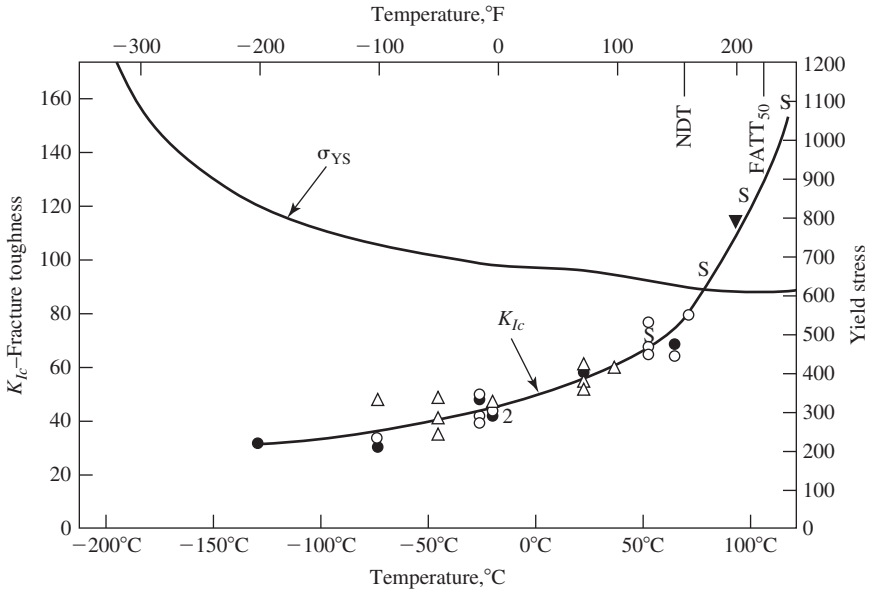
For the same B , compare the loads required to attain the same value of K_I for a compact specimen ($W = 50$ mm (1.97 in.), $a/W = 0.5$) and a center-cracked panel ($W = 200$ mm (7.87 in.), $a/W = 0.25$).

- 4-3.** Determine the residual strength diagram (σ_{\max} versus a) for a center-cracked panel of an aluminum alloy ($\sigma_{YS} = 350$ MPa (50.7 ksi), $K_{IC} = 50$ MPa \sqrt{m} (45.5 ksi \sqrt{m}), $W = 0.254$ m ($W = 10$ in.) for a/W values between 0.25 and 0.75.
- 4-4.** The stress intensity factor for a semicircular flaw of depth a (equal to 0.01 m [2.54 in.]) in a proposed cylindrical pressure vessel is given as $0.71 \sigma \sqrt{\pi a}$. The internal pressure is to be 15 MPa (2.2 ksi). The total volume of the pressure vessel is to be 1,000 m³ (35,000 in³). Three steels are available, and their characteristics are given in the following table. Structural weight and safety are primary considerations. The maximum stress is to be $\sigma_{YS}/2$, and a safety factor ≥ 1.1 is called for based upon the ratio of the fracture stress to the working stress. Which is the preferred steel?

Steel	Thickness, m (in.)	σ_{YS} , MPa (ksi)	K_{IC} , MPa \sqrt{m} ,
A	0.08 (3.15)	965 (140)	280 (255)
B	0.06 (2.36)	1,310 (190)	66 (60)
C	0.04 (1.57)	1,700 (246)	40 (36)

- 4-5.** A sharp penny-shaped crack with a diameter of 2.5 cm (1.0 in.) is completely embedded in a solid. Catastrophic fracture occurs when a stress of 700 MPa (100 ksi) is applied.
- (a) What is the fracture toughness of this material? [$K_{IC} = (2/\pi)\sigma_c\sqrt{\pi a}$].
- (b) If a sheet of this material is prepared for fracture-toughness measurement with the width of the sheet $w = 30$ cm (11.8 in.), a central crack of $2a = 7.5$ cm (2.95 in.), and the thickness of the sheet $B = 0.75$ cm (0.29 in.), would the fracture-toughness value be a valid number (the yield strength of the material is 1,100 MPa (160 ksi))?
- (c) What would be a sufficient thickness for valid K_{IC} measurement?
- 4-6.** A large-diameter turbine rotor is fabricated from a Cr-Mo-V steel with the temperature dependence of the yield strength and fracture toughness shown in the following figure. The rotor is designed to operate at 100°C at a stress that is 40% of the yield strength at that temperature. During a nonroutine shutdown due to a steam pipe failure, a technician discovered a 2.5 cm deep semicircular surface crack in the rotor that was oriented normal to the maximum stress direction. The supervisor decided to delay repair of the rotor until the next scheduled full-scale overhaul. Since the steam pipe repair was time-consuming, he was anxious to get the rotor online and used the “cold” start-up procedure

instead of the slower recommended start-up procedure. Was the supervisor's judgment correct? Use calculations to justify your answer.



Additional information for this question:

- Recommended startup procedure: (i) start up the rotor at 50% of the normal rotor design rpm level (ω_{op}); (ii) after the temperature of the rotor reaches 100°C, increase the rpm to $1.15\omega_{op}$ for 10 minutes to “proof-test” the rotor prior to its return to the normal service condition, where $\omega = \omega_{op}$.
- Cold startup procedure: (i) introduce the proof-test condition directly at ambient temperature (10°C) (i.e., $\omega = 1.15\omega_{op}$) and hold for 10 minutes; (ii) then reduce the rpm to $\omega = \omega_{op}$ and resume the normal service condition.
- The operational stress in the rotor varies with ω^2 and can be calculated with the following equation:

$$\frac{\sigma}{\sigma_{des}} = \frac{\omega^2}{\omega_{op}^2}$$

where σ_{des} is the rotor design stress at 100°C (i.e., 40% of the yield strength of the steel at that temperature).

5

Alloys and Coatings

I. INTRODUCTION

The characteristics of the materials involved in a failure are obviously of importance in carrying out a failure analysis. This chapter reviews the microstructural features and related matters, such as equilibrium and isothermal transformation diagrams of some of the more common alloys, as influenced by alloying and heat treatment. The nature of the coatings used in high-temperature applications is also discussed.

II. ALLOYING ELEMENTS

Figure 5-1 shows the periodic table of the elements. In solid form the elements are characterized by their crystal structure, with the elements considered to be ordered arrays of hard spheres. The three principal crystal structures are the face-centered cubic (fcc) with four atoms per unit cell, as in the case of aluminum and copper; the hexagonal close-packed (hcp) with six atoms per unit cell, as in the case of zinc and magnesium; and the body-centered cubic (bcc) with two atoms per unit cell, as in the case of iron. The unit cells of these crystal structures are shown in Fig. 5-2. If no atom is present on a lattice site, then a point defect, known as a *vacancy*, exists. Vacancies are important agents in diffusion processes, as we shall see.

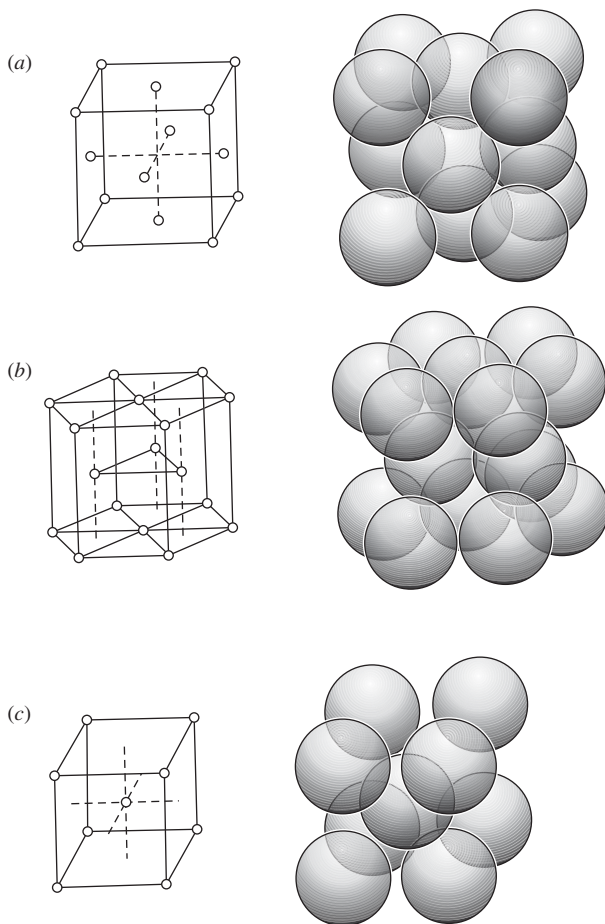
The yield strength of a pure element is usually quite low and unsuitable for structural application. A combination of elements is known as an *alloy*. The main purpose in alloying is to increase the strength properties. Additional reasons for alloying include the improvement in corrosion resistance, wear properties, and performance at elevated temperatures. There are other reasons for alloying as well. For example, if sulfur is present in a steel, during heat treatment the sulfur atoms may diffuse to the grain boundaries and cause temper embrittlement. To prevent this from happening, manganese is added to the steel and the sulfur atoms combine preferentially with the manganese to form manganese sulfide particles, thereby reducing the tendency for embrittlement.

Two types of common single-phase alloys are the *substitutional* and the *interstitial*. In a substitutional alloy, element A is replaced by element B on a lattice site. In an interstitial alloy, alloying elements such as H, C, N, and O are small enough to fit into spaces between lattice sites. Engineering alloys usually are made of a very large number of randomly oriented grains, each of which is a crystal; hence the term *polycrystalline alloy*. There are important exceptions however, such as the single crystals used in gas turbine engines of jet aircraft. Many other alloys are not single-phase alloys but may consist instead of two or more phases, as in the case of carbon steel, which consists of bcc α -iron and an intermetallic compound, Fe_3C .

III. PERIODIC TABLE

Group → ↓ Period	1	2	3	4	5	6	7	8	9	10	11	12	13	14	15	16	17	18
1	1 H																	2 He
2	3 Li	4 Be											5 B	6 C	7 N	8 O	9 F	10 Ne
3	11 Na	12 Mg											13 Al	14 Si	15 P	16 S	17 Cl	18 Ar
4	19 K	20 Ca	21 Sc	22 Ti	23 V	24 Cr	25 Mn	26 Fe	27 Co	28 Ni	29 Cu	30 Zn	31 Ga	32 Ge	33 As	34 Se	35 Br	36 Kr
5	37 Rb	38 Sr	39 Y	40 Zr	41 Nb	42 Mo	43 Tc	44 Ru	45 Rh	46 Pd	47 Ag	48 Cd	49 In	50 Sn	51 Sb	52 Te	53 I	54 Xe
6	55 Cs	56 Ba		72 Hf	73 Ta	74 W	75 Re	76 Os	77 Ir	78 Pt	79 Au	80 Hg	81 Tl	82 Pb	83 Bi	84 Po	85 At	86 Rn
7	87 Fr	88 Ra		104 Rf	105 Db	106 Sg	107 Bh	108 Hs	109 Mt	110 Ds	111 Rg	112 Cn	113 Uut	114 Fl	115 Uup	116 Lv	117 Uus	118 Uuo
Lanthanides				57 La	58 Ce	59 Pr	60 Nd	61 Pm	62 Sm	63 Eu	64 Gd	65 Tb	66 Dy	67 Ho	68 Er	69 Tm	70 Yb	71 Lu
Actinides				89 Ac	90 Th	91 Pa	92 U	93 Np	94 Pu	95 Am	96 Cm	97 Bk	98 Cf	99 Es	100 Fm	101 Md	102 No	103 Lr

Fig. 5-1. The PeriodicTable of the Elements.



The face centered cubic (FCC)
The hexagonal close packed (HCP)
The body-centered cubic (BCC)

Fig. 5-2. Unit cells. (a) Face-centered cubic (FCC); (b) hexagonal close packed (HCP); (c) body-centered cubic (BCC).

IV. PHASE DIAGRAMS

The phase diagram is a starting point in understanding microstructure-property relationships. These diagrams show the composition limits of phase fields as they exist under metastable or stable conditions. The important phase diagrams that are considered in the next sections include those for the iron-carbon system, the aluminum-copper system, the titanium-aluminum system, and the nickel-aluminum system. In

addition, the time-dependent aspects of the transformation in steels from austenite to ferrite, pearlite, bainite, or martensite are discussed.

A. Steels

For steels, the iron-carbon equilibrium diagram, Fig. 5-3 (1), together with the isothermal transformation diagrams, Fig. 5-4 (2), provide the key to understanding the multiplicity of microstructures and attendant properties that can be developed in this alloy system. Figures 5-5 to 5-9 provide examples of the variations in microstructure that occur as a function of carbon content and holding times beneath the eutectoid temperature, 723°C ($1,333^{\circ}\text{F}$).

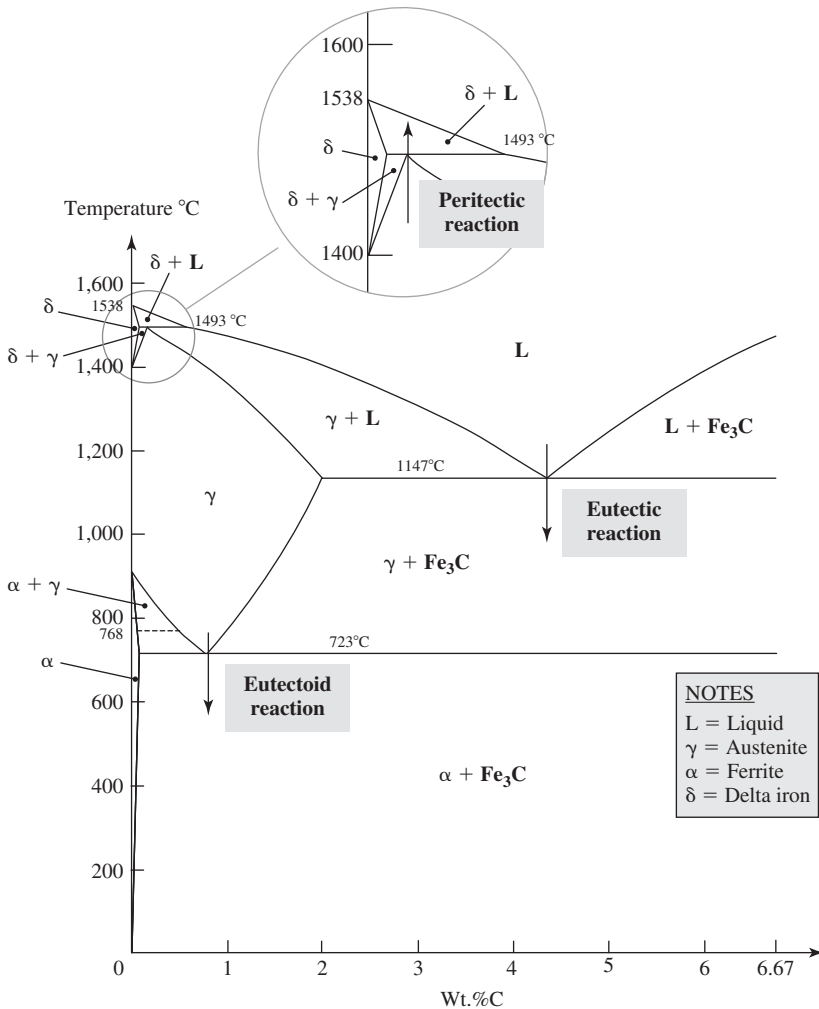


Fig. 5-3. The iron-carbon equilibrium diagram. (After *Smithells Metals Reference Book*, 1.)

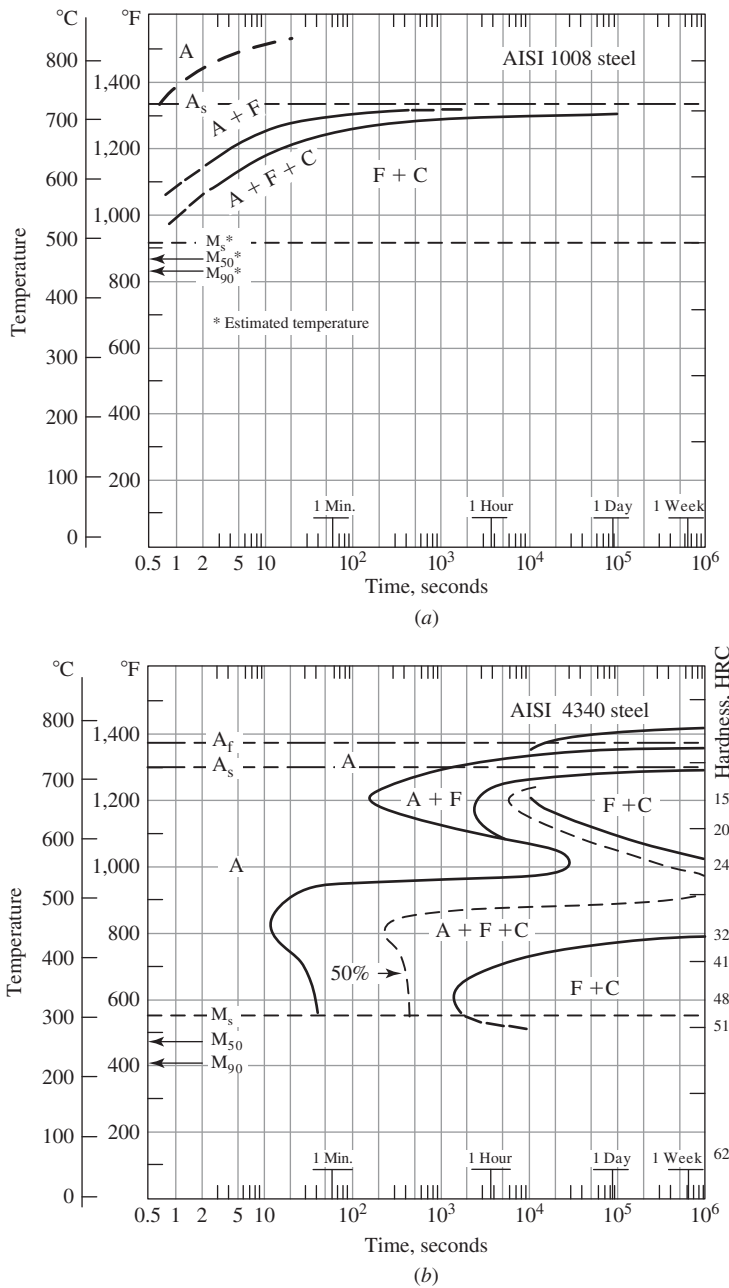


Fig. 5-4. Isothermal transformation diagrams (a) for a low- carbon steel, AISI 1008, (b) for a low-alloy steel, AISI 4340. (After *Isothermal Transformation Diagrams*, 2.)

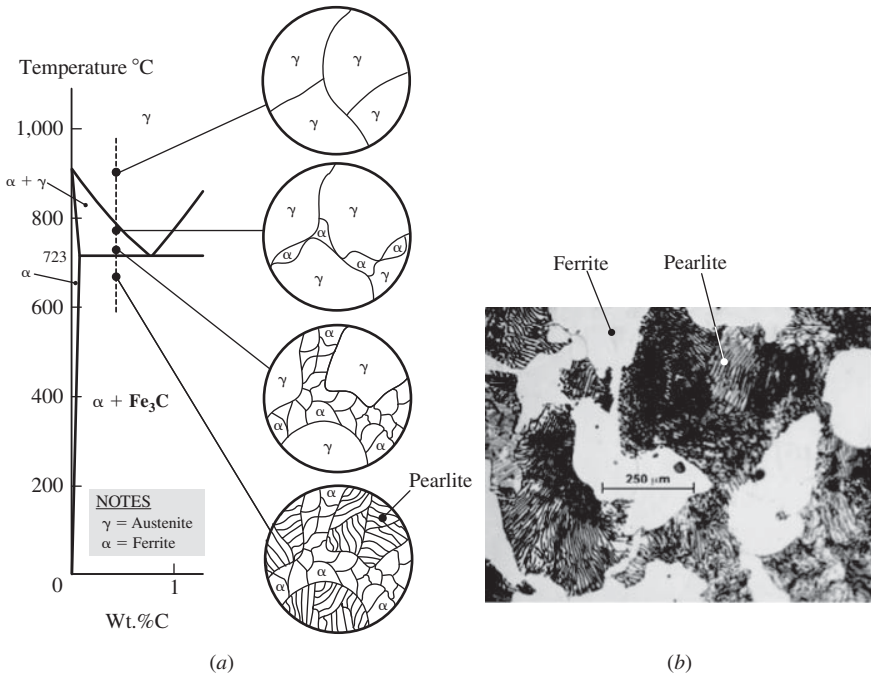


Fig. 5-5a,b. Various microstructures involving both ferrite (α) and pearlite that are developed upon slow cooling of a hypoeutectoid steel ($<0.8\%$ C) from the austenitic (γ) region. (Author created diagram; photo sourced from [http://accessscience.com/content/Heat-treatment\(metallurgy\)/311200](http://accessscience.com/content/Heat-treatment(metallurgy)/311200).)

Some definitions relating to these diagrams follow.

(a) *Ferrite*: A solid solution of one or more elements in body-centered cubic (bcc) iron. In the iron-carbon system, there are two ferrite regions separated by a region of austenite. The upper region is δ -ferrite, and the lower region is α -ferrite. Acicular ferrite is a nonequiaxed ferrite that forms upon cooling by a combination of diffusion and shear in a temperature range just above that for the formation of bainite. In low-carbon steels, the size of the ferrite grains has an important effect on the yield strength; the smaller the grain size, the higher the yield strength. The influence of grain size d on yield strength σ_Y is expressed in the Hall-Petch relationship:

$$\sigma_Y = \sigma_i + k_y d^{-1/2} \quad (5-1)$$

where σ_i is a measure of the inherent resistance of the lattice to plastic deformation and k_y is a constant. For a 0.2% carbon steel, the value of σ_i at the yield point is 70 MPa (10.1 ksi), and this value increases to 300 MPa (43.5 ksi) at a strain of 0.01, which is the maximum strain at the lower yield point. The corresponding values of k_y are 0.75 and 0.40 $\text{MPa}\sqrt{m}$ (0.68 and 0.36 $\text{ksi}\sqrt{\text{in.}}$). Changes in the values of the constants with strain occur because of the increase in dislocation density with strain.

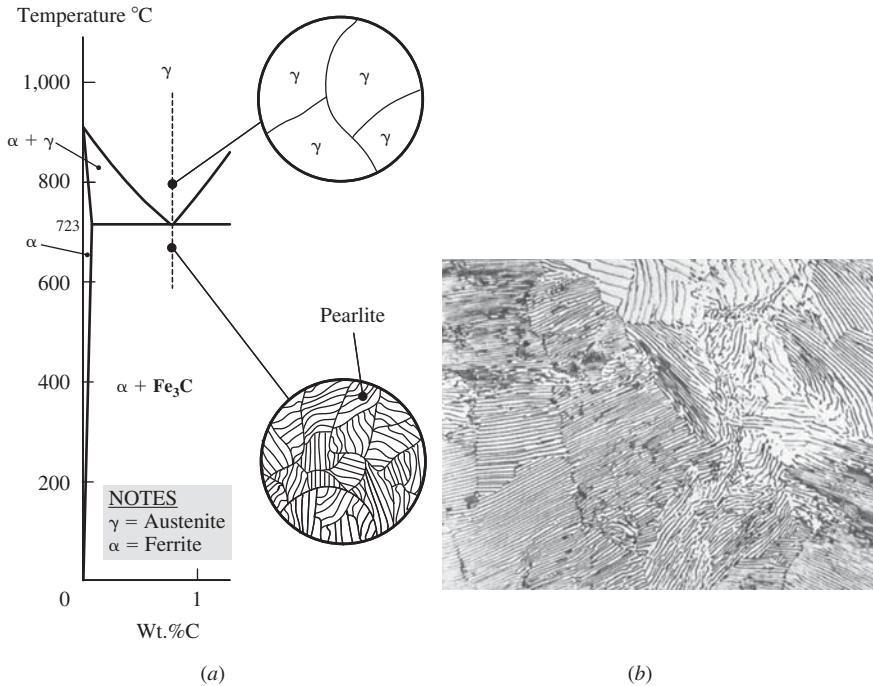


Fig. 5-6a,b. The microstructure of a eutectoid steel (0.8% C) upon slow cooling from the austenitic region. (Author created diagram; photo sourced from William F. Smith, Javad Hashemi, *Foundations of materials science and engineering*, 4th edition, McGraw-Hill International Edition, 2006, page 367.)

(b) *Austenite*: A solid solution of one or more elements in face-centered cubic (fcc) iron. In the iron-carbon system, it is known as the γ phase. The addition of 18% C and 8% Ni to low-carbon iron creates the class of alloys known as *austenitic stainless steels*, which are austenitic even at room temperature. They are noted for their resistance to corrosion, which is provided by a protective oxide. However, on cooling after welding some of the chromium can come out of solution to form grain boundary carbides, thus reducing the effectiveness of the protective oxide immediately adjacent to the weld and leading to “knife-line” attack, a form of intercrystalline corrosion.

(c) *Cementite*: A compound of iron and carbon having the formula Fe_3C ; it is also known as *iron carbide*.

(d) *Peritectic reaction*: On heating, the γ phase divides into liquid and δ (bcc) phases.

(e) *Eutectoid reaction*: On cooling, the γ phase divides into α and Fe_3C phases.

The amount of each phase present after the austenite decomposes can be determined with the aid of the *Lever Rule*. From Fig. 5-1 it is seen that the weight % of carbon present in the α -phase is 0.0025. The atomic weight of iron is 55.85; the atomic weight of carbon is 12.011. (Note that atomic weight is a dimensionless quantity, the ratio of the average mass of atoms of an element to 1/12 of the mass of carbon-12.)

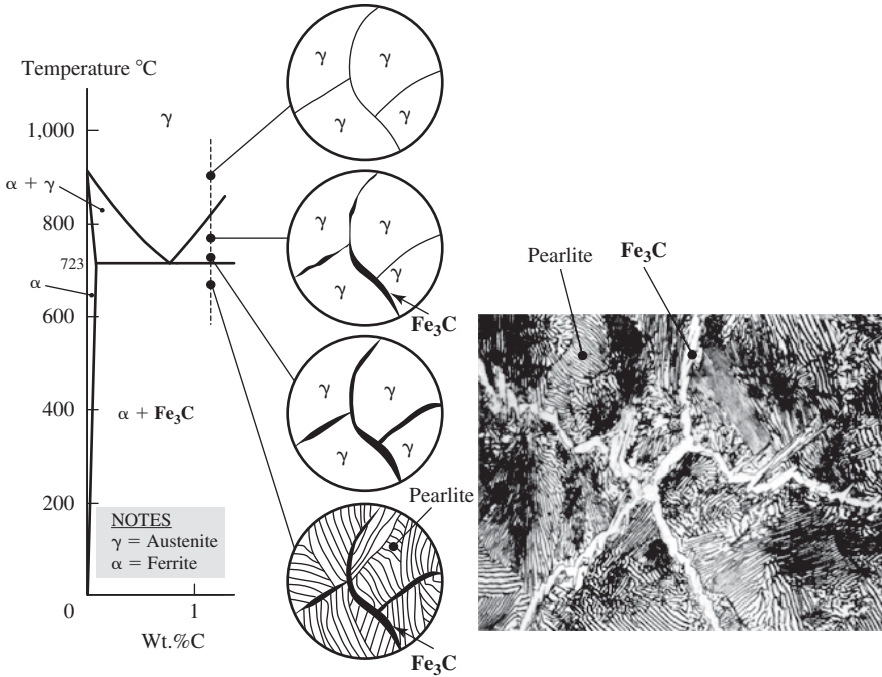


Fig. 5-7. Microstructures formed in a hypereutectoid steel ($>0.8\%$ C) upon slow cooling from the austenitic region. (Author created diagram; photo sourced from William F. Smith, Javad Hashemi, *Foundations of materials science and engineering*, 4th edition, McGraw-Hill International Edition, 2006, page 372.)

The weight % of carbon in Fe_3C is $12.011/(3 \times 55.85 + 12.011) \times 100 = 6.7 \text{ w/o}$. The weight % of carbon in a eutectoid steel is 0.8.

The fractional amount of carbon in the α phase is equal to $XC_\alpha = X(0.0025)$, where X is the fraction of α phase present. The fractional amount of carbon in the Fe_3C phase is $(1 - X) \times 6.7$. The sum of the fractional amounts of carbon in the α and Fe_3C phases must equal $1.0 \times$ the amount of carbon in the eutectoid alloy, 0.80 w/o. Therefore,

$$XC_\alpha + (1 - X) \text{ amount of C in } \text{Fe}_3\text{C} = \text{amount of C in the eutectoid alloy}$$

$$XC_\alpha - X \text{ amount of C in } \text{Fe}_3\text{C} + \text{amount of C in } \text{Fe}_3\text{C} = \text{amount of C in the eutectoid steel}$$

$$X(C_\alpha - \text{amount of C in } \text{Fe}_3\text{C}) + \text{amount of C in } \text{Fe}_3\text{C} = \text{amount of C in the eutectoid steel}$$

$$X = \frac{\text{amount of carbon in } \text{Fe}_3\text{C} - \text{amount of carbon in eutectoid}}{\text{amount of carbon in } \text{Fe}_3\text{C} - \text{amount of carbon in } \alpha}$$

$$X = \frac{6.7 - 0.8}{6.7 - 0.0025} = \frac{5.9}{6.7} = 0.88$$

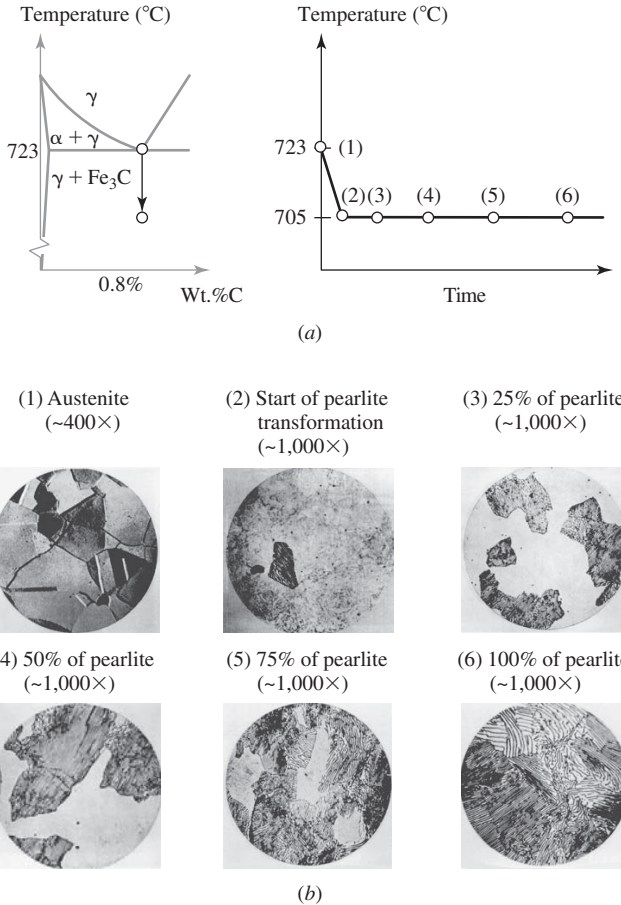


Fig. 5-8. (a) Diagrams showing temperatures and holding times involved in an isothermal transformation of a eutectoid steel. (b) The microstructures developed during isothermal transformation. (Author created diagram; source of photograph: Pat L. Mangonon, *The principles of materials selection for engineering design*. Prentice-Hall, International Edition, 1999, pages 813–815.)

That is, only 12% of the decomposed alloy is Fe_3C . The rest is α phase containing 0.0025 wt% carbon. This is an example of the use of the Lever Rule.

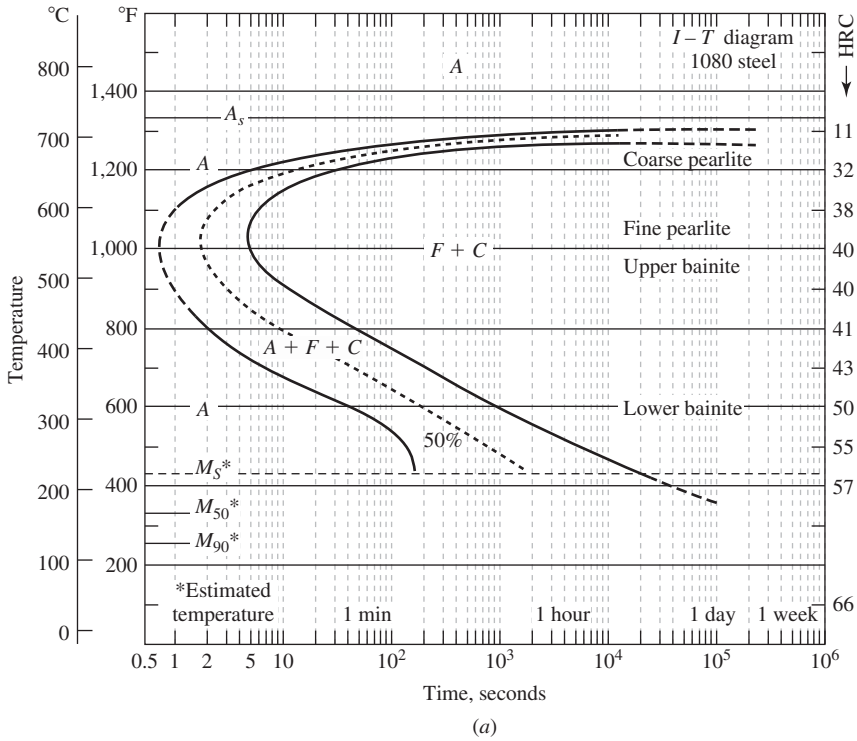
(f) *Eutectic reaction*: On cooling, the liquid phase divides into γ and Fe_3C phases.

(g) A_1 : This is the lower transformation temperature.

(h) A_3 : This is the upper transformation temperature.

(i) *Transformation range*: This is the region on the phase diagram between the A_1 and A_3 lines.

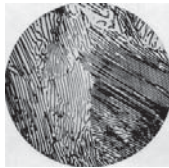
(j) *Pearlite*: This is a lamellar aggregate of ferrite and cementite occurring in steel and cast iron.



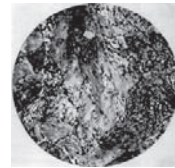
Coarse pearlite
formed at about 720°C
(Mag ~2,500×)



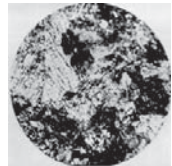
Coarse pearlite
formed at about 705°C
(Mag ~2,500×)



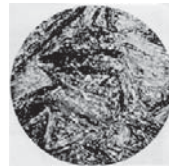
Fine pearlite
formed at about 595°C
(Mag ~3,000×)



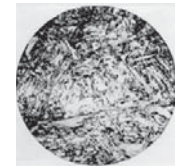
Upper bainite
formed at about 495°C
(Mag ~2,500×)



Lower bainite
formed at about 290°C
(Mag ~2,500×)



Martensitic structure
(Mag ~2,000×)



(b)

Fig. 5-9. (a) Isothermal transformation diagram of a eutectoid steel. (b) Microstructures at different holding temperatures. (Pat L. Mangonon, *The principles of materials selection for engineering design*. Prentice-Hall, International Edition, 1999, pages 815–816.)

(k) *Bainite*: This is a decomposition product of austenite that consists of an aggregate of ferrite and carbide and that forms at a temperature intermediate between the pearlite and martensite ranges.

(l) *Martensite*: A diffusionless transformation product of austenite that forms below the M_s (martensite start) temperature. Low-carbon martensites are bcc and have a ductile, lathlike microstructure. High-carbon martensites are bcc tetragonal and have a more brittle, platelike microstructure. There is a volume expansion of 1–3% when martensite forms, and the martensite is heavily deformed. As a result, martensite contains a high density of dislocations, which contribute to its high strength. The M_s temperature is dependent upon the alloy content. The following equation is typical of the empirical expressions that have been developed to relate the M_s temperature and composition in carbon and low-alloy steels (3):

$$M_s(^{\circ}\text{F}) = 930 - 570 \times \%C - 60 \times \%Mn - 50 \times \%Cr \\ - 30 \times \%Ni - 20 \times \%Mo - 20 \times \%W \quad (5-2a)$$

$$M_s(^{\circ}\text{C}) = 499 - 317 \times \%C - 33 \times \%Mn - 28 \times \%Cr \\ - 17 \times \%Ni - 11 \times \%Mo - 11 \times \%W \quad (5-2b)$$

It is seen that carbon has a particularly strong effect on the M_s temperature.

(m) *Retained austenite*: This is austenite that did not transform on cooling.

(n) *Cast iron*: An iron containing carbon in excess of the solubility in the austenite that exits at the eutectic temperature. In the case of a plain iron-carbon alloy, the solubility of carbon in austenite at the eutectic temperature is 4.3 wt%. Therefore, if the carbon content is in excess of 4.3 wt%, the alloy should be considered to be a cast iron.

Some common heat-treating and working operations are:

(a) *Recrystallization*: The formation of a new, strain-free grain structure from that existing in worked metal.

(b) *Hot working*: The deforming of a metal at a sufficiently high temperature that dynamic recrystallization occurs so that there is no strain hardening.

(c) *Cold working*: The deformation of a metal at a temperature below the recrystallization temperature.

(d) *Hot forging*: The forging of a metal, usually in the temperature range of 1,100–1,150°C (2,000–2,100°F).

(e) *Annealing*: Furnace cooling from a temperature just above A_3 .

(f) *Normalizing*: Air cooling from a temperature just above A_3 .

(g) *Hardenability*: With respect to the isothermal transformation diagrams, Fig. 5-4, hardenability relates to the time available on cooling austenite to avoid transformation to ferrite-pearlite and a transformation instead to bainite or martensite. The more time is available, the greater the hardenability. One of the principal

reasons for alloying steel is to increase its hardenability, and this is clearly seen in comparing Figs. 5-4a and 5-4b. The hardenability of certain steels, such as the maraging steels, is sufficiently high that heavy sections transform to martensite on cooling from the austenitic range. An increase in the austenite grain size will also increase hardenability, as this reduces the number of sites at which transformation is initiated.

(h) *Tempering*: Heating a quenched alloy to a temperature below the transformation range to produce desired changes in properties. The resistance to fracture of an alloy can be strongly dependent upon heat treating and processing parameters. For example, HY 80 steel, an alloy used for submarine hulls, is significantly tougher in the quenched and tempered condition than in the normalized condition due to differences in grain size and the distribution of precipitates.

(i) *Spheroidizing*: A heat treatment carried out just below A_1 during which lamellar cementite becomes globular.

(j) *Stress relieving*: Holding at a temperature near 650°C (1200°F), usually for several hours, to reduce residual stress. In the case of weldments, the weld microstructure will be tempered.

(k) *Carburizing*: The process of diffusing carbon into the surface layers of austenitic steel, usually carried out at temperatures of $925\text{--}980^{\circ}\text{C}$ ($1,700\text{--}1,800^{\circ}\text{F}$) in a time period of about an hour.

(l) *Nitriding*: The process of diffusing nitrogen into the surface layers of ferritic steel, usually carried out at temperatures of $480\text{--}540^{\circ}\text{C}$ ($900\text{--}1,000^{\circ}\text{F}$) in a time period of 8–24 hours.

(m) *Banding*. A heterogeneous microstructure with segregates aligned in filaments or planes parallel to the direction of working. An example is shown in Fig. 5-10.

(n) *Preheating in welding*: Heating the region to be welded just prior to welding in order to reduce the cooling rate after welding to prevent the formation of martensite. The recommended preheat temperature varies with the carbon content of the steel. For a 0.2% C steel it would be 95°C (200°F). For a 0.7% C steel it would be 315°C (600°F).

Some problems associated with hot working and heat treating and processing are:

(a) *Hot shortness*: This is a type of brittleness that develops in copper-containing steels in the hot working range where the solubility of copper in γ -iron is as much as 9%. The cracking associated with hot shortness occurs from the surface inward. In the presence of oxygen, three layers of iron oxides form. The outer oxide is hematite, Fe_2O_3 , and is reddish-brown to black in color. The intermediate layer is magnetite, Fe_3O_4 , and is black in color, and the inner layer is wustite, FeO , which is also black in color. At elevated temperatures, a metallic phase (95% Cu, 5% Fe) appears in the FeO . This phase remains dispersed in the FeO at relatively low temperatures near 900°C (1650°F) but is concentrated as a nearly continuous layer at temperatures of $1,050\text{--}1,200^{\circ}\text{C}$ ($1,920\text{--}2,190^{\circ}\text{F}$) along the metal/oxide interface. Since the melting point of copper is $1,084^{\circ}\text{C}$ ($1,983^{\circ}\text{F}$), detrimental penetration of the austenitic grain

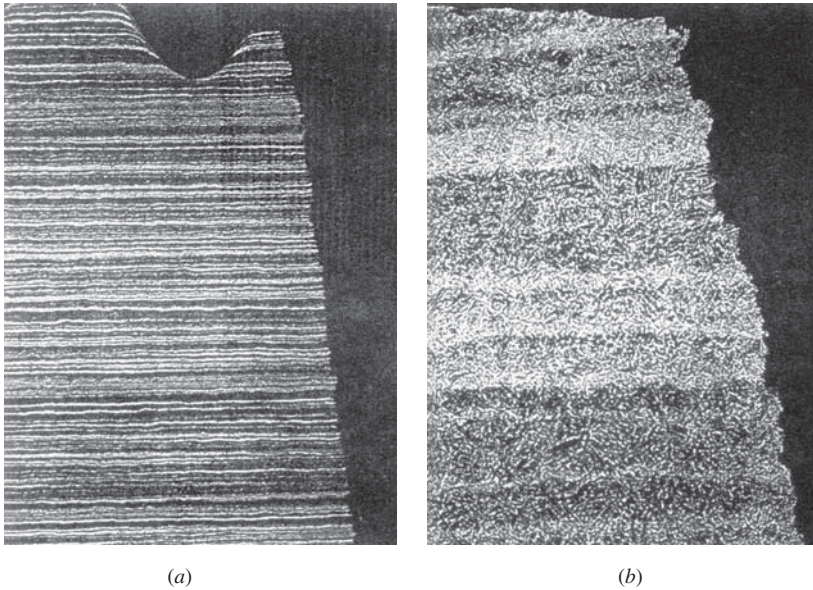


Fig. 5-10. An example of banding in a medium-carbon steel. (a) Magnification: 50 \times ; (b) Magnification: 400 \times . (Courtesy of S. Crosby.)

boundaries by the liquid or nearly liquid copper-rich phase occurs rapidly. Because of concerns about hot shortness, the amount of automotive scrap is limited in the making of quality steel due to the high copper content of this type of scrap.

(b) *Temper embrittlement*: Temper embrittlement occurs at a higher temperature than does blue brittleness, and is due to the segregation of elements such as antimony and phosphorus to prior austenitic grain boundaries. In the heat treating of heavy sections, either during temperature rise or temperature fall, there is a danger of temper embrittlement because the relatively slow rate of temperature change may provide sufficient time for deleterious forms of segregation to occur. A similar type of embrittlement can occur during long-time service at elevated temperatures. For example (4), the flues of a furnace were constructed of a steel that contained 0.09% phosphorus, a relatively high value, and after 30,000 hours of service at 430°C (806°F), the steel was found to be severely embrittled. The room temperature Charpy energy of the steel had decreased from an initial value of 80 J to 4 J. The addition of molybdenum can offset the embrittling effects of phosphorus, but molybdenum was not an alloying element in this steel, and the embrittlement was attributed to the high phosphorus content.

(c) *Blue brittleness*: This type of embrittlement is associated with strain aging and the precipitation of carbides at temperatures near 350°C (662°F). Since this reaction is promoted by cyclic or unidirectional plastic deformation, the working of steels in this range is not recommended. Figure 5-11 shows, for several low-carbon steels, the

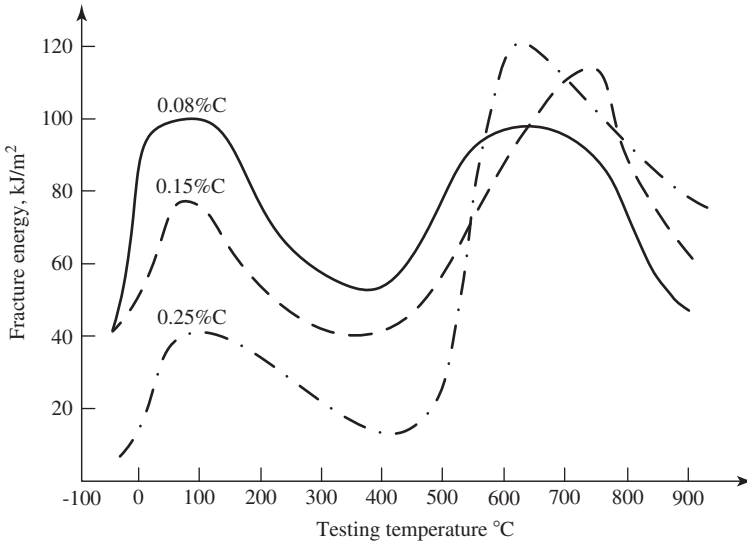


Fig. 5-11. Impact energy curves for low-carbon steels in which blue brittleness occurs at around 300°C (562°F). (After Rheinhold, 11.)

extent of the drop in toughness that occurs in this range. This type of embrittlement is referred to as *blue brittleness* because of the color of the oxide formed on a steel.

(d) *Quench cracking*: The objective in quenching a steel is to prevent transformation at temperatures above the martensite range. Susceptibility to quench cracking increases with the severity of the quench and with the carbon content. The influence of carbon is primarily due to its effect on the M_s temperature. The M_s temperature decreases from about 425°C (800°F) at 0.2% C to 150°C (300°F) at 1.0% C, and as the M_s temperature decreases, the volume expansion associated with the transformation increases. If the hardenability is high enough, when the interior transforms, the already transformed, relatively brittle surface will be placed in tension and may crack. Further, the potential for cracking is increased by the presence of stress raisers. In order to avoid delayed cracking after the quench, a tempering operation should immediately follow the quench. Allowing fully quenched pieces to stand overnight before tempering increases the probability of crack formation.

B. Aluminum Alloys

There are two classes of aluminum alloys, heat-treatable and non-heat-treatable. The former category attains strength properties by a process of quenching and aging, while the latter category is strengthened by cold work. The equilibrium diagram for the Al-Cu system, a typical heat-treatable alloy, is shown in Fig. 5-12 (5). Commercial alloys of this type also contain additional alloying elements such as silicon, iron, manganese, magnesium, lithium, and zinc. For those alloys in which copper is the

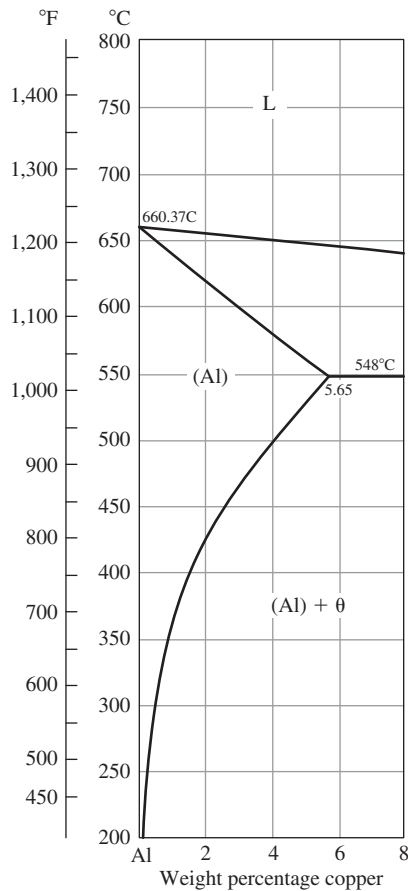


Fig. 5-12. Al-Cu phase diagram. (L = liquid.) (After ASM Metals Handbook, 5.)

principal alloying element, the amount of copper is about 4%. From Fig. 5-12, it is seen that this amount of copper is in solid solution at 500°C (932°F). However, on cooling from this temperature range, a phase boundary is crossed and precipitation occurs, either naturally at room temperature or artificially at a slightly elevated temperature. During aging, the first precipitates to form are copper-rich metastable regions known as *Guinier Preston (GP) zones*. There are two types. The first type to form is known as GP I, and upon further aging, the GP I zones evolve into GP II zones. Both of these zones are fully coherent with the parent fcc lattice, meaning that the crystallographic planes of the zones are continuous with the parent lattice in three dimensions, although the lattice parameters may differ slightly. As a consequence, at a sufficiently high shear stress, dislocations are able to pass from the parent matrix and shear through the coherent zones. With further aging, the semicoherent phase θ' appears, and with yet further aging, the noncoherent equilibrium phase θ (CuAl_2) with its own crystal structure appears. Maximum strength is reached when both GP II

and the θ' phases are present. When the precipitate is θ , the strength is less than that in the peak-aged condition, and the system is considered to be in an overaged condition.

In contrast to the ferrite-pearlite system, the grain size is not a factor determining the strength of aluminum alloys; rather, it is the spacing of the precipitates that governs the shear stress τ required for plastic deformation. The equation is

$$\tau = \frac{\mu b}{l} \quad (5-3)$$

where μ is the shear modulus, b is the Burger's vector, and l is the spacing between particles. At a spacing of several microns, typical of the overaged condition, the ratio of b to l is about 10^{-4} . For a shear modulus of 23 GPa (3.4×10^6 psi), the value of τ would be only 2.3 MPa (340 psi), a negligible amount. For particle strengthening to be effective, the value l must be much smaller.

C. Titanium Alloys

The density of titanium, 4.507 gm/cc, is midway between that of steel, 7.87 gm/cc, and that of aluminum, 2.699 gm/cc. It has a greater Young's modulus, 116 GPa (16.8×10^6 psi), than aluminum, 69 GPa (10×10^6 psi), and has useful long-term elevated properties up to 540°C (1,000°F), as well as good corrosion resistance. All of these characteristics make titanium and its alloys attractive for aerospace applications, and they are therefore used up to moderate temperatures in jet engines and as major structural components of aircraft as well. The three principal alloy types are known as α alloys, α - β alloys, and β alloys.

In pure titanium, there is an allotropic transformation at 885°C (1625°F) from the low-temperature hexagonal α phase to the high-temperature bcc β phase. The alloying elements aluminum, tin, carbon, oxygen, and nitrogen stabilize the α phase, and Ti-5Al-2.5Sn is an example of an important α phase alloy. Oxygen, carbon, and nitrogen are usually considered as impurities in titanium, but small quantities of oxygen are used as strengthening agents in most alloys, although extra-low interstitial (ELI) alloys are available if desired. The elements vanadium, zirconium, and molybdenum stabilize the β phase and cause it to exist as the stable phase at temperatures well below 885°C (1625°F). In fact, the Ti-4.5Sn-6Zr-11.5Mo alloy is β stable at room temperature and is therefore known as a β alloy.

Figure 5-11 is a pseudobinary equilibrium diagram for the (Ti-6Al)-V system (6). In this system, the aluminum and vanadium atoms are in solid solution above the β -transus. The addition of α -stabilizer aluminum to titanium increases the range of the α field, whereas vanadium expands the β field. Both of these elements are present in the most common α - β alloy, Ti-6Al-4V in weight %, or Ti-10Al-4V in atomic %. In common with steels, a variety of microstructures can be developed in titanium alloys, depending upon the composition and cooling rate. Ti-6Al-4V can be strengthened by quenching from above or below the β -transus followed by aging at moderately elevated temperature. However, at temperatures above the β -transus, the β grains grow rapidly, and therefore heat treating above the β -transus

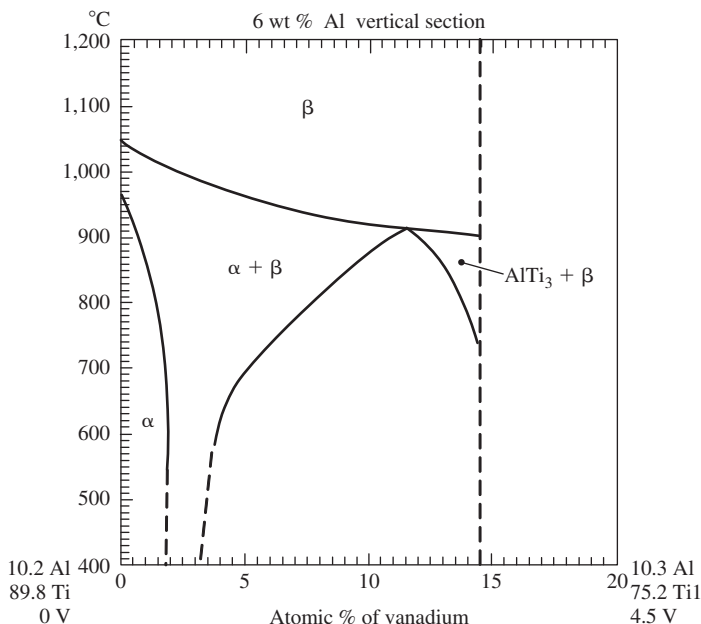


Fig. 5-13. (Ti-6Al)-V phase diagram. (After *Handbook of Ternary Alloy Phase Diagrams*, 6.)

may be undesirable. The alloy is therefore often heat-treated at a temperature some 15°C (59°F) below the β -transus to reduce the amount of α phase. It is then rapidly cooled to transform some of the β phase to martensite and then aged at a temperature of about 700°C . This type of heat treatment is referred to as a *solution treated and aged* (STA) heat treatment. If the aging treatment is carried out at a somewhat higher temperature, the material is said to be in a *solution treated and overaged* (STOA) condition. During these aging treatments, fine volumes of α form in the β phase. An aging heat treatment at temperatures below 510°C (950°F) can result in a β -to- ω transformation. The ω phase embrittles titanium alloys, but aging for sufficient time, for example, 8 hours, serves to eliminate the ω phase and to restore ductility.

An undesired nitrogen-stabilized phase, referred to as *hard α* , can be present in Ti-6Al-4V and act as a site for relatively easy crack initiation. To avoid the presence of this phase, triple vacuum-remelt procedures are used. Another undesired phase is known as *α case*. This phase can form as a surface oxide of some thickness if the heat-treating atmosphere contains oxygen. It is undesired because of its hard, brittle nature.

D. Nickel-Base Superalloys

Nickel-base superalloys are widely used in the hot sections of gas turbine engines. They may be in the form of forged or cast polycrystalline alloys, cast directionally solidified alloys, or cast single crystals. The use of directional solidification and

single crystals is aimed at minimizing or eliminating the deleterious effects of grain boundaries in the creep range.

The unique microstructure of nickel base superalloys permits the alloys to be used for short periods of time at remarkably high fractions of their melting points, for example, $0.8T_M$. The microstructure is based upon a two-phase system known as $\gamma - \gamma'$, where γ is the fcc nickel-rich matrix phase and γ' is a precipitate phase. The γ' phase is an ordered fcc phase based on the composition Ni_3Al . The unit cell of the γ' phase consists of aluminum atoms at the cube corners and nickel atoms at the centers of the cube faces. This ordered phase is coherent with the parent matrix and is often of cuboidal form, as indicated in Fig. 5-14. The lattice parameter of γ' can be either slightly larger or slightly smaller than that of the parent matrix, depending upon the particular alloy and temperature, a factor contributing to the stability of the phase at elevated temperatures. The coherency strains are also considered to contribute to the strength of these alloys. Since the γ' phase is ordered, the dislocations gliding through it do so in pairs. As the first dislocation glides through, the ordered arrangement of atoms along the glide plane is disturbed. The second dislocation is needed to restore order. The relatively high resistance to plastic deformation of $\gamma - \gamma'$ alloys has been attributed to the difficulty that the first dislocation experiences in entering the γ' phase from the γ phase. The climb of dislocations to bypass the γ' phase is also a possibility at elevated temperatures.

The phase diagram for the nickel-aluminum system is shown in Fig. 5-15 (7), and it is seen that the γ' phase (86.7 wt % Ni, 13.3 wt % Al) is ordered to the peritectic temperature, $1,395^\circ\text{C}$ ($2,543^\circ\text{F}$). However, commercial two-phase alloys contain less than 13.3 wt % Al, and also contain titanium as well as a number of additional alloying elements; therefore, they are a mixture of the phases γ and γ' . As shown in the following table, the composition of an alloy depends upon whether the alloy is to

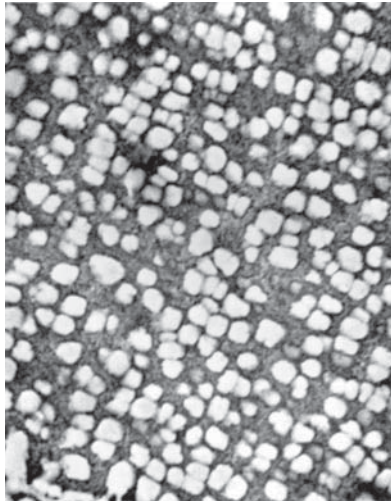


Fig. 5-14. An example of cuboidal γ' .

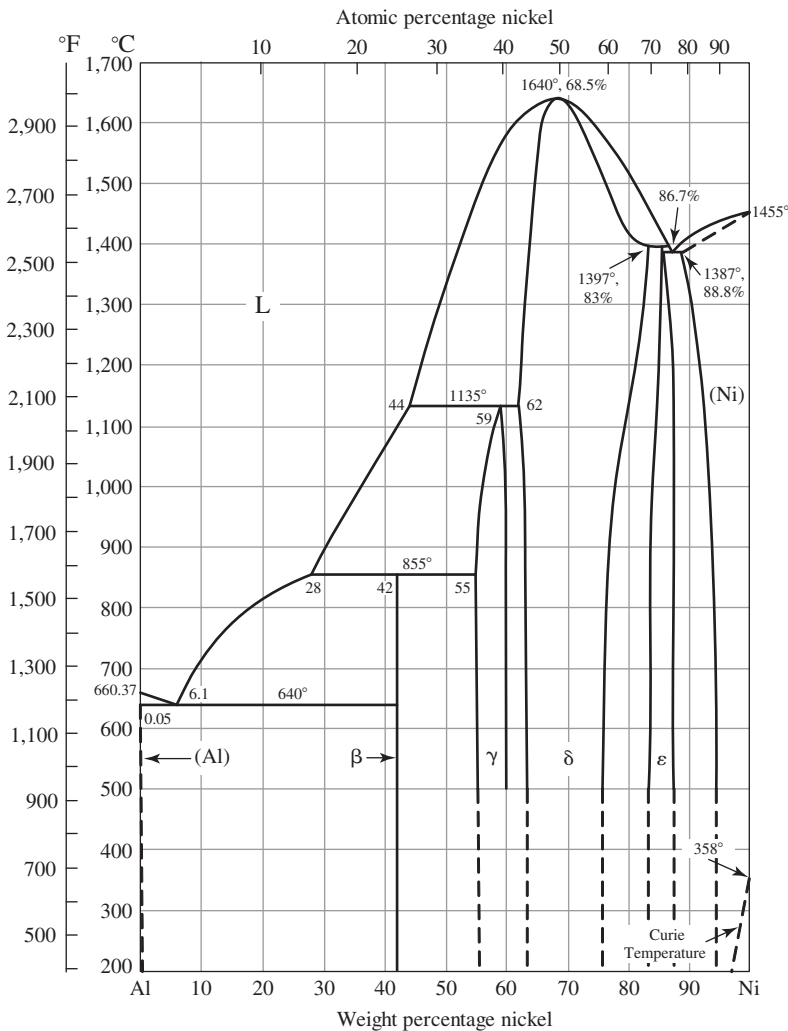


Fig. 5-15. Al-Ni phase diagram. (After ASM Metals Handbook, 7.)

be used as a polycrystal or a single crystal. The single crystal contains fewer alloying elements because many of the elements contained in the polycrystal are there to strengthen the grain boundaries, which, of course, are not present in single crystals. Single-crystal blades are inspected for casting porosity at the time of manufacture. However, if a turbine blade containing undetected porosity should enter service, there is a possibility that the pores will act as nuclei for fatigue crack formation. Another cause for concern is foreign object damage, since the damaged area may recrystallize in polycrystalline form and be more prone to crack initiation than an undamaged single crystal would be. As a result, the creep and fatigue properties can be significantly degraded.

Composition of MAR-M200

	Cr	W	Co	Al	Ti	Nb	C	B	Zr	Ni
Single Crystal	9.0	12.0	10.0	5.0	2.0	1.0	—	—	—	Bal.
Polycrystal	9.0	12.0	10.0	5.0	2.0	1.0	0.15	0.15	0.05	Bal.

Both polycrystal and single-crystal nickel-base superalloys exhibit an elevated temperature region in which the alloying elements are in solid solution. The γ' solvus marks the lower equilibrium boundary of this region. The temperature of the γ' solvus depends upon the sum of the aluminum and titanium weight percentages. At a sum of 4 wt %, the solvus is at 1,038°C (1,900°F), and at a sum of 8 wt % it is at 1,150°C (2,100°F). Upon aging below the γ' solvus, precipitation occurs. A typical aging treatment involves aging at a temperature below the solvus for several hours to develop primary precipitates, followed by further aging for up to 20 hours at a temperature some 200°C (392°F) less than the solvus temperature to bring about secondary precipitate formation. The secondary precipitates are smaller than the primary and are said to improve the creep strength. Figure 5-16 (8) shows an example of the effect of aluminum plus titanium content on the 100-hour creep rupture strength of several nickel-base superalloys at 870°C (1600°F).

If the temperature of a blade should rise in service due to poor convective cooling or improper operating conditions, it is possible for the γ' solvus to be exceeded. The γ' phase would then go back into solution and reprecipitate later on slow cooling as fine γ' . An example of this is shown in Fig. 5-17. Therefore, some information on the thermal history of a blade may be obtained through examination of microstructure.

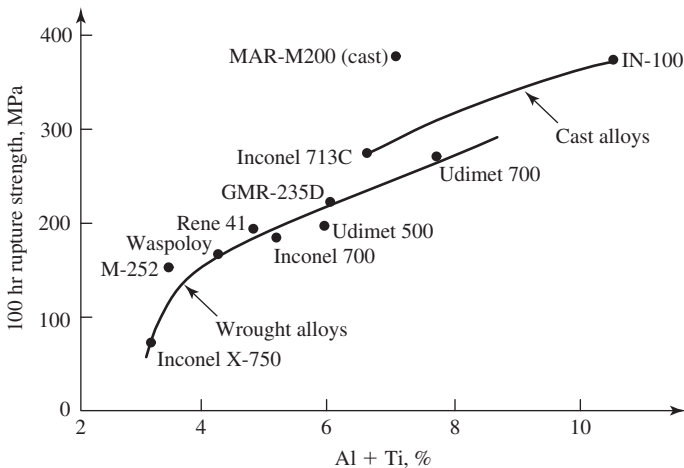


Fig. 5-16. Effect of the (Ti + Al) content on the 100-hour rupture strength of nickel-base superalloys at 870°C (1,600°F). (After Cross, 8.)

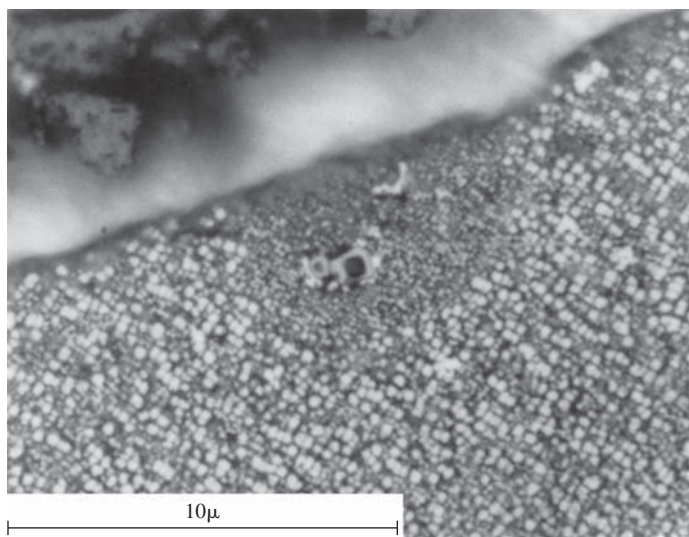


Fig. 5-17. Reprecipitated γ' .

Up to about 850°C ($1,560^{\circ}\text{F}$), the γ' particles retain their cuboidal shape, and during deformation they are cut by dislocations. At higher temperatures, γ' precipitates tend to transform to platelike particles known as *rafts*, which for most superalloys under uniaxial stress lie perpendicular to the tensile stress axis or parallel to the compressive stress axis (8). Usually these rafts accelerate the creep rate and thus reduce the creep strength. The rate of fatigue crack propagation is also enhanced when the rafts lie perpendicular to the stress axis. Conversely, the rate is decreased when the rafts are parallel to the axis of cyclic stressing.

An interesting characteristic of single crystals of γ' (Ni_3Al) is that the yield stress is a function of strain and temperature, as shown in Fig 5-18 (9). At a strain of 10^{-6} the yield stress is independent of temperature, but at a strain of 10^{-2} the yield strength rises remarkably with temperature before decreasing to a temperature of about 700°C ($1,300^{\circ}\text{F}$). The increase of the yield stress with temperature has been attributed (10) to the cross slip of screw dislocations from $\{111\}$ planes where they are glissile onto $\{100\}$ planes where they are sessile. However, at temperatures above 700°C ($1,300^{\circ}\text{F}$) the dislocations can glide on the $\{100\}$ planes, and the yield strength decreases with further increase in temperature.

V. COATINGS (9)

The turbine blades and vanes in the hot sections of jet aircraft engines and in stationary power plants are often coated for protective reasons. After solution heat treating, the coating application process is carried out at a high temperature just

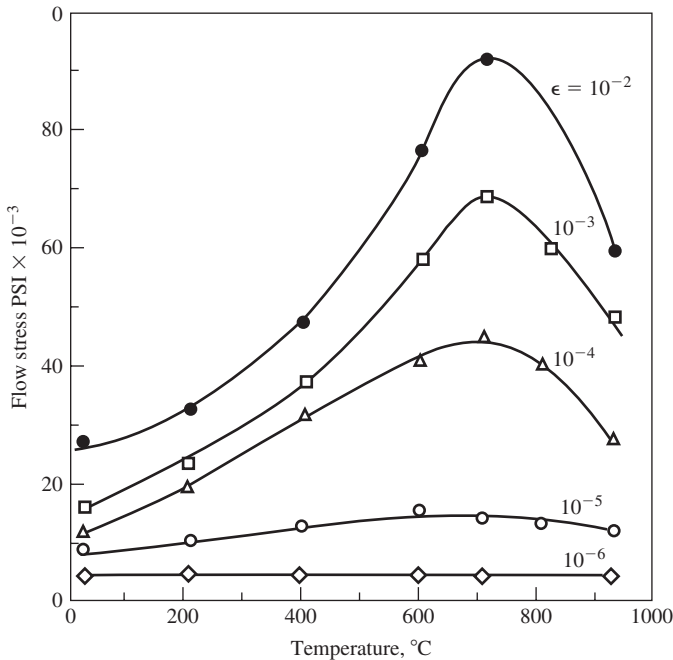


Fig. 5-18. The microstrain yield stress as a function of temperature for Ni_3Al . (After Thornton et al. (9).)

below the γ' solvus, and therefore primary γ' precipitates as the coating is being applied. After the coating has been applied, a secondary precipitation of γ' may take place at lower temperatures. As a result, there will be a bimodal distribution of γ' sizes, as shown in Fig. 5-19, with the larger size being associated with the coating process and the finer precipitate sizes being associated with aging at a lower temperature. The optimum γ' size is considered to be in the range of 0.5 to 1.0 μm .

The maximum in-service temperature of nickel-based superalloys is about 950°C (1,740°F); above this temperature the γ' phase tends to coarsen, with attendant loss in properties. In addition, the channel between γ' particles may tend to rupture, depending upon the degree of misfit between the phases.

The coatings that are used to protect components in the hot section of gas turbine engines are of two types: (a) oxidation-resistant coatings and (b) thermal barrier coatings (TBCs). The latter are used to reduce the operating temperatures of blades and vanes by reducing the heat flux across the component wall. The characteristics of a TBC and a turbine blade are shown in Fig. 5-20, the superalloy walls themselves may be only 1 mm thick. The TBC consists of the outer coating, a thermally grown oxide that develops in service, a bond coat to promote the adhesion of the outer coating and the substrate. Some interdiffusion occurs between the substrate and the bond coat. As can be seen, passageways for cooling gases make up a large fraction of the blade's cross section.

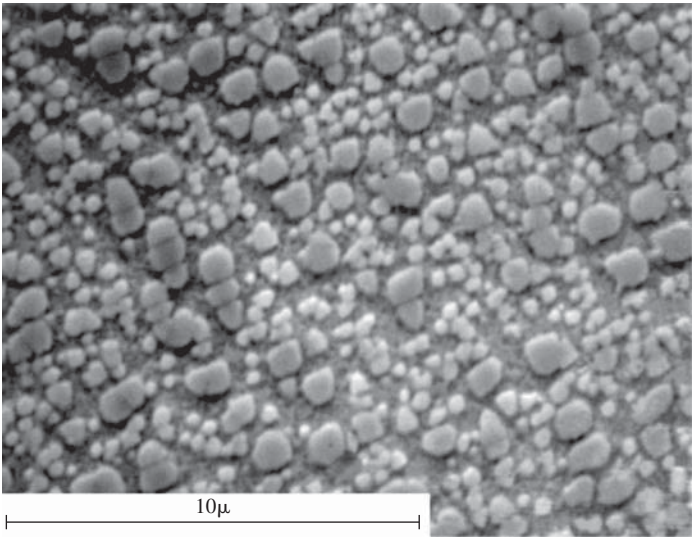


Fig. 5-19. Bimodal distribution of γ' .

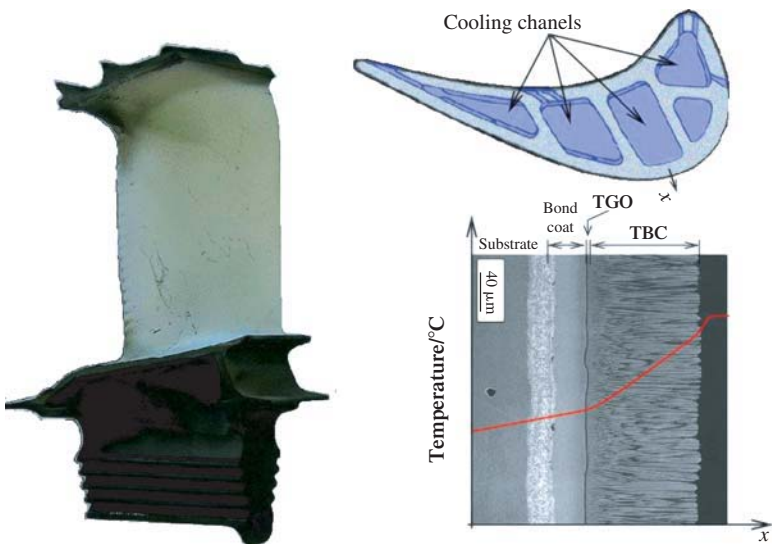


Fig. 5-20. A jet engine turbine blade. Note the cooling passages in the blade and the structure of a thermal barrier coating (TBC).

Oxidation coatings are used on the first- and second-stage superalloy blades and vanes of most of the advanced gas turbines, as well as on the internal cooling passages of the hotter parts of blades.

There are two standard coating groups: (a) diffusion coatings, including aluminides and modified aluminides, and (b) overlay coatings including TBCs that are of the MCrAlY type, where M can be either nickel or cobalt or a combination of the two.

Diffusion coatings are designed to form stable, continuous, and slow-growing, protective alumina oxides. Diffusion coating is a surface modification process wherein the coating element are deposited on the surface, and then the coating species is diffused into the substrate to form a protective layer, which is usually 10–100 μm thick. The phase providing the aluminum for the protective oxide layer is $\beta\text{-NiAl}$. The incorporation of platinum into the aluminide diffusion coating improves the oxidation, hot corrosion, and sulfidation resistance.

MCrAlY overlay coatings are often deposited by plasma spraying, and in contrast to diffusion coatings, they do not consume the substrate. However, a bond coat is usually involved, and there is diffusional interaction between the bond coat and substrate. The fact that the overlay coatings (TBCs) do not consume the substrate is an advantage in repair or replacement since the stripping of a diffusion coating can lead to appreciable loss of the substrate material. On average, TBCs are replaced after 2,000 hours of service, and the replacement process may be carried out three times during the lifetime of a component such as a turbine blade. In general, the mechanical properties of overlay coatings are better than those of aluminide coatings.

Thermal barrier coatings consist of either an MCrAlY or platinum-modified aluminide coating known as a *bond coat* together with a ceramic top coat. In electron beam physical vapor deposition (EB-PVD) coatings, a continuous, thin (1 μm) thermally grown oxide (TGO) layer is developed prior to the deposition of the ceramic. The layer imparts good adhesion to the TBC and protects the substrate from oxidation and corrosion. A ceramic outer layer, the topcoat, which consists of 6–8 wt % yttria-stabilized zirconia (YSZ), may then be deposited by EB-PVD. The top coat then grows in the form of columnar grains on the bond coat. The typical thickness of a TBC on a turbine blade is 125–200 μm . The grains are strongly bonded to the substrate but weakly bonded to each other, thereby providing good thermal strain tolerance. However, during service, silicon dioxide, SiO_2 , aluminum oxide, Al_2O_3 , and magnesium oxide, MgO ash particles accumulate between the grains and sinter them together, thereby reducing the strain tolerance.

Air plasma sprayed (APS) coating are also used. These coatings are deposited in layers, and their microstructure does not have a columnar structure, but consists instead of individual platelets formed from droplets impinging on the surface during the spraying process. For APS coatings, the TGO between the top coat and the bond coat develops under service conditions.

In service, the lifetime of components that are protected by an oxidation-resistant coating can be limited by the premature cracking of the protective layer, due to thermal mechanical fatigue or thermal shock, thereby exposing the substrate alloy to incipient cracking and to attack by the oxidizing atmosphere. The tendency for cracking under thermal-mechanical loading is a function of the difference between the coefficients of thermal expansion (CTE) of the coating and substrate as well as of the thickness of the coating, for thicker coatings fail at lower strains than do thinner coatings. With TBCs, on the other hand, the interface between the coating and substrate is often the weak link. The cracking of this interface can result in large-scale delamination due to the spalling off of the top coat from the underlying bond coat. In the failure process the difference in CTE is again an important factor, with spallation of the top coat being triggered by small buckles that develop in the bond coat as the result of ratcheting.

VI. SUMMARY

This chapter has briefly reviewed some of the principal characteristics of widely used alloys and coatings. In a failure analysis, it is at times important that the microstructure of the material examined be in the condition specified. If not, the cause of the discrepancy may have to be established, and this may require a more detailed knowledge of material processing than has been provided herein. The many volumes of the *ASM Handbook* series are valuable sources of such information.

REFERENCES

- (1) *Smithells Metals Reference Book*, 6th ed., ed. by E. A. Brandes, Butterworth, London, 1983, pp. 11–143.
- (2) *Isothermal Transformation Diagrams*, US Steel, Pittsburgh, PA, 1963.
- (3) P. Payson and C. H. Savage, Martensite Reactions in Alloy Steels, *Trans. ASM*, vol. 33, 1944, pp. 261–275.
- (4) D. R. H. Jones, “Failures of Structures and Components Which Fracture Mechanics Would Have Prevented,” in *Fracture Mechanics: Applications and Challenges*, ed. by M. Fuente, M. Elices, A. Martin-Meizoso, and J.M. Martinez-Esnaola, ESIS Pub. 26, Elsevier, Oxford, 2000, pp. 29–46.
- (5) *ASM Metals Handbook*, vol. 8, ASM, Materials Park, OH, 1973, p. 259.
- (6) *Handbook of Ternary Alloy Phase Diagrams*, vol. 4, ed. by P. Villars, A. Prince, and H. Okamoto, ASM, Materials Park, OH, 1973, p. 4389.
- (7) *ASM Metals Handbook*, vol. 8, ASM, Materials Park, Ohio, 1973, 262.
- (8) H. C. Cross, *Metals Progress*, vol. 87, 1965, p. 67.
- (9) P. R. Thornton, R. G. Davies, and T. L. Johnston, The Temperature Dependence of the Flow Stress of the γ' Phase Based upon Ni_3Al , *Metallurgical Trans.*, vol. 1, 1970, pp. 207–218.
- (10) B. H. Kear and H. G. F. Wilsdorf, *Trans. TMS-AIME*, 1962, vol. 224, pp. 382–386.
- (11) H. Mughrabi, in *Fracture Mechanics, Applications and Challenges*, ed. by M. Fuentes, M. Elices, A. Martin-Meizosa, J. M. Martinez-Esanola, ESIS Pub. 26, Elsevier, Oxford, 2000, pp. 13–28.
- (12) J. Bressers, S. Peteves, and M. Steen, in *Fracture Mechanics, Applications and Challenges*, ed. by M. Fuentes, M. Elices, A. Martin-Meizosa, J. M. Martinez-Esanola, ESIS Pub. 26, Elsevier, Oxford, 2000, pp. 115–134.
- (13) O. Reinhold, The Mechanical Properties of Ingot Iron and Steel at Different Temperatures, *Ferrum*, vol. 13, 1916, pp. 97–107.

PROBLEMS

- 5-1. Why is the amount of recycled automobile body scrap limited in steel making?
- 5-2. A cross-recessed forging die was made of D5 tool steel and fractured after only a short service life. The cause of the failure was found to be severe carbon

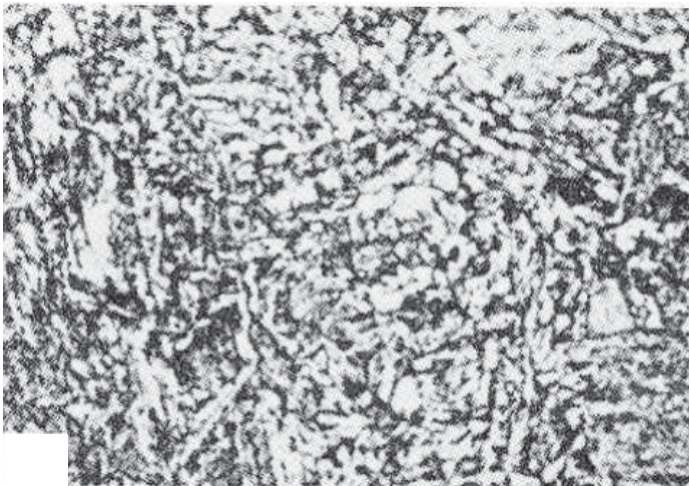
segregation. A client has asked for your recommendation for correction of this problem. In response to this request, please address the topics (a) to (c) first and then provide your recommendation.

- (a) Find out the nominal composition of D5 tool steel.
- (b) Is this steel suitable for such applications? Why?
- (c) Why is D5 tool steel prone to severe carbon segregation?
- (d) Provide your recommendation to correct the problem. (Your can recommend changing materials, modifying the heat treatment schedule, or anything else you think will work. Remember, this is a real-world problem; thus, the solution is not bounded by anything.)

- 5-3.** (a) Derive the Hall–Petch relation, $\sigma_y = \sigma_i + k_y d^{-1/2}$.
 (b) For a mild steel, σ_i 70.6 MPa and $k_y = 0.74 \text{ MPa } \sqrt{m}$, plot the yield strength as a function of $d^{-1/2}$.
 (c) Compare with an aluminum alloy for which the corresponding constants are 15.69 1 and 0.07.

- 5-4.** A lift truck manufacturer has to recall several thousand lift trucks to change lifting-fork arms because many lifting-fork arms had fractured prematurely. The failed lifting-fork arms were made of forged EN25 steel and had been subjected to shock loading while in service. A metallographic study showed that a coarse bainitic microstructure (shown below) was present at the fracture site.

What experiments would you do to determine the reason for these failures? Was there anything wrong with the processing steps? What would be the correct processing conditions?



Coarse bainitic structure of the failed fork arm made of EN25 steel.

6

Examination and Reporting Procedures

I. INTRODUCTION

Important aspects of failure analyses are the safekeeping and recording of evidence, the determination of dimensional characteristics, alloy identification, the study of fracture surfaces (fractography), and the determination of residual stresses by X-ray analysis. Some of the tools used in the examination of materials are quite simple, such as a small permanent magnet used to determine whether or not a metal is ferromagnetic. On the other hand, some tools are quite sophisticated, such as a scanning electron microscope used in the determination of fractographic detail. This chapter describes some of the more common methods used in the examination of materials and fracture surfaces, both in the field and in the laboratory. In addition, the topics of report preparation and testifying are discussed.

II. TOOLS FOR EXAMINATIONS IN THE FIELD

The equipment needed for an on-site investigation will vary depending upon the particular circumstances. Some of the more useful items are as follows:

- (a) Video camera
- (b) Polaroid camera

- (c) 35 mm camera or digital camera equipped with close-up lens
- (d) Permanent magnet to determine if a part is ferromagnetic (steel)

or not

- (e) Micrometers of various sizes
- (f) Rulers
- (g) Tape measure
- (h) Log book
- (i) Writing equipment
- (j) Polishing, etching, and replicating equipment
- (k) Dye penetrant kit (cleaner, penetrant, and developer)
- (l) Magnifying lens
- (m) Tape recorder

III. PREPARATION OF FRACTURE SURFACES FOR EXAMINATION

One of the complications associated with the examination of a fracture surface is that corrosion subsequent to fracture may have obscured some of the fractographic features. This can be a particular problem with carbon steel and cast iron components, since they rust very quickly in humid atmospheres. Fortunately, aluminum alloys and stainless steels are much less prone to corrosion. In some litigations, steel components have been stored outdoors for years and have become heavily coated with rust prior to examination. If the rust coating on a fracture surface is a light one, it can be removed by brushing on a commercial rust remover such as naval jelly and wiping it off after a few minutes. Nevertheless, sharp fractographic features are likely to be rounded. Where the rust coating is heavy, important fractographic features may be absent upon removal of the rust layer.

Ultrasonic cleaning is used to rid a fracture surface of debris, dirt, and oil coatings. Ultrasonic cleaning uses sound waves passed at very high frequency through liquid cleaners, which can be alkaline, acid, or even organic solvents. The passage of ultrasonic waves creates tiny gas bubbles, which offer vigorous scrubbing action on the parts being cleaned. This action results in an efficient cleaning process and is used as a final cleaner only, after loosely adherent debris has been removed.

IV. VISUAL EXAMINATION

Visual examination is one of the most important steps in fractographic analysis, but there are some commonsense precautions to be observed. For example, in the examination of the two halves of a failed component, the broken halves should not be fitted together to see how they fit because fractographic information contained on the surfaces may be altered. The fracture surfaces should not be touched because the salt contained in the moisture on fingertips may lead to corrosion. If possible, apply

a removable coating of oil or plastic compound to the surfaces to prevent any further corrosion.

The instruments used in visual examinations include dental mirrors, borescopes, and flexible fiberoptic scopes for use in examining internal surfaces that are not accessible to direct viewing. Steel rules, tapes, calipers, and weld gages are among the tools used to check on dimensional characteristics of failed components. A variety of cameras, including Polaroid and video cameras, are used to record the macroscopic features of failures. When making observations or when taking photographs, it is good practice to maintain a detailed log listing the observations and the sequence of photographs together with the subject matter of each photograph. A tape recorder is also useful in this regard.

Much information about the nature of a fracture can be obtained through visual examination. The human eye has a good depth of field, so even though a fracture may be rough, it will appear to be in focus to the viewer. Differences in color and evidence of corrosion or wear can be detected, the extent of plastic deformation or necking can be observed, and evidence of fatigue is often visible to the naked eye. The main limitation of a visual examination is the inability to resolve fine detail. The Rayleigh criterion for the limit of resolution gives the linear separation z of two just resolvable point objects at a distance of 250 mm (the minimum distance of distinct vision) as

$$z = \frac{0.61\lambda_0}{\text{NA}} \quad (6-1)$$

where λ_0 is equal to 550 nm, the wavelength to which the eye is most sensitive, and NA is the numerical aperture of the eye. The NA is expressed as $n \sin u$, where n is the index of refraction, equal to 1.0 in air, and $\sin u$ is the sine of the half-angle of the cone of light admitted to the eye from a point 250 mm from the eye. Since the half-diameter of the pupil is 1 mm, the value of NA is 0.004. Therefore, the value of z is approximately 0.1 mm or 100 μm , which, as a point of reference, is about the diameter of a human hair and 100 times larger than the micron, a common length standard in discussing metallurgical microstructures.

V. CASE STUDY: FAILURE OF A STEERING COLUMN COMPONENT

In the course of an accident investigation of an automobile crash in which there was a fire and the two occupants perished, it was found that a carburized pinion gear tooth of a steel component of the steering mechanism had fractured. Visual examination of the fracture surface of the component revealed two distinctly different color patterns. At the edge of the carburized tooth where the fracture had initiated, the fracture surface was flat and deep blue in color. Farther into the tooth, the fracture was in shear at an angle to the flat portion of the fracture. The color in the sheared region was purplish-pink. Because these two different color patterns were present on the same fracture surface, it was asserted that the part had been exposed to an elevated temperature twice in its history. It was claimed that the component must have been cracked during manufacture prior to final heat treatment, during which some oxide

had formed on the cracked surfaces. It was further claimed that this crack caused the component to fail and thus caused the accident. The claim was that both the old fracture surface and the new fracture surface were oxidized during the ensuing fire, but the old fracture surface had a different appearance because of two exposures to elevated-temperature oxidizing conditions.

To check on these allegations, a pinion gear was broken from an identical component and then exposed to 350°C for 20 minutes. It was found that this single exposure developed a color pattern similar to that observed on the failed pinion gear tooth. Additional tests with fatigue-cracked steel specimens were carried out to support these observations. The specimens were precracked in fatigue to develop a short fatigue crack and a corresponding flat fracture surface. The remaining ligament was then broken by overloading to develop a rough fracture surface. These specimens were then heated in air to a temperature of 350°C. It was found that the flat fatigue-cracked regions developed a blue oxide, whereas the rough fractures associated with the overload developed a pink-purple oxide. On the basis of such tests, it was shown that the fracture of the pinion gear tooth was the result of the crash rather than its cause.

VI. OPTICAL EXAMINATION

The magnification of a simple magnifying lens is given as

$$M = \frac{250}{f} \quad (6-2)$$

where f is the focal length of the lens expressed in millimeters. For a focal length of 50 mm, a magnification of five times would be obtained. Small magnifying lenses are useful in inspecting fracture surfaces and provide greater detail than is available by visual inspection alone.

The binocular stereomicroscope can provide magnifications up to 50 times and is a useful tool for the examination of fracture surfaces. This type of microscope has a good depth of field, and when equipped with a camera, it is useful for taking macrographs of fracture surfaces.

Optical microscopes are capable of obtaining much higher magnifications up to about 400 \times . Higher magnifications do not increase the detail but may allow a larger image to be viewed more easily. If an oil immersion lens is used, the numerical aperture NA can be increased to 1.60, and the limit of resolution z (see Eq. 6-1) is equal to 0.2 μm , of the order of one-half the wavelength of light, and 500 times better than that of the eye. The main drawback is that, as the magnification increases, the depth of field decreases, and specimens have to be extremely flat to be in focus. While this latter requirement can be met with metallurgically mounted and polished specimens, the inherent roughness of most fracture surfaces limits the usefulness of optical microscopes at high magnification.

In the examination of fracture surfaces, the use of oblique illumination is helpful in bringing out detail by creating a shadowing effect. Normal illumination is useful in observing differences in color or texture, but it is not recommended for fractography

because it does not produce the degree of topological contrast obtainable with oblique illumination. A trial-and-error process should be used to find the best inclination angle of the light source with respect to the fracture surface being examined. Rotation of the specimen will help to bring out the fine detail and aid in the identification of fractographic features.

VII. CASE STUDY: FAILURE OF A HELICOPTER TAIL ROTOR

A helicopter containing three passengers and a pilot was on a sight-seeing flight when the tail rotor blade separated from the helicopter. The purpose of the tail rotor blade is to counteract a torque induced by the main rotor blades, and with the loss of the tail rotor blade the helicopter goes into a spin. To counteract this spin, the pilot is trained to disengage the main rotor blades from the rotor and allow the main blades to windmill. Ordinarily, he can then bring the helicopter down safely. However, in this case the pilot did not do this. As a result, one passenger was hurled to his death from the spinning helicopter, and the other three occupants were injured in the ensuing crash. In the subsequent investigation, it was found that a component connecting the tail rotor to the engine had failed in fatigue, and this failure allowed the tail rotor to separate.

What caused the fatigue failure of the component? Was it due to poor design or to some other factor? The tail rotor blade was recovered, and it was noted that the tip of the blade showed signs of contact damage. This type of damage can occur as the helicopter is maneuvered on or near the ground on takeoff or landing, and the FAA regulations allow for some minor scratches and indents by specifying the allowable depth of such defects.

To check on the depth of the observed scratches and indents, a 100 power light microscope, which was equipped with a calibrated barrel, was used. Such a microscope has a limited depth of field, and by focusing first on the end surface of the tail rotor blade and then on the bottom of a defect, a determination of its depth could be made. The results of such an examination revealed that the depths of a number of the scratches and indents were in excess of the allowables, and it was concluded that tail strikes had induced abnormally high fatigue loads, which led to the failure of the component. In this case, a small depth of focus turned out to be an asset rather than a detriment. It is also noted that some helicopter manufacturers mount the tail rotor within a containment to protect the blade tips from tip strikes.

VIII. THE TRANSMISSION ELECTRON MICROSCOPE (TEM)

Prior to the advent of the scanning electron microscope (SEM), the TEM was used to study the topography of fracture surfaces. This was usually done with thin replicas of the surface. These replicas allowed the electron beam to pass through and create image contrast that depended upon thickness variations in the replica. To increase the contrast, the replicas were shadowed by evaporating a metal in a metal evaporator. Today the SEM is the preferred instrument for such studies. However, the scanning

TEM is used in research studies of thin sections of a metal that contains a fracture surface to obtain both an image of the surface and an image of the underlying dislocation microstructure.

A schematic of the essential features of an electron microscope is shown in Fig. 6-1. There is a source of electrons, the electron gun, and a series of electromagnetic lenses that focus the electron beam on the specimen. The resolving power of an electron microscope is quite high because of the short wavelengths associated with the electron beam. From Eq. 6-1, it can be seen that the smaller λ is, the smaller is the separation of points that can just be resolved. An electron can be considered to have a wavelength that is related to its momentum mv by

$$\lambda = \frac{h}{mv} \quad (6-3)$$

where h is Planck's constant, equal to 6.62×10^{-34} J-sec, m is the mass of an electron equal to 9.11×10^{-31} kg, and v is the velocity of the electron. The velocity of the electron can be expressed as

$$v = \sqrt{\frac{2eV}{m}} \quad (6-4)$$

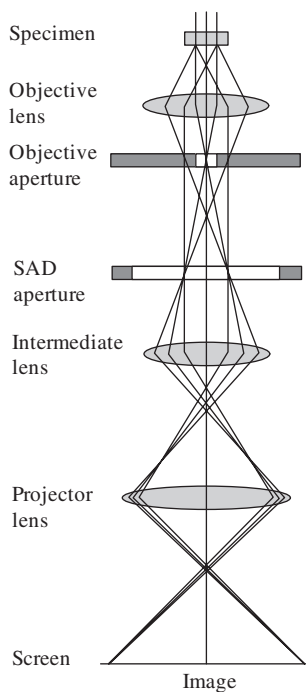


Fig. 6-1. Schematic diagram showing the essential features of an electron transmission microscope. (SAD = selected area diffraction.) (After Williams and Carter, 2.)

where V is the accelerating voltage and e is the charge on the electron equal to 1.602×10^{-19} coulombs. This leads to

$$\lambda = \frac{h}{\sqrt{2meV}} = \frac{1.224}{\sqrt{V}} \text{ nm} \quad (6-5)$$

For an accelerating voltage of 100,000 volts, the value of λ is 0.0038 nm—orders of magnitude smaller than the wavelength of visible light. The theoretical resolution in a TEM image approaches the wavelength of the incident electrons, although this resolution is not attained due to such lens defects as spherical and chromatic aberration and aperture diffraction. Typical resolutions obtained in modern TEMs are approximately 0.2 nm.

IX. THE SCANNING ELECTRON MICROSCOPE (SEM)

The basic elements of a SEM, one of most valuable tools in failure analysis, are shown in Fig. 6-2. As in the TEM, there is an electron source and a series of lenses that focus the electron beam on the surface being examined. In contrast to the TEM, there is no objective lens, and as a result, the electron beam in the SEM is very narrow. This results in a large depth of field, which is very useful in fractography,

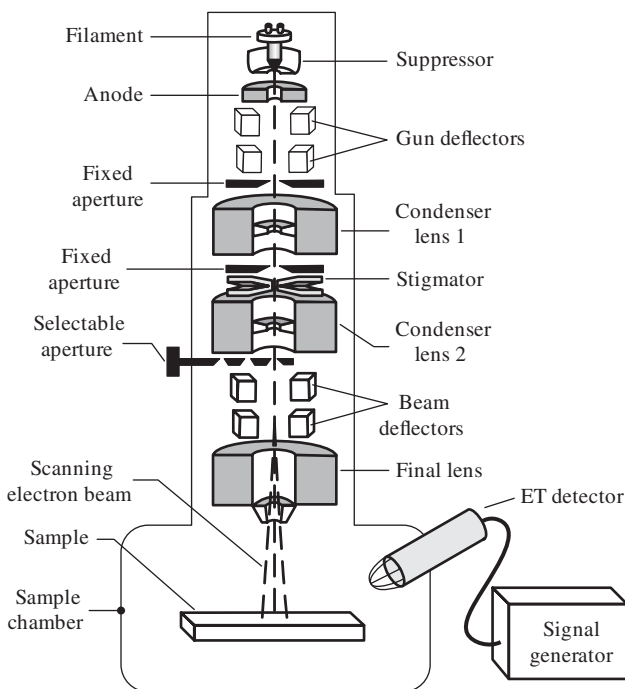


Fig. 6-2. Basic elements of an SEM.

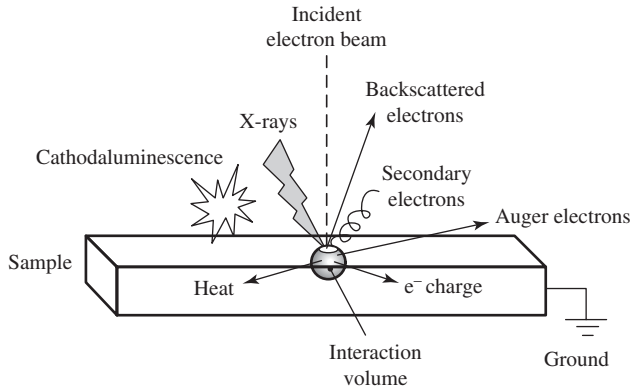


Fig. 6-3. Electron/sample interactions taking place in the SEM sample.

as well as good resolution, often about 10–20 nm. Figure 6-3 indicates the variety of electron/sample interactions that take place in the SEM. The SEM is usually equipped with an auxiliary energy dispersive X-ray spectroscopy (EDS) unit that can provide quantitative information on the chemical composition by analyzing the characteristic energies of the X-rays emitted through a depth of about 2 μm below the specimen surface. These characteristic X-rays are emitted when a primary electron displaces an inner electron from its orbit in an element and an outer electron replaces it. This information is displayed in chart form as a plot of X-ray intensity versus wavelength and is usually sufficient for purposes of alloy identification. To detect light elements such as carbon, nitrogen, and oxygen, special “windowless” detectors, or detectors sensitive to wavelength rather than energy, are used. The X-ray information can also be displayed as a map indicating the distribution of the element within a grain.

In the examination of fracture surfaces, the magnifications usually range from approximately 100 up to 5,000 times. One limitation of the SEM is that there is an upper limit to the size of specimen that can be examined, which commonly is about 15 cm \times 5 cm \times 5 cm, although some specialized instruments have a provision for much larger samples. If the available space is too small for the specimen being examined, then a replica technique may be employed. This technique is also useful in obtaining information about fracture surfaces in the field.

In the SEM, an electron beam is scanned (rastered) over the specimen’s surface, and images are formed either by the backscattering of the primary electrons or by the emission of secondary electrons. The backscattered electrons are collected by a solid-state device located just below the objective lens pole piece of an SEM, see Fig. 6-4, and are useful in compositional analysis because brighter regions in the image are an indication of material of higher average atomic number. These electrons can also be detected by a charge-coupled device in determining the orientation of individual grains in a polycrystal.

The secondary electrons are electrons that have been displaced from the specimen due to interaction with either primary or backscattered electrons. These electrons are

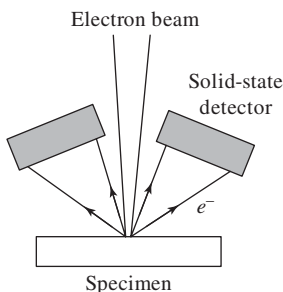


Fig. 6-4. Collector located below the pole piece for backscattered electrons.

important in bringing out the topography of a fracture surface. The energy associated with the primary electrons is usually in the range of 10–25 keV, whereas the energy of the secondary electrons is much less, for example, 10–50 eV. The emitted secondary electrons are collected by a Everhard-Thornley (ET) detector, which consists of a scintillator biased at +200 volts and a photoemission multiplier, Fig. 6-5. The image created by the collected secondary electrons is displayed on a cathode ray tube (CRT) and can be collected digitally or photographed. Image contrast is due to electron collection differences arising from the tilt of portions of the surface with respect to the electron detector. A region tilted toward the electron detector will give rise to an enhanced signal, while the signal will be reduced if the surface is tilted away from the detector. In addition, contrast is due to emission differences caused by variations in the beam-surface tilt angle. Asperities on heavily oxidized materials as well as nonconductors such as ceramics tend to develop charges during SEM observation

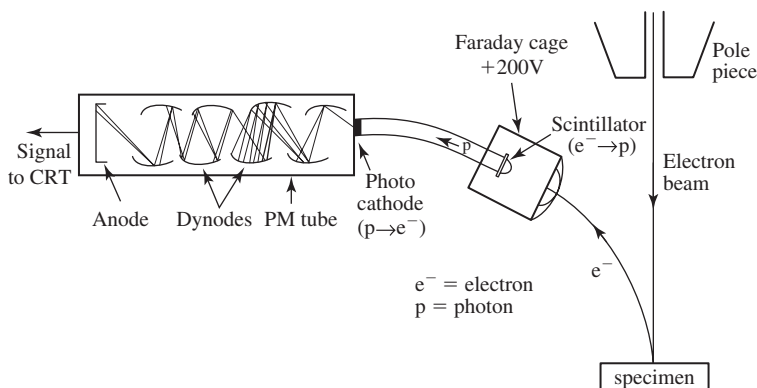


Fig. 6-5. An ET detector. Electrons from the specimen surface are drawn into the scintillator, generating visible light, which travels via fiber optics to the photocathode. There the light is reconverted to electrons. The electrical signal is multiplied by several electrodes in the photo-multiplier (PM) tube and transmitted to the cathode ray tube (CRT). (After Williams and Carter, 2.)

that detract from the quality of the image. The use of a lower operating voltage or the evaporation of a metallic coating onto the surface will help to reduce the extent of charging.

The ET detector collects both secondary electrons (SE) and backscattered electron (BS) signals, but there are differences in the characteristics of these signals that affect the topological contrast in the SEM. The SE signal is relatively weak and is symmetrically distributed in space. The ET detector attracts this signal by means of an electric field, so the signal loses directionality and the resulting contrast is low and the image looks even (within a close range of grays) but with fine details revealed. On the other hand, the highly energetic BS signals are very directional. As a result, the ET detector collects not only SE but also those BS electrons that are in its “line of vision.” Those edges and surfaces that are inclined toward the detector will produce a bright contrast, and the overall image (SE plus BS) will show bright lines in the edges and tilted surfaces (toward the detector), as well as gray and even contrast where the surface is flat and normal to the beam. This whole situation may produce a contrast that is not what the observer expects based on optical examinations, and very often it can be the opposite of the contrast obtained by light microscopy. For example, a pore may appear to be a particle. Therefore, the microscopist needs to be aware of this situation when interpreting SEM images.

The yield of both SE and BS electrons increases with atomic number, and this fact gives rise to atomic number contrast, which is used in compositional analysis. However, if the observer is trying to obtain compositional images by atomic number contrast, since an inclined surface or a sharp edge will produce a stronger BS signal, it might be mistaken as a region of higher atomic number (Z), since a heavy Z element also produces more signal.

The resolution of the SEM is determined primarily by the magnification, the spacing of the lines on the CRT screen, and the probe size. The spacing of lines on the CRT, δ , is usually about 0.1 mm, as is the size of the pixels, that is close to the resolution of the eye. In order for the image to be resolved on the screen, the probe size on the specimen multiplied by the magnification must equal this limit of resolution, that is, the spacing of the lines. At a magnification of $1,000\times$, the optimum probe size would be $0.1/1,000 = 10^{-4}$ mm = 100 nm. With SE and a small probe size, the resolution is usually of the order of 10–20 nm. For a 10 nm resolution, the minimum magnification needed to bring 10 nm up to the 100 μ m that the eye can resolve on the CRT screen would be about 10,000 times. At a magnification of $1,000\times$, a resolution of only 100 nm would be needed.

The depth of field D in an SEM can be expressed as

$$D = 0.2 \frac{1}{NA \times M} = 0.2 \frac{W_D}{R \times M} \text{ mm} \quad (6-6)$$

where NA is the numerical aperture, W_D is the working distance (focal distance below the final aperture, approximately 5–25 mm), R is the radius of the objective aperture of the microscope (0.050–0.200 μ m), and M is the magnification (less than 10,000). Equation 6-6 indicates that the depth of field can be increased by using a

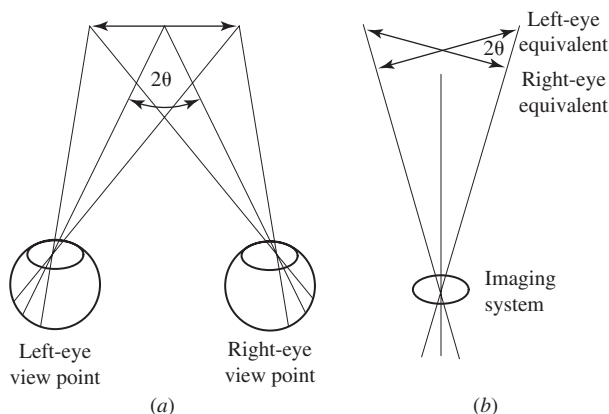


Fig. 6-6. Stereo pairs. (a) The twin images observed by the left and right eyes. (b) An equivalent to the image pair recorded before and after tilting a specimen about a known angle. (After Brandon and Kaplan, 1.)

long working distance and a small aperture. (For high resolution, a short working distance is required). For $M = 1,000$, $R = 100\text{ }\mu\text{m}$, and $W_D = 25\text{ mm}$, the value of D is $50\text{ }\mu\text{m}$, a much greater value than can be obtained in the light microscope. For example, for an oil immersion lens with NA of 1.60, W_D of 1 mm, and M of $400\times$, D would be only $0.3\text{ }\mu\text{m}$.

In the examination of rough fracture surfaces in the SEM, the use of the stereo-pair technique is helpful in obtaining a better sense of the three-dimensional nature of fractographic features. Our normal depth perception is due to the viewing of an object by both eyes, each from a slightly different angle than the other. In the stereo-pair technique, two micrographs are obtained, one with the specimen rotated 5° clockwise to the beam direction and the second at 5° counterclockwise to the beam direction, as indicated in Fig. 6-6. To observe the three-dimensional image, the two micrographs are then viewed simultaneously in a viewer that superposes the micrographs and allows the left eye to see one micrograph and the right eye the other.

X. REPLICAS

The replication of a limited region of a surface is a useful nondestructive method for the examination of large components. Repeated replication can be used to provide a historical record of an area of interest over a period of time, as in fatigue testing. Fatigue cracks that are as small as $10\text{ }\mu\text{m}$ in length have been detected by this method.

In making a replica of a fracture surface, either a single-stage or a two-stage replica is used. The first step in either process is to clean the surface to be replicated to remove rust, loose debris, and any oily deposits. A solvent such as acetone is often suitable for this purpose.

To make a replica once a clean surface is available, one side of a strip of cellulose acetate film is moistened with acetone to soften it, and then the soft side of the film

is pressed lightly against the fracture surface and allowed to dry. This process takes approximately 5 minutes. The film is then carefully peeled from the fracture surface. In some cases, the area being replicated may be polished and etched prior to the application of the acetate film in order to bring out microstructural features. Once the replica is obtained, it can then be observed in a light microscope, although in order to enhance the contrast of features, the film can be shadowed in a metal evaporator unit with a metal such as gold or chromium. The replica can be examined either with a light microscope or an SEM. However, the single-stage replica is not well suited for TEM, because the film does not stand up well in a high-energy electron beam. To get around this difficulty, the two-stage replica process has been developed. In this procedure, a single-stage replica is prepared as described above. The replica is then placed in a metal evaporator, replica side up, and shadowed at 45° with a metal such as germanium to enhance contrast in the electron beam. A thin layer of carbon is then deposited at normal incidence on the plastic replica. The original cellulose acetate film is then dissolved away in acetone, and the resultant shadowed carbon film is ready for examination in the TEM. Under the electron beam, it is much more robust than the single-stage plastic replica because the carbon conducts heat away much more effectively than does the cellulose acetate film. The production and evaluation of metallographic replicas obtained in the field is covered in ASTM Designation E 1351.

XI. SPECTROGRAPHIC AND OTHER TYPES OF CHEMICAL ANALYSIS

If more precise analyses of chemical compositions are desired than are provided by the EDS technique, then some form of spectroscopic analysis is usually used. Spectroscopy is the study of emission and absorption spectra and is widely employed in quantitative chemical analyses. In a prism spectrograph, a small sample of an alloy is vaporized, and as the electrons of each element present fall to an orbit of lower energy, electromagnetic radiation in the visible and ultraviolet ranges of a wavelength characteristic of that element is emitted. The index of refraction of a substance is defined as the ratio of the speed of light in vacuum to that in the substance. This index is also dependent upon the wavelength, and is larger the shorter the wavelength. This results in a greater deviation for violet light and a lesser deviation for red light. In spectroscopy the emitted radiation passes through a prism that diffracts and separates the various wavelengths that are present, and the resultant spectrum is photographed. The determination of the diffracted angle, as well as the intensity of the spectral lines, are then used to determine the nature and amount of each element present in the alloy. This technique works well for sodium and higher elements in the periodic table. Therefore, for the determination of the amount of light elements such as carbon, nitrogen, or oxygen, other methods are used. For example, one commercial unit determines the carbon content of a steel by combining the carbon with oxygen to form CO. The amount of CO produced is then used to determine the carbon content.

The etching characteristics of the various aluminum alloys are sensitive to composition. This fact can be used to determine if a particular sample is of one type or another, for example, Al-Zn-Mg or Al-Cu.

The relative amount and distribution of sulfur in steel can be of concern. A sulfur print provides a macrographic method for obtaining the distribution of sulfide inclusions. To obtain a sulfide print, a sheet of photographic bromide paper is immersed for 3 to 4 minutes in a dilute solution of sulfuric acid. The emulsion side of the sheet is then placed in contact with a polished steel surface for 1 or 2 minutes under moderate pressure. The sheet is then removed from the surface, rinsed, and fixed by placing it in a photographic fixing solution for about 15 minutes. A sulfur print will display the location and extent of sulfur inclusions on the prepared surface of the steel. ASTM Designation E 1180 provides detailed instructions for preparing sulfur prints for macrostructural examination.

A macroscopic examination of a polished steel surface can yield information about the type, number, and distribution of inclusions in general. ASTM charts are used to characterize the nature of the distribution of inclusions. Modern methods of quantitative metallography also are used in the analysis of such distributions.

XII. CASE STUDY: FAILURE OF A ZINC DIE CASTING

Die castings made of zinc alloys are relatively inexpensive and are used in a variety of applications. In one case, a zinc die casting was used in an electrically heated apparatus that circulated 82°C (180°F) water to keep an automobile engine warm overnight under extremely cold climatic conditions. One day, the car owner happened to notice that the zinc die casting was leaking, and made the mistake of jostling the die casting. It fractured, and scalding hot water was spewed on him.

One of the well-known problems with a zinc die casting is that, if lead is present in the alloy, it can lead to weakening due to segregation of the lead to the grain boundaries. In fact, the phase diagram for the Pb-Zn system, Fig. 6-7, shows that lead

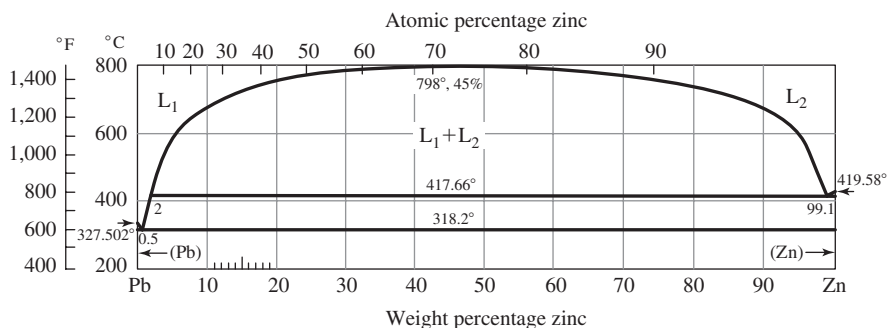


Fig. 6-7. Equilibrium phase diagram for the Pb-Zn system. (After ASM Metals Handbook, 3.)

has no solid solubility in zinc. Therefore, during casting, as the alloy is cooled from the molten state, any lead present will segregate to the grain boundaries. Concern about lead is reflected in chemical specifications for zinc alloys, which limit the amount of lead to less than 0.005 wt %. Unfortunately, lead is often found together with zinc ores, and it is therefore important that they be separated in the refining process.

A spectrographic analysis was carried out to determine the lead content of the zinc die casting. The results showed that there was 0.009 wt % lead present, well above the allowable level.

The melting point of lead is 318°C, and that of zinc is 418°C. At an operating temperature of 90°C, the lead in the grain boundaries was unable to withstand the stresses developed in the circulating water system, and grain boundary cracks developed, which led to the final failure.

XIII. SPECIALIZED ANALYTICAL TECHNIQUES

(a) Small spot electron spectroscopy (EPS) is a surface analysis technique that provides composition and chemical bonding analysis for the first 2 nm of a sample beneath the surface. EPS can detect all elements except hydrogen and helium. In failure analysis, it is useful in determining corrosion products and the chemical degradation of surfaces.

(b) Fourier transform infrared spectroscopy (FTIR) is used to determine the chemical composition and the nature of bonding of organic, polymeric, and many inorganic materials.

(c) Scanning Auger microanalysis (SAM) or Auger electron spectroscopy (AES) is a technique for the determination of the composition within 2–3 nm of the surface. It can detect all elements except hydrogen and helium. The sample is scanned with a focused electron beam that causes Auger electrons of low energy, 20–2,500 eV, to be emitted from the surface. The energies of the emitted Auger electrons are measured to provide an elemental analysis of the top few layers of the surface.

(d) Electron probe microanalysis (EPMA) uses a finely focused beam of electrons to generate X-rays to analyze the composition of a volume as small as a cubic micron. For example, the composition of nitride layers deposited within a grinding crack can be analyzed by this technique.

(e) In electron energy loss spectroscopy (EELS), electrons are transmitted through a thin film of metal. As the electrons interact with atoms in the specimen they lose energy, and the amount of energy lost is a characteristic of the atoms with which the electrons have interacted. Spectrographic analysis of the energy distribution of the electrons can be used for chemical analysis of the specimen. This technique is well suited to the detection of elements of atomic number 10 or less.

(f) Secondary ion mass spectrometry (SIMS) is used to provide high-sensitivity spatial information about the elements present in the top few atomic surface layers with 100 nm resolution and has the unique ability to detect hydrogen. In SIMS, a

beam of focused ions is directed at the surface in a high vacuum. These primary ions cause sputtering of the surface atoms and molecules. The sputtered ions are termed *secondary ions* and are mass analyzed using a mass spectrometer. A focused gallium ion gun is employed, together with a magnetic sector mass analyzer. A secondary ion image of the surface can be generated to provide a spatially resolved analysis of the surface. Secondary electrons are also emitted, and an ET electron detector can also be used to obtain secondary electron images.

(g) Scanning atomic force microscopy (AFM) permits the study of surface topography of an area $30\text{ }\mu\text{m} \times 30\text{ }\mu\text{m}$ with atomic-scale resolution. A probe that has one atom at its tip is suspended by a thin cantilever beam. The probe is scanned across a surface, and the supporting beam flexes in response to topographical changes. The beam deflections can be measured optically or with a capacitor. The method has been used to periodically monitor changes in slip-band topography during fatigue cycling, for example.

XIV. STRESS MEASUREMENT BY X-RAYS (4)

When stress is applied to a body in the elastic range, elastic strains are induced that manifest themselves at the atomic level as changes in the normal separation distance between atomic planes. X-ray diffraction techniques are used to measure these changes at the surface of a body. These changes are converted into strains, and a modification of Hooke's law is then used to convert the strains into the corresponding stresses. Residual stresses that may be introduced during manufacture or in service are often studied by this technique, since they may play a role in promoting fatigue or stress corrosion cracking failures. The following analysis indicates the nature of the procedures used in the analysis of stresses by X-ray techniques.

Consider a polycrystalline specimen loaded in tension. To measure the longitudinal strain by X-rays would require diffraction from planes perpendicular to the axis of the bar. Since this is usually impossible, the Poisson's contraction is measured instead. Similar considerations apply to a plane surface loaded under biaxial stress conditions.

Bragg's law (see Fig. 6-8) is used in the analysis. This law is

$$n\lambda = 2d \sin \theta \quad (6-7)$$

where n is the number of wavelengths, λ is the wavelength, d is the spacing between planes, and θ is the angle of reflection, that is, the angle between the tangent to the plane and the reflected beam. When the lattice is strained by an amount $\Delta d/d$, there will be a change in $\sin \theta$. It is desired to make the change in θ as large as possible in order to increase the sensitivity of the method. By taking the differential of Eq. 6-7, this condition can be written as

$$d \cos \theta \Delta \theta + \Delta d \sin \theta = 0$$

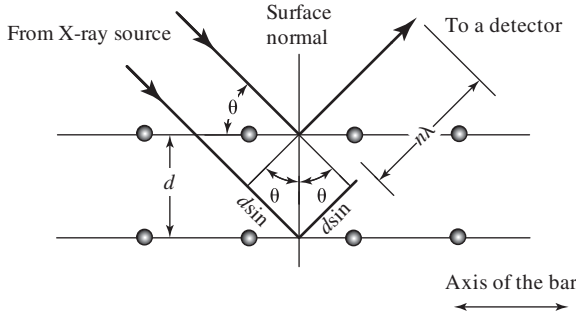


Fig. 6-8. X-ray diffraction and Bragg's law.

or

$$\Delta\theta = -\frac{\Delta d}{d} \tan \theta \quad (6-8)$$

Therefore, for a given change in d , the larger the value of θ , the larger will be the change in θ , the quantity being measured. This means that the angle of incidence should be as close to 90° as can be arranged.

The following indicates the principles involved in making an X-ray stress analysis. Consider a free surface with a biaxial stress present in the plane of the surface, as shown in Fig. 6-9. The strain in the direction normal to the surface is a principal strain and can be written as

$$\varepsilon_3 = -\frac{\nu}{E}(\sigma_1 + \sigma_2) \quad (6-9)$$

where σ_1 and σ_2 are principal stresses in the surface plane. This equation can be rewritten as

$$\frac{\Delta d_z}{d_z} = -\frac{\nu}{E}(\sigma_1 + \sigma_2) \quad (6-10)$$

and from Eq. 6-8,

$$\Delta\theta = \frac{\nu}{E}(\sigma_1 + \sigma_2) \tan \theta \quad (6-11)$$

In general, only the sum of the principal stresses can be obtained from a diffraction pattern obtained at normal incidence. With information about the loading conditions

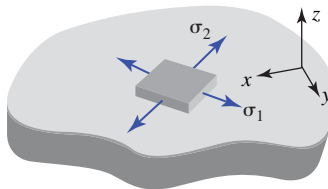


Fig. 6-9. Biaxial stress field.

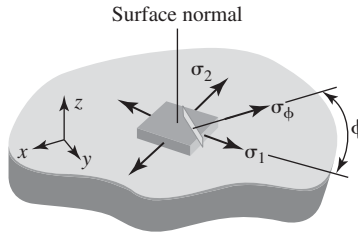


Fig. 6-10. Angular relationships in X-ray stress analysis.

or state of residual stress, it may be possible to determine the values of σ_1 and σ_2 . For example, the compressive residual stresses in a shot-peened surface are equal in all directions in the surface.

If instead of obtaining the sum of principal stresses it is desired to measure the stress acting in a given direction in the surface, then a different procedure has to be followed. Figure 6-10 shows the angular relations between the stress to be measured σ_ϕ , the principal stresses σ_1 and σ_2 , and the arbitrary x -, y -, and z -axes. In this procedure, the diffraction peak is measured at the surface normal and at one or more angles ψ , Fig. 6-11, which are in the plane of the normal and the desired surface direction. Here only one value of ψ will be considered for purposes of illustration. The normal-incidence pattern (Fig. 6-11a) measures the strain approximately normal to the surface, and the inclined-incidence pattern (Fig. 6-11b) measures the strain approximately parallel to OA . These measured strains are therefore approximately equal to ε_3 and ε_ψ , respectively, where ε_ψ is the strain in a direction at an angle ψ to the surface normal.

It can be shown that the following relation gives the difference between these two strains:

$$\varepsilon_\psi - \varepsilon_3 = \frac{\sigma_\phi}{E} (1 + \nu) \sin^2 \psi \quad (6-12)$$

but

$$\varepsilon_\psi = \frac{d_i - d_o}{d_o} \quad (6-13)$$

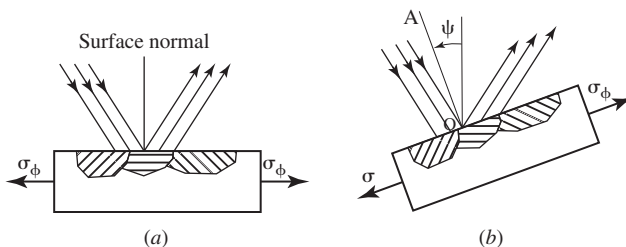


Fig. 6-11. (a) Normal-incidence pattern. (b) Inclined-incidence pattern.

and

$$\varepsilon_z = \frac{d_n - d_o}{d_o} \quad (6-14)$$

where d_i is the spacing of the inclined reflecting $\{hkl\}$ planes, approximately normal to OA , d_n is the spacing of the $\{hkl\}$ planes reflecting at normal incidence under stress, and d_o is the spacing of the same $\{hkl\}$ planes in the absence of stress. Combining Eqs. 6-12, 6-13, and 6-14, we get

$$\frac{d_i - d_o}{d_o} - \frac{d_n - d_o}{d_o} = \frac{d_i - d_n}{d_o} = \frac{\sigma_\phi}{E}(1 + \nu) \sin^2 \psi \quad (6-15)$$

Since d_o can be replaced by d_n with little error, Eq. 6-15 can be written as

$$\sigma_\phi = \frac{E}{(1 + \nu) \sin^2 \psi} \left(\frac{d_i - d_n}{d_n} \right) \quad (6-16)$$

and a knowledge of d_o is not required.

Modern X-ray stress analysis diffractometer units are programmed to make a series of readings at at least five different ψ settings. The experimental and analytical procedures are similar to that described above but provide a more accurate evaluation of σ_ϕ .

There are also other methods for the determination of residual stresses. For example, ASTM Designation E 837 deals with a method for determining residual stresses by the hole-drilling strain-gauge method. The method is semidestructive, and the residual stresses are determined near the surface of isotropic elastic materials. Strain gauges in the form of a three-element rosette are cemented to a selected area, and a hole is drilled at the center of the rosette to a depth 1.2 times greater than the hole diameter. The creation of the hole causes the residual stresses in the vicinity of the hole to relax, and the relieved strains are recorded. From these measurements, the initial state of the residual stress can be calculated.

XV. CASE STUDY: RESIDUAL STRESS IN A TRAIN WHEEL

A derailment of a passenger train was caused by the failure of one of the forged steel wheels. A chemical analysis indicated that the wheel met the specifications for a Class A passenger wheel. Its carbon content was 0.56 wt %. In contrast, the carbon content of freight car wheels is more like 0.75 wt %. The wheel had been shot-peened by the manufacturer to develop a residual biaxial compressive stress of magnitude 172–207 MPa (25–30 ksi) in both the rim and plate of the wheel. There was concern that the possible relaxation of the original residual stresses in service might have contributed to the failure. The X-ray method utilizing chromium $K\alpha$ was therefore used to determine the state of residual stress in the failed wheel. It was found that the residual stresses were still within the manufacturer's original range, and therefore that relaxation of residual stress did not play a role in this failure. This

determination was made as the result of tensile tests, fracture toughness tests, fatigue tests, sulfur print analysis, inclusion studies, and metallographic determination of the microstructure, all of which indicated that the wheel itself was not defective in any way. The actual cause of failure was traced to the presence of a fatigue crack that had been initiated at the corner of the rim due to an overhanging brake shoe. Normally, a brake shoe is seated on the tread of the wheel away from the rim corner. During braking action, there is an increase in temperature at the tread-shoe interface, which can be high enough for the steel to be heated to the austenitic range. Upon subsequent cooling, the austenite can transform to untempered martensite, which appears as a white layer on etching. In addition, thermal checks (fine cracks) can develop. When the brake shoe is in its proper position, these thermal checks are in the central part of the tread and are worn away before they can grow to a critical size for fracture. However, when a crack is created due to an overhanging brake shoe at a rim corner, there is no subsequent wear at this location, and a crack can grow to critical size, as happened in this case. To guard against overhanging brake-shoe problems, visual inspections of wheels and of the placement of the brake shoes are made at specified intervals. If discoloration of the rim corner due to overheating is noted, the wheel should then be more carefully inspected for the presence of cracking. However, in the case described above, the inspection procedure was not successful in detecting the problem in time, and the accident occurred.

XVI. THE TECHNICAL REPORT

An important aspect of any investigation is the preparation of the technical report. The following section provides an outline of the steps to be taken in involved in report preparation.

A. An Outline for Preparing the Technical Report

1. Introduction
 - A. What is the problem?
 - a. Manner and date of your first involvement with the case at hand.
 - b. Known circumstances relating to the failure.
 - c. Description of the components received and the date received. (It is important to maintain the “chain of evidence.”)
 - d. Documentation received (depositions, technical literature, manuals, etc.).
 - e. Purpose of the investigation.
 - B. What is known about the failure?
 - a. More detailed overall description of the failed component. Include macrophotographs.
 - b. History of the component: loads, environments, and so on.
 - C. What will you do?
 - a. Approach to be taken during analysis (hardness tests, chemical analysis, SEM work, site visits, and so on).

2. The Investigation

- A. Observations and related photographs at the site, if applicable.
- B. Laboratory analyses (SEM, micrographs, chemical analysis, hardness, etc.).
 - a. In a product liability case, it is generally preferred that the investigator take all photographs. If this is not feasible, the investigator should be present when the photographs are taken. This includes SEM work. The name of the person making the observations, if not the investigator, should be listed, along with the date and place of observation.
 - b. For chemical analyses carried out by a commercial laboratory, a description of the samples provided and the type of examination requested should be recorded.
- C. Stress analyses
 - a. It is preferred that the investigator carry out the stress analysis. If not, the person and organization that did the actual analysis should be identified.

3. Current status of evidence

- A. Was it returned or is it still in your possession?

4. Conclusions: On the basis of the above observations, it is concluded that:

- A. The type of failure was (“undoubtedly” or “most likely”) ____.
- B. The cause of the failure was (“undoubtedly” or “most likely”) due to ____.

XVII. RECORD KEEPING AND TESTIMONY

The importance of keeping good records cannot be overemphasized, particularly in legal matters. The following section reviews some of the steps that should be taken in preparing for trial testimony in a product liability case.

A. Maintain a “Chain of Custody”

(a) Be sure to keep a log of the date a piece of evidence was received and from whom. The party giving the part to you should get a receipt, a copy of which should be in your file. Photograph the part to show its “as received” condition.

(b) When the part is returned, enter the date and the recipient’s name in your file and obtain a receipt. It is good practice to photograph the part again to show its condition at the time of transfer.

(c) While the part is in your custody, record the types of examinations made and the associated dates.

B. Photos and Other Records

(a) When taking a series of photographs, use a voice recorder to identify each photo by number and also indicate the subject matter.

- (b) When prints are received, label each print with the subject matter identification and date taken. Keep prints with the case file.
- (c) If copies of prints are supplied to other parties, record the names of the recipients and the dates given.
- (d) Copies of EDS readouts should be labeled with date and subject matter and then placed in the case log book.
- (e) SEM photos should be dated and identified, and then stored with the case file.

C. Examination in Your Laboratory (or Service Laboratory)

(a) Initially, use only nondestructive types of examination (NDE). If destructive examination is required, be sure to get permission in writing from your attorney as to the specific form of examination. He or she may have to contact the opposing side for their permission as well. For example, the removal of a rust layer to better observe a fracture surface should only be done with the attorney's permission. Similarly, a hardness indentation may be considered by some to be destructive, and therefore permission should be obtained before doing such testing. Obviously, the sectioning of a part requires prior approval.

(b) Record in the log book the date and types of examinations made.

(c) List all data obtained: photographs, hardness values, chemical compositions, SEM work, and so on.

D. Storage

Keep any parts received in a safe and secure place while they are in your custody, preferably in a locked cabinet or secure room. The parts may be in your custody for a year or more at times. Protect the parts from corrosion; for example, coat the fracture surfaces of steel specimens with a light oil.

E. Depositions

If you give a deposition before a trial, be sure to answer all questions as directly and simply as possible. If you feel that an answer should be further clarified, ask for a break and discuss the matter with your attorney. He or she will have an opportunity to ask you some questions for clarification after the opposing attorney has completed his or her portion of the questioning. Be prepared. Any uncertainties, inaccuracies, or inconsistencies may be brought up later at the trial.

F. Pretrial Preparation

Most trial lawyers are not technically trained, and in a technical case they may not have grasped all of the details of the technical aspects of the matter completely. Their lack of understanding may lead them to ask questions that do not bring out all the points you as an expert would like to make to convince the jury of the correctness

of your views. One way of avoiding difficulties would be to meet with the attorney prior to the trial and provide a list of questions that will develop your testimony in a logical and complete fashion. The following is a suggested list of questions.

- (a) What is your name?
- (b) What is your professional address?
- (c) Please describe your education.
- (d) Please describe your employment history and consulting experience, particularly as it relates to the present case.
- (e) Please describe your publications in terms of numbers and general content.
- (f) Have you been previously qualified to be an expert witness at a trial? Approximately how many times? Over what period of time?
- (g) Have you done any research or consulting work on topics related to the present case?
- (h) How and when did you become involved in this case?
- (i) What documents did you receive?
- (j) What meetings of a technical nature did you attend in connection with this case? (These meetings may have been with a group of consultants on your side of case or with the manufacturer's representatives. There may have also been plant and site visits.)
- (k) What components did you receive for examination?
- (l) What types of examinations did you carry out? (As you answer this question during the trial, your photos, chemical analyses, similar occurrences, etc. may be placed in evidence.)
- (m) Did you examine the whole unit rather than just a component?
- (n) Did you examine any similar units?
- (o) What were your overall evidentiary factual findings? (For example, "the part failed in fatigue.")
- (p) Did you discuss your findings with anyone else who may have helped you in reaching your conclusions (professionals, technicians, mechanics, etc.)?
- (q) What were your conclusions?
- (r) How did you reach these conclusions? (In a failure analysis, there is often a sequence of events leading up to the final failure. You may have to offer your opinion as to what was the most likely sequence.)

These questions can obviously be modified to fit a particular case. But if you and your attorney agree beforehand on an appropriate list and sequence of questions and your attorney follows them at the trial, you will be better prepared and more confident on the witness stand.

In addition:

- (a) Before the trial, review the depositions of opposing side in the case, if any.
- (b) Prepare a list of questions for your attorney to ask during cross-examination.

G. Trial Testimony

(a) Be well groomed; dress in a professional style (a shirt, tie, and business suit for a man, a suitable equivalent for a woman).

(b) After you have responded to the first seven questions from the list in Section F, the opposing attorney may challenge your expertise as it applies to this particular case, and the judge will make a final decision. Normally, this is not a problem for an expert in the type of failure analysis that relates to the matter of the trial, and the answers to the above questions should be sufficient to qualify you. Obviously, if you have never worked in the field of electronics, you would not want to put yourself forward as an expert in that field. Once you are qualified as an expert witness, you are permitted to give your opinion concerning technical aspects of the matters at hand.

(c) During the trial, the judge may make some comments relating to your testimony. Listen carefully and don't interrupt. Some judges may seem to be rather abrupt and impatient. Take a deep breath and try not to get flustered. Answer questions calmly, accurately, and directly.

H. Cross-Examination

Answer the questions simply and directly. If you don't know an answer, say so. Do not attempt to argue; hopefully, your attorney will know if there is any need for further questioning during the redirect portion of the trial to give you the opportunity to clarify an answer given during the cross-examination. For example, during the cross-examination you may have said that it is possible for a part to have failed in a certain way (although you don't think it likely). During the redirect examination, your attorney may ask the question that will give you a chance to state that the probability of such an event is quite small in your opinion, given the general circumstances of the failure at hand.

I. A Final Point

If, during the trial, you are present for the testimony of the opposing side, prepare a list of comments and possible questions concerning this testimony for your attorney to use on cross-examination of the opposing witnesses.

XVIII. SUMMARY

This chapter has provided an introduction to many of the most common procedures used in carrying out a failure investigation. These procedures range from fairly simple to highly sophisticated. The investigator needs to be aware of these resources and to make use of the appropriate ones in a given analysis. The importance of maintaining proper custody of evidence, and of correct record keeping, report writing, and presentation of results, cannot be overemphasized.

REFERENCES

- (1) D. Brandon and W. D. Kaplan, *Microstructural Characterization of Materials*, Wiley, New York, 1999.
- (2) D. B. Williams and C. B. Carter, *Transmission Electron Microscopy*, Plenum, New York, 1999.
- (3) *ASM Metals Handbook*, 8th ed., vol. 8, ASM, Material Park, OH, 1973, p. 330.
- (4) B. D. Cullity, *Elements of X-ray Diffraction*, Addison-Wesley, Reading, MA, 1956.

PROBLEM

- 6-1.** A two-beam X-ray stress analysis is carried out on a high-strength steel component for which $E = 200$ GPa and $\nu = 0.25$. The part contains a biaxial residual stress system, and it is desired to measure the residual stress in a particular direction. The values of the (511) spacings for normal incidence and incidence at $\psi = 45^\circ$ are 0.0550 nm and 0.0552 nm, respectively. Determine the stress.

Brittle and Ductile Fractures

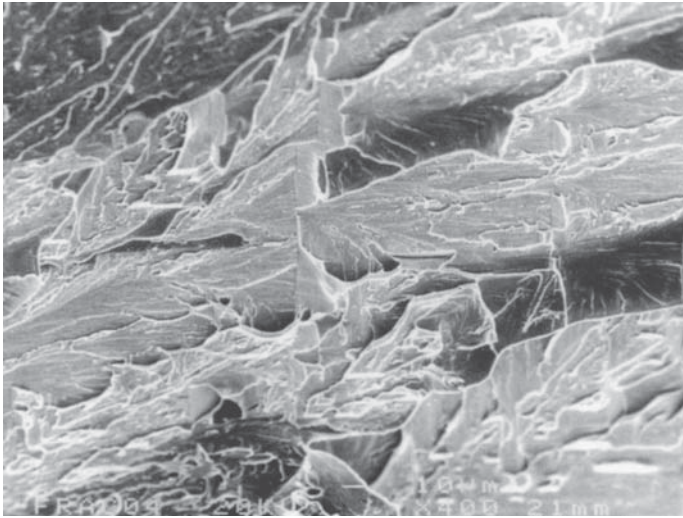
I. INTRODUCTION

In a polycrystalline material there are only two types of fracture, transgranular or intergranular. Under tensile loading, the transgranular mode can be subdivided into brittle and ductile types of failure. Failures that occur under cyclic loading are usually transgranular, whereas long-term creep failures occur in an intergranular mode. Other types of failure, such as stress corrosion cracking, can take place in either a transgranular mode or an intergranular mode.

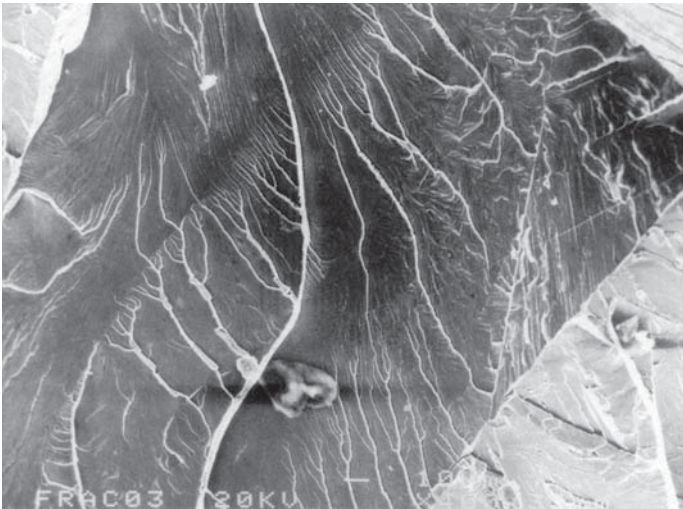
This chapter deals with brittle fracture and ductile fractures, and the transition from brittle to ductile fracture that occurs in steels as the temperature is increased from a low to a higher level.

II. BRITTLE FRACTURE

Transgranular brittle fracture in steel is characterized by a separation process known as *cleavage*, which occurs along the (100) crystallographic planes of the ferrite. If one examines a piece of steel that has failed in a brittle manner, either by eye or with a low-power microscope, bright specular reflections can be seen. These planar bright facets are the (100) cleavage planes. On a microscopic level, these facets usually



(a)



(b)

Fig. 7-1. Examples brittle fracture. (a) Cleavage facets. (b) River patterns. (Courtesy of Dr. J. Gonzalez.)

contain tear lines, visible at $100\times$, Fig. 7-1. These are created at a grain boundary as the crack front passes from one grain to another, since the (100) plane of one grain is in general not aligned with that of its neighbor. These tear lines are steps within a grain that join parallel (100) planes, and their creation adds to the energy required for fracture. As a crack front advances farther into a grain, there will be a tendency



Fig. 7-2. An example of chevron markings on the fracture surface of a 25 mm thick steel plate involved in the collapse of an Allegheny County, Pennsylvania, oil tank in 1988. The origin of the fracture is to the left. (Courtesy of Dr. I. Le May.)

for the number of tear lines to merge and disappear, thus creating what is known as a *river pattern*, that is, a merging of the tributaries with the main stream. These river patterns are a useful aid in the determination of the local direction of crack propagation. Since tear lines tend to be perpendicular to the crack front, the merging of the tear lines indicates that the local crack front curvature was convex with respect to the direction of crack propagation. Since the creation of tear lines requires an expenditure of energy, they exert a drag on crack propagation and therefore can affect the local shape of the crack front.

On a macroscopic level, the brittle fracture of a steel plate is characterized by so-called chevron markings. These markings are useful in failure analysis, as the tips of the chevrons point toward the origin of the fracture. An example is shown in Fig. 7-2. These chevron markings are macroscopic tear lines that run perpendicular to the curved crack front and diverge as the crack extends. Crack front curvature is due to a slower rate of crack propagation in the plane-stress surface region than in the plane-strain interior region.

Brittle cracks in steel travel at a high velocity, that is, 0.1–0.2 times the speed of an elastic wave in steel. This means that the strain rates along the crack front are extremely high. As will be discussed, high strain rates, as well as low temperatures, both contribute to the tendency for brittleness in steel. Brittleness also means that there is a lack of ductile deformation. Note that the fracture in Fig 7-2 is quite flat and there is no lateral contraction, as would be the case if a process akin to tensile necking had taken place.

Intergranular fractures are also brittle. Such fractures occur because of a weakness of the grain boundaries, which is often due to the segregation of impurity elements to the grain boundaries during processing and heat treatment. The term *rock candy* is used to characterize the appearance of intergranular fractures, Fig. 7-3. At low magnification, regions of intergranular fracture will appear to be bright because of the planar rock-candy topography, but the crystallographic planarity associated with cleavage fracture is absent.

In contrast to these two types of brittle fracture, a ductile fracture is noncrystallographic and takes place by plastic shear deformation. Because of the absence of crystallographic facets, it is duller in appearance than a brittle fracture.



Fig. 7-3. Intergranular fracture in steel. (Courtesy of Dr. J. Gonzalez.)

III. SOME EXAMPLES OF BRITTLE FRACTURE IN STEEL

Some interesting examples of well-known of brittle fractures in steel are listed below.

(a) In January 1919, a steel tank in Boston that contained 2,300,000 gallons of molasses suddenly collapsed. In the ensuing flood of molasses, 12 persons along with several horses either drowned or died of the injuries sustained (1).

(b) In the 1930s, several truss bridges failed in Europe at low temperatures. The failures were subsequently found to have initiated at weld defects. Charpy impact tests showed that the bridge steel was brittle at room temperature (1).

(c) During World War II, of 4,694 merchant ships studied from February 1942 to March 1946, 970 had developed cracks that required repairs. Between 1942 and 1952, more than 200 ships sustained fractures classified as serious, and at least nine T-2 tankers and seven Liberty ships broke completely in two as a result of brittle fractures. These events led to investigations that resulted in a rapid decrease in the number of these failures. Whereas there had been 130 failures per month in March 1944, there were only 5 per month in March 1946, although the total number of ships had nearly doubled. The improvements that were made included changes in design (including elimination of square corners at hatchways, etc.) and changes in fabrication procedures and retrofits, as well as impact requirements on the materials of construction (1, 2).

(d) At 5 p.m. on December 15, 1967, a suspension bridge spanning the Ohio River connecting Point Pleasant, West Virginia, with Kanauga, Ohio, suddenly collapsed. Forty-six people were killed in the accident. The cause of the failure was traced to



Fig. 7-4. Two flaws, upper left, 3 mm and 1.5 mm in radius, that existed prior to fracture of the critical eyebar of the Point Pleasant Bridge. (From NTSB, 3.)

two adjacent small semicircular flaws of the order of a few millimeters in radius, Fig. 7-4, in one of the eyebars that were linked together to make up the suspension system. These eyebars were 9.1 m (30 ft) or so in length, arranged in pairs so that four bars met at a pin connector, Fig. 7-5. However, the structure was not redundant, for if one member failed, the resulting load on its companion member would be sufficient to bring about its failure as well. One of the flaws was 3.2 mm (1/8 in.) in radius and the other was 1.6 mm (1/16 in.) in radius. These flaws had initiated at corrosion pits and had developed due to a combination of corrosion fatigue and

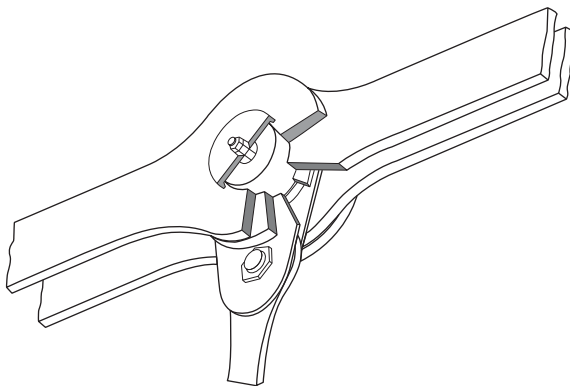


Fig. 7-5. A typical eyebar chain joint of the Point Pleasant Bridge. (From NTSB, 3.)

stress-corrosion cracking, processes that were not known to occur in bridges when the bridge had been designed in 1927. Unfortunately, these flaws developed in a portion of the structure not accessible to inspection. The steel had a yield strength of 552 MPa (80 ksi), but because it was lacking in fracture toughness, the small flaws were able to initiate brittle fracture, which led to the collapse (3).

(e) On January 2, 1988, a large aboveground fuel storage tank located in Allegheny County, Pennsylvania, suddenly collapsed, releasing 3.9 million gallons of diesel fuel. The crest of this wave washed over nearby earthen dikes, and much of the oil found its way into the Monongahela and Ohio Rivers. The steel shell of the failed tank was twisted and contorted, and massive steel columns and other internal support members were bent and thrown dozens of feet from their original locations. The shell itself was displaced about 36.6 m (120 ft) to the east of its original location. This tank had originally been located at another site and had been taken apart and reassembled at the Pennsylvania site, and failed on the first filling. Construction deficiencies attributable to reassembly, however, did not materially contribute to the collapse of the tank. Rather, the immediate causes of the collapse were found to be:

1. A decades'-old flaw due to a burn from a cutting or welding torch located near the top edge of a steel plate in the first level (in burning, steel is permanently damaged by incipient melting or intergranular oxidation)
2. Ambient temperatures cold enough that the steel in use was prone to brittle failure
3. Static stress from filling the tank to its permissible capacity.

In addition, the tank had not been subjected to a complete hydrostatic test after reassembly.

(f) In March 1985, a new water main was being tested in Hartford, Connecticut. The ambient temperature was 5°C (41°F), and water was flowing in the system when a control valve was suddenly shut; as a consequence, the water main ruptured. Chevron markings were clearly evident on the fracture surfaces of the pipe, and the markings indicated the region in which the fracture had originated. No defects were observed at the fracture origin. The failure had originated as a result of a phenomenon known as *water hammer*, which is a surge in the water pressure that occurs when a fluid in motion is suddenly stopped. In most cases, water hammer is evidenced by a banging noise in a piping system, but in extreme cases rupture can occur. In August 2012, also in Hartford, at an ambient temperature of 28°C (82°F), a truck hit and broke a fire hydrant. In response to the impact, a safety valve closed rapidly, causing pressure surges to occur that resulted in four brittle-type breaks in three interconnected water mains.

IV. DUCTILE-BRITTLE BEHAVIOR OF STEEL

A. The Charpy Test

Steels, and many other materials as well, fail in a brittle manner below a certain temperature range and fail in a ductile manner above this range. Aluminum alloys and

copper alloys, on the other hand, remain ductile even at extremely low temperature. The Charpy V-notch impact test, ASTM Designation E 23, is often used in the study of the ductile-to-brittle transition. A common specimen for this test is shown in Fig. 7-6a. The specimen is a square bar, 10 mm \times 10 mm in cross section and 55 mm in length, with a notch at midlength transverse to the bar. The notch is 2 mm deep, with a 45° included angle, and a tip radius of 0.25 mm. In some cases, the specimen is precracked by cyclic loading prior to impact testing.

In a test, the bar is removed from its cooling or heating medium (if any) and placed horizontally on the anvils of a pendulum-impact machine, with the V-notch vertical (Fig. 7-6b). Within 5 seconds after positioning a cooled or heated specimen, the pendulum is released from a predetermined height, and its potential energy is transformed into kinetic energy. A striker on the pendulum impacts the specimen on the side opposite the notch, generally breaking the specimen. The height to which the pendulum rises after breaking the specimen is then compared to its initial height, and the difference is used to determine the energy absorbed in the impact process. The striker may be equipped with strain gauges to provide a force-time readout during the fracture process (instrumented Charpy test). If a fatigue precracked the specimen, this information can be used to determine the dynamic fracture toughness of the material.

The Charpy test can be used in conjunction with, and at times to substitute for, more expensive fracture mechanics-type tests. Consider the following case (4).

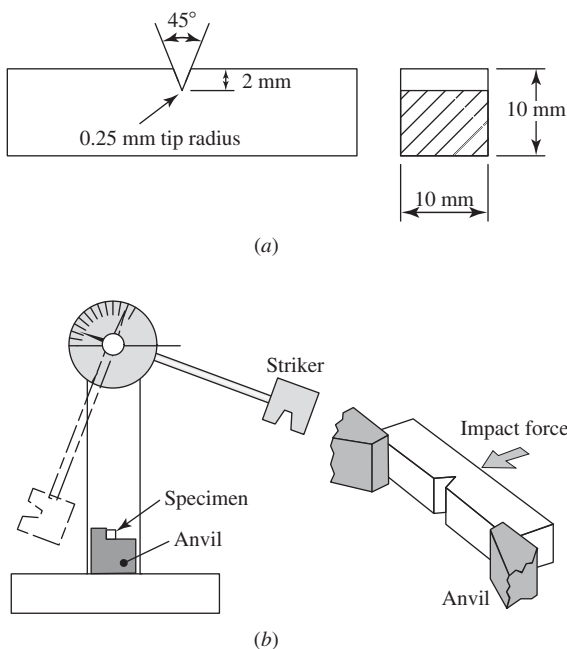


Fig. 7-6. (a) The Charpy V-notch specimen. (b) Pendulum-impact machine.

A steel producer has a contract to supply plate steel for an offshore platform. The plate material needs to meet criteria for mechanical properties that are quite rigorous for safety and end product reliability reasons. Before full-scale production of the order can begin, the steel supplier needs to demonstrate to the buyer that the material is capable of meeting such criteria. To accomplish this, the supplier qualifies the material for the project. The process begins by making the steel grade and then testing a portion of the plate to determine if all requirements have been met. Steel mill equipment imposes limits on plate size; therefore, individual units need to be welded together in the field to produce lengths that can reach to great depths. Small sections of the sample plate are welded together, and fracture mechanics tests are conducted to determine the crack tip opening displacement (CTOD) toughness in the heat-affected zone (HAZ) and along the fusion line where the weld metal meets the base metal. Then a steel supplier might correlate the CTOD results with the CVN 50% ductile-to-brittle transition temperature (DBTT). By agreement, this correlation can allow the steel supplier to use the Charpy test instead of the more expensive and time-consuming CTOD test. Empirical correlations between Charpy V-notch test results and K_{Ic} and K_{Id} (the fracture toughness obtained at a high strain rate) values have been obtained by Rolfe and Barsom (1) for particular grades of steels as a function of temperature. It is noted that design criteria for bridge steels have been based upon such correlative procedures.

An example of the influence of temperature and carbon content on the amount of energy absorbed in a Charpy test is shown in Fig. 7-7. The midpoint of the transition temperature range for a given steel is a measure of the DBTT. Other measures of the transition temperature may be related to the amount of lateral expansion on the compression side of the specimen or to the amount of shear fracture present on the fracture surface (picture window). In other cases, the transition temperature may be specified as a function of the level of energy absorbed—for example, 41 J (30 ft-lb).

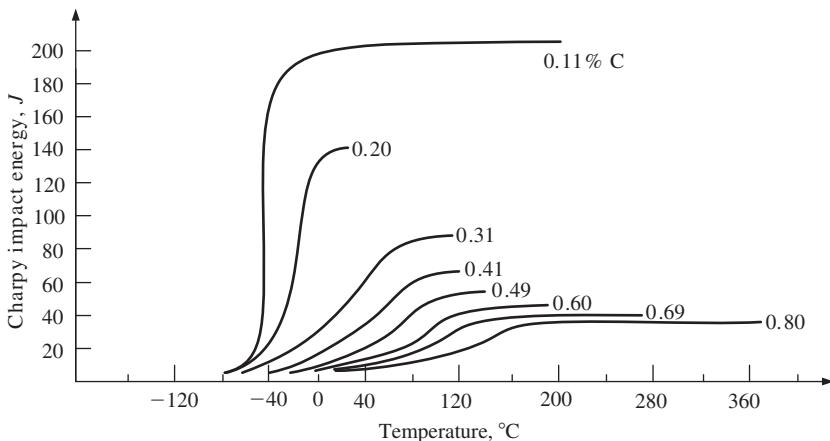


Fig. 7-7. The influence of the carbon content of steels on Charpy V-notch energy as a function of temperature. (After Burns and Pickering, 14.)

The failure of the welded ships at temperatures of the order of -1°C (30°F) during World War II focused attention on the factors that led to brittle behavior. Whether or not a steel will behave in a brittle or ductile manner depends upon a number of factors, the principal ones being composition, strength level, thickness, temperature, and strain rate. Higher levels of carbon, phosphorus, molybdenum, and arsenic in steel increase the transition temperature, whereas nickel, silicon, manganese, and copper decrease it. If loading conditions are such that dislocations within the steel move and multiply to accommodate the imposed strain rate before fracture is initiated, then the steel will behave in a ductile manner; otherwise, the steel will be brittle. In steels, dislocation motion at low temperatures is strongly influenced by interaction with the lattice. This interaction is known as the *Peierls force*, and it is much more pronounced in body-centered cubic (bcc) materials such as ferritic steels and hexagonal close-packed (hcp) materials such as zinc than it is in face-centered cubic (fcc) materials such as aluminum and copper.

Steels are referred to as *strain-rate-sensitive* materials since their low-temperature strengths are dependent upon the strain rate. In contrast, the strength properties of copper and aluminum are much less dependent upon the strain rate. This strain-rate sensitivity has consequences, not only with respect to fracture, but also in other areas, such as high-rate forming, as well. A simple expression can be derived for the stress required to move a dislocation at a given strain rate $\dot{\epsilon}$ and temperature T . It is assumed that the process is thermally activated and follows Arrhenius-type behavior, and that the activation energy Q is reduced by the applied stress acting within an activation volume v . The resultant equation is

$$\dot{\epsilon} = Ae^{-\left(\frac{Q-v\sigma}{RT}\right)} \quad (7-1)$$

where A is called a *frequency factor*, R is the universal gas constant ($8.314 \text{ J mol}^{-1}\text{K}^{-1}$), and T is the absolute temperature.

Thus,

$$\ln \frac{\dot{\epsilon}}{A} = -\frac{Q - v\sigma}{RT} \quad (7-2)$$

which can be expressed as

$$\sigma \frac{v}{R} = \frac{Q}{R} - T \ln \frac{A}{\dot{\epsilon}} \quad (7-3)$$

Equation 7-3 indicates that the stress required to move a dislocation at a given strain rate decreases with the increase in temperature and increases with the increase in strain rate. The parameter $T \ln(A/\dot{\epsilon})$ is known as the *rate-temperature parameter*, and it can be used to correlate yield strength behavior for steels as a function of temperature and strain rate, as shown in Fig. 7-8, with A equal to $10^8/\text{sec}$. Note that the strain-rate sensitivity decreases with increase in yield strength.

It is noted that a limited amount of plastic deformation usually takes place in steel even for nominally completely brittle fracture, as indicated by the fact that the fracture stress in tension of smooth bars tested in liquid nitrogen is equal to the

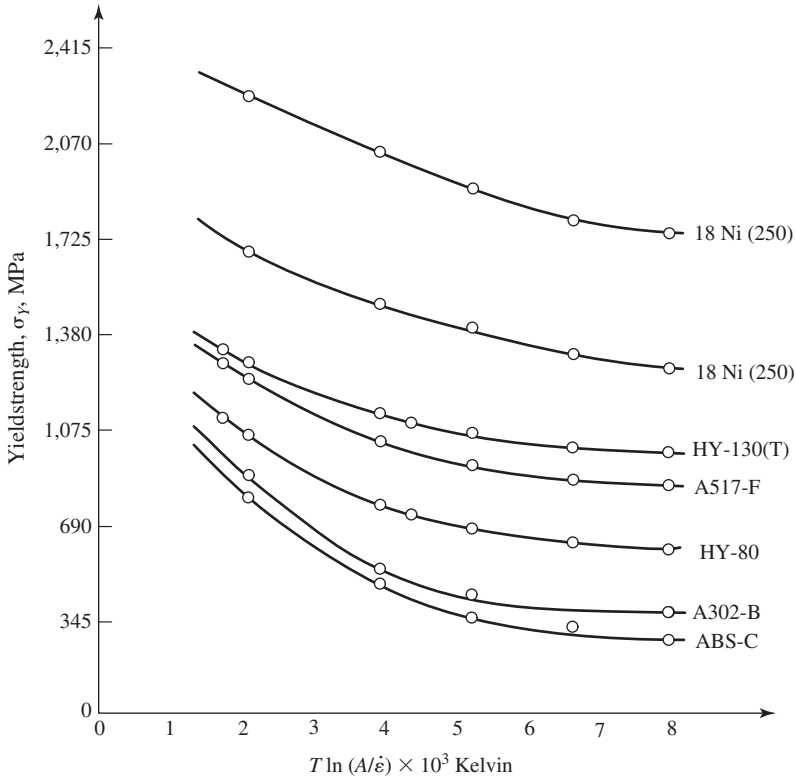


Fig. 7-8. Yield strength of several steels as a function of the parameter $T \ln A/\dot{\epsilon}$ with $A = 10^8/\text{sec}$ and the temperature T in degrees Kelvin. (After Rolfe and Barsom, 1. Based on Bennett and Sinclair, 13.)

yield strength measured in compression (5). This is interpreted to mean that plastic deformation is necessary to trigger brittle fracture. When this plastic deformation occurs, locally high stresses develop due to the blockage of dislocations at barriers (dislocation pileups). In carbon steels, these stresses then initiate the local fracture of grain boundary carbides, which act as the barriers to the dislocations.

One way to view the brittle fracture process in steel is to consider that the steel has a fixed local fracture strength σ_f , independent of temperature and strain rate. Should the stress in a component reach this value, brittle fracture will occur. In Chapter 3, we saw that under plane-strain conditions, the yield stress ahead of a U-shaped notch could be increased due to constraint by a factor of 3 over the yield strength when the von Mises criterion was used. In the case of the V-notched Charpy bar, this factor is somewhat less, 2.5, since the flanks of the V-notch are at 45° to each other rather than parallel. If we assume that brittle fracture at low temperatures in steels occurs when the local yield stress, σ_Y , equals the fracture strength σ_f , then brittle fracture of a Charpy bar will occur at a stress $1/2.5$ that of the fracture stress required for brittle

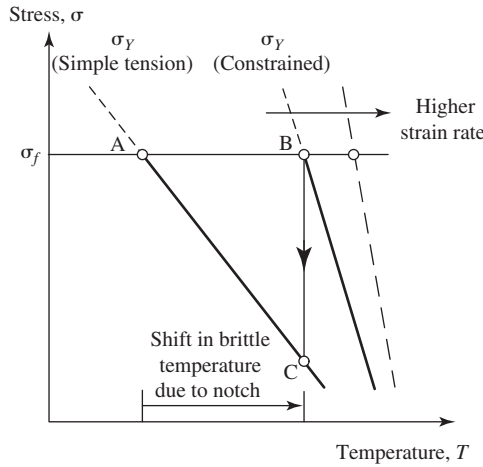


Fig. 7-9. Effect of a notch on the brittle transition temperature.

fracture. That is, the stress at point C in Fig. 7-9 is $1/2.5$ that of the stress at point B. This has the effect of moving the temperature at which the specimen is brittle to a higher value compared to the brittle temperature for an unnotched specimen, Fig. 7-9.

Similarly, an increase in strain rate will increase the transition temperature, since it increases the yield strength in a strain-rate-sensitive material such as carbon steel. The Charpy notched-impact test, therefore, provides a conservative measure of the transition temperature, since it involves both notch constraint and a high strain rate.

Grain boundaries per se block plastic deformation from progressing from one grain to the next because of differences in orientation of the slip systems from grain to grain. As a result, the grain size d can influence the yield strength of annealed polycrystalline alloys in which precipitation is absent. As a simplification, we consider a grain that is square in cross section, as shown in Fig. 7-10a. Under the action of an applied shear stress, the shear strain γ is given as (Fig. 7-10b)

$$\gamma = \frac{\tau}{G} = \frac{\Delta}{d} \quad (7-4)$$

When plastic deformation occurs in this grain, the elastic displacement Δ is relaxed and replaced by a plastic displacement (Fig. 7-10c), that is,

$$\Delta = \left(\frac{\tau}{G} d \right)_{el} = (nb)_{pl} \quad (7-5)$$

where n is the number of dislocations and b is their Burger's vector. These dislocations are blocked and pile up at the grain boundary. As a result, a stress concentration develops whose magnitude τ_{\max} is given by the simple expression

$$\tau_{\max} = n\tau \quad (7-6)$$

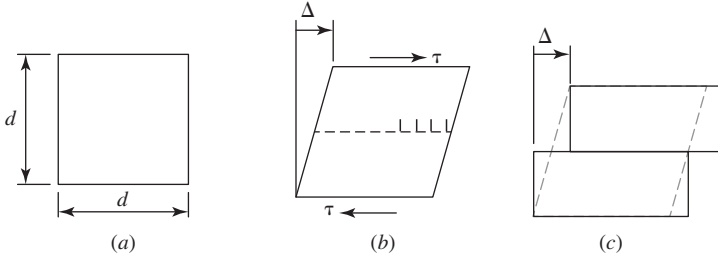


Fig. 7-10. (a) Square grain. (b) Square grain subjected to shear stress. (c) Square grain after relaxation of elastic strain due to the motion of dislocations.

The quantity n , appearing in Eq. 7-6, can therefore be replaced by τ_{\max}/τ , which leads to

$$\tau_y = (Gb \tau_{\max c})^{1/2} d^{-1/2} \quad (7-7)$$

where τ_y is the yield stress in shear and $\tau_{\max c}$ is the local stress at the tip of the dislocation pileup required to initiate slip in the next grain. This equation is rewritten in terms of the tensile yield stress as

$$\sigma_y = \sigma_i + k_y d^{-1/2} \quad (7-8)$$

where $k_y = 2(Gb \tau_{\max c})^{1/2}$ and σ_i is the lattice friction, that is, the stress required to move a dislocation in a single crystal. This equation is known as the *Hall-Petch relation*.

An interesting and useful outcome of this derivation is that, in single-phase materials or carbon steels having a ferritic-pearlitic microstructure in which plastic deformation occurs primarily in the soft ferritic phase, a decrease in grain size is seen to result in an increase in the yield strength. Further, if a certain level of $\tau_{\max c}$ has to be reached before fracture of a grain-boundary carbide can occur, then a decrease in grain size requires an increase in τ_y . Therefore, the yield strength and the fracture resistance are both raised by a decrease in grain size. This is a singular result, for generally any other modification that increases the yield strength of a given alloy results in a decrease in fracture resistance.

As the test temperature increases above the highest temperature at which a steel is completely brittle, a brittle-to-ductile transition occurs. The results of Charpy impact tests are shown schematically in Fig. 7-11. The term *upper shelf* refers to the region in Fig. 7-11 that is above the transition region, and the term *lower shelf* refers to that portion of the diagram below the transition region. Whereas a high strain rate below the transition temperature promotes brittle behavior by lessening the time available for the motion and multiplication of dislocations, a high strain rate above the transition temperature may increase the resistance to fracture, that is, the fracture toughness, since the fracture toughness depends upon both strength level and ductility (extension to fracture). Therefore, a high strain rate in the ductile

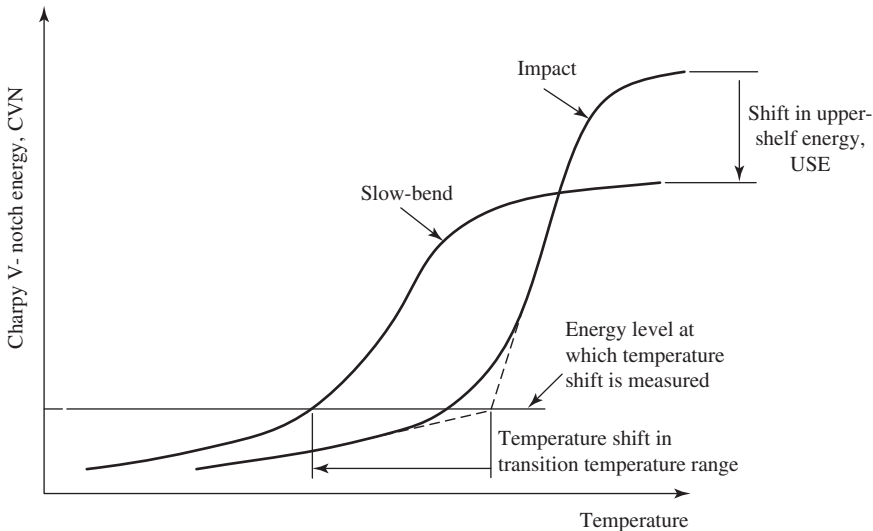


Fig. 7-11. A schematic representation of the upward shift in temperature of the Charpy V-notch transition temperature and the upper-shelf energy level due to an increase in strain rate. (After Barsom and Rolfe, 1.)

range that increases the yield strength may actually improve toughness, as indicated in Fig. 7-11.

V. CASE STUDY: THE NUCLEAR PRESSURE VESSEL DESIGN CODE

A. Prevention of Brittle Failure (4)

In a nuclear power plant, it is essential that the nuclear reactor be operated in a manner that ensures that pressure vessel integrity is maintained under both normal and transient operating conditions. This is accomplished by postulating limiting flaws and using linear-elastic fracture mechanics (LEFM) to calculate the allowable coolant temperature (T) and pressure (P) during heat-up, cool-down and leak/hydro testing (P - T curves). The P - T limits are revised periodically throughout the life of a plant to account for neutron damage to the pressure vessel. Over a period of time, neutron bombardment in the reactor beltline region shifts the ductile-to-brittle transition, as measured by the 41-J (30 ft-lb) energy level, to a higher temperature. The amount of the shift in the ductile-to-brittle transition is then used to shift the ASME reference stress intensity factor (K_{IR}) curve upward in temperature to account for the effects of embrittlement due to neutron bombardment, as shown in Fig. 7-12.

Since it is impractical to test large fracture toughness specimens throughout the life of a nuclear power plant, surveillance programs use Charpy and tensile specimens to track the neutron-induced embrittlement. The nuclear industry uses the 41-J index to define a ductile-to-brittle transition temperature (DBTT). Neutron

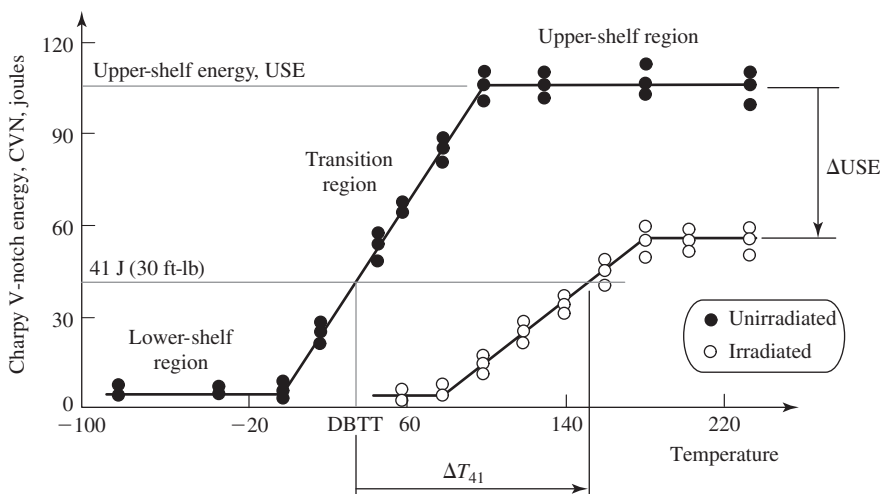


Fig. 7-12. A schematic indication of the effect of neutron irradiation on Charpy impact behavior. (After Manahan et al., 4.)

irradiation shifts the transition region to higher temperatures (ΔT_{41}), and the Nuclear Regulatory Commission (NRC) sets screening limits on the maximum shift that can occur during the life of the plant. If the screening limits are exceeded, then the plant must be shut down or a thermal anneal test must be conducted to restore the material properties.

The ability of a nuclear pressure vessel to withstand ductile fracture is judged by the upper shelf energy (USE). In older plants built before fracture toughness testing was widely used, Charpy testing was used to qualify individual heats of material. The ASME code and the Code of Federal Regulations prescribe minimum plate properties that must be attained prior to service (e.g., at least 102 J of energy on the upper shelf prior to service). The NRC requires an in-depth fracture mechanics assessment if the Charpy USE is expected to drop below 68 J during the operating life of the plant. If Charpy data can be used to extend the life of a plant by 1 year beyond the initial design life, a plant owner could realize revenues as large as \$150,000,000. Further, the cost avoidance from a vessel-related fracture is expected to be in the billion-dollar range. To date, the NRC has shut down one U.S. plant (Yankee Rowe) as a result of Charpy data trends (one concern was that the surveillance specimens were not from the same heat as the plates used for the pressure vessel). This plant's pressure vessel was constructed from a one-of-a-kind steel (which contained a small but higher level of copper than is now allowed, which promoted neutron damage at 288°C (550°F)) and is not representative of the U.S. reactor fleet.

The specified toughness requirements are obtained using Charpy V-notch test specimens coupled with the determination, as described below, of the nil-ductility transition temperature (NDTT). The NDTT is the highest temperature at which fracture occurs without macroscopic plastic deformation. The approach involves

a reference temperature, designated RT_{NDT} , and the reference fracture toughness curve K_{IR} .

The value of RT_{NDT} is obtained by measuring the drop weight NDTT of steels 15.9 mm (5/8 in.) and thicker. To determine the NDTT (ASTM Designation E 208) for a plate of 25.4 mm (1 in.) thickness, a specimen 356×89 mm (14×3.5 in.) is used. A single-pass, crack-starter weld, 63.5 mm (2.5 in.) long, is deposited in the center of the plate running longitudinally, and then a notch is made in the weld. The plate is mounted weld side down in a drop weight testing rig and is impacted by a drop weight whose kinetic energy equals 816 J (600 ft-lb) at the temperature of interest. Several specimens are needed to determine the NDTT. Above the NDTT, plastic deformation occurs and the specimen is restrained from breaking. At the NDTT, the specimen breaks without plastic deformation.

After the NDTT is determined, a set of three Charpy V-notch specimens is tested at a temperature 33°C (60°F) higher than the NDTT to measure the toughness, T_{CV} , to ensure an increase of toughness with temperature. A Charpy energy of 68 J (50 ft-lb) and a lateral expansion of 0.89 mm (35 mil) are required. The NDTT becomes the reference temperature RT_{NDT} if the Charpy results meet or exceed these requirements. If not, additional tests are performed at increasing temperatures (in steps of 10°F) until the requirements are satisfied. The RT_{NDT} then is designated to be this temperature minus 33°C . (See Fig. 7-13.)

The K_{IR} curve is then referenced to the RT_{NDT} . The data used to construct the lower bounding function K_{IR} curve used dynamic fracture toughness at the lower end as well as crack arrest toughness results to fix the upper end, and is used only for

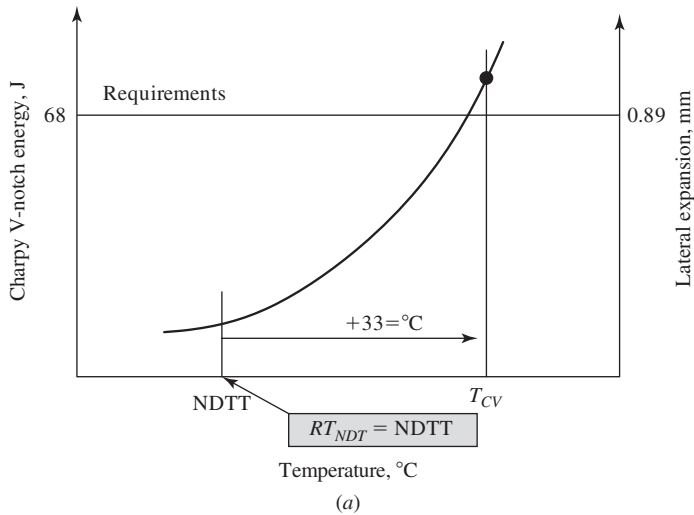


Fig. 7-13. Toughness requirements for nuclear pressure vessel steels. (a) Determined using the reference temperature, RT_{NDT} approach, where $NDTT = RT_{NDT}$. (b) Determined using the reference temperature approach, where $NDTT \neq RT_{NDT}$. (c) Determined using the reference fracture toughness, K_{IR} , curve. See text for details (4).

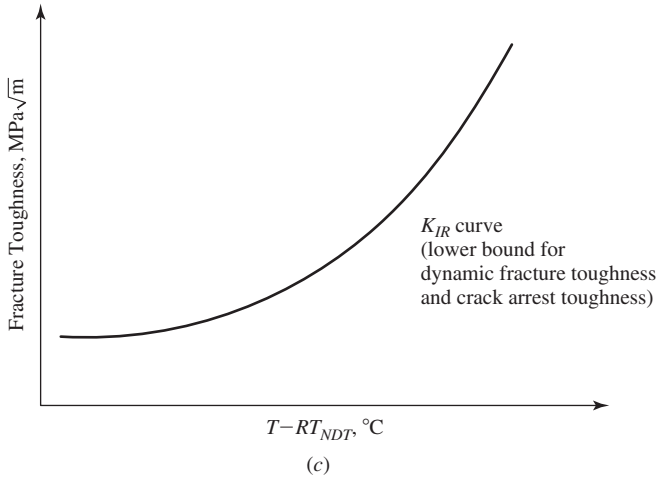
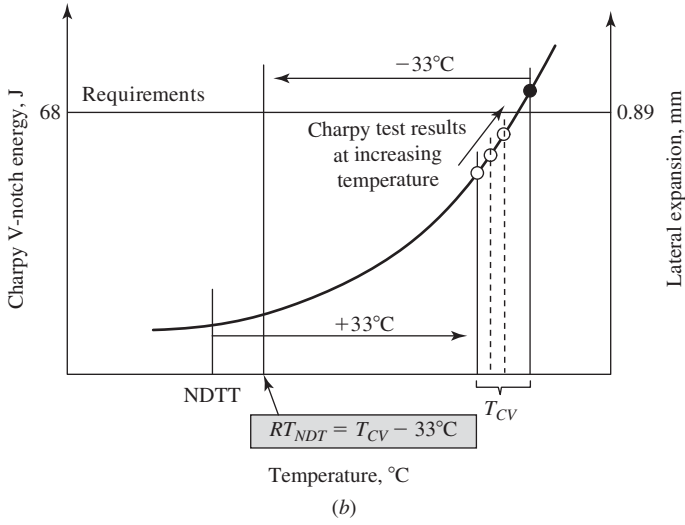


Fig. 7-13. (continued)

steels having a yield strength of 345 MPa (50 ksi) or less. The expression for the K_{IR} curve is

$$K_{IR}(\text{in ksi}\sqrt{\text{inches}}) = 26.777 + 1.223 \exp\{0.014493[T(^{\circ}\text{F}) - (RT_{NDT}(^{\circ}\text{F}) - 160)]\} \quad (7-9a)$$

$$K_{IR}(\text{in MPa}\sqrt{\text{m}}) = 24.36 + 1.129 \exp\{0.2029[T(^{\circ}\text{C}) - (RT_{NDT}(^{\circ}\text{C}) - 91.4)]\} \quad (7-9b)$$

VI. CASE STUDY: EXAMINATION OF SAMPLES FROM THE ROYAL MAIL SHIP (RMS) *TITANIC* (6)

In April 1912, the RMS *Titanic* struck an iceberg while steaming at 20+ knots and sank off Newfoundland in less than 3 hours with a loss of over 1,500 people. The wreckage was not located until 1985, and in 1991 a piece of the hull material was recovered and Charpy impact tests were carried out on test specimens machined from the sample. It was found that the steel fractured in a 100% brittle fashion at ice brine temperatures. These results led to the speculation that the impact with the iceberg had shattered the brittle hull plates, thereby allowing rapid flooding of the ship. In 1996, a section of the hull plating and several hull and bulkhead rivets were recovered, and metallurgical and mechanical analyses were performed on them. It was again found that the pieces of the hull steel possessed a ductile-to-brittle transition temperature that was very high with respect to the service temperature, making the material brittle at icewater temperatures, Fig. 7-14. This brittleness was attributed to both chemical and microstructural factors. The following tables provide information on the chemical and mechanical properties of the hull steel.

A. Chemistry

The following table gives the composition of the *Titanic*'s hull steel in weight % and compares this composition with that of a comparable modern steel.

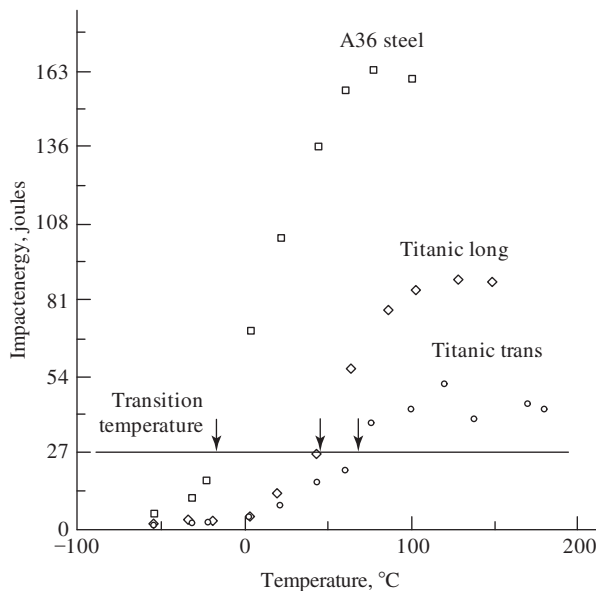


Fig. 7-14. Charpy impact energy versus temperature for specimens taken longitudinal and transverse to the rolling direction of the *Titanic*'s hull steel. Results for a modern steel, A36, are shown for comparison. The transition temperature is arbitrarily defined to be at the 27-J level. (After Foecke, 6.)

Element	<i>Titanic</i>	AISI 1018
Carbon	0.21	0.18–0.23
Sulfur	0.065	0.05 max
Manganese	0.48	0.6–1.0
Phosphorus	0.027	0.04 max
Silicon	0.021	—
Copper	0.025	—
Nitrogen	0.004	0.0026
Oxygen	0.013	—
Rare earths	—	—
Mn/S ratio	7.4:1	12:1–20:1
Mn/C ratio	2.3:1	3:1–7:1

Both sulfur and phosphorus decrease upper shelf toughness. It is noted that both the sulfur and phosphorus levels in the *Titanic*’s ship plates are much higher than those in modern steels, where sulfur levels of 0.002% and phosphorus levels of less than 0.01% are common. The steel was low in manganese, which could lead to embrittlement if there was not enough manganese (atomic weight 54.93) to combine with sulfur (atomic weight 32.06) in the form of MnS particles, where the ratio of manganese to sulfur is 1.71:1. However, in the case of the *Titanic*’s hull steel, there was sufficient manganese to tie up the sulfur in the form of MnS. Manganese is also a solid-solution toughening agent, and the relatively low amount of manganese in the hull steel, as well as the low manganese-to-carbon ratio, may have had a detrimental effect on impact toughness.

B. Tensile Properties

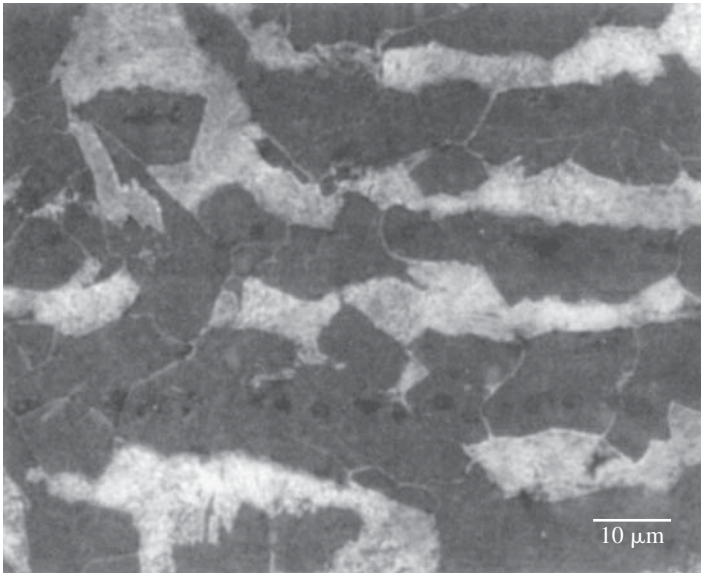
Yield strength	276 MPa (40 ksi)
Tensile strength	427 MPa (62 ksi)
Percent elongation	30 (50 mm [1.97 in.] gauge length)

These results showed that the hull steel met the specifications for the mechanical properties.

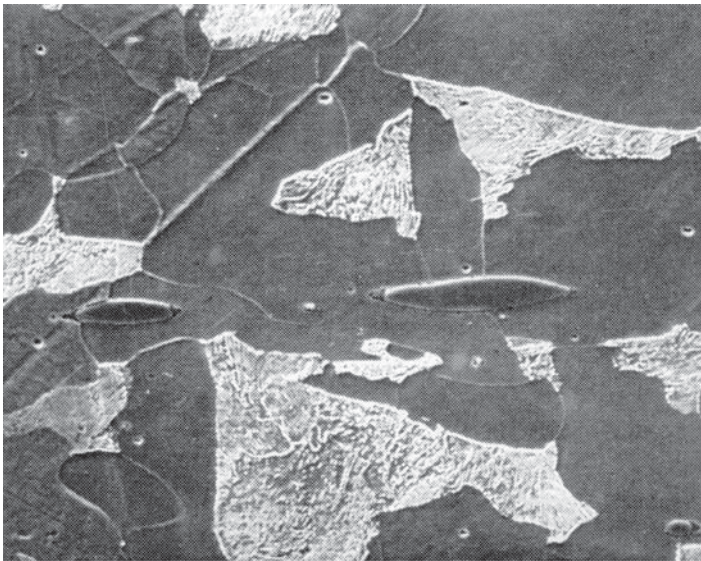
C. Microstructure

Figure 7-15 shows the microstructure of the *Titanic*’s hull steel and compares it to that of a modern steel of similar composition. The microstructure consists of large, coarse pearlite colonies (roughly 0.2 μm lamella thickness) and large ferrite grains (ASTM grain-size number 4–5, 100–130 μm in diameter). The ASTM grain-size number n is related to N^* , the number of grains per square inch at a magnification of 100 \times , by the relationships

$$N^* = 2^{n-1} \tag{7-10}$$



(a)



(b)

Fig. 7-15. (a) The microstructure of a longitudinal section of modern 1018 steel. (b) In comparison, that of the *Titanic*'s hull steel. The grain size, the pearlite lamellar spacing, and the MnS particle sizes are all larger in the *Titanic*'s hull steel. (From Foecke, 6.)

and

$$n = 3.32 \log 2N^* \quad (7-11)$$

The microstructure shows a large amount of banding in the rolling direction. MnS and oxide particles are present throughout the material and are quite large, occasionally exceeding $100 \mu\text{m}$ in length. The MnS particles had been deformed into lenticular shapes instead of being in the form of a series of elongated stringers, an indication of a low rolling temperature (6). The large grain size and the coarse pearlite indicate that the plate was hot rolled and air cooled, consistent with production in a low-speed rolling mill, as was the norm in the early 1900s. A large grain size is detrimental in the brittle range, because the intensity of stress where dislocations pile up against microstructural barriers such as pearlite or carbides increases with the increase in grain size. On the other hand, a small grain size not only improves toughness by reducing the size of pileups, but also raises the yield strength. The yield strength can be expressed as a function of grain size by means of the Hall-Petch relation, Eq. 7-8.

Modern steels processed in high-speed rolling operations have much smaller grain sizes and much finer pearlite compared to the *Titanic*'s hull steel. In the hull steel, both the large ferrite grain size and the coarse lamellar structure of the pearlite contributed to a higher transition temperature and lower upper shelf toughness. The high strain rate associated with the impact with the iceberg at 20+ knots would also have contributed to the brittle behavior because of the strain-rate sensitivity of the steel.

D. Fractography

The fracture surfaces of Charpy specimens from the *Titanic* fractured at 0°C (32°F) were 95% cleavage and 5% ductile. No evidence of intergranular fracture was found. Ten percent of the cleavage fractured area was seen to originate at fractured MnS particles.

E. Corrosion

Corrosion was not a factor in the sinking of the *Titanic*. However, at the 3,658 m (12,000 ft) depth at which the wreck rests, there is sufficient oxygen to allow the corrosion process to proceed, and *rusticles*, large stalactites of rust, have been observed. It is estimated that the ship, originally consisting of 60,000 tons of steel, is losing a ton per day to corrosion. At that rate, by 2076 AD the hull will be completely gone.

F. Rivets

In 1997, a panel concluded that the principal damage to the *Titanic*'s hull was due to parting of the plates, not to a 90 m (1,295 ft.) gash in the brittle plate steel, as had been proposed, thereby implying that failure of the rivets had played a role. Only 2 hull

rivets were examined in detail (out of 3,000,000 total), and the mechanical properties of these rivets figured in further speculation as to the sequence of events leading to the rapid flooding of the ship. Wrought iron usually consists of relatively pure iron, which contains 2–3% by volume iron silicate slag. However, metallographic analysis of the rivet shown in Fig. 7-16 revealed that it contained 9.3% slag, more than three times the expected level. Some of this slag was in the form of stringers more than $200\text{ }\mu\text{m}$ in length. These stringers are not bound to the matrix, and at low temperatures they can fracture and nucleate cracks in the iron. At the time of construction, the wrought iron rivets had been hydraulically driven through the hull plates and were flattened on the inside. Residual tensile stresses developed in the rivets on cooling, and these stresses reduced the resistance of the rivets to fracture.

The mechanical properties of wrought iron are highly anisotropic. In the direction of the stringers, wrought iron is as strong as mild steel. However, it is much weaker in the direction perpendicular to the stringers, and the ductility measured perpendicular to the stringers can be an order of magnitude less than that in the direction of the

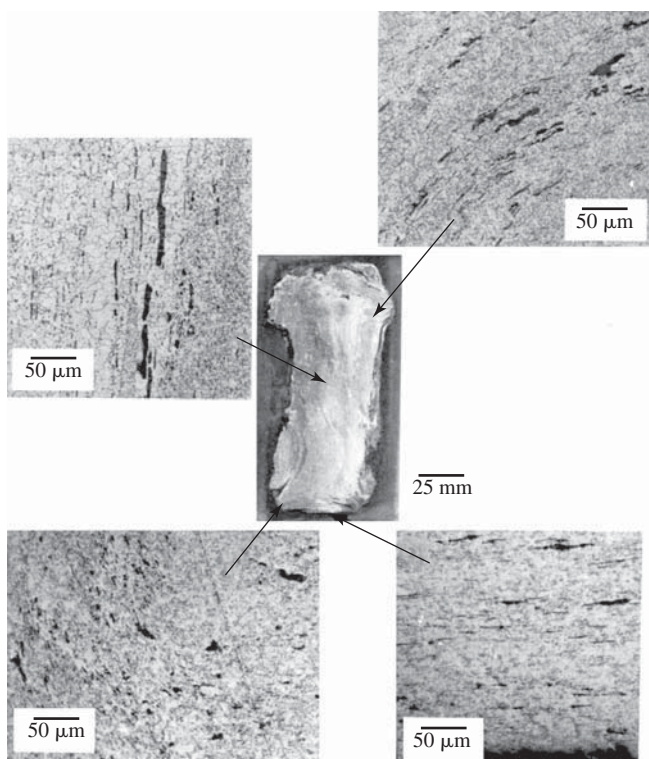


Fig. 7-16. The orientation of silicate slag at various locations within a cross section of a *Titanic* hull rivet. At the bottom right near the fracture surface created when the inner rivet head popped off, the stringers are oriented perpendicular to the tensile axis due to deformation when the inner head was formed. (From Foecke, 6.)

stringers. The two recovered rivets lacked their interior heads, an indication that they were popped off on impact due to a component of tensile stress acting across the stringers in the rivet heads. Therefore, pending further information, the investigators concluded that fracture of the rivets and the resulting parting of seams, rather than brittle fracture of the hull plates, may have been the critical factor involved in the sinking of the *Titanic*.

VII. DUCTILE FRACTURE

The process of ductile rupture on both the macroscale and the microscale differs from that of brittle rupture in that extensive plastic deformation is involved. The term *ductile failure* includes not only the separation process but, in certain forming operations, the process of necking as well. In this chapter, the topics of necking, which involves the use of the concepts of true stress and true strain, and ductile separation are treated. The microstructural characteristics of ductile fracture are also discussed.

VIII. DUCTILE TENSILE FAILURE, NECKING

In sheet forming, metals are extensively deformed. One of the forming limits imposed upon the extent of deformation in operations such as the forming of external automobile body sheet is that necking should not occur during the forming operation. An understanding of the causes of necking is therefore needed in dealing with this potential problem in manufacturing.

A. Condition for Necking of a Bar

On a load-extension plot, Fig. 7-17, the point at which necking begins is at P_{\max} . The rate of increase of load-carrying capacity per unit of area is given by

$$\frac{dF}{A d\varepsilon} = \frac{d\sigma}{d\varepsilon} \quad (7-12)$$

where σ is the true stress and ε is the true strain. The rate of decrease of load-carrying capacity per unit of area due to loss of cross-sectional area is given by

$$\frac{dF}{A d\varepsilon} = -\frac{\sigma dA}{A d\varepsilon} \quad (7-13)$$

We next make use of the fact that, for purely plastic deformation, the volume is constant, and we neglect any elastic dilatation. Therefore, $dV = 0$, and since $V = Al$, where l is the length of the element, we can write

$$dV = d(Al) = A dl + l dA = 0 \quad (7-14)$$

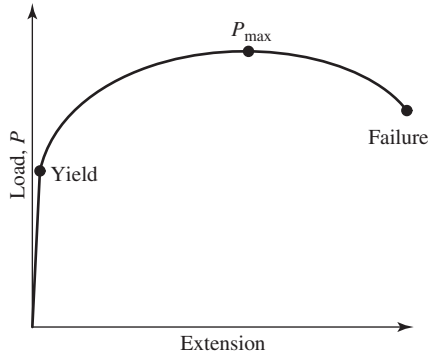


Fig. 7-17. Load (P) versus extension (Δ) plot used in the analysis of necking.

or

$$\frac{dA}{A} = -\frac{dl}{l} = -d\varepsilon \quad (7-15)$$

and Eq. 7-12 can be rewritten as

$$\frac{dF}{A d\varepsilon} = \sigma \quad (7-16)$$

At P_{\max} the rate of increase in load-carrying capacity due to strain hardening is no longer able to compensate for the rate of area decrease, and an instability develops, the condition for which is

$$\frac{d\sigma}{d\varepsilon} = \sigma \quad (7-17)$$

This can also be expressed in the following way: At P_{\max} , $\Delta P = 0$, and since $P = \sigma A$, where σ is the true stress and A is the current cross-sectional area, it follows that

$$\sigma dA + A d\sigma = 0 \quad \text{or} \quad \frac{d\sigma}{\sigma} = -\frac{dA}{A} \quad (7-18)$$

Hence,

$$\frac{d\sigma}{\sigma} = d\varepsilon \quad \text{or} \quad \frac{d\sigma}{d\varepsilon} = \sigma \quad (7-19)$$

which is the same condition for necking of a bar as given in Eq. 7-17.

The true stress-strain curve can be approximated by the following expression due to Ludwik:

$$\sigma = \sigma_o + k\varepsilon^n \quad (7-20)$$

where n is the strain-hardening exponent. At large strains, as assumed in the present case, σ_o can be neglected. Hence,

$$\frac{d\sigma}{d\varepsilon} = nk\varepsilon^{n-1} \quad (7-21)$$

If this expression for $d\sigma/d\varepsilon$ is substituted in the condition for necking, it is found that the strain at necking is

$$\varepsilon_n = n \quad (7-22)$$

Hence, the greater the strain-hardening exponent, the greater is the strain to necking.

Another stress-strain relationship that is often used in the analysis of plastic deformation is known as the *Ramberg-Osgood equation*, that is,

$$\varepsilon = \frac{\sigma}{E} + k_{RO} \left(\frac{\sigma}{E} \right)^m \quad (7-23)$$

where k_{RO} and m are material constants.

B. Strain Localization

In 4340 steel treated to have a high yield-strength-to-tensile-strength ratio, that is, 94%, when plastic deformation occurs, particularly if hydrogen is in the steel, a deleterious form of nonuniform localized deformation can occur due to plastic instability. Irregular grooves form in plastically deformed regions, as shown in Fig. 7-18, and in one case, the crash of a helicopter occurred because of the development of such markings in the main rotor spindle lugs. The subsequent fatigue

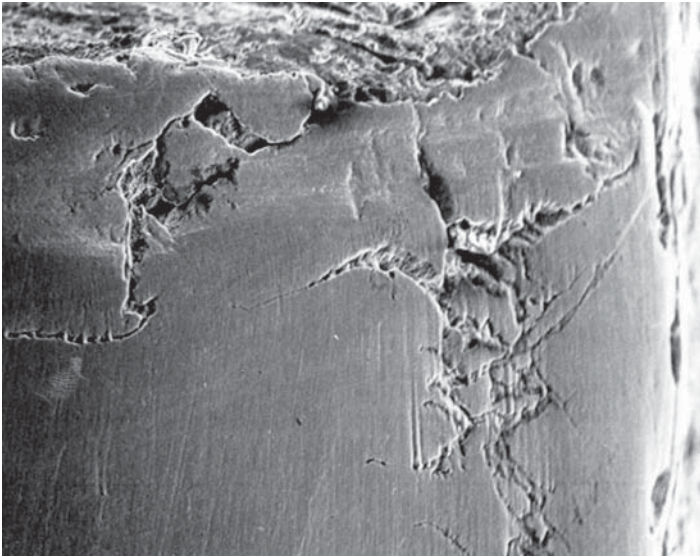


Fig. 7-18. Indications of localized plastic deformation in 4340 steel. (The yield-stress-to-tensile-strength ratio is 0.94). (Reprinted from *Materials Characterization*, vol. 26, A. J. McEvily and I. Lemay, Hydrogen assisted cracking, pages 253–268, Copyright 1991, with permission of Elsevier Science.)

crack growth from these grooves, which acted as stress raisers, resulted in the crash (7). The damaging plastic deformation was thought to have occurred under the severe loading conditions experienced during practice emergency landings.

C. Axisymmetric Stress in Necking

When a neck forms in a round bar, material at the minimum cross section of the neck attempts to contract more than the material just above and below the minimum cross section. As a result, the material above and below the minimum cross section constrains the material at the minimum cross section from freely contracting, and a triaxial state of hydrostatic stress is developed within the neck. This hydrostatic stress does not contribute plastic deformation since no shear stresses are associated with a state of hydrostatic stress, but the hydrostatic stress does increase the true tensile stress P/A required for plastic flow. By increasing the peak tensile stress, the hydrostatic stress does promote fracture of particles and interfaces and thereby affects the fracture process.

In the minimum cross section of a neck in a round tensile bar, the hydrostatic components of stress are given by

$$\sigma_{\theta\theta} = \sigma_{rr} = \sigma_z - \bar{\sigma} \quad (7-24)$$

Bridgman (8) derived the following relation to indicate the amount by which the local tensile stress acting at each point in the minimum cross section of a necked tensile bar had to be increased over the flow stress to overcome the effects of triaxiality:

$$\frac{\sigma_z}{\bar{\sigma}} = 1 + \ln \left(\frac{a}{2R} + 1 - \frac{r^2}{2aR} \right) \quad (7-25a)$$

$$\frac{\sigma_{\theta\theta}}{\bar{\sigma}} = \ln \left(\frac{a}{2R} + 1 - \frac{r^2}{2aR} \right) \quad (7-25b)$$

where $2a$ is the diameter of the necked region, r is the distance measured from the centerline in the plane of minimum cross section, and R is the radius of the neck.

Note that $\sigma_{\theta\theta}$ is zero at the surface and rises to a maximum at the centerline of the bar.

The above equation is used to determine how much the applied tensile stress must be raised as a function of the bar size and the radius of the neck to obtain plastic flow. The hydrostatic stress must be subtracted from the total stress to find the equivalent flow stress. Figure 7-19 (9) gives the ratio of the equivalent stress $\bar{\sigma}$ to the total nominal true stress P/A in a necked tensile specimen. The calculation for the average applied stress is obtained by integrating $\sigma_z 2\pi r dr$ over the cross-sectional area to get the total force and then dividing by the area to get the average stress. The nonhydrostatic component is simply $\bar{\sigma}$.

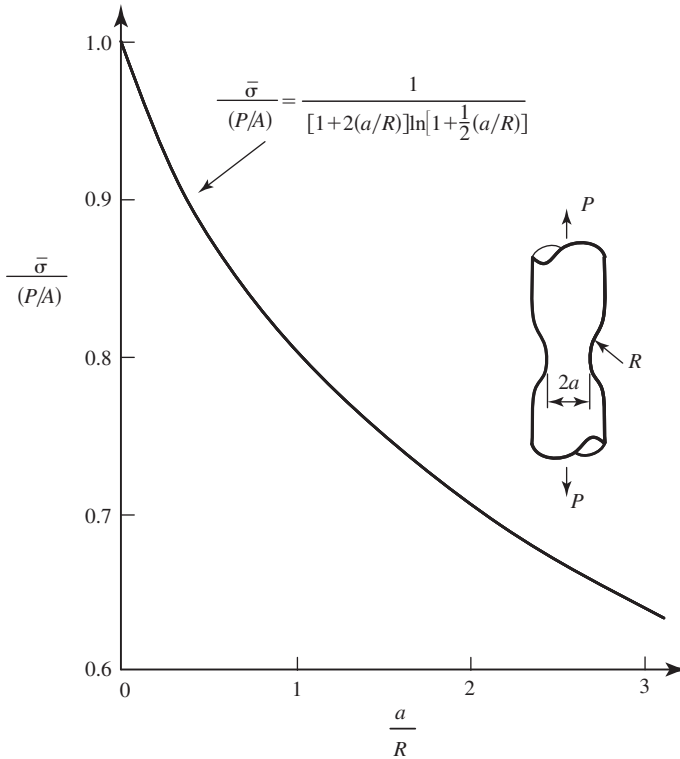


Fig. 7-19. The ratio of the effective stress $\bar{\sigma}$ to the nominal stress in a necked tensile specimen, where $2a$ is the diameter of the bar at the neck and R is the radius of the neck. (After Bridgman, 8, and McClintock and Argon, 9.)

D. Necking in a Thin Strip Under Tension

In a thin strip under tension, two types of necks can develop. One is referred to as *diffuse*, the other as *localized*. The condition for diffuse necking is the same as for bar necking, and this type of neck precedes the formation of the localized neck. A localized neck is a form of plane-strain deformation, the strain along the direction of the neck being zero. It is of interest that the localized neck in a thin sheet strip under tension does not develop in the transverse direction, but rather at a pronounced angle to the transverse direction. If a localized neck were to develop in the transverse direction, a constraint on plastic deformation would develop in the transverse direction, and according to the von Mises criterion, further deformation would require that the tensile stress be increased by $2/\sqrt{3}$. A higher axial stress would be required to cause the local deformation in the neck than is required to cause general deformation throughout the strip. Therefore, localization would not occur in the transverse direction. A direction of the neck in which localized deformation is possible is needed. From the Mohr circle for strain, Fig. 7-20a, it is seen that the

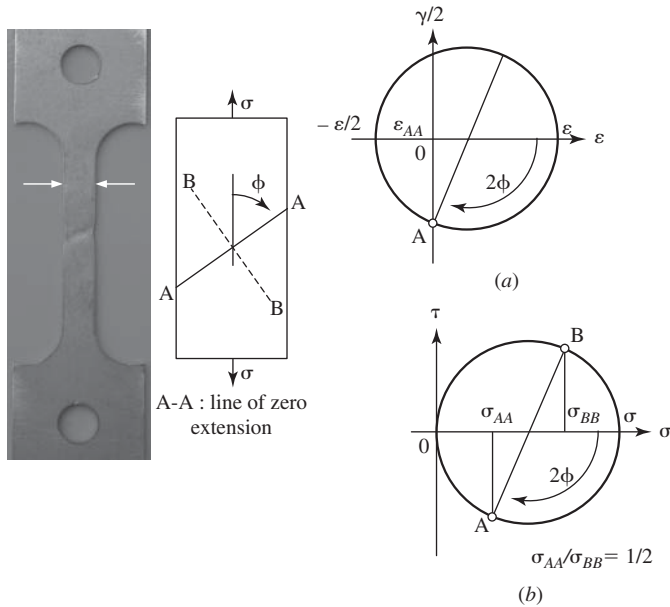


Fig. 7-20. Conditions for localized necking in a sheet. (a) Mohr circle for strain. (b) Mohr circle for stress.

strain is zero in a direction 54.7° from the axial direction. It also follows from the Mohr circle for stress, Fig. 7-20b, that the stresses parallel and normal to the direction of zero strain are in the ratio 1:2, which is consistent with the stress state required for plane strain plastic deformation. Analysis (10) indicates that the localized neck develops when the following condition is reached:

$$\frac{d\sigma}{d\epsilon} = \frac{\sigma}{2} \quad (7-26)$$

Use of the Ludwik relation indicates that at localized necking $\epsilon_n = 2n$. Therefore, it is to be expected that the localized neck will develop at twice the strain required for the formation of the diffuse neck. This is important in some sheet-forming operations where diffuse necking of the sheet is acceptable but localized necking is not, especially since fracture rapidly follows the development of a localized neck.

An example of a forming limit diagram for a low-carbon steel is given in Fig. 7-21. To use this diagram, the ratio of the minor to the major engineering strain is determined for a given forming operation. This ratio determines the slope of a line drawn from the origin. Where this line intersects either the diffuse necking, localized necking, or forming limit (fracture) lines on the diagram, the corresponding forming limit is reached, depending upon the particular considerations associated with a given forming operation. Note that, for biaxial tension straining, localized necking does not occur, since for this loading condition there is no direction in which the strain is zero.

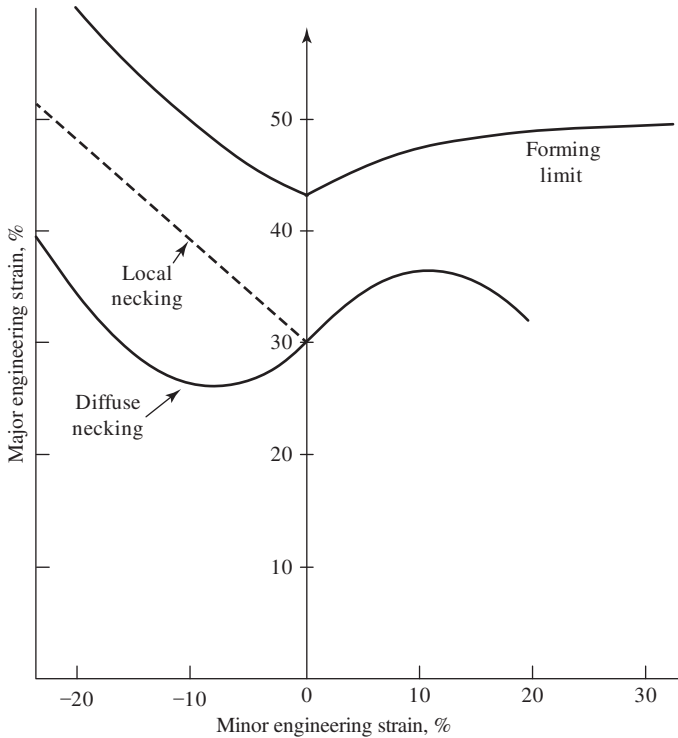


Fig. 7-21. An example of a forming limit diagram for sheet metal. (Adapted from Hosford and Caddell, 10.)

IX. FRACTOGRAPHIC FEATURES ASSOCIATED WITH DUCTILE RUPTURE

As the result of the triaxial state of stress developed in a neck in alloys containing carbides, oxides, and so on, the particles may break or the interface between particle and matrix may separate. By either process, transgranular, noncrystallographic voids are formed within the central portion of the neck. With further deformation these voids grow and link up, thereby reducing the effective cross-sectional area and bringing about final separation. The final overall appearance of the broken tensile bar is usually in the form of a cup and cone, where the central flat portion of the fracture developed by the void linking process, and the outer cone developed by a shearing-off process at the surface where the triaxial stresses were low.

At the microscopic level, these linked-up voids give rise to distinctive fractographic features known as *dimples*. In the flat part of the fracture, these dimples are circular in shape, whereas in the cone portion of the fracture rupture where shearing is dominant, the dimples are elongated. Figures 7-22 and 7-23 provide examples of both types of features. These features are usually of a size that is best examined in a SEM. They are not usually found using optical microscopy.

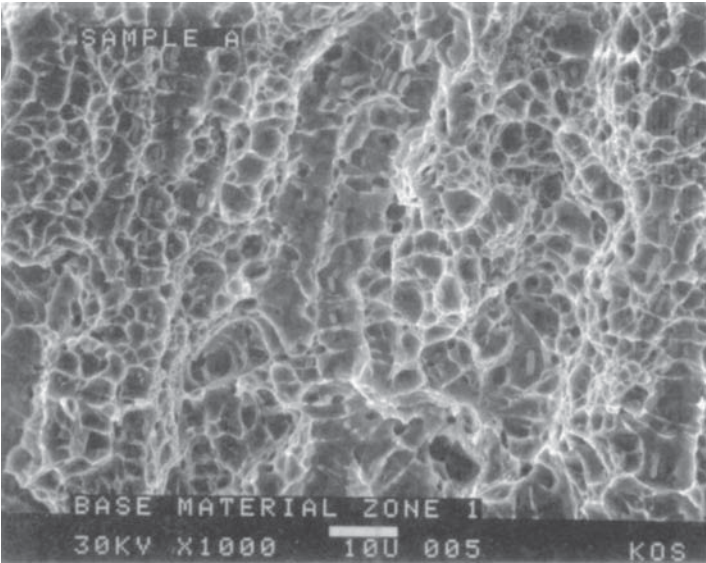


Fig. 7-22. Equiaxed dimples formed during ductile tensile fracture.

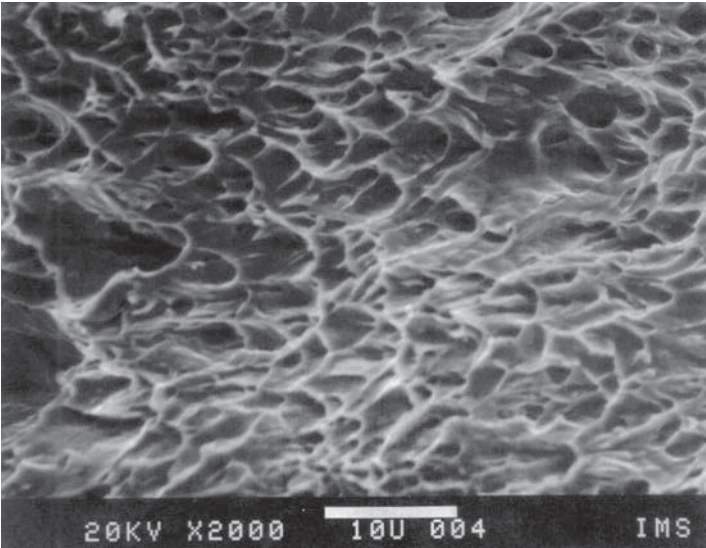


Fig. 7-23. Elongated dimples formed during ductile shear fracture.

Each of these dimples is nucleated at a particle. These fractographic features are always found on the tensile rupture fracture surfaces of face-centered cubic (fcc) alloys—for example, aluminum, copper, and nickel alloys. They are also found on the fracture surfaces of steels that have failed in tension above their ductile-to-brittle transition temperature.

In a copper specimen of normal commercial quality, oxides are dispersed in the copper, and in a tensile test it is at these oxides that the voids are nucleated, dimples form, and a cup-cone type of fracture results. It is of interest that, if copper of exceptionally high purity is tested in tension, the final separation process is quite different. Since there are no particles to nucleate voids upon the onset of necking, the specimen will continue to elongate and neck down to a point much like taffy before finally separating. At sufficiently elevated temperatures, where the flow stress is much less, even copper of commercial purity can behave this way, since the stresses are low, strain hardening is eliminated by dynamic recrystallization, and the triaxial stresses developed during necking are not sufficient to nucleate voids within the necked region.

The fracture toughness of a material is a function of strength, modulus, and elongation to failure. For a very-low-carbon steel alloy, a change from air melting to vacuum melting may have little effect on the strength and modulus, but the elimination of carbides and oxide particles can lead to an increase in ductility, as measure by the percentage of elongation and the percentage of reduction in area, which in turn can improve toughness. This increase in ductility comes about because of the absence of void-nucleating particles.

X. FAILURE IN TORSION

A round bar of a low-carbon steel can be twisted through several revolutions before it fails. When it does fail, the failure is in a plane of maximum shear stress at right angles to the axis of the bar, and there is little reduction in area and little, if any, elongation. On the other hand, when a round bar of brittle material such as gray cast iron is twisted to fracture, the strains involved are much less and the failure is of a helical nature. The fracture plane is at 45° to the axis of the bar, perpendicular to the direction of principal tensile stress. It has been noted that when the hardness of a tool steel is above 720 Vickers Hardness (HV), it behaves more like cast iron and fractures in a helical manner (9).

The cyclic loading of a round bar of a ductile material subjected to fully reversed torsion in the low-cycle regime will also result in a flat fracture that is perpendicular to the bar. However, the fracture surface of the same material that develops in high-cycle fatigue has been described as a “factory roof” because of the zigzag nature of the cracking process as cracks grow under the influence of the principal tensile stress.

XI. CASE STUDY: FAILURE OF A HELICOPTER BOLT (12)

In failure analysis, in order to determine whether or not a component has failed under monotonic or cyclic loading, it is sometimes necessary to develop reference standards for each type of failure, especially when the fracture surface of a part that has failed in service contains features that may be ambiguous in their interpretation. Such is

the case in the present case study, where in order to characterize the fractographic features of an AISI 9310 carburized steel, failures under monotonic and cyclic loading had to be obtained.

The component under investigation was a trunnion bolt, a critical part of a helicopter rotor mechanism. The helicopter had crashed in the ocean, and it was alleged that the bolt had failed due to fatigue, thereby causing the accident. To complicate matters, it was several months before the helicopter was recovered, and during this time some corrosion had occurred. The bolt was made of AISI 9310 steel and had been carburized. Examination of the fracture surface revealed the presence of markings in the case that could be interpreted to be fatigue markings. In addition, an unusual secondary crack was present that ran circumferentially in the case. It was suggested that this secondary crack had developed due to stress corrosion cracking during the time the component was submerged in the ocean. Reference standards such as the *ASM Metals Handbook* volume on fractography did not contain comparable fractographic examples, and it was therefore decided to carry out a set of tests to develop fractographic standards for this carburized steel. Since the fracture had occurred in bending at a reduced section of the bolt, a carburized specimen containing a semicircular notch was tested in four-point bending, as shown in Fig. 7-24. Two types of testing were carried out, monotonic bending to fracture and cyclic fatigue tests to fracture.

Figure 7-25 is a plot of the bending moment versus the deflection of a specimen in a monotonic test to failure. Discontinuities accompanied by loud cracking sounds were observed, which indicated progressive cracking in the case prior to final separation. Similar behavior is observed in tension tests of carburized steel where the case first cracks, with an accompanying loud noise at a load below that required for fracture of the tougher core.

The macroscopic fracture appearance of this specimen is shown in Fig. 7-26. As with the failed helicopter bolt, a circumferential crack in the case can be seen, a direct indication that this crack did not develop because of stress corrosion. It was surmised that the state of triaxial stress at the root of the notch, together with a radial

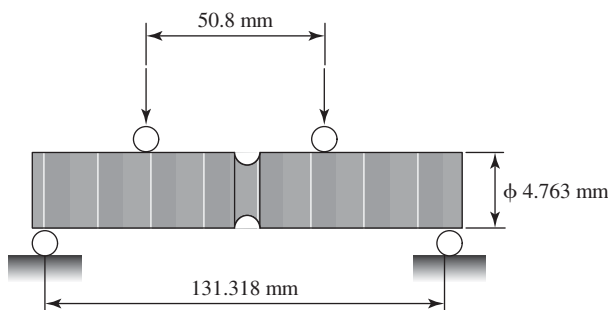


Fig. 7-24. Four-point bend test of a carburized, notched bar simulating the bolt. (After McEvily et al., 12.)

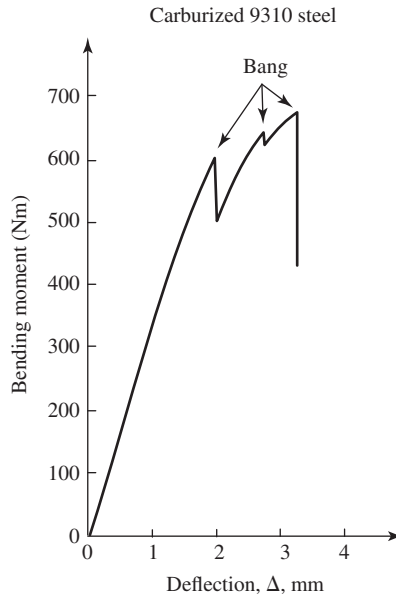


Fig. 7-25. Load-deflection plot of the carburized test specimen. (After McEvily et al., 12.)

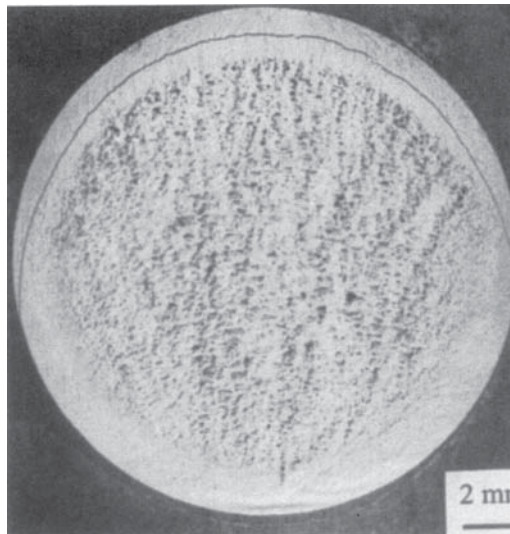


Fig. 7-26. Macroscopic fracture appearance after failure under monotonic loading, 12. (Reprint from Materials Characterization, vol. 36, No. 4/5, A. J. McEvily et al., A Comparison of the Fractographic Features of a Carburized Steel Fracture under Monotonic or Cyclic Loading, pp. 153–158, Copyright 1996, with permission of Elsevier Science.)

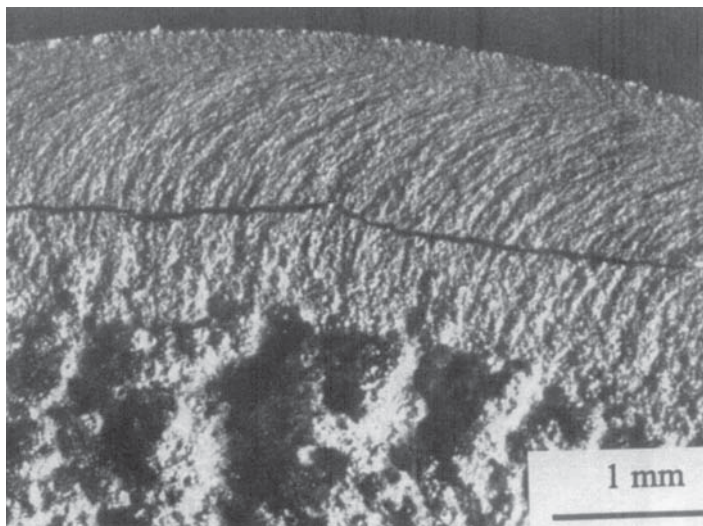


Fig. 7-27. Region of the fracture origin after failure under monotonic loading, 12. (Reprint from Materials Characterization, vol. 36, No. 4/5, A. J. McEvily et al., A Comparison of the Fractographic Features of a Carburized Steel Fracture under Monotonic or Cyclic Loading, pp. 153–158, Copyright 1996, with permission of Elsevier Science.)

tensile stress due to a difference in Poisson ratios between the case and the plastically deforming core, had developed to cause the circumferential crack.

Figure 7-27 shows the appearance of the case at higher magnification. The case contains markings that could be interpreted as being due to fatigue, whereas the fracture is known to be due to monotonic loading. The appearance of the core is shown in Fig. 7-28. Here, dimples representative of ductile overload failure are evident. In addition, manganese sulfide stringers can be seen.

For comparison, Figs. 7-29 and 7-30 show the fracture appearance after fatigue failure. The case is smooth, and markings known as *fatigue striations* can be observed in the core at higher magnification, Fig. 7-31. (Such markings are discussed more fully in Chapter 11.) Note that a secondary crack had developed in the case at the point where the fatigue crack had grown through most of the cross section and the remaining material failed by overload.

On the basis of such information, it was concluded that a fatigue fracture of the trunnion bolt had not occurred. Fracture of the bolt was a consequence of the crash rather than its cause.

XII. SUMMARY

This chapter has focused on the mechanical behavior and fractography of both brittle and ductile materials. A number of case studies have indicated the steps involved

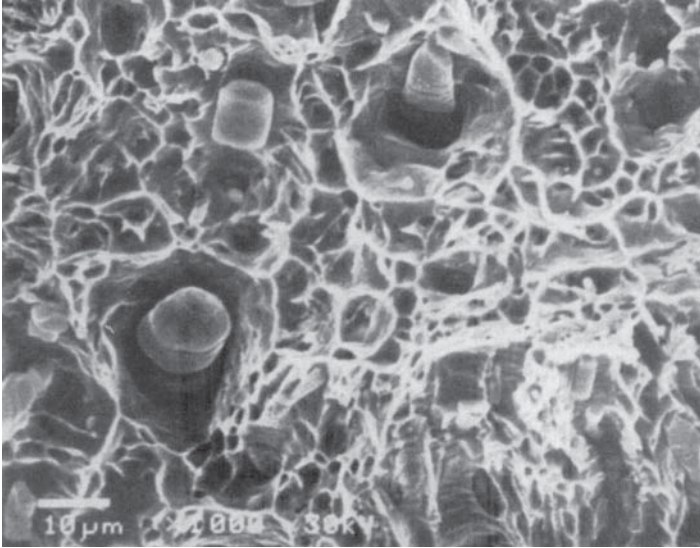


Fig. 7-28. Detail of the fracture surface after monotonic loading showing dimples and manganese sulfide particles in the core, 12. (Reprint from *Materials Characterization*, vol. 36, No. 4/5, A. J. McEvily et al., *A Comparison of the Fractographic Features of a Carburized Steel Fracture under Monotonic or Cyclic Loading*, pp. 153–158, Copyright 1996, with permission of Elsevier Science.)

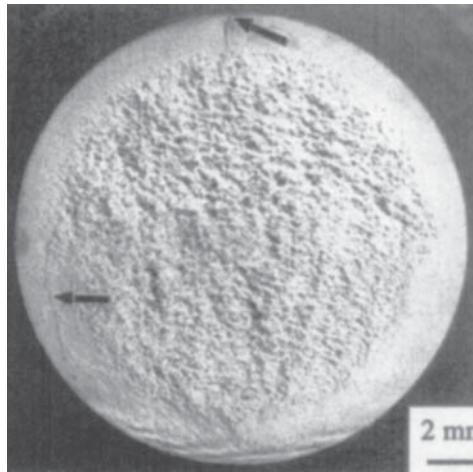


Fig. 7-29. Macroscopic view of the fracture surface after fatigue loading, 12. (Reprint from *Materials Characterization*, vol. 36, No. 4/5, A. J. McEvily et al., *A Comparison of the Fractographic Features of a Carburized Steel Fracture under Monotonic or Cyclic Loading*, pp. 153–158, Copyright 1996, with permission of Elsevier Science.)

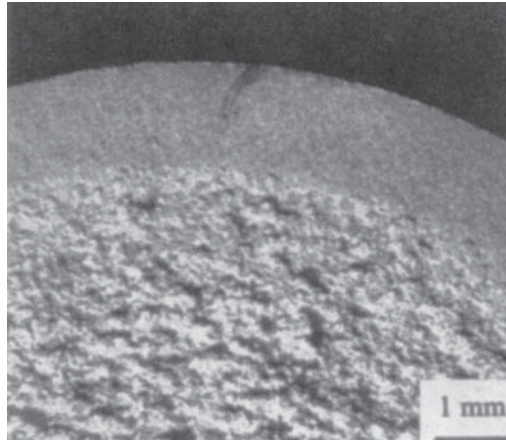


Fig. 7-30. A view of the area of fatigue crack initiation, 12. (Reprint from *Materials Characterization*, vol. 36, No. 4/5, A. J. McEvily et al., *A Comparison of the Fractographic Features of a Carburized Steel Fracture under Monotonic or Cyclic Loading*, pp. 153–158, Copyright 1996, with permission of Elsevier Science.)

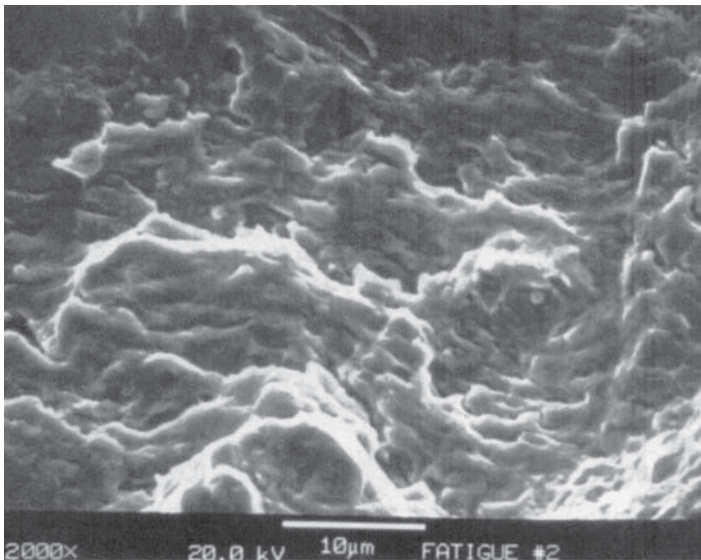


Fig. 7-31. A view of the core area showing fatigue striations, 12. (Reprint from *Materials Characterization*, vol. 36, No. 4/5, A. J. McEvily et al., *A Comparison of the Fractographic Features of a Carburized Steel Fracture under Monotonic or Cyclic Loading*, pp. 153–158, Copyright 1996, with permission of Elsevier Science.)

in carrying out an investigation to ascertain the nature of either brittle or ductile overload failure. In order to establish the type of failure, the failure analyst should be familiar with a wide variety of fractographic features.

REFERENCES

- (1) S. T. Rolfe and J. M. Barsom, *Fracture and Fatigue Control in Structures*, Prentice-Hall, Englewood Cliffs, NJ, 1977.
- (2) A. S. Tetelman and A. J. McEvily, *Fracture of Structural Materials*, Wiley, New York, 1967.
- (3) *Collapse of U.S. 35 Highway Bridge, Point Pleasant, West Virginia, December 15, 1967*, NTSB Report NTSB-HAR-71-1, Washington, DC, 1971.
- (4) M. P. Manahan, C. N. McCowan, T. A. Siewert, J. M. Holt, F. J. Marsh, and E. A. Ruth, Notched Bar Impact Testing Standards Have Yielded Widespread Benefits for Industry, *ASTM Standardization News*, Feb. 1999, pp. 30–35.
- (5) J. R. Low, Jr., “The Relation of Microstructure to Brittle Fracture,” in *Relation of Properties to Microstructure*, ASM, Cleveland, 1953, p. 163.
- (6) T. Foecke, *Metallurgy of the RMS Titanic*, National Institute of Standards and Technology Report NIST-IR 6118, Gaithersburg, MD, 1998.
- (7) G. Wold and J. Skaar, Strain Localization, 515–525, 39th Annual Forum of the American Helicopter Society, St Louis, May 1983.
- (8) P. W. Bridgman, The Stress Distribution in the Neck of a Specimen, *Trans. ASM*, vol. 32, 1944, p. 553–574.
- (9) F. A. McClintock and A. S. Argon, *Mechanical Behavior of Materials*, Addison-Wesley, Reading, MA, 1966.
- (10) W. F. Hosford and R. M. Caddell, *Metal Forming*, 2nd ed., Prentice-Hall, Englewood Cliffs, NJ, 1993.
- (11) G. E. Dieter, Jr., *Mechanical Metallurgy*, McGraw-Hill, New York, 1961.
- (12) A. J. McEvily, K. Pohl, and P. Mayr, A Comparison of the Fractographic Features of a Carburized Steel Fractured under Monotonic or Cyclic Loading, *Mater. Char.*, vol. 36, no. 4/5, 1996, pp. 153–158.
- (13) P. E. Bennett and G. M. Sinclair, Parameter Representation of Low Temperature Yield Behavior of Body-Centered-Cubic Transition Metals, *Trans. ASME, J. Basic Eng., Series D*, vol. 88, 1966, pp. 515–525.
- (14) K. W. Burns and F. B. Pickering, *J. Iron Steel Inst.*, vol. 202, 1964, p. 899.

PROBLEMS

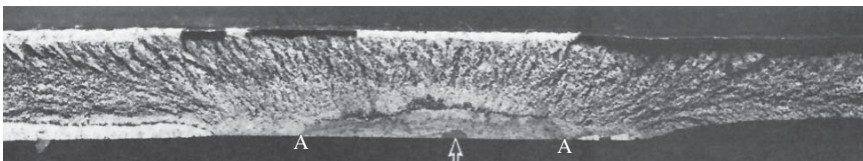
- 7-1.** In Fig. 7-8, suppose that the strain rate is fixed at 10^{-4} /sec. Assume a local fracture stress for ABS-C steel of 1,380 MPa (200 ksi). What is the highest temperature at which fracture will occur in a brittle manner for a Charpy V-notch specimen of this steel at the same strain rate according to the von Mises criterion?

- 7-2. The strength of a low-carbon steel is 622 MPa (90 ksi) for ASTM grain size #2 and 663 MPa (96 ksi) for ASTM grain size #8. What will the strength be for ASTM grain size #10? (Assume that the grains have a square shape.)
- 7-3. Plot the value of the hydrostatic stress in the neck of a tensile bar in terms of $\bar{\sigma}$ as a function of r/a for values of a/R of 1/3, 1, and 2.
- 7-4. For a given alloy, the condition for necking $\frac{d\sigma}{d\varepsilon} = \sigma$ is met at a true stress of 350 MPa (50.7 ksi) and a true strain of 0.50.
- Determine the corresponding values for the ultimate tensile strength and the engineering strain at necking.
 - What is the work per unit of volume required to strain this alloy to the point of necking, assuming that $\sigma = k\varepsilon^n$?
- 7-5. In a tensile test, what is the effect of the gauge length on the calculated strain
- before necking?
 - after necking?
- 7-6. The stress concentration factor (based on net section stress), K_T , for the notched-round bar in bending shown in Fig. 7-24 is given as

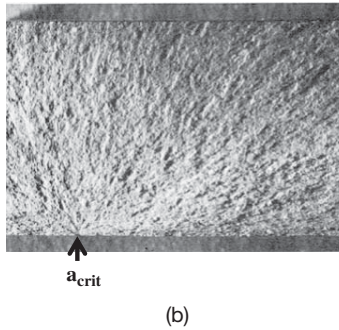
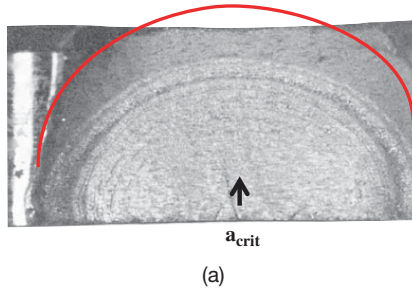
$$K_T = 3.04 - 7.236 \left(\frac{2h}{D} \right) + 9.375 \left(\frac{2h}{D} \right)^2 - 4.179 \left(\frac{2h}{D} \right)^3$$

where h is the notch depth, 3.175 mm, and D is the diameter of the bar. Determine K_T for this bar.

- 7-7. The figure below shows the cross-sectional image of the wall of a failed rocket-motor case.
- Based on the characteristics of fracture morphology, identify the crack initiation site.
 - Provide a brief explanation of the reasoning you used to identify the crack initiation site.
 - Show the boundary between the stable and unstable crack propagation regions on the image below. (You can draw the boundary directly on the image.)
 - Estimate the tensile stress that results in unstable crack propagation.
- Hint: The formula of the stress intensity factor, K , for a semielliptical surface crack in a plate can be utilized for this estimation.



- 7-8.** Below are shown the fracture surfaces of two metallic components. Discuss the possible differences between these two components in terms of (a) the magnitude of the stress and (b) the strength and fracture toughness of the material.



- 7-9.** Below is shown the fracture surface of a failed rocket-motor case. It is found that dark regions A and B are covered with oxides.
- Identify the crack initiation site(s) for the brittle fracture. Justify your answer based on the fracture morphology.
 - Use the fracture mechanics formula to estimate the final fracture stress. Assume that the material has a fracture toughness of $50 \text{ MPa}\cdot\text{m}^{1/2}$.
 - One of the possible causes for brittle fracture is the presence of quench cracks. What would you do and what evidence would you provide to prove that this is indeed the case? (Remember, this is a real-world problem; thus, you can use any resources and tools to prove the cause of the failure.)



- 7-10.** For a bridge steel, an empirical relationship was used to relate K_{IC} and the Charpy V-notch impact energy. This relation is shown below. At a given

temperature in the ductile-to-brittle transition region the Charpy V-notch energy value was 30 J/m^2 .

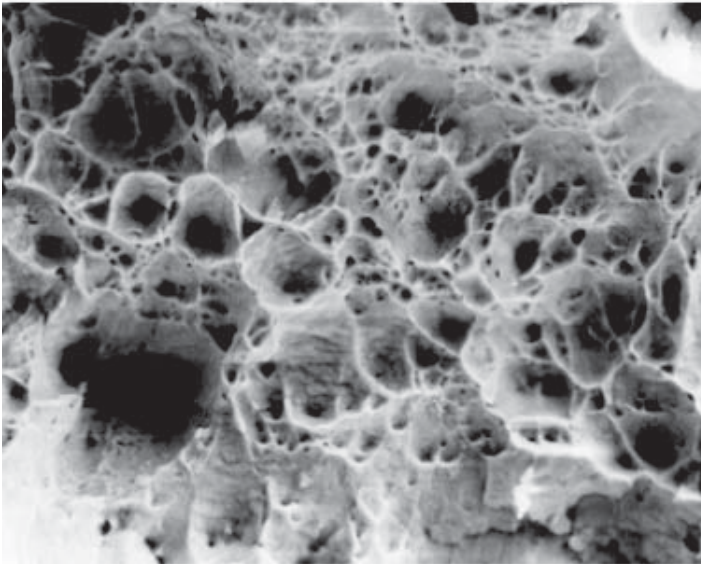
$$\frac{K_{IC}^2}{E} = 655 \text{ CVN}$$

where K_{IC} , E , and Charpy V-notch energy are in units of $\text{Pa}\cdot\text{m}^{1/2}$, Pa, and J/m^2 , respectively. E is the elastic modulus of the steel.

Compute the fracture toughness of the steel at this temperature.

7-11. The fractographs shown below were obtained from Charpy V-notch specimens. Unfortunately, the pictures were not labeled, so we do not know from what conditions and what materials they were obtained. Nevertheless, some conclusions can be drawn based on the fractographs.

- (a) If the two specimens are from the same material, will this material exhibit a ductile-to-brittle transition? Why?
- (b) If photograph (a) is representative of the fracture surface of Material X at all temperatures, what type of material is it likely to be in terms of crystal structure and yield strength?
- (c) If photograph (b) is representative of the fracture surface of Material Y at all temperatures, what type of material is it likely to be in terms of crystal structure and yield strength?
- (d) If photographs (a) and (b) are present in one Charpy V-notch specimen, at what locations would you be likely to find them?



(a)



(b)

8

Thermal and Residual Stresses

I. INTRODUCTION

Thermal stresses arise in components that are subject to temperature gradients, and the thermal transients associated with engine operations are of particular concern. Residual stresses arise because of nonuniform plastic deformation. They are important because they affect resistance to fatigue and stress corrosion cracking, and also can cause distortion during machining and heat treating. This chapter briefly reviews how these types of stress are developed.

II. THERMAL STRESSES, THERMAL STRAIN, AND THERMAL SHOCK

A. Thermal Stresses

Consider the bimetallic strip shown in Fig. 8-1. In order to avoid bending during heating, equal amounts of material 1 are placed on either side of material 2. The initial length of the strip is L_0 ; the area of material 1 is designated as A_1 and that of material 2 as A_2 . The corresponding coefficients of expansion are α_1 and α_2 .

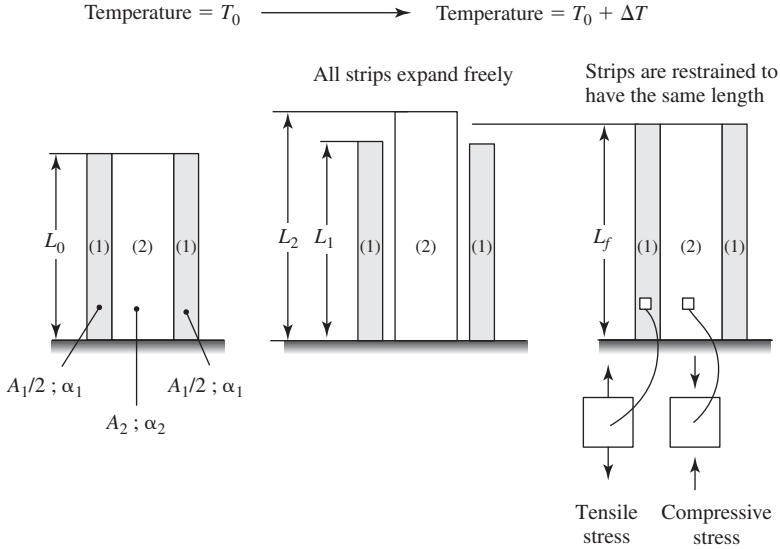


Fig. 8-1. A bimetallic strip.

If the strips were free to expand due to a temperature change of ΔT , the lengths of each material would be

$$L_1 = L_0(1 + \alpha_1 \Delta T) \quad (8-1)$$

$$L_2 = L_0(1 + \alpha_2 \Delta T) \quad (8-2)$$

But the final lengths must be equal, or $L_{1f} = L_{2f}$, or

$$L_0(1 + \alpha_1 \Delta T) + \frac{\sigma_1}{E_1} L_0 = L_0(1 + \alpha_2 \Delta T) + \frac{\sigma_2}{E_2} L_0 \quad (8-3)$$

Also, for equilibrium, $P_1 + P_2 = 0$ or $\sigma_1 A_1 + \sigma_2 A_2 = 0$.

There are thus two equations with two unknowns, and the stresses σ_1 and σ_2 can therefore be determined:

$$\sigma_2 = \frac{(\alpha_1 - \alpha_2) \Delta T E_1 E_2}{E_1 + E_2 (A_2/A_1)} = \frac{(\alpha_1 - \alpha_2) \Delta T E_2}{1 + (E_2/E_1)(A_2/A_1)} \quad (8-4)$$

$$\sigma_1 = -\sigma_2 \frac{A_2}{A_1} \quad (8-5)$$

As long as the stresses are in the elastic range, there will be no residual effects when the temperature returns to its initial value, and the above equations hold. However, if the stresses exceed the yield strength of the materials involved, a state of residual stress will develop when the temperature returns to its initial value. For

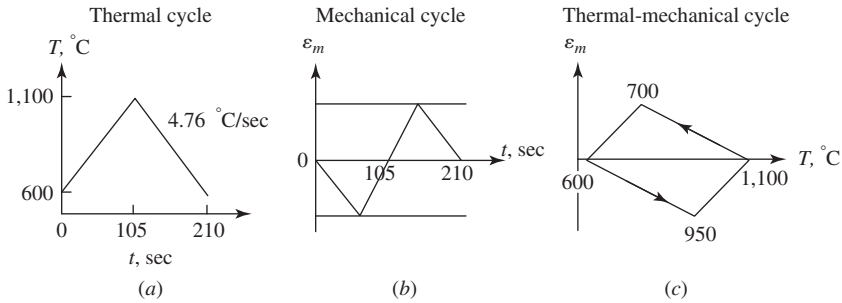


Fig. 8-2. Thermal-mechanical cycle. (a) Temperature versus time. (b) Strain versus time. (c) Thermal-mechanical hysteresis loop. (After Remy, 1.)

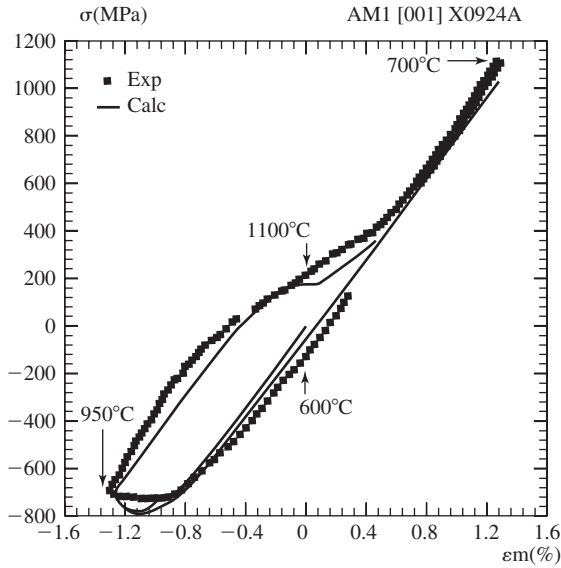
example, if material 2 in the above example had a lower coefficient of expansion and a relatively low yield stress, it could undergo plastic extension as the temperature increased. Subsequently, when the temperature was lowered, material 2 would be left in a state of residual compression, and material 1 would be in residual tension.

B. Thermal-Mechanical Cyclic Strains

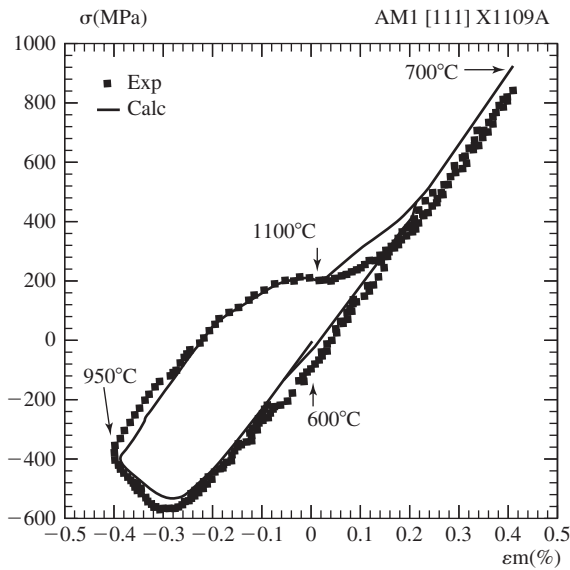
Transient thermal strains of a cyclic nature can arise in jet engine components such as disks, blades, and vanes. Figure 8-2 shows a simplified thermal-mechanical cycle for blades in a gas turbine (1). Under cruise conditions, the blades are at 600°C ($1,112^{\circ}\text{F}$). When engine power is increased, the surface temperature rises to $1,100^{\circ}\text{C}$ ($2,012^{\circ}\text{F}$) in 105 seconds, Fig. 8-2a. Engine power is then returned to the cruise condition, and the temperature falls to 600°C ($1,112^{\circ}\text{F}$) in another 105 seconds. The rate of heating and cooling is 4.76°C/sec (8.57°F/sec). The total strain is the sum of the strain due to thermal expansion plus the strain due to the thermal stresses developed. The mechanical strain versus time plot, shown in Fig. 8-2b, includes both elastic and plastic strains. On heating, the outer surface initially goes into compressive strain, but then the strain reduces to zero as the interior of the blade heats up. On cooling, the reverse procedure occurs. Figure 8-2c shows the counterclockwise diamond cycle that is the thermal-mechanical hysteresis loop for this transient thermal history. The corresponding stress versus mechanical strain hysteresis loops for single crystals in the [001] and [111] orientations are shown in Fig. 8-3. It is noted that the mean stress for the cycle is close to zero. For the [001] orientation, plastic deformation (or viscoplastic deformation) is pronounced at a strain of -0.8 . For the [111] orientation, plastic deformation begins at a strain of -0.25 . Such thermal mechanical histories are complex, but they are also obviously important in assessing the fatigue life of such components.

C. Thermal Shock

Thermal shock denotes the rapid development of a steep temperature gradient and accompanying high stresses that can result in the fracture of brittle materials. It can occur either on heating or cooling. For example, the sudden shutdown of turbine



(a)



(b)

Fig. 8-3. (a, b) Stress versus mechanical strain hysteresis loops for [001] and [111] thermal mechanical fatigue single-crystal specimens of AM1 superalloy using the cycle depicted in Fig. 8-2. Comparison between a viscoplastic model (solid line) and an experiment (symbols). (After Remy, 1. Reprinted from *Low Cycle Fatigue and Elastic-Plastic Behaviour of Materials*, edited by K.-T. Rie and P. D. Portella, pp. 119–130. Copyright 1998, with permission of Elsevier Science.)

engine can result in cracking of protective platinum-aluminide coatings due to the tensile stresses that develop as the surface cools and tries to shrink but is restrained by the interior.

An example of thermal shock that occurs during heating is as follows.

Consider a glass bowl whose thermal conductivity is low.

1. A hot liquid is poured into the bowl.
2. The inside surface of the wall tries to expand because of the sudden rise in temperature.
3. A biaxial compressive stress develops on the inside surface because expansion is resisted by the surrounding, still cool, wall material.
4. This compressive stress system sets up a balancing tensile stress system in the outer, still cool, portion of the wall.
5. Fracture can initiate in the outer region if the magnitude of the tensile stress developed is sufficient to nucleate a crack at a weak point.

III. RESIDUAL STRESSES CAUSED BY NONUNIFORM PLASTIC DEFORMATION

Residual stresses arise because of a gradient in plastic deformation caused either by mechanical deformation or by a thermal gradient caused during cooling of a metal or alloy from a high temperature to a low temperature. The sign of the residual stress is always opposite to the sign of the applied stress that gave rise to the residual stress. Residual stresses are important in fatigue and stress corrosion cracking, where they can be either beneficial or detrimental. If residual stresses are present prior to heat treatment or machining, they can be detrimental, because they can result in distortion (warping).

A. An Example of Mechanically Induced Residual Stresses: Springback After Bending into the Plastic Range (2)

In sheet bending (Fig. 8-4), the width w is much greater than the thickness t , and width changes are negligible. Therefore, bending can be considered to be a plane-strain operation with $\varepsilon_y = 0$, $\varepsilon_z = -\varepsilon_x$. Let z be the distance measured from the midplane of the sheet in the thickness direction, and let r be the radius of curvature of the midplane. The value of ε_x varies linearly from $-t/2R$ at the inside of the bend ($z = -t/2$) to zero at the midplane ($z = 0$) to $+t/2R$ at the outside of the bend ($z = t/2$).

Figure 8-5 shows the stress through the cross section. The principle of superposition is used to show that unloading can be considered to be the reverse of loading, so that for purely elastic bending there is no residual stress after unloading.

Next, assume that the material is elastic ideally plastic, that is, there is no strain hardening in the plastic range. If the tensile yield stress is σ_Y , the flow stress in plane strain σ_0 will be $1.15 \sigma_Y$. Figure 8-6a shows the stress distribution throughout the

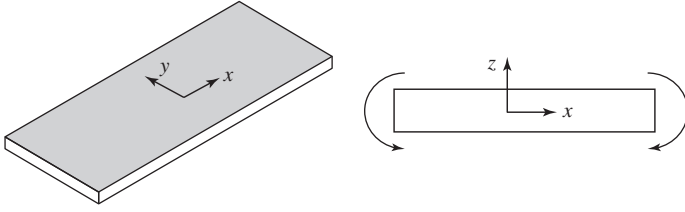


Fig. 8-4. Sheet bending.

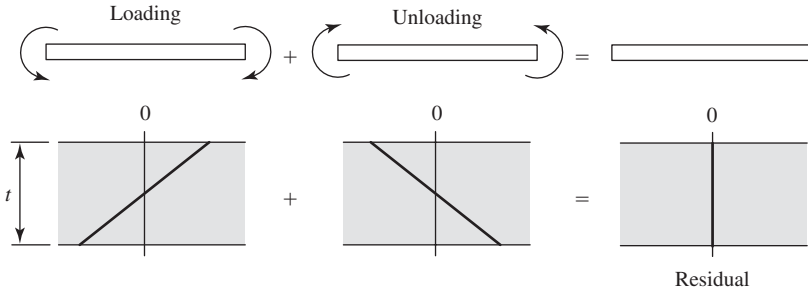


Fig. 8-5. Strip bending, elastic strains.

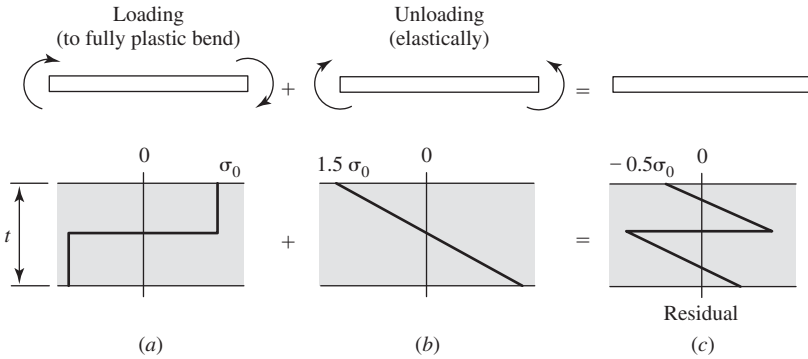


Fig. 8-6. (a) Strip bending, (b) plastic strains on loading, (c) elastic on unloading.

sheet for fully plastic behavior. Except for an elastic core at midplane (which will be neglected), the entire section will be at a stress, $\sigma_x = \pm\sigma_0$.

To calculate the bending moment M needed to create this fully plastic bend, note that $dF_x = \sigma_x w dz$ and $dM = z dF_x = z \sigma_x w dz$. Therefore, the fully plastic bending moment is

$$M = \int_{-t/2}^{+t/2} w \sigma_x z dz = 2 \int_0^{t/2} w \sigma_0 z dz = w \sigma_0 \frac{t^2}{4} \quad (8-6)$$

(Note that the elastic bending moment needed to have σ_x just equal to σ_0 would be $w\sigma_0 t^2/6$ so that the fully plastic bending moment is 50% higher.)

When the external moment is released, the internal moment must go to zero. As the material springs back elastically, the internal residual stress distribution must result in a zero bending moment (Fig. 8-6*b*). Since the unloading is elastic,

$$\Delta\sigma_x = \frac{E}{1 - \nu^2} \Delta\varepsilon_x = E' \Delta\varepsilon_x \quad (8-7)$$

The change in strain is given as $\Delta\varepsilon_x = z/r - z/r'$, where r' is the radius of curvature after springback. This causes a change in bending moment ΔM , where

$$\begin{aligned} \Delta M &= 2w \int_0^{t/2} \Delta\sigma_x z \, dz \\ &= 2w \int_0^{t/2} E' \left(\frac{1}{r} - \frac{1}{r'} \right) z^2 dz. \\ \Delta M &= \frac{wE't^3}{12} \left(\frac{1}{r} - \frac{1}{r'} \right) \end{aligned} \quad (8-8)$$

$M - \Delta M = 0$ after springback, and therefore equating M and ΔM gives

$$\frac{w\sigma_0 t^2}{4} = \frac{wE't^3}{12} \left(\frac{1}{r} - \frac{1}{r'} \right) \quad (8-9)$$

or

$$\left(\frac{1}{r} - \frac{1}{r'} \right) = \frac{3\sigma_0}{tE'} \quad (8-10)$$

The resulting residual stress

$$\begin{aligned} \sigma'_x &= \sigma_x - \Delta\sigma_x \\ &= \sigma_0 - E' \Delta\varepsilon_x \\ &= \sigma_0 - E' z \left(\frac{1}{r} - \frac{1}{r'} \right) \\ &= \sigma_0 - E' z \left(\frac{3\sigma_0}{tE'} \right) \\ \sigma'_x &= \sigma_0 \left(1 - \frac{3z}{t} \right) \end{aligned} \quad (8-11)$$

On the outside surface, $z = t/2$, and the residual stress σ'_x equals $-\sigma_0/2$. On the inside surface, the residual stress is $+\sigma_0/2$. The distribution of stresses is shown in Fig. 8-6*c*.

Note that the sign of the residual stress at the surface is opposite to the sign of the stress that caused it. Also, plastic deformation is required, but the plastic deformation must be nonuniform. There is no residual stress associated with a tensile bar that has been uniformly stretched into the plastic region. On the other hand, residual stresses will develop at notches, and so on, if the material at the base of the notch is strained into the plastic range while the surroundings remain elastic.

An important state of residual stress is that formed at the tip of a notch in a component that has been loaded in tension and then unloaded. Under load, the stress at the notch tip is higher than elsewhere and there is a sharp stress gradient. If the peak stress at the notch is lower than the yield strength of the material, upon unloading no residual stress will form. However, a more interesting situation is that in which the applied tensile stress is high enough to develop a plastic zone at the notch tip, for in this case a residual compressive stress will develop upon unloading. Why does this residual stress develop?

When the plastic zone at the notch forms, there is a large increase in tensile strain at the notch root as compared to purely elastic loading. In order to accommodate this large local tensile strain, additional material is needed. This material is provided by the formation of a concave dimple in the plastic zone at the crack tip and the transport of material in the z -direction of the specimen. Note that there is a plane-stress operation at the surface of the component in which the volume of material is constant. Upon unloading, because there is now extra material in the subsurface region, a compressive residual stress is developed at the notch tip. If the component had been loaded in compression high enough to form a plastic zone at the notch tip, then the material in the plastic zone would have bulged outward from the component's surface, thereby lessening the amount of material in the subsurface layers. Upon unloading, because there is now less material in the subsurface region, a tensile stress would be developed at the notch tip. To sum up, in order for a residual stress to develop, there must be plastic deformation as well as a stress gradient. Further, the sign of the residual stress is always opposite to the sign of the stress in the loading phase.

Surface compressive residual stresses are beneficial in fatigue and in stress corrosion cracking. For example, they are often deliberately introduced by a process known as *shot peening*, which develops a biaxial compressive residual stress in the surface. The fatigue crack growth rate of any fatigue crack that might form would be retarded because of this compressive residual stress field.

An important state of residual stress is that formed at the tip of a growing fatigue crack due to an overload in plane specimens. During fatigue crack growth, if a 100% overload is applied, the fatigue crack will subsequently undergo a period of reduced rate of crack growth as the crack penetrates the plastic zone created by the overload. This slowdown is related to an increased level of compressive residual stress brought about by the overload. This residual stress is largely a plane stress in the surface regions, and is brought about by the lateral contraction of material at the surface that occurs in the overload plastic zone. In ductile materials, this lateral contraction leads to the formation of an obvious dimple immediately ahead of the crack tip. The compressive stress develops as the load is reduced from the overload level, and for

now, because of the lateral contraction, there is more material in planes parallel to and just below the surface of the overload plastic zone than before the overload. As the crack grows through the overload zone, these residual stresses are released, giving rise to an increased level of crack closure in the wake of the crack tip (see Chapter 10), which results in a slowdown of the rate of fatigue crack propagation. The extent of the slowdown in crack rate is a function of the overload level and the thickness of the specimen, being much more pronounced in thin compared to thick specimens. The reason for this difference is that, in thick specimens, plane-strain conditions prevail throughout most of the specimen's thickness, and the lateral contraction associated with plane stress is absent under plane-strain conditions. Hence, the level of enhanced residual compressive stress due to an overload is much less in thick compared to thin specimens.

B. Case Study: Shaft of a Golf Club

At a golf driving range in Connecticut the shafts (tapered hollow tubes) of the clubs were sometimes bent or otherwise damaged in use and had to be replaced. A supply of replacement shafts was kept in a storage shed, which at times was damp and humid. The shafts were made of a low-alloy steel that had been chrome plated, which protected the exterior of the shaft from corrosion. Whereas new shafts were sealed to the club head as well as at the grip end, and thereby were protected from corrosion on the inside of the shaft, the replacement shafts were not sealed; as a result, the interiors of these replacement shafts underwent corrosion over a period of time.

A golfer was driving balls with a club whose shaft was a replacement. As he struck a ball, the shaft fractured and the end he was holding struck him in the eye. Fortunately, the damage to his eye was not serious, and he recovered completely.

Upon examination of the shaft, it was noted that the fracture origin was at a small dent in the shaft that existed before the accident. The fracture had initiated at this dent on the inside of the shaft. The fracture origin shown in Fig. 8-7 was more planar and brittle in appearance than was the fracture away from the origin, shown in Fig. 8-8, which exhibited the dimples characteristic of ductile fracture. It was concluded that the fracture was due to hydrogen embrittlement, which was associated with corrosion and the seemingly innocuous dent that, because of springback, resulted in a residual tensile stress on the inside of the shaft at the periphery of the dent. When the dent was formed, material on the inside near the periphery of the dent went into compression and material near the center of the dent went into tension. Upon springback, the signs of the stresses were reversed and a residual tensile stress was left on the inside surface at the periphery of the dent.

IV. RESIDUAL STRESSES DUE TO QUENCHING

On cooling a metal part from an elevated temperature, residual stresses may be developed. For example, if a massive piece of copper is cooled rapidly, the surface layers will cool before the interior, thus setting up tensile strains and stresses in the

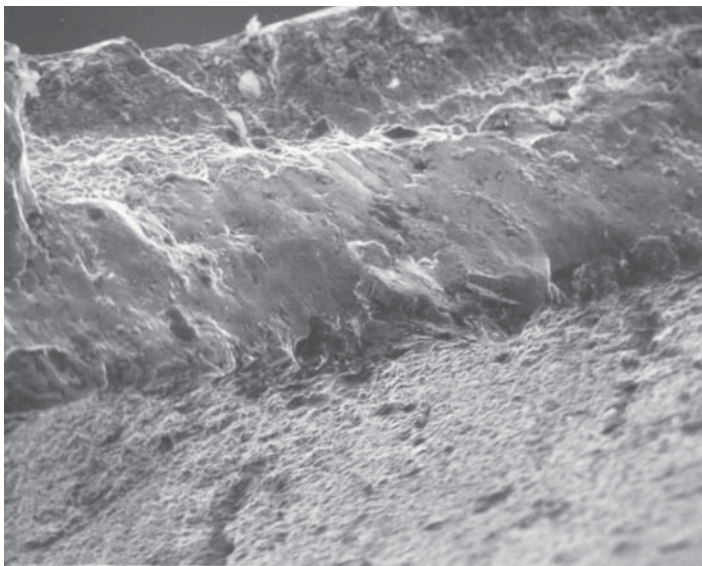


Fig. 8-7. Macroscopic view of the area of the fracture origin in a failed golf shaft. The rough area at the bottom is the corroded inside surface of the shaft. (Reprinted from *Materials Characterization*, Vol. 26, A.J. McEvily and I. LeMay, pp. 253–268, Copyright 1991, with permission of Elsevier Science.)

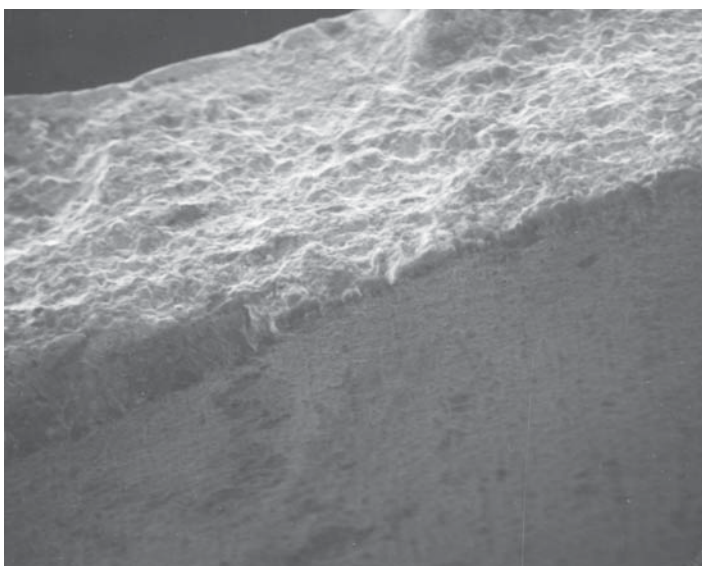


Fig. 8-8. Macroscopic view of the fracture surface away from the fracture origin in a failed golf shaft. (Reprinted from *Materials Characterization*, Vol. 26, A.J. McEvily and I. LeMay, pp. 253–268, Copyright 1991, with permission of Elsevier Science.)

surface that are counterbalanced by compressive stresses in the interior. At elevated temperatures, these tensile and compressive stresses are relaxed due to the low yield strength of the material. However, at a later point in the cooling process, the already cooled surface layer will be subjected to compression as the interior finally cools and shrinks. In general, the resultant compressive stress in the surface layers is beneficial, except when machining follows and distortion results from the nonuniform removal of the surface.

When steel is quenched to form martensite at a low temperature, the transformation from austenite to martensite is associated with a volume expansion of the order of 1–3%. At the surface, this initially results in a compressive stress, as in the case of copper, but when the underlying layer finally cools and expands, the surface is put into tension. These tensile stresses can be reduced by using a steel of lower hardenability so that the interior does not go through a martensitic transformation, but instead transforms to bainite at a higher temperature.

A. Quench Cracking

In a steel, there is always the possibility of immediate quench cracking due to the level of tensile residual stresses developed when untempered martensite is formed. However, cold cracking (or delayed cracking) is the more probable event; for this reason, alloy steel parts that have been quenched are quickly transferred to tempering furnaces or salt baths in order to minimize the time available for cold cracking to develop. If cracks develop on quenching into water and the part is then transferred to a salt bath for tempering, an explosive reaction can occur as the water trapped in the cracks transforms into steam. Therefore, personnel carrying out this operation need to wear protective face masks and protective clothing.

It is also possible to develop quench cracks above the quench temperature if, during the quench of a material with low ductility, the tensile surface stresses that develop due to the temperature gradient in the material exceed the resistance to cracking of the material, as indicated in Fig. 8-9.

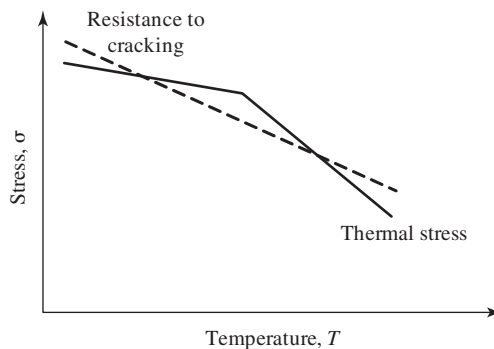


Fig. 8-9. A schematic of thermal stress versus resistance to cracking as a function of temperature.

To avoid the development of residual stresses, heat-treating procedures are used that minimize the temperature gradients responsible for the residual stresses. Such methods are:

- (a) *Martempering*: The steel is rapidly cooled to a temperature above M_s and held to allow a uniform temperature to develop before further cooling to martensite (Fig. 8-10a).
- (b) *Austempering*: The steel is rapidly cooled to a temperature above M_s and held there until the transformation to bainite is complete before further slow cooling to room temperature (Fig. 8-10b).

V. RESIDUAL STRESS TOUGHENING

If the outer surface of the bowl discussed in Section II on thermal shock had been treated to have a residual compressive stress in the surface region, the resistance to thermal shock would have increased. Glass can be toughened by diffusing large atoms into the surface to develop residual compressive stresses on cooling as, for example, in Corningware. Tempered glass is created by cooling rapidly from an elevated temperature to develop compressive surface residual stresses, much as in the case of a block of copper. This type of glass is used in the side windows of automobiles. When such glass breaks, it fractures into many small fragments. However, the glass used in windshields is not tempered. A windshield consists of a sandwich of two sheets of glass between which is bonded a sheet of plastic. In a crash, the windshield is intended to be flexible enough to reduce head injuries but resistant enough to overall fracture to prevent front seat occupants from being ejected through the windshield. In this case, the glass generally breaks into large shards that remain attached to the plastic membrane.

VI. RESIDUAL STRESSES RESULTING FROM CARBURIZING, NITRIDING, AND INDUCTION HARDENING

A. Carburizing

Carburizing is carried out in the austenitic range and can lead to the development of a compressive residual stress at the surface in a low-alloy steel during quenching for the following reason (3, 4). Carbon is one of the elements that depresses the M_s temperature of a steel. The M_s temperature of the carburized surface layer, therefore, can be much lower than that of the interior because of the differential in carbon contents. On quenching, the interior, even though it is at a higher temperature than the surface, is the first to transform due to its higher M_s temperature. Later on, the surface transforms and tries to expand, but it is now restrained by the already transformed interior. As a result, the surface is left in a state of residual compression, as indicated in Fig. 8-11.

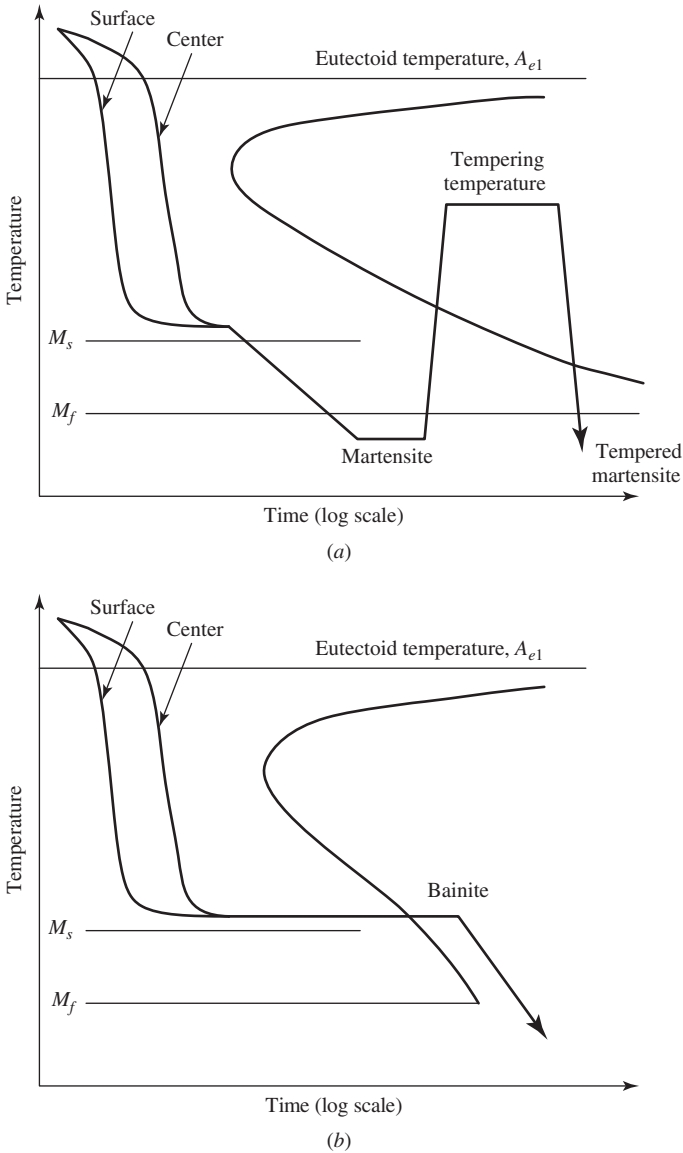


Fig. 8-10. Cooling curve. (a) Martempering. (b) Austempering.

B. Nitriding

Nitriding is carried out at an elevated temperature below the eutectoid temperature for time periods of the order of 9–24 hours, and during the nitriding process any prior residual stresses are relaxed. The purpose of nitriding is to improve the surface wear and fatigue properties. Since the temperatures are lower than those in carburizing and no phase transformation is involved, problems with distortion are minimized,

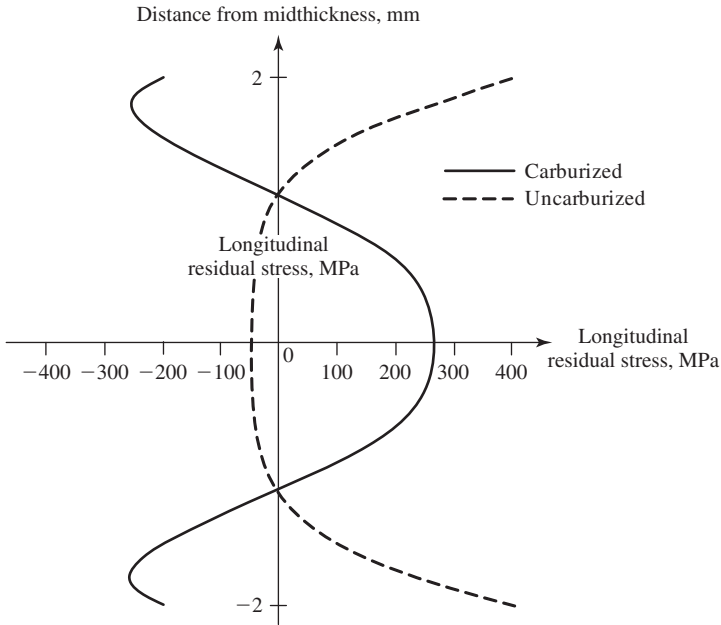


Fig. 8-11. Effect of carburization on the residual stresses in a quenched and tempered (1 hour at 180–200°C) (356–392°F) 0.93 Cr-0.26 C steel. (After Ebert, 3, and Krauss, 4).

an important consideration when heat treating carefully machined parts such as crankshafts. The formation of nitrides leads to a beneficial compressive residual stress in the surface even after the usual slow cooling because of a lower coefficient of expansion of the nitrides.

C. Induction Hardening

Induction hardening is a surface-hardening process in which only the surface layer of a suitable ferrous workpiece is heated by electrical induction to above the transformation temperature and immediately quenched. Compressive residual stresses develop as the surface layers transform from austenite on quenching.

VII. RESIDUAL STRESSES DEVELOPED IN WELDING

In welding operations, the parts being joined often provide a large heat sink, and therefore cooling rates are rapid. As a result, untempered martensite may form in a residual tensile stress field and lead to weld cracking, either through cold cracking or quench cracking. The susceptibility to weld cracking increases as the number of unfavorable welding conditions increases. For example, a medium-carbon steel welded with an electrode not of the low-hydrogen type, and without preheat or postheat, may perform satisfactorily even though there may be a HAZ containing a region of martensite about 1.6 mm (1/16 in.) thick if joint restraint is low and cyclic

loading in service is limited. However, if the section thickness is doubled, the level of residual stress rises due to greater constraint, and the thickness of the martensitic zone is increased due to a higher cooling rate, and cracking may develop. Even the use of low-hydrogen electrodes may not prevent cracking of the thicker section, but the use of a 315°C (600°F) preheat will prevent cracking by retarding the rate of cooling, thereby reducing the level of the residual stresses and the amount of martensite formed.

On cooling below the M_s temperature, two forms of martensite can form, depending upon the carbon content. In low-carbon steels, the martensite is made up of laths that contain a high density of dislocations. In higher-carbon steel, the martensite is made up of plates that also contain a high dislocation content but, in addition, may be twinned. Preheating is used to reduce the cooling rate in order to minimize the likelihood of the formation of brittle martensite, particularly twinned martensite. The preheat temperature increases with carbon content and with the thickness of the plates being welded, with recommended preheat temperatures ranging from 38°C (100°F) for a 0.2 wt % C steel up to 315°C (600°F) for a 0.6 wt % C steel.

Postweld heating of a weldment serves two purposes. One is to relieve the residual stresses that may have been developed during the welding process. The second is to temper both the weld deposit and HAZ to improve their fracture toughness. It is now mandatory that weldments in all nuclear components and in most pressure vessels be postweld heat treated (PWHT). These postweld heat treatments are carried out at a temperature of the order of 650°C (1,200°F) for 1 hour.

The residual stresses that are developed both parallel to and transverse to a butt weld due to shrinkage of the weld metal on cooling are shown in Fig. 8-12 (5) To minimize distortion, weld passes were made from each edge of the plate toward the center, which accounts for the transverse residual stress distribution, since the last weld metal to solidify was in the central region of the butt weld. The residual stress developed during welding can sometimes be beneficial. For example, the fatigue strength of steel lap-welded joints for automotive use was improved by

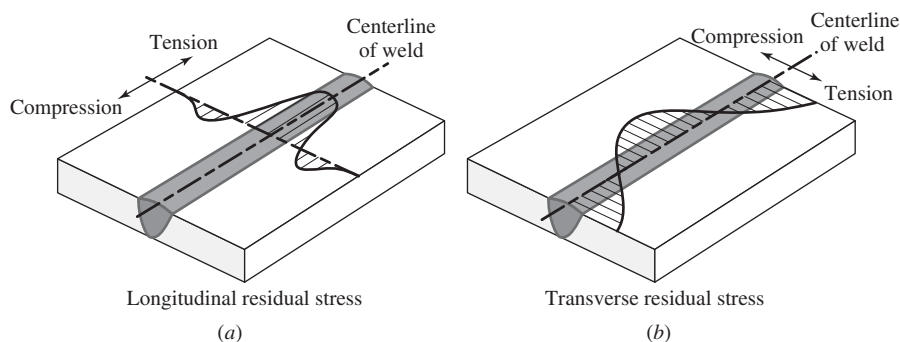


Fig. 8-12. Residual stress developed at a butt weld. (a) Longitudinal direction. (b) Transverse direction. (After Gurney, 5.)

using low transformation temperature (M_s 200°C [392°F] M_f 20°C [68°F]) welding wire (10Cr-10Ni), which induced compressive residual stresses in the surface layers. The fatigue strength at 10^8 cycles was increased from 300 MPa to 450 MPa by this procedure (6).

VIII. MEASUREMENT OF RESIDUAL STRESSES

The two main methods for the determination of the magnitude of residual stress, the X-ray method and the metal removal method, were described in Chapter 6. Another example of the metal removal method is known as the *boring-out method*. This method can be used to determine residual stress levels in cannon or other cylindrical bodies. In the case of a cannon barrel, as a last step in the manufacturing process, a pressure is developed within the barrel of sufficient magnitude to expand the interior of the barrel into the plastic range. When the pressure is removed, a beneficial state of residual compressive stress is developed on the inner surface, a process known as *autofrettage*. Determination of the magnitude of the residual stresses by the boring-out method involves the machining away of successive layers from the interior of the barrel. As each layer is removed, some of the residual stress is relieved. As a result, on the outer surface of the barrel, longitudinal and circumferential strains develop that are measured by strain gauges. From these measurements the magnitude of the initial residual stress state can be deduced.

IX. SUMMARY

The thermal stresses that arise in engineered items, such as the turbine disks of jet aircraft engines, are no longer a major problem because of improvements in materials as well as better design procedures. Nevertheless, their presence must be taken into account. Problems with thermal cracking during heat treatment continue. Residual stresses are still a problem because their presence may not be recognized until a cracking problem associated with them develops.

REFERENCES

- (1) L. Remy, "Thermal and Thermal-Mechanical Fatigue of Superalloys, a Challenging Goal for Mechanical Tests and Models," in *Low Cycle Fatigue and Elasto-Plastic Behavior of Materials*, ed. by K.-T. Rie and D. P. Portella, Elsevier, Oxford, 1998, pp. 119–130.
- (2) W. F. Hosford and R. M. Caddell, *Metal Forming*, 2nd ed., Prentice-Hall, Englewood Cliffs, NJ, 1993.
- (3) L. J. Ebert, The Role of Residual Stresses in the Mechanical Performance of Case Carburized Steel, *Met Trans. A*, vol. 9A, 1978, pp. 1537–1551.
- (4) G. Krauss, *Principles of Heat Treatment of Steel*, ASM, Materials Park, OH, 1980.
- (5) T. R. Gurney, *Fatigue of Welded Structures*, Cambridge University Press, Cambridge, 1968, p. 58.

- (6) A. Ohta, Y. Maeda, and N. Suzuki, "Improvement in Fatigue Properties by Beneficial Welding," in *Proceedings of the 25th Symposium on Fatigue*, Japan Society of Materials Science, 2000, pp. 284–287.

APPENDIX 8-1: CASE STUDY OF A FRACTURE DUE TO THERMAL STRESS

Ceramic materials are usually quite strong in compression but relatively weak in tension, especially in the presence of defects. Figure A8-1 shows a ceramic bowl. The wall thickness of the bowl is 4.8 mm (0.18 in.). When a hot liquid was poured into the bowl, it suddenly developed a circumferential crack, as shown in Fig. A8-2. Why did this crack form? When the hot liquid was poured into the bowl, the ceramic material on the inside of the bowl, which was in direct contact with the fluid, tried to expand but was prevented from doing so by the adjacent cooler material. As a result, a biaxial compressive was developed on the inside surface of the bowl. To balance this compressive stress, tensile stresses developed on the outer surface of the bowl. A small defect was present in the outer surface, and when it was subjected to these tensile stresses, a crack nucleated and then propagated to failure. Figure A8-3 shows the region of fracture origin. Note that a series of "hesitation" lines can be seen. These lines differ from the chevron patterns observed in the brittle fracture of steel. Hesitation lines are created due to plane stress-plane strain interaction. The plane strain portion of the fracture front travels faster than does the plain stress portion. As a result, the crack front is strongly curved. When the plane strain portion gets too far



Fig. A8-1. Ceramic bowl containing a circumferential crack. The two halves mated together so well it is difficult to see the crack.



Fig. A8-2. Two halves of bowl shown in Fig. A8-1 separated to show crack.

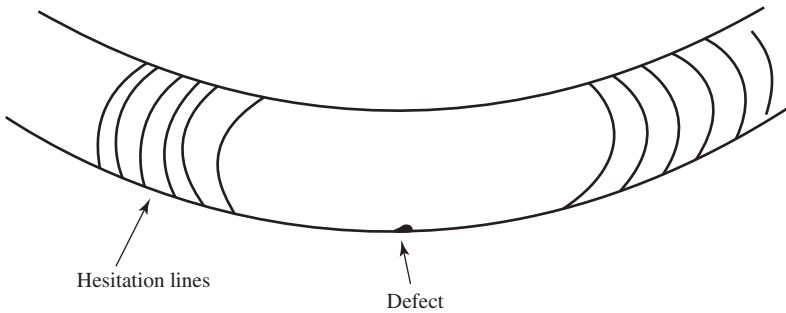


Fig. A8-3. Sketch of fracture surface appearance in vicinity of fracture origin.

ahead of the plane strain portion, a “hesitation” line is formed due to the arrest of the crack by the trailing plane stress portion. As the plane stress portion catches up, the crack front is again free to move forward rapidly. The pattern of markings formed by these hesitation lines enables one to locate the origin of fracture with ease.

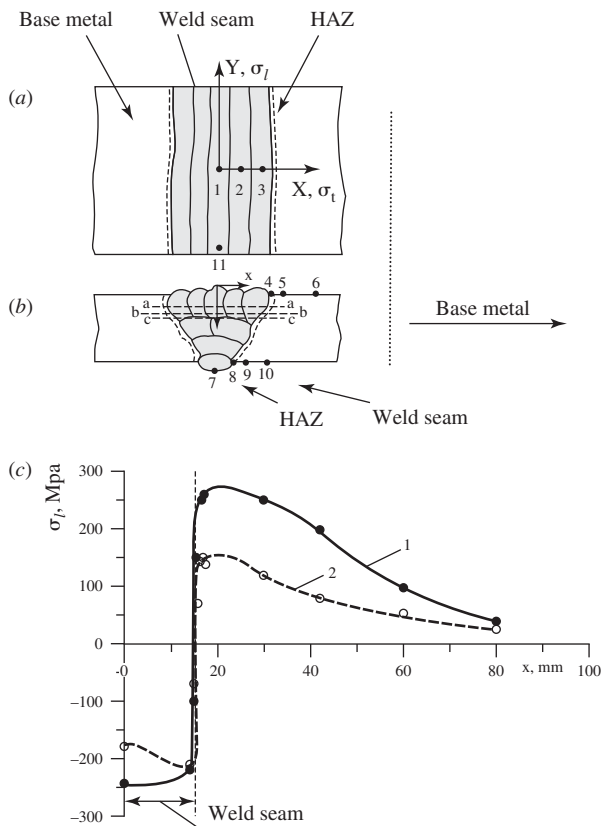
PROBLEMS

- 8-1.** What problems might you anticipate with a ceramic coating that experiences a sudden rise in temperature such that the temperature rise in the metal beneath the coating is much less than that of the coating?

8-2. Consider the bimetallic strip figure shown in Fig. 8-1. Assume that material 1 is steel ($\alpha = 0.00001176/^{\circ}\text{C}$) and material 2 is aluminum ($\alpha = 0.0000236/^{\circ}\text{C}$). The yield stress of the aluminum is 69,000 Pa and that of the steel is 690,000 Pa. The total area of steel equals that of aluminum.

- What temperature rise is needed for the aluminum to reach its yield stress?
- Discuss what happens to the system if the temperature rises above that in (a).
- If the yield stress of the aluminum is exceeded and 0.05% plastic deformation of the aluminum occurs as the temperature continues to rise, what is the state of stress in the strip when the temperature returns to its original value?
- Why is α higher for fcc aluminum than for bcc iron?

8-3. The following figures show a linear butt weld between steel plates and the residual stress distribution around the linear weld seam. Provide an explanation as to why the residual stress distribution of Curve 1 in (c) has the shown profile.



- (a) Top view of a linear butt weld of steel plates and (b) the cross-sectional view of the linear butt weld of steel plates. (c) The distribution of residual stresses as a function of the location measured from the center of the weld seam. 1– the residual stresses parallel to the weld seam – and 2– the residual stresses perpendicular to the weld seam along the positions 1, 2, 3, 4, 5, etc. shown in (a) and (b).
- 8-4.** (a) Why does quenching typically result in compressive stresses at the surface of the component if there is no phase transformation involved in the quenching process? In contrast, tensile stresses are produced at the surface of the component when there is martensite formation during quenching. Why?
- (b) Carburizing, nitriding, and induction hardening can all introduce residual compressive stresses to the surface of the workpiece. What is the mechanism for each of these processes that creates compressive stresses at the surface of the workpiece?
- 8-5.** One of the methods used to decrease the residual stress in cylindrical bars is simply to subject the bar to a tensile plastic stretch. Why does a simple stretching reduce the residual stress?
- 8-6.** Temperature gradients in a material can lead to a well-known phenomenon termed *thermal-mechanical loading*. Use the turbine blade as an example to explain thermal-mechanical loading and what impact it has on the material's performance.

9

Creep

I. INTRODUCTION

The time-dependent deformation of materials under stress is known as *creep*. In metals, it is primarily an elevated-temperature diffusion-controlled process that is terminated by rupture. This chapter reviews the creep mechanisms and creep lifetime prediction procedures. The several failure mechanisms are also discussed.

II. BACKGROUND

At temperatures above $0.4T_M$, where T_M is the melting point in K , time-dependent deformation, that is, creep and rupture processes of materials, are primary design considerations. In many applications—for example, the aircraft gas turbine engine—the operating temperature, and hence the efficiency, are limited by the creep characteristics of materials, so that there is therefore an economic incentive to develop alloys with superior creep resistance. Designs are usually based on a maximum permissible amount of creep, such as 0.1 or 1% during the expected lifetime of a particular component. These service lives can vary from minutes for a rocket engine component, to tens of thousands of hours for jet engine components, to hundreds of thousands of hours for high-pressure steam lines. At elevated temperatures, creep deformation may not be the only mechanism governing service lifetime, for alloys have been found to fracture after very limited extension (1) or after unexpectedly short service lifetimes. However, today creep rupture is not a common occurrence. This is because of advances in alloy development, particularly in the aircraft

field, inspection procedures, and the development of codes such as the American Society of Mechanical Engineers (ASME) Boiler and Pressure Vessel Code and the recommended rules of the American Petroleum Institute (API). Creep problems with carbon steels can be avoided by limiting their use to temperatures below $0.4T_m$, that is, below the creep range. Therefore, in boiling water and pressurized nuclear reactors, which operate at 288°C (550°F), creep is not a problem. However, some pressurized boiler components, such as superheater headers, superheater tubes, and steam pipes, do operate in the creep range using creep-resistant alloys such as $1\frac{1}{4}$ Cr $\frac{1}{2}$ Mo and $2\frac{1}{4}$ Cr-1 Mo steels. Gas turbine engines also operate above $0.4T_m$, and therefore creep is of concern. When creep failures occur, it is often because a power plant or engine has been operated beyond its safe lifetime or because the safe operating conditions have exceeded prescribed limits. In addition, unanticipated creep failures have occurred during normal service at welds and other locations in high-pressure steam lines, as will be discussed subsequently.

In a review of failures in fossil-fired steam power plants, it was found that 81% of the failures were mechanical in nature and that the remainder was due to corrosion. Of the mechanical failures, 65% were classified as short-time, elevated-temperature failures. Only 9% were due to creep, with the rest being due to such causes as fatigue, weld failures, erosion, and so on (2).

III. CHARACTERISTICS OF CREEP

Figure 9-1 shows typical creep extension plots for constant stress conditions. The characteristic regions of the load extension curve are:

- (a) The primary creep region in which the creep strain rate decreases with time.
- (b) The secondary creep region in which, under constant true stress, the creep strain rate has a minimum and steady-state value $\dot{\epsilon}_{ss}$. However, under constant load conditions, no steady-state value may be evident.
- (c) The tertiary creep region in which, even under constant true stress conditions, the creep strain rate accelerates with time.

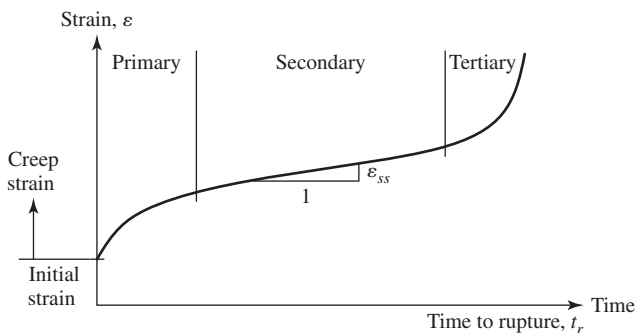


Fig. 9-1. Creep extension as a function of time for constant stress loading conditions.

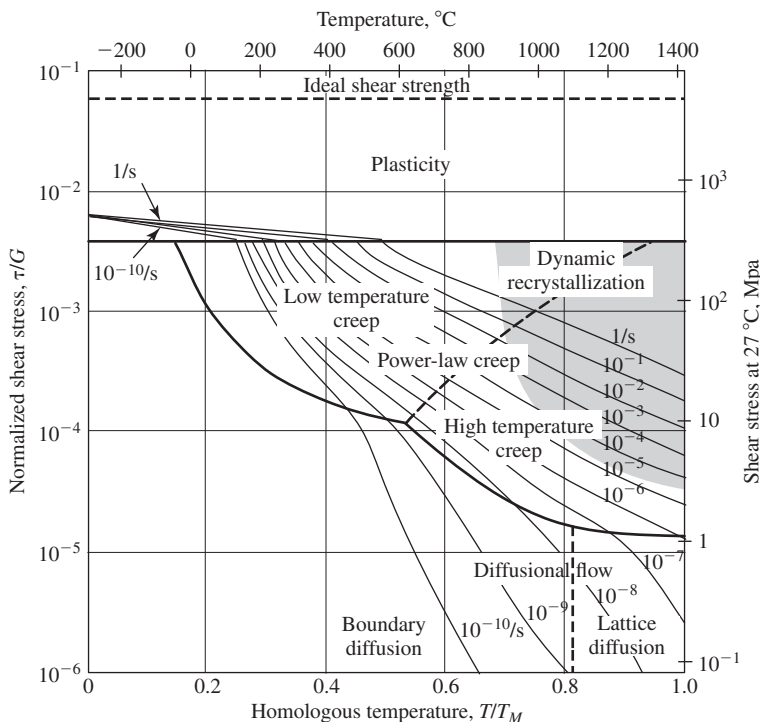


Fig. 9-2. An example of a creep deformation map for pure nickel of grain size 0.1 mm, work hardened. (After Frost and Ashby, 3.)

A major development in recent years has been the introduction of creep deformation maps (3). These maps indicate, for a given alloy, the creep deformation and rupture mechanisms as a function of temperature and stress level, and permit creep analyses to be carried out on a more rational basis. Figure 9-2 is an example of a creep deformation map. The ordinate is τ/G , where τ is the shear stress and G is the shear modulus that decreases with temperature increase. The abscissa is T/T_M , where T_M is the absolute melting temperature. Such maps indicate the mechanism of deformation corresponding to a given combination of stress level and temperature. At temperatures below $0.4T_M$, the deformation is largely either elastic or plastic, whereas above this temperature under constant loading conditions, creep deformation occurs by either one of two mechanisms, power law creep or viscous creep. Both of these mechanisms are diffusion controlled. At low temperatures in the creep range, creep occurs by diffusion along short circuit paths, that is, the grain boundaries or the cores of the dislocations. At high temperatures, the diffusion path is through the bulk of the material.

In power law creep, the rate-limiting step is known as *climb*. In this process, blocked glide dislocations move perpendicular to their glide planes rather than along them as atoms diffuse away from or to the core lines of the dislocations. By climbing, the dislocations are able to circumvent obstacles such as precipitates in

their glide paths. Power law creep occurs in components such as turbine blades and high-pressure steam pipelines. In the latter case, stresses may be quite low, that is, 45.5 MPa (6.6 ksi). Viscous creep occurs at still lower stress levels. The viscous creep mechanism does not involve the climb of dislocations, but only the diffusion of atoms in such a way as to lead to elongation accompanied by a decrease in cross-sectional area under tensile stress. The equations governing these two types of creep are given below.

In power law creep, the steady-state creep rate is proportional to the stress raised to a power n , where n takes on values that are commonly in the range 3–6. The creep strain rate is related to the diffusion-controlled climb of dislocations and is expressed as

$$\dot{\epsilon}_{ss} = G\sigma^n e^{-Q/RT} \quad (9-1)$$

where $\dot{\epsilon}_{ss}$ is the steady-state creep strain rate, G is a material constant, Q is the stress-modified activation energy, R is the gas constant equal to $8.314 \text{ J mol}^{-1} \text{ K}^{-1}$, and T is the absolute temperature.

The value of the exponent n has a strong influence on the shape of a bar during creep. Let l denote the length of the bar and A the cross-sectional area. As in plastic deformation, volume is conserved during creep; then:

$$Al = \text{constant} \quad (9-2)$$

$$A dl + l dA = 0 \quad (9-3)$$

$$\frac{dA}{A} = -\frac{dl}{l} = -d\epsilon \quad (9-4)$$

$$\frac{dA}{A dt} = -\frac{d\epsilon}{dt} = -H\sigma^n = -H\left(\frac{F}{A}\right)^n \quad (9-5)$$

$$A^{n-1} dA = -HF^n dt \quad (9-6)$$

which after integration leads to

$$A_t = (A_0^n - nHF^n \Delta t)^{1/n} \quad (9-7)$$

where A_0 is the initial cross-sectional area and A_t is the cross-sectional area after a time, t . If $n = 1$, as in diffusion creep or linear viscous flow, then a reduced cross section draws down only slightly faster than the rest of the bar, and this is why molten glass can be drawn down into a thin fiber. For example, consider the creep deformation of a bar with an initial cross section A_{01} , which initially contains a reduced section A_{02} equal to $0.9A_{01}$. When, under viscous creep deformation, the reduced section reaches $0.5A_{01}$, the remainder of the bar would have an area of $0.6A_{01}$. That is, the ratio of the two areas at that time would be only 0.833 as compared to the initial ratio of 0.9. However, if n were equal to 3–5, as in power law creep, then as can be seen from Eq. 9-5, the reduced cross section would draw down much more rapidly than the rest of the bar, with the result that a sharp neck would be developed.

IV. CREEP PARAMETERS

A number of parametric relationships have been developed for design purposes in the attempt to relate stress, creep rate, time to rupture, and temperature in order to extrapolate available data to longer rupture times at lower stresses under the assumption that the mechanism of creep remains the same in the range of interest. One of the more widely used of these parameters is the Larson-Miller parameter. In the Larson-Miller approach, data on the steady-state creep rate or the creep rupture life at a given stress level at one temperature are used to estimate the creep rates and lifetimes at the same stress level at other temperatures. The starting point for the development of this parameter is the Arrhenius type of equation:

$$\dot{\epsilon}_{ss} = Ae^{-Q(\sigma)/RT} \quad (9-8)$$

or

$$T \log(\dot{\epsilon}_{ss} - C) = -2.3 \frac{Q}{R} = -f(\sigma) \quad (9-9a)$$

where T is in K , $\dot{\epsilon}_{ss}$ is in $m/m/hr$, and $C = \log A$, or

$$\log \dot{\epsilon}_{ss} = C - f(\sigma) \frac{1}{T} \quad (9-9b)$$

If the log of the steady-state creep rate data for a series of stress levels is plotted versus $1/T$, such a plot will produce a series of straight lines with a common intercept C , as in Fig. 9-3a, provided that the data conform to Eq. 9-8. Once the value of C is determined, a master plot of $\log \sigma$ versus $T \log(\dot{\epsilon}_{ss} - C)$, the Larson-Miller parameter, can be constructed, as shown in Fig. 9-4.

When the extension in tertiary creep is small compared to the extension in steady-state creep, the empirical Monkman-Grant law,

$$\dot{\epsilon}_{ss} t_r = \text{constant} = B = \epsilon_r \quad (9-10)$$

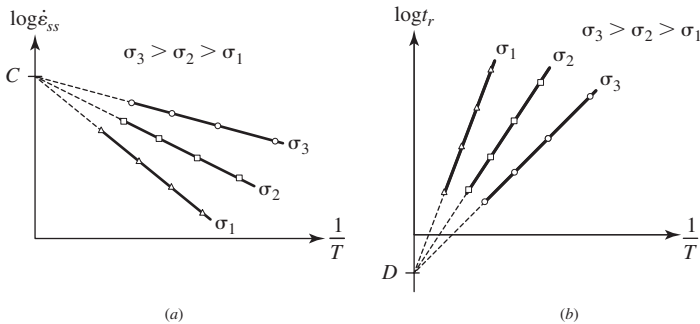


Fig. 9-3. Plots used in the determination of Larson-Miller constants. (a) $\log \dot{\epsilon}_{ss}$ vs. $1/T$. (b) $\log t_r$ vs. $1/T$.

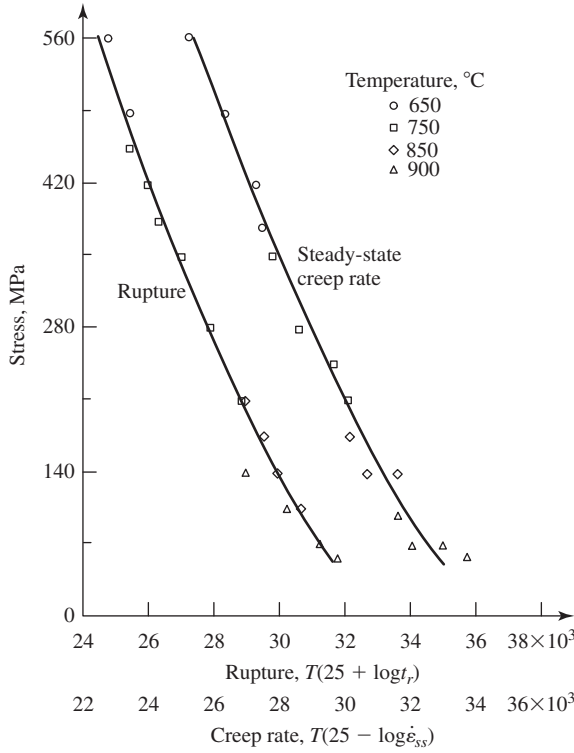


Fig. 9-4. Larson-Miller plot for Inconel X. (After Tetelman and McEvily, 4.)

where t_r is the time to rupture and ϵ_r is the strain to rupture, can be used to develop an alternate form of the Larson-Miller parameter,

$$T \left(\log \frac{B}{t_r} - C \right) = -f(\sigma) \quad (9-11)$$

or

$$T(\log B - \log t_r - C) = -f(\sigma)$$

or

$$T(D + \log t_r) = f(\sigma) \quad (9-12a)$$

or

$$\log t_r = -D + f(\sigma) \frac{1}{T} \quad (9-12b)$$

The constant D is determined by plotting experimental data for a series of stress levels, as shown in Fig. 9-3b. Once D is determined, a master plot of $\log \sigma$ vs. $T(D + \log t_r)$ can be constructed, as shown in Fig. 9-4.

To estimate the time to failure under variable loading and temperature conditions during the creep lifetime, a linear damage rule, known as *Robinson's life fraction rule*, is used. To carry out the calculations, data are needed on the time to rupture under constant loading conditions at the temperatures of interest. This rule is

$$\sum_{i=1}^{i=i} \frac{t_i}{t_{fi}} = 1 \quad (9-13)$$

where t_i is the time spent at the i th stress level at a given temperature and t_{fi} is the time to failure under the same loading conditions.

In using any extrapolation approach to predict long-time behavior, it is assumed that the microstructure remains essentially unaltered. However, this may not be the case, and the predictions may be nonconservative. For example, at temperatures above 425°C (800°F), carbon steels in long-time service are subject to graphitization, a process that leads to loss of strength and overall ductility. In this process Fe_3C is replaced by iron and carbon. Above 470°C (875°F), carbon-molybdenum steels are similarly affected. In welded structures, this transformation from carbide to graphite takes place preferentially along heat-affected zones adjacent to the welds and can lead to creep failures requiring repair or replacement (5). For service above 425°C (800°F), the use of carbon-molybdenum steels containing 1/2% or more chromium eliminates the danger of graphitization. It is also reported that carbon-molybdenum steels deoxidized with silicon are not prone to graphitization after prolonged exposure to elevated temperatures (6).

V. CREEP FRACTURE MECHANISMS

The modes of creep failure are compared to the modes of low-temperature failure in Fig. 9-5 (7). The creep failure modes are:

(a) *Intergranular creep failure*: This is the most likely mode of creep fracture in long-time exposure to temperature and stress. In this failure process, voids nucleate along grain boundaries and wedge cracks appear at triple points (1). Figure 9-6 shows examples of a wedge crack and grain boundary voids. In time, these defects grow and link up; as a result, there is little reduction in cross-sectional area and a "flat" or thick-walled fracture results. This mode of failure is associated with components that have been in service for many years. Because grain boundaries are weak areas in creep, due to grain boundary sliding that contributes to creep elongation, and also because they are sites for void nucleation, means have been developed to minimize the effects of grain boundaries. Directional solidification is used to grow columnar grains that are parallel to, rather than at an angle to, the principal creep stress. Single crystals are used in order to completely eliminate the negative contributions of grain boundaries to creep. The use of directionally solidified and single-crystal components has permitted gas turbine engine operating temperatures to be raised significantly. Single crystals were first used in the hot stage of aircraft gas turbine engines.

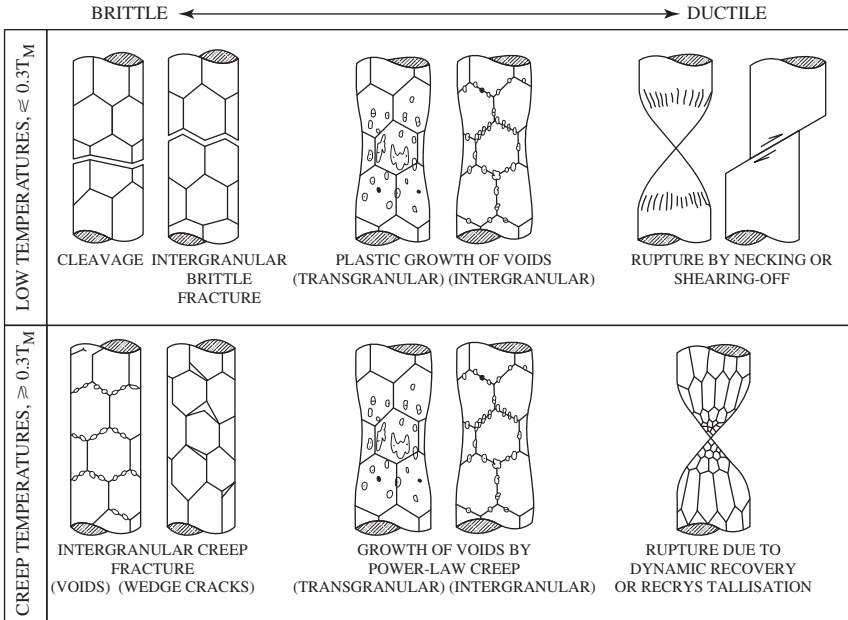


Fig. 9-5. Broad classes of fracture mechanisms. The upper row refers to low temperatures ($< 0.3T_M$) where plastic flow does not depend strongly on temperature or time; the lower row refer to the high temperature range ($> 0.3T_M$) in which materials creep. (After Ashby et al., 7. Reprinted by permission.)

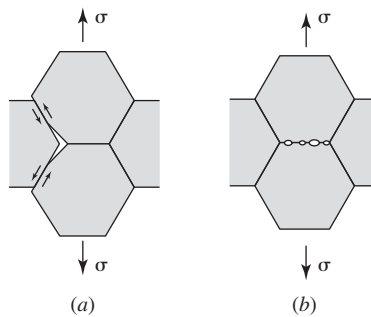


Fig. 9-6. (a) Example of a wedge crack. (b) Example of grain boundary voids.

Advances in casting technology now permit the use of single crystals in industrial gas turbines where the blades are much larger than in aircraft engines.

(b) *Transgranular creep fracture*: This mode of failure can occur in short-time creep failures, and the failure process is similar to that of tensile rupture below the creep range. The ductility and reduction in area are usually large and much greater

than at room temperature, with the result that a heat exchanger tube will locally balloon and lead to a thin-walled fracture.

(c) *Point rupture fracture*: At sufficiently high temperatures and low stresses, dynamic recrystallization, that is, recrystallization during creep, can remove microstructural creep damage. As a result, voids do not nucleate, and necking down to a point can occur.

VI. FRACTURE MECHANISM MAPS (6)

These maps are analogous to creep deformation maps and indicate the mode of failure as a function of stress and temperature. An examination of a creep fracture surface together with the information contained in these maps can give an indication of the operating conditions at the time of failure. Figure 9-7 is an example of a fracture mechanism map.

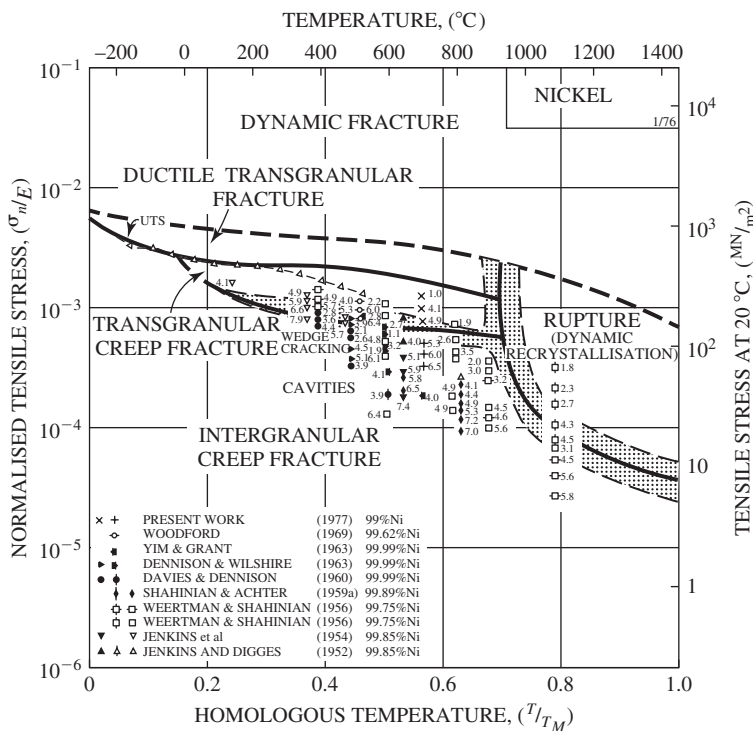


Fig. 9-7. An example of a fracture mechanism map for round bars of commercially pure nickel tested in tension. The map shows four fields corresponding to four modes of failure. Individual tests are marked by symbols and (for creep tests) labeled with the logarithm, to base 10, of the time to fracture in seconds ($\log t_f$). Solid symbols mean that the fracture was identified as intergranular. Shading indicates a mixed mode of fracture. (After Ashby et al., 7. Reprinted with permission.)

VII. CASE STUDIES

A. Failure at Longitudinally Welded Pipe (8)

After 12 years of service at 538°C (1,068°F) a low-chromium alloy steel pipeline of wall thickness equal to 25.4 mm (1 in.) failed at a longitudinal, submerged-arc weld. The pipeline should have lasted for over 30 years based upon creep rupture analyses that assumed that the weld and base metals had the same creep properties and were stressed at 45.5 MPa (6.6 ksig), but in this case, the weld metal was less creep resistant than the base metal. It is noted that pipelines are nominally in a state of plane strain. The nominal stresses in a pipeline are the hoop stress $\sigma_1 = \sigma$ (hoop), $\sigma_2 = \sigma/2$ (longitudinal) and $\sigma_3 \approx 0$ (through-thickness). The strain in the longitudinal direction is given as

$$\varepsilon_2 \propto \left(\sigma_2 - \frac{1}{2}\sigma_1 \right) = 0 \quad (9-14)$$

For constancy of volume, $\dot{\varepsilon}_1 = -\dot{\varepsilon}_3$. Therefore, during creep, a pipeline expands in the circumferential direction and grows thinner in the radial direction, and there is no change of length in the longitudinal direction.

The weld was a symmetric double-V weld, Fig. 9-8, and had lower creep resistance than that of the base metal. For purposes of illustration, assume that all of the circumferential creep strain occurred in the weld material. Designate the length of the weld at the circumference to be l_{co} and the length of the weld at midthickness to be l_{mo} . Over a period of time the creep strain at both of the above locations will be the same. However, the length change of the weld at the circumference will be $\Delta l_c = \dot{\varepsilon} l_{co}$, and that at midsection will be $\Delta l_m = \dot{\varepsilon} l_{mo}$. Since $l_{co} > l_{mo}$, the shape of the weld would change. To prevent this change, a tensile stress would develop at the midsection. In addition, in the low-chromium alloy steel, a high density of spherical inclusions associated with the submerged arc welding process was present along the fusion line. A sulfur coating on the inclusions prevented good bonding with the matrix, and the high tensile stress at the root of the weld promoted the early formation and growth of cavities at the inclusions. As these cavities grew, they

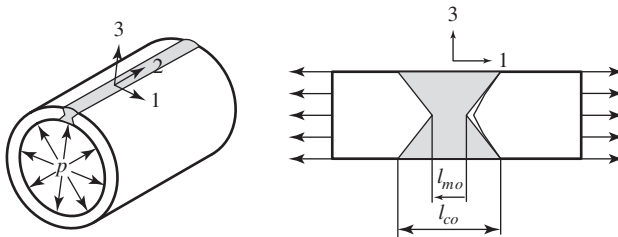


Fig. 9-8. An idealized model of a longitudinal pipe weld. The curvature of the pipe is neglected and plane-strain conditions are assumed. The arrows represent the uniform hoop stress in the pipe away from the weld.

linked up to form a crack along the fusion line within 1–2 years of service. The crack then extended along the fusion line toward the inner and outer surfaces of the pipe as additional cavities formed at grain boundary inclusions in the high-strain field ahead of the crack. These cavities then grew and coalesced with the crack tip. A detailed analysis involving power law creep behavior, $\dot{\epsilon} = B\sigma^n$, and elastic-plastic creep crack growth relationships led to a predicted lifetime of 10 years, a value close to the time involved in the actual failure.

B. Failure of a Heat Exchanger Tube

An oil-fired power plant had been in service for a number of years when, during the 1970s, an oil shortage developed. Since the shortage appeared to be of long duration, management decided to convert the plant to a coal-fired operation. The plant was therefore modified to accommodate the use of coal. During the modification, a vertical bank of new heat exchanger tubes was installed. In operation, the tubes are heated externally by hot gases from the furnace, and there is a flow of steam within the tubes. The tubes were made of 1018 steel and were 50 mm (2 in.) in diameter, with a wall thickness of 5 mm (0.2 in.). The steam pressure was 10 MPa (1,450 ksig), resulting in a hoop stress of 40 MPa (5.8 ksig). The plant had been in operation for only a day or so following the modification when rupture in a transgranular, thin-walled mode of one of the tubes occurred, see Fig 9-9*a,b*, necessitating a costly shutdown of the plant. The fact that the failure was of a thin-walled type was a direct indication of a short-time fracture due to overheating. The reduction in wall thickness is much less pronounced in long-time creep failures, since they occur due to the linking up of grain boundary voids. In addition, in long-time failures, there is usually considerable intergranular cracking in regions adjacent to the thick-walled fracture (Fig. 9-9*c*), which, of course, did not occur in the case under consideration.

The tube was repaired by welding in a replacement section, but again, after the plant had been in operation for only a short while, the replacement section failed, also in a thin-walled manner. During the second repair operation, a member of the repair crew happened to look up into the failed tube and noticed that an obstruction was present. The obstruction turned out to be a wrench that had been accidentally dropped into the tube during the plant conversion and had wedged itself midway down the tube. The wrench had disrupted the flow of steam in the tube, causing a hot spot to develop. As a result, the tube temperature had risen to a point where the flow strength of the metal was exceeded, and rupture occurred in the observed short-time, thin-walled fashion.

The microstructure in the vicinity of the break can give an indication of the maximum temperature reached as well as an indication of the subsequent cooling rate. For example, in one instance when an attempt was made to remove the upper end of an oil drum made of a low-carbon steel by flame cutting with an oxyacetylene torch, an explosion occurred. The procedure involved in flame cutting is to preheat an area to a cherry red color with the oxygen supply to the cutting torch set at a low level and then to increase the oxygen supply for the cutting operation itself. In this case, as soon as the cutting flame penetrated the metal, the fumes in the drum ignited

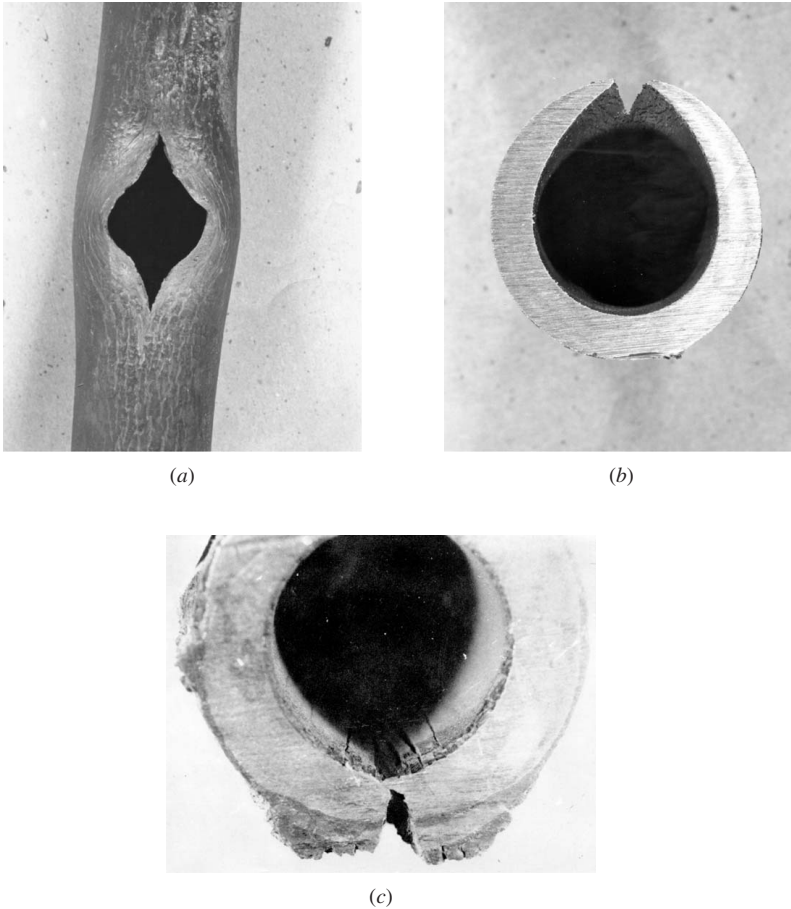


Fig. 9-9. (a) Longitudinal view of a thin-walled creep fracture. (b) Cross-sectional view of a thin-walled creep fracture. (c) Cross-sectional view of a thick-walled creep fracture. (After French, 2. Reprinted with permission.)

with explosive force. Subsequent metallographic examination of the preheated area revealed an acicular microstructure rather than a ferritic-pearlitic microstructure, thereby indicating that the area had been heated into the austenitic range during preheating and then cooled rapidly after the explosion. In the case of the failed heat exchanger tube, the microstructure at the break was ferritic-pearlitic, an indication that it had been heated to a temperature below the transformation temperature but high enough to allow softening and rupture to occur.

When excessive amounts of creep are found in jet aircraft engines, the microstructure can be examined to determine if high thermal excursions due to improper engine operation had occurred. Similarly, the examination of the microstructure in any creep failure can lead to an indication of the thermal history of the component.

C. An Ovalized Tube (9)

When a tube of oval cross-sectional shape is subjected to internal pressure in addition to the hoop stress, a bending stress will also be introduced (Fig. 9-10). Under pressure, the tube cross section tries to become more circular, thereby introducing the bending stresses, which are at a maximum at the end of the major axis of the ellipse. At this location, the bending stress adds to the hoop stress on the inside surface and subtracts from the hoop stress on the outside surface. Ovalization occurs at tube bends, with attendant pipe wall thickening at the inner radius of the bend and thinning at the outer radius of the bend (Fig. 9-10). To minimize ovalization, it is standard practice to hot form the bend after first packing the pipe with sand.

In one instance, a Cr-Mo tube with an outer diameter of 44.5 mm (0.82 in.) and a nominal wall thickness of 7.5 mm (0.3 in.) failed by cracking longitudinally at a bend after operating for only 3,500 hours at 538°C (1,000°F) at a pressure of 13.7 MPa (2.0 ksig). The nominal hoop stress was calculated to be 33.8 MPa (4.9 ksig). Measurement of the tube wall thickness revealed that it was 8.5 mm (0.34 in.) at the inner radius of the bend and 6.1 mm (0.24 in.) at the outer radius of the bend. There was also significant ovalization, with the maximum tube diameter exceeding the minimum by 4 mm (0.16 in.). It was confirmed that the tube bending had been carried out without packing with sand and without the use of proper bending equipment.

The allowable ASME code stress for the material at the operating temperature is 53.8 MPa (7.8 ksig). When the draft methodology of API (American Petroleum Institute) 579 Recommended Practice was used to calculate the combined bending and hoop stress, the resultant value for the observed degree of ovality was found to be well in excess of the allowable limit, and the reason for the premature failure is readily seen.

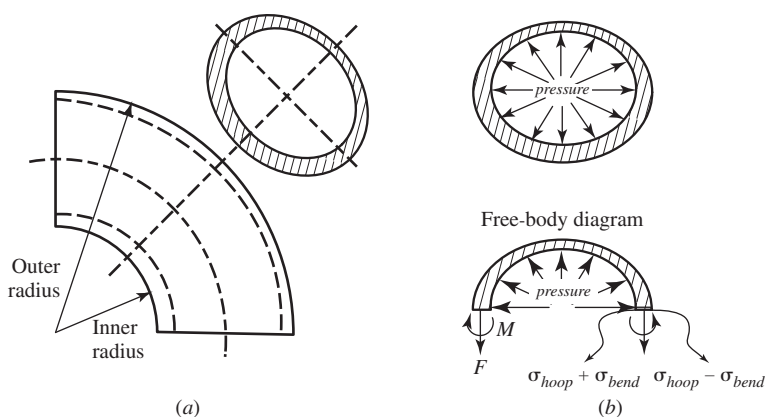


Fig. 9-10. (a, b) Ovalized tube under internal pressure.

D. Failures in Fossil-Fired Boilers (2)

D.1. Oil-Fired Steam Boiler An oil-fired steam boiler had been in service for 2 years when a furnace side-wall tube ruptured. The steam temperature was 540°C (1,005°F), and the steam pressure was 14.7 MPa (2,150 psig). The fracture occurred at the downstream edge of a circumferential weld and was of the short-time, knife-edge type. The microstructure at the failure location was in a spheroidized condition, whereas farther away from the failure, it contained pearlite. It was deduced that the weld upset the smooth steam flow and formed an area of turbulence, leading to the formation of an insulating steam blanket. As a result, the metal temperature rose to 650–700°C (1,292°F), at which point the metal was not able to withstand the internal pressure and the rupture occurred.

In other failures, the formation of insulating scales on the interior of tubes is due to the reaction between steam and iron to form magnetite. These scales have led to catastrophic increases in metal temperature. The reduction of tube wall thickness due to corrosion or erosion can also be a contributing factor.

D.2. Waterwall Tube A waterwall tube failed in a short-time, knife-edge manner. The nominal temperature was 540°C (1,000°F), and the steam pressure was 15.4 MPa (2.2 ksig). The microstructure at the point of failure consisted of ferrite and bainite, whereas away from the failure the microstructure consisted of ferrite and pearlite. The presence of bainite indicated that the tube had been heated above the A_1 temperature into the two-phase $\alpha - \gamma$ region and rapidly cooled. From the relative amounts of these two phases, an estimate of the maximum temperature reached can be made through the use of the Lever Rule. The Lever Rule states that the amount of % α -phase present at a given temperature is given by

$$\% \alpha = \frac{\% \text{ carbon in } \gamma - \% \text{ carbon in alloy}}{\% \text{ carbon in } \gamma - \% \text{ carbon in } \alpha} \times 100 \quad (9-15)$$

In this case, the Lever Rule indicated that the highest temperature had been in the range 790–820°C (1,454–1,508°F). The cause of the failure was attributed to hot spots, which developed as the result of poor circulation of the furnace gases.

In another failure, the microstructure was entirely bainitic, indicating that a temperature in excess of 870°C (1,600°F) had been reached.

D.3. Superheater Tube A 2 1/4 Cr-1 Mo steel superheater tube experienced a nominal temperature of 540°C (1,000°F) at a pressure of 13.5 MPa (1.96 ksig). The tube outside diameter (OD) was 44 mm (1.76 in.), and the wall thickness was 6.6 mm (0.26 in.). After some time in service, the tube failed in a classic creep type of fracture, as shown in Fig. 9-9c, with a 38mm-long (1.52-in.) longitudinal split. The wall thickness at the fracture showed virtually no reduction. The wall thickness 180° from the fracture was 7.6 mm (0.30 in.), which included an outer scale of 1.3 mm (0.05 in.) and an inner scale of 0.8 mm (0.03 in.). It was estimated that, with

the insulating scales present, the outer skin temperature had risen to about 650°C, whereas the safe upper temperature limit for the avoidance of severe oxidation was 605°C (1,120°F). The cause of the creep failure was due to prolonged exposure to the 650°C (1,200°F) temperature.

Overheating can also result in the formation of methane (CH₄) gas as hydrogen from the flue gas atmosphere combines with carbon in the steel and decarburizes it. If the methane forms at subsurface sites, the gas can create an internal pressure leading to blister formation on the OD.

VIII. RESIDUAL LIFE ASSESSMENT

Design codes have traditionally been about design only, and have not been intended to cover the assessment of an operating plant that has been in service for some time. In the case of boilers, pressure vessels, and tanks, periodic inspections are carried out, but they have not provided a complete engineering evaluation and have not been governed by a regulatory code in terms of engineering assessment of damage and the prediction of the remaining safe life (10). An immediate reaction upon finding defects such as cracks or pores during an evaluation is to condemn the equipment as not meeting code requirements and indicating that repair is necessary. Recently, however, *fitness for service codes* have been and are being developed by the ASME and the API, codes that provide rules and guidelines for repairs and alterations based upon risk-based inspection procedures. Three levels of analysis may be involved: qualitative, semiquantitative, and fully quantitative. As an example, cracks in a tee connection weld that operated at 585°C (1,085°F) at 4.5 MPa (0.65 ksig) were discovered during an unplanned shutdown. After a qualitative analysis of the risks involved and as a temporary expedient, weld repairs were made, even though grinding prior to welding did not completely eliminate the cracks. Later, however, it was found to be desirable to extend the period of operation before a major repair was undertaken, and a more detailed analysis, including the use of computer codes for creep crack growth, was therefore undertaken to evaluate the safety of the system. Based upon the size of the crack, an evaluation of the loading during operation and shutdown, and the time required to grow the crack by creep to a critical size, it was concluded that the tees needed to be replaced much sooner than desired by plant management.

This example relates to the important question concerning a plant that has been in service for some time: “How much longer can the plant operate before major problems start to develop?” Answers to this question are needed in order to plan for major overhauls and perhaps replacement of the plant. It turns out that for components that operate in the creep range, this is not an easy question to answer. However, the following procedures in the following sections A and B have been developed to provide a partial answer.

A. Microstructurally Based Approach

This approach relies upon the observation of grain boundary voids. The procedure involves the cleaning, polishing, and etching of suspect areas in situ and then making

replicas for observation under the microscope. If voids are found, and depending on their stage of development into cracks, an estimate of the residual life of the component can be made that is usually of the order of several years or less. Care in polishing the surface is needed, for it has been shown (11) that grain boundary cavities in Cr-Mo low-alloy steels are enlarged by the polish-etch procedures used and may not be apparent upon more careful polishing. In fact, the apparent voids may have been locations at which grain boundary carbides were removed during polishing. However, if voids are not found, a definitive life assessment cannot be made, except for the fact that the component will last at least as long as the time required for observable voids to develop, grow and link up, and cause failure. This may require at least 5 years, so that at least this amount of time is available to plan for repairs and replacement.

An alternative procedure is to examine the microstructure for the degree of spheroidization that may have occurred in service as an indication of residual life (9). A Cr-Mo superheater stub failed after 175,000 hours at a temperature of 515°C (960°F) and extensive spheroidization had taken place, with little evidence of the original pearlite being evident. However, when a Cr-Mo steam tube failed after 70,000 hours at 490°C (914°F), extensive void formation and cracking on grain boundaries could be observed, but with no detectable change in the original ferrite-pearlite microstructure. Longer times and higher temperatures may be needed before spheroidization is apparent.

B. Accelerated Creep Testing

In this procedure for determining the remaining creep lifetime, material is taken from a component that has been in service for some time. Creep tests are then conducted on this material at higher stresses and/or higher temperatures than at the in-service conditions. The creep rupture life, t_r , for each test condition is then plotted against a parameter such as the Larson-Miller parameter, $LMP = T(C + \log t_r)$, as shown schematically in Fig. 9-11. Note that the value of the parameter is reduced

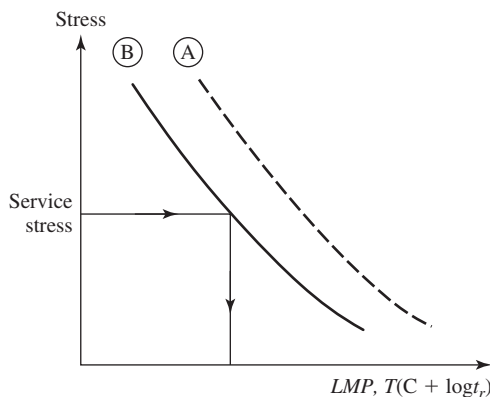


Fig. 9-11. Stress rupture curves for virgin material (Curve A) and for material after many years of in-service use (Curve B).

by in-service exposure. Next, the *LMP* at the operating stress is determined and the time to rupture of a specimen at the operating stress and temperature is predicted. This rupture life of a specimen is supposed to be the remaining life of a component.

IX. STRESS RELAXATION

The substitution of elastic strain by inelastic (creep) strain at elevated temperatures leads to a loss of tensile stress in bolted connections and is therefore a problem. This process occurs at constant displacement and is known as *stress relaxation*.

As shown in Fig. 9-12, a component of length L , perhaps a bolt, is subjected to a displacement δ , which is then maintained throughout the life of the component. The total strain in the member is δ/L . If the component is used in the creep range, stress relaxation will ensue. The equations governing this process are as follows:

$$\varepsilon_t = \varepsilon_e + \varepsilon_{pl} \quad (9-16)$$

where ε_t is the total strain, ε_e is the elastic strain, and ε_{pl} is the inelastic strain. Since the total strain is fixed in time,

$$\dot{\varepsilon}_t = 0 = \dot{\varepsilon}_e + \dot{\varepsilon}_{pl} \quad (9-17)$$

and

$$\dot{\varepsilon}_e = -\dot{\varepsilon}_{pl} \quad (9-18)$$

which leads to

$$\frac{1}{E} \frac{d\sigma}{dt} = -A\sigma^n \quad (9-19)$$

The variables are then separated to yield

$$\sigma^{-n} d\sigma = -AE dt \quad (9-20)$$

and upon integrating

$$\frac{1}{-n+1} \sigma^{-n+1} \Big|_0^{\sigma(t)} = -AE \Delta t \quad (9-21)$$

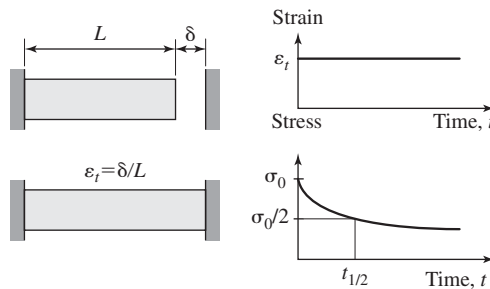


Fig. 9-12. Stress relaxation.

The stress varies in time from its initial value σ_0 to a lower value $\sigma(t)$, which leads to

$$\frac{1}{\sigma(t)^{n-1}} - \frac{1}{\sigma_0^{n-1}} = (n-1)AE \Delta t \quad (9-22)$$

The time $\Delta t_{1/2}$ required for the stress to relax to one-half of the initial value is obtained by setting $\sigma(t) = \sigma_0/2$, so that

$$\Delta t_{1/2} = \frac{(2^{n-1} - 1)}{(n-1)AE\sigma_0^{n-1}} \quad (9-23)$$

X. ELASTIC FOLLOW-UP

In the previous section, it was shown that if a structural member is deformed and the strain is maintained at a constant value, the stress will decrease from its initial value because of the conversion of elastic strain to creep strain. But if the strained component is connected to another member, which does not undergo creep deformation, the strain in the component undergoing creep will increase over time, even though the total displacement remains constant. This phenomenon, known as *elastic follow-up*, can be understood with the aid of Fig. 9-13. In Fig. 9-13a, the displacements initially developed in members 1 and 2 are shown. Component 1 is not in the creep range, whereas component 2 is. In Fig. 9-13b, the initial displacements of member 1, Δ , and member 2, δ , are represented by points A and B, and the total displacement is considered to be fixed. If, over a period of time, due to stress relaxation the load carried by member 2 decreases, then since member 1 is in series with member 2, the load carried by member 1 will also decrease, leading to a decrease in elastic strain in member 1. As the elastic strain in member 1 decreases from point A to point C, the plastic strain in member 2 must increase to maintain a constant total displacement, that is, point B moves to point D.

Elastic follow-up can occur in a high-temperature piping system—for example, in a pipe expansion loop. When the pipe is subjected to thermal expansion, a straight

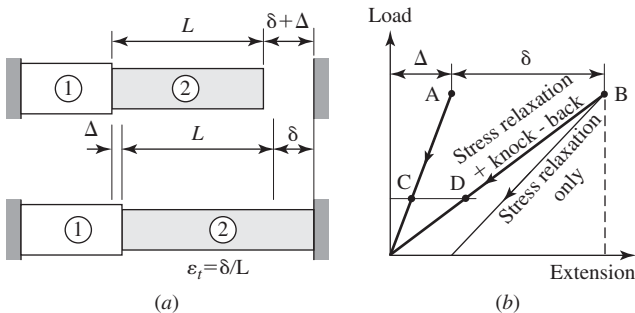


Fig. 9-13. (a, b) Elastic follow-up.

pipe that has a higher stiffness can cause accumulation of creep strain in an elbow that has a lower stiffness.

XI. SUMMARY

This chapter has dealt with the nature of the creep process and creep failure modes. Design procedures were reviewed, and the topics of residual life determination and stress relaxation and elastic follow-up were discussed. Several case studies have served to illustrate the variety of problems that can arise because of creep.

REFERENCES

- (1) H. E. Evans, *Mechanisms of Creep Fracture*, Elsevier Applied Science, Oxford, 1984.
- (2) D. N. French, *Metallurgical Failures in Fossil Fired Boilers*, Wiley, Hoboken, NJ, 1983.
- (3) H. J. Frost and M. F. Ashby, *Deformation-Mechanism Maps*, Pergamon Press, Oxford, 1982.
- (4) A. S. Tetelman and A. J. McEvily, Jr., *Fracture of Structural Materials*, Wiley, Hoboken, NJ, 1967.
- (5) *Fossil Power Systems*, ed. by J. G. Singer, Combustion Engineering, Windsor, CT, 1981, pp. 10–22.
- (6) H. Thielsch, *Defects & Failures in Pressure Vessels & Piping*, Reinhold Publishing Co., New York, 1965.
- (7) M. F. Ashby, C. Ghandi, and D. M. R. Taplin, Fracture Mechanism Maps and Their Construction for F.C.C. Metals and Alloys, *Acta Met.*, vol. 27, 1979, pp. 699–729.
- (8) G. R. Stevick and I. Finnie, Crack Initiation and Growth in Weldments at Elevated Temperature, in *Localized Damage IV*, ed. by H. Nisitani, M. H. Aliabadi, S.-I. Nishida, and D. J. Cartwright, Computational Mechanics Publishers, Southampton, UK, 1996, pp. 473–484.
- (9) H. C. Furtado, J. A. Collins, and I. Le May, “Additional Experiences in Evaluating Power Station Component Failures and Indications,” in *Risk, Economy and Safety, Failure Minimization and Analysis; Failures '98*, ed. by R. K. Penny, Balkema, Rotterdam, 1998, pp. 75–80.
- (10) H. C. Furtado and I. Le May, “Fitness for Service Assessment of Boiler Plant and Pressure Vessels,” in *Risk, Economy and Safety, Failure Minimization and Analysis; Failures '96*, ed. by R. K. Penny, Balkema, Rotterdam, 1996, pp. 151–157.
- (11) T. L. da Silveira and I. Le May, Effects of Metallographic Preparation Procedures on Creep Damage Assessment, *Mater. Char.*, vol 28, 1992, pp. 75–85.

PROBLEMS

- 9-1.** The bolts of an elevated-temperature unit are tightened to 70 MPa at a temperature of 550°C where Young’s modulus is 175 GPa. The $\dot{\epsilon}_{ss}$ at this stress

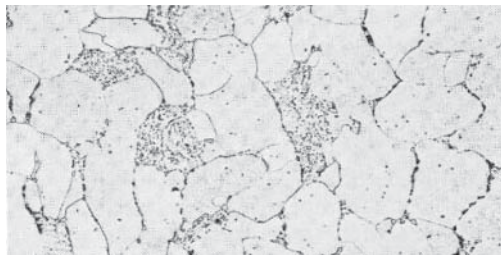
and temperature is $5.0 \times 10^{-8}/\text{hr}$, and the power-law creep exponent is 4.0. Determine the stress in the bolts after 1 year.

- 9-2.** A turbine engine operates at constant speed at 750°C , and the blades initially have a 1 mm clearance. The blades are proportioned such that along a main section 100 mm in length the centrifugal stress is constant at 40 MPa. Tests have shown that at the steady state, the power-law creep rate at 800°C is $7.5 \times 10^{-8}/\text{sec}$ and at 950°C it is $1.3 \times 10^{-5}/\text{sec}$. Estimate the time required for the tip clearance to be reduced to zero.
- 9-3.** The power-law creep relation for a Ni-Cr-Mo steel at 454°C is given as

$$\dot{\epsilon} = 3 \times 10^{-13} \text{sec}^{-1}$$

where σ is in MPa.

- (a) A 2 m long round tension member is to support a load of $4.48 \times 10^4 \text{N}$ for 10 years without exceeding 2.5 mm of creep deformation. What is the maximum stress that can be applied?
- (b) If after 3 years it is decided to lower the total deformation allowed to 1.5 mm, what then is the maximum allowable stress?
- (c) What cross section is required?
- 9-4.** Under a tensile stress of 276 MPa, the creep rupture lifetime at 597 K of the nickel-base alloy Udimet 700 is 100 hours. At this stress level the value of the Larson-Miller parameter is 28×10^3 . What is the value of the constant C in the Larson-Miller parameter? Note that t_R is in hours.
- 9-5.** A steam boiler tube made of a 0.3% carbon steel failed. The microstructure near the fracture is shown in Fig. P9.5S. It can be seen that spheroidization of the pearlite and the formation of grain boundary voids have occurred.
- (a) Point out the regions exhibiting spheroidization and grain boundary voids.
- (b) Based upon the above microstructural features, discuss the estimated temperature to which the tube had been exposed.

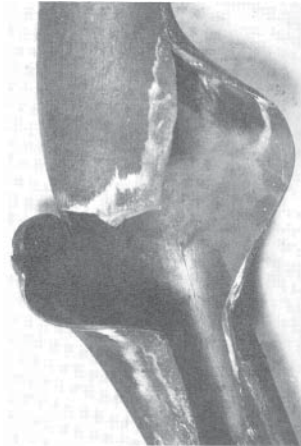


(a)

9-6. A boiler tube made of 1.25Cr-0.5 Mo steel ruptures, with a “cobra” appearance (see the figure) because of its operation under an overheating condition.

Based on this image, discuss the following issues:

- (a) Will this failure likely be a thin-walled or a thick-walled fracture? Why?
- (b) Will this failure be likely to result from substantial overheating or slight overheating? Why?



10

Fatigue

I. INTRODUCTION

Fatigue is a leading cause of failure in mechanical components that are subjected to cyclic loading. This chapter deals with the historical background of fatigue and mechanisms of crack initiation and growth of fatigue cracks, together with a consideration of design procedures and a discussion of some case studies.

II. BACKGROUND

A fatigue failure is the result of the repeated application of stress below the tensile strength of the material but above a stress amplitude that corresponds to the fatigue strength of the material. Fatigue failure consists of three processes: initiation of one or more cracks, the growth of a dominant crack, and final separation (fracture). Research has shown that plastic deformation is necessary for both the initiation and propagation of fatigue cracks. A perfectly brittle material such as diamond cannot fail in fatigue. Another requirement is that the cross-slip of screw dislocations is possible. *Cross-slip* is that process wherein a screw dislocation is able to move from one slip plane to an intersecting slip plane. In those materials where cross-slip is not an easy process, such as sodium chloride (NaCl), magnesium oxide (MgO), and lithium fluoride (LiF), fatigue failure does not occur. It would appear therefore that cross-slip should be involved in any mechanism for fatigue crack initiation.

In the first half of the nineteenth century, a number of train wrecks occurred in England and Germany as the result of fatigue failure of railroad car axles. The cause

of the first failures must have been a complete mystery, for the existence of fatigue was not known at the time, but as more accidents occurred, engineers realized that they had a new phenomenon on their hands that had to be dealt with, and as result a number of investigations were initiated. The term *fatigue* was first used in 1839 by Poncelet in describing failure due to the repeated action of tension and compression. Rankine (1843) observed that the growth of fatigue cracks in axles was an important aspect of the fatigue process. McConnell in England (1849) claimed, probably because of the brittle appearance of the fatigue fracture surfaces he observed, that “a change from fibrous to crystalline character occurred during fatigue,” an unfounded idea that has long appealed to shop mechanics. Fairbairn (1864) carried out fatigue tests on components and was able to propose allowable stresses for bridge structures subject to cyclic loading.

Probably the most influential fatigue research in that era (1858–1870) was carried out by Wöhler, a German railroad engineer. He was the first to carry out extensive fatigue test programs on small test specimens rather than on actual components, and to use both rotating bending and axial loading test methods. He was primarily interested in determining the maximum stress amplitude below which an axle would not fail. Because of his pioneering contributions to the field of fatigue research, plots of stress amplitude versus fatigue life are commonly referred to as *Wöhler’s curves* in Europe. In the United States such plots are known as *S/N curves*.

The exact shape of these *S/N* curves is material dependent, particularly in the high-cycle regime. For low-carbon steels, the *S/N* curves exhibit a well-defined “knee” at about 10^6 cycles, as shown in Fig. 10-1. Beyond the knee the curves are horizontal, and we can speak of a *fatigue limit*. A useful relationship for steels, as indicated in Fig. 10-1, is that the fatigue limit is about one-half of the tensile strength. For most other alloys, however, the knee is absent and the *S/N* curve at high numbers of cycles continues to decline slowly with an increase in the number of cycles to failure, as indicated in Fig. 10-2. For such materials, it is customary to define the

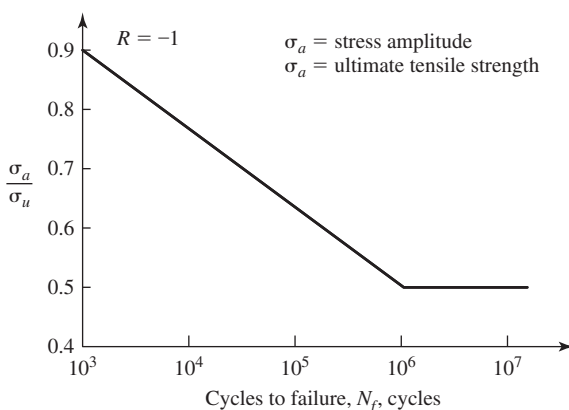


Fig. 10-1. Typical *S/N* behavior for steels.

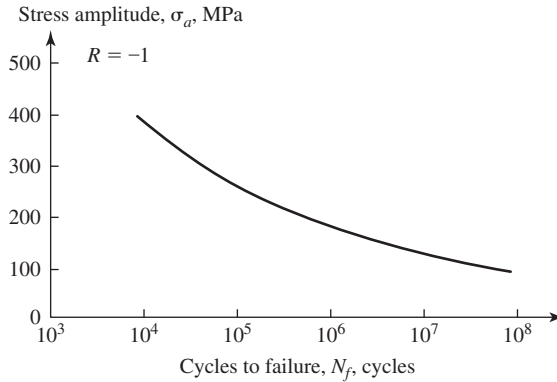


Fig. 10-2. S/N curve for an aluminum alloy.

fatigue strength as the stress amplitude corresponding to a specific number of cycles, often 10^7 . Brown (1) has found that the fatigue strength of face-centered cubic (fcc) alloys is often about one-third of their tensile strength.

Some components will experience huge numbers of fatigue cycles in their lifetimes and, for reliable operation, will be designed such that the stress amplitudes experienced are below the fatigue curve by some margin of safety. Such components are designed for infinite life. However, to design an aircraft structure on such a basis would result in too severe a weight penalty, and such structures where the stress amplitudes are above the fatigue strength are designed for finite life. In such cases, periodic inspections are often warranted to ensure safe operation.

Under variable amplitude loading, certain components may experience stresses, some of which are above and some below the fatigue strength. In such cases, it is not safe to assume that stresses below the fatigue strength do no damage. This is because stresses above the fatigue strength may initiate cracks that are then able to propagate at stress amplitudes that lie below the original fatigue strength.

In addition to S/N curves, cyclic stress-strain curves are of interest. These curves may differ to some extent from the stress-strain curves developed under unidirectional loading conditions. If a cyclic test is carried out under fully reversed total strain conditions, a change in the stress amplitude may be required to attain the given strain limits. That is, the material may undergo cyclic hardening or softening (cold-worked metals soften, annealed metals harden), but with continued cycling a steady-state hysteresis loop may be obtained. If a number of such tests are carried out at increasing strain amplitude and the results are plotted, a line drawn from the origin through each of the points of saturation in the first quadrant will lead to the formation of the cyclic stress-strain curve. Cyclic stress-strain curves are mainly of interest when the plastic amplitude is much larger than the elastic strain amplitude. This is the realm of low-cycle fatigue where fatigue failures occur within 10^3 cycles or so. When the plastic strain amplitude is much less than the elastic strain amplitude, we are in the realm of high-cycle fatigue, and the number of cycles to failure can be 10^6 or more.

III. DESIGN CONSIDERATIONS

The fatigue lifetime is strongly affected by a number of factors, such as the type of loading—for example, bending, axial, multiaxial, or torsion. The presence of a notch or hole will reduce the fatigue resistance, but not simply as a direct function of the notch stress concentration factor; the size of the notch or hole is also a consideration. For example, a plate of steel that contains a hole of 1 mm (0.04 in.) diameter will have a higher fatigue strength than a plate containing a hole of 1 cm (0.4 in.) diameter, despite the fact that in both cases the stress concentration factor is 3.0. Materials in engineering usage are often cyclically loaded in corrosive environments that degrade the fatigue properties. For example, ship propellers and drilling platforms operate in sea water, which accelerates both the crack initiation process and the crack growth process. The term *corrosion fatigue* is used to describe the combined action of cyclic loading and corrosion. A related form of fatigue is known as *fretting corrosion fatigue*, with fretting being due to the relative motion of surfaces under pressure—for example, between a rivet head and the clamped sheet metal in an aircraft structure.

Aircraft turbine blades experience huge numbers of vibratory cycles during their lifetimes; for this reason, there is interest in fatigue at ultra-high cyclic lifetimes, such as 10^{10} cycles. In some of these ultra-high fatigue lifetime studies, it has been observed that for certain steels at high numbers of cycles, a drop in fatigue resistance can occur due to the growth of subsurface fatigue cracks. In assessing the fatigue performance of turbine blades, the possibility of foreign object damage (FOD) due to the ingestion of hard particles into an aircraft turbine engine must be taken into account. The effect of bird strikes on turbine blade performance is another consideration, one that, until recently, precluded the use of composite materials as first-stage turbine blades because of their low resistance to bird-impact damage.

Much of the early testing in fatigue was carried out under fully reversed loading, where the mean stress was zero, as in the case of a railroad car axle. However, components are often cycled about a mean stress other than zero, and the designations R and A are used to describe such loading conditions. These designations are defined as

$$R = \frac{\sigma_{\min}}{\sigma_{\max}} \quad (10-1)$$

and

$$A = \frac{\sigma_a}{\sigma_m} \quad (10-2)$$

where σ_{\min} and σ_{\max} are the minimum and maximum stresses in a loading cycle, respectively, σ_a is the stress amplitude, and σ_m is the mean (average) stress. The stress range $\Delta\sigma$ is equal to $\sigma_{\max} - \sigma_{\min}$. The stress amplitude σ_a is equal to $\Delta\sigma/2$.

For certain components, the value of R may change significantly during use due to changes in the mean stress. For example, consider a point on the lower side of an aircraft wing. While the plane is taxiing on the ground, the mean stress is in compression and R is negative, but in flight the same point is in tension and R is positive.

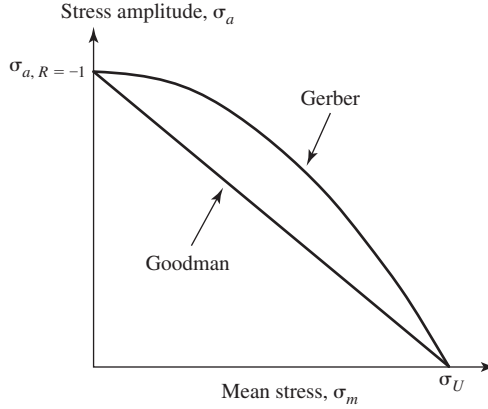


Fig. 10-3. The Goodman and Gerber relations for the prediction of the effect of mean stress on the allowable stress amplitude for a given fatigue life.

Gerber (1873) and Goodman (1899) proposed relationships to deal with the dependence of allowable stress amplitudes on positive mean stresses, and their relationships are depicted in Fig. 10-3. The Gerber relation is parabolic and is given by

$$\sigma_a = \sigma_{a,R=-1} \left[1 - \left(\frac{\sigma_m}{\sigma_U} \right)^2 \right] \quad (10-3)$$

where σ_a is the stress amplitude corresponding to a given lifetime; $\sigma_{a,R=-1}$ is the stress amplitude for a given fatigue lifetime under fully reversed loading, which is known from experiments; σ_m is the mean stress; and σ_U is the ultimate tensile strength. The Goodman relation is linear and is given by

$$\sigma_a = \sigma_{a,R=-1} \left(1 - \frac{\sigma_m}{\sigma_U} \right) \quad (10-4)$$

Alloys differ in their conformity to either of these empirical relationships. Today, such relationships are still important in design, although fracture mechanics considerations are also becoming more widely used as well, as will be discussed.

Two analytical relationships are commonly used in fatigue analyses. One is due to Basquin, who in 1910 proposed that a linear relationship exists between the log of the stress amplitude and the log of the number of cycles to failure, or

$$N_f = C\sigma_a^{-g} \quad (10-5)$$

where C and g are constants and σ_a is the stress amplitude. The other relationship is due to Coffin and Manson, who in the 1950s independently proposed that the log of the plastic strain range, $\Delta\epsilon_p$, is linearly related to the log of the number of cycles to

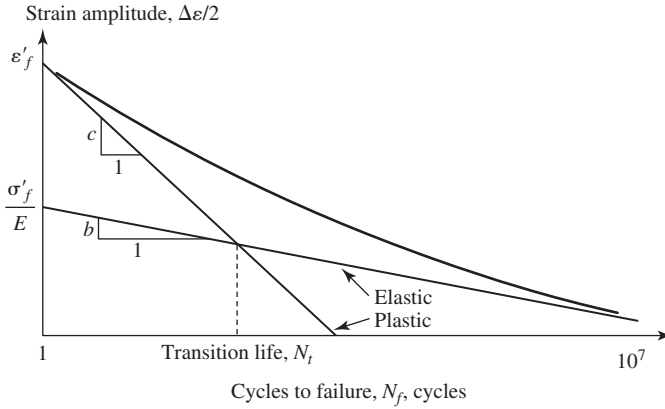


Fig. 10-4. The log of the number of cycles to failure as a function of logs of the elastic, plastic, and total strain amplitudes, where b and c are, respectively, the slopes of the elastic and plastic components of the total strain versus the number of cycles to failure.

failure, or

$$N_f = D(\Delta\varepsilon_p)^{-d} \quad (10-6)$$

where D and d are constants. This is an important relationship for cases in which the plastic strain amplitude is large with respect to the elastic strain amplitude, that is, the low-cycle fatigue regime.

A strain-life curve for fully reversed strain is shown in Fig. 10-4. The Coffin-Manson and Basquin relationships plot as straight lines as a function of either the elastic or plastic component of strain in Fig. 10-4. That is,

$$\frac{\Delta\varepsilon_p}{2} = \varepsilon'_f (N_f)^c \quad (10-7)$$

and

$$\frac{\Delta\varepsilon_e}{2} = \frac{\sigma'_f}{E} (N_f)^b \quad (10-8)$$

where the empirical constants are σ'_f , the fatigue strength coefficient; ε'_f , the fatigue ductility coefficient; b , the fatigue strength exponent; and c , the fatigue ductility exponent.

The fatigue life where the two straight lines cross is known as the *transition life*. At this life, the plastic strain amplitude is equal to the elastic strain amplitude, and it can be considered that fatigue lives to the left of the intersection represent the low-cycle fatigue range, and fatigue lives to the right of the intersection represent the high-cycle fatigue range. The transition life can be obtained by setting the elastic and plastic strains in the above equations equal to each other and solving for N_t to obtain

$$N_t = \left(\frac{\varepsilon'_f E}{\sigma'_f} \right)^{1/(b-c)} \quad (10-9)$$

The principal variables are ε'_f and σ'_f . As ε'_f increases σ'_f usually decreases, with the result that the value of N_f is much higher for low-strength alloys (perhaps 10^5 cycles) than for high-strength alloys (perhaps 10 cycles).

In using either the Basquin relation or the Coffin-Manson relation for calculating the fatigue life, the average fatigue life is considered. In designing to allow for scatter in fatigue strength, for corrosion, and for in-service surface damage, the design allowable stress for a critical part, such as an aircraft propeller, may be a small fraction of the smooth bar average fatigue strength. The determination of such low design allowables has often stemmed from experience more than from analysis.

Components in service are generally subjected to variable amplitude loading rather than the constant amplitude loading used to generate S/N curves, and the Palmgren-Miner Law is used to make an approximate prediction of the fatigue lifetime under variable amplitude loading conditions. The law is referred to as a *linear damage summation rule* and is expressed as

$$\sum_{i=1}^m \frac{n_i}{N_{fi}} = 1 \quad (10-10)$$

where n_i is the number of cycles applied at the i th loading level, N_{fi} is the number of cycles to failure at that level, and m is the number of load levels. This law is used in estimating the fatigue life where not only the stress amplitude varies but the mean stress does as well. An example would be the case of aircraft structures, which experience repeated ground-air-ground (GAG) cycles associated with takeoff, cruising, and landing. In such a GAG cycle, the mean stresses vary significantly, as do the loads resulting from maneuvers, wind gusts, and accelerations.

Jet aircraft engine components, such as the disks into which the turbine blades are inserted, are subjected to a type of cyclic loading known as *thermal-mechanical fatigue* (TMF). During engine startup, the temperature at the surface of a disk increases more rapidly than does that of the interior of the disk. As a result, a compressive stress is developed in the surface, and compressive plastic strains can result. On shutdown, the reverse situation can develop, with tensile stresses being developed in the surface of the disk. It is possible for these cyclic stresses and strains to result in low-cycle fatigue crack initiation in the disk, with possible disastrous consequences, unless the disks are carefully inspected at appropriate intervals.

In dealing with notches and their effect on fatigue, a relation due to Neuber (2) is often used. The relation is

$$K_T^2 = K_\sigma K_\varepsilon \quad (10-11)$$

This relation states that the square of the stress concentration factor, K_T , is equal to the product of the stress concentration factor, K_σ , defined as $\sigma_{loc}/\sigma_{app}$, times the strain concentration factor, K_ε , defined as $\varepsilon_{loc}/\varepsilon_{app}$, where the subscripts refer to the local conditions at the notch and to the applied loading conditions, respectively. This relation was derived for Mode III loading in the elastic-plastic range but has been used for other modes of loading as well. This relationship is obviously true in the

elastic range, but it also appears to hold reasonably well for cases where the material at the tip of a notch is in the plastic range as well, for when plastic deformation occurs at a notch under a continuously rising load, the stress concentration factor will decrease and the strain concentration factor will increase. For applied stress within the elastic range, the Neuber relation can be written as

$$K_T^2 = \frac{\sigma_{loc}}{\sigma_{app}} \frac{\varepsilon_{loc}}{\varepsilon_{app}} = \frac{\sigma_{loc}\varepsilon_{loc}}{\sigma_{app}^2/E}$$

or

$$K_T\sigma_{app} = \sqrt{E\sigma_{loc}\varepsilon_{loc}} \quad (10-12)$$

The last of these equations is used as follows. Unnotched specimens are cycled to failure at different strain amplitudes under fully reversed strain conditions, the cyclic amplitude stress associated with each strain amplitude is noted, and the square root quantity on the right-hand side of the equation is calculated. Then it is assumed that when the magnitude on the left-hand side equals the magnitude on the right-hand side, both sides of the equation represent equal fatigue lifetimes. On this basis, fatigue data obtained with unnotched specimens can be used to estimate the fatigue life for a notched specimen of any K_T value. However, as mentioned above, it is observed in fatigue testing that K_f , the stress concentration factor determined under cyclic loading conditions, is less than K_T , the theoretical stress concentration factor. This effect has been attributed to the crack length emanating from the stress raiser and to crack closure (3). To account for it, empirical expressions such as the following, which is also based upon Neuber's (4) work, have been used:

$$K_f = 1 + \frac{K_T - 1}{1 + \sqrt{\rho'/\rho}} \quad (10-13)$$

where ρ' is considered to be a material constant, which in the case of steel decreases in magnitude with an increase in tensile strength.

A design procedure that has been developed by the Japanese Society of Mechanical Engineers (5, 6) takes into account the effect of the part geometry and the tensile strength level in determining the fatigue strength, σ_w , of a component. The basic equation is

$$\sigma_w = \frac{\sigma_{w0}\zeta_s}{\beta} \quad (10-14)$$

where σ_{w0} is the fatigue strength of a polished specimen, ζ_s is an empirically determined fatigue strength reduction factor for surface finish and material, and β is determined with the aid of a design chart. For example, consider the bending of a shaft with a shoulder. To use the design chart for this case, Fig. 10-5, information is needed on: the tensile strength of the material, σ_U ; the diameter of the shoulder, D ; the diameter of the shaft, d ; and the radius of the transition from shaft to shoulder, ρ . Let us assume a tensile strength of 50 kgf/mm² (490 MPa), $D = 50$ mm, $d = 25$ mm, and $\rho = 2.5$ mm. Therefore, $d/\rho = 10$, and $1 - d/D = 0.5$.

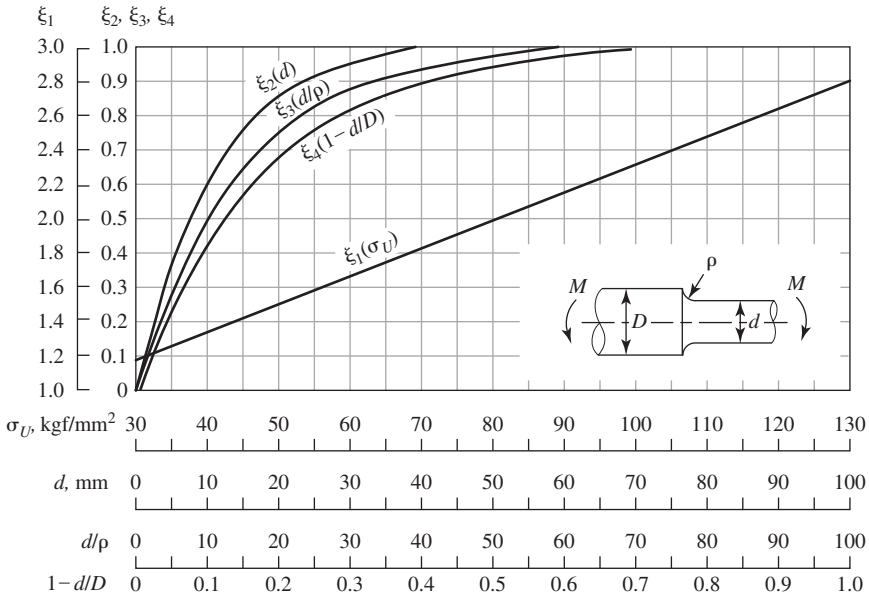


Fig. 10-5. The notch factor for a steel shaft with a shoulder in bending as a function of the tensile strength, σ_U , the major and minor diameters, and the transition radius, ρ . (After Nishida 6, based on *Design Handbook for the Fatigue Strength of Metals*, 5.)

From the chart, $\xi_1 = 1.45$, $\xi_2 = 0.92$, $\xi_3 = 0.48$, and $\xi_4 = 0.93$. The notch factor β is defined as

$$\beta = 1 + \xi_1 \xi_2 \xi_3 \xi_4 = 1 + 1.45 \times 0.92 \times 0.48 \times 0.93 = 1.60 \quad (10-15)$$

Therefore, the fatigue strength of the shaft is estimated to be $0.625\sigma_{w0}\zeta_s$. σ_{w0} can be estimated to be one-half of the tensile strength, so that $\sigma_w = 15.6 \text{ kgf/mm}^2 (153 \text{ MPa}) \times \zeta_s$. Additional design charts are available to cover other geometries and loading conditions.

Although design analysis precedes the manufacture of a fatigue-critical component, fatigue testing is an important part of the certification process, as in the case of aircraft. For the Boeing 717, parts were tested under simulated in-service loading (spectrum loading) to five times the planned number of operational cycles (7). The fatigue testing of components is an essential part of vehicle development in the ground transportation industry as well. In the case of a part that has failed in service, it may be possible to carry out an analysis to determine why the part did not have the requisite strength to sustain the applied loads.

It is of interest to see how knowledge of fatigue is used in the development of design rules. Albrecht and Wright (8) have reviewed the procedures used in the design of welded steel bridges against fatigue. For each of eight different types of weld detail, a basic S/N plot is constructed that consists of two straight lines on a

log-log plot. The finite-life line is drawn through the data points at a slope of $1/3$. This line intersects a horizontal line representing the fatigue limit at what is referred to as the *transition life*. The design curve in the finite-life range is set at two standard deviations to the left of the mean S/N line, and the design fatigue limit is set at one-half of the constant-amplitude fatigue limit to account for variable-amplitude loading, since if cracks are nucleated at stresses above the fatigue limit, then stresses applied below the fatigue limit are significant. The standard deviation ranges from 0.221 for plain rolled I beams to 0.101 for cover plates welded to the flange of an I beam, and the transition lives range from 14×10^6 to 180×10^6 cycles, depending upon the detail.

IV. MECHANISMS OF FATIGUE

A. The Initiation of Fatigue Cracks

From 1850 to 1950, very little work was done to establish the mechanism(s) of fatigue crack initiation, the development of Wöhler curves being of paramount interest. However, there were some exceptions. For example, Ewing and Humphrey in 1903 used a light microscope to observe the slip bands that formed in iron under either unidirectional loading or cyclic loading conditions. They found that under cyclic loading the slip bands widened and, more importantly, fatigue cracks were initiated within these slip bands. In the 1920s, Gough showed that plastic deformation was an essential part of the crack nucleation process, and also that the environment influenced the process of crack initiation.

From the 1950s to the 1980s, a number of factors came together to spur interest in fatigue crack initiation, such as the advent of the transmission and scanning electron microscopes. In 1958 Wood (9) used taper sectioning to magnify the profile of fatigue slip bands. In this procedure, a flat specimen containing fatigue slip bands is sectioned in the loading direction along a plane whose normal is about 10° from the normal to the specimen surface. This procedure in effect magnifies the size of slip band features only in the direction of the taper. Wood observed that the fatigue slip bands had a notch-peak topography and that cracks were initiated at the notches, and his observations formed the basis for one mechanism of fatigue crack initiation. Figure 10-6 is a taper section transverse to the direction of loading of a 3% Si-Fe specimen which had been subjected to cyclic loading. Many extrusions are seen, and fatigue cracks as well. The cracks initiate at re-entrant corners of the extrusions and also where two extrusions happen to meet. These sites are stress concentrators which evidently promote the initiation of fatigue cracks. It is noted that there is no evidence of an intrusion, which is considered to be the counterpart of an extrusion. A 3% Si-Fe alloy is a planar slip material, meaning that the slip lines tend to be quite straight and cross slip is difficult. Materials such as copper and iron, are examples of materials in which wavy slip lines occur and cross slip is easy.

Another mechanism for fatigue crack nucleation involves what are known as *persistent slip bands*, *dislocation annihilation*, and *vacancies*. Slip bands that

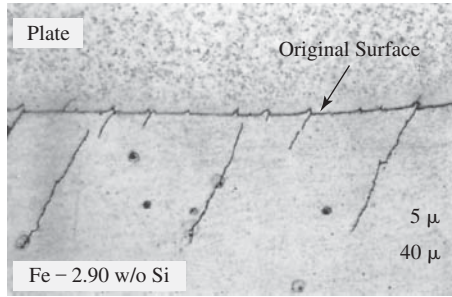


Fig. 10-6. Fatigue crack initiation at extrusions in a 3% Si-Fe alloy, as seen in a taper section. (After Boettner and McEvily, 10.)

reappear after surface polishing and recycling are known as *persistent slip bands* (PSBs). Transmission electron microscopy has shown that beneath the surface these bands are ladder-like in appearance, with few dislocations between the rungs of the ladder. It has been proposed that the annihilation of edge dislocations within these bands leads to the formation of vacancies, which in turn cause an expansion within the bands and the formation of surface fatigue slip bands (11). Fatigue cracks are formed at the surface along the intersection of the PSB with the matrix.

In commercial alloys, in contrast to the pure metals described above, crack initiation often occurs at inclusions and pores.

B. Fatigue Crack Closure

B.1. Overview According to ASTM E 647, the Standard Test Method for Measurement of Fatigue Crack Growth Rates (12), the term *crack closure* refers to the phenomenon whereby the fracture surfaces of a fatigue crack come into contact during the unloading portion of a force cycle and force is transferred across the crack. In many materials, crack closure can occur while the force is above the minimum force in the cycle even when the minimum force is tensile. Upon reloading from the minimum force, some increment of tensile loading must be applied before the crack is fully open. It is also noted that ASTM STPs 982 (13) and 1343 (14) provide excellent overviews of the subject of fatigue crack closure.

In 1970, Elber (15) showed that crack closure had an important influence on fatigue crack growth behavior. By means of experiments with the aluminum alloy 2024-T3 ($\sigma_Y = 350$ MPa), Elber demonstrated that at a given R value, the crack opening level increased with ΔK , where ΔK is the range of the stress intensity factor in a loading cycle and R is the ratio of the minimum stress to the maximum stress in a loading cycle. Elber showed that only the portion of a loading cycle above the crack-opening level was effective in propagating a fatigue crack.

Similar results have been obtained with other low- and medium-strength aluminum alloys—for example, 6061-T6 ($\sigma_Y = 276$ MPa), Fig. 10-7. This type of crack closure is referred to as *plasticity-induced fatigue crack closure* (PIFCC), and Elber

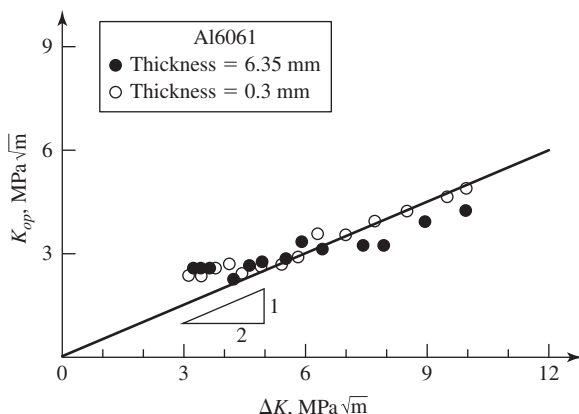


Fig. 10-7. K_{op} versus a ΔK plot of a 6061 aluminum alloy for two compact tension (CT) specimen thickness. (After Ishihara et al., 17.)

proposed that PIFCC was due to the residual stretch of material in the wake of the crack tip. Budiansky and Hutchinson (16) have provided a mathematical analysis of plasticity-induced crack closure that is consistent with Elber's interpretation. However, higher-strength aluminum alloys may not exhibit PIFCC—for example, 7090-T6 ($\sigma_Y = 650$ MPa) and IN9021-T4 ($\sigma_Y = 530$ MPa) (18).

Soon after Elber's initial studies, other forms of crack closure were found, including a type of material-related crack closure now known as *roughness-induced fatigue crack closure* (RIFCC). This type of crack closure occurs as the result of asperity contact on the opposing surfaces of a fatigue crack. In RIFCC the crack opening level is constant and independent of ΔK , in contrast to PIFCC. An example of this type of RIFCC is shown in Fig. 10-8 for a 6 mm (0.24 in.) thick 9Cr-1Mo steel specimen ($\sigma_Y = 530$ MPa, [77 ksi]). Here the K_{op} level, the stress intensity factor at the crack opening level, is approximately $2.5 \text{ MPa}\sqrt{\text{m}}$ ($2.3 \text{ ksi}\sqrt{\text{in.}}$).

Another form of crack closure is known as *oxide-induced crack closure*. This form of closure is particularly important for carbon steels at elevated temperatures when thick oxides form on the fracture surfaces. It is also noted that the effect of crack closure on the rate of fatigue crack growth is most pronounced in the near-threshold range at low R levels.

Elber introduced the concept of an effective range of the stress intensity factor ΔK_{eff} that is defined as

$$\Delta K_{eff} = K_{\max} - K_{op} \quad (10-16)$$

where K_{op} is the stress intensity factor at the crack opening level. For 2024-T3, he proposed that ΔK_{eff} be given by the following equation:

$$\Delta K_{eff} = (0.5 + 0.4R)\Delta K \quad (10-17)$$

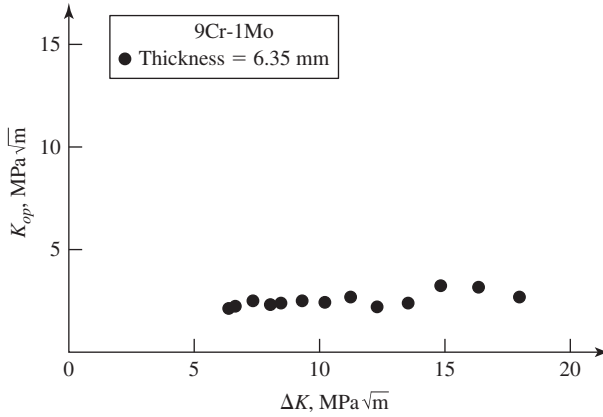


Fig. 10-8. K_{op} versus a ΔK plot of 9Cr-1Mo steel. (After Ishihara et al., 17.)

Although there has been much research on crack closure, it appears that the reason why some aluminum alloys exhibit PIFCC while steels exhibit RIFCC has not yet been made clear, although it has been suggested (19, 20) that factors influencing the crack tip opening displacement (CTOD) may be of importance. The expression for the CTOD under plane stress conditions is

$$CTOD = \frac{\Delta K_{eff}^2}{\sigma_y E} \quad (10-18)$$

Aluminum alloys, with their relatively low Young's modulus as compared to steel, will have a CTOD three times larger than that of steel of the same yield stress level, meaning that there will be a much larger plastic stretch at the surface and a higher degree of PIFCC in the plane stress region than at the surface of steel. It also follows that if PIFCC is surface related, then machining away the surface layers should reduce the PIFCC level. No such effect would be expected for RIFCC. For PIFCC it is also to be expected that as the thickness of a compact specimen is increased, the fatigue crack growth rate will also increase as the relative importance of PIFCC decreases. No such thickness effect will be expected in the case of RIFCC.

B.2. Effect of Surface Removal In previous work (21) that involved the effect of an overload on subsequent fatigue crack growth behavior, it was shown that the removal of 0.5 mm (0.02 in.) from each surface of a compact specimen immediately following the overload resulted in the elimination of much of the effect of the overload. It was therefore concluded that the retardation due to an overload was largely due to an enhanced level of surface-related PIFCC as the result of the overload. In the present study, we have repeated this type of surface-removal experiment, but without any overload being involved.

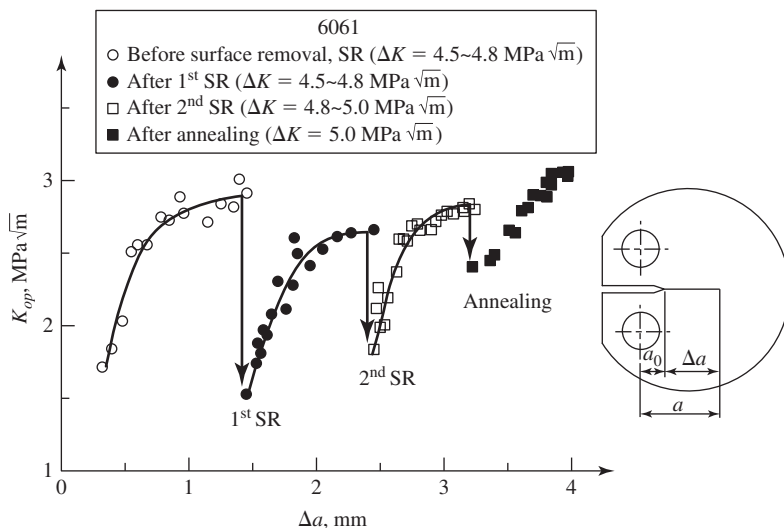


Fig. 10-9. Effect of surface removal (SR) on 6061. (After Ishihara et al., 17.)

Figure 10-9 shows the effect of surface removal on the crack opening level of 6061. The specimen had been tested at a ΔK level of 4.5 to 5.0 $\text{MPa}\sqrt{\text{m}}$. During each surface removal step, 0.5 mm (0.02 in.) was removed from each specimen surface by electro-discharge machining, after which the surfaces were electropolished. These results show a marked effect of surface removal on the crack opening level of 6061, and indicate that the crack closure level at the surface was at least 1 $\text{MPa}\sqrt{\text{m}}$ higher than that of the interior crack opening level. Since 6061 exhibits PIFCC (22), we conclude that the plane-stress plastic zone at the specimen surface is an important factor in PIFCC. It is noted that annealing at 673K for 0.5 hour resulted in a decrease in the surface crack opening level. This effect may be due to compression creep in the contact areas in the surface region.

Figure 10-10 shows the effect of stepwise removal by electro-polishing of about $30\mu\text{m}$ in each step from each specimen face of a 6 mm (0.24 in.) thick 6061 specimen that had been cycled at a ΔK of 5 $\text{MPa}\sqrt{\text{m}}$. After $300\mu\text{m}$ of material had been removed from each the surface, PIFCC was eliminated and only RIFCC remained. The K_{op} level for RIFCC was 1.5 $\text{MPa}\sqrt{\text{m}}$, about half of the PIFCC level.

Figure 10-11 shows the effect of surface removal on the K_{op} level for S25C that had been cycled at 11 $\text{MPa}\sqrt{\text{m}}$. Characteristic of RIFCC, surface removal has little if any effect on the K_{op} level as determined by the strain gauge method. However, previous work (23) using the replica technique has shown that even in the case of RIFCC, there is a small amount of PIFCC at the surface that is not detected by the strain gauge technique.

B.3. Effect of Crack Wake Removal In these experiments, a fatigue crack was grown at a ΔK level of 6.3 $\text{MPa}\sqrt{\text{m}}$ in 6061-T6 and at 11 $\text{MPa}\sqrt{\text{m}}$ in S25C.

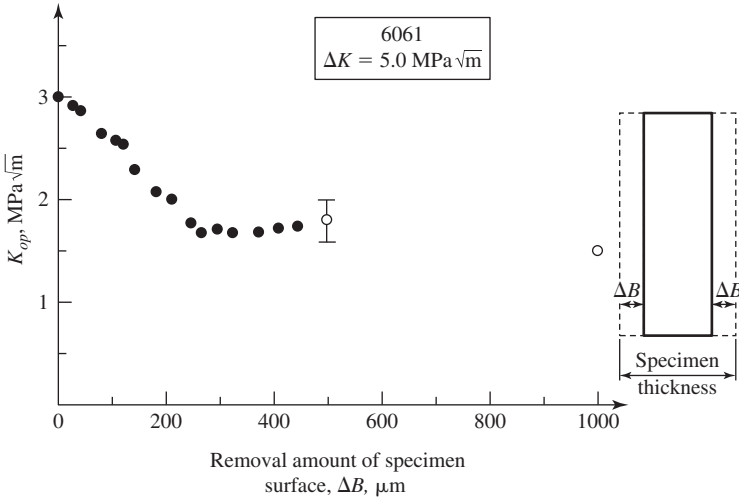


Fig. 10-10. Effect of stepwise surface removal on the K_{op} level in 6061. (After Ishihara et al., 17.)

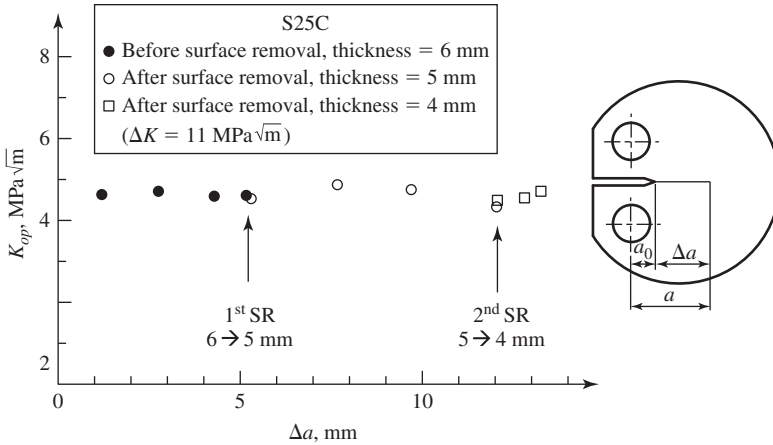


Fig. 10-11. Effect of surface removal (SR) on S25C. (After Ishihara et al., 17.)

The crack wake was then removed in steps to determine the K_{op} level, a function of distance from the crack tip. (This procedure is the reverse of the procedure in which crack closure was developed as an initially closure-free crack grew.)

As seen in Fig. 10-12, the value of K_{op} can be fitted with the following equation:

$$K_{op} = (1 - e^{-k\lambda})(K_{op\max} - K_{\min}) + K_{\min} \quad (10-19)$$

where K_{op} is the transient value of the opening level, k is a material constant that governs the rate of crack closure development, λ is the distance in this case measured

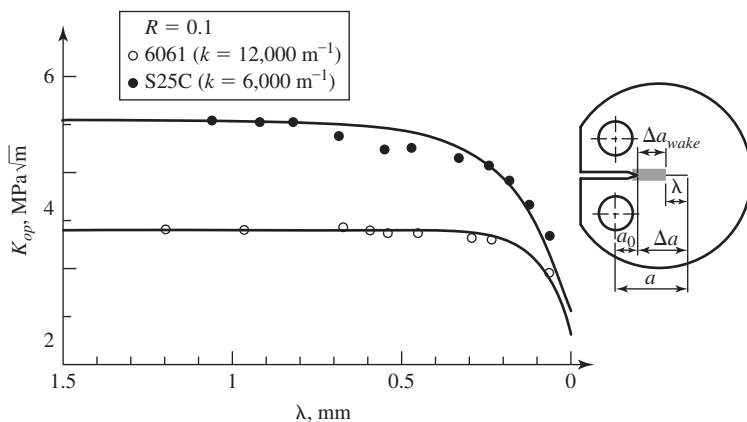


Fig. 10-12. The effect of wake removal on K_{op} ; the curves are in accord with Eq. 10-19. (After Ishihara et al., 17.)

back from the crack tip, and $K_{op\max}$ is the crack opening level associated with a crack of macroscopic length. It is noted that the values for k of $12,000 \text{ m}^{-1}$ for 6061 and $6,000 \text{ m}^{-1}$ for S25C are consistent with values obtained in prior investigations (24, 25) that were obtained under increasing λ conditions. The wake removal procedure provides an alternative means for the determination of the magnitude of the material constant k .

We note that K_{op} is the integral of the effects of crack closure between the crack tip and the λ value at which K_{op} is determined. K_{op} does not increase with an increase in λ beyond the point at which $K_{op\max}$ is reached. That is, due to the wedging effect of the crack closure developed up to the point of $K_{op\max}$ the opposing crack surfaces do not make contact beyond the λ value associated with $K_{op\max}$. During the uploading process, as load is applied, the crack begins to open at a λ value corresponding to the λ value at which $K_{op\max}$ is developed. As the load continues to increase, the value of λ continues to decrease until the crack tip itself is open at a ΔK value corresponding to $K_{op\max}$. During unloading, this process is reversed.

Fatigue striations range in spacing from 0.1 to $10 \mu\text{m}$. They are created cycle by cycle at the crack tip in the plane-strain region by localized crack tip opening and closing plastic deformation processes at ΔK levels above K_{op} . Therefore, crack closure is not involved in the process of striation formation.

C. The Propagation of Fatigue Cracks

In the 1950s, it was thought that cracks initiated early in life in the low-cycle fatigue range but very late in life in the high-cycle fatigue range. Today, mainly as the result of Ishihara's studies (26), we know that even in the high-cycle range cracks are initiated early in life, that is, in less than 10% of the total life. Ishihara used a replica technique in making this finding. In this procedure, a test fatigue specimen is carefully polished, and a replica is made of the test section by taking a thin cellulose

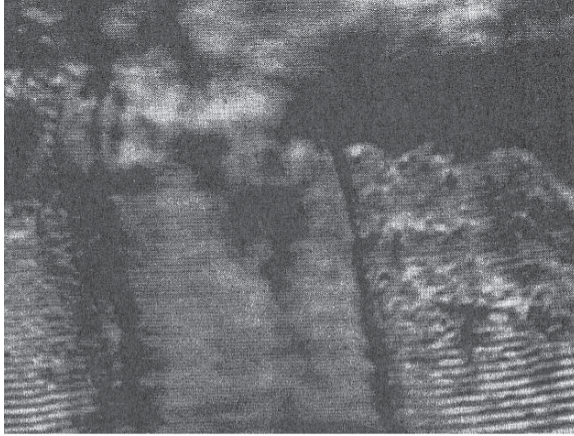


Fig. 10-13. A first micrograph of fatigue striations (7075-T6 aluminum alloy). (From Zapffe and Worden, 27, with permission of ASM International[®]. All rights reserved.)

acetate sheet, moistening one surface with acetone, and then pressing the sheet to the specimen surface. When the sheet is dry, it is removed and set aside. Then the specimen is cycled for some number of cycles and a second replica is made and examined. This procedure is repeated at an increasing total number of cycles until a crack is finally identified on a replica. Then the preceding replicas are examined in reverse order at the crack site to find how early in life a crack can be identified. In general, it has been found that a $10\text{ }\mu\text{m}$ crack forms in less than 10% of the total fatigue lifetime. This means that most of the fatigue lifetime is spent in fatigue crack propagation, not initiation. Therefore, the process of propagation is of great interest.

The study of fatigue crack propagation was given a huge boost by the finding of unique markings, now known as *striations*, on a fatigue fracture surface by Zapffe and Worden (27) in 1951. Figure 10-13 provides an example of these striations as seen with a light microscope. (Zapffe also coined the term *fractography*, meaning the study of fracture surfaces.) Research was quickly directed at finding the mechanism of striation formation and at determining whether or not a fatigue crack advanced in each cycle. Another goal was to be able to express the rate of fatigue crack growth per cycle in terms of the controlling parameters.

Forsyth and Ryder (28) answered the question of whether or not a fatigue crack advanced in each cycle using the following experiment. They grew a fatigue crack in an aluminum alloy under constant-amplitude conditions. Then they applied five cycles of higher amplitude before returning to the constant-amplitude level. Upon examination of the fracture surface, they observed five distinct striations whose spacing was larger than that of the constant-amplitude loading. Clearly, the crack had advanced in each loading cycle.

Laird and Smith (29) showed that a fatigue crack advanced in a stable fashion by crack tip bunting (opening) and crack advance in the loading portion of a cycle, and by crack resharpener (closing) in the unloading portion of a cycle.

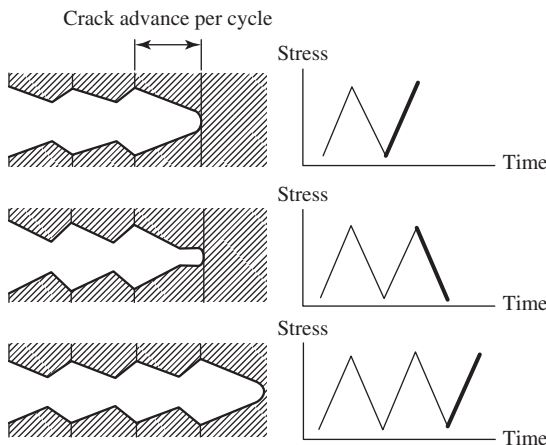


Fig. 10-14. Sawtooth striations created in the crack propagation sequence. (After McMillan and Pelloux, 30.)

McMillan and Pelloux (30) used stereo viewing in a scanning electron microscope to provide detailed information about the mechanism of striation formation. Their model of the process is shown in Fig. 10-14. The fatigue crack blunts and advances during the loading portion of the cycle but closes only over a portion of the advance during unloading. During the next cycle, the blunting of the tip causes a rotation of the closed portion and the formation of a striation. Such striations are known as *staircase striations*. The height of a striation is related to the crack growth rate. For example, in low-carbon steels, below a growth rate of about $0.1 \mu\text{m}$ per cycle, striations may not be resolvable. For most ductile alloys, they are observed at growth rates between 0.1 and $10 \mu\text{m}$ per cycle. Above this range other modes of separation, known as *static modes*, occur prior to final separation.

An interesting characteristic of striations is that they are not present if the fatigue crack growth test is conducted in vacuum. It has been observed (31) that for Type 304 stainless steel, the CTOD in vacuum is some 50 times larger than in air, with the result that the striation created in the previous cycle is swept into the flanks of the blunted crack tip region in the next cycle and eliminated.

V. FACTORS AFFECTING FATIGUE CRACK INITIATION

A. Surface Roughness

As mentioned above, plastic deformation is essential to the nucleation and growth of fatigue cracks. Anything that promotes plastic deformation will decrease the fatigue resistance of a material. The surface is the region at which fatigue cracks usually initiate, although when the surface is harder than the interior, subsurface

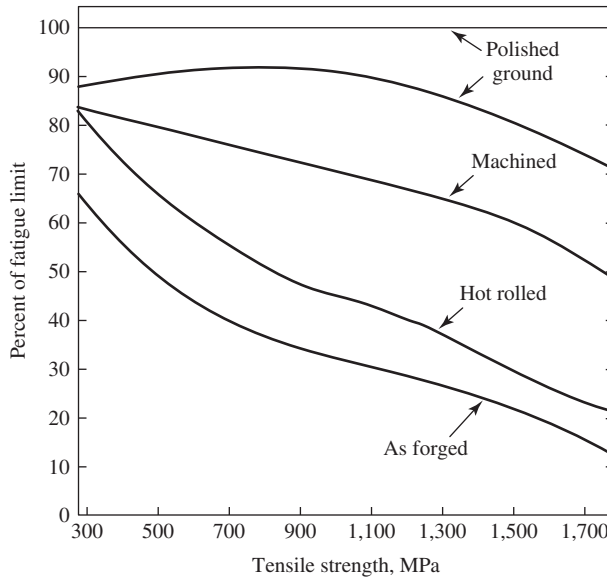


Fig. 10-15. The effect of surface finish on the fatigue knockdown factor as a function of tensile strength. (After Juvinall, 32.)

fatigue cracks may initiate. Stress concentrators such as notches and corrosion pits will degrade fatigue resistance. The handbook values for fatigue strength are generally given for highly polished specimens tested under fully reversed loading conditions ($R = -1$). Care should therefore be used in applying these values to actual components. The degree of surface roughness, which is a function of the machining or processing method, will be a factor, since roughness acts as a stress concentrator. Figure 10-15 indicates how the surface finish varies as a function of the mode of processing, affecting the fatigue strength (32).

B. Carburization

The decarburization that occurs during the hot-forging of a steel will lead to a soft surface layer in which resistance to plastic deformation is reduced, with a corresponding decrease in fatigue strength. An increase in strength properties may increase fatigue strength, at least in steel, where it is observed that the endurance limit is one-half of the tensile strength. However, in high-strength aluminum alloys, this is not the case, that is, fatigue strength does not increase with tensile strength but can be rather insensitive to the strength level. The behavior of aluminum alloys indicates that, despite a high strength level, local soft spots exist in the microstructure that permit plastic deformation at relatively low stress levels. Compressive residual surface stresses are useful in preventing the development of fatigue cracks. On the other hand, tensile residual surface stresses are to be avoided.

C. Shot Peening

Shot peening is used as a means to remove brittle oxide scales that form on steel during heat treatment, but Almen at General Motors (33) noted that shot peening also improved fatigue resistance by imparting a residual compressive stress to the peened surface. The shot peening process involves the use of a stream of metal or glass shot of a selected size, moving at a chosen velocity and impinging upon the surface being treated. The peening conditions are standardized by means of test strips (Almen strips). Shot peening a thin strip leaves the shot-peened surface in compression, the midportion of the strip in tension, and, so that there be no net moment, the surface opposite to the peened surface in compression. This state of stress leads to a curvature of the strip, as in the bending of a beam, such that, if the peening is from above, the strip adopts a convex upward shape, that is, it rises in the Almen test. During a check calibration, the Almen strips are peened and the height of the strip as a function of time is noted. After some time, the height will not change significantly. If the height differs from that specified, the peening conditions are altered accordingly.

It should be noted that shot peening has a beneficial effect on torsional fatigue strength (34).

D. Environments

The environment can have a strong effect on fatigue behavior, as shown in Fig. 10-16. Corrosion has two effects: (a) it can lead to the formation of corrosion pits, stress

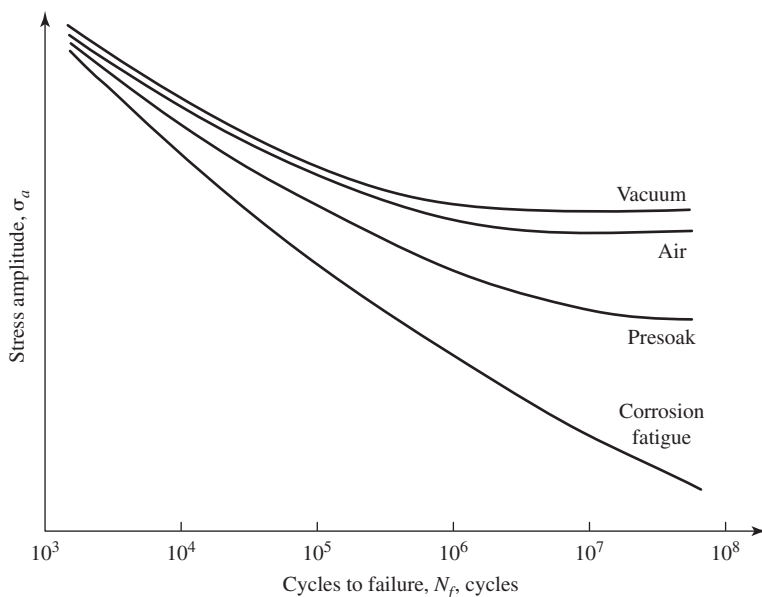


Fig. 10-16. Effect of various environments on the S/N curve of a steel. (After Fuchs and Stephens, 36.)

raisers that degrade the fatigue resistance of a material, and (b) it accelerates the crack propagation process. These corrosion processes are of particular concern with respect to aging aircraft. A review of the current understanding of pitting corrosion and corrosion fatigue in aluminum airframe alloys has been presented by Wei and Harlow (35).

VI. FACTORS AFFECTING FATIGUE CRACK GROWTH

A number of factors can affect the rate of fatigue crack growth. Among these are the deleterious effect of the environment; the application of overloads, which can retard the rate of fatigue crack growth; and the application of underloads, which can accelerate the rate of fatigue crack growth. Figure 10-17 schematically indicates the formation of a fatigue crack within a slip band at the surface and its subsequent propagation under cyclic tensile loading. In clean material, the initial crack propagates along a slip plane within the slip band and is referred to as a *Stage I* crack. At some point, usually within the first grain or two, the crack will change orientation and begin *Stage II (Mode I)* propagation in a direction perpendicular to the principal tensile stress. In material containing inclusions, a crack may initiate at an inclusion, and the slip band process of initiation may be bypassed. In calculations of the fatigue life, the cycles spent in crack initiation are sometimes neglected, and the lifetime is computed on the basis of the growth of micron-sized cracks to a critical size for failure in Mode I.

In the ultra-long life fatigue regime of steels, that is, 10^6 – 10^9 cycles to failure, fatigue cracks can originate at subsurface inclusions rather than at the surface. Of particular concern is that these ultra-high-cycle fatigue failures can occur at stresses

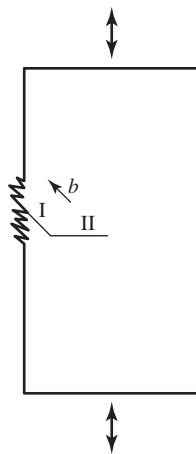


Fig. 10-17. A schematic diagram of Stage I and Stage II fatigue crack growth. (b is the Burgers vector.)

below the nominal fatigue limit (37). In some cases, subsurface cracking occurs because the surface had been strengthened by residual compressive stresses due to shot peening, heat treatment, machining, a protective oxide, and so on. In other cases, the stress-raising effect of the largest subsurface inclusion within the most highly stressed volume may lead to subsurface crack nucleation, particularly in axial loading. Small amounts of bainite within a martensitic matrix have also led to subsurface fatigue crack formation (38).

In the case of an inclusion-nucleated subsurface fatigue crack, optical examination of the region immediately adjacent to the inclusion has revealed the presence of a faceted, optically dark area (ODA) (38). The ODA can vary in radial extent from a few microns to as large as 50 μm , increasing in size the longer the fatigue lifetime. Secondary ion mass spectroscopy (SIMS) has shown that hydrogen is present in the ODA, and the initiation of the fatigue crack is thought to be promoted by hydrogen that had segregated to the inclusion. The fact that the ODA increases in size with an increase in fatigue lifetime indicates that the hydrogen was able to diffuse along with the crack and promoted crack growth at the lowest crack growth rates. As the fatigue crack propagates beyond the ODA while still subsurface, it propagates in vacuum without the aid of hydrogen, and the optical image becomes relatively bright. However, once the crack penetrates through to the surface, it propagates in air and the optical image darkens. The overall effect that is created is known as a *fish-eye*, Figs. 10-18 and 10-19. In Fig. 10-18, a subsurface crack grew to the surface before fracture occurred. In Fig. 10-19, the fatigue crack was still a subsurface crack when fracture occurred. The change from a dark (ODA) to a light and then to a dark optical appearance is due to changes in fracture surface roughness. The fracture surface is rough in the ODA but much smoother in the surrounding optically bright area. It then

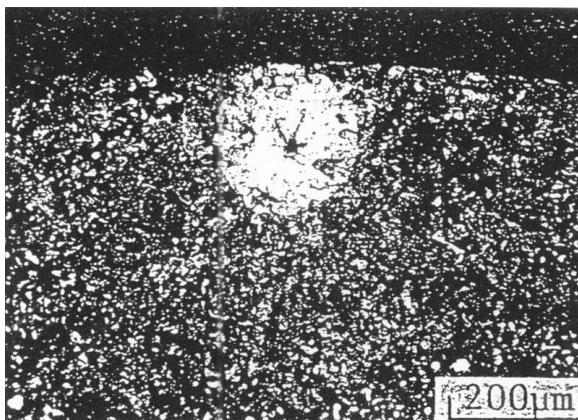


Fig. 10-18. An example of a fish-eye fracture in SAE 9254 steel. (From Murakami et al., 39. Originally published in ISIJ International.)

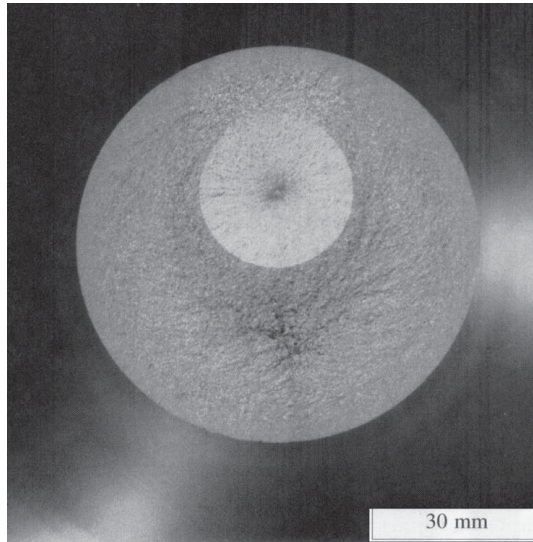


Fig. 10-19. A complete subsurface fish-eye fracture. (Courtesy of Y. Murakami.)

becomes rough again if the crack has penetrated to the surface. The fatigue crack propagation process involves the opening and closing of the crack tip in each loading cycle. The rough appearance created in air is due to the fracturing of the oxide at the crack tip at different levels around the periphery of the crack front during the loading portion of a fatigue cycle. In vacuum, the crack advance along the crack front is much more coplanar, and an optically bright region results. It is also noted that similar differences in roughness occur, for example, in elevated-temperature fatigue tests conducted in either air or vacuum.

Figure 10-20 provides examples of fatigue striations that are created during fatigue crack propagation. These markings are most easily observed in ductile metals and may be difficult to observe in high-strength alloys of limited ductility. They are created on a cycle-by-cycle basis and are usually observed at crack growth rates ranging from $0.1\text{ }\mu\text{m}$ per cycle up to more than $10\text{ }\mu\text{m}$ per cycle. The striations often have a staircase profile, which is created in the manner shown in Fig. 10-21. Their presence or absence may be critical in deciding the nature of a fracture. When striations are present on a fracture surface, they can at times be used to trace the loading history of the failed part. For example, in the fatigue failure of a support beam for a wing landing flap, the fatigue crack initiated at a bolt hole, and striations were observed to be in pairs. The flap beam saw two dominant loads in each flight, a high load during landing (flap out) and a lower load during takeoff (flap partially out), and the width of the striation spacing created on landing was twice that created on takeoff. A count of these striations indicated that the crack growth life was about

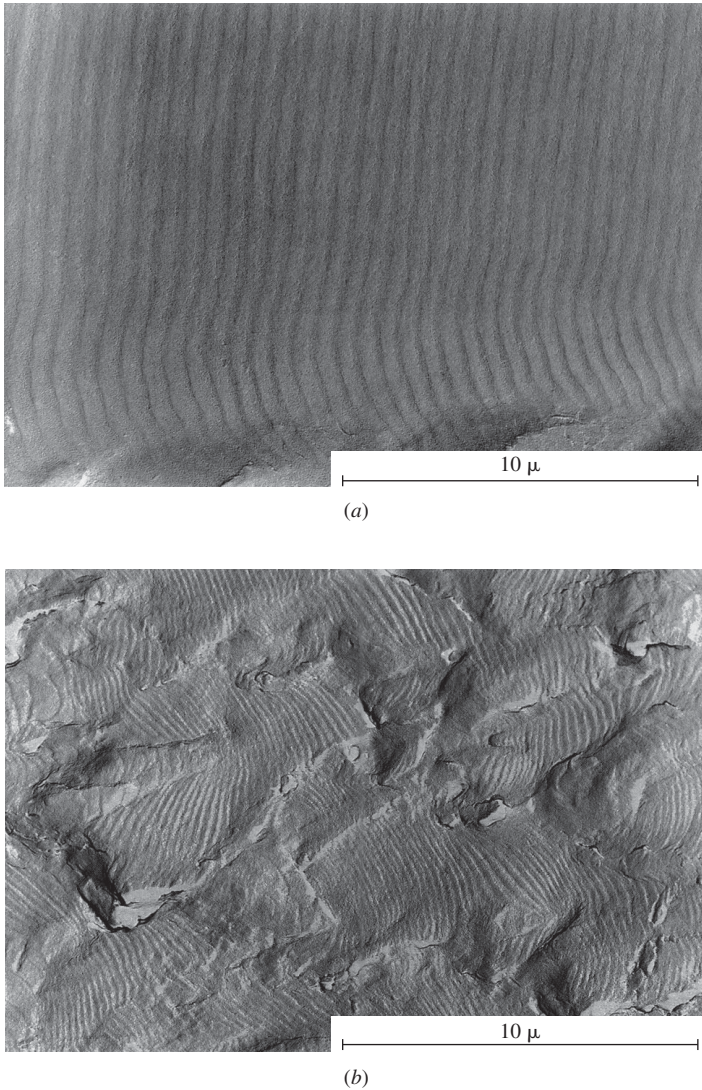


Fig. 10-20. (a, b) Examples of fatigue striations observed in aluminum alloys.

5,000 flights, long enough for the crack to have been detected by periodic inspection (40). In the case of an aluminum helicopter blade containing a fatigue crack, the main cyclic loading occurs as the blade is brought from rest up to speed and then back to rest again. A count of the striations created by this loading can also indicate the number of flights spent in crack propagation. This is true of other rotating parts such as aircraft engine crankshafts.

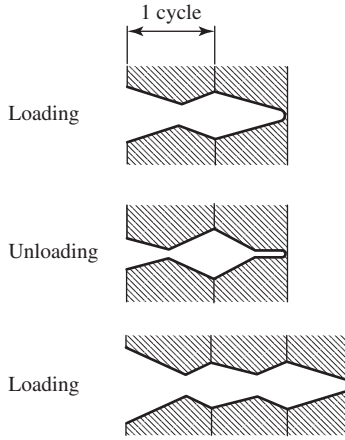


Fig. 10-21. A model for the formation of staircase-profile type fatigue striations. (After Schijve, 41.)

VII. ANALYSIS OF THE RATE OF FATIGUE CRACK PROPAGATION

A. Crack Tip Stress Approach

The first successful correlation of the rate of fatigue crack propagation with loading parameters was that of McEvily and Illg (42).

In the 1950s, it was well known that the ratio of the fatigue strength of an unnotched specimen to that of a notched specimen K_f was less than the theoretical stress concentration factor K_T . Kuhn and Hardrath (43) used the following empirical relationship due to Neuber (4) in order to relate K_f and K_T :

$$K_f = 1 + \frac{K_T - 1}{1 + \sqrt{\frac{\rho'}{\rho}}} \quad (10-20)$$

where ρ is the radius of the notch and ρ' is a material constant.

In the analysis of the rate of growth of a fatigue crack, it was assumed that whatever events occurred at the tip of a fatigue crack were in response to the elastic stress range S at the crack tip, given by $K_N S$, where S is the applied stress range at a given R ratio, which is the ratio of the minimum stress to the maximum stress in a loading cycle. The value of K_N was set equal to the right-hand side of the Eq. 10-20. However, in order to assign a value to K_N for a fatigue crack, it was necessary to assign an effective crack tip radius ρ_e , which was done empirically. As a simplification, it was assumed that the tip radius ρ was equal to ρ' , and therefore,

$$K_N = 1 + \frac{1}{2}(K_T - 1) = \frac{1}{2}(K_T + 1) \quad (10-21a)$$

And since K_T is large,

$$K_N \approx \frac{1}{2}K_T \quad (10-21b)$$

or

$$K_T \propto K_N \quad (10-21c)$$

From an analysis of the experimental results, values for ρ_e of 0.076 mm (0.003 in.) for 2024-T3 and 0.051 mm (0.002 in.) for 7075-T6 were assigned. We note that since 1958, ample evidence has been obtained—for example, Bowles and Schijve (44)—that shows that because of crack surface roughness, the tip radius in the offloaded condition is finite rather than zero. However, it is doubtful that the experimental values for the tip radii would agree with those given above, since a number of factors, such as crack tip plasticity, were not considered in the analysis. The da/dN values as a function of $K_N S_{net}$ are shown in Fig. 10-22 for the aluminum alloy 7075-T6 and in Fig. 10-23 for the aluminum alloy 2024-T3.

The equation fitted to the master curve in the log da/dN versus $K_N S_{net}$ in both Fig. 10-22 and Fig. 10-23 is

$$\log \frac{da}{dN} = 0.00509 K_N S_{net} - 5.472 - \frac{34}{K_N S_{net} - 34} \quad (10-22)$$

where a is in inches, S_{net} is expressed in ksi units, and 34 represents the fatigue strength at $R = 0.05$ in ksi units. Note that the same master curve was used for both 2024-T3 and 7075-T6, and that a threshold is predicted when $K_N S_{net}$ equals to the fatigue strength.

From Eq. 10-21c, $K_T \propto K_N$. The quantity $K_T S_{net}$ represents the stress at the crack tip, where K_T is based upon the net section. The quantity $K_{TG} \sigma_G$ is identical to $K_T S_{net}$, since it also represents the stress at the crack tip. Here K_{TG} is the theoretical stress concentration factor based upon the gross section stress and σ_G is the gross section stress.

In 1958 Irwin (45) showed that the stress ahead of a crack, σ_y , was given by

$$\sigma_y = \frac{K}{\sqrt{2\pi r}} \quad (10-23)$$

And in 1961, Paris, Gomez, and Anderson (46) astutely used the stress intensity factor, K , as a characterizing parameter to correlate successfully fatigue crack growth data, including data from Ref. 42. In 1965, Paris and Erdogan (47) expressed the fatigue crack growth rate in the form of a power law, that is,

$$\frac{da}{dN} = C(\Delta K)^m \quad (10-24)$$

and found that the value of m for aluminum alloys was about 4.0. Since the time of the work of Paris and Erdogan, a plot of $\log da/dN$ versus $\log \Delta K$ has been the standard way of displaying fatigue crack growth data.

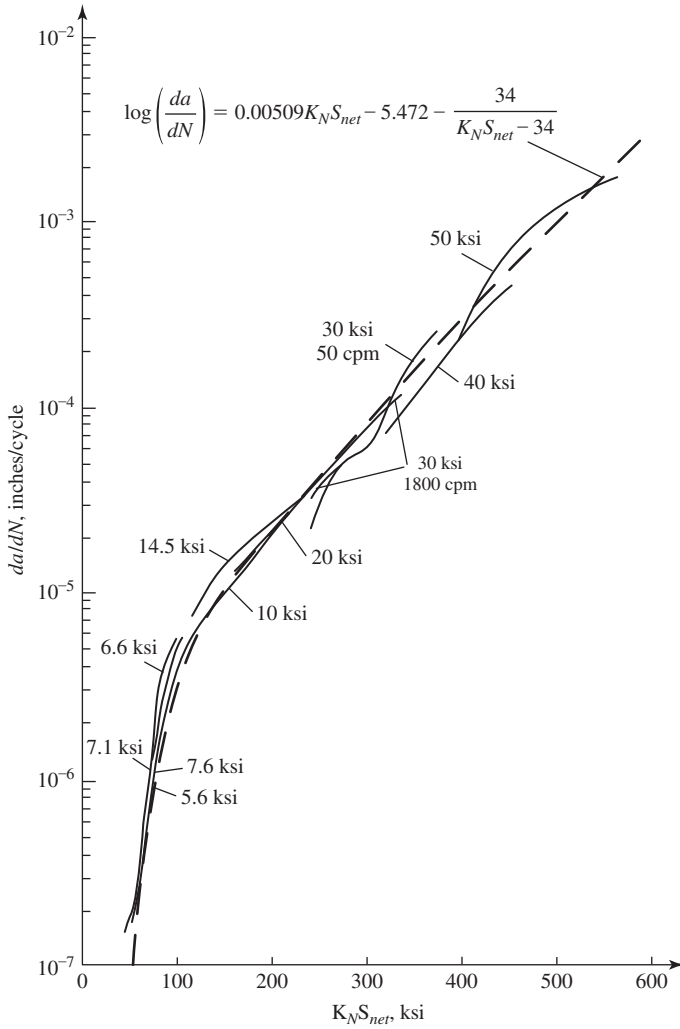


Fig. 10-22. The rate of fatigue crack growth in the aluminum alloy 7075-T6 as a function of $K_N S_{net}$. The stress values on the curve represent the initial values of the net section stress used in the tests. (After McEvily and Illg, 42.)

An important link between the $K_N S_{net}$ parameter and the stress intensity factor K was provided by Irwin (48), who in 1960 showed that K was related to $K_{TG} \sigma_G$ as follows:

$$K = \lim_{\rho \rightarrow 0} K_{TG} \sigma_G \sqrt{\frac{\pi \rho}{4}} \quad (10-25)$$

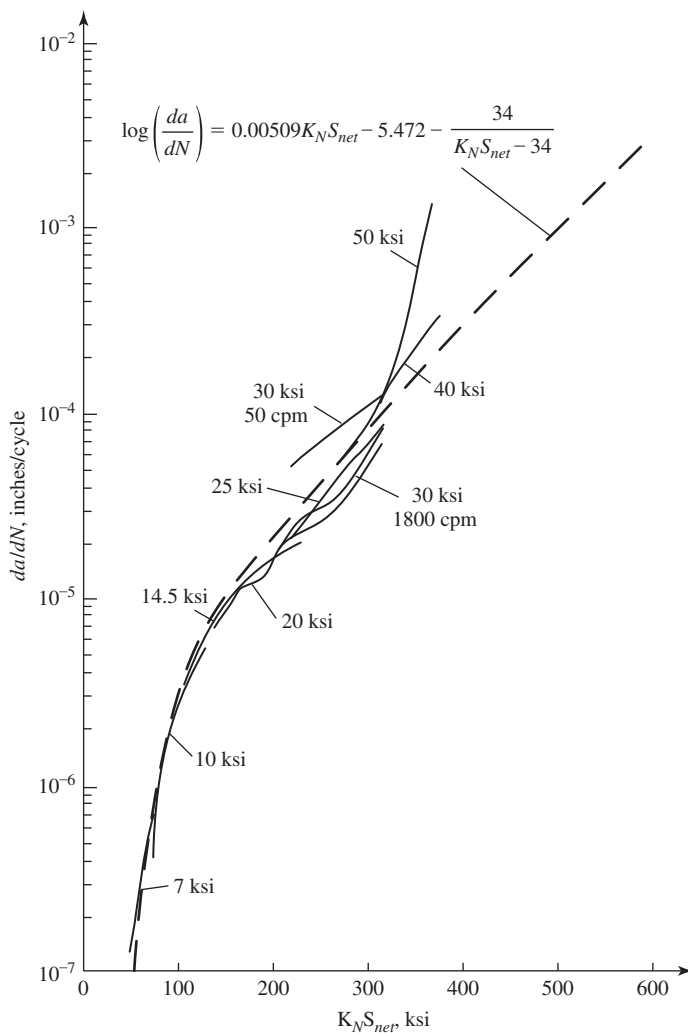


Fig. 10-23. The rate of fatigue crack growth in the aluminum alloy 2024-T3 as a function of $K_N S_{net}$. The stress values on the curve represent the initial values of the net section stress used in the tests. (After McEvily and Illg, 42.)

For a wide center-cracked panel containing a small, flat, elliptically shaped crack of radius ρ and of length $2a$,

$$K_{TG} = 1 + 2\sqrt{\frac{a}{\rho}} \quad (10-26)$$

and therefore the corresponding stress intensity factor is the well-known expression

$$K = \sigma_G \sqrt{\pi a} \quad (10-27)$$

But if $\rho \rightarrow \rho_e$ instead of zero,

$$K = \sqrt{\frac{\pi \rho_e}{4}} \sigma_G + \sigma_G \sqrt{\pi a} \quad (10-28)$$

Note that Eq. 10-28 contains an additional term and a constant ρ_e that are not present in Eq. 10-27. The magnitude of the constant for 2024-T3 is $7.6 \times 10^{-5} \text{ m}$ (0.003 in.), and for 7075-T6, it is $5.0 \times 10^{-5} \text{ m}$ (0.002 in.). Therefore, with respect to the large crack data in Ref. 42, the first term in Eq. 10-28 is negligible. However, in dealing with cracks of extremely small lengths where a in the second term of Eq. 10-28 approaches zero, the values are significant, as will be discussed.

Equation 10-21a can be rewritten as

$$K_T = 2K_N - 1 \quad (10-29)$$

And in a very good approximation for the data shown in Fig. 10-23 as

$$K_T = 2K_N \quad (10-30)$$

$K_N S_{net}$ therefore can be written as

$$K_N S_{net} \propto K_T S_{net} = K_{TG} \sigma_G \quad (10-31)$$

We can therefore use $K_{TG} \sigma_G$ as a correlating parameter. Next, we use Eq. 10-25 for the case of a centrally cracked panel,

$$K = \lim_{\rho \rightarrow 0} K_{TG} \sigma_G \sqrt{\frac{\pi \rho}{4}} = \sqrt{\frac{\pi \rho_e}{4}} \sigma_G + \sigma_G \sqrt{\pi a} \quad (10-32)$$

which is the same expression given by Eq. 10-28. Therefore, the link between K and $K_N S_{net}$ has been established. Further, if we plot the data as $\log da/dN$ versus $\log \Delta K$, a plot similar to that shown in Fig. 10-24 is obtained, and in agreement with Paris and Erdogan, the value of the slope m is about 4.0. As will be discussed subsequently, a value for m of 2.0 reflects more accurately the basic mechanism of fatigue crack growth. The reason why a value of 4.0 is obtained is that in the near-threshold range the growth rates are lower than expected for an m value of 2.0, whereas in the high rate of fatigue crack growth near K_c , the rates are higher than expected for an m value of 2.0 because of the increasing occurrence of localized rupture events as the fracture level is approached. Both of these factors contribute to the rotation of a line through the data toward higher values of m . This is particularly true for high-strength aluminum alloys, for which the range of ΔK values between the threshold and K_c is much less than for low-carbon steels, where m values of 2.0 are obtained.

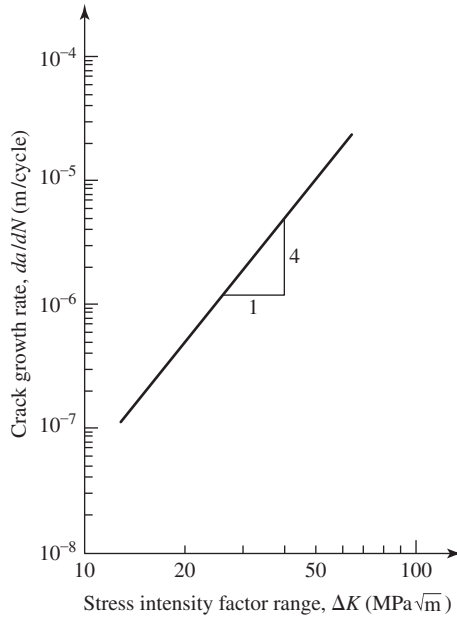


Fig. 10-24. The rate of fatigue crack growth as a function of the stress intensity factor range.

B. A Fatigue Crack Growth Relationship

B.1. Long Cracks Long cracks are defined as those cracks in which crack closure has been fully developed to the level of $K_{op\max}$.

Equation 10-24 is an example of empirical fatigue crack growth laws. As has been pointed out by Frost and Dugdale (49) and Liu (50), such relationships are not dimensionally correct. However, if we take the growth increment per cycle da as being proportional to the effective CTOD and include the effect of the threshold, we obtain the dimensionally correct expression

$$\frac{da}{dN} = A' \frac{1}{\sigma_Y E} (\Delta K_{eff} - \Delta K_{effth})^2 = A (\Delta K_{eff} - \Delta K_{effth})^2 \quad (10-33)$$

This expression for the rate of fatigue crack growth has been successfully used in the long crack regime. For example, Fig 10-25a shows the experimental results for da/dN in Ti-6Al-4V as a function of ΔK (51). Fig. 10-25b shows the same data plotted after correction for crack closure has been made (52). As originally proposed by Elber (15), there is no R effect on da/dN when da/dN is plotted as a function of ΔK_{eff} . In addition, correction for crack closure has also been successful in correlating data from overload and underload tests once the corresponding crack closure values have been determined (53).

The transition in crack growth rate at about 10^{-8} m/cycle is thought to be due to the size of the crack-tip plastic zone relative to a microstructural feature, in this

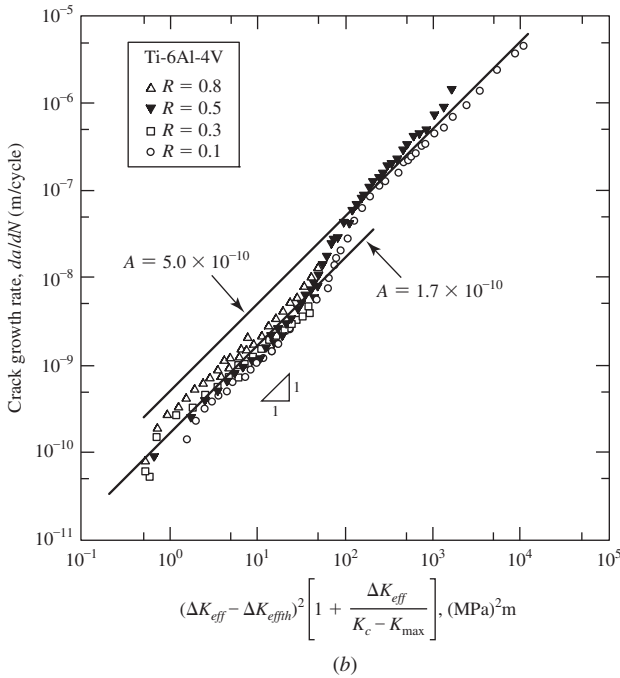
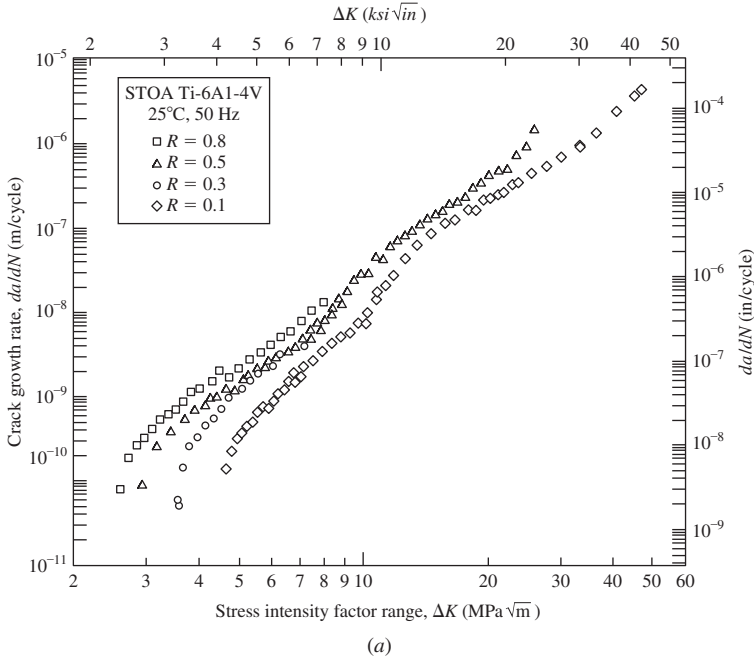


Fig. 10-25. (a) Fatigue crack growth rate for Ti-6Al-4V as a function of ΔK (51). (b) Fatigue crack growth rate for Ti-6Al-4V as a function of ΔK_{eff} (52).

case the size of an alpha grain, about $10\mu\text{m}$. At low growth rates the plastic zone is entirely contained within the alpha phase, but at high growth rates the plastic zone is larger than an alpha grain. At low growth rates a single slip system may be operating, whereas at high growth rates two systems may be operating, thereby providing a necessary condition for striations to form.

B.2. Short Cracks Short cracks are defined as those cracks in which the crack closure level varies from zero to $K_{op\max}$ as a newly formed fatigue crack grows in length. The maximum length of a short crack is about 0.5 mm. (0.02 in.) However, in order to use Eq. 10-33 in the analysis of short crack behavior, it is necessary to make three modifications to that equation.

(a) *Modification for elastic-plastic behavior:* Crack growth can be elastic-plastic in nature rather than linear-elastic because of a high ratio of fatigue strength to yield strength and the consequent large ratio of the plastic zone size to the crack length. (54) proposed that the linear-elastic approach could be extended to include elastic-plastic behavior, that is, those cases where the crack-tip plastic zone size is large with respect to the crack length, by increasing the actual crack length, a , by one-half of the plastic zone size. If the plastic zone size is taken to be that as defined by Dugdale (55), then the modified crack growth length, a_{mod} , is given as

$$\begin{aligned} a_{\text{mod}} &= a + \frac{1}{2} \left(\sec \frac{\pi}{2} \frac{\sigma_{\max}}{\sigma_Y} - 1 \right) a \\ a_{\text{mod}} &= \frac{a}{2} \left(1 + \sec \frac{\pi}{2} \frac{\sigma_{\max}}{\sigma_Y} \right) = aF \end{aligned} \quad (10-34)$$

where σ_{\max} is the maximum stress in a loading cycle, σ_Y is the yield strength, and F is termed the *elastic-plastic correction factor*, and

$$F = \frac{1}{2} \left(1 + \sec \frac{\pi}{2} \frac{\sigma_{\max}}{\sigma_Y} \right) \quad (10-35)$$

(b) *Modification for transient crack closure:* The level of crack closure developed in the wake of a crack varies from zero for a newly formed crack up to $K_{op\max}$ for a macroscopic crack. The following expression has been proposed (56) to describe this transient in crack closure behavior:

$$\Delta K_{op} = (1 - e^{-k\lambda})(K_{op\max} - K_{\min}) \quad (10-36)$$

where ΔK_{op} is the value of $K_{op} - K_{\min}$ in the transient range, k is a material constant (units m^{-1}) that determines the rate of crack closure development, λ is the length of the newly formed crack (m units), and $K_{op\max}$ is the magnitude of the crack opening level associated with completion of the transient period of growth. The value of λ when $K_{op\max}$ is reached is generally less than 1 mm (0.04 in.). The dependency of ΔK_{th} and ΔK_{effth} for steels as a function of yield strength is shown in Fig. 10-26 (56).

Experimentally determined values of k as a function of tensile strength for several steels are shown in Fig. 10-27 (56).

(c) *Modification for the Kitagawa effect:* In the very small crack range, the rate of crack growth is determined by the range of cyclic stress rather than the range of the stress intensity factor (Kitagawa effect (57)). An example of the Kitagawa effect is given in Fig. 10-28.

In this regard, Eq. 10-33 is of interest. In a straightforward application of the fracture mechanics approach, as the crack length approaches zero, so does the stress intensity factor, and there is no way to deal with very short crack growth behavior. However, we see that in Eq. 10-33 there is an additional term, $\sqrt{\pi\rho_e/4}\sigma_G$. We set σ_G equal to the fatigue strength and equate this quantity to the effective stress intensity factor at the threshold level, ΔK_{effth} . But rather than make use of such an equation directly, we replace ρ_e with an effective crack length, r_e . This is done by equating the peak stress at the tip of the crack, $K_{TG}\sigma_G$, to the same stress, σ_y , given by Eq. 10-23, that is,

$$K_{TG}\sigma_G = \lim_{\rho \rightarrow \rho_e} \frac{K_T\sigma_G\sqrt{\frac{\pi\rho}{4}}}{\sqrt{2\pi r_e}} \quad (10-37)$$

which leads to $r_e = 8\rho_e$.

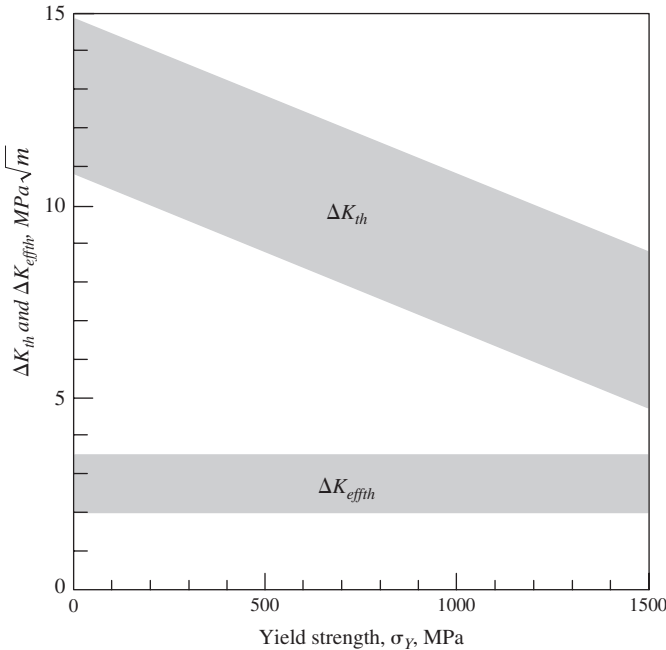


Fig. 10-26. The variation of ΔK_{th} and ΔK_{effth} as a function of yield strength for steels. $R = 0$. (After Endo and McEvily, 56.)

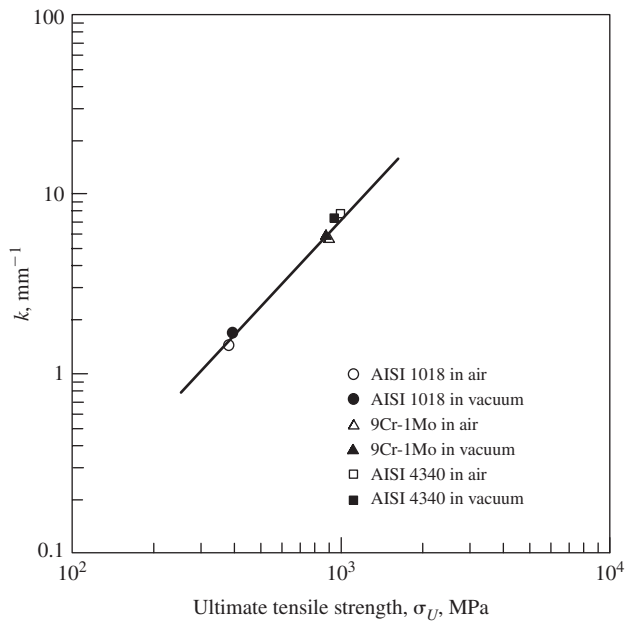


Fig. 10-27. The dependence of the material constant k on tensile strength for a variety of steels. (After Endo and McEvily, 56.)

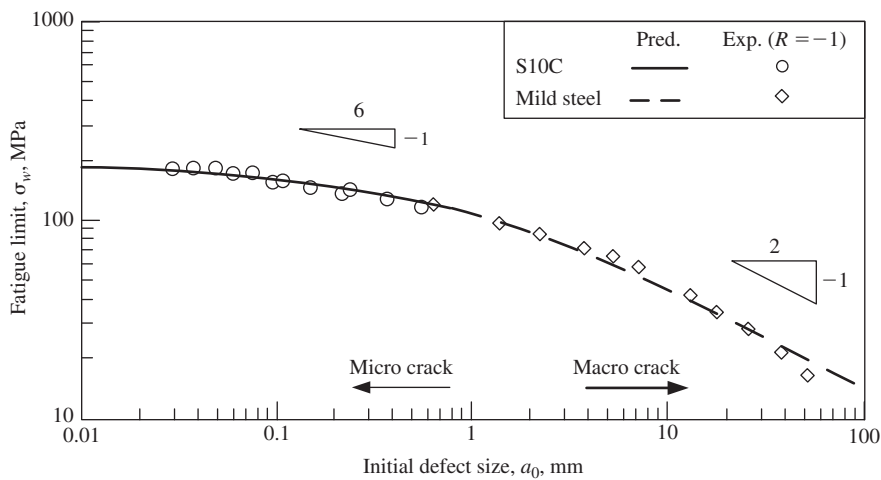


Fig. 10-28. An example of the Kitagawa effect. For very small defect sizes the fatigue strength, σ_w , becomes the controlling parameter. (After Endo and McEvily, 56.)

The resultant stress intensity factor at the condition for fatigue crack growth is then written as

$$\Delta K_{effth} = \left(\sqrt{2\pi r_e} + Y\sqrt{\pi r_e} \right) \sigma_w \quad (10-38)$$

where σ_w is the fatigue strength and Y is a factor related to the shape of the crack.

The magnitude of the material constant r_e is given by

$$r_e = \left[\frac{\Delta K_{effth}}{\left(\sqrt{2\pi} + Y\sqrt{\pi} \right) \sigma_w} \right]^2 \quad (10-39)$$

It is noted that in this analysis the threshold for fatigue crack propagation is linked to the fatigue strength, in a manner similar to that used in Ref. 42. The magnitude of r_e is about $1\mu\text{m}$ for steels, aluminum alloys, and titanium alloys.

Hence, all three of the above modifications are taken into account, and Eq. 10-33 becomes

$$\frac{da}{dN} = A \left[\left(\sqrt{2\pi r_e F} + Y\sqrt{\pi a F} \right) \Delta\sigma - \Delta K_{effth} - (1 - e^{-k\lambda}) (K_{op\max} - K_{\min}) \right]^2 \quad (10-40)$$

An example of the use of Eq. 10-40 is given in Fig. 10-29 for the case of fatigue cracks grown from circular holes of differing radii. As crack closure develops, the stress range required to propagate a crack at just above the threshold level for crack lengths greater than 0.01 m (0.4 in.) increases. In order for a crack to grow to failure from a hole of 0.20 mm (0.008 in.) radius, a stress range of 300 MPa (43.5 ks) would be required. At lesser stress ranges, nonpropagating cracks would form. A similar situation applies to cracks grown from a hole of 0.48 mm (0.02 in.) radius, but for a hole of 4.8 mm radius, once a crack is initiated, it can propagate to failure, that is, there is no crack closure barrier.

B.3. Very High Cycle Fatigue (VHCF) Some components, such as turbine blades, may be subjected to huge numbers of cycles of the order of 10^{10} during their service lifetimes, and in recent years an interest in VHCF has developed. A characteristic of failures in this realm is that failure usually initiates in a subsurface mode. The mechanism of fatigue failure in VHCF is not yet known, but some mechanisms have been proposed. One of them is based upon the reduction of the crack closure level due to wear 59. In this model as applied to $\alpha - \beta$ Ti-6Al-4V, it is assumed that a cleavage facet forms early in life in an alpha grain. However, a crack from this facet cannot grow initially because the barrier due to crack closure is too high. But with continued cycling, this barrier is worn away to permit the crack to grow by a small increment. Then more wear must occur at the crack tip to allow another small increment of crack growth to occur. The overall process is indicated in Fig. 10-30. In this view, the reason why so many cycles are required for failure is that most of the lifetime is consumed in the wear process.

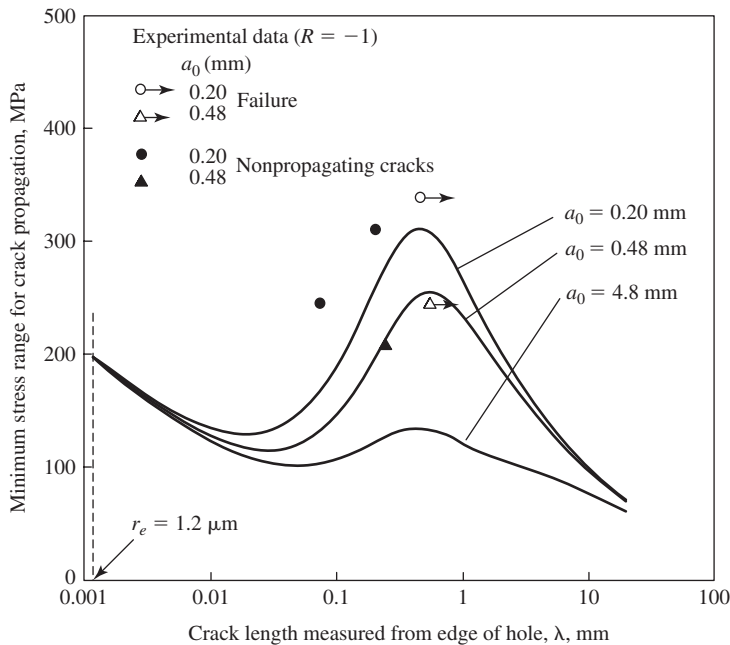


Fig. 10-29. Minimum stress range required to propagate a fatigue crack in a carbon steel at a rate of 10^{-11} m/cycle from small holes of different radii as a function of the distance from the hole. (After Endo and McEvily, 56. Experimental data points are from Haddad et al., 58.)

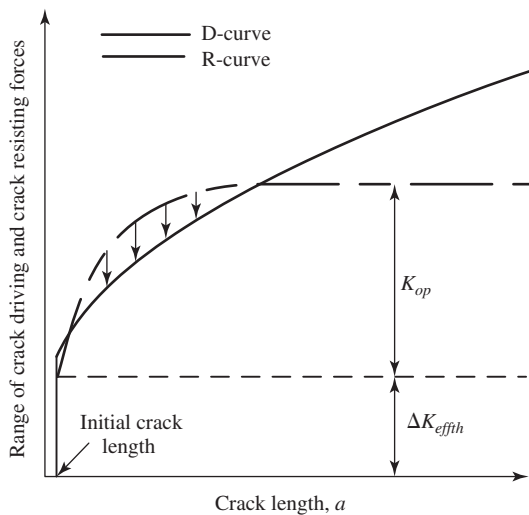


Fig. 10-30. Schematic illustration of the reduction by wear in VHCF of the R (resisting) curve down to the level of the D (driving) curve. (After McEvily et al., 59.)

VIII. FATIGUE FAILURE ANALYSIS

A. Macroscopic

When a component fails in fatigue, an examination of the fracture surfaces may provide substantiating evidence such as well-defined *beach mark* patterns. These patterns can be created by environmental interactions with the crack front, and the term *thumbnail fracture* is often used to describe their shape around the origin of fatigue cracking. In steel parts that are subjected to reversed loading, the fatigue fracture surfaces can rub together, as in $R = -1$ loading, and develop a highly polished appearance, particularly near the origin of fatigue cracking. In such cases, no fine details will be observed, but the macroscopic beach markings may be apparent, as in Fig. 10-31. Such markings can develop when the part experiences periods of cycling followed by periods of rest. During the rest period, corrosion occurs at the crack tip to outline the crack front, thereby creating the beach mark. Variable-amplitude loading may also create beach marks, particularly if there are many cycles of small amplitude mixed with a few high-amplitude cycles. In this case, the texture of the fracture may vary from smooth for the low-amplitude cycles to rough for the high-amplitude cycles, and it is the roughness that leads to the creation of the beach marks. A well-defined transition between the fatigue region and the region of final overload failure can also establish that the fracture was due to fatigue.

B. Microscopic

An examination of a fatigue fracture surface using light microscopy or scanning electron microscopy will reveal whether the fracture is intergranular or transgranular. If the fracture is transgranular, which is the usual mode, the fracture may be faceted,



Fig. 10-31. Fatigue beach markings on a steel component. The markings are visible to the eye, and the fatigue crack initiated at a weld defect at the top of the figure.

indicating a crystallographic path for crack growth. This mode is observed in aluminum alloys at low growth rates and in single crystals of nickel-base superalloys, for example. Transgranular fractures are often noncrystallographic in that faceted growth is not observed. It is on such fracture surfaces that fatigue striations are observed.

At higher ranges of the stress intensity factor corresponding to growth rates greater than $0.1\text{ }\mu\text{m}$ per cycle, fatigue striations may be visible, and their presence can be related to the magnitude of the stress amplitudes that had been applied. They are observable only over a limited range of growth rates because at too low a growth rate, that is, usually below $0.1\text{ }\mu\text{m}$ per cycle, they are not resolvable in a scanning electron microscope, and at high growth rates, that is, above 10^{-3} mm/cycle , the fracture surface contains increasing amounts of what are called *static fracture patches*, which are the precursors to final separation. Because of these limitations, striations may provide only limited information about the past in-service history. However, even this information can be critical in trying to determine whether a particular fracture occurred by fatigue or not. The spacing of striations is da/dN , and if a plot of da/dN versus ΔK is available for the appropriate R condition, the applied ΔK values can be determined. However, the presence of high residual stresses, such as may be present in a welded joint, can make this type of analysis more difficult. Striations can also provide information on the number of cycles or flights that a part experienced during the crack propagation phase of a fatigue failure. In some cases, only the major loadings may be reflected, as in the case of an aluminum helicopter blade where a relatively few start-up cycles of high stress amplitude create a different fracture surface texture than do the cycles experienced during flight. In such a case, it may not be possible to resolve individual striations because of rubbing of the fracture surfaces. Similarly, a failed crankshaft of a propeller-driven aircraft may exhibit two different but repetitive textures, one associated with takeoff and the other with cruise conditions. In such a case, it may be possible to determine the number of flights since the last inspection, for example.

Since fatigue striations are not usually observed below a crack growth rate of $0.1\text{ }\mu\text{m}$ per cycle, it is not possible to reconstruct the loading history of a failed part on the basis of spacing of striations in this range of crack growth rates. However, an alternative procedure has been developed in which the fracture surface roughness is measured with a profilometer either transverse to (60) or parallel to (61) the direction of fatigue crack propagation. As shown in Fig. 10-32, the fracture surface roughness of a 12CrMo steel increases with an increase in crack growth rate, and from this information the corresponding ΔK values and loading history can be estimated. The method has potential applicability in the range of fatigue crack growth rates from 10^{-9} to 10^{-7} m/cycle , but a reference fracture surface of known loading history is needed for comparison with the fatigue fracture surface of a failed component. As in the case of striations, corrosion of the fracture surfaces will increase the difficulty of establishing a good correlation between the roughness parameter and the rate of fatigue crack growth.

For materials in which fatigue striations are difficult to observe, it may be worthwhile to conduct laboratory fatigue and fracture tests to establish standards that

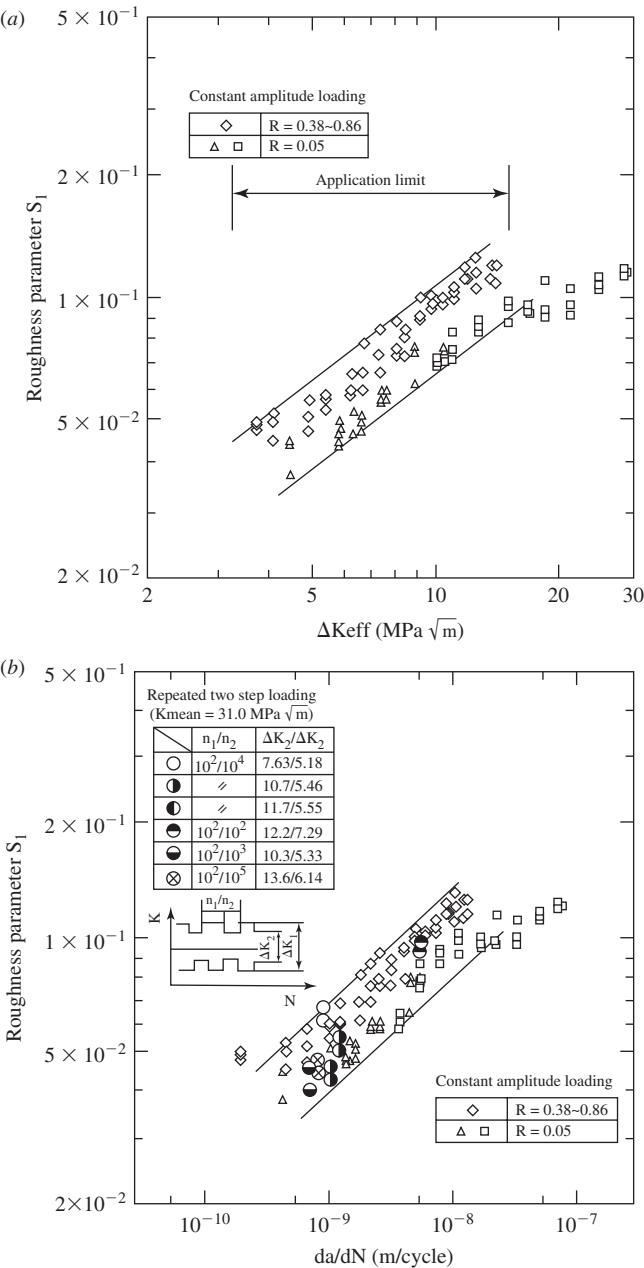


Fig. 10-32. (a) The relation between the roughness parameter S_1 and ΔK_{eff} for a 12CrMo steel. (b) The relation between the roughness parameter S_1 and da/dN for a 12CrMo Steel. (From Fujihara et al., 60. Reprinted with permission of the Society of Materials Science, Japan.)

can be used to determine the characteristics of the fracture surfaces associated with each type of fracture. Knowledge of the loading history of a failed part is helpful in the examination of a fracture surface, for it is important to establish that a set of striation-like markings under investigation are the result of cyclic loading, since markings that are similar in appearance to fatigue striations have been observed in cases of creep failure, stress corrosion cracking, and overload failures. Such markings may correspond to an intermittent mode of crack growth or to a hesitation in growth rate of the crack front. In brittle materials such as glass, *Wallner lines*, which resemble striations, may be present on the fracture surface. These lines are the result of interaction between the expanding crack front and reflected elastic waves in the body.

In some cases, it may not be feasible to examine the actual fractured component in the laboratory. In such instances, replicas of the fracture surface can be made in the field and examined later in the laboratory, as described in Chapter 6.

IX. CASE STUDIES

A. Hydroelectric Generator Power Failure (62)

The failure of an epoxy-coated, low-carbon steel cooling fan blade occurred in one unit of a 10-year-old Pelton-wheel hydroelectric station, and the detached blade cut into the stator windings, short-circuited the unit, and caused a fire. Six months earlier another blade had failed, and this failure was attributed to fatigue initiating at a pit that had been introduced during manufacture. Following this failure, all blades were stripped of their coatings and subjected to examination. A number of small cracks were detected, and the affected blades were replaced. Because of a shortage of replacement blades, the number of blades at the top and bottom of the generator units had been reduced from 24 to as few as 12. Following the fire, cracks that had developed in a 1-month period were found in two blades of another generating unit. These blades, as well as the failed blade that led to the fire, were adjacent to gaps that had been created where blades had been removed to provide them for another unit. Examination of the fracture surfaces showed that the cracks were high-cycle fatigue cracks, and it was clear that blade vibration was a major problem.

Both finite element method analysis and an experimental modal analysis were made, and both indicated that the first natural frequency of the blades in the regions where the cracks initiated was 70 Hz. An estimate of the cyclic stress range was made based upon the observed striation spacings, and it was found to be high enough to indicate that a resonant condition must have been present. However, this condition must have been intermittent for the blades to have lasted even a month at 70 Hz. It was concluded that the cracking problem was caused by air-induced vibration brought about by the absence of some of the blades and associated with periodic vortex shedding. The problem was solved by installing complete new sets of fan blades that were heavier than the original blades and therefore had a higher natural frequency. Prior to installation, the blades were carefully inspected to be sure that no surface defects were present that might trigger fatigue cracking.

B. Fatigue of a B747 Fuse Pin (63)

In 1992, a B747-200 freighter was 6 minutes out of the Amsterdam airport at an altitude of 2,000 m (6,500 ft) and climbing, when suddenly the right inboard engine and pylon separated from the wing. When this engine separated, it was under full power, and because of a gyroscopic moment, it moved into the path of the right outboard engine and struck it, causing the outboard engine also to separate from the wing. (These two engines fell into a lake and were not recovered for several months.) The aircraft became unstable, crashed into an apartment complex, and was destroyed. The 4 persons on board the aircraft, as well as approximately 50 persons in the apartment complex, lost their lives. The 747 was 22 years old and had accumulated 45,746 flight hours and 10,107 flight cycles. A total of 257 flight cycles had elapsed since the last ultrasonic inspection of critical parts involved in the accident.

Each engine weighed 38.3 kN (8,600 lb) and developed 222 kN (50,000 lb) of thrust at full power, and these forces, as well as another 89 kN (20,000 lb) of force due to the pitching of the engine during takeoff and climb, had to be resisted by the support structure. Figure 10-33 (63) is a sketch of the pylon structure that attaches the engine to the wing. The design incorporates 4340 low-alloy steel fuse pins, which are intended to shear off should the engine strike the ground, thereby allowing the engine to separate from the wing, thus minimizing the chance of a fire due to rupture of a fuel tank. A sketch of a fuse pin is shown in Fig. 10-34 (64). Each fuse pin transmits load from two lugs on the pylon to a clevis that is attached

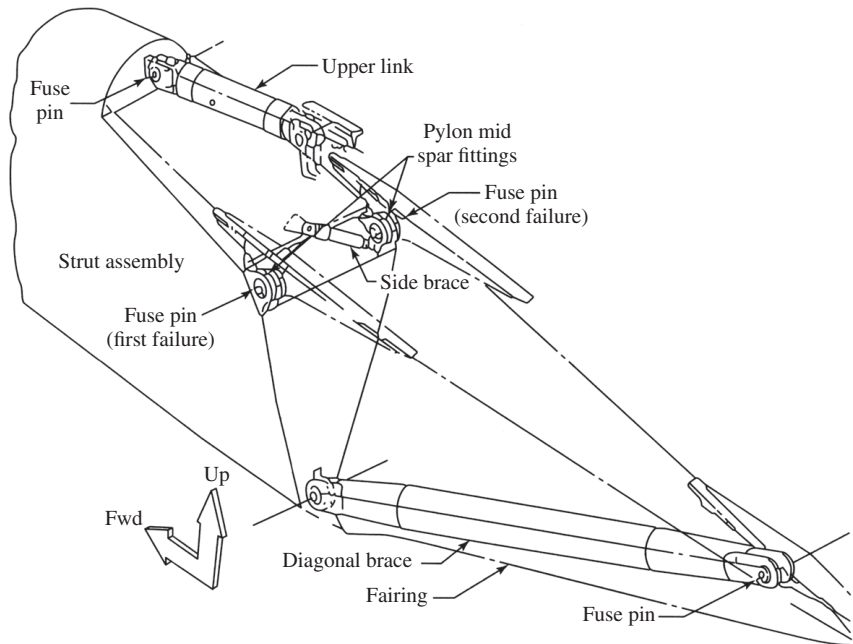


Fig. 10-33. Pylon to wing attachments (63).

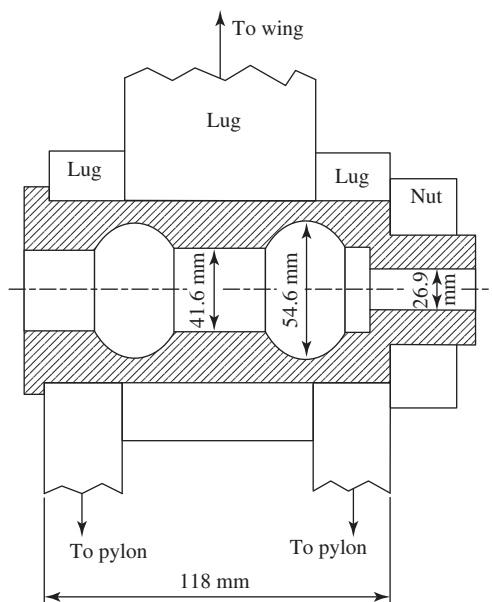


Fig. 10-34. A sketch of a fuse pin showing the attachment lugs (64).

to the wing. The investigation showed that the midspar fuse pins of the right inboard engine were critical. Unfortunately, the inboard midspar fuse pin was not recovered. However, because the outer lug on the inboard pylon fitting had broken under combined bending and tensile loading, it was clear that the inboard side of the midspan fuse pin had failed first due to fatigue, and that, as a result, the load on the outboard midspar fuse pin had been greatly increased. The midportion of the outboard fuse pin was recovered and was still within the clevis. On the inboard side it had failed in shear, but on the outboard side it had failed by fatigue. The main fatigue crack had initiated at multiple sites on the inner surface of the fuse pin at a reduced section where machining grooves were present and had grown in a radial direction. Examination of the fatigue fracture surface revealed the presence of striations spaced at approximately 1- to 3 μm intervals. An example of these striations is shown in Fig. 10-35 (65). Approximately 1,900 major striations were present, and at a depth of 2.2 mm (0.088 in.), they were spaced at intervals of 1.0 μm . The striation spacing indicated a fatigue crack growth rate of a $1\text{--}3 \times 10^{-3}\text{ mm}$ per cycle, which in 4340 steel corresponds to a ΔK of 50–70 $\text{MPa}\sqrt{\text{m}}$ (59).

A question arose as to whether the major striations represented cycle-by-cycle events or flight-by-flight events. If they were flight-by-flight indications, the fatigue crack should have been detected by the ultrasonic method at the time of the last inspection, 257 flight cycles before the crash. If, on the other hand, they were cycle-by-cycle striations, they must have been created by engine oscillations after failure of the inboard fuse pin and just before the inboard engine separated. Detailed

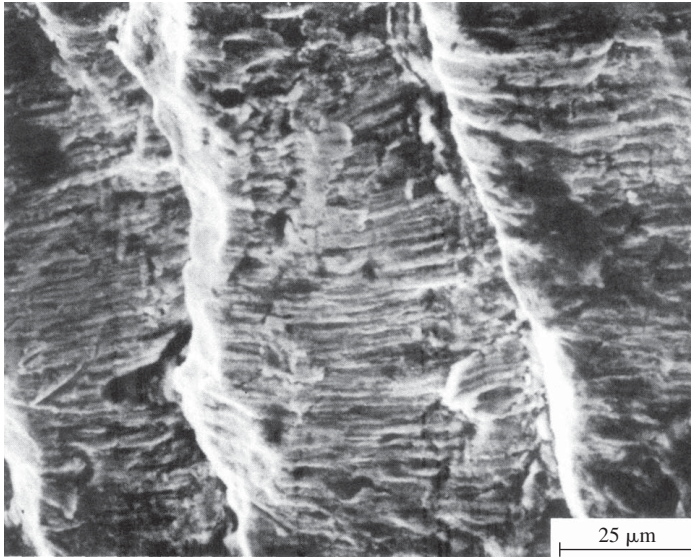


Fig. 10-35. Fatigue striations found on a failed outboard fuse pin. (From Oldersma and Wanhill, 65.)

examination of the striations revealed the presence of minor striation-like markings between striations. In the flight-by flight interpretation, these striation-like markings were indications of in-flight loading events due to gusts and maneuver loads. However, the interpretation of these minor markings was not straightforward, for in auxiliary tests under constant load amplitude conditions, it was observed that, at growth rates of the order of $1\text{--}3\text{ }\mu\text{m}$ per cycle, minor markings were created between striations. The Netherlands Aviation Safety Board (638) found that no firm conclusion could be drawn as to whether or not a fatigue crack in the outboard midspar fuse pin was detectable at the last ultrasonic inspection.

A stress intensity factor can be calculated to obtain an estimate of the range of stress that was actually applied. Since the length-to-depth ratio of the crack was large, a single edge notched configuration in pure bending is assumed, and at a depth of 2.2 mm (0.88 in.) and a total thickness of 7 mm (0.28 in.), ΔK is equal to $0.03\ \Delta\sigma$ (51). For a nominal load of 267 kN (60 kips) per fuse pin, a maximum stress of 400 MPa (58 ksi) has been calculated (654). At a crack depth of 2.2 mm, the calculated value of ΔK is then $12.0\text{ MPa}\sqrt{\text{m}}$. This is too low a value to create an observable striation in steel under the flight-by-flight conditions that existed prior to the failure of the inboard fuse pin. Therefore, the stress intensity must have been higher. It could have been higher due to higher load amplitudes and also if the crack tip deformation had been elastic-plastic rather than linear-elastic. To account for elastic-plastic behavior, Irwin (45) has suggested increasing the actual crack size by one-half of the plastic zone size. The size of the plane-stress plastic zone $r_{pzs-P\sigma}$,

as given by Dugdale (52), is

$$r_{pzs-P\sigma} = a \left[\sec \left(\frac{\pi}{2} \frac{\sigma}{\sigma_Y} \right) - 1 \right] \quad (10-41)$$

In plane-strain, the expression for the plastic zone size using the Irwin plastic constraint factor is

$$r_{pzs-P\epsilon} = \frac{a}{3} \left[\sec \left(\frac{\pi}{2} \frac{\sigma}{\sigma_Y} \right) - 1 \right] \quad (10-42)$$

The estimated tensile strength of the 4340 fuse-pin steel is 860 MPa (125 ksi), based upon a Brinell Hardness Number (BHN) of 240, and the yield strength is estimated to be 745 MPa (108 ksi) (66). If one-half of the plastic zone size is added to the crack length, the expression for $\Delta K_{EP-P\epsilon}$, the elastic-plastic value of ΔK for plane-strain conditions at a crack depth of 2.2 mm (0.088 in.) becomes

$$\Delta K_{EP-P\epsilon} = 1.11 \Delta \sigma \sqrt{\frac{\pi}{6} a \left[\sec \left(\frac{\pi}{2} \frac{\sigma}{\sigma_Y} \right) + 5 \right]} \text{ MPa } \sqrt{\text{m}} \quad (10-43)$$

which is equal to 12.2 MPa $\sqrt{\text{m}}$.

The elastic-plastic value results in a small increase in ΔK over the linear-elastic fracture mechanics (LEFM) value, but not enough to create well-defined striations, for which a ΔK of at least 30 MPa $\sqrt{\text{m}}$ (27 ksi $\sqrt{\text{in}}$) is needed. Therefore, the observed striations, even on a flight-by-flight basis, could not have been created at the nominal stress amplitude that existed prior to the failure of the inboard fuse pin. For a striation spacing of 1 μm at a depth of 2.2 mm (0.088 in.) and a corresponding ΔK of 50 MPa $\sqrt{\text{m}}$, (45 ksi $\sqrt{\text{in}}$) the required $\Delta \sigma$, according to Eq. 10-43, for plane-strain would be 728 MPa (106 ksi). This value is much higher than the nominal 400 MPa (58 ksi) that existed prior to the fatigue failure of the inboard fuse pin. The calculations, therefore, indicate that fatigue crack growth in the outboard fuse pin had occurred on a cycle-by-cycle basis under the high load amplitudes that developed after the inboard fuse pin failed.

As a result of this accident, several changes were made in the pylon-to-wing connections. The original type of fuse pin was replaced by a stainless steel fuse pin that did not have thin-walled regions. In addition, the pylon fittings and bracing were strengthened.

C. Aircraft Gas Turbines

Modern gas turbine engines for aircraft feature a significant reduction in the number of engine parts, low operating and maintenance costs, and high reliability, with thrust values per engine varying from 44.5 kN (10,000 lb) to over 444.8 kN (100,000 lb). For the 100-seat Airbus A318, thrust is in the range of 71.2 to 106.8 kN (16,000 to 24,000 lb), whereas for the long-range B777, thrust will exceed 444.8 kN. The PW6000 engine proposed for the A318 will have an initial on-wing engine time of 15,000 hours about 6–8 years after entering service, at which time 900

high-temperature turbine blades will be replaced. The life-limiting parts, such as the turbine disks, are designed for 25,000 cycles, meaning that these parts should last until the second overhaul (68).

The PW6000 engine relies upon proven materials, simplified mechanical systems, and advanced aerodynamics. The 1.44 m (56.5 in.) diameter first-stage fan utilizes shroudless (no midspan supports), solid titanium fan blades, together with a titanium fan case. The inlet vanes in the low-pressure compressor are fabricated from titanium for bird-strike resistance, and the unit's single-piece drum rotor is also forged from titanium. Integrally bladed disks (blisks) are not used in order to facilitate the replacement of damaged blades in the field. Blades in the first two stages of the high-pressure compressor are made of titanium, while the blades in the remaining stages are made from a nickel-based alloy. The unit's disks are also made of a nickel-based alloy. The single-piece turbine exhaust case is made of Howmet C263 alloy. To cope with debris ingestion and erosion, a splitter spacing arrangement is used between the fan and the low-pressure compressor so that debris such as sand, brake dust, and tire remains can be centrifuged out of the engine's flow path and into the fan duct. This centrifuging also helps the engine shed rain and hail, protecting against flameouts. The addition of a fourth stage to the low-pressure compressor allows for supercharging, which results in a temperature drop of 17°C (30°F) in the high-pressure turbine. This translates into a significant increase in component life.

Today, aircraft turbines are remarkably durable. For example, 50 years ago, an aviation piston engine manufacturer could expect to sell 20–30 times the original cost of the engine in after-market parts. With the advent of the jet engine, this after-market figure dropped to 3–5 times. Despite this marked improvement, fatigue still remains as a cause for concern (68). In gas turbine engines, low cycle fatigue (LCF) failures are usually caused by large cyclic excursions between zero stress and the operating stress. For example, a rotor disk would experience one LCF cycle as it accelerates from rest to operating speed, then decelerates to shutdown. In the mid-1970s, manufacturers and the U.S. Air Force (USAF) initiated the development of fracture mechanics–based damage-tolerant design criteria aimed at reducing the risk of unexpected failure from LCF. These criteria were eventually embodied in the Engine Structural Integrity Program. LCF assessments consist of an LCF-safe life determination, which is the life to expected crack initiation, and a fracture mechanics–based assessment to determine the remaining life to failure from an assumed crack, defect, or inspection limit. Both assessments are made and are used to determine an appropriate safety inspection interval, if required, and an eventual retirement life for the component.

On the other hand, high cycle fatigue (HCF) failures generally occur due to numerous smaller cyclic excursions between two or more stress states. These excursions result from the following drivers:

- (a) *Aerodynamic excitation:* Caused by engine flow path pressure perturbations affecting primarily blades and vanes
- (b) *Mechanical vibration:* Caused by rotor imbalance that affects external components, plumbing, and static structures; and rub, affecting blade tips and gas path seals

- (c) *Airfoil flutter*: Caused by aerodynamic instability, affecting blades
- (d) *Acoustic fatigue*: Affecting mostly sheet metal components in the combustor, nozzle, and augmentor

HCF has been identified as the cause of 24% of the maintenance problems in aircraft turbine engines, and is the USAF's number one readiness issue. Nearly half of the affected components are blades and vanes, and since these components can accumulate up to 10^{10} HCF cycles, design methods, criteria, and prediction approaches have been improved to address HCF. However, dramatic increases in engine performance and concurrent reductions in weight have driven up temperatures, stresses, and individual stage loading, and HCF problems have persisted. Although the rate of failure has remained steady, the percentage of HCF problems has actually increased.

Design for HCF tends to be based on experience and safety factors. The Goodman diagram is a basic design tool. Failure is expected to occur for combinations of mean stress and stress amplitude that lie above the line on this diagram corresponding to a given fatigue lifetime. As the number of cycles to failure increases, the allowable stress amplitude correspondingly decreases. The Goodman diagram approach as currently employed is highly empirical and does not adequately address in-service damage or interaction of HCF with other damage modes (fretting, LCF, etc.). Ultimately, HCF problems result from repeated stresses that are higher than the material's ability to resist them, as indicated by the reliability curves shown in Fig. 1-2. The intersection of the tails of these two curves indicates instances where the operating stresses are greater than the material strength—therefore, where failures occur. The HCF program is intended to shift these curves away from each other by altering mean values and reducing standard deviations.

The Palmgren-Miner Rule is used to estimate the number of cycles to failure under variable amplitude loading conditions in which the components may experience both HCF and LCF loading. Experience has shown that this summation often depends upon the load sequence, and the value of the summation can be greater or less than unity. However, the HCF alternating stresses in turbine blades and vanes are often difficult to predict or measure, and as a result, there is significant uncertainty in the actual vibratory stress levels experienced by these components. This is why extensive testing of fatigue-prone components is done in the aircraft industry to evaluate the influence of edges, holes and attachments, shot peening, and coatings.

Foreign object damage (FOD) is common for fan and compressor blades, with the relatively sharp airfoil leading edges being most susceptible. The size of the damaged areas varies from near microscopic to large tears, dents, or gouges. To assess the effect of FOD, the damage is simulated by V-notches in laboratory test programs, and airfoils are designed assuming reduced HCF capability in FOD-susceptible areas. Blade and disk attachment surfaces are also susceptible to fretting and/or galling surface damage. Both fretting and galling result from the relative motion of surfaces in contact with one another; and both are characterized by surface debris, wear, and reduced fatigue capability.

A USAF committee concluded that most titanium failures were attributable to HCF and recommended that the development of a threshold fracture-mechanics approach be undertaken as an alternative to the Goodman diagram approach. An improved HCF design system would consist of:

(a) A crack initiation analysis, improved over the current Goodman approach, to assess basic HCF capabilities. The intent would be to improve prediction approaches and reduce the level of empiricism. Factors to be considered include the effects of intrinsic defects, a local stress-strain approach, cyclic hardening and softening, maximum stresses, strain ranges, inelastic stress-strains, tensile and shear failures, HCF/LCF interaction, multiaxial stresses, processing effects, materials anisotropy, and material property variability.

(b) A fracture mechanics–based system capable of addressing ΔK_{th} behavior, small crack effects, crack closure, and HCF/LCF interaction.

Other goals include (a) the development of nonintrusive methods of accurately measuring the distribution and variation of dynamic stresses and pressures within gas turbine components and (b) the development of real-time measurement capabilities to ensure safe operation in the field.

D. Coil Springs (69)

Heavily coiled springs, especially those having a coil diameter that is less than four times the wire diameter, often fail in service under loads that are well below the safe load determined by the use of ordinary helical-spring formulas. A better stress analysis taking into account the effects of curvature is therefore needed.

Consider a heavy, closely coiled helical spring of mean coil diameter $2r$ subjected to an axial load, as shown in Fig. 10-36. The forces acting on any element $aa'b'b$ cut out by two neighboring radial planes may be resolved into a twisting moment Pr acting in a radial plane and a direct shearing force P acting in the direction of the axis of the spring.

The twisting moment Pr will cause rotation of two sections aa' and bb' with respect to each other through a small angle $d\alpha$. But since the length of the fiber $a'b'$

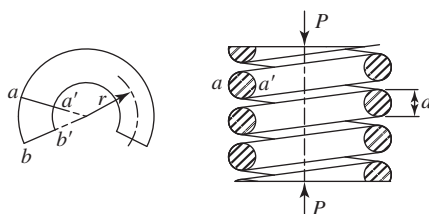


Fig. 10-36. A closely coiled helical spring. (After Wahl, 69.)

is much less than the length of the fiber ab , it is clear that the shearing strain, and hence the shearing stress, for any given angular rotation of the two cross sections will be much greater in $a'b'$ than in ab . The stress at a is further increased by the direct shearing stress due to the axial load P . This stress corresponds to the shearing stress at the neutral axis of a cantilever beam of circular cross section loaded with a load P .

The shear stress distribution, due to the twisting moment Pr , along a transverse diameter of wire is as shown in Fig. 10-37, the stress at a' being much larger than that at a . To this stress at a' must be added the direct shear stress due to the external load P .

In line with the above considerations, a more exact formula for determining the maximum shearing stress, τ_{\max} , at a' for an axially loaded helical spring was derived by Wahl (69):

$$\tau_{\max} = \frac{16 Pr}{\pi d^3} \left(\frac{4c - 1}{4c - 4} + \frac{0.615}{c} \right) \quad (10-44)$$

where P is the axial load on the spring, d is the diameter of the wire, r is the mean radius of the coil, τ_{\max} is the maximum shear stress, and

$$c = \frac{2r}{d} = \frac{\text{mean coil diameter}}{\text{wire diameter}} \quad (10-45)$$

The expression for τ_{\max} consists of the ordinary formula for stress in helical springs multiplied by a factor k , which depends on the ratio c . Values of k , which can be considered to be a stress multiplication factor, for various values of c are given in the following table:

c	3	4	5	6	8	10
k	1.58	1.40	1.31	1.25	1.18	1.15

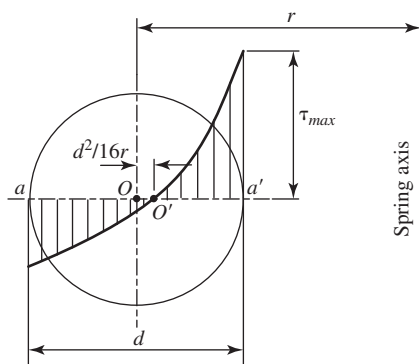


Fig. 10-37. Stress distribution in a coil spring along a transverse diameter, $a-a'$, assuming rotation about the point O . (After Wahl, 69.)

Example

Determine the maximum shear stress in a coil spring for an axial load of 5 kN for a wire diameter d of 25 mm and an r of 100 mm.

$$c = \frac{2 \times 100}{25} = 8, \quad k = 1.18$$

$$\tau_{\max} = \frac{16 \times (5 \times 10^3) \times (100 \times 10^{-3})}{\pi \times (25 \times 10^{-3})} (1.18) = 193 \text{ MPa}$$

Note that this stress occurs on the inside of the spring, the usual location for fatigue crack initiation.

X. THERMAL-MECHANICAL FATIGUE

A thermal-mechanical loading cycle was described in Chapter 8. As with other types of loading, the repeated application of such a cycle can result in fatigue. A traditional cause of concern has been the thermal fatigue cycle imposed upon the disks in the hot stages of a jet aircraft engine during takeoff and landing. Through a combination of design, testing, and in-service inspection, the modern disks now serve reliably, and for a greater number of flight cycles than in years past, before their fatigue lifetime is expended.

XI. CAVITATION

Cavitation is a form of liquid erosion that involves the formation and collapse of bubbles within the liquid. Cavitation damage has been observed on ship propellers and hydrofoils, in hydraulic pumps and structures, and infrequently in sliding bearings (70). Examples of cavitation damage in steel pump components are shown in Figs. 10-38*a* and 10-38*b*. When the local pressure in a liquid is reduced sufficiently, gas-filled bubbles can nucleate and grow. If these bubbles subsequently pass into a region of higher pressure, they can implode in a few milliseconds and form microjets of liquid that attain velocities ranging from 100 to 500 m/sec. A very small fraction of these jets impinges upon the adjacent surface and a form of Hertzian contact occurs, leading to the development of subsurface shear stresses sufficiently high to nucleate fatigue cracks. These fatigue cracks then grow to the surface, allowing small particles to break away and thereby creating observable cavitation damage.

The resistance of a metal to cavitation erosion is influenced by several factors, among which are hardness, the strain energy to fracture, and the corrosion-fatigue strength. Surface treatments such as shot peening are not very effective because they duplicate the processes that occur during the crack nucleation period.

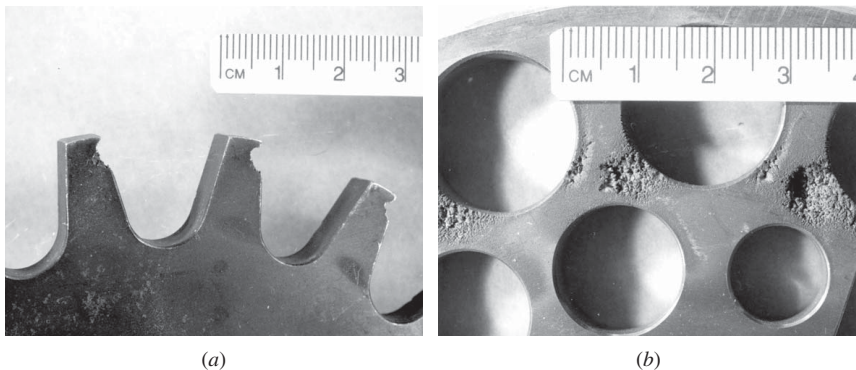


Fig. 10-38. (a,b) Examples of cavitation damage in pump components.

XII. COMPOSITE MATERIALS

Properly made composites can be quite resistant to fatigue; for example, the fatigue strength at 10^7 cycles can be as high as 90% of the tensile strength of the composite. However, environmental degradation of polymer matrix composites, as well as mechanical damage to fibers, can occur to degrade the fatigue resistance. The fatigue crack propagation process can be influenced by a phenomenon known as *bridging*, which is illustrated in Fig. 10-39. Unbroken fibers in the wake of the crack tip serve to reduce the level of the CTOD and thereby reduce the rate of crack propagation.

Composites can also be reinforced by particles and by short fibers known as *whiskers*, and there is current interest in strengthening aluminum with either SiC particles or fibers for automotive engine applications. Another type of composite, known as *Glare*, is made of alternating layers of aluminum and fiberglass bonded together. Its key structural property is better fatigue resistance, for in fatigue-critical areas it can take up to 20–25% higher loads than conventional aluminum. This

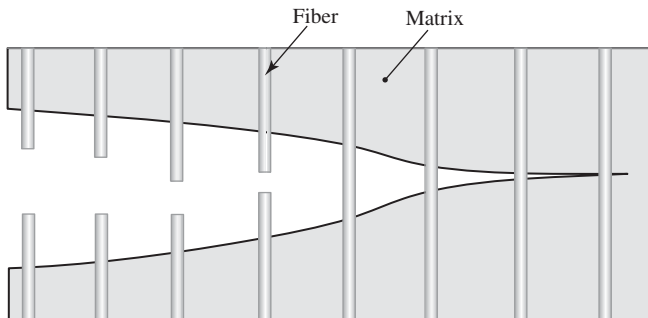


Fig. 10-39. The bridging of a crack in a composite material by unbroken fibers in the wake of the crack tip.

composite will be used for fuselage components of the 555 passenger plane, the Airbus A380 (71).

XIII. SUMMARY

This chapter has provided a broad coverage of the field of fatigue. The main topics were design procedures and factors influencing the initiation and propagation of fatigue cracks. One case study illustrated the use of fracture mechanics in a failure analysis. Another case study dealt with design considerations for gas turbine engines.

REFERENCES

- (1) C. M. Brown, Cambridge University, private communication.
- (2) H. Neuber, Theory of Stress Concentration for Shear-strained Prismatical Bodies with Arbitrary Stress-Strain Law, *Trans. ASME, J. Appl. Mech.*, vol. 28, 1961, p. 544–550.
- (3) A. J. McEvily and K. Minakawa, On Crack Closure and the Notch Size Effect in Fatigue, *Eng. Fract. Mech.*, vol. 28, 1988, pp. 519–527.
- (4) H. Neuber, *Theory of Notch Stresses*, Edwards, London, 1946.
- (5) Design Handbook for the Fatigue Strength of Metals, Japan Society of Mechanical Engineering (JSME), vol. 1, Tokyo, Japan, 1982, p. 125.
- (6) S.-I. Nishida, *Failure Analysis in Engineering Applications*, Butterworth-Heinemann, Oxford, 1986.
- (7) *Aviation Week and Space Technology*, Sept. 13, 1999.
- (8) P. Albrecht and W. Wright, “Bridge Design,” in *Fracture Mechanics: Applications and Challenges*, ed. by M. Fuentes, M. Elices, A. Martin-Meizoso, J. M. Martinez Esnaolo,ESIS Pub. 26, Elsevier, Oxford, 2000, pp. 211–234.
- (9) W. A. Wood, Formation of Fatigue Cracks, *Phil. Mag.*, vol. 3, no. 31, 1958, pp. 692–699.
- (10) R. C. Boettner and A. J. McEvily, *Acta Met.*, vol. 13, 1965, pp. 937–945.
- (11) K. Differt, U. Essmann, and H. Mughrabi, *Phil. Mag. A*, 1986, vol. 54, pp. 237–258.
- (12) ASTM E 647, Standard Test Method for Measurement of Fatigue Crack Growth Rates, *American Society for Testing and Materials*, Philadelphia, 1991.
- (13) ASTM STP 982, Mechanics of Fatigue Crack Closure, ed. by J. C. Newman and W. Elber, *American Society for Testing and Materials*, Conshohocken, PA, 1988.
- (14) ASTM STP 1343, Advances in Fatigue Crack Closure Measurement and Analysis, ed. by R. C. McClung and J. C. Newman, Jr., *American Society for Testing and Materials*, Conshohocken, PA, 1999.
- (15) W. Elber, Fatigue Crack Closure under Cyclic Tension, *Eng. Fract. Mech.*, vol. 2, 1970, pp. 37–45.
- (16) B. Budiansky and J. W. Hutchinson, Analysis of Closure in Fatigue Crack Growth, *J. Appl. Mech.*, vol. 45, 1978, pp. 267–276.
- (17) S. Ishihara, Y. Sugai, and A. J. McEvily, On the Distinction between Plasticity- and Roughness-Induced Fatigue Crack Closure, *Met. Trans.*, vol. 43A, no. 9, 2012, pp. 3086–3096.

- (18) K. Minakawa, G. Levan, and A. J. McEvily. The Influence of Load Ratio on Fatigue Crack Growth in 7090-T6 and IN9021-T4 P/M Aluminum Alloys, *Met. Trans.*, vol. 17A, 1986, pp. 1787–1795.
- (19) R. J. Donahue, H. MCI. Clark, P. Atanmo, R. Kumble, and A. J. McEvily, Jr., Crack Opening Displacement and the Rate of Fatigue Crack Growth, *Int. J. Fract. Mech.*, vol. 8, no. 2, 1972, pp. 209–219.
- (20) A. J. McEvily, On the Cyclic Crack-Tip Opening Displacement, *Fat. Fract. Eng. Mat. Struct.*, vol. 32, 2009, pp. 284–285.
- (21) A. J. McEvily and Z. Yang, The Nature of the Two Opening Levels Following an Overload in Fatigue Crack Growth, *Met. Trans.*, vol. 21A, 1990, pp. 2717–2727.
- (22) H. Bao and A. J. McEvily. On Plane-Stress-Plane-Strain Interactions in Fatigue Crack Growth, *Int. J. Fatigue*, vol. 20, 1998, pp. 441–448.
- (23) A. J. McEvily and Z. Yang, “On Transients in Fatigue Crack Growth,” in *Effects of Load and Thermal Histories*, ed. by P. Liaw and T. Nicholas, Metals Society, AIME, Warrendale, PA, 1987, pp. 3–12.
- (24) B. Gamache and A. J. McEvily, On the Development of Fatigue Crack Closure in *Fatigue '93*, vol. 1, ed. by J.-P. Bailon and J. I. Dickson, EMAS, Warley, UK, 1993, pp. 577–582.
- (25) A. J. McEvily, M. Endo, and Y. Murakami, On the Relationship and the Short Fatigue Crack Growth Threshold, *Fatigue Fract. Eng. Mat. Struct.*, vol. 26, 2003, pp. 269–278.
- (26) S. Ishihara and A. J. McEvily, On the Early Initiation of Fatigue Cracks in the High Cycle Regime, *Proceeding of the 12th International Conference on Fracture*, CD-ROM, Ottawa, Canada, July 12–17, 2009.
- (27) C. A. Zapffe and C. O. Worden, Fractographic Registrations of Fatigue, *Trans. ASM*, 1951, vol. 43, pp. 958–969.
- (28) P. J. E. Forsyth and D. Ryder, Some Results of the Examination of Aluminum Alloy Specimen Fracture, *Metallurgia*, vol. 63, 1961, pp. 117–124.
- (29) C. Laird and G. C. Smith, Crack Propagation in High Stress Fatigue, *Phil. Mag.*, vol. 8, 1962, pp. 847–857.
- (30) J. C. McMillan and R. M. Pelloux, Fatigue Crack Propagation Under Program and Random Loads, in *ASTM STP 415, Fatigue Crack Propagation*, ASTM, Conshohocken, PA, 1967, pp. 505–535.
- (31) A. J. McEvily and J. Gonzalez, Fatigue Crack Deformation Processes as Influenced by the Environment, *Met. Trans.*, vol. 23A, No. 8, 1992, pp. 2211–2221.
- (32) R. C. Juvinall, *Engineering Considerations of Stress, Strain and Strength*, McGraw-Hill, New York, 1967.
- (33) J. O. Almen and P. H. Black, *Residual Stresses and Fatigue in Metals*, McGraw-Hill, New York, 1963.
- (34) M. Wakita, T. Kuno, T. Hasegawa, K. Saruki, and K. Tanaka, Effects of Shot Peening on Torsional Fatigue Strength of High Strength Spring Steel, *J. Soc. Mat. Sci.*, vol. 57, no. 8, 2008, pp. 800–807.
- (35) R. P. Wei and D. G. Harlow, Corrosion and Corrosion Fatigue of Aluminum Alloys—an Aging Aircraft Issue, in *Fatigue '99*, vol. 4, ed. by X. R. Wu and Z. G. Wang, EMAS, West Midlands, UK, 1999, pp. 2197–2204.
- (36) H. O. Fuchs and R. I. Stephens, *Metal Fatigue in Engineering*, Wiley, Hoboken, NJ, 1980.

- (37) T. Sakai, M. Takeda, N. Tanaka, and N. Oguma, Very High Cycle Fatigue, *Proceedings of the 25th Symposium on Fatigue*, Japan Society of Material Science, 2000, Kyoto, pp. 191–194.
- (38) Y. Murakami, N. N. Yokohama, and K. Takai, The Opically Dark Area, *Proceedings of the 25th Symposium on Fatigue*, Japan Society of Material Science, 2000, Kyoto, pp. 223–226.
- (39) Y. Murakami, T. Toriyama, Y. Koyasu, and S. Nishida, Effects of Chemical Composition of Non-Metallic Inclusions on Fatigue Strength of High Strength Steels, *J. Iron Steel Inst. Japan*, vol. 79, 1993, pp. 60–66.
- (40) J. Schijve, in Predictions of Fatigue Life and Crack Growth as an Engineering Problem. A State of the Art Survey, *Fatigue '96*, vol. 2, ed. by G. Lütjering and H. Nowak, Pergamon, Oxford, 1996, pp. 1149–1164.
- (41) J. Schijve, in ASTM STP 415, *Fatigue Crack Propagation*, Conshohocken, PA, 1967, p. 533.
- (42) A. J. McEvily and W. Illg, The Rate of Fatigue-Crack Propagation in Two Aluminum Alloys, *NACA TN 4394*, 1958.
- (43) P. Kuhn and H. F. Hardrath, Engineering Method for Estimating Notch-Size Effect in Fatigue Tests on Steel, *NACA 2805*, 1952.
- (44) C. Q. Bowles and J. Schijve, ASTM STP 811, Crack Tip Geometry for Fatigue Cracks Grown in Air and Vacuum, *Fatigue Mech.*, 1983, pp. 400–425.
- (45) G. R. Irwin, *Encyclopedia of Physics*, vol. 6, Springer, Heidelberg, 1958.
- (46) P. C. Paris, M. P. Gomez, and W. P. Anderson, A Rational Analytic Theory of Fatigue, *Trend Eng.*, vol. 13, 1961, pp. 9–14.
- (47) P. C. Paris and F. Erdogan, A Critical Analysis of Crack Propagation Laws, *J. Basic Eng.*, *Trans. ASME*, vol. 85, 1965, pp. 528–534.
- (48) G. R. Irwin, *Fracture Mechanics, Proceedings of the First Symposium on Naval Structural Mechanics*, Pergamon, New York, 1960, pp. 557–594.
- (49) N. E. Frost and D. S. Dugdale, The Propagation of Fatigue Cracks in Sheet Specimens, *J. Mech. Physics Solids*, vol. 6, no. 2, 1958, pp. 92–110.
- (50) H. W. Liu, Crack Propagation in Thin Metal Sheets Under Repeated Loading, *J. Basic Eng.*, *Trans. ASME*, Series D, vol. 83, no. 1, 1961, pp. 23–31.
- (51) B. L. Boyce and R. O. Ritchie, Effect of Load Ratio and the Maximum Stress Intensity Factor on the Fatigue Threshold in Ti-6Al-4V, *Eng. Fracture Mech.*, vol. 68, (2001), pp. 129–147.
- (52) G. R. Irwin, A. J. McEvily, B. L. Boyce and R. O. Ritchie, unpublished results.
- (53) S. Ishihara, A. J. McEvily, T. Goshima, S. Nishino and M. Sato, 2008, The Effect of the R Value on the Number of Delay Cycles Following an Overload, *Int. J. Fatigue*, vol. 30, 1737–1742.
- (54) G. R. Irwin, Naval Research Laboratory Report No. 5486, Naval Research Laboratory, Washington, D.C. 1960.
- (55) D. S. Dugdale, Yielding of Steel Sheets Containing Slits, *J. Mech. Physics Solids*, vol. 8, 1960, pp. 557–594.
- (56) M. Endo and A. J. McEvily, Prediction of the Behavior of Small Fatigue Cracks, *Mat. Sci. Eng.*, vol. A 468–470, 2007, pp. 51–58.
- (57) H. Kitagawa and S. Takahashi, Applicability of Fracture Mechanics to Very Small Cracks, *Proceedings of the 2nd International Conference on Mechanical Behavior Of*

- Materials, Boston, USA, American Society of Materials, Materials Park, Ohio, 1976, pp. 627–631.
- (58) M. H. El Haddad, T. H. Topper and K. N. Smith, Prediction of Non Propagating Cracks, *Eng. Fract. Mech.*, vol 11, 1979, pp. 573–584.
 - (59) A. J. McEvily, R. Nakamura, H. Oguma, K. Yamashita, H. Matsunaga, and M. Endo, On the Mechanism of Very High Cycle Fatigue in Ti-6Al-4V, *Scripta Materialia*, vol. 59, no. 11, 2008, pp. 1207–1209.
 - (60) M. Fujihara, Y. Kondo, and T. Hattori, Fractography in the Near-Threshold Range, *Japan Soc. Mater. Sci.*, vol. 40, no. 453, 1991, pp. 712–717.
 - (61) K. Furukawa, Examination of Near-Threshold Fracture Surfaces, *Proceedings of the 25th Symposium on Fatigue*, Japan Society of Material Science, 2000, Kyoto, pp. 71–73.
 - (62) I. Le May and H. C. Furtado, Power Station Assessment and Failure Investigation, *Technol., Law and Ins.*, vol. 4, 1999, pp. 111–119.
 - (63) Netherland Aviation Safety Board, *Aircraft Accident Report 92-11*, El Al Flight 1862, Amsterdam, October 4, 1992.
 - (64) E. Zahavi, *Fatigue Design*, CRC Press, New York, 1996.
 - (65) A. Oldersma and R. J. H. Wanhill, Netherlands National Aerospace Laboratory, *NLR Contract Report 93030 C*, Amsterdam, the Netherlands, 1993.
 - (66) *ASM Metals Handbook*, 9th ed., vol. 1, ASM, Materials Park, OH, 1978, p. 426.
 - (67) *Aviation Week and Space Technology*, June 7, 1999, p. 43.
 - (68) B. A. Cowles, High Cycle Fatigue in Aircraft Gas Turbines—An Industry Perspective, *Int. J. Fract.*, vol. 80, 1996, pp. 147–163.
 - (69) A. M. Wahl, *Mechanical Springs*, 2nd ed., McGraw-Hill, New York, 1963.
 - (70) F. G. Hammitt and F. J. Heymann, in *ASM Metals Handbook*, vol. 10, 8th ed., Failure Analysis and Prevention, ASM, Materials Park, OH, 1975, p. 160.
 - (71) M. A. Dornheim, *Aviation Week and Space Technology*, 2001, pp. 126–128.

FOR FURTHER READING

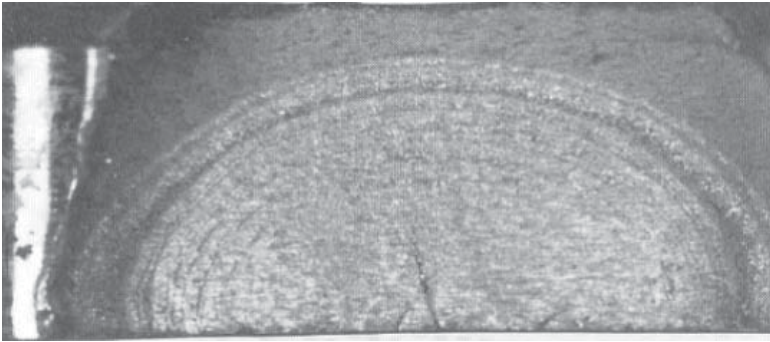
- (1) S. Suresh, *Fatigue of Materials*, 2nd ed., Cambridge University Press, Cambridge, 1998.
- (2) *Fatigue and Fracture*, ASM Handbook, vol. 19, Materials Park, OH, 1996.
- (3) J. A. Bannantine, J. C. Comer, and J. L. Handrock, *Fundamentals of Metal Fatigue Analysis*, Prentice Hall, Englewood Cliffs, NJ, 1990.
- (4) Y. Murakami, *Metal Fatigue*, Elsevier Ltd., 2002.
- (5) J. C. Newman Jr., E. L. Anagnostou, and D. Rusk, Fatigue Crack Growth Analyses, *Int. J. Fatigue*, 2013, in press.

PROBLEMS

- 10-1.** A thick-walled pressure vessel is made of steel for which $K_c = 50 \text{ MPa}\sqrt{\text{m}}$. Nondestructive testing shows that the component contains semicircular cracks

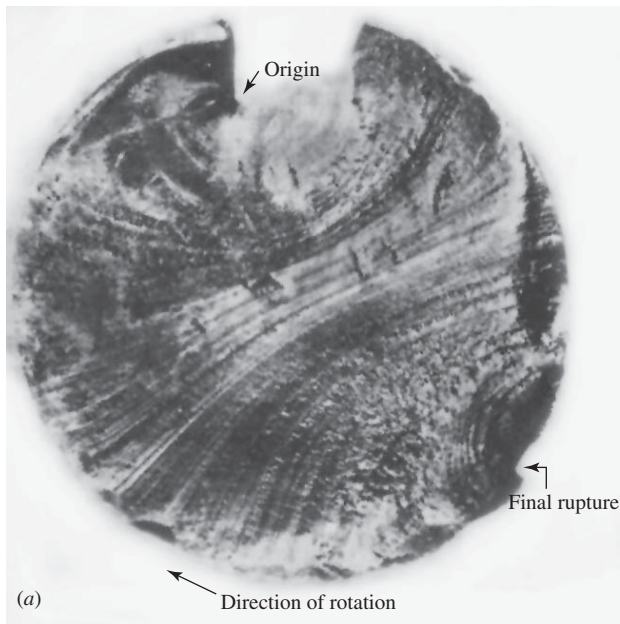
of depth up to $a = 0.2$ mm. The crack growth rate under cyclic loading is given by $da/dN = A(\Delta K)^2$, where $A = 10^{-10}(\text{MPa})^{-2}$. The component is subjected to an alternating stress range $\Delta\sigma = 200$ MPa ($R = 0$). Given that $\Delta K = 0.73\Delta\sigma\sqrt{\pi a}$, determine the number of cycles to failure.

- 10-2.** From Fig. 8-3, estimate the plastic strain range in the thermal cycle shown from the width of the hysteresis loop. Then use the Coffin-Manson Law, $N_f^{1/2}\Delta\varepsilon_p = C$, to determine the number of cycles to failure if the value of C is 0.6.
- 10-3.** The Basquin Law for an alloy tested at $R = -1$ is $N_f^b(\Delta\sigma/2) = C$. At a $\Delta\sigma$ of 300 MPa, N_f is 10^5 cycles, and at a $\Delta\sigma$ of 200 MPa, N_f is 10^7 cycles.
- Determine the values of the constants b and C .
 - What is N_f for a stress range of 250 MPa?
 - If a specimen is cycled at 250 MPa for 5×10^5 cycles, how many additional cycles based upon the Palmgren-Miner Rule will the specimen be able to sustain at a stress range of 200 MPa?
- 10-4.** A critical component whose fracture toughness is K_{Ic} is cyclically loaded at $R = 0$. The component must withstand at least N cycles before failure. The stress range is $\Delta\sigma$ and the rate of fatigue crack growth in the part is given as $da/dN = A(\Delta K)^2$, where $\Delta K = Y(\Delta\sigma)\sqrt{\pi a}$ is the range of the stress intensity factor for a fatigue crack or any initial flaws, if present. Assuming linear elastic behavior:
- Show that the magnitude of the proof stress to ensure satisfactory service that must be applied before the component is put into service is given by $\sigma_{proof} = \sigma e^{\frac{A}{2}Y^2\pi\Delta\sigma^2N}$. A procedure of this nature is used in safeguarding the wings of the F-111 swing-wing aircraft. If this were a pressure vessel, the working pressure would be raised by the same factor in conducting a proof test.
 - If $A = 2 \times 10^{-9}(\text{MPa})^{-2}$, $Y = 1.0$, $\sigma = 140$ MPa, and $N = 10,000$ cycles, determine the required proof stress level.
- 10-5.** The macrostructure shown on the right in the figure was from a fatigue fractured steel.
- Discuss what macrostructure features (beach marks, ratchet lines, flatness of the fracture surface, etc.) are present on the fracture surface.
 - Identify the crack initiation site.
 - Estimate the applied maximum stress, σ_{\max} , if the steel has a fracture toughness of $120 \text{ MPa}\sqrt{\text{m}}$ and the component failed with $R = 0$.
- (Note: the image was presented with the real dimensions.)



10-6. The macroscopic image below is the cross section of a shaft failed under cyclic rotational bending. Discuss

- (a) the locations of the crack initiation site and the final fracture region.
- (b) what other markings are present and what the possible reasons are for the appearance of these markings.
- (c) why the crack initiation site and the final fracture region are not located symmetrically.
- (d) whether the crack initiation site and the final fracture region change the location if the direction of rotation changes.



11

Statistical Distributions

I. INTRODUCTION

This chapter deals briefly with two types of statistical distribution, normal or Gaussian distribution and extreme value distributions. Normal distributions are useful in dealing with the scatter encountered in fatigue test results, for example. Extreme value distributions are useful in dealing with early failures in a population and in analyzing the influence of inclusions on fatigue strength.

II. DISTRIBUTION FUNCTIONS

There are two types of distribution functions. One is the relative distribution function, which gives the number of observations that fall between two limits—for example, in determination of the yield strengths of 449 tensile bars, the percentage of the results that fall between 828 and 841 MPa (122 ksi). The other distribution function is the cumulative distribution function, which gives, for example, the total number of specimens of the 449 tensile bars tested with yield strengths less than 841 MPa (122 ksi).

The central tendency of a relative distribution is often of interest, and it can be determined by one of three measures. These are:

1. *Arithmetic mean (average)*, μ : The sum of the values in the distribution divided by their number

2. *Median*: The value in an ordered set of values below which and above which there is an equal number of values
3. *Mode*: The value that occurs with the highest frequency

In a normal distribution, these three measures of central tendency are equal, whereas in an extreme value distribution they generally differ. The standard deviation is a measure of the spread in a population of n items and is expressed as

$$\sigma = \sqrt{\frac{\sum_{i=1}^{i=n} (x_i - \mu)^2}{n - 1}} \quad (11-1)$$

where x_i is the i th value in an ordered series. The variance is the square of σ and is also used as a measure of scatter. The coefficient of variation v is expressed as

$$v = \frac{\sigma}{\mu} \quad (11-2)$$

The normal distribution focuses on the central characteristics of a distribution and is characterized by a symmetric bell-shaped curve and two parameters, the mean of the population μ and the standard deviation σ . The Weibull extreme value distribution (1) is used in the assessment of the probability of early failure in a distribution, the left-hand side of a distribution, and is widely used in the bearing industry. The Gumbel extreme value distribution (2) is used to predict items on the right-hand side of a distribution such as the size of the largest inclusion to be found within a given volume.

III. THE NORMAL DISTRIBUTION

The equation derived by Gauss for the bell-shaped normal distribution is

$$f(x) = \frac{1}{\sigma \sqrt{2\pi}} e^{-(x-\mu)^2/2\sigma^2} \quad (11-3)$$

where $f(x)$ is the height of the frequency distribution curve at a particular value of x . An example of this distribution, the standardized normal frequency distribution, is given in Fig. 11-1a. The distribution is symmetrical about μ and extends from $-\infty$ to $+\infty$. (The German 10-mark banknote, which was issued in October 1993, features a portrait of Gauss, Eq. 11-3, and a bell-shaped distribution curve.) The relative frequency of a value of $(x - \mu)/\sigma$ falling between $-\infty$ and a specified value is given by the area under the curve between these limits, with the area under the entire curve being unity. The relative frequency is also known as the *cumulative distribution function* and is obtained by numerically integrating Eq. 11-3 between the limits of $-\infty$ and $(x - \mu)/\sigma$. Table 11-1 lists the areas under the curve for several ranges of σ .

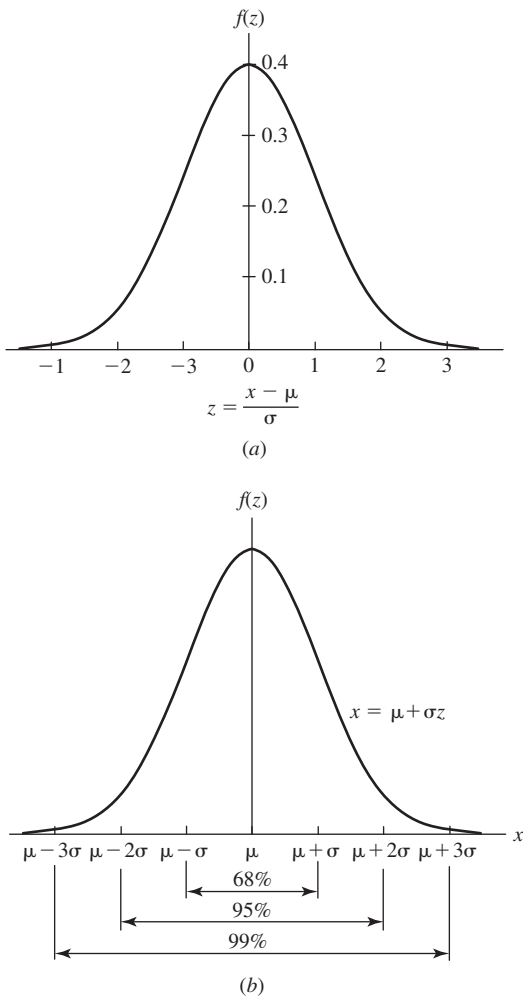


Fig. 11-1. (a) The bell-shaped curve associated with the standardized normal frequency distribution. (b) One, two, and three σ ranges about the mean of a normal distribution.

Table 11-1. Areas Under the Normal Frequency Curve for Given Ranges of σ

Range	Area Under the Curve
$\pm 0.5 \sigma$	0.3830
$\pm 1.0 \sigma$	0.6826
$\pm 2.0 \sigma$	0.9744
$\pm 3.0 \sigma$	0.9974
$-\infty$ to $(\mu - \sigma)$	0.1587
$-\infty$ to μ	0.5000
$-\infty$ to $(\mu + \sigma)$	0.8413
$-\infty$ to $(\mu + 2 \sigma)$	0.9772
$-\infty$ to $(\mu + 3 \sigma)$	0.9987

Table 11-2. Frequency Tabulation of Yield Strengths of a Steel (4)

Yield Strength, MPa	Frequency	Cumulative Frequency	Cumulative Frequency, %
786.0–799.1	4	4	0.9
799.8–812.9	6	10	2.2
813.6–826.7	8	18	3.8
827.4–840.5	26	44	9.6
841.2–854.3	29	73	16.1
855.0–868.1	44	117	25.9
868.8–881.9	47	164	36.4
882.6–895.7	59	223	49.5
896.4–909.5	67	290	64.5
910.1–923.2	45	335	74.5
923.9–937.0	49	384	85.4
937.7–950.8	29	413	91.9
951.5–964.6	17	430	95.7
965.3–978.4	9	439	97.7
979.1–992.2	6	445	99.0
992.9–1006.0	4	449	99.9

The area between $\pm \sigma$ of the mean is equal to 0.68, that is, 68% of the values fall between these limits in the normal distribution. Similarly, 95% of the values are between $\pm 2\sigma$ of the mean, and 99.7% of the values are between $\pm 3\sigma$ of the mean, as indicated in Fig. 11-1*b*. One commonly stated production goal in industry is the 6 σ goal, meaning that only 3.4 parts per million are expected to be outside of the specified tolerance range.

To determine if a distribution can be treated as a normal distribution, the cumulative frequency distribution is plotted on normal probability paper. In this type of plot, the cumulative frequency (in percent) is plotted against the parameter of interest—for example, the yield strength. If the distribution is indeed normal, it will plot as a straight line. The frequency distribution of the yield strengths of a steel is shown in Table 11-2 and is used as an illustration.

Figure 11-2 shows the above data plotted on normal probability data, and it is seen that the distribution can be fitted by a straight line, indicating a normal distribution. The mean value and the standard deviation can also be determined from Fig. 11-2. The mean is the value of the abscissa corresponding to a cumulative frequency of 50%. The standard deviation is equal to one-half of the difference between the abscissa value at the 84% cumulative frequency level and the abscissa value at the 16% cumulative frequency level.

IV. STATISTICS OF FATIGUE; STATISTICAL DISTRIBUTIONS

An important consideration in dealing with the reliability of a structure is the scatter in in-service loads encountered in practice compared to the scatter in a material's ability to resist the imposed loading conditions, Fig. 1-2. Figure 11-3 is a schematic diagram which indicates both the distribution of fatigue lives and as well as fatigue

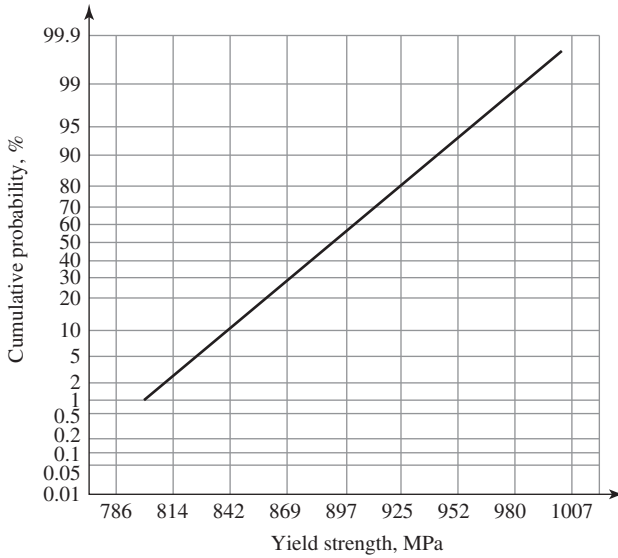


Fig. 11-2. Cumulative normal distribution plot of yield strengths plotted on normal probability paper. (After Dieter, 4.)

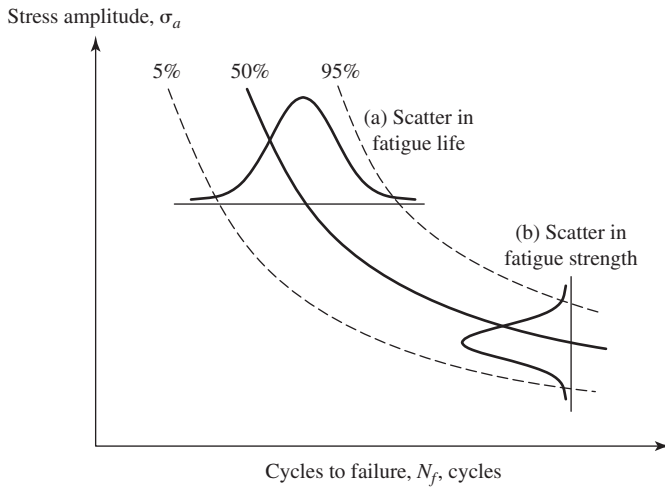


Fig. 11-3. (a) The scatter in fatigue lives. (b) The scatter in fatigue strengths. The probability of failure is indicated.

strengths. An example of the degree of scatter encountered in testing laboratory samples is given in Fig. 11-4 (5). This figure is a logarithmic-normal probability plot showing individual fatigue lifetimes obtained at different stresses for the aluminum alloy 7075-T6 under zero-tension loading. An even larger scatter may be found in service due to differences in nominal loading and environmental conditions.

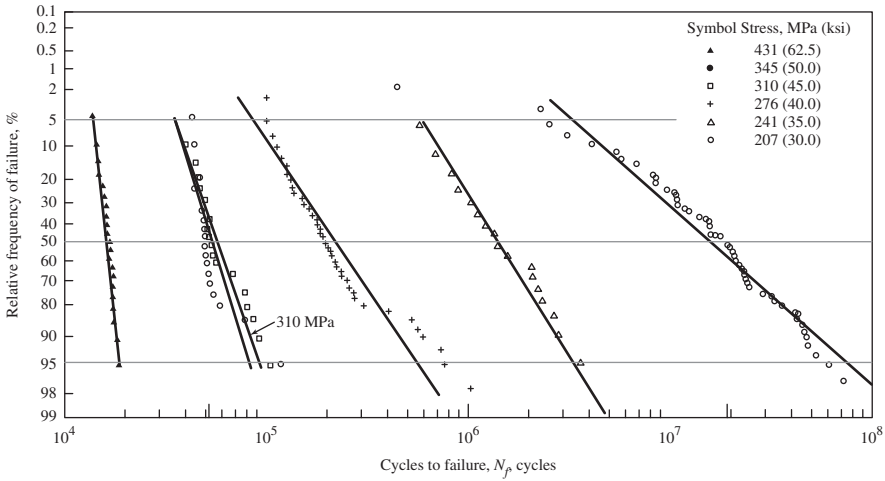


Fig. 11-4. Logarithmic normal probability diagram showing individual fatigue lifetimes obtained at different stress ranges at $R \approx 0$. (After Sinclair and Dolan, 5.)

A straight line on this plot corresponds to a log-normal distribution of data points, and the steeper the slope, the smaller the standard deviation in lifetimes. Note that the scatter increases with a decrease in σ_{\max} . The line corresponding to the highest stress amplitude is steep, and the scatter is relatively small. However, at the lowest σ_{\max} , 207 MPa (30 ksi), the line is much less steep and there is more than an order of magnitude difference in lifetimes.

The statistical distribution of the fatigue strengths indicated in Fig. 11-3 is usually analyzed either as a normal distribution rather than a log-normal distribution or as an extreme value distribution.

V. THE WEIBULL DISTRIBUTION (1)

The Weibull distribution function is the most widely used extreme-value distribution function. It is particularly useful in predicting the probability of an early fatigue failure. The Weibull probability density function is given by the following three-parameter equation:

$$f(x) = \frac{m}{\delta} \left(\frac{x - x_0}{\delta} \right)^{m-1} e^{-\left(\frac{x - x_0}{\delta} \right)^m} \quad (11-4)$$

where δ is the scale parameter, m is the shape parameter, a measure of the degree of scatter, and x_0 is the location parameter.

The cumulative probability distribution function is given by

$$F(x) = 1 - e^{-\left(\frac{x - x_0}{\delta} \right)^m} \quad (11-5)$$

The quantity $F(x)$ is estimated from a group of N samples that are arranged in order from the smallest to the largest, by noting the number of samples n that have value of x or less; thus,

$$F(x) = \frac{n}{N} \quad (11-6)$$

However, because N is generally small, it is preferable to define $F(x)$ as

$$F(x) = \frac{n}{N + 1} \quad (11-7)$$

The cumulative probability can be estimated from the rank number i of the arranged data by the following formula (6):

$$F_i = \frac{i - 0.3}{N + 0.4} \quad (11-8)$$

Equation 11-5 can also be written in a more useful form as

$$\ln[-\ln(1 - F)] = -m \ln \delta + m \ln(x - x_0) \quad (11-9)$$

If the data follow a Weibull distribution, a plot of $\ln \ln[1/(1 - F)]$ versus $\ln(x - x_0)$ will result in a straight line of slope m and the Weibull parameters can be estimated by the least squares method. δ is a scale parameter because a change in its value will result in a corresponding shift in the position of the line on the plot. For F equal to 0.632, $\ln \ln[1/(1 - F)]$ is zero, and $\ln \delta$ is equal to the corresponding value of the abscissa. The slope m provides an indication of the skewness of the frequency distribution. As shown in Fig. 11-5, an m value of 3.5 corresponds approximately to a normal bell-shaped distribution. As m decreases below 3.5, the spread of the data

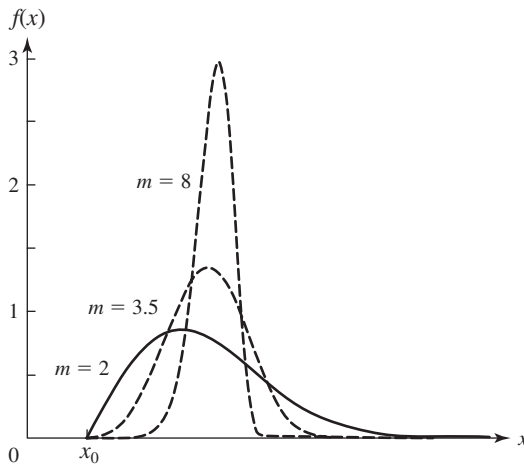


Fig. 11-5. Weibull relative frequency distribution as influenced by the shape parameter m .

increases and there is a large percentage of “infant mortalities.” For m values greater than 3.5, there is a benefit in that the dispersion of the data is low and the reliability of prediction is increased.

In some cases, it may be possible to fit a straight line only through the lower portion of the cumulative distribution curve, yet this may be sufficient for the particular application.

A. Application to Yield Strength

In a Weibull distribution of yield strengths, the probability that the yield strength σ_Y will fall in the range from 0 to σ_Y (i.e., the cumulative probability distribution function) is denoted by $F(\sigma_Y)$ and is given as

$$F(\sigma_Y) = 1 - e^{-\left(\frac{\sigma_Y - \sigma_{Y0}}{\sigma_0}\right)^m} \quad (11-10)$$

where σ_{Y0} is the expected lowest yield strength in the population.

Equation 11-10 is rewritten as

$$\ln \ln \left[\frac{1}{1 - F(\sigma_Y)} \right] = -m \ln \sigma_0 + m \ln(\sigma_Y - \sigma_{Y0}) \quad (11-11)$$

Figure 11-6 shows the yield strength data of Table 11-2 plotted in accord with Eq. 11-7 for various values of σ_{Y0} . It is seen that the best straight-line fit to the data at low values of F , the usual region of interest, is obtained for a value of σ_{Y0} equal to 724 MPa (105 ksi). The slope of this line is 4.69, and σ_0 is equal to 182.6 MPa (26.4 ksi). Special coordinate paper, known as *Weibull probability paper*, is commercially available to expedite the plotting of data.

B. Application to Fatigue Life

In a Weibull distribution of fatigue life, the cumulative probability distribution function $F(N_f)$ is given as

$$F(N_f) = 1 - e^{-\left(\frac{N_f - N_{f0}}{N_0}\right)^m} \quad (11-12)$$

Table 11-3 shows the results of 101 fatigue tests of the 6061-T6 aluminum alloy. The specimens were loaded axially at $R = -1$, with the loading direction parallel to the rolling direction and the maximum stress fixed at 144.8 MPa (21 ksi) (7). The fatigue lives are given in Table 11-3. Figure 11-7 shows the fatigue life data of Table 11-3 plotted in accord with Eq. 11-8, with the value of N_{f0} taken to be 181×10^3 cycles. The remaining Weibull parameters were estimated from a least squares fit of the data: $m = 3.30$, and $N_0 = 1,363 \times 10^3$ cycles. It should be noted that the shape parameter m is close to 3.5; therefore, this set of data can also be analyzed as a normal distribution. The mean and standard deviation of the normal distribution are $1,401 \times 10^3$ cycles and 391×10^3 cycles, respectively.

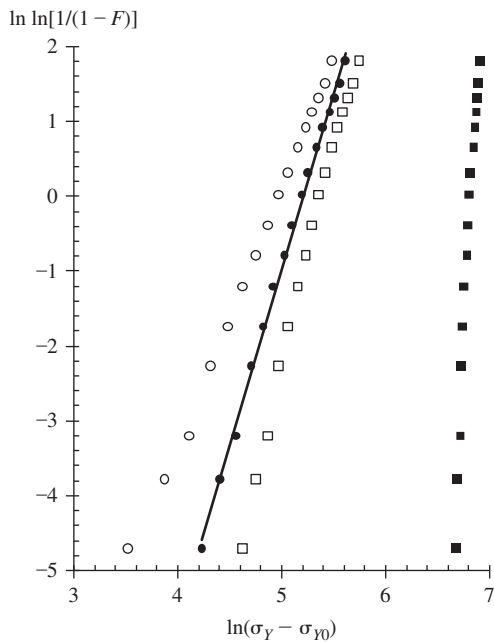


Fig. 11-6. Weibull plot of yield strengths. σ_{Y0} is the expected minimum value of the yield strength.

Table 11-3. Fatigue Lifetimes of 101 Specimens of Al 6061-T6 at a Maximum Stress of 144.8 MPa (21 ksi) and $R = -1$ (7). Lifetime in Cycle $\times 10^{-3}$

370	1,016	1,235	1,419	1,567	1,820
706	1,018	1,238	1,420	1,578	1,868
716	1,020	1,252	1,420	1,594	1,881
746	1,055	1,258	1,450	1,602	1,890
785	1,085	1,262	1,452	1,604	1,893
797	1,102	1,269	1,475	1,608	1,895
844	1,102	1,270	1,478	1,630	1,910
855	1,108	1,290	1,481	1,642	1,923
858	1,115	1,293	1,485	1,674	1,940
886	1,120	1,300	1,502	1,730	1,945
886	1,134	1,310	1,505	1,750	2,023
930	1,140	1,313	1,513	1,750	2,100
960	1,199	1,315	1,522	1,763	2,130
988	1,200	1,330	1,522	1,768	2,215
990	1,200	1,355	1,530	1,781	2,268
1,000	1,203	1,390	1,540	1,782	2,440
1,010	1,222	1,416	1,560	1,792	

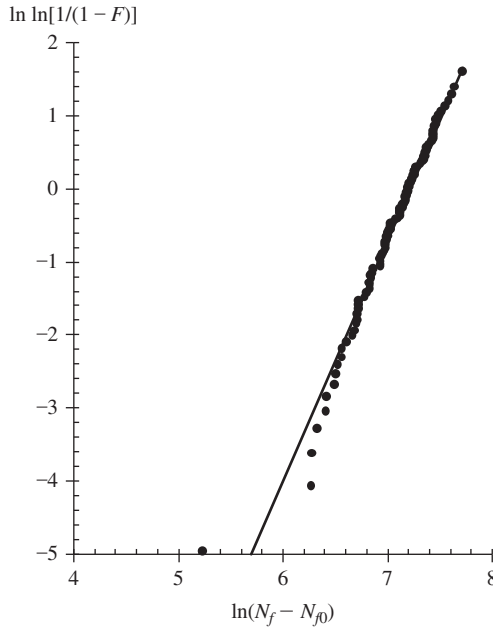


Fig. 11-7. Weibull plot of fatigue life.

VI. THE GUMBEL DISTRIBUTION (3)

Another type of extreme value distribution is due to Gumbel. Whereas the Weibull distribution is used in estimating the probability of early failure in a population, the Gumbel extreme value distribution is useful in predicting the likelihood of an event such as a hurricane or flood of a given magnitude. Murakami and co-workers (8,9) have applied Gumbel's extreme value distribution method to predict the maximum size of an inclusion within a given volume of metal, an important consideration with respect to quality control and fatigue strength.

In the procedure developed by Gumbel, the cumulative distribution function F_j is defined as

$$F_j = \frac{j}{N+1} \quad (11-13)$$

where N is the total number of observations and j is the j th observation when the N observations are arranged in order from smallest to largest.

A reduced variate y_j is then related to Eq. 11-13 by

$$y_j = -\ln \left[-\ln \left(\frac{j}{N+1} \right) \right] = -\ln[-\ln(F_j)] \quad (11-14)$$

This implies that

$$e^{-y_j} = -\ln\left(\frac{j}{N+1}\right) \quad (11-15)$$

and that

$$e^{-e^{-y_j}} = \frac{j}{N+1} = F_j \quad (11-16)$$

that is, the cumulative distribution function is a doubly exponential function.

Note that in a plot of a Gumbel distribution the abscissa scale is linear rather than logarithmic, as in a Weibull distribution.

The concept of the *return period* is introduced. If an event (e.g., a value equal to or larger than x) has a cumulative probability p , on average $1/p$ trials are needed for the event to happen once. The return period is defined as

$$T_j = \frac{1}{p} = \frac{1}{1 - F_j} \quad (11-17)$$

where p is the cumulative probability of the event with a value equal to or larger than x .

Upon substituting Eq. 11-13 into Eq. 11-17, we obtain

$$T_j = \frac{1}{1 - \left(\frac{j}{N+1}\right)} = \frac{N+1}{N+1-j} \quad (11-18)$$

A reduced variate y_j in Eq. 11-14 can be written in terms of a return period as

$$y_j = -\ln\left[-\ln\left(\frac{T_j - 1}{T_j}\right)\right] \quad (11-19)$$

The return period for the median of a distribution (cumulative probability = 0.5 or $F(y) = 0.5$) is 2, for the upper quartile (cumulative probability = 0.25 or $F(y) = 0.75$) it is 4, and so on. Scales other than time may be used; for example, a length scale is used in considering the cumulative probability that an inclusion of a given size or a corrosion pit of a given depth will be found in examining N numbers of metallographic sections. If the unit observation area is S_0 and if the total area to be inspected is S , then the return period is

$$T = \frac{S}{S_0} \quad (11-20)$$

A. Maximum Size of the Inclusion

Murakami and coworkers (8) have applied Gumbel's extreme value distribution method to predict the maximum size of the inclusion (defined by $\sqrt{\text{area}}$) present

within a given volume of metal, an important consideration with respect to quality control and fatigue strength.

The first step is to prepare a polished section of the metal and to determine the square root of the area of the largest inclusion, that is, $\sqrt{area_{max}}$, found within an area S_0 . Typical values for S_0 range from 0.075 to 0.482 mm². This operation is repeated on N different sections, where N is often set at 40. The values of $\sqrt{area_{max,i}}$ are classified, starting with the smallest, and indexed with $i = 1, \dots, N$. The cumulative distribution function F_i and the reduced variate y_i are then calculated from Eqs. 11-13 and 11-14. Next, the data are plotted on extreme value distribution probability paper with the reduced variate as the ordinate and $\sqrt{area_{max}}$ as the abscissa, as in Fig. 11-8. (The value of F_j , expressed in percent, may also be used as the ordinate, since F_j and y_j are related through Eq. 11-14. The return period T_j can also be used as the ordinate, since T_j is a function of F_j , that is, Eq. 11-17.)

If a straight line can be drawn thorough the data, as in Fig. 11-8, the distribution can be considered to be doubly exponential in accord with Gumbel's statistical method of the extremes. In this example, Fig. 11-8 indicates that the cumulative probability that the largest inclusion found will be of size 14.97 μm or less is 9.756% (corresponding to an i value of 4, $F_4 = 4/(40 + 1) = 0.09756$).

If a straight line is found, as in Fig. 11-8, it can be extended beyond the range of the data to make predictions concerning the probability of finding an inclusion larger than those already found within a given volume of metal. For example, consider the distribution in size of graphite nodules in ductile iron. Assume that S_0 , the inspected area in an examined section, is 1 mm² and that 50 sections are examined to determine the size of the largest graphite nodule in each section and its associated $\sqrt{area_{max}}$. With this information, a plot of the cumulative probability distribution as a function of the $\sqrt{area_{max}}$ similar to the plot in Fig 11-8 can be established. In this case F_{50}

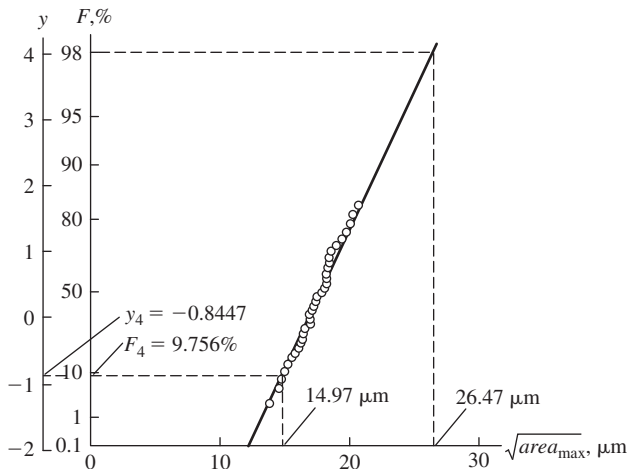


Fig. 11-8. Cumulative distribution of largest inclusion sizes ($N = 40$) plotted according to Gumbel's statistics of the extreme. (After Murakami et al., 8.)

is equal to 0.98, the reduced variate y_{50} is 3.9, and the return period, T_{50} , is 51. It can be estimated from Fig. 11-8 that the largest graphite nodule found in 50 sections with the cumulative distribution function of F_{50} is $26.47 \mu\text{m}$ for its $\sqrt{\text{area}_{\text{max}}}$. Therefore, in the examination of 50 sections on average, there is a 98% probability that a graphite nodule of the maximum size with its $\sqrt{\text{area}_{\text{max}}}$ being $26.47 \mu\text{m}$ will be found.

For the same inspection area $S_0, 0.16 \text{ mm}^2$, the straight line through the original 50 data points can be extrapolated to predict the return period for larger defects with their $\sqrt{\text{area}_{\text{max}}}$ larger than $26.47 \mu\text{m}$. For example, suppose that five fatigue samples are to be tested in bending. Each specimen has a diameter of 10 mm and a test length of 18 mm, and only graphite nodules at or just below the surface are of concern as nucleation sites for fatigue cracks. In this case S , the total surface area of the five specimens, would be $5 \times 10 \text{ mm} \times \pi \times 18 \text{ mm}$, or about $2,830 \text{ mm}^2$. Assume that we are interested in the cumulative distribution function and return periods of graphite nodules with their $\sqrt{\text{area}_{\text{max}}}$ being $32 \mu\text{m}$ or larger. We extrapolate the straight line for the 50 inspection areas and find that $F_i = 0.9939$ and the reduced variate $y_i = 5.1$. The return period for graphite nodules with their $\sqrt{\text{area}_{\text{max}}}$ being $32 \mu\text{m}$ or larger can be computed via Eq. 11-19 and is 164. In other words, we need 164 sections, on average, to find graphite nodules with their $\sqrt{\text{area}_{\text{max}}}$ being $32 \mu\text{m}$ or larger if the same inspection area, 0.16 mm^2 , is used for inspection. The total area of 164 sections of 0.16 mm^2 is 26.24 mm^2 . For the five samples of interest the total area is $2,830 \text{ mm}^2$, that is, about $108 \times 26.24 \text{ mm}^2$. Therefore, it can be concluded that one would expect to find graphite nodules with their $\sqrt{\text{area}_{\text{max}}}$ being $32 \mu\text{m}$ or larger at least 108 times in these five samples. Such information is useful in assessing the effect of the size of graphite nodules on fatigue strength as well as for quality control purposes.

B. Influence of Inclusion Size on Fatigue Strength

Extreme value distributions are important considerations in fatigue. Murakami (9) has used the statistics of the extreme to analyze the distribution of inclusion sizes in SKH51 tool steel. Figure 11-9 shows the extreme value distribution of the inclusions found at the fracture origin of 34 specimens. The distribution of inclusion sizes was plotted in terms of the statistics of the extreme for this steel. Murakami has shown that the lower bound on fatigue strength, σ_{wl} , is related to the size of the largest inclusion expected at or near the surface in a rotating bending fatigue test. As the number of specimens increases, the probability of encountering larger defects also increases, with the result that σ_{wl} is a function of the number of rotating beam specimens tested N , expressed as

$$\sigma_{wl} = \frac{1.41(\text{HV} + 120)}{(\sqrt{\text{area}_{\text{max}(N)}})^{1/6}} \quad (11-21)$$

where σ_{wl} is in MPa, HV is the Vickers Hardness Number expressed in units of kgf/mm^2 , and $\sqrt{\text{area}_{\text{max}(N)}}$ is in microns. For N values of 10 and 100 the expressions

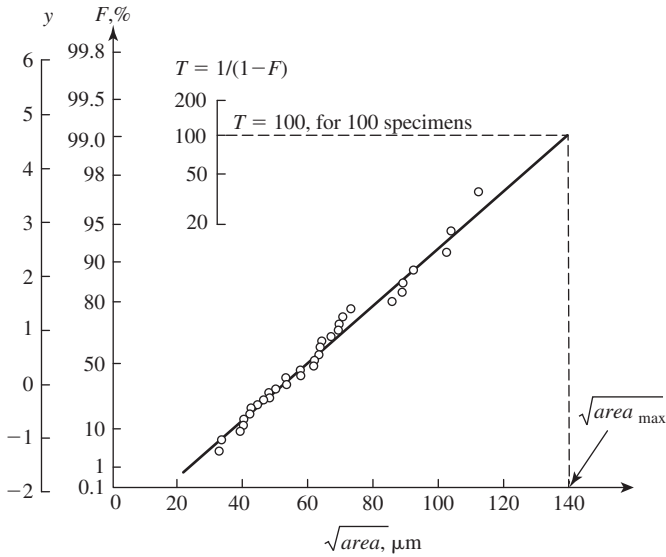


Fig. 11-9. Statistical distribution of the extreme values of the maximum size of the inclusion at the center of the fatigue fracture origin for SKH51 tool steel. (After Murakami, 9.)

for fatigue strength are

$$\sigma_{wl(10)} = \frac{1.41(HV + 120)}{(98)^{1/6}} = 0.66(HV + 120) \quad \text{MPa} \quad (11-22)$$

and

$$\sigma_{wl(100)} = \frac{1.41(HV + 120)}{(138)^{1/6}} = 0.62(HV + 120) \quad \text{MPa} \quad (11-23)$$

These equations are plotted in Fig. 11-10 and compared with experimental results. It is noted that the type of inclusion, whether it be an oxide, sulfide, or silicide, for example, did not affect the endurance limit; only the $\sqrt{\text{area}_{\text{max}}}$ parameter did. However, at stress amplitudes in the finite fatigue life range, the nature of the inclusion becomes a more important consideration.

C. Maximum Depth of the Corrosion Pit

Shibata (10) has used Gumbel extreme value statistics to determine the maximum depth of a corrosion pit that will grow in a 6 mm thick steel baseplate of an oil storage tank depth over a given period of time. The tank baseplate had a surface area S of 1,040 m². Ten sampling sites in the baseplate, each of an area equal to 1.85 m², were selected at random, and the depth of the maximum sized pit, d_{max} , in each of these test areas was determined. From these data, the corresponding cumulative probability F_i and the reduced variate y_i were calculated with the aid of Eqs. 11-13, and 11-14.

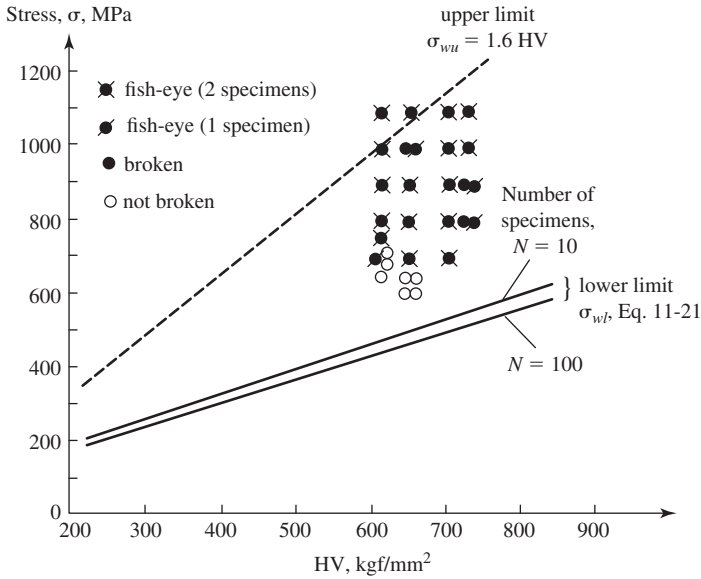


Fig. 11-10. A comparison of the predicted and experimental lower bounds of the fatigue strength of SKH51 tool steel as a function of hardness level, HV. (From Murakami, 9.)

Figure 11-11 is a plot of y_i as a function of d_{\max} . The equation of the straight line is

$$-\ln(-\ln F) = 1.848d_{\max} - 1.360 \quad (11-24)$$

The return period $T = S/S_0 = 1040/1.85 = 562$. Upon substitution of this value for T into Eq. 11-17, the value of F is found to be 0.9982. Equation 11-24 can then be used to determine the probable maximum depth of a corrosion pit that had grown over the period of time that the tank had been in service. The time for penetration of the tank by a corrosion pit can be found by substituting $d_{\max} = 6 \text{ mm}$ in Eq. 11-24 to obtain the corresponding value of F . The probability p is obtained from the relationship $p = 1 - F$. In this case, the probability p is about 6×10^{-5} . That is, there is the low probability of 6×10^{-5} that at some location in the baseplate a corrosion pit had penetrated the baseplate during the service lifetime.

VII. THE STAIRCASE METHOD

In 1948 Dixon and Mood (11) introduced the staircase method for testing the sensitivity of explosives to shock by dropping the explosives from various heights in a systematic manner to minimize the number of tests required for a given accuracy in determining the height above which an explosive would explode and below which it would not. Since 1948 the method has been applied in other situations, including the determination of the fatigue strength of a metal at a given number of cycles, such as

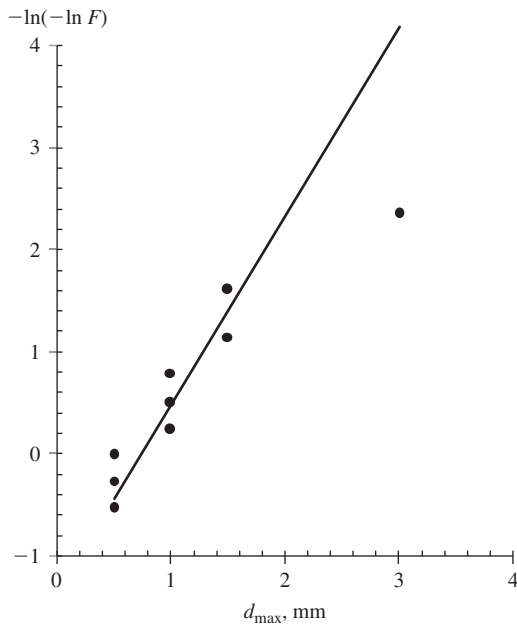


Fig. 11-11. Gumbel plot of maximum pit depth.

10^7 cycles. It is assumed that in the case of fatigue there is a critical stress amplitude, σ_0 , above which a fatigue specimen will fail in less than 10^7 cycles and below which it will not.

In the staircase method as applied to fatigue, the first step is to estimate the stress amplitude at the fatigue strength level, σ_0 , and then to select a succession of stress amplitudes $\sigma_1, \sigma_2, \sigma_3 \dots$ above σ_0 together with a succession of stress amplitudes $\sigma_{-1}, \sigma_{-2}, \sigma_{-3} \dots$ below σ_0 . The first specimen is then tested at a stress amplitude of σ_0 . If the specimen fails before 10^7 cycles, the second specimen will be tested at σ_{-1} ; otherwise, the second specimen will be tested at σ_1 . In general, any specimen will be tested at the level immediately below or immediately above the level of the previous test, according to whether or not there was a fatigue failure in the previous test. The results of such an experiment can be displayed as in Fig. 11-12, where the

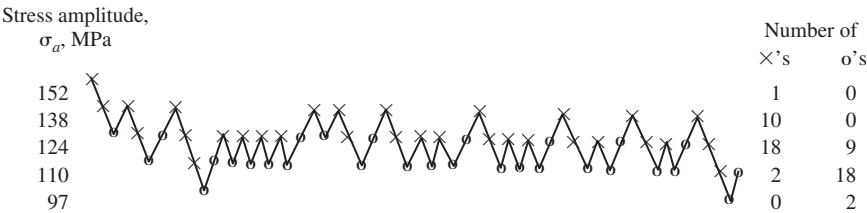


Fig. 11-12. Test sequence and results. \times denotes a fatigue failure; o denotes a run-out.

×'s represent fatigue failures and the o's nonfailures. The ×'s and o's are shown in the same sequence as that in which the tests were run. In this case, a total of 60 specimens were tested.

(for 20 tests, x's = 11, o's = 9, $n_0 = 1$ at 97 MPa, $n_1 = 6$ at 110 MPa,

$$n_2 = 2 \text{ at } 124 \text{ MPa; } N = 9$$

$$A = 1 \times 6 + 2 \times 2 = 10$$

$$B = 1 \times 6 + 4 \times 2 = 14$$

$$m = y' + d \left(\frac{A}{N} \pm \frac{1}{2} \right)$$

$$m = 96 + 13.8(10/9 + 0.5) = 96 + 14.6 = 118 \text{ MPa (vs. 120 MPa)}$$

$$s = 1.62d \left(\frac{N \cdot B - A^2}{N^2} + 0.029 \right) = 1.62 \times 13.8(126 - 100/81 + 0.029)$$

$$= 7.8 \text{ MPa (vs. 7.8 MPa)}$$

The primary advantage of the method is that it automatically concentrates testing near the mean, which increases the accuracy with which the mean can be estimated. The statistical analysis of the data can be quite simple, provided that the experiment satisfies certain conditions.

First of all, the analysis requires that the stress amplitudes at the fatigue strength be normally distributed. Secondly, the sample size must be large if the analysis is to be applicable. A determination of reliability may be misleading if the sample size is less than 40 or 50, which is often the case in fatigue testing where a number like 20 is more common. A further condition is that one must be able to estimate roughly in advance the standard deviation of the fatigue strengths in order to simplify the analysis. The interval between stress levels should be approximately equal to the standard deviation and preferably less than twice the standard deviation. Prior experience, such as knowledge of the standard deviation for aluminum alloys, is useful in setting the interval between test levels.

In the present case, we will be concerned with the determination of the fatigue strength (10^7 cycles) of an aluminum alloy. We assume that the distribution of fatigue strengths at 10^7 cycles is a normal distribution. Letting σ_a represent the stress amplitude, $y = \sigma_a$ will then be the normally distributed test variate. The mean is represented by μ and the variance of the distribution by σ^2 , where σ is the standard deviation. The experiment is performed by choosing an initial value of the stress amplitude, σ_0 (124 MPa), that is close to the anticipated mean. The other testing levels are chosen so that the values of the normalized stress amplitude y are equally spaced. If d (13.8 MPa) is the preliminary estimate of σ , the standard deviation, and if $y_0 = \sigma_0$, then the actual testing stress amplitudes are obtained by putting the σ_a values equal to $\sigma_0 \pm d$, $\sigma_0 \pm 2d$, $\sigma_0 \pm 3d$, ..., and solving for σ_0 .

In any experiment, the total number of fatigue failures will be approximately equal to the total number of nonfailures (run-outs). For estimating μ and σ , only the

failures or the nonfailures are used, depending on which has the smaller total. Let N represent the smaller total and let $n_0, n_1, n_2 \dots n_k$ denote the frequencies at each level for this less frequent event, where n_0 corresponds to the lowest level and n_k to the highest level at which the event occurs. We then have $\sum n_i = N$.

The estimate of μ , say m , is

$$m = y' + d \left(\frac{A}{N} \pm \frac{1}{2} \right) \quad (11-25)$$

where y' is the normalized height corresponding to the lowest level on which the less frequent event occurs. The plus sign is used when the analysis is based upon the run-outs; the minus sign is used when it is based upon the fatigue failures.

The estimate of σ , say s , is

$$s = 1.62d \left(\frac{N \cdot B - A^2}{N^2} + 0.029 \right) \quad (11-26)$$

A and B are defined as

$$A = \sum_{i=0}^{i=k} i n_i \quad \text{and} \quad B = \sum_{i=0}^{i=k} i^2 n_i$$

respectively.

The expressions for m and s are accurate when $(NB - A^2)/N^2 > 0.3$ and d is less than $2s$.

In the present example, the estimate of the mean, μ , is $m = 96 + 13.8(36/29 + 1/2) = 120$ MPa.

The estimate of the standard deviation σ , $s = 1.62 \times 13.8(270/841 + 0.029) = 7.8$ MPa

(Note: d (13.8 MPa) should be less than $2s < 15.6$), and $(NB - A^2)/N^2 = 0.32$ should be larger than 0.3.)

VIII. SUMMARY

The statistical treatment of data is useful in quality control and in establishing lower limits on properties such as the yield strength and fatigue strength. An awareness of the scatter in such properties is important in design as well as in failure analysis

REFERENCES

- (1) W. Weibull, *J. Appl. Mech.*, vol. 18, 1951, pp. 293–297; vol. 19, 1952, pp. 109–113.
- (2) E. J. Gumbel, *Statistics of Extremes*, Columbia University Press, New York, 1958.
- (3) F. B. Stulen, W. C. Schulte, and H. N. Cummings, "A Normal Distribution of Yield Strengths," in *Statistical Methods in Materials Research*, ed. by D. E. Hardenbergh, Pennsylvania State University Press, University Park, 1956.

- (4) G. E. Dieter, Jr., *Mechanical Metallurgy*, McGraw-Hill, New York, 1961.
- (5) G. M. Sinclair and T. J. Dolan, *Trans. ASME*, vol. 75, 1953, p. 867.
- (6) C. Lipson and N. J. Sheth, *Statistical Design and Analysis of Engineering Experiments*, McGraw-Hill, New York, 1973.
- (7) Z. W. Birnbaum and S. C. Saunders, A Statistical Model for Life-Length of Materials, *J. Am. Statist. Assoc.*, vol. 53, 1958, p. 159–167.
- (8) Y. Murakami, T. Toriyama, and E. M. Coudert, Instructions for a New Method of Inclusion Rating and Correlations with the Fatigue Limit, *J. Testing and Eval.* vol. 22, no. 4, 1994, pp. 318–326.
- (9) Y. Murakami, Inclusion Rating by Statistics of Extreme Values and Its Application to Fatigue Strength Prediction and Quality Control of Materials, *J. Res. Natl. Inst. Stand. Technol.*, vol. 99, no. 4, 1994, pp. 345–351.
- (10) T. Shibata, Evaluation of Corrosion Failure by Extreme Value Statistics, *ISIJ Int.*, vol. 31, no. 2, 1991, pp. 115–121.
- (11) W. J. Dixon and A. M. Mood, A Method for Obtaining and Analyzing Sensitivity Data, *J. Am. Statist. Assoc.*, vol. 43, 1948, pp. 109–126.

APPENDIX 11-1: METHOD OF LINEAR LEAST SQUARES (C. F. GAUSS, 1794)

Regression analysis is a statistical tool for the investigation of relationships between variables. In this section, the method used to obtain a best linear fit ($y = mx + b$) to a data set will be discussed. Such a fit is appropriate for the statistical functions discussed earlier, for examples, Figs. 11-4, 11-7, and 11-11. The method is directed at finding the line that minimizes the difference (error) between the data and the line.

For each pair of observations x_i, y_i the error is defined as

$$e_i = mx_i + b - y_i \quad (11A-1)$$

Then m and b are found in such a way that the sum of the square of the errors, $S(m, b)$, over all the n observations is minimized.

$$S(m, b) = \sum_{i=1}^n (mx_i + b - y_i)^2 \quad (11A-2)$$

Taking the derivative of S with respect to m and setting the result to zero yields

$$\begin{aligned} \frac{\partial S}{\partial m} &= \sum_{i=1}^n 2(mx_i + b - y_i)x_i = 0 \\ b \sum_{i=1}^n x_i + m \sum_{i=1}^n x_i^2 &= \sum_{i=1}^n x_i y_i \end{aligned} \quad (11A-3)$$

Taking the derivative of S with respect to b and setting the result to zero yields

$$\frac{\partial S}{\partial b} = \sum_{i=1}^n 2(mx_i + b - y_i) = 0$$

$$nb + m \sum_{i=1}^n x_i = \sum_{i=1}^n y_i$$

Therefore,

$$b = \frac{\sum_{i=1}^n y_i - m \sum_{i=1}^n x_i}{n} \quad (11A-4)$$

Substitute Eq. 11A-4 into Eq. 11A-3:

$$\frac{1}{n} \sum_{i=1}^n x_i \left(\sum_{i=1}^n y_i - m \sum_{i=1}^n x_i \right) + m \sum_{i=1}^n x_i^2 = \sum_{i=1}^n x_i y_i$$

$$\sum_{i=1}^n x_i \sum_{i=1}^n y_i - m \left(\sum_{i=1}^n x_i \right)^2 + mn \sum_{i=1}^n x_i^2 = n \sum_{i=1}^n x_i y_i$$

Therefore,

$$m = \frac{n \sum_{i=1}^n x_i y_i - \sum_{i=1}^n x_i \sum_{i=1}^n y_i}{n \sum_{i=1}^n x_i^2 - \left(\sum_{i=1}^n x_i \right)^2} \quad (11A-5)$$

A related quantity r , called the *linear correlation coefficient*, is a measure of how well a linear least squares fit is able to describe the data. The correlation coefficient is given as

$$r = \frac{n \sum_{i=1}^n x_i y_i - \sum_{i=1}^n x_i \sum_{i=1}^n y_i}{\sqrt{n \sum_{i=1}^n x_i^2 - \left(\sum_{i=1}^n x_i \right)^2} \sqrt{n \sum_{i=1}^n y_i^2 - \left(\sum_{i=1}^n y_i \right)^2}} \quad (11A-6)$$

The value of r is between -1 and $+1$. If x and y have a strong positive linear correlation, r is close to $+1$. If there is no linear correlation or a weak linear correlation, r is close to 0 . A value near zero means that there is a random, nonlinear relationship between the two variables. A correlation greater than 0.8 is generally described as *strong*, whereas a correlation less than 0.5 is generally described as *weak*.

The square of the correlation coefficient is known as the *coefficient of determination*, r^2 . This coefficient can have a value between 0 and 1.0, and is an indication of the strength of the linear association between x and y , that is, how well the regression line represents the data. If the regression line passes exactly through every point on the scatter plot, it would be able to explain all of the variation. The farther the line is away from the points, the poorer is the least squares fit.

Example

Determine the slope and intercept of a line that best fit to the following five pairs of data. Also, calculate the coefficient of determination r^2 .

x	y
1	2
2	5
3	3
4	8
5	7

Construct the following table to facilitate the calculation.

No.	x	y	xy	x^2	y^2
1	1	2	2	1	4
2	2	5	10	4	25
3	3	3	9	9	9
4	4	8	32	16	64
5	5	7	35	25	49
Summation	15	25	88	55	151

From Eqs. 11A-5 and 11A-4, with $n = 5$

$$m = \frac{n \sum_{i=1}^n x_i y_i - \sum_{i=1}^n x_i \sum_{i=1}^n y_i}{n \sum_{i=1}^n x_i^2 - \left(\sum_{i=1}^n x_i \right)^2} = \frac{5 \times 88 - 15 \times 25}{5 \times 55 - 15^2} = \frac{440 - 375}{275 - 225} = \frac{65}{50} = 1.3$$

$$b = \frac{\sum_{i=1}^n y_i - m \sum_{i=1}^n x_i}{n} = \frac{25 - 1.3 \times 15}{5} = \frac{25 - 19.5}{5} = \frac{5.5}{5} = 1.1$$

Therefore, the equation of the least squares line is

$$y = 1.3x + 1.1$$

Figure A11-1 represents a given set of data and a best fit line.

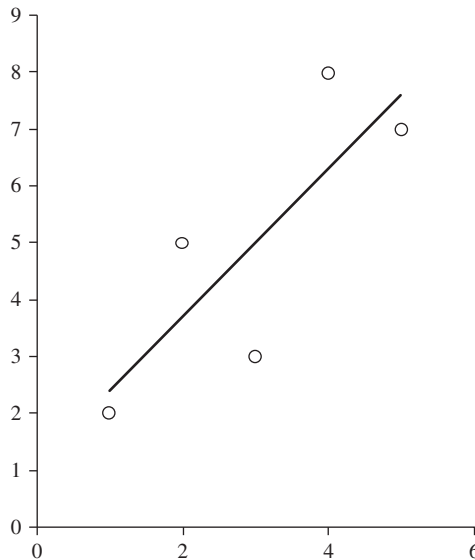


Fig. A11-1. x, y data pairs from the table together with the line representing the least square fit.

From Eq. 11A-6, with $n = 5$

$$r = \frac{5 \times 88 - 15 \times 25}{\sqrt{5 \times 55 - 15^2} \sqrt{5 \times 151 - 25^2}} = \frac{440 - 375}{7.07 \times 11.40} = \frac{65}{80.6} = 0.81$$

$$r^2 = 0.65$$

meaning that 65% of the variation in y can be explained by the independent variable, x .

PROBLEMS

11-1. Carry out the statistical analysis for the yield strength data listed in Table 11-2 using both Gaussian distribution and Weibull distribution functions.

- For the Gaussian distribution, find the arithmetic mean and the standard deviation.
- Arrange the yield strength data in the order of increasing values and find their corresponding probability and cumulative probability values.

- (c) Use the probability function to find out whether the data follow the Gaussian distribution.
- (d) Use the cumulative probability function to find out whether the data follow the Gaussian distribution.
- (e) For the Weibull distribution, use the cumulative probability function to find out whether the data follow the Weibull distribution. Choose $\sigma_{Y0} = 689.5$ MPa for this evaluation.
- (f) Determine the Weibull modulus, m , and the scale parameter, σ_0 .
- (g) Decide which distribution function can better describe the yield strength data listed in the table. Why?

11-2. For Problem 11-1, re-examine the suitability of the Weibull distribution using $\sigma_{Y0} = 0.0$ MPa.

- (a) What are the Weibull modulus and the scale parameter for $\sigma_{Y0} = 0.0$ MPa?
- (b) Will the Weibull distribution with $\sigma_{Y0} = 0.0$ MPa provide a better description of the yield strength data than the Weibull distribution with $\sigma_{Y0} = 689.5$ MPa? Why?

11-3. The following hardness data (HV, kg/mm²) are obtained from an oxide.

801.55	810.00	861.35	869.00	870.55	876.00
931.50	950.00	957.95	962.00	968.30	974.00
979.80	982.00	982.00	986.00	999.35	1,012.00
1,033.00	1,036.15	1,056.00	1,065.00	1,066.05	1,087.90
1,106.30	1,160.00				

Use Excel software and the following steps to determine which distribution function, Gaussian or Weibull, is better for describing the data listed above.

- (a) For the Gaussian distribution, find the arithmetic mean and the standard deviation.
 - i. Arrange the hardness data in the order of increasing values and find their corresponding probability and cumulative probability values.
 - ii. Use the cumulative probability function to find out whether the data follow a Gaussian distribution.
- (b) For the Weibull distribution, use the cumulative probability function to find out whether the data follow a Weibull distribution. Choose $x_0 = 700$ kg/mm² (in Eq. 11-4) for this evaluation.
- (c) Determine the Weibull modulus, m , and the scale parameter, δ .
- (d) Decide which distribution function can better describe the hardness data listed above. Why?

11-4. Fig. 11-12 presents the experimental results obtained by the staircase method when 60 specimens were tested. If only 20 specimens had been tested, what would have been the estimated values of the fatigue strength and the standard deviation? Compare your results with those obtained when 60 specimens were tested.

12

Defects

I. INTRODUCTION

Failures of components have often been triggered by defects that were introduced during the manufacturing process. Because of the prevalence of defects, critical parts are inspected in the attempt to prevent defective parts from entering service, sometimes without success. For example, an undetected defect in a Ti-6Al-4V turbine disk led to the crash of a DC-10 aircraft. Since the resolution of any inspection method is limited, it is prudent to consider that defects of a size equal to the limit of resolution are present in assessing the integrity of a structure. Some defects are unavoidable, as in the case of welds, and allowance must be made for such defects to obtain reliable in-service performance. In this chapter, some of the more common types of defects encountered in welds, castings, and rolled or forged products are discussed.

II. WELD DEFECTS

A. General Characteristics

Weld defects are generally geometrical in nature. However, microstructural changes in the base metal also may be of concern, particularly when there is an accompanying decrease in mechanical properties and resistance to corrosion. These microstructural changes occur in that portion of the base metal that is adjacent to the weld that was not melted during the welding process. This region is known as the *heat-affected zone* (HAZ).

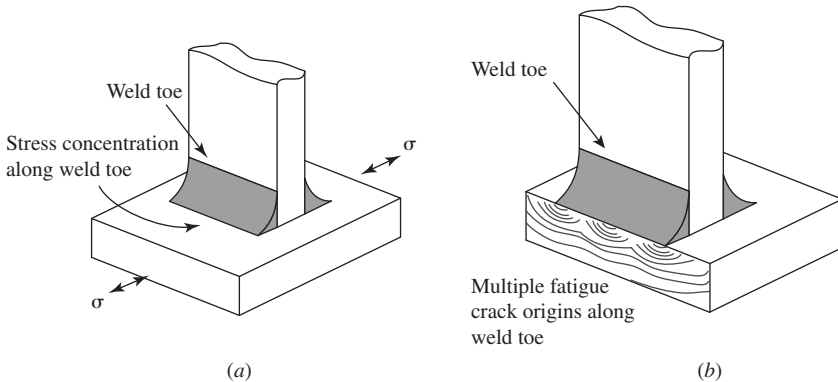


Fig. 12-1. (a) Fillet weld with weld toes indicated. (b) Failure of a plate at nonload carrying transverse fillet welds. (After the Welding Institute, 1.)

Certain defects, such as the porosity caused by the entrapment of gas evolved during weld metal solidification and an irregular shape, are inherent to the welding process. Figure 12-1a depicts a fillet weld, with the toe of the weld being the junction between the face of the weld and the base metal. Irregularities in shape at the toe of a fillet weld act as stress raisers. In addition, irregular surface ripples are formed in the wake of a weld pass and are concave with respect to the direction of the weld pass, Fig. 12-1b. These surface ripples, as well as those formed at the start and stop positions of the welding process, are geometric discontinuities that promote the initiation of fatigue cracks. Although the fatigue properties of many welded structures are strongly influenced by the presence of such defects, under monotonic loading these defects are much less of a problem. No failures due to porosity have been reported in welds where the porosity was within acceptable code requirements (1).

An example of a fatigue failure after 10 years of operation at a weld toe of a lifting lug in an oil pumping unit is given in Fig. 12-2. The lifting lugs were affixed

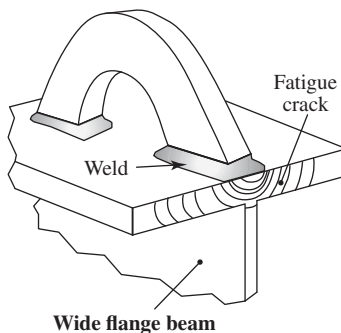


Fig. 12-2. Fatigue fracture at a weld toe. (After Larrainzar et al., 3)

to the unit by arc welding and were used simply to facilitate the assembly of the unit. Since these lugs were add-ons, little attention was paid to the integrity of the welds at these lugs, as is typical. Better welding practice would have greatly reduced the possibility of this type of failure.

Defects in welds also result from improper welding procedures. A number of common weld defects are shown in Fig. 12-3. These include the *undercut*, which is a groove melted into the base metal adjacent to the toe of a weld and left unfilled, and the *cold lap*, which is a protrusion of weld metal beyond the bond at the toe of weld. Lack of penetration indicates that weld metal did not completely fill the gap between the two plates being welded. Lack of fusion can occur if the base metal does not melt or, in a multipass weld, if there is a lack of melting of the previous pass between passes. One type of defect is due to a shoddy work practice known as “slugging a weld.” In making a long fillet weld, welders have been known to place a welding rod along the intersection of the two plates being welded and then to cover it over with weld metal, so that to the eye it would appear to be a sound weld. Incredibly, such defects have been found even on booster rockets for space launches.

Weld reinforcement is the excess of weld metal above the plane of the plates being joined by a butt weld. This is actually a misleading term, since the excess creates a stress concentration that lowers the fatigue resistance. *Underfill*, also referred to as a *weld cavity* or *weld crater*, denotes the opposite of reinforcement. The fatigue strength of a transverse butt weld is dependent upon the weld profile. The highest fatigue strength of a butt weld is obtained when the weld is flush with the plate surface, that is, it has zero reinforcement.

Weld porosity in the case of a fillet weld is not a great concern because the geometrical factors discussed above usually exert a stronger influence on fatigue behavior than does the porosity. On the other hand, porosity is of greater concern in butt welds subject to cyclic loading where the degree of porosity influences the fatigue life. To guard against failures due to porosity, radiographic inspection using a radioactive element such as cobalt 60, together with film, is used (see Chapter 14). Radiographic inspection standards exist to aid in the assessment of the degree of porosity and to determine in a given application whether a weld is acceptable or not.

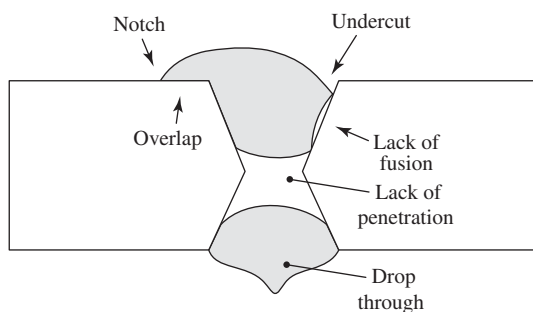


Fig. 12-3. Some typical weld defects.

Some of the other defects associated with welds are:

- (a) *Mismatch*: The plates that are being butt welded are offset by transverse or angular misalignment.
- (b) *Shrinkage*: Shrinkage of the weld and the adjacent area during cooling after welding can result in cracking of the base metal, as well as crater and fusion line cracking in the weld metal.
- (c) *Buried slag inclusions*: Slag inclusions result from the dissolution of the welding flux in the weld metal. In the case of multipass welding, the slag is normally on the outer portion of a solidified weld and is brushed off. However, if it is not completely removed, slag inclusions can develop between passes. These defects are generally less harmful than the design details associated with fillet and butt welds.
- (d) *Weld spatter*: Weld spatter refers to the metal particles expelled during arc or gas welding. Weld spatter can be particularly dangerous in the case of quenched and tempered steels, as it can lead to the formation of untempered martensite in the base metal as well as to surface irregularities, which can facilitate the nucleation of fatigue cracks.

In addition, the properties of the heat-affected zone (HAZ), the portion of the base metal that was not melted during the welding operation but whose microstructure and physical properties were altered by exposure to elevated temperature, are of concern with respect to mechanical behavior.

B. Effect of the Cooling Rate

Alloying elements such as carbon, manganese, chromium, and nickel all increase hardenability and decrease the critical cooling rate because they slow down the diffusive decomposition of austenite, but because phases such as hard, untempered martensite may form, these elements also increase the likelihood that weld cracking may occur on cooling. The effect of alloying elements on the tendency toward crack formation on cooling can be assessed using empirical formulas that express the alloy content in terms of a carbon equivalent, CE. An example of such a relationship is

$$CE = C + \frac{Mn}{6} + \frac{Cr + Mo + V}{5} + \frac{Ni + Cu}{15} \quad (12-1)$$

where the concentrations of each element are given in wt %. When the CE exceeds 0.45, the cooling rate must be controlled very carefully to produce sound welds. Since thermal stresses increase both with an increase in cooling rate and an increase in CE, cracking becomes more likely since the toughness, that is, the resistance to cracking, decreases as the CE increases. To minimize the tendency toward cracking, preheating of the weld region just prior to welding is done to reduce the cooling

rate after welding, with the specified level of preheat increasing with the increase in CE.

C. Laminar Tearing

When a tension-bearing member is fillet welded to a rolled steel plate, a tensile stress is developed normal to the plane of the plate. In this direction, the fracture resistance is less than that in the in-plane directions because of the anisotropy introduced during rolling. Manganese sulfide particles and other inclusions will be oriented perpendicular to the tensile stress. If this stress is high enough, a type of in-plane fracture known as *laminar tearing* can occur (Fig. 12-4). In critical structures such as submarines, the hull steels are processed in such a way as to reduce the anisotropy in fracture resistance.

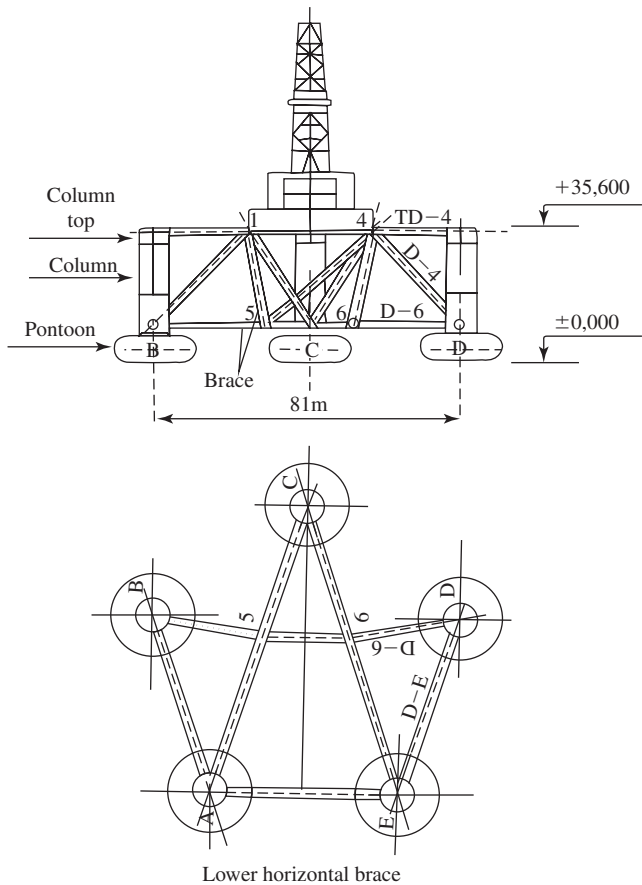


Fig. 12-4. Laminar tearing.

III. CASE STUDY: WELDING DEFECT

A. The Alexander Kielland Accident, March 27, 1980 (4)

The *Alexander Kielland* (AK) was built as a mobile, semisubmersible oil drilling platform of the pentagon type, where five cylindrical columns support the platform, see Fig. 12-5. A major design objective was to minimize platform movement in heavy seas. The AK was built in France and delivered in 1976, but was used as an accommodation platform to house the workers in North Sea offshore drilling operations rather than as a drilling platform. It originally had a capacity of 80 beds, but over time this was increased to 384.

In the 9 months prior to the accident, the AK was anchored close to the drilling platform "Edda 2/7 C." To each of the columns A, B, D, and E, two anchor wires were attached. Column C was not anchored. The connection between the AK and Edda was maintained by a movable walkway. In bad weather, the walkway was lifted onboard the AK, and the AK was shifted away from Edda. This was done by slackening the anchor wires from the B and D columns and tightening the anchor wires from the A and E columns.

On March 27, 1980, visibility was poor, and because the wind speed was 16–20 meters (m)/sec (45 mph) and the wave height was 6–8 m (20–26 ft.), the AK was shifted away from Edda by 1,750 hours. About half an hour later, column brace D-6

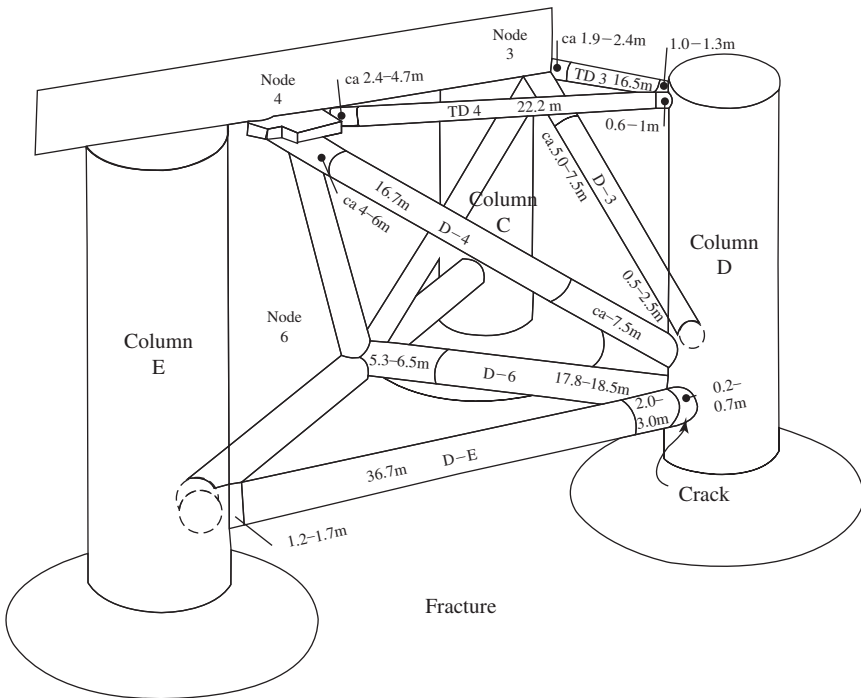


Fig. 12-5. The AK pentagon structure. (From *The Alexander Kielland Accident*, 4.)

failed and other braces then quickly failed, allowing column D to break away from the AK. The platform heeled almost at once, and when the angle of heel reached 35° the message “Mayday, Mayday. Kielland is capsizing” was sent out at about 1,829 hours.

On board the AK, a strong impact was experienced a few minutes before 1,830 hours, followed by some kind of trembling. This seemed to be a wave impact, typical of bad weather. Immediately after the first impact, however, there was another, again accompanied by shaking of the platform, accompanied by sounds of metal tearing. The platform started to heel further, and the situation became critical. The angle of heel almost stabilized at $30\text{--}35^\circ$, but then continued slowly to increase past 35° until the platform capsized. From Edda it appeared as if only the wire from column B had kept the platform from capsizing, but when this wire broke, the platform overturned at 1,853 hours and floated upside down in the sea.

As mentioned, the horizontal brace D-6 broke first; see Fig. 12-6. In this brace, an opening had been cut out, and a hydrophone for control of positioning had been welded in. The hydrophone was considered by the builder as equipment rather than as a load-bearing component of the structure. For this reason, no complete strength evaluation had been made of the welding-in of the hydrophone.

There were 212 men aboard the AK at the time of the accident. Most of them tried to reach the platform’s highest point, the B column. Several were unable to don life vests, as there was no time to go to the cabins to get them. The permanent crew on board, as well as the employees of some companies, had survivor suits. Eight were able to don these, but only four survived. There were seven covered lifeboats, each of which could take 50 men. An attempt to launch five lifeboats was made. Three of these lifeboats failed to release properly and were smashed against the platform and crushed. One lifeboat containing 26 men got away, and the men were rescued by Norwegian helicopters. Another lifeboat containing 14 people failed to launch properly, but came to the surface when the platform capsized and then picked up 19 survivors from the water. All 33 were rescued. A total of 16 men were saved when they swam to rafts that were self-launched at the time of capsizing or thrown from Edda. Seven survivors were picked up by supply boats in the area. A further seven survivors were brought on board Edda by a personnel basket. Of the 212 men on board, 89 were saved and 123 lost their lives.

B. Accident Investigation

The main structural support elements of the pentagon platform consisted of the five columns supported by pontoons, designated A through E. The existing rules required that the rig remain floating in a stable position after damage that resulted in flooding of two adjacent tanks in a column. No consideration was given to the possible loss of a column.

The pontoons were circular, 22 m (72 ft.) in diameter and 8.5 m (28 ft.) in height. Each pontoon supported a column with a diameter of 8.5 m (28 ft.). The columns were 27.1 m (89 ft.) in height and were connected with a set of horizontal and angular braces made of high-strength steel. Ten anchor lines, two from each column, were used together with a hydrophone system to keep the platform properly positioned at the selected location.

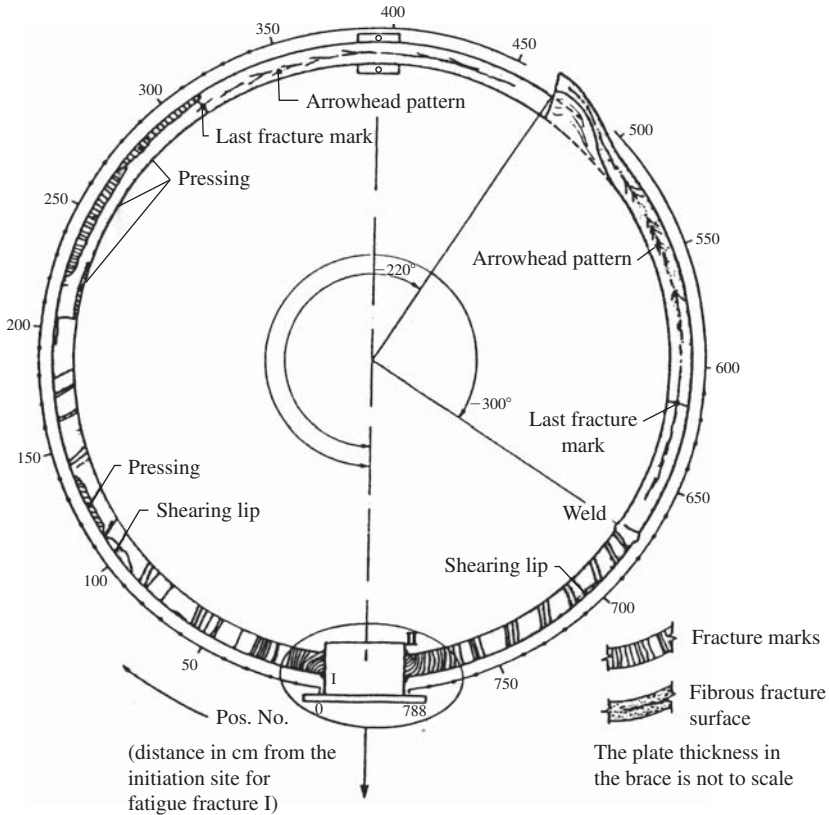


Fig. 12-6. Location of the fractures in the braces connected to column D. The fracture in brace D-6, the first to fail, was located at a hydrophone that had been welded to the brace. Approximate lengths of the structural components are given in meters. (From The Alexander Kielland Accident, 4.)

Annual inspections of limited extent and a more thorough inspection every 4 years were called for. Three annual inspections in situ had been carried out, but the lower horizontal braces could not be inspected. The main inspection of the hull and machinery was scheduled to begin in April 1980.

Corrosion protection was afforded by a coat of paint consisting of a brown undercoating and a covering paint (*brai epoxy*), as well as a red covering coat to protect against fouling on the external surfaces of the bracing. In addition, a cathodic protection system using an applied current was used. The system could supply a maximum current of 600 amps and was controlled by adjusting the potential on various parts of the structure. Sacrificial anodes were used during the period of construction.

Welding electrodes of the ESAB OK 48.30 type were used for manual fillet welds at braces and, in particular, in the fillet weld between the hydrophone fitting and brace D-6. Welds made from these electrodes have a yield strength 30% higher than that of the base metal, with tensile strength and ductility properties similar to those of the base metal. Based upon their perceived criticality, the welds were classified into

three groups, which affected the qualification requirements for the welders and the inspections to which the welds were subjected. The welding of hydrophones to the braces fell into the lowest category. The specifications called for 100% inspection of all critical joints. Inspection methods included radiography, dye penetrant, and magnetic particle methods.

To attach the hydrophone to the tubular brace, a hole was burned into the brace (26 mm thick (1 in.), 255 mm (10.2 in.) in diameter) of diameter 3–5 mm (0.12–20 in.) larger than that of the hydrophone (325 mm [13 in.] in diameter). The hydrophone was then welded into place with fillet welds by manual arc welding and 5 mm covered electrodes, with two passes being made, one on either side of the brace. There was no preheating. Examination of the hydrophone fitting on brace D-6 after the accident showed evidence of cold bending and welding from both sides of the brace (X-joint). The weld also showed a marked *root defect*. The weld had poor adhesion to the base metal in some places. The form of the weld was also unfavorable, with contact angles of up to 90° present. The fillet weld at the hydrophone fitting had been inspected for cracks with a dye penetrant.

C. Fracture in Bracing Member D-6

Two fatigue cracks were initiated: one from an outside fillet weld and one from an inside fillet weld; see Fig. 12-7. The exact origins were difficult to pinpoint because fracture markings and striations were weak, and the details on the fracture surfaces had been ruined by the hammering together of the opposing fracture surfaces. The first 200–300 mm (8–12 in.) of the fracture surfaces exhibited the typical markings of fatigue fracture. When the fractures had reached a length of about 300 mm (12 in.), growth occurred more rapidly in leaps, giving intermittent fracture marks. The fracture marks here were coarse and fibrous, and shear lips occurred along the edges. Contraction was small, of the order of 2–4%. The final break constituted about one-third of the circumference and was coarse, with some chevron-like markings, and there was considerable contraction.

A portion of the fracture surface in the weld between the hydrophone and the brace contained the remains of a coat of paint, indicating that cracks were present at the time of fabrication. This paint was present on both the fracture surface of the inside weld and the bracing D-6 to an extent of 70 mm (2.8 in.). A crack of this length must have existed at the time of paint application.

The fillet weld joints showed shallow, flat fractures in and near the fusion zone, typical tear-off fractures, and in part, fractures in the weld itself. The formation of the initial cracks could have been due to excessive thermal strains during welding, and/or excessively high external loads on the platform, or insufficient cracking resistance of the weld metal. In addition, the local strain level may have been too high. A load-bearing fillet weld will have as large a failure capacity as a butt weld when the fillet weld *a*-measure is of the order of 40–70% of the plate thickness; see Fig. 12-8. For a 26 mm (1 in.) plate, this indicates an *a*-measure of 10–18 mm (0.4–0.7 in.), while the nominal *a*-measure of the weld in question was 6 mm. In addition, the weld angle was not optimum and fusion in the hydrophone holder was low. These factors reduced the effective *a*-measure of the fillet weld.

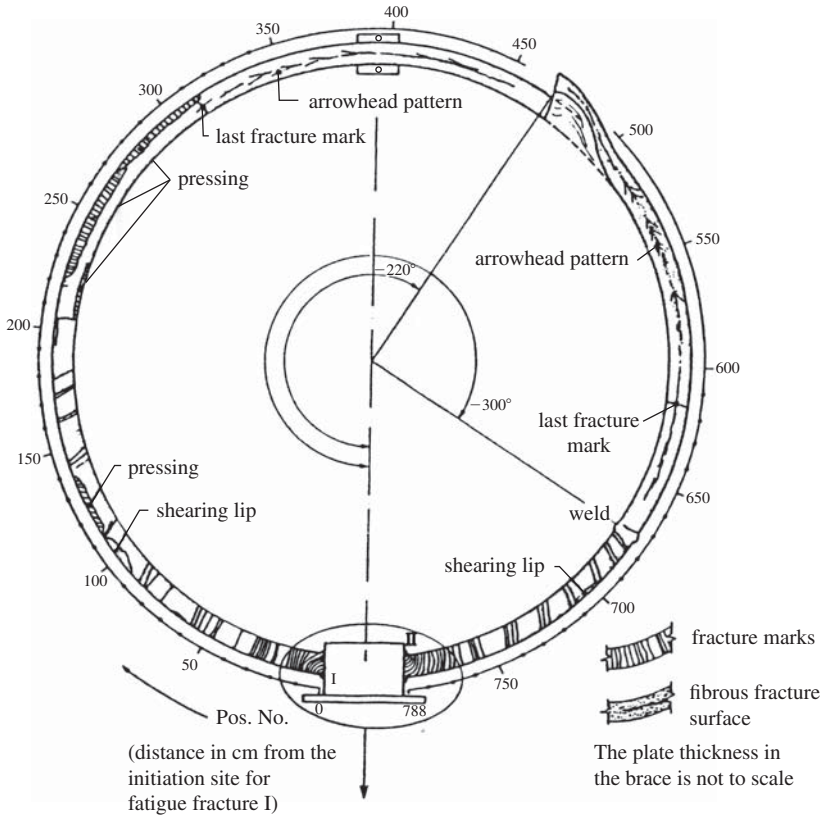


Fig. 12-7. Fracture surface features of the failed brace D-6. Note two fatigue origins at locations I and II at the welded in hydrophone. (From The Alexander Kielland Accident, 4.)

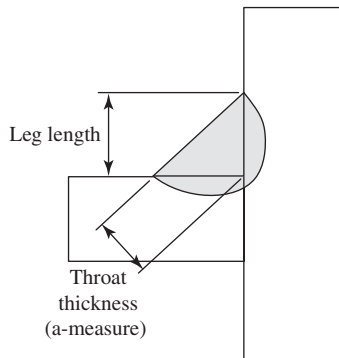
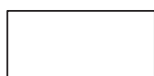


Fig. 12-8. Fillet weld a-measure.

D. Conclusions

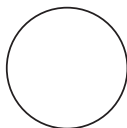
The accident report dealt with overall issues relating to the safety of mobile drilling platforms, such as the need for an improved analysis of potential problems in the design stage. A better system for exploring the consequences of all possible types of failure (in this case, the loss of a column had not been anticipated), together with fault trees, was needed. Fault trees are used to explore in a systematic manner the consequences of the failure of individual components. The symbols that are used in a fault tree study are shown in Fig. 12-9a. An example of a fault tree for a gasoline

Event symbols



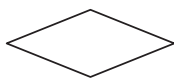
Event

Identified fault or event, produced by combination of other more basic causes; a “gate” input or output



Primary Failure

Basic events, malfunctions, or causes, with available data from test results or failure analysis information.



Undeveloped Event

Events not pursued to determine more basic faults, used mostly for information purposes; limit of fault tree resolution.



Normal Event

A system characteristic; event presumed to always occur.

Gate symbols



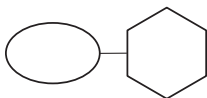
AND Gate

Output event exists or occurs only when all input events exist or occur simultaneously.



OR Gate

Output event can exist or occur if any one or more of input events exist or occur.

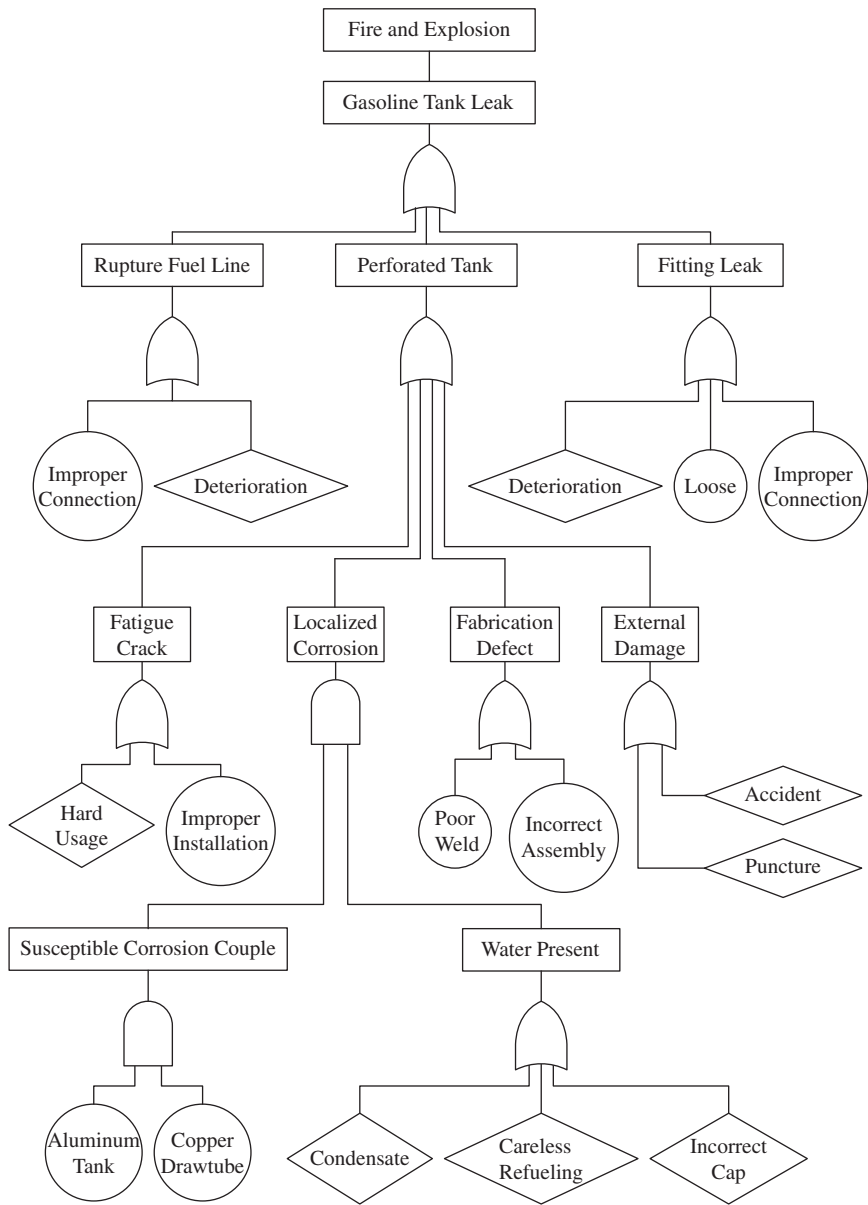


Inhibit (or Conditional) Gate

Output is conditional, depends upon occurrence restricting or qualifying event; controlling variable is described in adjoining symbol.

(a)

Fig. 12-9. Fault trees. (a) Fault tree symbols. (b) An example of a fault tree. (After Witherell, 5.)



(b)

Fig. 12-9. (continued)

tank in marine service is given in Fig. 12-9b. Stability of the platform in the event of major damage was also a consideration. With respect to metallurgical matters, the following can be concluded:

- (a) We should beware of weld add-ons.
- (b) When add-ons must be used on structural components, the welds should be stress relieved and carefully inspected.

IV. CASTING DEFECTS

Many types of potential defects are associated with the casting process, any of which can lead to product failure. For example, the new nuclear-powered French aircraft carrier *Charles de Gaulle* was engaged in long-distance sea trials in November 2000 when it was forced to return to its home port at reduced speed because a blade on one of its two propellers broke off. Each propeller weighs 17,000 kg (37.4 kips) and is 5.8 m (19 ft.) in diameter. The propellers were specially designed to keep noise to a minimum. The cause of the failure has not yet been established, but it is suspected that a defect in the failed propeller may have been created during the casting process.

Among the principal casting defects are the following:

- (a) *Metallic projections*: Fins, and so on, can occur.
- (b) *Cavities*: These might be porosity, blowholes, or pinholes. Porosity in cast single-crystal turbine blades is a cause of concern with respect to fatigue crack initiation, for example.
- (c) *Discontinuities*: One example of a discontinuity is a *cold shot*, which is a portion of an ingot or casting showing premature solidification caused by a splash of metal during solidification. Another discontinuity is known as a *cold shut*, which is a discontinuity that appears on the surface of cast metal as a result of two streams of liquid meeting and failing to unite. (Cold shuts can also develop during forging, where they appear as laps on the surface of a forging or billet that was closed without fusion during deformation.)
- (d) *Defective surface*: This can take the form of roughness or sand adherence.
- (e) *Incomplete casting*: A portion of the desired shape may be missing.
- (f) *Incorrect dimensions or shape*: Shrinkage, core shift, and so on, can occur. For example, in casting a hollow rectangular shape, a polymeric form (core) may be used to shape the inside cavity. If during the pouring operation this core shifts, the resultant casting will have walls of differing thicknesses, with the thinner wall being more prone to fatigue than the thicker wall.
- (g) *Nonmetallic inclusions*: Possible inclusions include slag, flux, sand, oxides, and so on.
- (h) *Centerline piping*: A pipe is a central cavity formed by contraction of an ingot during solidification.

V. CASE STUDY: CORNER CRACKING DURING CONTINUOUS CASTING

Corner cracking in continuous square casting occurs due to shrinkage, phase transformation, and the lack of mold support. To avoid oxidation, the mold is sealed with argon and oil is used as a lubricant, which is probably graphite at 1,649°C (3,000°F). During the early stage of the continuous casting process, the exterior of the casting solidifies while the interior remains a liquid. Since the casting direction has a vertical component, there is an increase in hydrostatic pressure with an increase in the vertical component. This increase can lead to cracking at the corners, which are prone to cracking due to trapped solute and an elongated grain structure. If such corner cracks are present after casting, the cracked corners have to be ground away, a costly operation. To avoid this problem, the mold should be double tapered to provide lateral support during the shrinkage and phase transformation processes.

VI. FORMING DEFECTS (6)

(a) *Over- and under-cambering*: In a rolling mill, in order to obtain a product of uniform thickness, the rolls may have a larger diameter (camber) at midwidth than at the edges to compensate for bending of the rolls during the rolling operation. Cracking in a rolled product can occur due to either over-cambering or under-cambering of the rolls. Over-cambering leads at midwidth to a thinning of the product and a greater tendency to extend in the rolling direction. This tendency is restrained by adjacent, less highly thinned material. As a result, the restraining material is placed in tension, which can lead to the development of transverse cracks. Under-cambering, on the other hand, results in the potential for cracking at midwidth.

(b) *Edge cracking* (Fig. 12-10a): In rolled sheet metal, edge cracking is due to a state of plane stress (rather than plane strain) at the edges and a lack of edge support. Since the material at the edges can expand in the transverse direction, less material is moving in the rolling direction than moving away from the edges. As a result, a tensile stress is set up at the edges in the rolling direction, and this stress can result in edge cracking.

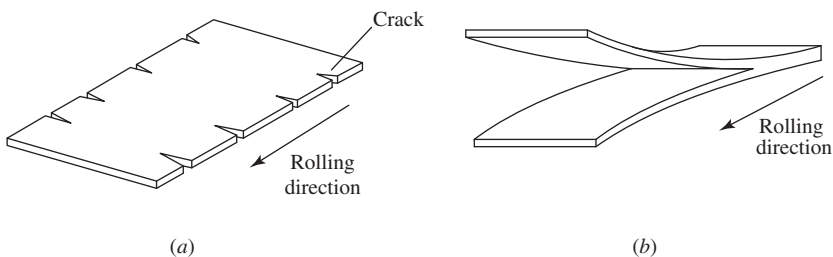


Fig. 12-10. Schematic of forming defects. (a) Edge cracking. (b) Alligatoring.

(c) *Stretcher strains*: Elongated markings that appear on the surface of a steel that has an upper and a lower yield level are known as *stretcher strains*. These are objectionable in exterior sheet metal automobile parts, as they detract from a smooth finish.

(d) *Alligatoring* (Fig. 12-10b): The longitudinal splitting of a rolled flat slab in a plane parallel to the rolled surface is called *alligatoring*.

(e) *Residual stresses*: Such stresses can develop during most cold forming operations. They may have a deleterious effect on subsequent machining operations because of distortion when the remaining residual stresses are equilibrated.

(f) *Banded microstructure*: A heterogeneous microstructure with the segregates aligned in a direction parallel to the rolling direction is known as a *banded microstructure*. In steels, bands of pearlite may be separated by bands of ferrite, Fig. 5-8. The microhardness will vary across a band, with bands of higher hardness being more prone to hydrogen-induced cracking.

(g) *Seams and laps (folds)*: These are defects created during extrusion, drawing, and forging operations. A lap is a surface defect, appearing as a seam, caused by folding over hot metal, fins, or sharp corners and then rolling or forging them into the surface but not welding them.

(h) *Undesirable flow patterns in forging*: During a forging operation, the grains elongate in the main direction of metal flow, which can lead to an anisotropy in material properties. If in use the principal tensile stress is transverse to the flow direction, cracking may occur due to material weakness in the transverse direction. A similar situation existed with respect to the *Titanic* rivet discussed in Chapter 7, where the slag inclusions were oriented perpendicular to the tensile stresses due to metal flow during the rivet head forming process.

VII. CASE STUDIES: FORGING DEFECTS

A. F-111 (7)

On the basis of its fatigue resistance, fracture toughness, and resistance to stress-corrosion cracking, a high-strength steel, D6ac, of 1,517–1,655 MPa (220–240 ksi) ultimate tensile strength, was selected for transferring load from the wing to the fuselage in the F-111 swing-wing aircraft. Machined forgings were used in the fabrication of the wing pivot fitting and the carry-through box. During the development of the F-111, three full-scale fatigue tests were carried out on wing assemblies, and these tests demonstrated a fatigue capability of six times the design life.

In December 1969, an F-111A was involved in an accident during a training mission. During a pull-up from a pass over a target area, the left wing separated in flight and the aircraft crashed. In the investigation, the flaw shown in Fig. 12-11 was found in the wing pivot fitting. A small band of fatigue striations, approximately 0.5 mm (0.02 in.) in depth, was found on the periphery of the flaw and was attributed to the 104.6 hours of flight operations prior to the accident. It was determined that the flaw had been initiated during the hot-forging process and had extended during the

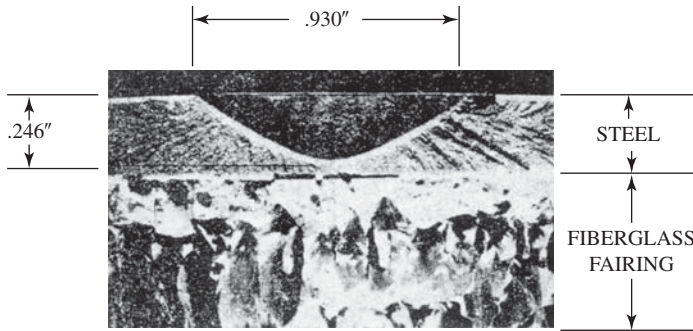


Fig. 12-11. Forging defect in the wing pivot fitting of an F-111 aircraft. (From Buntin, 7.)

subsequent cooldown. The flaw had escaped detection during inspection primarily because the flux fields used with magnetic particle inspection were inadequate for a tight flaw in a part of the unusual shape and size of the wing pivot fitting. Also, the sound wave transmission during ultrasonic inspection had been directed almost parallel to the flaw surfaces, and the reflected signal was insufficient to detect the flaw.

As a result of this accident, an unprecedented rigorous proof test and nondestructive examination of each F-111 were undertaken. This program was directed not only at the detection of flaws, but also at establishing inspection intervals for use with the fleet of F-111 aircraft in service. The inspection interval, which included a confidence factor, was determined by the initial size of an assumed flaw based upon the proof test, the growth of the flaw as a function of time under service loading and environmental conditions, and the critical size of the flaw for service operations.

B. Jet Engine Components

On January 2, 2001, a front-page article in the *Wall Street Journal* drew attention to problems with the General Electric Aircraft Engines (GEAE) CF-6 engines. These engines are used to power a broad range of Boeing and Airbus Industries planes, such as the DC-10, the A300, and the Boeing 767. Almost 6,000 of these engines are in service, and failures are quite rare. One problem first surfaced in 1991 when a type of cracking known as *dwell time fatigue* was found during inspection of a compressor component known as a *spool*, which is made of a forged titanium alloy. Since then, this type of cracking has led to two instances of engine failure on takeoff and a third instance in which the takeoff was aborted. Fortunately, these failures did not result in deaths or injuries. The cause of this type of fatigue cracking is not well understood, but it appears to be promoted in certain titanium alloys such as Ti-6Al-2Sn-4Zr-2Mo by large grains of susceptible orientation that are developed during a hot-forging process in which the billet is not heavily deformed. This type of fatigue is thought to be accelerated by hold periods at peak stress, hence the term *dwell time fatigue*.

Since the service temperatures involved are well below the creep range, creep does not appear to be a factor, but environmental factors may be involved. GEAE has changed both the forging technique and the titanium alloy in an effort to eliminate this type of cracking in the future.

A second problem was discovered in April 2000. It was found that the locking mechanism holding in place the ring containing the engine vanes had cracked, allowing the ring to rotate and wear through the casing, thereby releasing a shower of debris. To remedy this situation, GEAE has developed new locking mechanisms to secure the vanes.

Until the replacement parts have been installed, these problems will require a more intensive engine inspection program, involving the use of ultrasonic inspection methods, and a reduction in the spool's service life from 15,000 takeoffs to 12,500. There are clearly important economic considerations as well. For example, since the spool inspections now require the taking apart and reassembling of the whole engine, a 60 day process, a shortage of inspected engines could result. For this reason, GEAE is developing computerized inspection tools in an effort to reduce the inspection time to the order of 1 week.

VIII. CASE STUDY: COUNTERFEIT PART (8)

The following case describes a failure that occurred in 1976 in which a bogus part played an important role.

A four-engine, propeller-driven transport plane had just touched down when the left main wheel assembly separated. The aircraft slewed off the runway, and a fire damaged the wing and engines on the left side. It was found that the failure of a trunnion (a pin or pivot on which something can be rotated or tilted) arm shaft in the landing gear, which had occurred during the previous takeoff, was responsible for the accident. Progressive beach markings were found on the fracture surface of the trunnion arm, which suggested that fatigue may have been involved. However, in a detailed examination, intergranular fracture was observed without evidence of fatigue striations. It was concluded that the trunnion arm had failed because of stress corrosion cracking.

The trunnion arm was made of a fine-grained, through-hardened and tempered 4340 steel. It had been subjected to excessive wear in service, and during an overhaul it had been chrome plated to bring the dimensions of the worn trunnion arm back to the original level. Beneath the chrome plating and adjacent to the fracture, a regular pattern of intergranular cracks was found, some of which were not continuous through the chrome plating, an indication that they were not due to plating cracks. These cracks were about 0.5 mm (0.02 in.) in depth, and it was concluded that they were thermal checks, which had been created by overheating that occurred during a grinding operation at the time of an overhaul prior to hard chrome plating 18 months before the accident. A properly carried out magnetic particle inspection should have detected these cracks. Normally, local overheating due to coarse grinding leaves a

shallow, transformed, untempered martensitic layer, but fine grinding following a coarse cut may erase this layer, as was the case in this instance.

In comparing the failed trunnion shaft with a nominally similar trunnion shaft from the failed landing gear, certain differences were noted. The failed shaft had been ground undersize and then brought up to the correct size by plating, whereas the unfailed shaft had been machined undersize on a lathe with a single point tool prior to plating. The failed shaft was grit-blasted but not shot-peened, whereas the unfailed shaft was shot-peened. A fine crack network in the plating on the failed shaft was typical of a high-speed, low-crack plating bath, whereas a large crack network in the plating of the unfailed shaft was typical of a chromic/sulfuric conventional plating bath. The unfailed trunnion conformed to the overhaul facility's work statement procedures, whereas the failed trunnion did not. It was concluded that the failed trunnion was a substandard, counterfeit part. All manufacturers and overhaul facilities need to be on the lookout for the substitution of cheap parts for the parts specified by the original equipment manufacturer (OEM).

IX. THE USE OF THE WRONG ALLOYS; ERRORS IN HEAT TREATMENT, ETC.

Incorrect identification of alloys is another cause of failure (2). Examples include the misidentification of a monel alloy as a Type 304 stainless steel and the welding of monel with stainless steel electrodes, resulting in a brittle joint because the copper content of the monel led to hot-short cracking of the weld. Other examples include the substitution of Type 430 stainless steel for Type 304.

In-service failures have occurred where carbon steels have been substituted for chromium-molybdenum steels in high-temperature, high-pressure pipelines. Because of such mix-ups, the entire superheater tube sections in major steam power plants have had to be replaced in at least two instances. Mix-ups have even occurred in submarine construction, where welded pipe has been substituted for seamless pipe. Undoubtedly, there are many more instances of this sort of problem. To minimize such problems, it is recommended that parts be properly identified by stamping or by etching with an electric pencil. However, even this procedure is not foolproof, for there are instances where properly identified but incorrect alloys have been substituted for specified alloys because of careless erection practice.

Problems can also arise from improper heat treatment. In one welded structure, a quenched and tempered HY-80 alloy steel was specified, but the same steel in a normalized condition was used instead. The low toughness of the normalized steel resulted in hydrogen-induced cracking.

A punched-in trademark on a metal component can also serve as a site for crack initiation, particularly in a part that is used repetitively, such as a die. One is reminded of the wooden baseball bat with its burned-in label and the warning "Never hit the ball with the label facing forward." Too often, this sort of good advice is ignored by manufacturers.

X. SUMMARY

Defects are often the cause of premature failures. This chapter has provided a description of some of the more common types of defects. The avoidance of defects involves good quality control and inspection procedures.

REFERENCES

- (1) *Fracture Surface Replicas*, The Welding Institute, Abingdon, Cambridge, UK, 1973.
- (2) H. Thielsch, *Defects & Failures in Pressure Vessels and Piping*, Reinhold Publishing Co., New York, 1965.
- (3) C. Larrainzar, I. Korin, and J. Perez Ipiña, Analysis of Fatigue Crack Growth and Estimation of Residual Life of the Walking Beam of an Oilfield Pumping Unit, *Eng. Fail. Anal.*, vol. 17, 2010, pp. 1038–1050.
- (4) The Alexander L. Kielland Accident, Norwegian Public Reports, NOU 1981:11, Oslo, Norway, 1981.
- (5) C. E. Witherell, *Mechanical Failure Avoidance*, McGraw-Hill, New York, 1994.
- (6) W. F. Hosford and R. M. Caddell, *Metal Forming*, 2nd ed., Prentice-Hall, Englewood Cliffs, NJ, 1993.
- (7) W. D. Buntin, Concept and Conduct of Proof Test of F-111 Production Aircraft, *Aeronautical J.*, vol. 76, no. 742, 1972, pp. 12–27.
- (8) T. W. Heaslip, “Failure of Aerospace Components,” in *Metallography in Failure Analysis*, ed. by J. L. McCall and P. M. French, Plenum, New York, 1978, pp. 141–165.

PROBLEMS

12-1. The effect of the reinforcement angle at a butt weld in steel on the fatigue range, $\Delta\sigma$ at 2×10^6 cycles at $R = 0$ is given as $\Delta\sigma = 120 \left[2 - \cos \left(\theta - \frac{\pi}{2} \right) \right]$, MPa. Here θ is the reinforcement angle in radians.

- (a) Plot the value of $\Delta\sigma$ as a function of θ for values of θ between $\frac{\pi}{2}$ and π radians.
- (b) The ultimate tensile strength of the steel is 600 MPa. Use the Goodman relationship to determine the stress range, $\Delta\sigma$, at 2×10^6 cycles for $R = -1$ loading conditions.

For comparison purposes, plot $\Delta\sigma$ as a function of θ on the same graph as in part (a).

12-2. Several elbow subassemblies comprising segments of oil-line assemblies broke in service. The components of the subassemblies were made of aluminum alloy 6061-T6. The expected service life of each subassembly was at least 10 years, but the actual life was between 6 months and 1 year. Two subassemblies were returned to the laboratory for determination of the cause of failure. In one

(Fig. 1), the threaded boss had separated from the elbow at the weld. In the second, the failure was caused by fracture of the elbow near the flange (Fig. 2). Investigation revealed that penetration of the elbow wall section was entirely lacking in the first subassembly (Fig. 1). Furthermore, examination of the weld fracture surface showed evidence of beach marks at the apex of the V-notch and dimples at the top portion of the V-notch. The hardness values taken from the threaded boss and the tube were about 102 Bhn (Brinell hardness number). No sign of corrosion was found.

Study of the second elbow (Fig. 2) revealed that the welded joint attaching the threaded boss had also failed but had been rewelded by the user and returned to service. The second failure then occurred in the tube near the flange. The fracture surface showed evidence of beach marks and dimples at different regions. The hardness near the fracture was less than 53 Bhn. The manufacturing procedure stipulated that following the welding, the subassembly had to be solution treated and aged to the T6 temper.

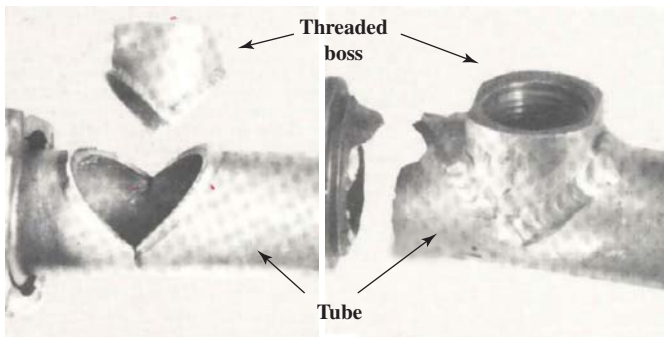


Fig. 1

Fig. 2

- (a) Find the nominal composition of Al 6061.
- (b) Find the treatment conditions for T6 treatment.
- (c) Find or estimate the hardness value of Al 6061 in the T6 condition.
- (d) Discuss the possible cause for the failure of the first elbow.
- (e) Discuss the possible cause for the failure of the second elbow.
- (f) What other experiments would you do if you cannot identify the root cause of the failure based on the information presented?

13

Environmental Effects

I. INTRODUCTION

Corrosion combined with steady or alternating stresses can play a major role in several types of failure processes. The interaction of the environment, stress, and an alloy can be quite complex, and in some cases, there may be no consensus as to the exact mechanisms involved. Nevertheless, on a macroscopic level, there is ample evidence of the deleterious effects that the environment can exert in promoting fracture. Corrosion is a time-dependent phenomenon, and its effects in service may not be realized until many years have passed. This is an important consideration, since many components are subjected only to short-time testing prior to being approved for in-service use. Consideration needs to be given to the time-dependent effects of corrosion in service, as in the case of aging aircraft. In this chapter, some basic aspects of corrosion processes will be reviewed and various types of corrosion-related fractures will be discussed.

II. DEFINITIONS

(a) *Corrosion*: The deterioration of a metal by a chemical or electrochemical reaction with its environment.

(b) *Stress-corrosion cracking (SCC)*: Failure by cracking due to the combined action of corrosion and stress, either external (applied) or internal (residual). Cracking

may be either intergranular or transgranular, depending on the metal and the corrosive medium.

(c) *Hydrogen embrittlement*: A condition of low overall ductility in metals resulting from the absorption of hydrogen. Steel tensile specimens charged with hydrogen exhibit a reduction in the percentage of elongation and in the percentage of reduction in area as compared to uncharged specimens. The failure mode may be either cleavage, intergranular, or ductile, but in the last case the dimples are more numerous and more shallow as compared to those in an uncharged specimen. Hydrogen embrittlement is most severe at room temperature and can lead to a delayed or time-dependent form of cracking. It is also referred to as *hydrogen-assisted fracture*, which can denote embrittlement on the atomic scale due to bond weakening or to the promotion of localized plastic deformation.

(d) *Hydrogen-induced cracking (HIC)*: A form of hydrogen embrittlement. HIC can occur in the absence of applied or residual stress as the result of the combining of two hydrogen atoms to form an H_2 molecule inside the metal matrix. This reaction takes place at a convenient location such as an inclusion interface. The formation of a hydrogen molecule from two hydrogen atoms results in a local increase in pressure. As more and more molecules form at a given site, the pressure increases to the point where, if the site is near the surface, a blister may form. If the site is remote from a surface, the formation and growth of a crack may take place, and if a number of such cracks form, they can link up and greatly degrade the fracture resistance. In some cases, when external stresses are present, it may be difficult to distinguish between hydrogen embrittlement due to atomic interaction with the lattice and HIC.

(e) *Hydrogen attack*: An elevated-temperature problem caused by the diffusion of hydrogen into steel, where it combines with carbon to form methane gas, leading to porosity within the steel.

(f) *Liquid metal embrittlement*: Loss of ductility of a metal such as aluminum as the result of direct contact with a liquid metal such as mercury, or austenitic steel in contact with molten zinc, or molten lead in contact with ferritic steel.

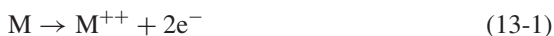
(g) *Corrosion fatigue*: The deleterious effect of an environment, including ambient air, on the purely mechanical fatigue process.

(h) *Localized deformation*: Plastic deformation involving the motion of dislocations in microscopically narrow zones.

(i) K_{ISCC} : The threshold value of the Mode I stress intensity factor for stress corrosion cracking for a given alloy and environment.

III. FUNDAMENTALS OF CORROSION PROCESSES

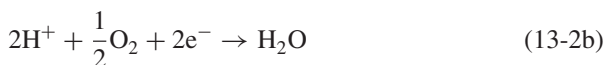
A basic aspect of the electrochemical corrosion process is that the dissolution of metal takes place at the anode and the removal of electrons takes place at the cathode. A typical dissolution reaction can be written as



a reaction referred to as an *oxidation reaction* in that electrons are liberated. A typical cathodic reaction can be written as



a reaction referred to as a *reduction reaction* in that electrons are consumed. Another cathodic reaction that is important in neutral and alkaline solutions containing dissolved oxygen is



in an electrochemical corrosion process, and it is basic that the total anodic current, I_A , be equal to the total cathodic current, I_C . Figure 13-1 shows the reactions occurring at a corrosion pit in aluminum where the reduction process involves oxygen (Fig. 13-1a) and where the reduction process involves hydrogen (Fig. 13-1b).

Faraday's law gives the mass in grams going into solution from an anode in a given time period. In some models of SCC, anodic dissolution at a crack tip is envisioned. This law is derived as follows:

1. A metal ion going from the anode to the cathode carries z units of charge, where z is the valence. This is equivalent to $z \times 1.602 \times 10^{-19}$ coulombs.
2. If N mols go from the anode to the cathode, then the number of coulombs transported would be $N \times (A_v \times z \times 1.602 \times 10^{-19})$, where A_v is Avogadro's number, 6.022×10^{23} .

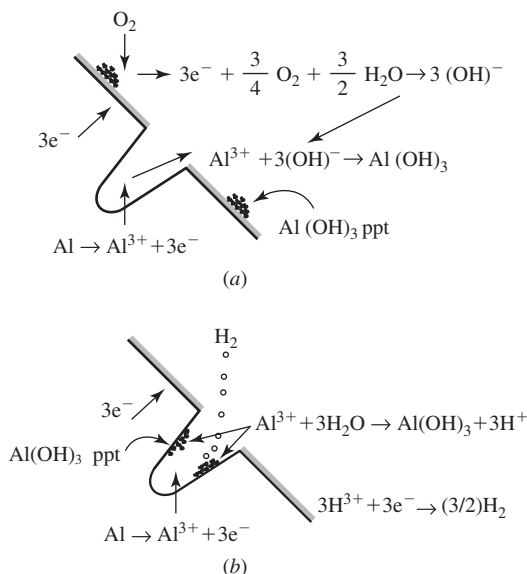


Fig. 13-1. Reaction at a corrosion pit in aluminum. (a) Reduction process involving oxygen. (b) Reduction process involving hydrogen.

3. This number of coulombs can be expressed as $N \times z \times 1.602 \times 10^{-19} \times 6.022 \times 10^{23} = N \times z \times 96,519$ coulombs $= N \times z \times F$, where F is Faraday's constant $= 96,519$ coulombs/mol.
4. The current is the number of coulombs transported per second, or $I_A = N \times z \times F/t$.
5. The above relation can be rewritten as $N = I_A t/zF$.
6. To convert this expression to the metal weight loss in grams from the anode, multiply both sides of the above equation by the molecular weight in grams/mol, W , to obtain

$$NW = \text{total mass in grams lost} = M = WI_A t/zF \quad (13-3)$$

This is Faraday's law. This expression can be rearranged to give the total anodic current, I_A :

$$I_A = MzF/Wt \quad (13-4)$$

Faraday's law can also be written in terms of the current density i_A , where $i_A = I_A/A$, that is, $M = Wi_A t/AzF$, where A is the area of the anode. For this reaction to proceed during SCC, it is necessary that any protective oxide film at the crack tip be ruptured. Continuing plastic deformation in the plastic zone at a crack tip may be required to expose the underlying base metal to the corrosive environment. In addition, chloride ions, if present, may serve to weaken oxide films so that they are more easily ruptured by plastic deformation.

It is also noted that the cathodic reaction may involve hydrogen ions. If, instead of combining with electrons, these ions diffuse into the metal, the possibility of hydrogen embrittlement develops, especially since the cathode may be quite close to the anode.

When metal ions are created and electrons are liberated at the anode, an electric potential develops. This potential is measured relative to a standard electrode when the following typical reversible reaction is established in a molar solution of metal ions:



By this means, a table of electrochemical potentials is established for the various metallic elements, which is similar to the Galvanic series. The potential for the reversible hydrogen reduction reaction,



is taken as zero, and it becomes the standard reference potential. The potential for the reaction in Eq. 13-5 is 0.440 volt below that of the standard hydrogen electrode. If the reduction process involves oxygen rather than hydrogen, the reduction reaction is



This reversible reaction occurs at potential of 0.82 volt above the standard hydrogen potential.

The actual potential in a corrosion process falls between that for the oxygen potential, +0.82 volt (if dissolved oxygen is more plentiful than hydrogen ions), and the metal potential, if iron, -0.44 volt. The realized potential is called the *mixed corrosion potential*, E_{corr} , which is associated with a corresponding corrosion current density, i_{corr} . The process whereby the potentials are altered is called *mutual polarization*, which occurs as the result of electron flow from the anode to the cathode. This information can be displayed on a potential-log current diagram, as in Fig. 13-2.

Pourbaix diagrams, or potential-pH diagrams, indicate the thermodynamically stable phases that can form during aqueous corrosion. Figure 13-3 is a simplified Pourbaix diagram for iron in aqueous solution. In Fig. 13-3, the upper dotted line represents the reaction given by Eq. 13-7 and the lower dotted line represents the reaction given by Eq. 13-6. At potentials above the oxygen reaction line, oxygen is evolved. At potentials below the hydrogen reaction line, hydrogen is evolved. Between the two lines, water is stable. At one time, it was thought that if the potential-pH values fell between these two lines, the stress corrosion cracking process could not involve hydrogen and anodic dissolution must control the cracking process. However, more recently, measurements of the pH at crack tips have shown that pH values can be much lower than the bulk values. Therefore, at a given potential, the crack tip pH value can lie below the line for the hydrogen reaction, meaning that hydrogen can be evolved and hydrogen embrittlement is possible. Figure 13-4 gives an example of this situation for a high-strength steel.

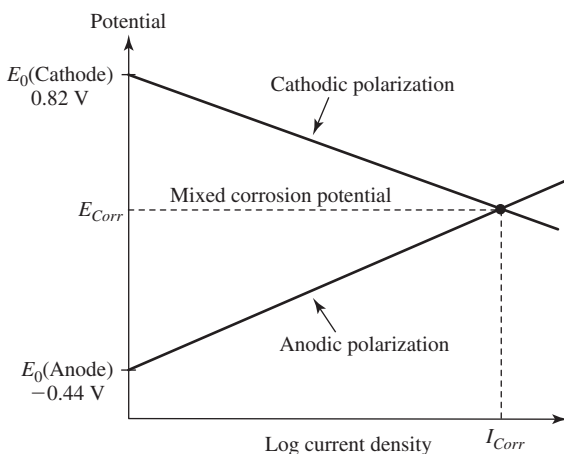


Fig. 13-2. A potential-log current diagram.

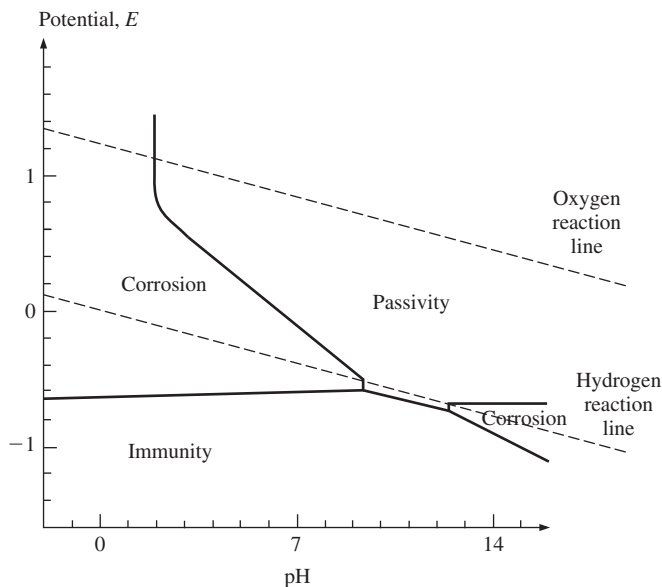


Fig. 13-3. A simplified Pourbaix diagram for iron.

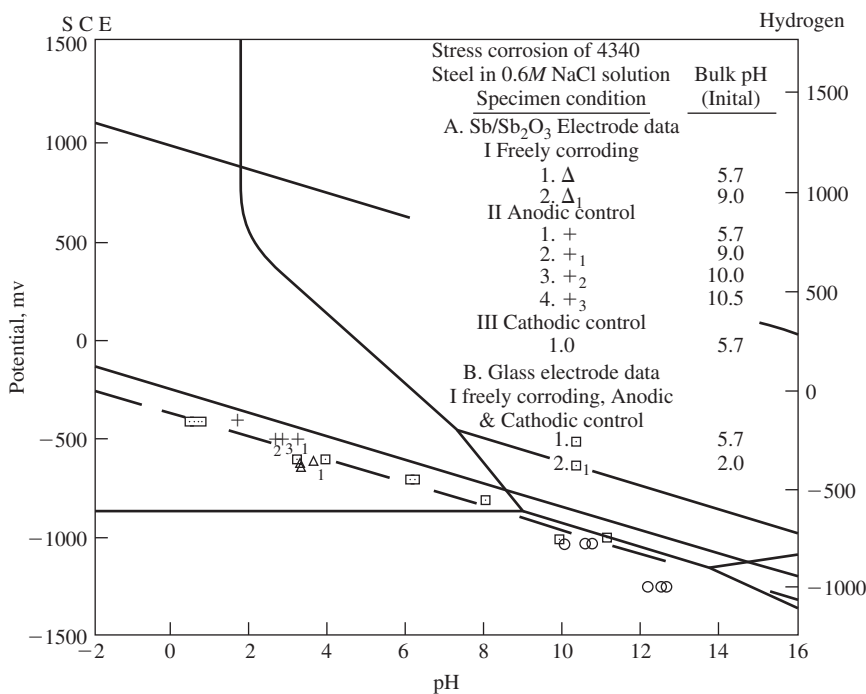


Fig. 13-4. A Pourbaix diagram showing the potential at a crack tip in 4340 steel as a function of the crack tip pH value. (From Brown, 13.)

IV. ENVIRONMENTALLY ASSISTED CRACKING PROCESSES

There are currently four types of mechanisms that are known to relate to the effects of the environment on cracking processes. One mechanism is based upon the repeated rupture and reformation of films at the tip of a growing crack. The second mechanism is based upon the process of anodic dissolution at a crack tip. The third is liquid metal embrittlement, involving either the weakening of atomic bonds or the promotion of localized deformation. The fourth is hydrogen-assisted fracture, and since aqueous corrosion is the most common type of corrosion, the potential for hydrogen-assisted cracking in many cases exists. There are two leading theories for hydrogen-assisted fracture. One is that hydrogen weakens atomic bonds, resulting in embrittlement. The other is that hydrogen promotes very localized plastic deformation, which results in high shear strains and fracture within the localized shear bands. There may not in fact be a single mechanism, as one or the other may be operative under a given set of circumstances. From a practical point of view, it is important to know the situations in which hydrogen-assisted cracking can occur and take appropriate preventive steps.

Figure 13-5 is a schematic showing how stress corrosion cracks can develop from a free surface. Figure 13-6 shows how the SCC process may proceed by a film rupture model in cartridge brass.

SCC tests are carried out on either smooth, notched, or precracked specimens. Results for smooth stainless steel specimens in boiling magnesium chloride, a standard but severe environment, are shown in Fig. 13-7. In SCC of stainless steel as well as other alloys, typical branching cracks are observed, which distinguish this form of cracking from fatigue cracking, where usually only a single major crack is observed, Fig. 13-8. Figure 13-9 is a schematic representation of the rate of stress corrosion crack growth as a function of K . Figure 13-10 shows results for precracked specimens of aluminum alloys. Note that a plateau exists where the rate of cracking is constant and independent of K . This plateau develops because the diffusion of the corroding species in the liquid at the crack tip becomes rate limiting. At the lowest rates of crack growth, the K_{ISCC} value is approached. The effect of flaw size on establishing the safe limits for the avoidance of SCC is shown in Fig. 13-11. In this

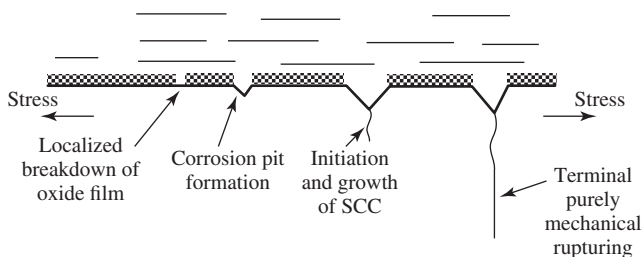


Fig. 13-5. Schematic of a stress corrosion crack developing at the surface. (After Brown, 14.)

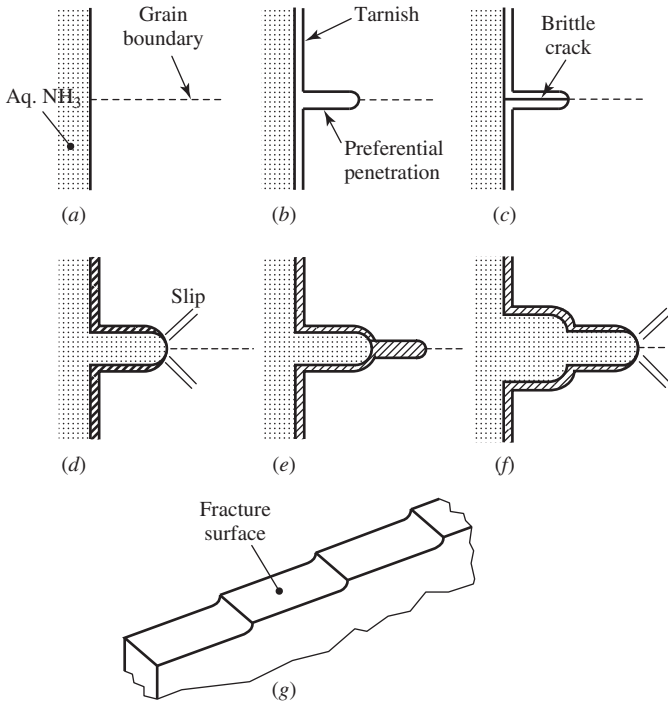


Fig. 13-6. A film rupture model for α -brass in a tarnishing solution. (After Pugh, 15.)

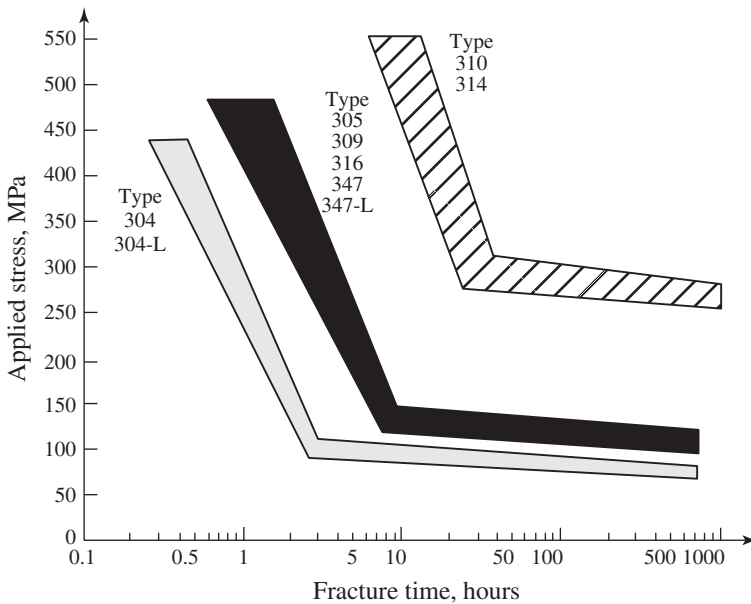
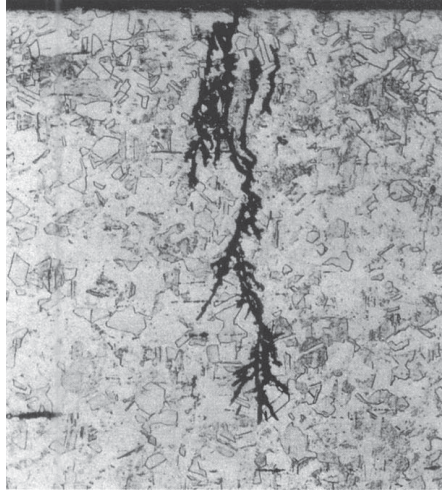
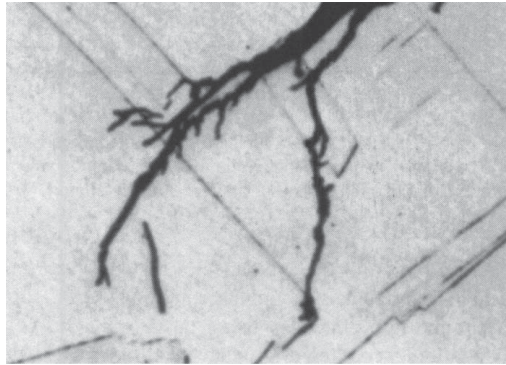


Fig. 13-7. Relative SCC behavior of austenitic stainless steels in boiling magnesium chloride solution. (After Denhard, 16.)



(a)



(b)

Fig. 13-8. (a, b) Examples of SCC branch cracking in AISI type 304 austenitic stainless steels. (From Brown, 14.)

case, the threshold found under smooth bar conditions sets the limit up to a flaw size of 1.5 mm (0.06 in.), where the stress intensity factor takes over. This behavior is analogous to a similar situation encountered in mechanical fatigue. The stress intensity factor for a long, shallow surface flaw is given as

$$K = \sqrt{\frac{1.2\pi\sigma^2 a}{1 - 0.212(\sigma/\sigma_Y)^2}} \quad (13-8)$$

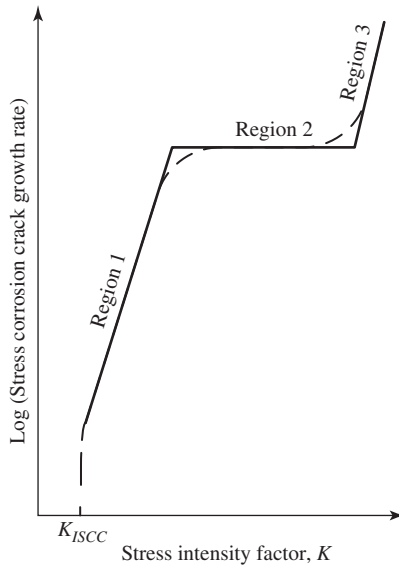


Fig. 13-9. Schematic of the rate of SCC as a function of the stress intensity factor, K . Region 3 is of little interest and is often missing. Region 1 is missing in some systems. Regions 1 and 2 are not always straight lines in such plots but may be strongly curved. (After Brown, 14.)

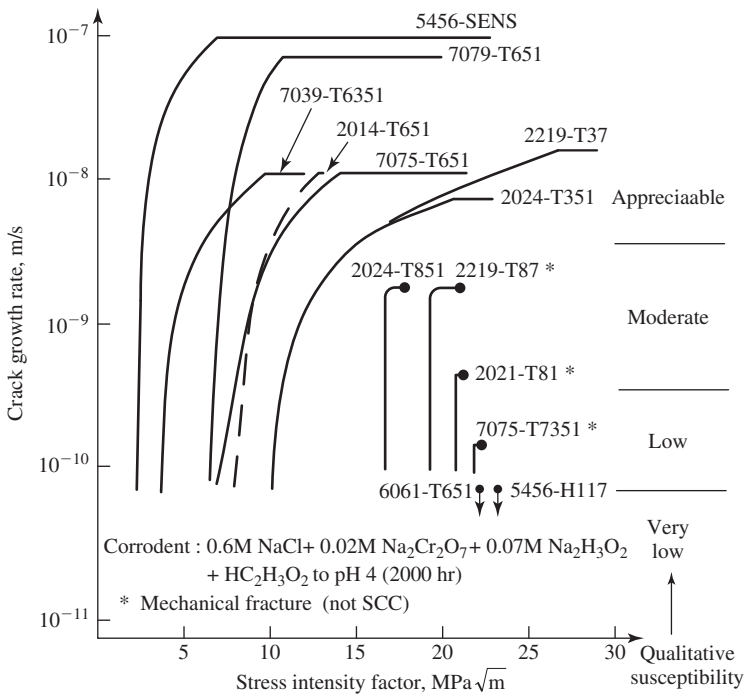


Fig. 13-10. The rate of SCC growth, da/dt , as a function of the stress intensity factor for aluminum alloys showing plateau levels. (After Brown, 14, and Sprowls et al., 18.)

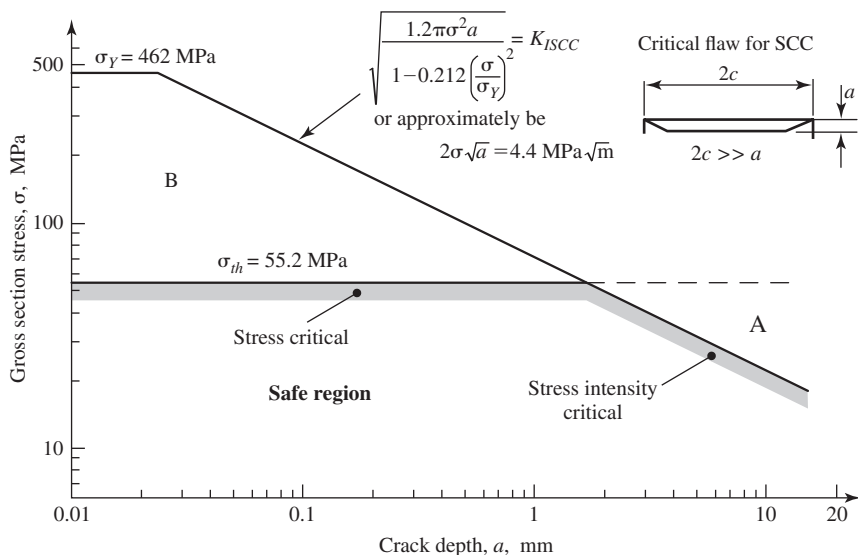


Fig. 13-11. Flaw depth a versus stress, showing the stress critical- (small cracks) and threshold stress critical- (large cracks) boundaries for the aluminum alloy 7079-T651 plate. (After Brown, 14.)

If, as an upper limit, σ is set equal to σ_Y , then a value for a_{cr} , where a_{cr} is the critical crack length at K_{ISCC} , can be expressed as

$$a_{cr} = 0.2 \left(\frac{K_{ISCC}}{\sigma_Y} \right)^2 \quad (13-9)$$

and $K_{ISCC} = \sqrt{5a_{cr}}\sigma_Y$. This last relationship plots as a straight line of slope $\sqrt{5a_{cr}}$ on a plot of K_{ISCC} versus σ_Y . The relationship gives the value of K_{ISCC} required for a given a_{cr} and σ_Y to avoid stress-corrosion crack growth. Figure 13-12 shows this level of K_{ISCC} for several crack lengths as a function of σ_Y , and includes experimental K_{ISCC} - σ_Y data points for a number of titanium alloys. Note that the K_{ISCC} datum point for Ti-8Al-1Mo-1V at a σ_Y just over 827 MPa (120 ksi) is quite low, as is the corresponding a_{cr} . Because of its relatively high strength, at one time the U.S. Navy considered using this alloy for submarine hulls. The alloy performed well in smooth-bar stress corrosion tests, but its low K_{ISCC} value precluded further consideration for such an application.

Cathodic protection by the use of either an impressed current or sacrificial anodes can be used to lower the rate of SCC, as shown in Fig. 13-13. However, too much of a reduction in the corrosion potential can result in hydrogen embrittlement due to larger amounts of hydrogen being required at the cathode to maintain a higher i_c , as shown in Fig. 13-14. The effect of a reduction in potential, therefore, is to reduce the anodic current but to increase the cathodic current.

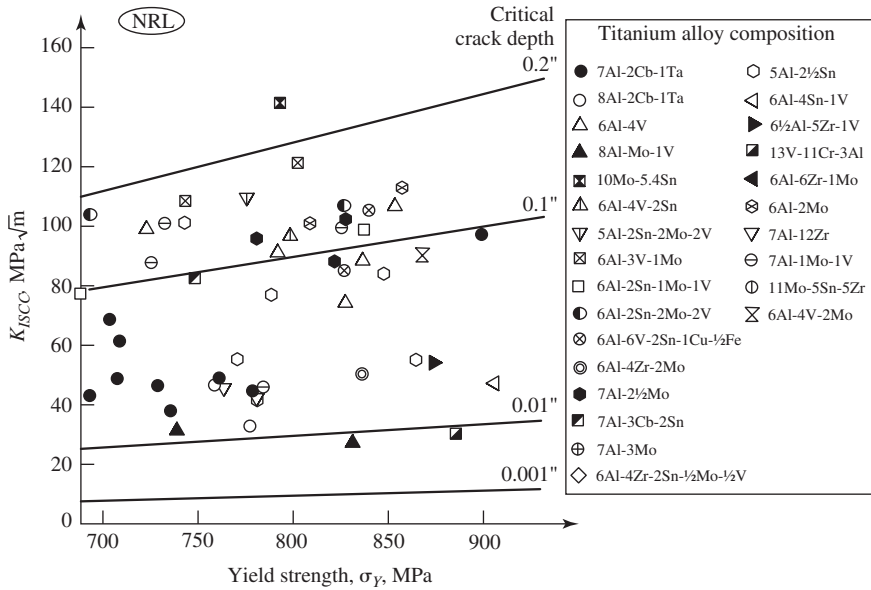


Fig. 13-12. K_{ISCC} data on titanium alloys in sea water. The critical flaw size as a function of K_{ISCC} and yield strength level is indicated (NRL = Naval Research Laboratories). (After Brown, 14.)

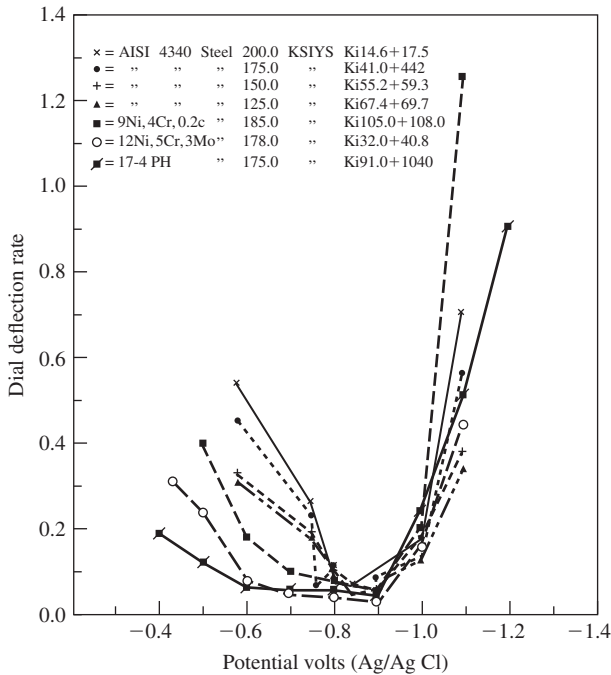


Fig. 13-13. Effect of varying degrees of cathodic protection on the stress-corrosion cracking rates of several steels. The rate of cracking was taken to be proportional to the dial deflection rate. (From Brown, 14.)

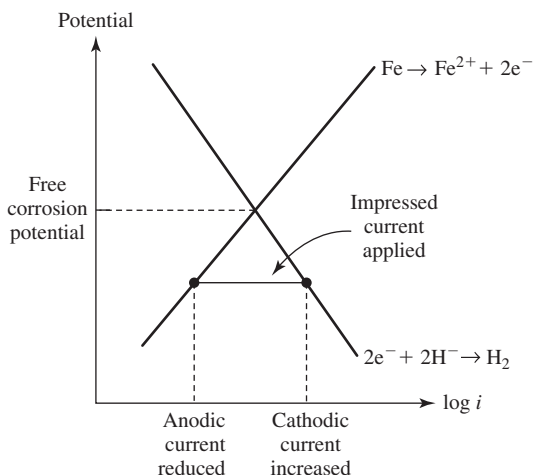


Fig. 13-14. Effect of an impressed current on reducing the corrosion rate of iron through cathodic protection.

V. CASE STUDIES

A. Spring Failures

Failures associated with hydrogen-assisted cracking are delayed failures that involve discontinuous crack growth. They often occur without warning and with severe or potentially disastrous consequences. For example, consider an encased, precompressed spring in a fire-protection system. In the event of a fire, a low-melting-point component melts, thereby releasing the spring and activating a water sprinkler system. However, if the spring contains hydrogen because of a plating operation, or if it corrodes with the uptake of hydrogen, it may fail prior to its time of need. Such a failure can remain undetected, which would negate the protective scheme, with obvious potential for disaster. The extent of corrosion may depend upon the surface, for a highly polished surface often shows less corrosive attack than a rough surface under the same service conditions.

Spring failures can also occur because the spring material was inappropriate for the intended use (1). For example, a pressure relief valve was provided to vent gas from a high-pressure unit in the event that the pressure in the unit built up beyond the 7.6 MPa (1,100 psi) operating conditions. The gas contained 1,000 ppm by weight of H_2S at 20°C (68°F). The valve included a high-strength compressed coil-spring that was essential for the proper operation of the safety valve but that was not resistant to the effects of the H_2S environment. Fortunately, the relief valve was never called upon to operate, for after 9 months of service the spring was found to have broken.

The National Association of Corrosion Engineers (NACE) Standard MR-01-75 (2) provides information regarding the selection of materials to be resistant to sulfide stress cracking (SSC), a form of hydrogen-assisted cracking. The standard indicates

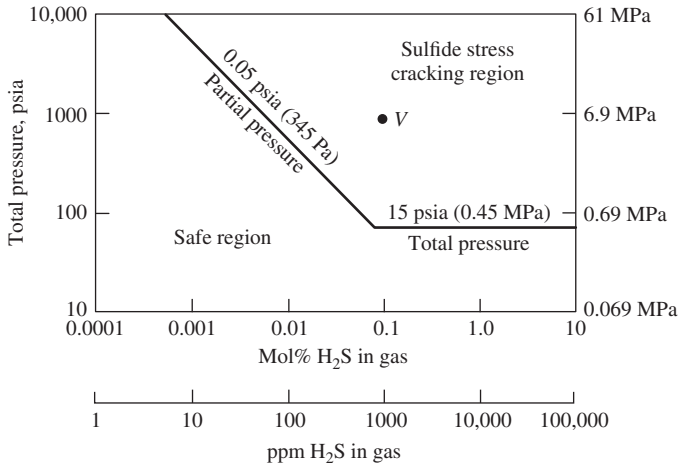


Fig. 13-15. Graph showing the limit of susceptibility of steels to SSC in sour gas systems. Point V represents the conditions as seen by the pressure release valve spring. (After NACE Standard MR-01-75-1980.)

that for the operating conditions, 1,000 ppm of H₂S and 6.9 MPa (1ksi) total pressure (indicated by the V in Fig. 13-15), a material should have been selected that was resistant to SSC. MR-01-75 lists applicable materials for springs intended for such in-service conditions. The allowable hardness is normally restricted to below 22 HRC (Rockwell C Scale Hardness), whereas the failed spring was a martensitic stainless steel with a hardness of 45–50 HRC. This failure was clearly due to a lack of awareness of the danger of hydrogen-assisted cracking in the presence of H₂S.

B. Failure of a Ladder Rung

Step-rungs are used to enable workers to mount the towers that support high-tension lines. At the lower levels of a tower, the rungs are removable to prevent children from climbing the towers. Workers install portable rungs in slots as they mount a tower and remove them as they come down. The rungs are made from a single rod of normalized 1018 steel, which has been cold formed to a shape consisting of the horizontal rung and two vertical legs welded together, with the vertical legs fitting into the slots on the tower. On one occasion, as a rung was being tapped into a slot, the rung failed, and an investigation into the cause of failure followed. The appearance of the fracture surface is shown in Fig. 13-16 (1). After the cold forming operation, the rung had been cleaned and phosphated prior to painting in order to improve the adhesion of the paint. The dark region in the lower portion of Fig. 13-16 contains phosphorous, indicating that hydrogen-assisted cracking in this region occurred during the phosphating process. Fracture adjacent to the dark region occurred by a cleavage mechanism. Failure of the remaining ligament at the top of the figure occurred by a ductile tearing process.

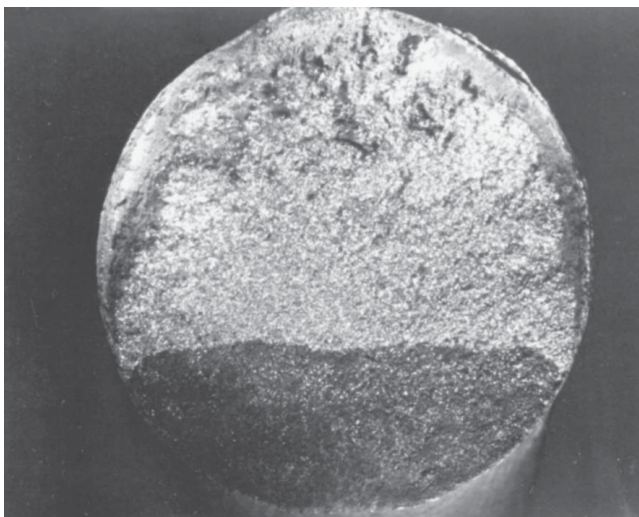


Fig. 13-16. Ladder rung fracture surface appearance. (Reprinted from *Materials Characterization*, vol. 26, A. J. McEvily and I. Le May, Hydrogen assisted cracking, pages 253-258, Copyright 1991, with permission from Elsevier Science, 1.)

Hydrogen is produced in the phosphating process but generally does not lead to cracking in low-strength steels such as 1018. However, in this case, the properties of the steel had been modified by the cold forming operation. The local hardness at the inside of a bend was equivalent to that of steel of 827 MPa (120 ksi) tensile strength, as compared to the original strength of 496 MPa (72 ksi); in addition, the bending operation had resulted in a state of residual tensile stress at the inside of the bend. The combination of high hardness, residual tensile stress, and hydrogen ions led to crack formation. The solution to this cracking problem was relatively simple. The flame from the welding torch that was used to weld the legs together after forming was directed at the bends to bring them to a cherry red color, and then the rung was allowed to cool in air. This procedure softened the steel and removed the residual tensile stresses, thereby rendering the material resistant to hydrogen-assisted cracking.

VI. CRACKING IN OIL AND GAS PIPELINES

The prevention of oil or gas pipeline failures is a matter of prime concern in the petroleum industry, and ASME and API codes are widely used in specifying, fabricating, and inspecting the steels used for pipelines. Nevertheless, on average, two failures per day due to corrosion-induced leaks or ruptures have occurred in Alberta, Canada, alone (3). Pipelines are often coated with a bituminous layer to protect against corrosion, and, if laid on a seabed, they may be encased in concrete to protect against external damage. To further guard against corrosion, the pipeline may be cathodically protected with an impressed current or by sacrificial anodes of

aluminum or magnesium. For internal corrosion control, the most often used method involves the use of inhibitors. If a pipeline containing oil were to fail, there would not only be the loss of product, but also the danger of damage to the environment. When a pressurized gas pipeline fails, not only may there be an explosion endangering lives, but also 1 km (3,280 ft.) or more of pipeline may be destroyed due to a running crack that moves faster than the gas pressure can be relaxed.

These pipelines can be examined by internal electromagnetic or ultrasonic inspection devices known as *smart pigs* (pipe internal gauging system), which move along inside the pipeline with the oil or gas, measuring wall thicknesses, metal loss, and internal diameter and detecting dents and flaws. In addition, external examination methods using nondestructive examination techniques, such as radiographic and ultrasonic inspection, are used to check the welds for defects and to determine wall thickness. Because of economic considerations, the control of risk may have a higher priority than the control of corrosion per se (4). Risk R is defined as the probability of failure P multiplied by the consequence of failure C :

$$R = P \times C \quad (13-10)$$

For example, a higher probability of failure may be tolerated in a remote area than in a densely populated area because the consequence of failure may be much lower in a remote area.

Much of the concern with respect to fracture of pipelines in addition to general corrosion has to do with hydrogen-assisted cracking, particularly when H_2S is present in the moisture contained within the gas or oil. A gas that has an H_2S concentration of less than 20 ppm is known as *sweet gas*, and problems due to H_2S are not severe. When the concentration of H_2S exceeds 20 ppm, however, the deleterious effects of H_2S become pronounced; for this reason, the gas is referred to as a *sour gas*. The reason why H_2S is of concern is that, when it dissociates in water, the sulfide anion acts as a "poison" and promotes the penetration of hydrogen ions into a metal. Hydrogen ions are produced by the corrosion reaction between iron and moist sulfide (5). In pipeline steels, cracks that form because of hydrogen embrittlement (HIC) often develop at and follow manganese sulfide stringers because the interface is weak and hydrogen is trapped at such inclusions. Planar cracks can form near the midthickness of the pipe, where the concentration of manganese sulfide particles is greatest, but they do not reduce the structural integrity of the pipe per se. However, several noncoplanar cracks may be linked up by short radial cracks, forming a *stepwise crack*, and thereby a critical crack length for fracture under the influence of the hoop stress may be reached.

Cracking in a buried pipeline can occur because of potential differences that develop between the soil and the pipe. For example, a 863.6 mm (34 in.) diameter, spirally welded Grade X-60 spheroidized steel pipe with a wall thickness of 7.8 mm (0.305 in.) was used in the fabrication of a pipeline in accord with API Specification 5L. The maximum allowable pressure in the line was 52 bar (775 psi), but leakage occurred at an operating pressure of 42 bar (626 psi). The line was cathodically protected by an impressed current as well as by sacrificial magnesium anodes. At the failure location, it was noted that the bituminous asphalt coating had been stripped

off and the supporting ground had subsided, thereby inducing additional stresses at a low strain rate into the steel. Cracks had initiated on the outside of the pipe and tended to follow the manganese sulfide inclusions. Scanning electron microscope examination revealed evidence of transgranular quasi-cleavage-like brittle fracture. A jagged crack appearance with a tendency for stepwise cracking suggested that hydrogen was involved in the cracking process.

Cathodic protection is widely used to protect gas pipelines from corrosion. However, hydrogen evolution can occur during cathodic protection when the pipe-soil potential is more negative than -850 mV with reference to a Cu/CuSO₄ reference electrode. In one case, the actual pipe-soil potential was $-1,100$ mV, which was sufficiently negative for hydrogen evolution. In addition, the sacrificial anodes had come in direct contact with the steel, further lowering the potential. It was considered that slow plastic deformation due to the subsidence of the soil had occurred, which had facilitated the entry of hydrogen into the steel. To check on this possibility, slow strain rate tests (strain rate = 10^{-6} /sec) were carried out in artificial brackish groundwater with steel specimens held at a potential of $1,100$ mV. The reduction in area at fracture in these tests dropped from a normal value of over 60% to less than 30%, and it was concluded that the leakage had occurred because of hydrogen-assisted cracking (6).

In another instance (1), a steel pipeline had been heat-treated to have a spheroidized microstructure, and because of a relatively low yield strength (414 MPa [60 ksi]), it was not considered to be susceptible to hydrogen-assisted cracking. The pipeline was laid in winter, and soil and snow were trapped within the line. No cleaning was done until the summer months, by which time the snow in the line had melted. The ground through which the line had been laid had an acid topsoil and an alkaline lower layer, and when they were mixed together with water, a visible reaction occurred. When the line was pressure tested in summer, numerous intergranular failures occurred at bends in the line where laying stresses occurred. At the failures, there was an absence of corrosion products, further evidence that hydrogen-assisted cracking had occurred because of poor housekeeping procedures in laying the line.

Stress corrosion cracking has been observed in gas-transmission pipelines downstream of a compressor station (7), where the pipe temperatures are the highest. The cracks originated on the external surface, and a black oxide layer formed on the fracture surfaces. Iron carbonate or bicarbonate was detected on the fracture surfaces, having been produced at a pore in the pipe coating as the hydroxide created by the cathodic potential was converted by the CO₂ in the soil to a carbonate-bicarbonate environment. The fractures were intergranular and typical of SCC; the cracks were branched.

VII. CRACK ARRESTORS AND PIPELINE REINFORCEMENT

Steel rings are used as crack arrestor devices in steel gas-transmission pipelines to reduce the possibility of long running longitudinal cracks. These arrestors have the effect of reducing the pipe opening as the crack propagates. This decreases

the available crack-driving force and, as a result, crack arrest can take place. This essentially is a second line of defense against catastrophic failure in the event that crack initiation cannot always be prevented (8).

For economic reasons, it is often undesirable to shut down a pipeline to replace sections in which defects or loss of wall thickness have been discovered during inspection. Instead, a *sleeve* is used to reinforce the original section. These sleeves are sections of steel that snugly encase the original pipeline and are welded in place. A modified method uses an epoxy layer between the original pipe and the outer steel sleeve. When the epoxy sets, it expands and can create a radial pressure equal to that in the pipeline, thereby taking load off the original pipe and transferring it to the reinforcing sleeve.

VIII. PLATING PROBLEMS

During the electroplating of steel with protective coatings of chromium, cadmium, or zinc, large amounts of hydrogen are generated at the metal surface, some of which diffuses into the steel. In steels of high hardness, this hydrogen can lead to embrittlement. For example, it was found that zinc-plated steel screws of 28-36 HRC failed after being in service for only 2 weeks. This particular problem was remedied when the fasteners were replaced by zinc-coated ones having a lower hardness, 100 Rockwell B Hardness (HRB).

In cases where plated high-strength steels must be used, it is common practice to bake out the components after plating. The solubility of hydrogen at room temperature is extremely low, of the order of 1 ppm. A plating operation results in a supersaturation of hydrogen, and some of this hydrogen will diffuse out of the steel after the plating operation. However, critical amounts of hydrogen will be retained in the steel, particularly at so-called trapping sites. To reduce the hydrogen content, it is common practice to bake out the component after plating. It has been shown (9) that, after baking a hydrogen-charged 4130 steel at 150°C (302°F) for 24 hours, embrittlement is almost completely eliminated.

IX. CASE STUDIES

A. Welding Electrodes (10)

A highway bridge in Melbourne, Australia, was supported by girders made of a high-strength, low-alloy steel (yield strength 550 MPa, 80 ksi), as schematically shown in Fig. 13-17a. The girders were reinforced at midspan by welding coverplates on to the lower flange at the erection site. From Fig. 13-17b, it can be seen that the coverplates were narrower than the flange and were machine-welded to the flange by a pair of single-pass fillet welds. In order to smooth out the load transfer between the reinforced and nonreinforced portions of the flange, the width of the coverplate was reduced gradually over the last 460 mm (18.4 in.) of its length from its full width of

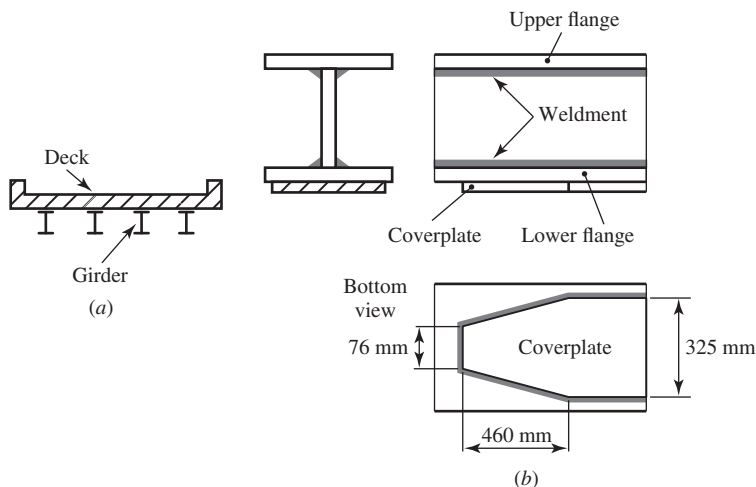


Fig. 13-17. (a) Transverse cross section of a bridge. (b) Orthographic views of the girder at the location near the end of a coverplate.

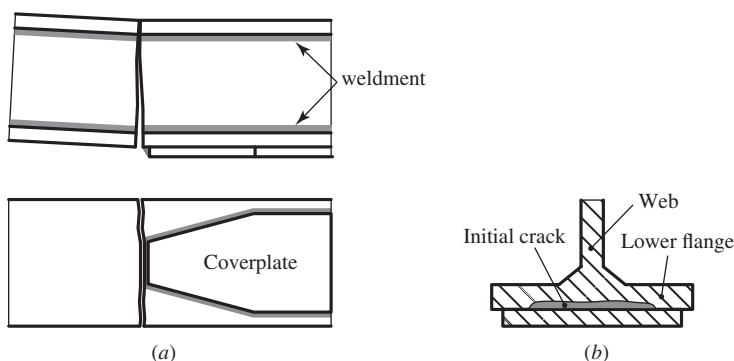


Fig. 13-18. (a) Location of the fracture. (b) Location of the initial crack.

325 mm (13.0 in.) down to 76 mm (3.0 in.). It is important to note that the tapered regions, as well as the transverse ends of the coverplates, were welded by hand using three-pass fillet welds. After a year of service, a partial collapse of the span occurred as the result of progressive crack formation at the ends of the coverplates (see Fig 13-18a). Some of these cracks (see Fig. 13-18b) had existed for some time, as indicated by the paint primer and rust on the crack surfaces. All fractures had initiated in the heat-affected zone (HAZ) at the toe of the coverplates and showed no evidence of corrosion products.

The HAZ cracks were most likely due to hydrogen-assisted cracking, with the source of the hydrogen being the moisture in the flux coatings on the electrodes. The specifications called for the flux coatings to be of a low-hydrogen type, but the flux coatings could still have absorbed moisture from the atmosphere. It was therefore

important to bake out the electrodes immediately prior to use at a temperature of 150°C (302°F) for 30 minutes. After the accident, however, it was determined that a higher temperature should have been used. Further, there was evidence that the electrodes used in the hand-welding operations had been lying about and were exposed to the atmosphere prior to use.

Concern about moisture absorbed in the flux coatings arises because, during welding, the moisture provides hydrogen that is dissolved in the weld pool and diffuses into the HAZ. As the HAZ cools, the steel becomes increasingly saturated with hydrogen, and upon transformation from austenite to ferrite, bainite, or martensite, the solubility of hydrogen in the steel is markedly decreased. There is a strong tendency for the hydrogen either to escape from the metal or to be trapped at sites such as dislocations, grain boundaries, and particle-matrix interfaces. The shrinkage of the weld metal during cooling leads to the development of tensile residual stresses in the HAZ, which increase with the hardness of the weld metal. The tensile residual stresses are locally further increased by the stress concentrations associated with the irregular geometry of the weld toes. Rapid cooling can also result in the presence of brittle, untempered martensite within the HAZ, which is susceptible to hydrogen-assisted cracking.

In the case of the Melbourne highway bridge, it was concluded that the combination of hydrogen, tensile residual stresses, and a susceptible HAZ resulted in the observed delayed cracking.

B. Stack Corrosion (11)

A 123 m (403.5 ft.) high flue gas stack of 3 m diameter was built from 7 m tubular sections of a self-weathering copper-bearing steel. The wall thickness varied from 38 mm (1.5 in.) in the lower sections to 19 mm (0.76 in.) in the upper sections. Flanges were welded at either end of the sections and provided the means for bolting sections together. After 18 months of service, severe corrosion was observed on the upper two-thirds of the interior surface of the stack, with metal losses approaching 1 mm (0.04 in.). In addition, bolt failures due to fatigue were found in both the upper and lower sections. The severe interior corrosion was attributed the formation of H_2SO_4 , sulfuric acid, as the result of the condensation of sulfur-containing flue gases on the upper 100 m (328 ft.) of the stack. The corrosive fluid also ran into the bolted joints and caused additional damage. Examination of the broken bolts also showed evidence of fatigue due to the cyclic nature of the wind loading of the stack. The fatigue problem had been made more severe because of the mode of fabrication of the flanges. The flanges were fillet welded to the tubular sections, and then triangular reinforcing gusset plates were added. These welding operations were performed without first bolting the flanges together. As a result, severe distortions were introduced when the flanges were finally bolted together, which increased the mean stress on the bolts and decreased their resistance to fatigue under the fluctuating wind loads.

Subsequent repairs were extensive and included lining the upper tube section with stainless steel, welding stainless steel coverplates over each flange location, completely insulating the exterior of the stack so that the dew point temperature,

150°C (302°F), would be above the rim of the stack, and adding a tuned mass damper to reduce wind-induced deflections.

C. Backing Rings

In the 1960s, it was common practice to place a backing ring in the interior of a steam pipe at the site of a butt weld to ensure that full penetration of the weld would be achieved. However, it was found that branched stress corrosion cracks often initiated in areas of pitting at such sites due to (1) a stress concentration at the weld root and (2) the interface between the backing ring and the pipe, providing an ideal place for ions such as Cl^- , which emanated from the water phase during shutdown periods, to concentrate. Thermal cycling may have assisted crack growth when units were used over a long periods for peak load operations only (11).

X. PITTING CORROSION OF HOUSEHOLD COPPER TUBING

The pH level in the home water supply carried by copper tubing can be a critical factor affecting corrosion and pitting. In some municipalities, the pH level is maintained at 7.5. A pH value below 7 is not desirable because of concerns about lead from piping in the distribution system entering the water. A pH above 8 is usually not desirable because the water becomes hard and less suitable for washing purposes. However, in some communities, the water may contain large amounts of carbonates, and it is necessary to maintain a high pH, above 8.5, to prevent the carbonate from precipitating onto the walls of the copper tubing to form a layer of cupric carbonate hydroxide $[\text{CuCO}_3 \cdot \text{Cu}(\text{OH})_2]$, a greenish-white substance whose color is a direct indication that copper is corroding to form the compound. At susceptible sites, this corrosion of copper may occur as pitting, and as the pits grow, the wall of the copper piping may be penetrated and leaks develop. The solders used in joining sections of copper tubing are also of concern. The appropriate solder fluxes minimize the content of constituents that are known to promote pitting corrosion on copper, such as zinc and chlorides. It is also noted that the depth of the maximum size corrosion pit developed as a function of time has been studied using the statistics of the extreme (17).

XI. PROBLEMS WITH HYDROGEN AT ELEVATED TEMPERATURES

The above examples relate to the effect of hydrogen at room temperature. At elevated temperatures, there can be a different hydrogen-related problem. For example, a carbon steel that was used in a catalytic cracking unit was found to have lost its strength because of hydrogen diffusing into the metal. The hydrogen combined with carbon in the Fe_3C (cementite) to form methane and eliminated the pearlite phase. Figure 13-19 (1) shows the microstructure with voids caused by the methane gas produced in the hydrogen-methane reaction. Such problems can be avoided by the use of low-alloyed steels, which contain carbide-stabilizing elements. The Nelson diagram, Fig. 13-20, is an important guide in the selection of materials for service in hydrogen environments at elevated temperatures.

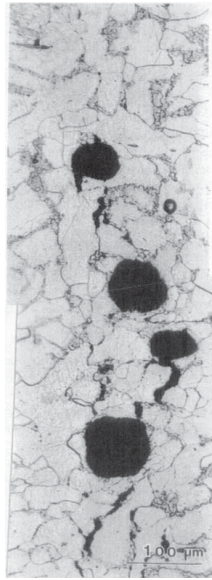


Fig. 13-19. Example of hydrogen attack. (Reprinted from Materials Characterization, vol. 26, A. J. McEvily and I. LeMay, Hydrogen assisted cracking, pages 253–268, Copyright 1991, with permission from Elsevier Science, 1. Photo courtesy of Dr. Tito Luiz da Silveira, Rio de Janeiro, Brazil.)

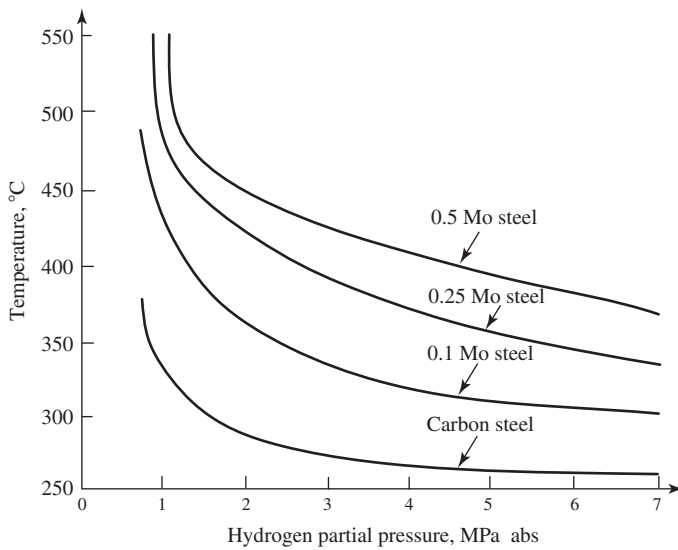


Fig. 13-20. Nelson diagram. (After API, 12.)

XII. HOT CORROSION (SULFIDATION)

The nickel-base and cobalt-base components of a jet aircraft engine are subject to a form of high-temperature corrosion known as *sulfidation*, which is related to the amount of sulfur in the fuel. Sodium sulfate in the environment can lead to a depletion of the alloying elements required to form a protective film on the parts. When nickel combines with sulfur, the melting point drops from 1,455°C (2,650°F) for pure nickel to 635°C (1,175°F) for Ni-22% sulfur. Unless the alloy is protected by a coating, excessive creep and intergranular fracture may occur. The high velocity of flow through the engine can also result in loss of material through a process referred to as *erosion-corrosion*.

XIII. SUMMARY

The corrosion process can degrade resistance to fatigue and fracture by causing loss of cross section, etch pits, pack-out, stress corrosion cracking, and accelerating fatigue crack growth rates. In addition, the corrosion process can lead to the introduction of hydrogen into materials with consequent embrittlement. Where aggressive environments are anticipated, it is particularly important to carefully select the material best suited to withstand the effects of the environment.

REFERENCES

- (1) A. J. McEvily and I. Le May, Hydrogen Assisted Cracking, *Mater. Char.*, vol. 26, 1991, pp. 253–268.
- (2) NACE Standard MR-01-75 (1980 rev.), Sulfide Stress Cracking Resistant Material for Oil Field Equipment, NACE, Houston, TX, 1980.
- (3) *Pipeline Performance in Alberta 1980–1997*, Report 98-G, Alberta Energy and Utilities Board, Calgary, Alberta, Canada, December 1998.
- (4) R. W. Revie, Trends in Corrosion R&D, with a Focus on the Pipeline Industry, <http://www.nrcan.gc.ca/picon/Journal/2000/paper1.asp>.
- (5) D. A. Jones, *Principles and Prevention of Corrosion*, Macmillan, New York, 1992.
- (6) A. Punter, A. T. Fikkers, and G. Vanstaen, Hydrogen-Induced Stress Corrosion Cracking on a Pipeline, *Mater. Perform.*, vol. 31, 1992, pp. 24–28.
- (7) R. J. Eiber and J. F. Kiefner, *ASM Metals Handbook*, vol. 11, 9th ed., ASM, Materials Park, OH, 1986, pp. 695–706.
- (8) P. E. O'Donoghue and Z. Zhuang, A Finite Element Model for Crack Arrestor Design in Gas Pipelines, Fatigue and Fracturing, *Eng. Mater. Struct.*, vol. 22, 1999, pp. 59–66.
- (9) J. O. Morlett, H. Johnson, and A. Trioano, Hydrogen Embrittlement, *J. Iron Steel Inst.*, vol. 189, 1958, p. 37–49.
- (10) D. R. H. Jones, *Materials Failure Analysis, Engineering Materials 3*, Pergamon Press, Oxford, UK, 1993.

- (11) C. Bagnall, H. C. Furtado, and I. Le May, "Evaluation of Steam Generating Plant: Some Problems Encountered and Their Solution," in *Lifetime Management and Evaluation of Plant, Structures and Components*, ed. by J. H. Edwards, P. E. J. Flewitt, B. C. Gasper, K. A. McLarty, P. Stanley, and B. Tomkins, EMAS, West Midlands, UK, 1999, pp. 295–302.
- (12) *Steels for Hydrogen Service at Elevated Temperatures and Pressures in Petroleum Refineries and Petrochemical Plants*, API Pub. 941, American Petroleum Institute, Washington, DC, June 1977.
- (13) B. F. Brown, in *The Theory of Stress Corrosion Cracking in Alloys*, ed. by J. C. Scully, NATO Scientific Affairs Division, Brussels, 1971, pp. 186–204.
- (14) B. F. Brown, *Stress Corrosion Cracking Control Measures*, NBS Monograph 156, National Bureau of Standards, Washington, DC, 1977.
- (15) E. N. Pugh, in *The Theory of Stress Corrosion Cracking in Alloys*, ed. by J. C. Scully, NATO Scientific Affairs Division, Brussels, 1971, pp. 418–441.
- (16) E. Denhard, Stress Corrosion Cracking of Austenitic Stainless Steels, *Corrosion*, vol. 16, no. 7, 1960, pp. 131–144.
- (17) *Application of Statistics of the Extreme to Corrosion* (in Japanese), ed. by M. Kowaka, Japan Society for the Prevention of Corrosion, Maruzen, Tokyo, 1984.
- (18) D. O. Sprowls, M. B. Shumaker, and J. D. Walsh, Marshall Space Flight Center Contract No. NAS 8-21487, *Final Report, Part I*, NASA, Washington, D.C. May 31, 1973.

PROBLEMS

- 13-1.** The rate of stress corrosion crack growth expressed in m/hr for an Al-Zn-Mg alloy in a saline solution is given as $\frac{da}{dt} = 8 \times 10^{-7} K^2$. The fracture toughness of the alloy is 30 MPa \sqrt{m} . Suppose that the material is used in the form of a pipe of wall thickness 12 mm and diameter 96 mm through which flows a saline solution at a pressure of 6 MPa. The pipe contains flaws on the interior surface that are 0.1 mm deep. Assume that $K = \sigma \sqrt{\pi a}$.
- (a) How long will it take for the pipe to either burst or leak through?
 - (b) If it is desired that the pipe last for at least 10,000 hours, what is the maximum pressure that can be applied?
 - (c) What proof test pressure has to be applied to ensure that the pipe lasts for 10,000 hours?
 - (d) If the system is operated at a pressure of 6 MPa for 2,000 hours, what is the life expectancy if the pressure is then reduced to 3.45 MPa?

14

Flaw Detection

I. INTRODUCTION

A combination of a fracture mechanics analysis and flaw-detection procedures provides the most reliable method for ensuring the integrity of critical structures. The most common nondestructive examination (NDE) methods for the detection of flaws are visual inspection, dye penetrant inspection, eddy current inspection, ultrasonic inspection, and radiography. Acoustic emission is also used but to a lesser extent. This chapter discusses the principal aspects of these inspection methods. Also included are case studies to illustrate the dangers that can be involved when NDEs are not carried out properly.

II. INSPECTABILITY

Inspectability is defined to indicate that all critical areas prone to fracture in a given structure are known and that appropriate techniques for the inspection of these areas are available. Figure 14-1 provides an example of a case in which this criterion was not met, and as a result, the consequences were catastrophic. The plane, a C-130 cargo plane, had been used for many years by the U.S. Air Force. At some point, it was declared surplus and sold to a company that fought forest fires. In 2002, while fighting a forest fire in Northern California, the starboard wing came off as the center wing box failed during a pull-out from a drop of a fire-retardant chemical on a forest fire. In less than 1 second the port wing also came off. The fuselage then rolled to an inverted position and crashed, killing all three crew members.



Fig. 14-1. A C-130 forest-fighting plane in the process of losing its wings.

In the subsequent investigation, it was found that the failure of the center box that provided support to the two wings had failed as the result of fretting fatigue at rivet holes, as shown in Fig. 14-2. Large-scale fatigue cracking ran in the forward-aft direction.

Normally, perhaps one would expect to find fatigue cracks at the wing roots, and these areas had presumably been inspected over the years. The occurrence of fatigue cracks in the center box had not been considered, and to make the situation even more difficult, a structural aluminum plate on the center box prevented direct observation of the critical area. These factors led to a complete lack of inspectability.

Another example of the consequences of lack of inspectability follows. The train wreck shown in Fig. 14-3 occurred in 1998 near the village of Eschede in Germany. The toll of 101 people dead and an estimated 88 injured was the deadliest accident in German history. It was caused by a single fatigue crack in one wheel that, when it failed, caused the train to derail at a switch.

The wheels on the train were unusual. As shown in Fig. 14-4, they consisted of outer and inner sections of steel separated by a layer of rubber that was intended to make the train ride more smoothly as compared to conventional solid steel wheels. The fatal fatigue crack initiated internally, along the boundary between the rubber layer and the outer steel ring. After the accident, all rubber-containing wheels were

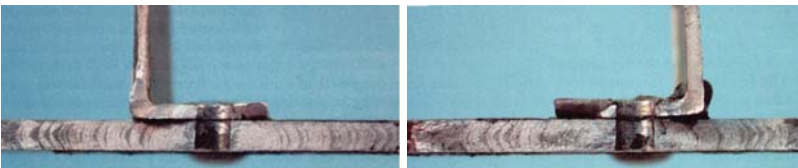


Fig. 14-2. Fatigue cracks initiating at rivet holes in the center wing box of the C130 aircraft.



Fig. 14-3. Wreckage of an Inter-City Express (ICE) train in Germany.

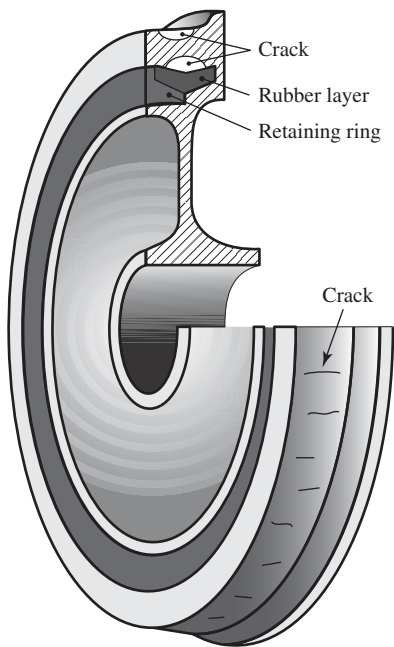


Fig. 14-4. Composite wheel of the ICE train.

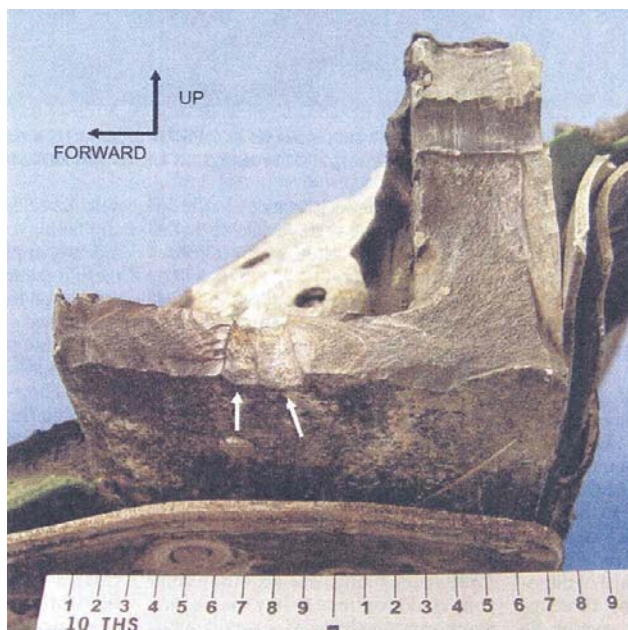


Fig. 14-5. Fracture surface of the lower wing spar in the Grumman Mallard seaplane.

replaced by solid wheels, for it was recognized that rubber-containing wheels lacked inspectability.

Even though a component may initially be inspectable, sometimes procedures carried out during maintenance may introduce additional factors that detract from inspectability. For example, in 2005, a 58-year-old Grumman Mallard seaplane lost its right wing on takeoff because of the failure of the wing spar. All 20 people aboard were killed. About 1 year prior to the accident, the aluminum skin on the lower portion of the right wing had been replaced. The NTSB determined that this accident was due to a maintenance program that failed to identify and properly repair fatigue cracks in the right wing. Figure 14-5 shows the appearance of the fracture in the lower wing spar after the accident. The fatigue cracks emerging from the rivet hole are evident, as is the fact that at one location, two rivet holes are side by side. It appears that the second of these rivet holes was drilled 1 year previously to accommodate the installation of the new wing skin. The stress concentration factor for the two side-by-side holes would be about 5.0, whereas for a single hole it would be about 3.0. Further, there was a lack of inspectability since the side-by-side hole configuration was not detected until after the accident.

Now that the important matter of inspectability has been introduced, we move on to a discussion of the more common inspection procedures that are used to detect cracks. These methods are visual, dye penetrant, magnetic particle, eddy current, ultrasonic, and radiographic.

III. VISUAL EXAMINATION (VE)

VE for surface flaws is widely used, for it is obviously a simple, fast, and inexpensive method. However, VE lacks good resolution, and eye fatigue, boredom, and distractions can reduce the quality of this type of inspection. Good illumination is needed, and the observations can be aided by such items as magnifiers, dental mirrors, tubular borescopes, and glass-fiberscopes (1).

IV. PENETRANT TESTING (PT)

PT is used for the detection of surface flaws. It is a low-cost, easy-to-use, rapid, and portable method. The procedure for a PT is shown in Fig. 14-6 and can be described as follows (1):

1. Carefully clean the surface (Fig. 14-6a).
2. Apply the penetrant (Fig. 14-6b), a liquid of low viscosity and high surface tension containing dyes, suspensions of colored particles, or a radioactive gas. Allow time for penetration (*dwell time*).
3. Remove the excess penetrant (special agents can be used), as shown in Fig. 14-6c.
4. Apply a developer to the surface (Fig. 14-6d). The developer acts as a blotter to draw the penetrant to the surface from the flaw and provides a contrasting background.
5. Observe with good illumination or, if fluorescent penetrants are used, with ultraviolet light in a darkened area.

For the penetrant to flow over the surface and migrate into flaws open to the surface, the liquid must wet the surface, that is, angle θ in Fig. 14-7 must be less

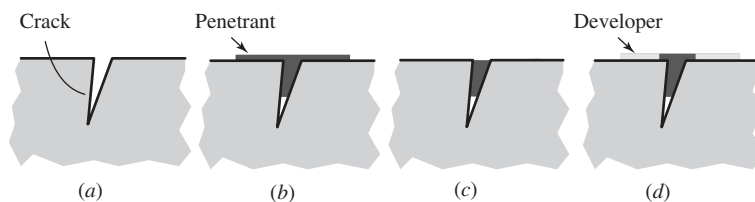


Fig. 14-6. Penetrant testing.

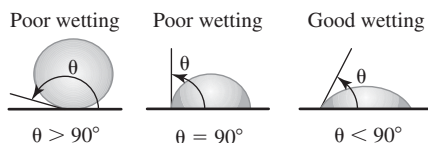


Fig. 14-7. The effect of the contact angle θ on wettability. (After Survey of NDT, 1.)

than 90° . A low viscosity is also desired. The depth of penetration increases with the surface tension T , as shown in the following example.

Example

Determine the depth d_L that the liquid penetrant will penetrate down into a flaw of width w , depth d_0 , and surface extent e (see Fig. 14-8).

The resistance to penetration is provided by the buildup of pressure as the entrapped air is compressed.

The volume of the flaw is d_0we , and $PV = C$ (ideal gas law at constant temperature). From equilibrium of forces (see Fig. 14-9):

$$Pwe = 2eT \cos \theta$$

$$\frac{C}{V}w = 2T \cos \theta \quad (14-1)$$

The volume of entrapped air is

$$V = we(d_0 - d_L) \quad (14-2)$$

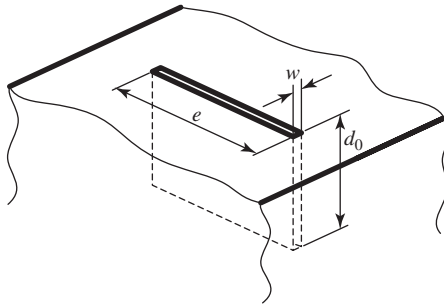


Fig. 14-8. Body having a surface flaw.

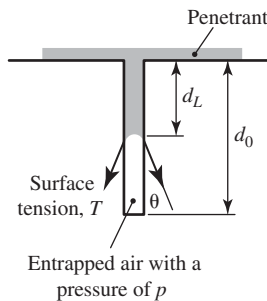


Fig. 14-9. Equilibrium condition at which the penetrant penetrates down into a flaw.

Substituting into Eq. 14-1 yields

$$\begin{aligned}\frac{C}{we(d_0 - d_L)}w &= 2T \cos \theta \\ \frac{C}{2eT \cos \theta} &= d_0 - d_L \\ d_L &= d_0 - \frac{C}{2eT \cos \theta} = d_0 - \frac{P_0 V_0}{2eT \cos \theta} = d_0 - \frac{P_0 w d_0}{2T \cos \theta} \\ d_L &= d_0 \left(1 - \frac{P_0 w}{2T \cos \theta} \right) \quad (14-3)\end{aligned}$$

Therefore, the smaller the width of the flaw, and the higher the surface tension and the smaller the θ , the greater will be the depth of penetration.

As indicated in Figs. 14-7 and 14-10, in order for a liquid to wet a solid, angle θ must be less than 90° .

$$\gamma_{sa} = \gamma_{sl} + \gamma_{la} \cos \theta = \gamma_{sl} + T \cos \theta \quad (14-4)$$

$$T \cos \theta = \gamma_{sa} - \gamma_{sl} = \Delta \gamma_{sa-sl} \quad (14-5)$$

where γ and T are surface tensions. The subscripts a , s , and l refer to air, solid, and liquid, respectively.

The surface tension of a liquid can be determined from a capillary rise experiment, Fig. 14-10,

$$T = \frac{h(\rho_l - \rho_g)gr}{2 \cos \theta} \quad (14-6)$$

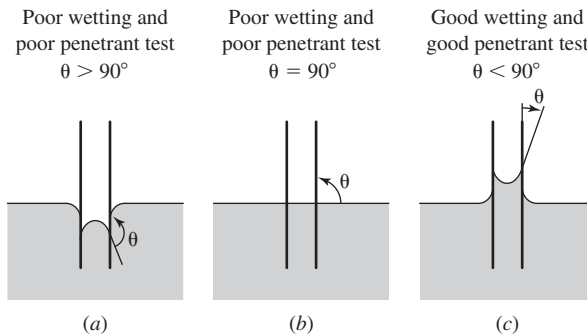


Fig. 14-10. The effect of the contact angle on penetrability. (a) Liquid depressed in a capillary tube. (b) No capillary rise or depression. (c) Liquid rise in a capillary tube. (After Survey of NDT, 1.)

where h is the capillary rise, ρ_l is the density of the liquid, ρ_g is the density of the gas in the capillary, g is the acceleration due to gravity, r is the radius of the capillary, and θ is the contact angle of the liquid in the capillary. If T is assumed to be fixed, $\cos \theta$ then depends on the difference in the surface energies of the solid and the solid-liquid interface. The smaller is γ_{sl} for a given T , the larger will be $\cos \theta$, and hence the smaller θ will be; the liquid is therefore considered to be more wettable. Making the liquid more wettable increases $\cos \theta$ and therefore also increases the depth of penetration.

The surface energy of water is 72 dynes/cm (0.072 J/m²). The surface energy for solids is much higher, thousands of dynes per centimeter. The surface energy of glass is 1.75×10^3 dynes/cm = 1.75 J/m².

V. CASE STUDY: SIOUX CITY DC-10 AIRCRAFT (2)

A. Summary

On July 19, 1989, at 1516 hours, a DC-10-10 aircraft, tail number N1819U, operated by United Airlines as Flight 232, while en route from Denver to Chicago, experienced a catastrophic failure of the tail-mounted No. 2 engine during a cruise flight at Mach 0.83. The separation, fragmentation, and forceful discharge of Stage 1 fan rotor assembly parts from the No. 2 engine led to the loss of three hydraulic systems that powered the airplane's flight controls. The flight crew experienced severe difficulties controlling the airplane, which subsequently crashed during an attempted landing at Sioux Gateway Airport, Iowa. There were 285 passengers and 11 crew members onboard. One flight attendant and 110 passengers were fatally injured.

In aircraft gas turbine engines, the engine shroud is designed to contain small pieces of hardware, such as turbine blades, should they break loose during engine operation. However, since the disk is much more massive, its kinetic energy is so high that it would not be feasible to design it to contain the disk fragments should the disk fracture. Instead, reliance is placed upon the detection of fatigue cracks long before they reach a critical size. However, in this case this procedure did not work. The NTSB determined that the probable cause of this accident was the inadequate consideration given to human factor limitations in the inspection and quality control procedures used by the United Airlines engine overhaul facility. This resulted in the failure to detect a fatigue crack originating from a previously undetected metallurgical defect located in a critical area of the stage 1 fan disk that was manufactured by General Electric Aircraft Engines (GEAE). The subsequent catastrophic disintegration of the disk resulted in the liberation of debris in a pattern of distribution and with energy levels that exceeded the level of protection provided by design features of the hydraulic systems that operate the DC-10's flight controls.

B. Factual Information

About 1 hour and 7 minutes after takeoff, the flight crew heard a loud bang, followed by vibration and shuddering of the airframe. The No. 2 engine had failed, and the airplane's main hydraulic pressure and quantity gauges indicated zero. The flight crew deployed the air-driven generator (ADG), which powered an auxiliary hydraulic pump, and the hydraulic pump was selected "on." However, this action did not restore the hydraulic power. The captain reduced the thrust on the wing-mounted left-side engine (No. 1 engine), and the airplane, which had entered a right descending turn, began to roll to the wings-level attitude. Fuel was jettisoned to the level of the automatic system cutoff, leaving 15,195 kg (33,500 lb). About 11 minutes before landing, the landing gear was extended by means of an alternate gear extension procedure. The airplane touched down slightly to the left of the runway at 1600 hours (44 minutes after the engine failure). First ground contact was made by the right wing tip, followed by the right main landing gear. Witnesses saw the plane ignite and cartwheel. The airplane was destroyed by impact and fire.

The airplane, valued at \$21,000,000, had been delivered to United Airlines in 1971. It had acquired 43,401 flight hours and 16,997 cycles. It was powered by GEAE CF6-6D high-bypass-fraction turbine engines. The CF6-6 engine had been certified by the FAA in 1970. The total time on the No. 2 engine was 42,436 hours, and the number of cycles it had undergone was 16,899. A total of 760 cycles had elapsed since the last maintenance, and the engine had been installed on October 15, 1988. The engine could be installed in either the wing or tail position.

C. Stage 1 Fan Disk Historical Data

The stage 1 fan disk had been processed in the GEAE Evandale, Ohio, factory from September 3 to December 11, 1971. It was a new part in an engine that was shipped to Douglas Aircraft on January 22, 1972, where it was installed on a new DC-10-10. During the next 17 years, the engine was removed six times for inspection, the last being in February 1988, 760 cycles prior to the accident. This disk was accepted after each of six fluorescent penetrant inspections (FPIs). (The second inspection was at the GEAE Airline Service Department in Ontario, Canada. The other five inspections were at the United Airlines CF6 Overhaul Shop in San Francisco.) FPI is the accepted industry inspection technique for interrogating nonferrous (nonmagnetic) component surfaces for discontinuities or cracks. The technique relies upon the ability of the penetrant (a low-viscosity penetrating oil containing fluorescent dyes) to penetrate by capillary action into surface discontinuities of the component being inspected. The penetrant fluid is applied to the surface and allowed to penetrate into any surface discontinuities. Excess penetrant is then removed from the component surface. A developer is then applied to the component surface to act as a blotter and draw the penetrant back out of the surface discontinuity, producing indications that fluoresce under ultraviolet (black) lighting.

About 3 months after the accident, parts of the No. 2 stage 1 engine fan disk were found in farm fields near Alta, Iowa. There were two sections that constituted nearly

the entire disk, each with fan blade segments attached. These parts were initially taken to the GEAE facility in Evendale, Ohio, for examination under the direction of the NTSB. The smaller of the two segments was later taken to the NTSB laboratory in Washington, D.C., for further evaluation.

The stage 1 fan disk weighs about 168 kg (370 lb) and is a machined titanium alloy forging (Ti-6Al -4V) about 81 cm (32 in.) in diameter. The various portions of the disk are the rim, the bore, the web, and the disk arm. These are shown in Figs. 14-11*a* and 14-11*b*. The rim is about 12.7 cm (5 in.) thick and is the outboard portion of the disk. The rim contains the axial “dovetail” slots, which retain the fan

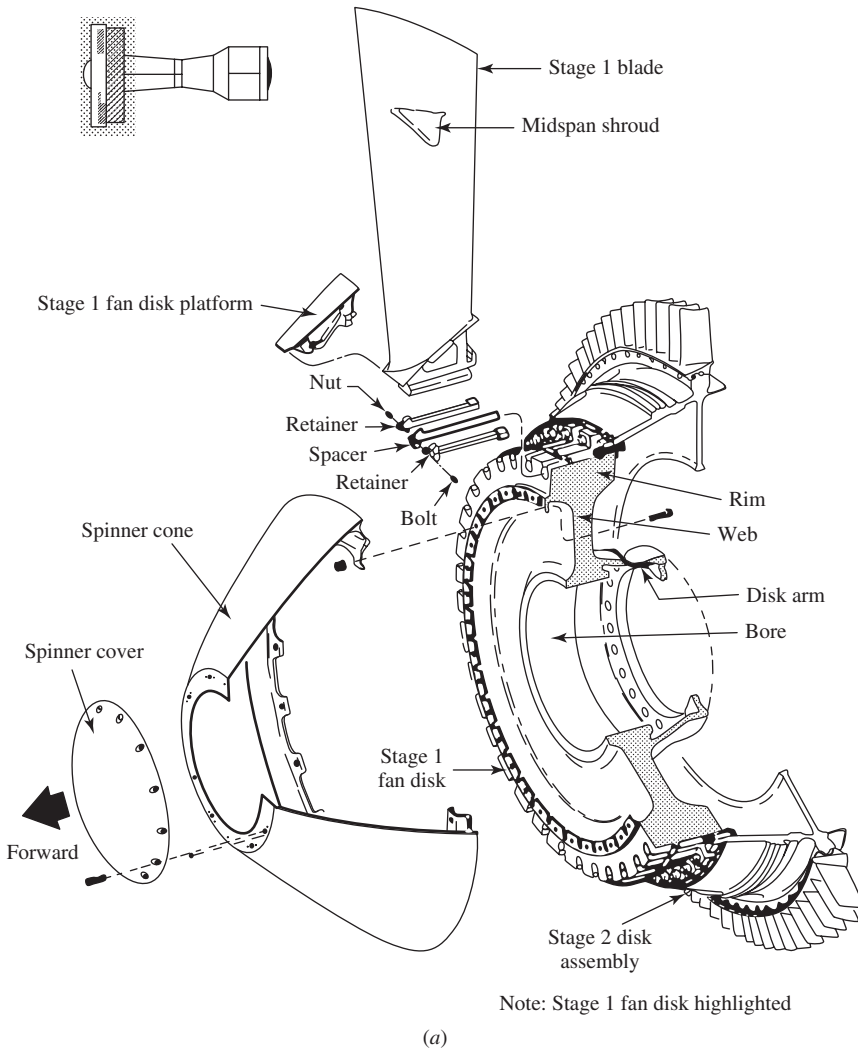


Fig. 14-11. (a, b) The stage 1 fan disc. (From NTSB, 2.)

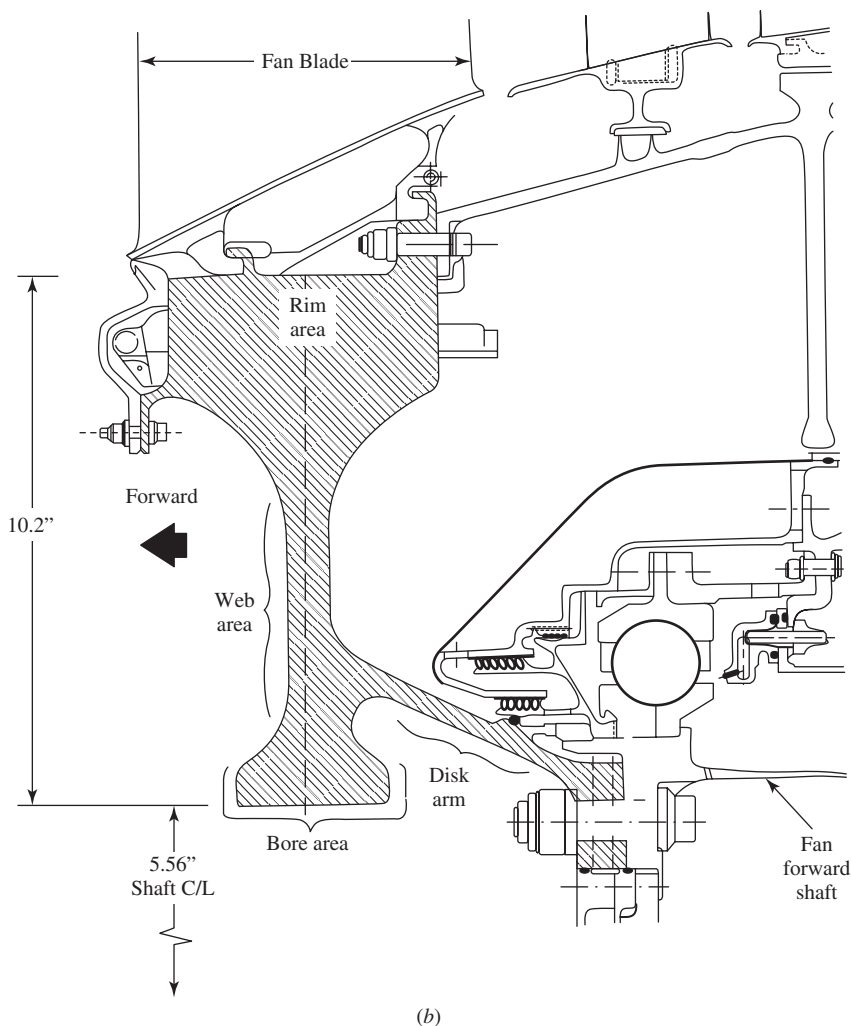


Fig. 14-11. (continued)

blades. The stage 2 fan disk is bolted to the aft surface of the rim. The bore is about 7.6 cm (3 in.) thick and is the enlarged portion of the disk adjacent to the 27.9 cm (11 in.) center hole. Extending between the rim and the bore is the disk web, which is about 1.9 cm (0.75 in.) thick. The conical disk arm extends aft from the web at a diameter of about 40.6 cm (16 in.). The conical arm diameter decreases in the aft direction to about 25.4 cm (10 in.) at the disk arm flange, where the disk bolts to the fan forward shaft.

The primary loads imposed on the stage 1 fan disk are radially outboard loads in the dovetail slots, which arise as the disk holds the fan blades against centrifugal force

during rotation of the assembly. These loads result in radial stresses in the disk rim, which decrease toward the disk bore, where they are supplanted by circumferential (hoop) stresses. These hoop stresses are at a maximum along the inside diameter of the bore. Because the disk arm acts to strengthen the aft face of the disk, the forward corner of the bore is the area on the disk that experiences the maximum hoop stress.

D. Examination of the No. 2 Engine Stage 1 Fan Disk

The two recovered pieces of the No. 2 engine fan disk comprised the entire separated disk, with the exception of an unrecovered dovetail post. Figure 14-12 shows the reconstructed pieces of the disk after the larger disk piece had been cut during metallurgical examination. The gap between the smaller and larger pieces does not represent missing material but is the result of mechanical deformation that occurred during disk separation. The disk contained two principal fracture areas, resulting in about one-third of the rim separating from the remainder of the disk. One of the fracture areas progressed largely circumferentially through the web and the rim. The other fracture area was on a near-radial plane, progressing through the bore, the web, the disk arm, and the rim. Features on the circumferential fracture were typical of overstress separation stemming from multiple origin areas in the radius between the disk arm and the web. The near-radial fracture surface also contained overstress features over most of its surface. However, on this break, the overstress features stemmed from a preexisting radial/axial fatigue crack region in the bore of the disk. Figure 14-13 shows the fatigue region at the bore.

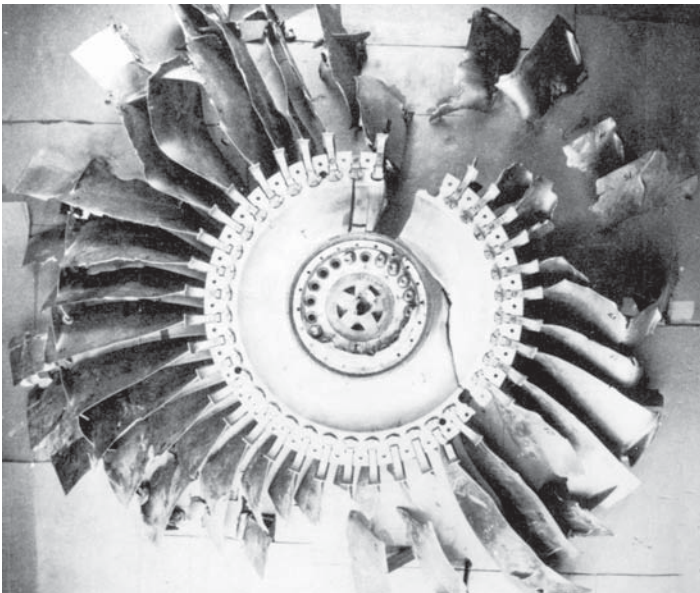


Fig. 14-12. The reconstructed stage 1 fan disk of the No. 2 engine. (From NTSB, 2.)

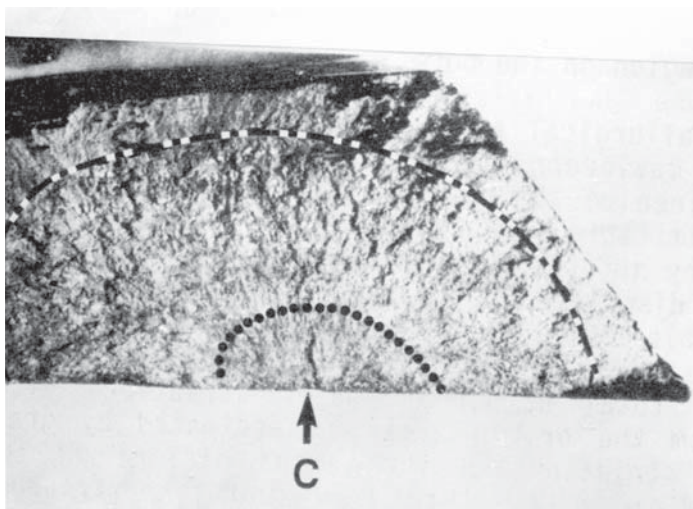


Fig. 14-13. Fatigue crack fracture area of the stage 1 fan disk. The fatigue crack extends from the cavity (arrow C) to the dashed-line position. The discolored portion of the fatigue crack (an indication of dye penetrant) is between the cavity and the dotted line. Magnification: 2.26x. (From NTSB, 2.)

The fatigue crack initiated near a small cavity on the surface of the disk bore about 22 mm (0.86 in.) aft of the forward face of the bore. A portion of the fatigue crack around the origin was slightly discolored. The topography of the main fracture surface in the fatigue zone was the same outside the discolored area as it was inside the discolored area. The overall sizes of the fatigue crack, the discolored area, and the cavity were as follows:

	Length	Radial Depth
Fatigue zone	31 mm (1.24 in.)	14 mm (0.56 in.) [†]
Discolored area	12 mm (0.48 in.)	4.6 mm (0.18 in.)
Cavity	1.4 mm (0.055 in.) [*]	0.4 mm (0.015 in.)

^{*}The width of the cavity across the mating fracture surfaces was also 1.4 mm (0.055 in.).

[†]GEAE estimated that the fatigue crack was 13 mm (0.5 in.) deep at the time of the last inspection.

Fractographic, metallographic, and chemical analyses of the fatigue region revealed the presence of an abnormal nitrogen-stabilized hard- α phase around the cavity. This phase extended slightly outboard of the cavity to a maximum radial depth of 0.46 mm (0.018 in.) and an overall length of 11.2 mm (0.44 in.). The altered microstructure associated with this hard phase extended significantly beyond the area containing only stabilized α -structure, gradually blending into the normal

microstructure, which consisted of a mixture of approximately equal amounts of primary α -structure and transformed β -structure. The stabilized α -region contained microcracks that were generally oriented parallel to the cavity surface, and some microporosity was also found.

Scanning electron microscopic (SEM) examination revealed that fatigue striations existed just outboard of the stabilized α -region. Close to the cavity, areas of brittle fracture intermixed with ductile-appearing bands were observed. The fatigue striation spacing generally increased as the distance from the origin increased. At a radial distance of 3.7 mm (0.145 in.), areas with more closely spaced striations were also found. The more closely spaced striations were referred to as *minor striations*, and the more widely spaced striations were referred to as *major striations*. The total number of major striations along a radially outward direction from the origin area was estimated by graphically integrating a plot of striation density versus distance. The estimate correlated reasonably well with the total number of flight cycles on the disk, indicating that fatigue crack growth had been taking place since early in the life of the disk.

Analytical procedures were developed to determine if chemical residues from the United Airlines dye penetrant inspection were present on the fatigue fracture surface. The fracture surface was gently washed with deionized water and then in an ultrasonic unit also using deionized water. Secondary ion mass spectroscopy (SIMS) measurements showed an ion fragmentation pattern that was consistent with chemical compounds used in the FPI fluid. Gas chromatographic (GC) mass spectroscopy (MS) of the water used in the ultrasonic cleaning provided further evidence for the presence of the dye penetrant on the fracture surface.

E. Fan Disk Manufacturing Process and Hard Alpha Material

The three primary steps in the manufacture of titanium alloy fan disks are material processing, forging, and final machining. In the first step, metals are combined in a heat, which is numbered and then processed into a titanium alloy ingot in a vacuum furnace melting operation. The ingot is then mechanically formed into a billet. The billet is then cut into smaller pieces, which are then forged. The next step is the machining of the forged shape into the final configuration and the shot peening of fatigue-critical regions.

Hard α -inclusions constitute one of the three main anomalies in titanium alloys, the other two being high-density inclusions and alpha segregates or β -flecks. Most of the hard α -inclusions result from a local excess of nitrogen and/or oxygen introduced through atmospheric reactions with titanium in the molten state. A typical hard α -inclusion contains an enriched α -zone in the α -plus β -matrix, and voids and cracks are frequently associated with these zones. Hard α -inclusions have a melting point significantly higher than that of the normal structure, and to promote their melting or dissolution, it is desirable to increase the temperature of the molten pool in the furnace or to increase the time during which the material is in the molten state. Successive melting operations, such as double or triple vacuum remelting, provide additional opportunities for dissolution of hard inclusions but do not guarantee their complete dissolution, and all GEAE fan disks manufactured after January 1972

have been triple-vacuum remelted. The double-melted 40.6 cm (16 in.) billet for the failed disk was produced in 1971, and the NTSB concluded that, at the time of the manufacture of the disk, the cavity at the fatigue origin was filled with hard alpha material, making the defect difficult to detect by ultrasonic inspection.

During the manufacture of the failed disk, GEAE inspected the forged shape using a macroetch technique to bring out any anomalies on the surface; a final FPI procedure was carried out in December 1971, with no anomalies found. The United Airlines FPI procedure warned inspectors that titanium parts resist the capillary action of the penetrant and that "complete penetrant coverage is required for these materials." Also, United Airlines inspectors were cautioned not to overwash the parts or the penetrant might be flushed out of true indications. Along with certain other areas, the disk bore was mentioned as a critical area for inspection.

F. Initiation and Propagation of the Fatigue Crack

Fracture mechanics calculations by GEAE were consistent with the fatigue crack reaching critical size at the time of separation. The analysis was also consistent with fatigue crack initiation on the first application of stress from a defect slightly larger than the cavity found at the fatigue origin. The NTSB concluded that the hard alpha defect area cracked upon the first application of stress during the disk's initial exposure to full-thrust engine power conditions and that the crack continued to grow and entered material unaffected by the hard alpha defect. From that point, the crack followed established fracture mechanics predictions for the Ti-6Al-4V alloy until it reached the critical size for fracture. It seems a bit odd that fracture occurred under cruise conditions rather than under the full-thrust conditions of the last takeoff.

VI. CASE STUDY: MD-88 ENGINE FAILURE (3)

The plane was equipped with Pratt & Whitney JT8D-219 turbofan engines. During the flight's takeoff roll the aircraft experienced an uncontained, catastrophic turbine engine failure that caused debris from the front compressor hub of the No. 1 left engine to penetrate the left aft fuselage (Fig. 14-14). The impact left two passengers dead and two severely injured; all were from the same family. The pilot aborted the takeoff and the airplane stopped on the runway. Although the rotor (Fig. 14-15) had recently been inspected by the FPI method, no cracks were detected. It has been suggested that water from the cleansing procedure may have been trapped in the fatigue crack, thereby preventing the penetrant from entering the crack. It is also possible that, as in the DC-10 case, since the parts were shot-peened, the compressive stresses from shot peening may have kept the cracks closed, so that little if any of the penetrant could enter the cracks.

In the case of the MD-88, the cause of fatigue cracking (Fig. 14-16) was also due to a hard alpha case that had been created during machining of the tie-rod holes. Due to poor lubrication, high temperatures were generated during the machining process that resulted in the uptake of nitrogen from the atmosphere.

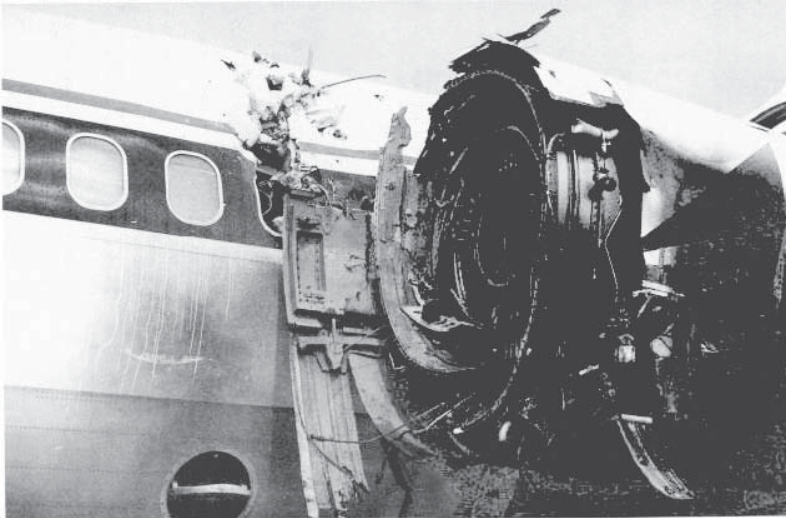


Fig. 14-14. Damaged area of the airplane near the No.1 engine. (From NTSB, 3.)

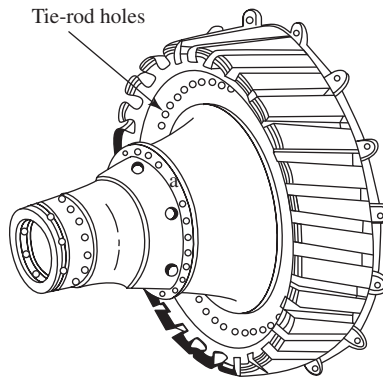


Fig. 14-15. Pratt & Whitney JT8D-200series engine fan hub. (From NTSB, 3.)

VII. MAGNETIC PARTICLE TESTING (MT)

MT is used for the detection of surface and near-surface flaws and is low cost, fast, and portable. However, the material must be ferromagnetic and the surface must be clean. The method is more sensitive than dye penetrant inspection for the detection of tightly closed cracks, which may also contain corrosion products (4).

The MT procedure involves (1):

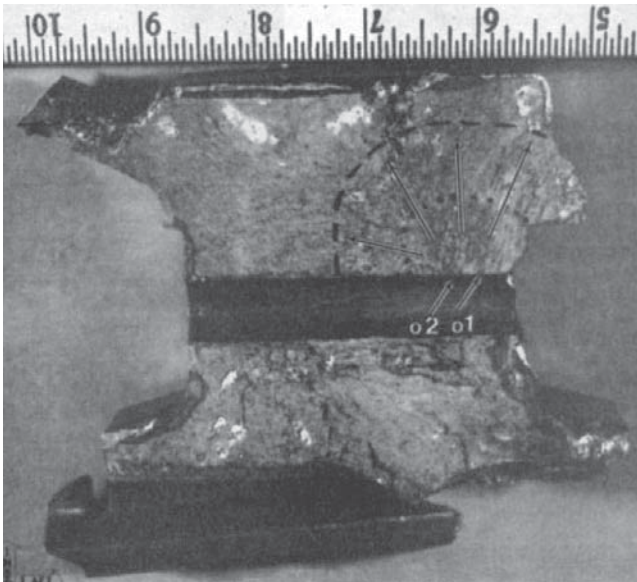
1. The establishment of a magnetic field in the part, usually by an electric current
2. The application of magnetic particles in the form of a liquid suspension or dry powder

3. An examination and evaluation
4. A repeat test with the magnetic field at 90° to the original direction of magnetization

If there is a flaw, a leakage flux of the magnetic field in the part will develop, as shown in Fig. 14-17. This leakage flux will attract the magnetic particles and



(a)



(b)

Fig. 14-16. (a) Failed piece. (b) Fracture surface. (Dashes indicate the size of the fatigue crack at the time of the last FPI inspection.) (From NTSB, 3.)

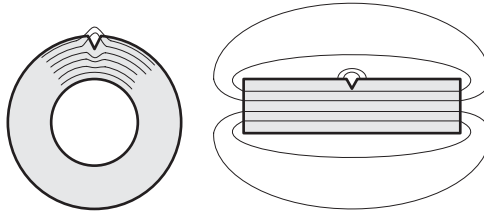


Fig. 14-17. Leakage of magnetic flux lines due to surface discontinuities. (After Survey of NDT, 1.)

indicate the location of the discontinuity. For an indication to form, it is necessary that the flaw be at a large angle (90°) to the lines of flux. If the flaw is parallel to the lines of flux, no leakage current will occur and the flaw will be undetected. At angles between 0° and 90° , the leakage flux will be proportional to the sine of the angle between the discontinuity and the lines of flux.

When an electric current passes through a conductor, a magnetic field is formed around the conductor. The direction of the lines of flux is determined by the right-hand rule. If the current flows along a bar, then the lines of flux will form as a circular field along the conductor, and the MT method will be sensitive to longitudinal flaws (Fig. 14-18a). If the conductor is a coil around the specimen, then the lines of flux

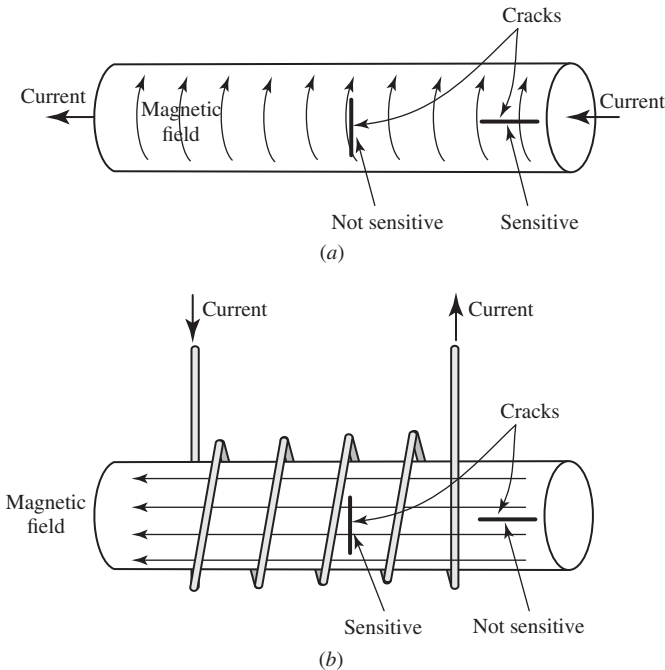


Fig. 14-18. The magnetic fields set up by (a) a "head shot" and (b) a coil.

will form a longitudinal field in the specimen (Fig. 14-18*b*), and the MT method will be sensitive to circumferential flaws. In the magnetic particle inspection of an aircraft crankshaft, a “head shot” using alternating current (AC) or rectified AC, which develops greater penetrating ability, is used to establish a circular magnetic field for the detection of longitudinal flaws (Fig. 14-18*a*). A coil is then used to establish a longitudinal magnetic field for the detection of circumferential flaws (Fig. 14-18*b*). In both cases, the applied currents can range up to 3,000 amps. After the examination, the part may be demagnetized by applying an AC current whose magnitude gradually decreases in a controlled manner.

The current I in amps required to develop an adequate magnetic field with a coil is given as $I = 45,000D/LN$, where D is the specimen diameter, L is the specimen length, and N is the number of turns. L/D should be at least 2 to avoid end effects but not greater than 15.

A standard practice is to use fluorescent particles that are suspended in a liquid. The liquid is sprayed over the part being examined, and those particles attracted to a flaw will remain, while the rest are washed away. The observation is made under ultraviolet light.

VIII. CASE STUDY: FAILURE OF AN AIRCRAFT CRANKSHAFT

A single-engine, piston/propeller, four-passenger private plane had taken off with a pilot and two passengers when, shortly after the takeoff, power was lost. The pilot attempted an emergency landing, but unfortunately, the plane struck power lines and all persons on board perished. It was subsequently determined that the cause of the accident was the fatigue failure of the crankshaft. Since the crankshaft had been examined by the MT method only 80 flight hours prior to the crash without detection of a defect, the organization that carried out the inspection was accused of negligence.

The crankshaft was a 4340 low-alloy steel forging. At the time of manufacture, it had been nitrided to improve both its wear and fatigue resistance. After 2,000 hours in service, the crankshaft had been worn enough to warrant surface refinishing by grinding and renitriding. After an additional 1,000 hours of service, the engine was overhauled. No work was done on the crankshaft, but because it had been removed from the engine during the overhaul, it was inspected by MT in accord with regulations. Eighty flight hours later, the accident occurred. Examination of the failed crankshaft revealed that in addition to the fatal fatigue crack, a number of additional small surface cracks were present, as shown in Fig. 14-19. It is thought that these cracks were grinding cracks that had been introduced at the time of the 2,000-hour overhaul. It is noted that the cracks were filled with a white substance, which is related to the renitriding process. This material is Fe_4N (iron nitride) and is a by-product of nitriding. Where it forms on the smooth surface of the crankshaft, it is easily removed by polishing prior to putting the crankshaft back into service.

Figure 14-20 is the phase equilibrium diagram for the Fe-N system. Of particular interest is the fact that the Fe_4N phase is ferromagnetic at room temperature. In

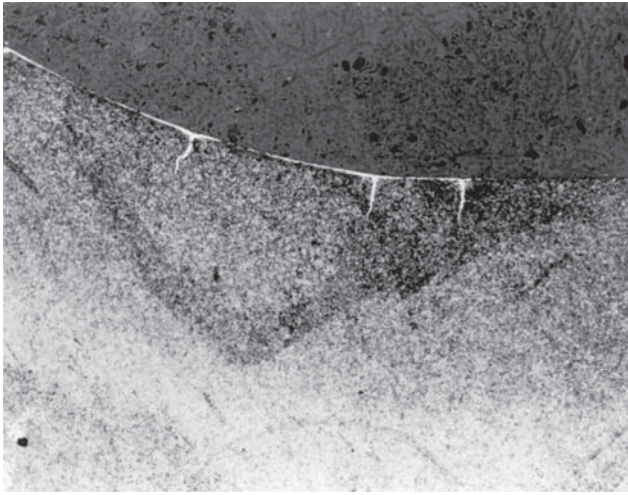


Fig. 14-19. An example of tight grinding cracks completely filled with nitride. Magnification: 50.

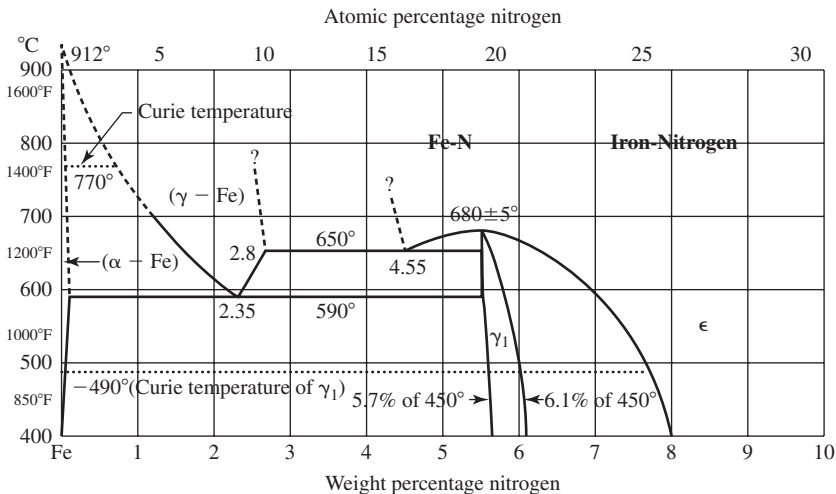


Fig. 14-20. The iron-nitrogen phase diagram. (From ASM Metals Handbook, 5, with permission of ASM International.)

addition, as shown in Fig. 14-21, the magnetic properties of this phase are remarkably similar to those of 4340 steel. The implication is that, if a tight crack such as a grinding crack is completely full of this phase, then in a magnetic field there will be no disruption of the flux lines and the crack will go undetected if examined by the MT method. To check on this possibility, a fatigue crack was grown in a 4340 compact specimen, and the specimen was examined by the MT method. Figure 14-22a clearly shows the distribution of magnetic particles along the fatigue crack. The specimen

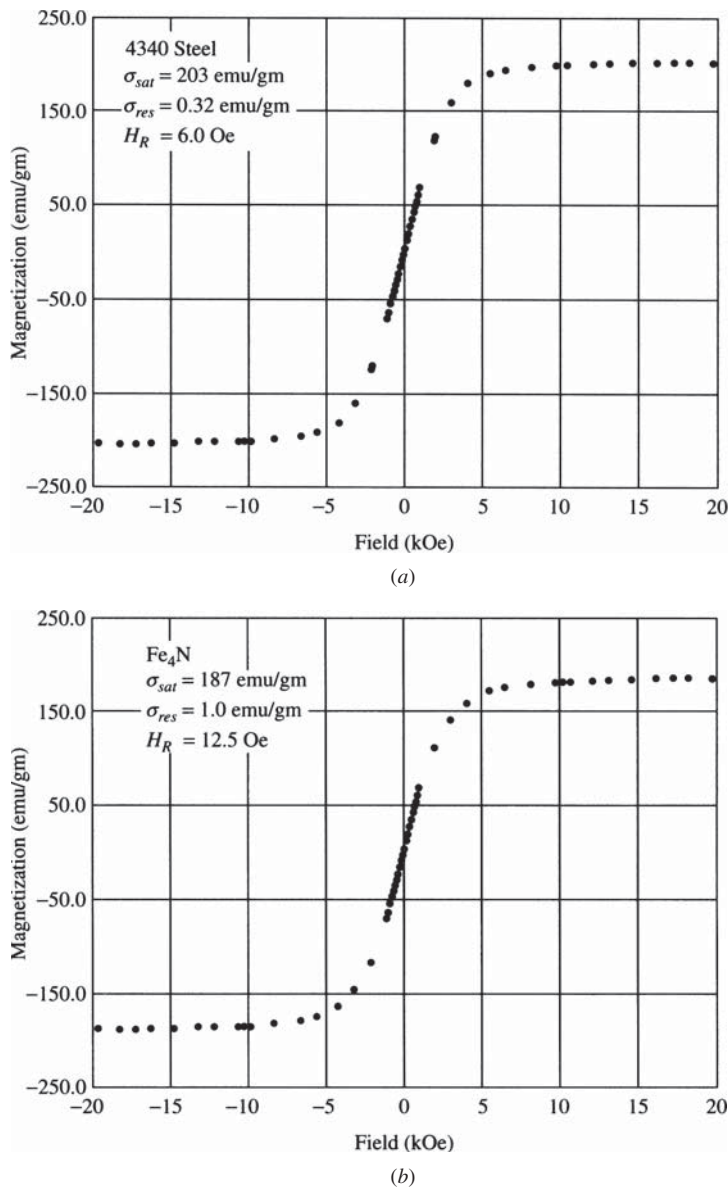
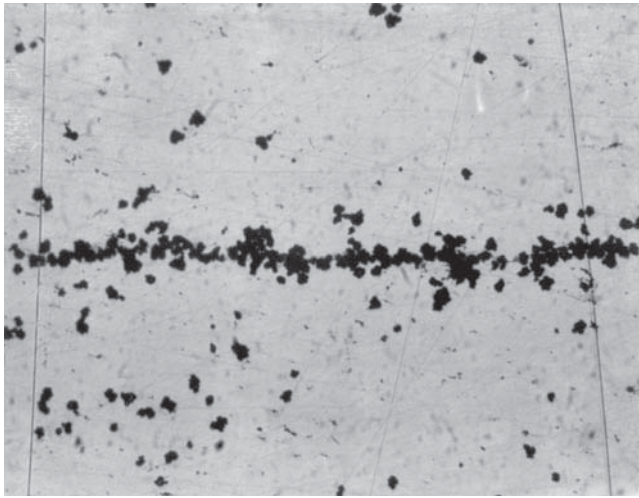


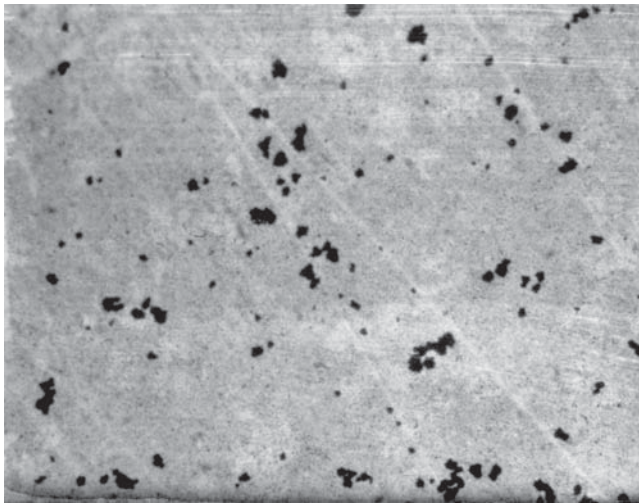
Fig. 14-21. (a, b) Comparison of the magnetization behavior of 4340 steel with Fe₄N (γ'). (Courtesy of W. A. Hines, University of Connecticut.)

was then nitrided and reexamined by the MT method. As shown in Fig. 14-22b, the fatigue crack could no longer be detected.

The conclusion drawn is that the organization that performed the last MT inspection had not been negligent. It was not possible to detect the grinding cracks



(a)



(b)

Fig. 14-22. Magnetic particle distribution at a fatigue crack. Magnification: 200 \times . (a) Prior to nitriding. (b) After nitriding with the white layer removed.

after nitriding. It was the organization that performed the 2,000-hour overhaul that was at fault, for they should have inspected the crankshaft by the MT method prior to renitriding. Based upon an analysis of the fatigue striations, it appears that the grinding cracks did not propagate until after the second overhaul. An increase in the compression ratio at that time may have raised the stress intensity factor at the critical grinding crack to a level above the propagation threshold.

IX. EDDY CURRENT TESTING (ET)

Eddy current testing is used for the detection of surface and near- surface flaws that are within 6 mm (0.24 in.) of the surface. The method is rapid and can be automated and provide a permanent record. In addition it is quite sensitive to the presence of flaws, and surface contact is not necessary. The method is based on inducing small circular electrical currents (eddy currents) in metallic materials using a coil excited by electrical current, Fig. 14-23*a*. Disruption of the eddy currents by a discontinuity is similar to the disruption of magnetic fields except that a wider variety of discontinuities and physical properties affect eddy currents. The depth of penetration S is frequency dependent; the higher the frequency, the less the penetration.

$$S(\text{in.}) = 1980\sqrt{r/\mu f}, \quad S(\text{mm}) = 50,292\sqrt{r/\mu f} \quad (14-7)$$

where r is the resistivity in ohm-cm, μ is the magnetic permeability (taken to be 1 for nonmagnetic materials), and f is the frequency in hertz. The following table (1) lists the depths of penetration for several metals as a function of the frequency.

Metal	Conductivity (% IACS)*	Standard Depth of Penetration† in Mils (mm) at a Frequency of		
		1 kHz	100 kHz	10 MHz
Copper	100	80 (2.0)	8 (0.2)	0.8 (0.02)
Aluminum	61	160 (4.0)	16 (0.4)	1.6 (0.04)
Titanium	3.1	800 (20)	80 (2.0)	8.0 (0.2)
Iron	10.7	14 (0.36)	1.4 (0.04)	0.1 (0.004)
304 SS	2.5	550 (14.0)	55 (1.4)	5.5 (0.14)

*International Annealed Copper Standard.

†Depth at which signal intensity is $1/e$ that at the surface.

As can be seen from Fig. 14-23*b*, a flaw in the specimen can affect the eddy currents and produce a change in the impedance of the coil. Impedance changes in either primary or secondary (sensing) coils are sensed as changes in current through the coil or as phase changes in the voltages or currents. The readout of these changes may be the deflection of a meter, an oscilloscope presentation, a strip chart recording, lights or alarm activation, digital readouts, or operational control of manufacturing processes.

Specimen-to-probe effects include:

(a) Edge effects resulting from a distortion of the magnetic field near the edge of a specimen. Inspecting within 3.2 mm (1/8 in.) from the edge of a nonmagnetic material or within 152 mm (6 in.) of the edge of a magnetic material is likely to produce signal distortions.

(b) The gap between a circular specimen and the encircling coil can greatly affect readings. The closer the specimen comes to filling the hole in the center of the coil, the greater will be the sensitivity (fill factor = 1).

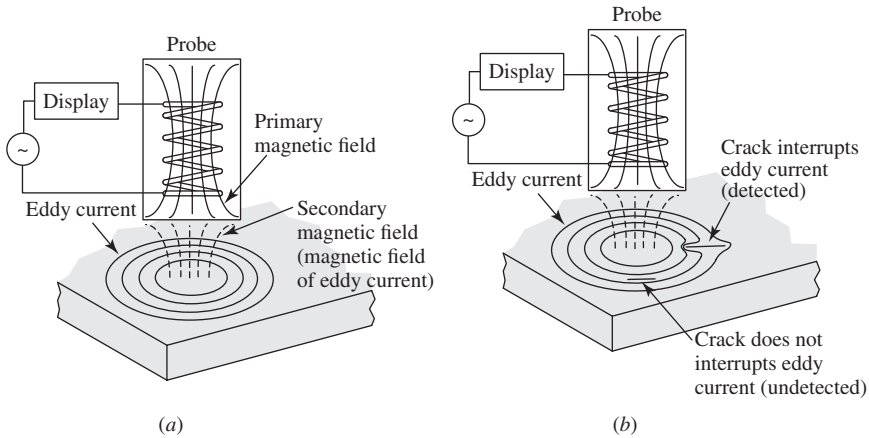


Fig. 14-23. (a) The inducement of eddy currents by an alternating magnetic field. (b) Disruption of the eddy current by discontinuities.

(c) A gap between the specimen and the probe decreases the sensitivity of the test because the field of the coil is strongest close to the coil. The “lift-off” effect can be used to measure the thickness of paint or nonmagnetic plating on a magnetic substrate. Probes often use spring loading to maintain a constant gap.

ET inspections are also used to determine the thickness of coatings and other dimensional characteristics, but a degree of sophistication in the proper use of the technique is needed. In one case, the method was specified as a check on the positioning of cooling passages in turbine blades. However, none of the technicians was properly trained to carry out the inspection; as a result, turbine blades with improperly positioned cooling passages entered service. Fortunately, no harm resulted from this oversight.

Figures 14-24 and 14-25 demonstrate the eddy current readout due to the existence of a crack and a simulated delamination.

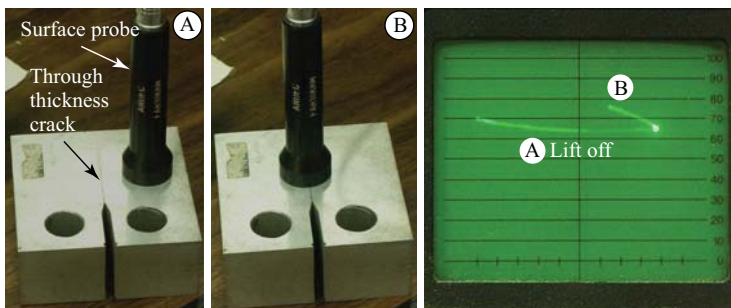


Fig. 14-24. Eddy current readout due to a crack. (Courtesy of C. Kunpanichkit, Chulalongkorn University.)

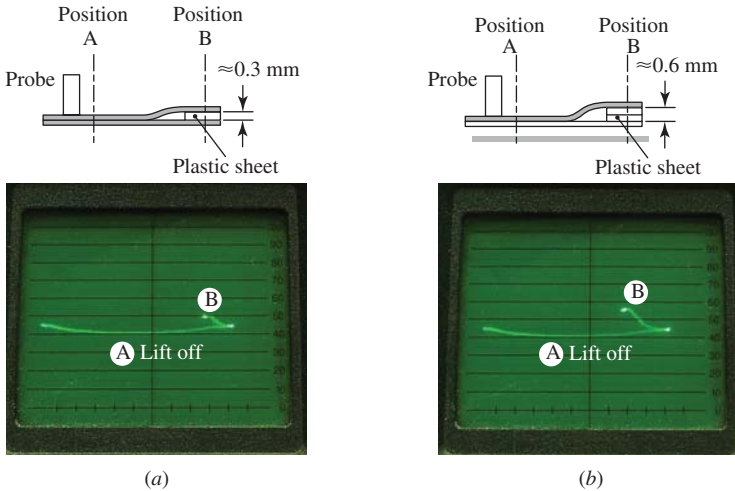


Fig. 14-25. (a, b) Eddy current readout due to a simulated delamination. (Courtesy of C. Kunpanichkit, Chulalongkorn University.)

X. CASE STUDY: ALOHA AIRLINES

This case was discussed in Chapter 1. The ET method had been used prior to the accident in the inspection of the 737 Aloha Airlines fleet. However, readily detectable flaws such as the disbonding of skins and fatigue cracks emanating from multiple rivet holes were not discovered. Inadequate training and monitoring of the inspectors in the use of this technique were the main factors contributing to the failure of the method in this case.

XI. ULTRASONIC TESTING (UT)

UT is used for the detection of surface and subsurface flaws (1). It can give the location and size of a flaw; it is portable but slow, and a couplant is required. The orientation of the flaw is important; the results are operator dependent, and good standards are needed. Sound waves with frequencies ranging from 0.5 to 10 MHz are often used in inspections, much higher than the 20,000 Hz associated with the limit of human hearing. The most common UT technique is called *pulse-echo*, in which a pulse of sound waves is introduced into the specimen by a piezoelectric transducer (an anisotropic crystal capable of converting an applied voltage into vibration of the crystal or converting deformation of the crystal into a voltage). The pulse of sound waves travels through the specimen until it is reflected at the back surface of some discontinuity, Fig. 14-26. The oscilloscope presentation relates the distance (time) traveled by the pulse of sound to the signal detected. The echo indication of the discontinuity will appear in the oscilloscope presentation in the same position relative to the front and back reflections that the discontinuity occupies in the specimen.

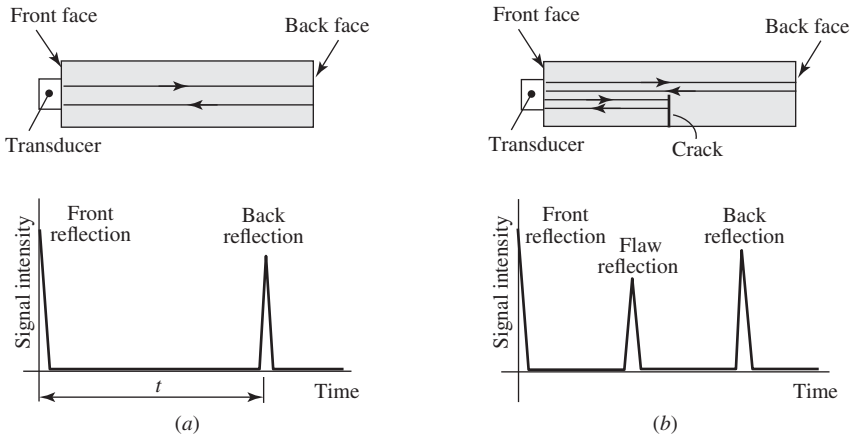


Fig. 14-26. Signals developed in the pulse-echo UT technique (a) No disturbance from the crack. (b) Disturbance from the crack exists.

There are three scan modes: A, B, and C. In the A-scan mode, the one most widely used, a quantitative display of signal intensity (size of the flaw) and time of flight (depth of the flaw) is obtained at one point on the surface of the test piece. The method uses a fixed transducer and provides information on the flaw type, its depth, and its location. In the B-scan mode, a quantitative display of the time of flight along a line on the surface is obtained. In a B-scan, the transducer and the test piece move with respect to each other. The method can provide information on the size (in one direction), position, and depth, and, to a certain degree, the shape and orientation of internal flaws. The C-scan mode results in a two-dimensional semiquantitative display of the echo intensity of the test piece. It displays a plane section of the test piece but provides no depth or orientation information. In a C-scan the entire surface is traversed or rastered.

A problem with UT is the transmission of the ultrasonic energy from the transducer to the test piece. Placing a transducer in direct contact with a surface usually results in a very small amount of energy transfer because of the presence of air in the interface. The acoustic impedances Z of the air and the test piece are very different. ($Z = \rho V$, where ρ is the density and V is the wave velocity.) A couplant is used to couple the transducer ultrasonically with the test piece to ensure efficient sound energy transmission. The couplant acts to smooth out surface irregularities and to exclude all air between the surfaces. Ideally, the couplant should have an acoustic impedance between the transducer and the test piece. Two methods of coupling are used: immersion and contact.

In immersion testing, clean, deaerated water with a wetting agent is used as a couplant. In contact testing, transducers are held directly on the test surface with a thin liquid film for a couplant. The couplant is an oil- or grease-like material that fully wets the surface of the transducer and the test piece. Contact testing consists of three techniques, which are determined by the sound wave mode: normal beam (longitudinal wave), angle beam I (shear waves), and angle beam II (surface waves).

A. Normal Beam Technique

In the normal beam technique, the ultrasonic pulse is projected into the test piece perpendicular to the surface. This technique is further subdivided into pulse-echo techniques and transmission techniques. The transmission technique uses a detector on the back face of the test piece. The pulse echo technique uses either a single transducer (to send and receive signals) or two transducers (one to send the signal and the other to receive the reflected signals).

B. Critical Angles

For normal incidence, transmission and reflection occur with no change in beam direction. For other angles of incidence, however, some interesting and useful changes in beam direction occur in accord with Snell's Law:

$$\frac{\sin \theta_I}{V_I} = \frac{\sin \theta_R}{V_R} \quad (14-8)$$

where θ_I is the angle of incidence, θ_R is the angle of reflection or refraction, V_I is the velocity of the incident wave, and V_R is the velocity of the reflected or refracted wave.

When an incident longitudinal sound wave passes through an interface between materials with different acoustic impedances (see Fig. 14-27), Snell's Law can be written as

$$\frac{\sin \theta_I}{V_{L_1}} = \frac{\sin \theta_L}{V_{L_1}} = \frac{\sin \theta_T}{V_{T_1}} = \frac{\sin \phi_L}{V_{L_2}} = \frac{\sin \phi_T}{V_{T_2}} \quad (14-9)$$

A single incident, nonnormal longitudinal beam results in two refracted waves, one longitudinal and one transverse, and a similar pair of reflected waves. As the angle of incidence is increased, the angle of the refracted longitudinal wave approaches 90° . At 90° the first critical angle of incidence is found, Fig. 14-28a.

$$\sin \theta_{I_1} = \frac{V_{L_1}}{V_{L_2}} \quad (14-10)$$

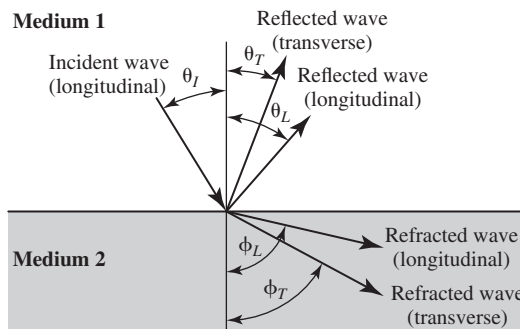


Fig. 14-27. Waves generated by the incidence of an oblique longitudinal sound wave on a medium of different acoustic properties. (After Survey of NDT, 1.)

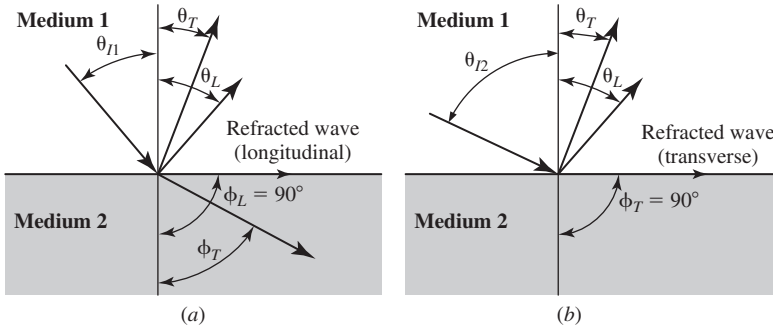


Fig. 14-28. (a, b) The first and second critical angles of incidence of a longitudinal wave. (After Survey of NDT, 1.)

As the angle of incidence is increased further, only shear waves are present in the second medium. The second critical angle is reached when the angle of the refracted transverse wave is increased to 90° , Fig. 14-28b

$$\sin \theta_{I2} = \frac{V_{L1}}{V_{T2}} \quad (14-11)$$

At the second critical angle, the shear wave has become a surface wave. If the angle of incidence is increased further, no energy will be transmitted to the second medium.

C. Angle Beam Techniques

The angle beam technique is used to transmit sound into the test piece at a predetermined angle to the surface. Figure 14-29 shows a typical angle beam search unit with the transducer mounted on a plastic wedge. Depending upon the angle of incidence, there may be mixed longitudinal and shear modes, shear modes only, or a surface mode only produced in the test specimen, as indicated in Fig. 14-27. Having

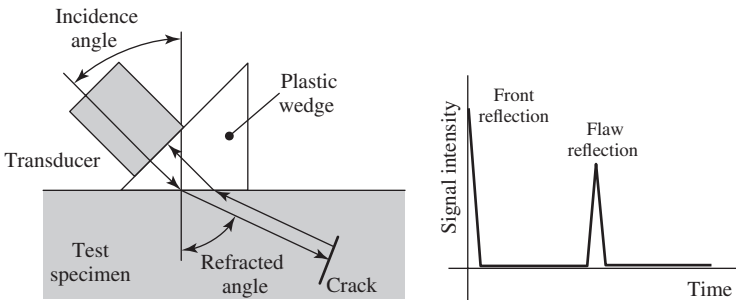


Fig. 14-29. Illustration of the setup for the angle beam technique with the transducer mounted on a plastic wedge. (After Survey of NDT, 1.)

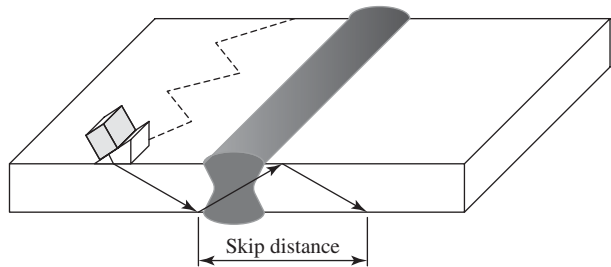


Fig. 14-30. Illustration of the use of the angle beam technique. (After Survey of NDT, 1.)

more than one mode present in the test piece is unacceptable because interpretation becomes difficult. Therefore, angle beam transducers are always used at angles of incidence greater than the first critical angle. The use of the angle beam technique is illustrated in Fig 14-30. This method requires a signal detector. The method is also used with a single transducer-detector unit.

D. Wave Velocities and Acoustic Properties

The velocity of a plane longitudinal wave is given as

$$V_L = \sqrt{\frac{E(1 - \nu)}{\rho(1 + \nu)(1 - 2\nu)}} \tag{14-12}$$

The velocity of a shear wave is given as

$$V_T = \sqrt{\frac{G}{\rho}} \tag{14-13}$$

The acoustic properties of some common materials are given in the following table (1)

Material	Density, g/cm ³	V_L , cm/μ sec	V_T , cm/μ sec	Z_L , g/cm ² -μ sec
Carbon steel	7.85	0.594	0.324	4
Al 2117-T4	2.80	0.625	0.310	1.75
304 SS	7.9	0.564	0.307	4.46
Air	0.000129	0.0331	—	0.00004
Glass	2.5	0.577	0.343	1.44
Lucite	1.18	0.267	0.112	0.32
Water	1.0	0.149	—	0.149
Copper	8.89	0.470	0.226	4.18

E. Other Considerations

(a) *The reduction of signal intensity as a function of the distance traveled (attenuation):* $I = I_0 e^{-kd}$, where I is the intensity at d , I_0 is the incident intensity, k is the absorption coefficient, and d is the distance into the specimen.

(b) *The near field:* Close to the transducer emitting sound, the intensity of sound is very irregular due to interference between the sound waves emitted from different parts of the transducer. The length of the near-field L_{nf} is given as $L_{nf} = D^2/4\lambda$, where D is the diameter of the transducer and λ is the wavelength of the ultrasonic beam. Interpretation of data obtained from the near field may be difficult.

XII. CASE STUDY: B747

In Chapter 10 the fatigue failure of fuse pins on a B747 freighter was discussed. A related matter involves the ultrasonic inspection of the fuse pins. No cracks were detected at the time of the last inspection, and yet it appears likely that a fatigue crack was probably present on the inboard side of the inboard fuse pin. Why was this crack not found? The UT inspection procedure was based upon the assumption that any fatigue crack would grow normal to the axis of the fuse pin. However, the recovered portion of the outboard fuse pin indicated that the crack grew at an angle to the radial direction of the fuse pin. In the UT inspection technique, a signal is sent from one end of the pin that is reflected from a radial crack, as shown in Fig. 14-31a, and appears on the CRT before the signal from the inclined portion of the fuse pin is received. However, if the crack were oriented as in Fig. 14-31b, the path length of the reflected signal would be longer and might not appear on the CRT in the expected location for a crack. Further, if the crack were oriented as in Fig. 14-31c, the return signal might not be detected at all. In addition to these complications, it was found that the fuse pins in service did not simply bend, as had been assumed, but instead developed a “crankshaft” configuration that may also have had an effect on the ability to detect fatigue cracks. It is noted that the Netherlands Aviation Safety Board recommended that a review be made of the NDE inspection techniques.

XIII. RADIOGRAPHIC TESTING (RT)

RT is used for the detection of subsurface flaws, particularly in welded joints. It is low cost, provides a permanent record, and is portable, but it cannot detect laminations, is a radiation hazard, and needs trained operators (1).

In radiography the specimen is exposed to a beam of X-rays, gamma rays, or neutrons. If the beam encounters a flaw of lesser density than that of the basic material, then more than the normal amount of radiation will transit that region and reach the detector, usually film. This leads to a darker area on the film when processed, Fig. 14-32.

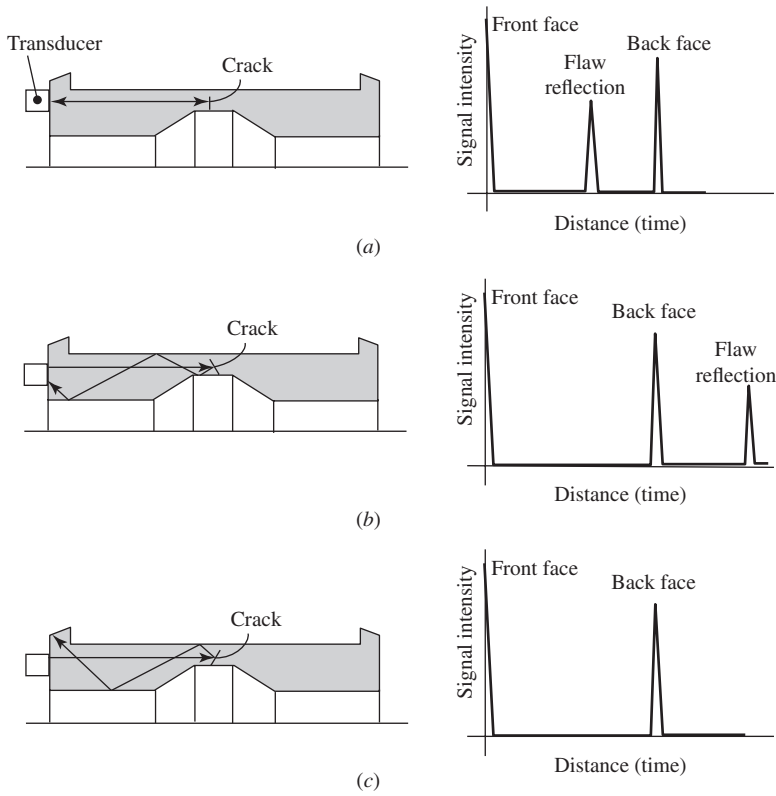


Fig. 14-31. The effect of crack orientation on an ultrasonic signal. (a) Crack perpendicular to the ultrasonic beam and oscilloscope display corresponding to the (a), (b), and (c) ultrasonic signal paths when the crack is not perpendicular to the ultrasonic beam.

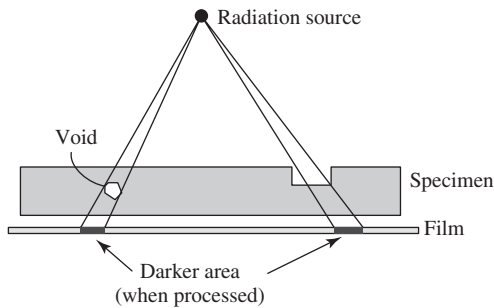


Fig. 14-32. The basic radiographic process. (After Survey of NDT, 1.)

Gamma Radiation Sources (1)

Source	Half-Life	Energy, MeV	Steel Thickness	
			in.	mm
Iridium-192	74 days	0.31, 0.47, 0.60	0.25–3	6–75
Cesium-137	30.1 years	0.66	0.5–4	13–100
Cobalt-60	5.3 years	1.17, 1.33	0.75–9	19–230

Some X-ray machines can produce photons with energies in the 10–100 MeV range, which far exceeds the energies available from radioactive isotopes. Increasing the applied voltage used in generating the X-rays increases their penetrating power. The great advantage of isotopes is their portability for in situ inspection.

X-ray and gamma ray quality is usually expressed in terms of the thickness of a reference attenuator material (aluminum, copper, or iron) required to reduce the intensity of the beam to one-half of its original value. This thickness is referred to as the *half-value layer* (HVL).

A. Penetrators

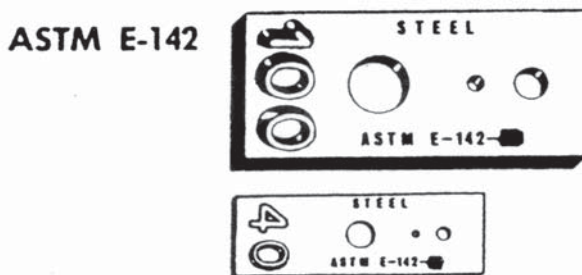
The two basic overall parameters that the interpreter must know in regard to a given radiograph are the radiographic sensitivity and the definition that have been achieved. Radiographic sensitivity is measured in terms of the minimum percentage of the subject item that corresponds to the least discernible change in the photographic density of the final radiograph. *Definition* refers to the smallest-size (in lateral dimension) flaw of given (equivalent) thickness. Both sensitivity and definition are established by the use of penetrators.

A *penetrator* is a device placed on the film side of a specimen whose image in a radiograph is used to determine the radiographic quality. The standard penetrator is a rectangle of metal with three drilled holes of set diameter, which is composed of a metal similar to that being radiographed. Normally, the thickness of the penetrator T is selected to be 2% of the thickness of the specimen. The penetrator contains holes that may be $1T$, $2T$, $4T$, and $8T$ in diameter. A standard 2% sensitivity requires the technique to image the penetrator whose thickness is 2% of the test piece and the $2T$ hole of the penetrator. (See Fig. 14-33.)

The six methods discussed so far in this chapter are all passive methods in that the component being inspected need not be under stress or in service.

XIV. ACOUSTIC EMISSION TESTING (AET)

AET is used for the detection of surface and subsurface flaws (1). It can provide remote and continuous surveillance and a permanent record, but it may need many contact points and may be expensive. This is an active method in that the component being inspected is loaded during an inspection or a crack grows under load during surveillance.

**IDENTIFICATION:**

The rectangular penetrameter is identified with a lead number attached to the penetrameter. The number indicates the thickness of the penetrameter in thousandths of an inch. The penetrameter thickness must be selected to indicate the proper quality level.

GENERAL DIMENSIONS:

2 1/2" & smaller Length 1 1/2" Width 1/2"
 2 3/8" to 8" incl. Length 2 1/4" Width 1"
 9" & larger Diameter equal to 4 x thickness
 (Number of holes — 2)

Thickness: 2% of the thickness, of the section, to be radiographed.
 (To nearest standard fractional size)
 Minimum thickness005"

Hole sizes: Small hole dia. 1 x Thickness
 Medium hole dia. 2 x Thickness
 Large hole dia. 4 x Thickness
 Minimum hole dia.010"

ASTM E-142-72 & 74 are identical.

Fig. 14-33. Examples and dimensions of penetrameters. (From Survey of NDT, 1.)

Acoustic emission is defined as the high-frequency (30 kHz–5 MHz) stress waves generated in a material by the rapid release of strain energy during crack growth, plastic deformation, or phase transformation (which also involves plastic deformation). Using electronic sensing and analysis of data from a multiplicity of sensors, the location and relative severity of a flaw can be determined. AET can be combined with hydrostatic testing so that catastrophic failure from the growth of defects can be prevented. Nuclear reactor pressure vessels can be continuously monitored to guard against the growth of flaws. Careful interpretation of data is required to distinguish between plastic deformation and crack growth. As cracks increase in length, the strain energy released per increment of growth also increases, and so does the acoustic signal. Applications include checking on the safety of bridge structures, monitoring fatigue and stress corrosion crack growth, and monitoring the delayed cracking associated with hydrogen embrittlement.

XV. COST OF INSPECTIONS

In carrying out an inspection program in order to ferret out defective parts, it is clear that the more parts that are examined in the case of a production run or the greater the frequency of inspections in the case of an aircraft structure, the more likely it is that the defective parts will be discovered (1). However, each of these inspections has an associated cost. A balance between the cost of inspection and the benefit gained needs to be struck. The following example illustrates the considerations involved.

Assume that the losses due to substandard products decrease with the number of inspections N as

$$\text{total losses} = A - CN^{1/2} \quad (14-14)$$

where A and C are constants. Assume further that the cost of inspections is given by

$$\text{cost of inspections} = BN \quad (14-15)$$

where B is a constant. The total cost as a function of N is therefore equal to

$$\text{total overall cost} = A - CN^{1/2} + BN \quad (14-16)$$

The optimum number of inspections N_{opt} is the one that will minimize the total cost. N_{opt} is obtained by taking the derivative of the total cost with respect to N and setting it equal to zero, which leads to

$$N_{opt} = \left(\frac{C}{B} \right)^2 \quad (14-17)$$

Note that the constant A does not appear in this result. In a specific case where $A = \$100$, $C = \$2.00$, and $B = \$0.10$, the optimum number of inspections would be 100. The total cost as a function of the number of inspections for this example is plotted in Fig. 14-34. If the cost per inspection C were to increase, then N_{opt} would decrease. On the other hand, if C were to increase, then N_{opt} would also increase.

When a new product is introduced, the term *bathtub curve* is used to describe the history of failures. The number of failures per unit time may be high initially due to bugs in the manufacturing process or poor inspection procedures. Once these problems have been corrected, the number of failures per year remains fairly steady over a period of time before rising again as the useful life of the product is exceeded.

For further reading on nondestructive examination see reference (1).

XVI. SUMMARY

The inspection for defects and cracks is a vital part of the procedures used to ensure the safety of structures. The use of fracture mechanics in design is coupled with a need for adequate inspection methods. This chapter has provided a review of

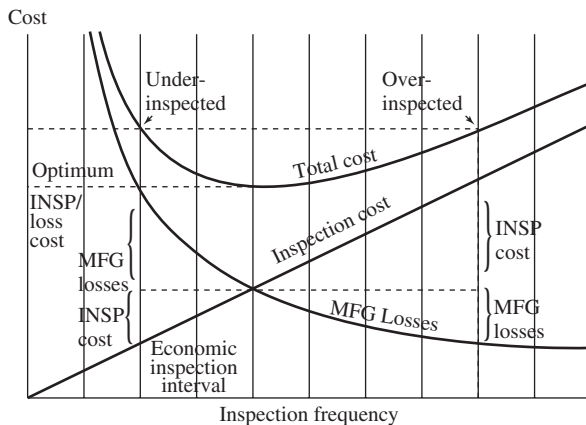


Fig. 14-34. Relationship of cost to inspection frequency. (After Survey of NDT, 1.)

the principal nondestructive techniques, and in case studies has pointed out their shortcomings.

REFERENCES

- (1) *Survey of NDE*, EPRI Nondestructive Evaluation Center, Charlotte, NC, 1986.
- (2) *NTSB Aircraft Accident Report, NTSB/AAR-90/06*, United Airlines Flight 232, Sioux City, Iowa, Washington, DC, 1989.
- (3) *NTSB Aircraft Accident Report, NTSB/AAR-98/01*, Uncontained Engine Failure, Delta Airlines Flight 1288 McDonnell Douglas MD-88, N927DA Pensacola, Florida, Washington, DC, 1996.
- (4) C. Bagnall, H. C. Furtado, and I. LeMay, "Evaluation of Steam Generator Plant: Some Problems Encountered in Their Solution," in *Lifetime Management and Evaluation of Plant, Structures and Components*, ed. by J. H. Edwards, P. E. J. Fleitt, B. C. Gasper, K. McLarty, P. Stanley, and B. Tomkins, EMAS, West Midlands, UK, 1999, pp. 295–302.
- (5) *ASM Metals Handbook*, 8th ed., vol. 8, ASM, Materials Park, OH, 1973, p. 303.

PROBLEMS

- 14-1. A sound beam traveling in water impinges upon a steel plate. What percentage of the energy of the beam is reflected? What percentage is transmitted?

The energy reflected, IR, is given by $IR = \left(\frac{Z_2 - Z_1}{Z_2 + Z_1} \right)^2$.

$$Z_{\text{water}} = 0.149 \text{ g/cm}^2\text{-}\mu \text{ sec}$$

$$Z_{\text{steel}} = 4.68 \text{ g/cm}^2\text{-}\mu \text{ sec}$$

- 14-2.** The longitudinal velocity of sound in Lucite is 0.267 cm/ μ sec. In steel, the longitudinal wave velocity of sound is 0.594 cm/ μ sec and the transverse wave velocity is 0.324 cm/ μ sec.
- Determine the first critical angle of incidence for sound transmission from the Lucite into the steel.
 - Determine the second critical angle for sound transmission from the Lucite into the steel.
 - There is no critical angle when sound goes from the steel into the Lucite. Why?
- 14-3.** A fatigue crack in a steel is completely filled with an impermeable substance whose magnetic properties are the same as those of the steel. Will the MT technique detect the crack? Will the PT method detect the crack? Will the ET method detect the crack? Will the UT method detect the crack?

15

Wear

I. WEAR

Tribology is the study of the wear process that occurs when two contacting surfaces move relative to each other. Two important factors that influence the wear process are friction and lubrication. One objective of tribologists is to be able to predict the rate of wear, for this rate determines the useful lifetime of such items as roller bearings and gears. This objective has not yet been fully met, but some simplified relationships together with a good deal of experimental data have provided a reasonable view of a very complex subject. The wear rate is commonly expressed as Q/S , where Q is the wear volume for a given sliding distance S . Various models lead to relationships in which the wear rate is proportional to the normal load L and inversely proportional to the hardness H , that is, $Q/S = kL/H$. This type of linear wear equation is often ascribed to Archard (1), as will be discussed.

The consequences of wear can vary from the trivial to the very serious. An example of the latter is the crash of Alaska Airlines Flight 261 on January 30, 2000, in the Pacific Ocean off Los Angeles in which 88 people perished. This tragedy appears to have been brought about by the excessive wear of a gimbal nut through which passed a jack screw that controlled the position of the horizontal tail stabilizer. The stripping of the threads of the gimbal nut may have led to the loss of control of the horizontal stabilizer and the resultant crash. Both the lubricants and the maintenance procedures are suspect.

II. THE COEFFICIENT OF FRICTION

When two solids are placed in contact, the apparent area of contact is A . However, only some regions of their surfaces will touch; others will not. Those regions that make contact are known as *junctions*, and the sum of all the junction areas is known as the *area of contact* A_c . When these junctions form, they are considered to be welded together. (The purpose of a lubricant is to prevent these welded junctions from forming.) Based upon considerations of plastic deformation, an estimate of the area of contact can be made:

$$P_N = A_c \sigma_Y \quad (15-1a)$$

$$A_c = \frac{P_N}{\sigma_Y} \quad (15-1b)$$

where P_N is the normal load between the two interfaces, σ_Y is the yield stress, and A_c is the actual area of contact. It is considered that plastic deformation occurs at all of the high points of contact, thereby increasing the area of contact. The plastic deformation process then continues and A_c grows until the conditions of Eq. 15-1a are satisfied. If we try to slide one contacting surface over the other, and if it is assumed that all junctions are welded together, then all of the junctions must be sheared in the sliding process. The shearing force P_T is given as

$$P_T = \tau A_c = k A_c \quad (15-2)$$

where τ is the shear stress required to shear the junctions, which is set equal to the yield stress in pure shear k . However, because of work hardening during the deformation process, an accurate value of the yield stress may be difficult to assign.

In this model the coefficient of friction μ is given as

$$\begin{aligned} \mu &= \frac{P_T}{P_N} \\ &= \frac{k A_c}{\sigma_Y A_c} = \frac{k}{\sigma_Y}, \text{ a constant} \end{aligned} \quad (15-3)$$

If k is taken to be $0.5\sigma_Y$ then μ is 0.5. This is Coulomb's Law of Friction, ($P_T = \mu P_N$), with the coefficient of friction being 0.5, a not unreasonable value for direct metal-to-metal contact in air. The coefficient of friction can vary widely. For metal-to-metal contact in vacuum, μ may be greater than 5.0, and since in air the value of μ is much smaller than in vacuum, it is clear that the environment exerts a strong influence. However, this influence has not been considered in the above analysis for μ . Perhaps oxide coatings make the welding of junctions less feasible, thereby reducing the value of μ . Whereas the highest values for μ are obtained in

vacuum, the lowest values for μ are obtained under conditions of good hydrodynamic lubrication, where μ may be 0.0001. Intermediate values are obtained for steel on aluminum, 1.3. For titanium on titanium μ has a value of 0.5 (2).

There are two types of wear, abrasive and adhesive. *Abrasive wear* involves the plowing action of a hard particle over a softer surface, as in the polishing of a metal with diamond paste. In *adhesive wear*, material is transferred at a junction from one contacting surface to the other. However, as this type of wear process continues, hard, oxidized wear particles form, leading to the development of abrasive wear. Therefore, the term *sliding wear* rather than *adhesive wear* may be preferred (3). The purpose of a lubricant filtering system is to remove such particles from the lubricant, thereby forestalling abrasive wear by these oxidized particles.

In addition to wear, heat is generated during a frictional wear process, sometimes with disastrous results. For example, ignition of titanium has occurred in jet aircraft engines due to the rubbing of titanium alloy compressor blade tips against a containment constructed of a titanium alloy. As a result, a titanium alloy is no longer used for the containment.

III. THE ARCHARD EQUATION(1)

In the case of adhesive wear, the Archard equation given can be used to estimate the total volume of wear debris produced per unit of sliding distance, Q/S , where Q is the total volume of wear produced and S is the sliding distance. The wear rate is assumed to be proportional to the normal load P_N and inversely proportional to the hardness H , that is,

$$\frac{Q}{S} = \frac{KP_N}{H}$$

or

$$Q = \frac{KP_N S}{H} \quad (15-4)$$

where K is a dimensionless constant. Note that since $P_T = \mu P_N$, Q is proportional to the work done by the friction forces $P_T S$.

Equation 15-4 can be derived by first examining the behavior of a single asperity.

The local load δP_N supported by an asperity that is assumed to have a circular cross section with a radius a is

$$\delta P_N = \sigma_Y \pi a^2$$

If the yield strength σ_Y of the asperity, which is assumed to be plastic, is assumed to be proportional to the indentation hardness H of the asperity, that is, $\sigma_Y = cH$, where c is a constant, then

$$\delta P_N = cH\pi a^2 \quad (15-5)$$

The volume of wear debris δV for a particular asperity is considered to be a hemisphere sheared off from the asperity, so that

$$\delta V = \frac{2}{3} \pi a^3 \quad (15-6)$$

The sliding distance involved in forming this hemispherical fragment is $2a$. Hence, the wear volume of material produced from this asperity per unit of sliding distance is

$$\delta Q = \frac{\delta V}{2a} = \frac{\pi a^2}{3} \quad (15-7)$$

But from Eq. 15-5, $\pi a^2 = \frac{\delta P_N}{cH}$, so that

$$\delta Q = K \frac{\delta P_N}{H} \quad (15-8a)$$

and

$$Q = K \frac{P_N}{H} \quad (15-8b)$$

The constant K in Eq. 15-8 is used to incorporate all of the various constants used in the derivation of Eq. 15-8 and is a measure of the severity of wear. Typically for “mild” wear, $K \approx 10^{-8}$, whereas for “severe” wear, $K \approx 10^{-2}$.

IV. AN EXAMPLE OF ADHESIVE WEAR

Adhesive wear takes place during intense automotive or truck braking action when rubber from the tires is transferred to the roadway, creating skid marks. If it is assumed that all of the kinetic energy of the vehicle is expended as frictional energy with the roadway, then

$$\frac{1}{2} \frac{W}{g} v^2 = \mu W d \quad (15-9)$$

$$v = \sqrt{2\mu g d} \quad (15-10)$$

where W is the weight of the vehicle, v is its velocity, g is the acceleration due to gravity, μ is the coefficient of friction, and d is the length of the skid marks. A typical value for μ that is used by traffic accident investigators in determining a vehicle's velocity is 0.75. It is interesting to note that the estimated velocity is independent of the weight of the vehicle.

V. FRETTING FATIGUE

Fretting is a wear process, often combined with corrosion, and is due to the relative motion of two components, usually metal, that are held together by a compressive force. The amplitude of the relative motion can vary but may be only a few microns. If the relative motion is cyclic and continues for some time, it can lead to increased roughening of the surfaces in the area of contact and the creation of hard oxide particle debris that can increase the rate of wear. Under continued cyclic loading conditions, the roughened surface can lead to the formation of a fatigue crack and

to fretting fatigue failure. This type of failure is of particular concern in the aircraft field, where the fretting that takes place between the aluminum aircraft skin and the rivet head has led to a number of crashes, that is, C130 and 707. To avoid this type of fatigue failure, aluminum sheets can be bonded together by an epoxy rather than by rivets, as in the Boeing 737. The use of composite materials, as in the Boeing 787 and the Airbus A380 aircraft, can also eliminate problems with rivets simply by doing away with rivets. Nevertheless, fretting problems remain a matter of concern, as for example in the dovetail joint of turbine engines where the turbine blade is inserted into the turbine disc. Since the mid-1980s, attempts have been made to avoid blade-disc fretting by making blades and discs as a single unit called an *integrally bladed* unit. During the fretting fatigue process, load is transferred from the specimen into the pads by interfacial friction. In the transfer area a fretting scar will develop, as shown in Fig. 15-1. During the fretting process the sharp edge of the fretting pad, a location of high stress concentration, will be worn and rounded. It is at this location that a small semicircular fatigue crack will form. The crack will propagate at a 45° angle, perpendicular to the first principal stress, at a rate governed by the normal components of the applied load and the compressive load of the pads. As the crack lengthens, it will eventually turn to a path that is perpendicular to the applied cyclic load and then propagate to failure.

In order to eliminate fretting fatigue failures in turbine rotors, some rotors together with the turbine blades have been manufactured as integral units. Such rotors are designated as Rotor (IBR) or more commonly as *blisk* (blade-disk). Blisk manufacturing was first used in 1985 for the compressors of a helicopter engine; since then, its use has continued to increase in major applications for both compressors and fan blade rotors. A main disadvantage of a blisk is that any major damage to IBR blades requires the full removal of the engine so that the IBR can be replaced or, if

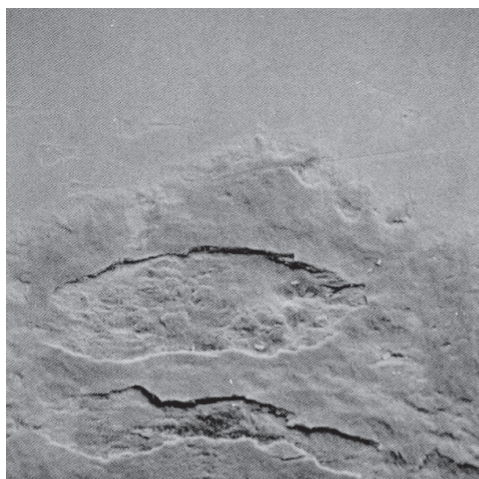


Fig. 15-1. Fretting scar. (From Lutynski et al., 4.)

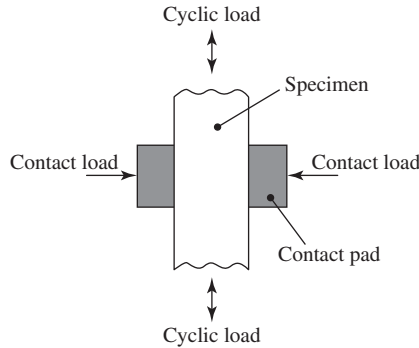


Fig. 15-2. Schematic of a fretting fatigue experiment.

possible, replacement blades welded on. Maintenance of this nature must often be performed at a specialized facility. In addition, IBR blades must undergo harmonic vibration testing, as the natural damping of the dovetail attachment of a typical turbine blade is no longer present.

The fretting fatigue process is usually studied using laboratory setups in which metal pads are clamped to a flat test specimen, as shown in Fig. 15-2. A compressive load of desired magnitude is applied to the pads by means of two bolts attached to a proving ring equipped with strain gauges that provide a means of calibration. Fretting fatigue S/N curves can then be determined by cyclically loading at various stress amplitudes to establish the degree of fatigue strength degradation resulting from the use of various pad-metal combinations and various compressive stresses.

The laboratory tests can be supplemented by Finite Element Analysis (FEA) to gain further insight into the fretting fatigue process. Figure 15-3 shows the stress distribution in the region of fretting as obtained by FEA. The FEA procedure has led to the development of plots as shown in Fig. 15-4, in which the maximum interfacial shear stress is plotted against the maximum compressive stress under the pads. The plot is made up of a series of parallel lines, each for a given lifetime. The fretting fatigue behavior of a dovetail joint is consistent with the method of analysis used. Stress amplitude versus the compressive test plots will show similar trends. Resistance to fretting can be improved by any surface treatment that improves wear resistance, such as carburizing or nitriding. Other modifications, such as lubrication or the use of polymeric materials in the interface, also improve the resistance to fretting. Figure 15-5 shows that the shot peening of Ti-6Al-4V can markedly improve the resistance of this alloy to fretting fatigue (4).

The fundamental way to prevent fretting is to design for no relative motion of the surfaces at the contact. The surface finish plays an important role, as fretting normally occurs by the contact of the asperities of the mating surfaces. Lubricants are often employed to mitigate fretting because they reduce friction and inhibit oxidation.

Soft materials often exhibit higher susceptibility to fretting than hard materials of a similar type. The hardness ratio of the two sliding materials also has an effect on fretting wear (5). However, softer materials such as polymers can show the opposite

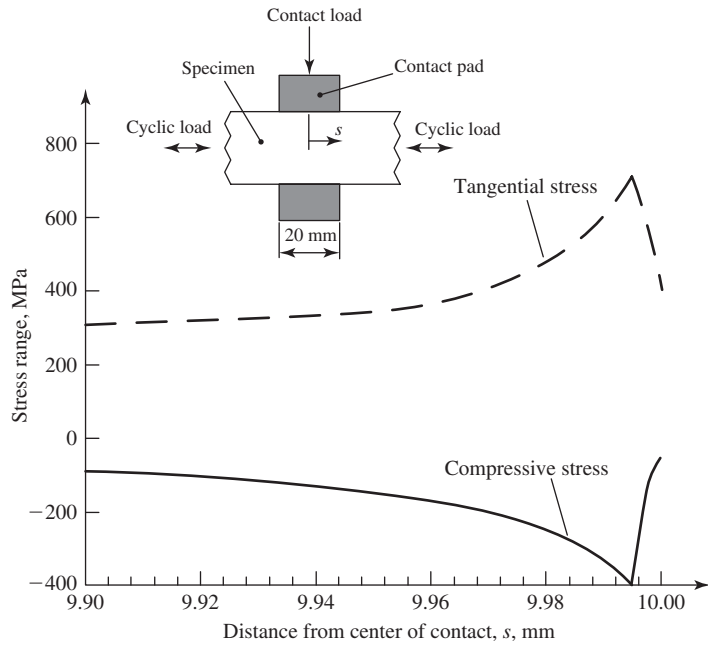


Fig. 15-3. Stress distribution in the fretting region.

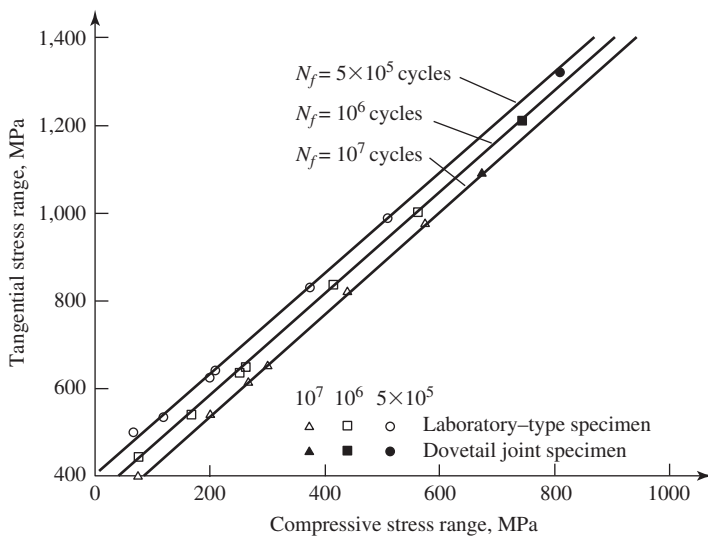


Fig. 15-4. Fretting fatigue design curve based on the tangential stress range and the compressive stress range near a contact edge. (After Lutynski et al., 4).

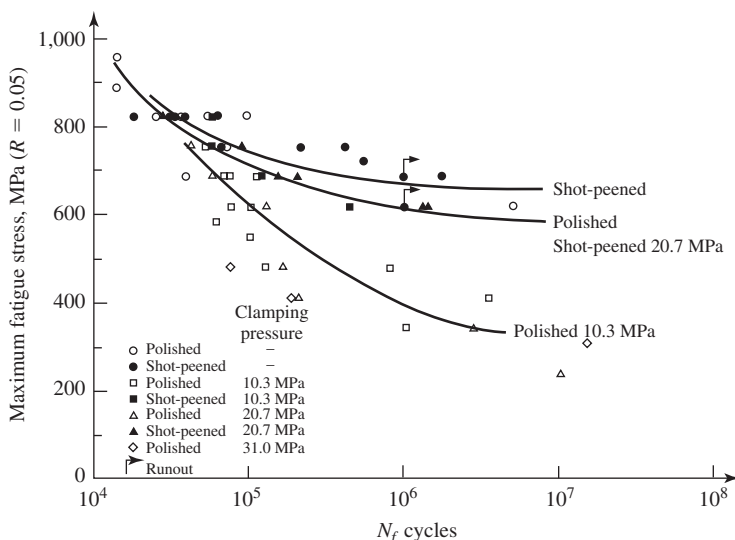


Fig. 15-5. Fretting fatigue results of shot-peened and non-shot-peened specimens tested under fretting and nonfretting conditions. The trend lines are indicated. (After Lutynski et al., 4.)

effect when they capture hard debris that becomes embedded in their bearing surfaces. They then act as very effective abrasive agents, wearing down the harder metal with which they are in contact.

VI. CASE STUDY: FRICTION AND WEAR; BUSHING FAILURE

In the course of a 2,000-hour overhaul, a small plane had the two steel bushings and the steel shaft that held a carburetor butterfly valve replaced in the fall of the year. The bushings were short, thin, hollow cylinders used as guides and nonroller bearings. After the overhaul, the plane was not flown until the following spring. After only a few hours of flying, the pilot, in making an approach for a landing at an airport, found that the control linkage to the carburetor would not operate, and he began to lose altitude. He therefore attempted a landing on a highway, but unfortunately, the plane struck a car, killing an occupant. In the course of the accident investigation, it was discovered that the carburetor shaft was frozen in one of the bushings, thereby accounting for the mishap. The only lubrication provided to the shaft-bushing system came from the fuel vapors of the carburetor.

In a subsequent investigation of the frozen shaft-bushing system, it was found that a great deal of force was required to separate the two; they had to be pressed apart, that is, the combination was truly frozen. Examination of the shaft showed that an abrasive scratch ran for some distance from the bushing along the length of the shaft. Evidently, when the shaft was inserted in the bushing, a work-hardened burr on the bushing had scratched the shaft, and the plowed-out material from the

shaft had lodged in the interface between the bushing and shaft. During the winter this debris had oxidized and hardened. This hardened mass caused further abrasive damage during flight operations until the shaft froze in the bushing and the accident occurred.

It was next discovered that the manufacture of the parts by a firm now bankrupt and out of business had involved a process known as *reverse engineering*, a term indicating that a part originally designed and made by one manufacturer had been copied by another. In this reverse engineering process, every detail of the original part save one had been faithfully replicated. Both bushings and shaft were of the same stainless steel (AISI 416: 0.15C, 12–14Cr, 1.25 Mn, 0.60 max Mo [optional], 0.06 max P, 0.15 min S, 1.00 max Si), and in fact had been machined from the same rod. The essential difference was that the original design called for the shaft to be heat treated to a hardness of 24 HRC, with the bushings to be much softer at a 95 HRB. In the shaft-bushing system that seized, the hardness of both components was 92 HRB. In the course of reverse engineering, this important difference had been overlooked.

Had the shaft been at the proper hardness, the burr on the bushing would not have caused the observed abrasive scratch and the accident would not have occurred. Even without abrasive damage, the soft shaft wore excessively due to adhesive wear, as shown by examination of similar shafts that had seen 2,000 hours of service. Had the shaft been at 25 HRC, only the bushings would have been worn, which is usually the desired situation.

In a final report issued by the NTSB on this matter, the board held the repair facility largely responsible and placed little blame on the manufacturer, a decision that seems a bit strange given the circumstances.

VII. ROLLER BEARINGS

A tapered roller bearing is shown in Fig. 15-6a (6). This type of bearing will be considered in some detail. The causes of failure of other bearing types, that is, spherical roller bearings, needle bearings, and so on, have many characteristics in common with the cause of this type of bearing.

A tapered roller bearing consists of four basic components: the inner race or cone, the outer race or cup, the tapered rollers, and the roller retainer or cage. The forces acting on a tapered roller bearing are shown in Fig. 15-6b. Under proper operating conditions, all components carry the load with the exception of the cage, whose primary function is to space the roller around the cone. The roller bearings as well as the races are tapered on the principle of a cone, and because of the tapered races, the bearing will handle a combination of radial and thrust loads. The rollers are crowned to ensure uniform contact across the entire roller length. This improves fatigue behavior and extends the bearing life. The nominal contact stress between roller and race under rated loading is 1,379–1,724 MPa.

The bearing cups and cones are machined from high-quality forged steel (52100, 58–60 HRC) of low nonmetallic inclusion content. Rollers are either cold formed

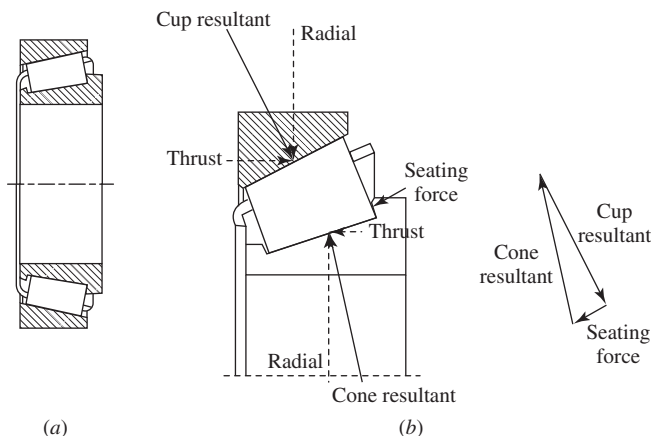


Fig. 15-6. (a) Example of a tapered roller bearing, type TS (pressed steel cage). (b) The forces acting on a tapered roller. (After Tapered Roller Bearings, 6.)

from cold-drawn wire or machined from hot-rolled rods and bars. The steels are low-carbon carburizing grades, vacuum degassed bearing-quality alloy steels. After machining, carbon is added to the surfaces of the bearing components to a depth adequate to sustain bearing loads. This results in a hard, fatigue-resistant case and a tough, ductile core in the carburized and heat-treated part. An additional benefit from the carburizing is the compressive residual surface stress, which improves fatigue resistance. As cleaner steels have become available, the surface finish has become critical in controlling the fatigue life. Therefore, surface finishes are kept in the range $0.63\text{--}2\text{ }\mu\text{m}$, and bearing noise levels are checked to ascertain that they meet the specifications.

There are two fundamental load ratings for tapered roller bearings: a *basic dynamic* load rating and a *static* load rating. The basic dynamic load rating is used to establish the life expectancy of a rotating bearing. The static load rating is used to determine the maximum permissible load that could be applied to a bearing when it is not rotating without producing false Brinell markings. (False Brinelling occurred when automobiles were shipped by rail over long distances. Under the vibratory loads experienced, the balls in ball bearings in the wheel assemblies wore indentations into the bearing races, causing the bearings to “run noisy” when the cars were subsequently driven. The indentations looked like Brinell hardness indentations, hence the term *false Brinelling*.)

The basic dynamic load rating is subdivided into a basic dynamic radial load rating C_{90} and a basic dynamic thrust load rating C_{a90} . The bearing K -factor indicates the ratio of the two, or

$$K = \frac{C_{90}}{C_{a90}} \quad (15-11)$$

K can also be expressed in terms of one-half of the included cup angle α as

$$K = 0.389 \cot \alpha \quad (15-12)$$

The life of a tapered roller bearing is considered to be completed after repeated stressing causes pitting or spalling over 1 % of the contact surfaces. These defects result because of Hertzian contact of the bearing components, which leads to subsurface shear stresses, which alternate in sign as a roller passes a given spot; see Fig. 15-7. The repeated alternating shear stresses lead to fatigue cracking and spalling in a process known as *rolling contact fatigue*. In this process, small subsurface fatigue cracks are formed that grow and break through to the surface, leading to pitting and spalling as fragments break away from the surface. This type of fatigue is found in many components of mechanical systems, including railroad tracks and train wheels.

Since bearings exhibit considerable life scatter, a statistical method is used to evaluate their life. The Weibull extreme value distribution is used to determine the statistical life of bearings at any reliability level. The rated life for bearings is usually given in terms of the L_{10} level, where L_{10} is defined as the number of revolutions (cycles) that 90 % of a group of identical bearings will exceed under standard loading conditions before the fatigue failure criterion is reached.

The basic dynamic load ratings for properly aligned and lubricated bearings are based on a rated life of 90×10^6 cycles (3,000 hours at 50rpm). The races should be less than 3–4 minutes out of alignment. Misalignment can occur due to shaft deflection, inaccuracies in machining of the shaft or housing, and inaccuracies

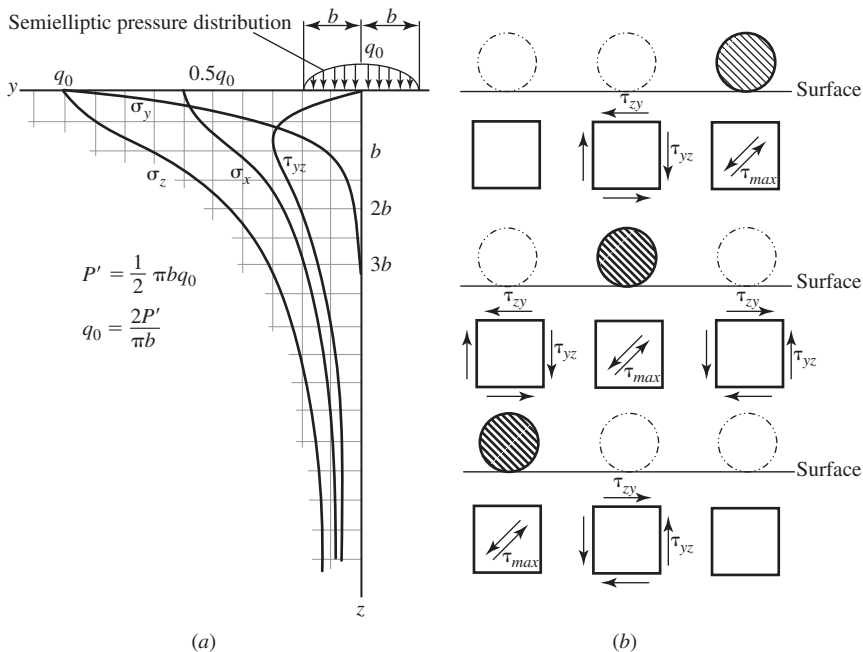


Fig. 15-7. (a) Subsurface stresses developed due to contact of a cylinder with a plane surface. (b) Subsurface shear stresses developed at three fixed positions as a cylinder rolls from right to left. ((a) After Timoshenko, 7. (b) After (8) ASM Metals Handbook, 8th Edition, Vol. 10, Failure Analysis and Prevention, 1975.)

introduced during press fitting. The empirical relationship between rated life of a roller bearing and load is

$$L_{10}P^{10/3} = \text{constant} \quad (15-13)$$

For $L_{10} = 90 \times 10^6$ cycles, the corresponding load P is designated as C_{90} ; therefore, the L_{10} life for any other radial load P is given by

$$L_{10}P^{10/3} = 90 \times 10^6 C_{90}^{10/3} \quad (15-14)$$

or

$$L_{10} = 90 \times 10^6 \times \left(\frac{C_{90}}{P} \right)^{10/3} \text{ revolutions} \quad (15-15)$$

(To account for thrust loads, P can be expressed as a P_{eq} .) The bearing catalog lists the C_{90} load for each bearing, and therefore the L_{10} life for other loads can be determined.

A. Bearing and System Reliability

The rated life of a bearing is an expression of reliability, that is, 90 % reliability that a bearing will equal or exceed a give life. In some bearing applications, greater than 90 % reliability is required. Figure 15-8 is an empirical Weibull plot that can be used to select the appropriate reduced life to give the increase in reliability.

Alternatively, to obtain the L_{10} life of a bearing at a level of reliability R other than 90 %, the following relationship can be used:

$$a_i = 4.48 \left(\ln \frac{100}{R} \right)^{2/3} \quad (15-16)$$

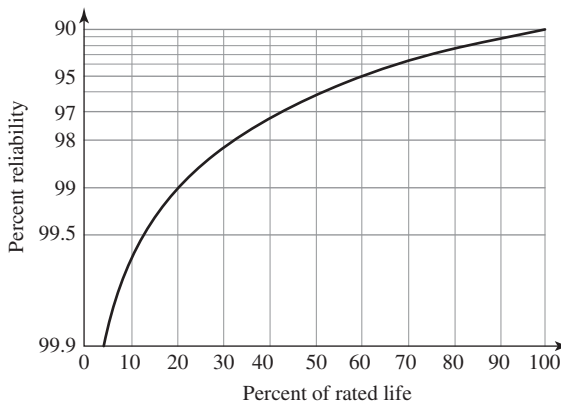


Fig. 15-8. Weibull plot indicating product reliability as a function of the percentage of the rated life. (After Tapered Roller Bearings, 6)

where a_i is a life adjustment factor and R is the % reliability. (For 90 % reliability, $a_i = 1.0$.)

$$R = 100e^{-\left(\frac{a_i}{4.48}\right)^{3/2}} \quad (15-17)$$

is the equation of the line in Fig. 15-8, where $100a_i$ is the percentage of the rated life. Multiply the L_{10} life by a_i to obtain the LR life, which is the life for reliability of R percent. For a reliability greater than 90 %, a_i will be less than unity, and for a reliability less than 90 %, a_i will be greater than unity.

B. First Example

What is the adjusted rated life for an application that requires 98 % reliability?

$$a_i = 4.48 \left(\ln \frac{100}{98} \right)^{2/3} = 0.33 \quad (15-18)$$

Then $L_R = L_2 = 0.33 L_{10}$. (Note that this factor can be obtained directly from the chart, Fig. 15-8.) If 10,000 hours of life are required at 98 % reliability, then a L_{10} life of 30,300 hours would be required. For one company's bearings, the average or mean life is approximately 4 times L_{10} . Median life L_{50} is approximately 3.5 times L_{10} .

System reliability is encountered when it is desired to consider the probability that all of several bearings will survive to a certain life, that is,

$$\text{reliability(system)} = R_1 \times R_2 \times R_3 \dots \times R_n \quad (15-19)$$

where R_1 , R_2 , and so on, represent the reliability of each bearing in a system to a required system life.

C. Second Example

What is the reliability of a system that requires 6,000 hours of life when the rated lives of the four bearings in the system are 12,000, 10,000, 9,000, and 8,000 hours?

Rated Life	System Life as % of Rated Life	% Reliability Bearing to System Life
12,000	50	96
10,000	60	95
9,000	66.7	94
8,000	75	93

$$\begin{aligned} \text{reliability(system)} &= 0.96 \times 0.95 \times 0.94 \times 0.93 \\ &= 0.80 \text{ or } 80\% \text{ for } 6,000 \text{ hours} \end{aligned}$$

The L_{10} life of a system life for a number of bearings each having the same or a different L_{10} life is

$$L_{10\text{system}} = \left[\left(\frac{1}{L_{10A}} \right)^{3/2} + \left(\frac{1}{L_{10B}} \right)^{3/2} + \cdots + \left(\frac{1}{L_{10n}} \right)^{3/2} \right]^{-2/3} \quad (15-20)$$

For example, if four bearings in a system each had an L_{10} life of 3,000 hours at 50 rpm, the system L_{10} life would be approximately 1,200 hours.

D. Bearing Failures (9)

Normally, the cause of bearing failure is rolling contact fatigue with subsurface crack initiation occurring at nonmetallic inclusions or carbides. The major factors that lead to premature failure are incorrect fitting, excessive preloading during installation, insufficient or unsuitable lubrication, overloading, impact loading, vibration, excessive operating or environmental temperature, contamination by abrasive matter, ingress of harmful liquids, and stray electric currents. The deleterious effects resulting from the above conditions are flaking or pitting (fatigue), fluting (grooved pitting), cracks or fractures, rotational creep, smearing, wear, fretting, softening, indentation, case crushing (heavy loads, thin case, soft core), and corrosion.

Proper lubrication of bearings is important for good performance. The intent of lubrication is to prevent direct metal-to-metal contact. There are two types of oil films: the *reaction film* and the *elastohydrodynamic film*. The reaction film is also known as a *boundary lubricant* and is produced by physical adsorption and/or chemical reaction to form a desired film that is soft and easily sheared but difficult to penetrate or remove from the surface. The elastohydrodynamic film forms dynamically on the wear surface as a function of surface speed. This film is very thin, has a very high shear strength, and is only slightly affected by compressive loads as long as constant temperature is maintained. Analysis of wear debris in a lubricant after a period of service can provide information as to the nature and extent of wear processes.

The basic life rating of a bearing assumes that the lubricant film thickness is at least equal to the composite roughness of the contacting surfaces σ_q , where

$$\sigma_q = \sqrt{R_{q1}^2 + R_{q2}^2} \quad (15-21)$$

and R_{q1} and R_{q2} are the root mean square (RMS) roughness measurements of the two surfaces. The film thickness divided by the composite roughness is designated as λ , and the fatigue life increases with increase in λ . The mode of bearing fatigue failure is also influenced by λ . For values of λ in the range of 1.0 – 3.0, fatigue cracks initiate at subsurface inclusions and surface roughness is of relatively minor importance. When the value of λ is less than 1.0, surface roughness is of much greater importance. A common cause of bearing failure, known as *burnup*, is due to inadequate lubrication, too high a preload, or excessive speed. During burnup, the bearing temperature rises and the material flows plastically, thereby destroying the bearing geometry.

VIII. CASE STUDY: FAILURE OF A RAILROAD CAR AXLE

During the late 1970s and early 1980s, weight saving was a strong driving force in the design of cars, trucks, buses, and trains because of anticipated fuel shortages. In one case involving passenger trains, hollow axles were substituted for solid axles to save weight. These axles were equipped with press-fitted tapered roller bearing assemblies that transferred the car loading to the axles, then to the wheels, and finally to the tracks. The cars had not been in service for long when an axle failed on one of them, and a wheel came off. Fortunately, there were no injuries. Examination of the failed axle revealed that it had been worn and overheated where the bearing had been seated. The wheel failure prompted inspection of the other axles in the fleet, and in many cases, excessive wear at the bearing seat was found. Excessively worn axles were taken out of service. To guard against any further failures of the axles while a fix was being developed, temperature-sensing devices were installed in the wheel hubs. These devices were examined for signs of overheating at selected stops along the route of the trains. Unfortunately, these examinations were time-consuming and resulted in considerable delay and expense. In addition, ultrasonic inspections of the bearing-axle interfaces were made to determine if a gap had developed due to excessive wear. These examinations were facilitated by the fact that the axles were hollow. When excessive wear was found, the axle was removed from service.

The use of hollow axles was not new. They had been used successfully before, but in prior usage the ratio of the inside to the outside diameter had been 0.5. In the case under consideration, the ratio was 0.6. In other words, the axles under discussion were more hollow than the older ones had been, and this turned out to have serious consequences. An analysis was carried out to determine how the axles deformed under load. It was found that the residual compressive stress on the bearing after pressing the bearing onto the axle was less for the hollow axle than for the solid axle. Insufficient compressive stress on the bearing can encourage interfacial fretting, resulting in the reduction of the interference fit at the interface. It was also found that, in contrast to solid axles, which remain essentially round under load, the cross section of these hollow axles “ovalized” into an elliptical shape under load. Because the interference fit was not sufficiently high, the ovalization caused cyclic relative motion of the bearing with respect to the axle. As a result, at a given location on the axle under the bearing, shear stresses were developed that oscillated in magnitude with each revolution of the axle. These shear stresses, in turn, led to the observed excessive wear at the bearing-axle interface.

The final fix was to replace the hollow axles with solid axles.

IX. GEAR FAILURES (10,11)

The main factors controlling gear life are the accuracy of the tooth geometry, the gear-tooth contact conditions including lubrication, and the material. Figure 15-9 gives an indication of the stresses that are developed in a spur gear tooth as the result of rolling contact with a mating gear tooth. Figure 15-10a is an example of the

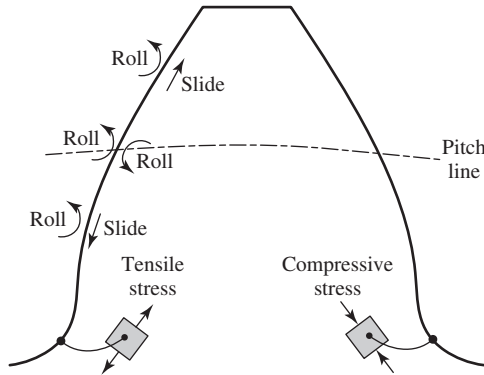


Fig. 15-9. The stresses developed in a spur gear tooth due to rolling contact. (After Alban, 11.)

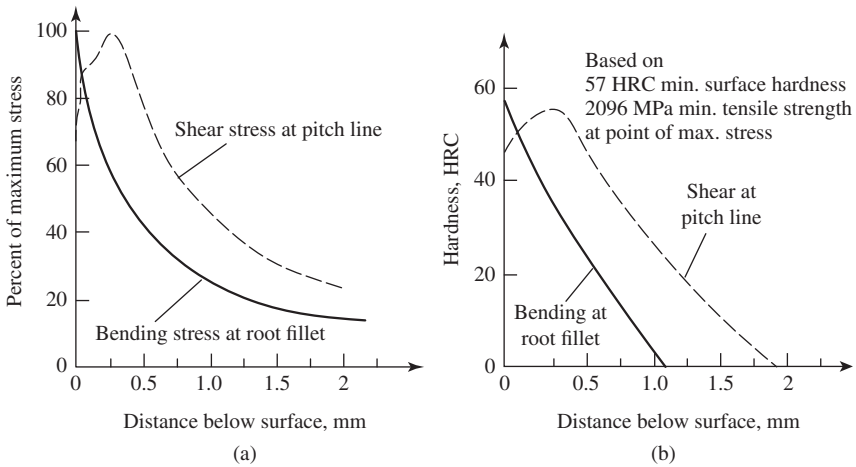


Fig. 15-10. (a) Subsurface stresses in a spur gear tooth. (b) The hardness gradients necessary to prevent subsurface failure. (After Alban, 11.)

subsurface stresses developed on contact between mating gear teeth, and Fig 15-10*b* shows the level of subsurface hardness required to resist these stresses. Gears can fail in a number of different modes, and as with bearings, an increase in the level of noise or vibration is an indication of impending failure. The leading cause of failure is either tooth bending, which leads to fatigue crack initiation at the root of a gear tooth, or rolling-contact fatigue, which induces small-scale pitting, which leads to larger-scale spalling. Additional causes of failure are impact, wear, and stress rupture. In at least one instance, the striking of a blade of a boat propeller has been known to cause enough of an impact to rupture gear teeth. In addition, other gear in the gear train contained cracks that were not detected, and a failure occurred shortly

after the gear system was put back into service. Therefore, careful inspection of all gear teeth after an impact is warranted. Each part of a gear tooth surface is in action for only short periods of time. This continual shifting of the load to new areas of cool metal and cool oil makes it possible to load gear surfaces to stresses approaching the critical limit of gear metal without failure of the lubricating film. The maximum load that can be carried by gear teeth also depends upon the velocity of sliding between the surfaces, because the heat generated varies with the rate of sliding and the pressure. Too much frictional heat can cause scuffing and the destruction of tooth surfaces.

A. Gear Material Problems

A number of issues related to materials can contribute to fatigue failure in gears. These include the size and nature of nonmetallic inclusions, poor forging patterns, pitting, banding, segregation, forging laps, and improper material selection. Misidentification has led to the use of an incorrect steel in some instances, and the wrong grade of steel has sometimes been used in weld repairs.

Steel gears are usually case-hardened by carburization, nitriding, or induction hardening, and the properties of the case are important both at the midprofile and at the root radius of the gear tooth. Case depth is usually understood to mean the *effective case depth*, defined as the distance from the surface to the location where the hardness drops to specified level. For a carburized gear, this level is usually 50 HRC, whereas for an induction-hardened gear, the level depends upon the carbon content, being 35 HRC for a steel containing 0.3 wt % carbon and 50 HRC for a steel containing more than 0.53 wt % carbon. The shear stress due to rolling contact is at its maximum about 0.25 mm (0.01 in.) below the surface at the contact region of the mating teeth, and in order to avoid fatigue failure, the hardness in this region is typically specified to be at least 58 HRC at the surface with an effective case depth of 0.5 mm, and the case depth at the root radius where the bending stress is a maximum is specified to be 0.3 mm (0.012 in.).

The carburization process results in a biaxial compressive state of stress in the carburized layer, which is balanced by tensile stresses in the core of the gear tooth. This system of stresses can result in a time-delayed form of cracking of the gear tooth that initiates beneath the surface and that is probably hydrogen-related, as shown in Fig. 15-11. The tendency for this type of fracture increases with case depth, since a greater tensile residual stress will be needed to balance a larger residual compressive force.

Another type of subsurface-initiated failure as the result of cyclic loading has also been observed in gear teeth (12). If the yield strength of the substrate is low and the forces developed along the pitch line are high, case crushing may occur, Fig. 15-12, particularly with a thin case. In cases where induction hardening is used to harden the entire gear, quench cracking can occur. Such a quench crack is distinguishable from a forging lap because the fracture surface of a quench crack is free of scale or oxides. The induction hardening process needs to be controlled to avoid irregular hardening patterns that can lead to easy fatigue failure.

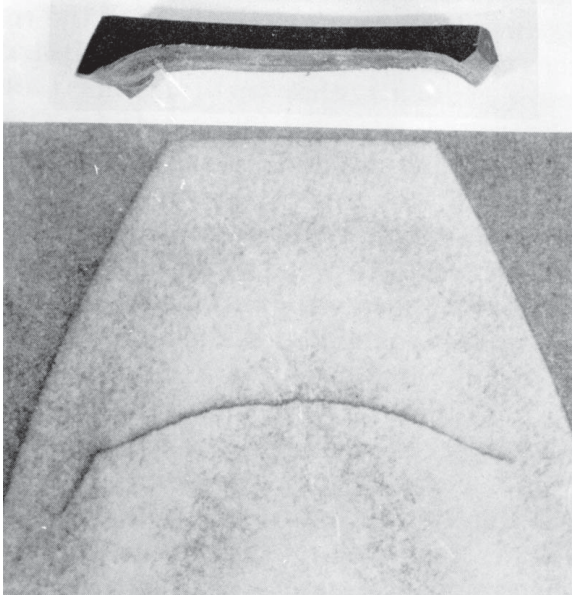


Fig. 15-11. An example of a gear tooth failure due to carburizing-induced residual stresses. (From Alban, 11. With permission of ASM International.)

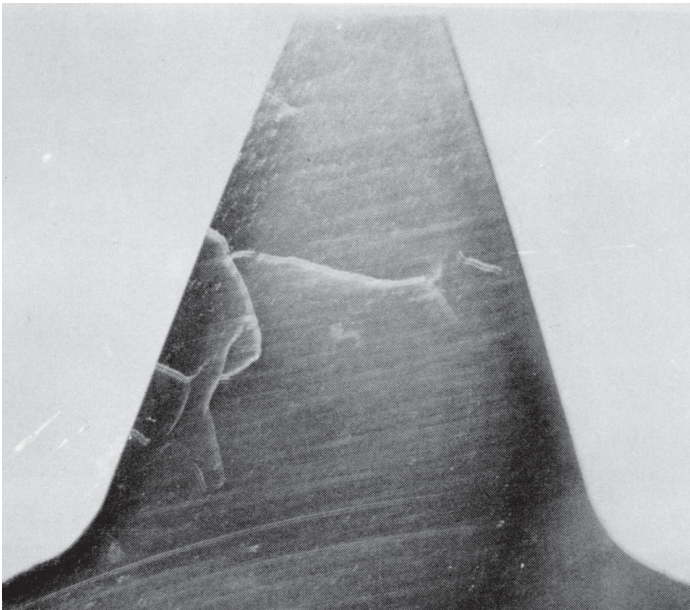


Fig. 15-12. An example of case crushing. (From Mackaldener and Olssen, 12.)

B. Design and Manufacturing Problems

Problems associated with design and manufacturing arise because of the presence of geometric stress raisers such as oil holes, excessive machining of the case, undercutting, the characteristics of the gear teeth, and dimensional changes due to heat treating. In addition, the grinding process usually leaves the surface in a state of residual tensile stress, and may also cause grinding checks and burns.

X. SUMMARY

In this final chapter, we have reviewed the role of contact stresses and wear in determining the useful lifetimes of roller bearings, bushings, and gears. Case studies were used to illustrate a number of types of failure involving wear.

REFERENCES

- (1) J. F. Archard and W. Hirst, The Wear of Materials Under Unlubricated Conditions, *Proc. Royal Soc.*, vol. A-236, 1958, pp. 71–73.
- (2) E. Rabinowicz, “Friction and Wear,” in *Mechanical Behavior of Materials*, ed. by F. A. McClintock and A. S. Argon, Addison-Wesley, Reading, MA, 1966, pp. 657–674.
- (3) M. F. Ashby and D. R. H. Jones, *Engineering Materials I*, Pergamon Press, Oxford, UK, 1980, pp. 223–235.
- (4) C. Lutynski, G. Simansky, and A. J. McEvily, Fretting Fatigue of Ti-6Al-4V Alloy, Materials Evaluation Under Fretting Conditions, ASTM STP 780, 10822, ASTM, Conshohocken, PA, 1982, pp. 150–164.
- (5) D. A. Rigney, Sliding Wear of Materials, *Annu. Rev. Mater. Sci.*, vol. 18, 1988, pp. 141–163.
- (6) Tapered Roller Bearings, Section 1, *Engineering Journal*, The Timken Co., Canton, OH, 1972.
- (7) S. Timoshenko, *Theory of Elasticity*, McGraw-Hill, New York, 1934.
- (8) *ASM Metals Handbook*, 8th ed., vol. 10, ASM, Materials Park, OH, 1975, p. 428.
- (9) C. Moyer, Fatigue and Life Prediction of Bearings, *ASM Handbook*, vol. 19, ASM, Materials Park, OH, 1996, pp. 355–362.
- (10) D. W. Dudley, Fatigue and Life Prediction of Gears, *ASM Handbook*, vol. 19, ASM, Materials Park, OH, 1996, pp. 345–354.
- (11) L. E. Alban, *Systematic Analysis of Gear Failures*, ASM, Materials Park, OH, 1985.
- (12) M. Mackaldener and M. Olssen, Interior Fatigue Fracture of Gear Teeth, *Fat. Fract. Eng. Mater. Struct.*, vol. 23, 2000, pp. 283–292.
- (13) R. J. Roark and W. C. Young, *Formulas for Stress and Strain*, fifth ed., McGraw-Hill, New York, 1982.

PROBLEMS

- 15-1.** The outer radius of a hollow steel axle is designated as a , the inner radius as b . The change in a , Δa , due to an external pressure q is given on p. 504 in Roark and Young (13) as

$$\Delta a = \frac{-qa}{E} \left(\frac{a^2 + b^2}{a^2 - b^2} - \nu \right)$$

For a given Δa , plot the variation in q as a function of b/a . $E = 210$ GPa, $\nu = 0.25$, $a = 20$ cm

- 15-2.** (a) What is the life adjustment factor for a bearing reliability of 95 %?
 (b) Determine the B5 life for a system containing four bearings whose rated lives are 12,000, 10,000, 9,000, and 8000 hours.
- 15-3.** What is the reliability of a system containing four bearings that requires 5,000 hours life when the rated lives of the bearings are 12,000, 10,000, 9,000, and 8000 hours?

Concluding Remarks

The previous 15 chapters have provided a basic and, it is hoped, an interesting introduction to the subject of metal failures. For more extensive information, there is a large body of literature that deals with this subject. The ASM Metals Handbook Series provides additional details, in particular Volume 19 on fatigue and fracture, Volume 11 on failure analysis and prevention, and Volume 12 on fractography. The weekly publication *Aviation Week and Space Technology* provides excellent coverage of aircraft accidents and safety-related matters. The Internet is now another source of information. For example, a 1-year conference on pipeline integrity is available. Failures differ greatly in terms of loading conditions, environments, and material characteristics, and the competent investigator should be aware of pertinent information already in the literature in carrying out a failure analysis.

Some additional sources of information concerning fatigue and failures are listed below.

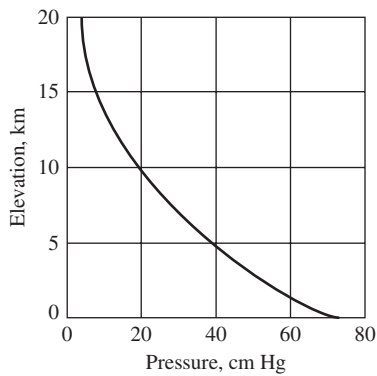
- C. R. Brooks and A. Choudhury, *Metallurgical Failure Analysis*, McGraw-Hill, New York, 1993.
- V. J. Colangelo and F. A. Heiser, *Analysis of Metallurgical Failures*, Wiley Interscience, New York, 1987.
- J. A. Collins, *Failure of Materials in Mechanical Design*, Wiley Interscience, New York, 1981.
- D. R. H. Jones, *Materials Failure Analysis*, International Series on Materials Science and Technology, Pergamon, Press, Oxford, 1993.
- G. A. Lange, ed., *Systematic Analysis of Technical Failures*, DGM Informations Gesellschaft, Oberursel, Germany, 1986.
- J. M. Newman, Jr., "Prediction of Fatigue Crack Growth under Variable-Amplitude and Spectrum Loading Using a Closure Model," in *Design of Fatigue and Fracture Resistant*

- Structures, in ASTM STP 761, P. R. Abelkis and C. M. Hudson, eds., ASTM, Conshohocken, PA, 1982, pp. 255–277.
- S.-I. Nishida, *Failure Analysis in Engineering Applications*, Butterworth Heinemann, Oxford, 1992.
- C. E. Witherell, *Mechanical Failure Avoidance*, McGraw-Hill, New York, 1994.
- D. J. Wulpi, *How Components Fail*, 2nd ed., ASM, Materials Park, OH, 1999.
- B. Ziegler, Y. Yamada, and J. C. Newman, Jr., “Crack Growth Predictions Using a Strip-Yield Model for Variable-Amplitude and Spectrum Loading,” Second Symposium on Structural Durability, Darmstadt, Germany, 2008, pp. 1–15.

Solutions to Problems

CHAPTER 1

1-1. Solution:



$$p = 76 - 8.45h + 0.285h^2$$

At 2.37 km, $p = 76 - 8.45 \times 2.37 + 0.285 (2.37)^2 = 57.6 \text{ cm Hg}$

Note that 76 cm Hg is equivalent to $1.013 \times 10^5 \text{ Pa}$

$$\frac{57.6}{76} = \frac{x}{1.013 \times 10^5 \text{ Pa}}, x = 0.76 \times 10^5 \text{ Pa} = 0.076 \text{ MPa}$$

At 10 km, $p = 76 - 8.45(10) + 0.285(100) = 20.0 \text{ cm Hg}$

$$\frac{20}{76} = \frac{x}{1.013 \times 10^5}, x = 0.027 \text{ MPa}$$

$$\Delta p = 0.076 - 0.027 = 0.049 \text{ MPa}$$

1-2. (a) As designed: Bearing load at upper balcony is $5 \times 10^4 N$

(b) As built: Bearing load at upper balcony is $1 \times 10^5 N + 0.5 \times 10^5 N = 1.5 \times 10^5 N$

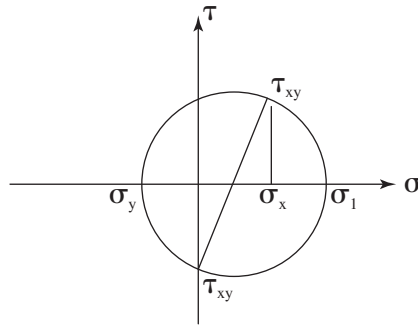
CHAPTER 2

2-1. (a) $\sigma_h = 0.049 \times 3.7/2 \times 0.00091 = 99.6 \text{ MPa}$

(b) $99.6 \times 3 = 298.8 \text{ MPa}$

Note that although a repeated stress of 99.6 MPa would probably not cause a fatigue failure in a structural aluminum alloy, a repeated stress of 298.8 MPa would.

2-2. A thin-walled box beam is subjected to bending and torsion. Assume that the crack propagates in a direction that is normal to the first principal stress. Bending results in a longitudinal tensile stress in the lower surface of the beam where cracking occurs. The Mohr circle for this case (tension plus shear) is shown.



The angle 2θ , which is twice the angle between the direction of the first principal stress and the longitudinal direction x , is 60° . From the Mohr circle diagram,

$$\tan 2\theta = \frac{\tau_{xy}}{\sigma_x/2} = \sqrt{3}, 2\theta = 60^\circ$$

$$\tau_{xy} = (\sqrt{3}/2)\sigma_{xy}; \quad \sigma_{xy}/\tau_{xy} = \sigma_{xy}/(\sqrt{3}/2)\sigma_{xy} = 1.15$$

and the ratio of the bending stress to the shear stress is

$$\sigma_x = 2\tau_{xy}/\sqrt{3} = 1.15$$

Note that the radius of the Mohr circle is

$$r = \sqrt{(\tau^2 + \sigma_x^2/4)} = \sqrt{[(3/4)\sigma_x^2 + \sigma_x^2/4]} = \sigma_x$$

Therefore, the first principal stress $= \sigma_x(1/2 + 1) = 1.5 \sigma_x$.

2-3. (a) In plane stress

At $a \pm 0$,

$$\varepsilon_y = \frac{207 \text{ MPa}}{200,000 \text{ MPa}} = 0.00104, \varepsilon_x = \varepsilon_z = -0.25 \times 0.00104 = -0.00026$$

$$\Delta = \varepsilon_x + \varepsilon_y + \varepsilon_z = 0.00104 - 0.00026 = 0.00078$$

At $0 \pm a$,

$$\varepsilon_x = \frac{-69 \text{ MPa}}{200,000 \text{ MPa}} = -0.00035, \varepsilon_y = \varepsilon_z = +0.25 \times 0.00035 = 0.00009$$

$$\Delta = -0.00035 + 0.00009 = -0.00028$$

(b) In plane strain

At $\pm a$, $0 \varepsilon_z = 0$, $\sigma_z = \nu\sigma_y$, $\sigma_x = 0$, $\sigma_y = 207 \text{ MPa}$,

$$\sigma_z = 0.25 \times 207 = 51.75 \text{ MPa}$$

$$\varepsilon_y = \frac{1}{E}(\sigma_y - \nu\sigma_z) = \frac{1}{200,000}(207 - 0.25 \times 51.75) = 0.00097$$

(slightly less than in plane stress)

$$\varepsilon_x = \frac{1}{200,000}[-0.25 \times (207 + 51.75)] = -0.00032$$

(slightly more than in plane stress)

$$\Delta = -0.00032 + 0.00097 = 0.00065 \text{ (slightly less than in plane stress)}$$

At $0 \pm a$, $\varepsilon_z = 0$, $\sigma_z = \nu\sigma_x$, $\sigma_y = 0$;

$$\sigma_x = -69 \text{ MPa}, \sigma_z = -17.25 \text{ MPa}$$

$$\varepsilon_x = \frac{1}{E}(\sigma_x - \nu\sigma_z) = \frac{1}{200,000}[-69 - 0.25(-17.25)] = -0.00032$$

(slightly less than in plane stress)

$$\varepsilon_y = \frac{1}{200,000}[-0.25(-69 - 17.25)] = 0.00011$$

(slightly more than in plane stress)

$$\Delta = -0.00032 + 0.00011 = -0.00022 \text{ (slightly less than in plane stress)}$$

2-4. Consider a cube with each edge equal to 1.0 length units. In this case $\Delta l = \varepsilon_x$, etc.

The original volume, V , is 1.0.

The volume under stress is $(1 + \varepsilon_x)(1 + \varepsilon_y)(1 + \varepsilon_z) = 1 + \varepsilon_x + \varepsilon_y + \varepsilon_z +$ higher order terms that can be neglected. Hence $\Delta V = \varepsilon_x + \varepsilon_y + \varepsilon_z$, so $\frac{\Delta V}{V} = \Delta = \varepsilon_x + \varepsilon_y + \varepsilon_z$.

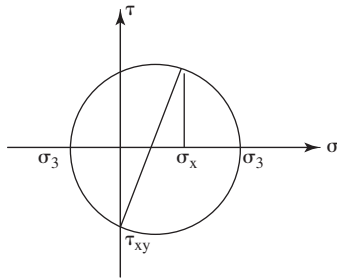
CHAPTER 3

3-1. 1. Use the Mohr circle to determine the principal stresses

$$\sigma_1 = \frac{\sigma_x}{2} + \left(\frac{\sigma_x^2}{4} + \tau_{xy}^2 \right)^{1/2}$$

$$\sigma_2 = 0$$

$$\sigma_3 = \frac{\sigma_x}{2} - \left(\frac{\sigma_x^2}{4} + \tau_{xy}^2 \right)^{1/2}$$



For the von Mises criterion for yielding, substitute in Eq. 3-18 to obtain

$$\left(\frac{\sigma_x}{\bar{\sigma}} \right)^2 + 3 \left(\frac{\tau_{xy}}{\bar{\sigma}} \right)^2 = 1 \quad (1)$$

For the Tresca criterion for yielding, substitute in Eq. 3-23 to obtain

$$(\sigma_x^2/4 + \tau_{xy}^2)^{1/2} = k = \bar{\sigma}/2$$

$$(\sigma_x^2/4 + \tau_{xy}^2) = (\bar{\sigma}/2)^2$$

$$(\sigma_x^2 + 4\tau_{xy}^2) = (\bar{\sigma})^2$$

$$(\sigma_x^2/\bar{\sigma}^2 + 4\tau_{xy}^2/(\bar{\sigma})^2) = 1$$

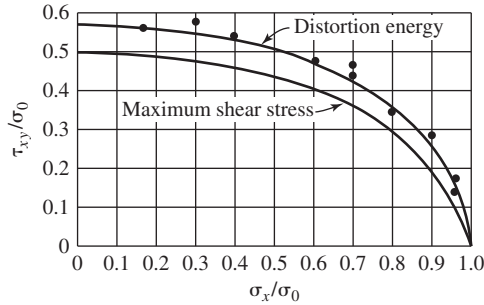
$$\left(\frac{\sigma_x}{\bar{\sigma}}\right)^2 + 4\left(\frac{\tau_{xy}}{\bar{\sigma}}\right)^2 = 1 \quad (2)$$

(or from the Mohr circle, $(\frac{\sigma_x}{2})^2 + \tau_{xy}^2 = k^2 = (\frac{\bar{\sigma}}{2})^2$)

Equations 1 and 2 each define an ellipse, as shown in the accompanying figure.

Tresca: Maximum shear stress

Von Mises: Distortion energy



3-2. $\sigma_{kyd} = k - 2k\theta$. θ in this case is equal to $-(\frac{\pi}{2} - \frac{1}{2}\frac{\pi}{4} = \frac{3}{8}\pi)$.

Therefore, $\sigma_{hyd} = k + 2k\frac{3}{8}\pi = k + \frac{3}{4}\pi k$, and $\sigma_1 = k + k + \frac{3}{4}\pi k = 2k(1 + \frac{3}{8}\pi)$.

From Eq. 3-34,

$$\frac{\sigma_1}{2k} = 2.18 = 1 + \ln\left(1 + \frac{x}{R}\right), \ln\left(1 + \frac{x}{R}\right) = 1.18, \left(1 + \frac{x}{R}\right)$$

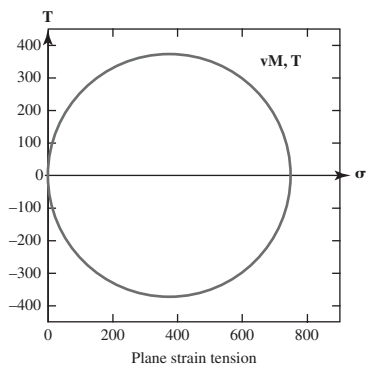
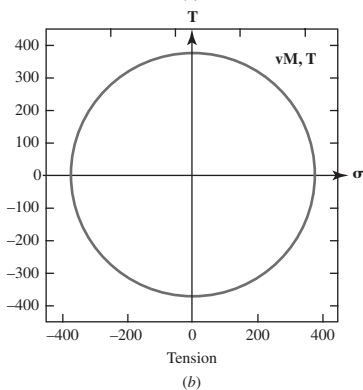
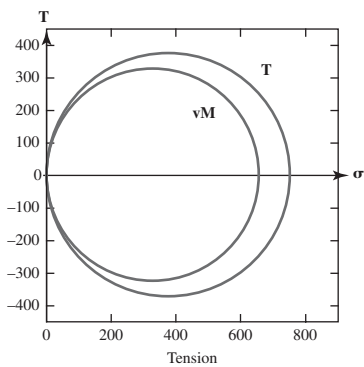
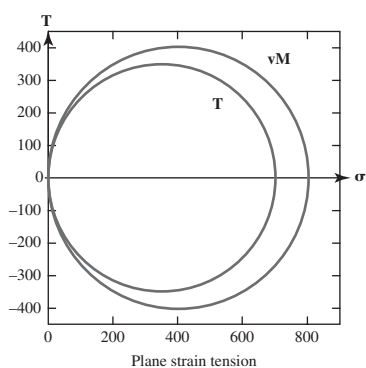
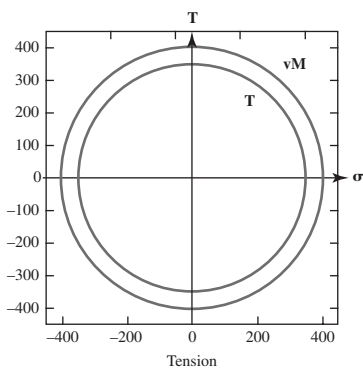
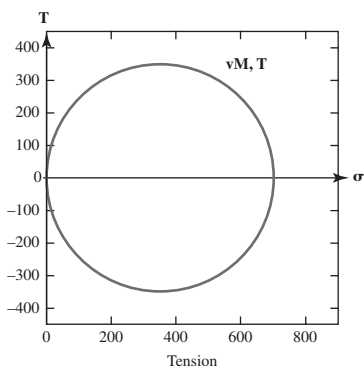
$$= 3.25, \frac{x}{R} = 2.25, x = (0.25) 2.25 = 0.56 \text{ mm}$$

$$\sigma_1 = 2.18 (2k) \quad k = \frac{\sigma_y}{2} \text{ Tresca; } k = \frac{\sigma_y}{\sqrt{3}} \text{ von Mises}$$

According to the Tresca criterion, σ_1 is 2.18 times the yield stress in simple tension.

According to the von Mises criterion, σ_1 is $2.18 \times 1.15 = 2.51$ times the yield stress in simple tension.

Note that when the yield stress in torsion (pure shear) is taken as the basis for the yield criterion rather than the yield stress in tension, the Tresca hexagon circumscribes the von Mises circle. For tension loading, according to the Tresca criterion, the tensile yield will equal $2k$, but according to the von Mises criterion, the tensile yield stress will be equal to $(2/\sqrt{3})k = 2.30k$.



- 3-4.** $\sigma_y = 275$ MPa, $\sigma_1 - \sigma_3 = 2k = 275 < 300$, material yields according to the Tresca criterion.

$$\sigma_{ys} = 275 \text{ MPa}, \sigma_1 = 300 \text{ MPa}, \sigma_2 = 150 \text{ MPa}, \sigma_3 = 0$$

$$\bar{\sigma} = \sqrt{\frac{1}{2}[(300)^2 + (150 - 300)^2 + (150)^2]} = 259.8 \text{ MPa} < 275 \text{ MPa}$$

The effective stress (or equivalent stress) is less than the yield stress; therefore, according to the Von Mises criterion, the biaxially loaded specimen will not yield.

The Tresca Mohr circle is centered at $275/2 \text{ MPa} = 137.5 \text{ MPa}$ = radius of circle

The Von Mises Mohr circle is centered at $275 \frac{2}{\sqrt{3}} \frac{1}{2} = 158.8 \text{ MPa}$ = radius of circle

According to the Von Mises criterion, for the same ratio of stresses, yield would occur when $\sigma_1 = 317.6 \text{ MPa}$.

- 3-5. (a)** Find σ_1 first:

$$\sigma_1 = \frac{\text{Pressure} \times \pi R^2}{2\pi Rt} = \frac{\text{Pressure} \times R}{2t} = \frac{(5 \times 10^6 \text{ Pa}) \times (1.25 \text{ m})}{2.(5 \times 10^{-3} \text{ m})} = 625 \text{ MPa}$$

Under the plane-stress condition, $\sigma_3 = 0$; $\sigma_1 = \sigma_2$ because of the symmetry; thus, the equivalent normal stress ($\bar{\sigma}$) can be obtained by using Eq. 2-24a:

$$\bar{\sigma} = 1/\sqrt{2}[(\sigma_2)^2 + (-\sigma_1)^2]^{1/2}$$

Substitute $\sigma_1 = \sigma_2 = 625 \text{ MPa}$ in the above equation and obtain $\bar{\sigma} = 625 \text{ MPa}$.

$$\therefore \bar{\sigma}(625 \text{ MPa}) < \sigma_{ys}(1,000 \text{ MPa})$$

Thus, the thin-walled container will not yield under the Von Mises criterion.

- (b)** For a safety factor of 4.0, we have $4 \times \bar{\sigma} = 2,500 \text{ MPa}$, which is higher than the yield strength of the alloy steel (1,000 MPa).

$$\therefore 4 \times \bar{\sigma}(2,500 \text{ MPa}) > \sigma_{ys}(1,000 \text{ MPa})$$

The yield strength of the container will not be high enough when the safety factor of 4.0 is used to guard against yielding. Thus, the thickness of the container has to be increased or the operating pressure has to be reduced. Alternatively, a steel with an extremely high yield strength (2,500 MPa) should be used.

3-6. Find the shear stress (τ):

$$\tau = \frac{5000 \text{ N}}{\pi (5 \times 10^{-3} \text{ m})^2} = 63.66 \text{ MPa}$$

Since τ (63.66 MPa) is less than the shear strength of the cylindrical fillet (400 MPa), the fillet with $D = 10 \text{ mm}$ will be sufficient to prevent shear yielding.

For a safety factor of 4.0, the selected fillet is still sufficient to prevent shear yielding because $4\tau = 254.64 \text{ MPa}$ is still smaller than the shear strength of the cylindrical fillet (400 MPa).

The design above does not include consideration of fatigue loading. The corners of the square fillet are the regions of high stresses. The increased stresses in these areas make them more prone to fatigue cracking. In order to prevent fatigue failure of the fillet, shaft, and impeller, the fillet can be redesigned to have round corners.

3-7. (a) Total force on the cap = Pressure $\times \pi R^2 = 20 \text{ MPa} \times (\pi (12.5 \times 10^{-3} \text{ m})^2) = 9,817.5 \text{ N}$

Note: $1 \text{ N/m}^2 = 1 \text{ Pa}$.

(b) The tensile force in each bolt = $\frac{9,821 \text{ N}}{6} = 1,636.25 \text{ N}$

(c) The tensile stress in each bolt = Tensile force in each bolt / Area of a bolt

$$= \frac{1,636.25 \text{ N}}{50 \times 10^{-6} \text{ m}^2} = 32.73 \text{ MPa}$$

(d) The tensile stress in each bolt is (32.73 MPa) $< \sigma_{ys}$ (400 MPa); therefore, all the bolts will not plastically deform when the vessel has a hydrogen pressure of 20 MPa.

(e) With a safety factor of 4.0, the tensile stress in each bolt would be $4 \times 32.7 \text{ MPa} = 131 \text{ MPa}$, which is still less than σ_{ys} (400 MPa). \therefore 6 bolts are sufficient to safeguard against yielding with a safety factor of 4.0.

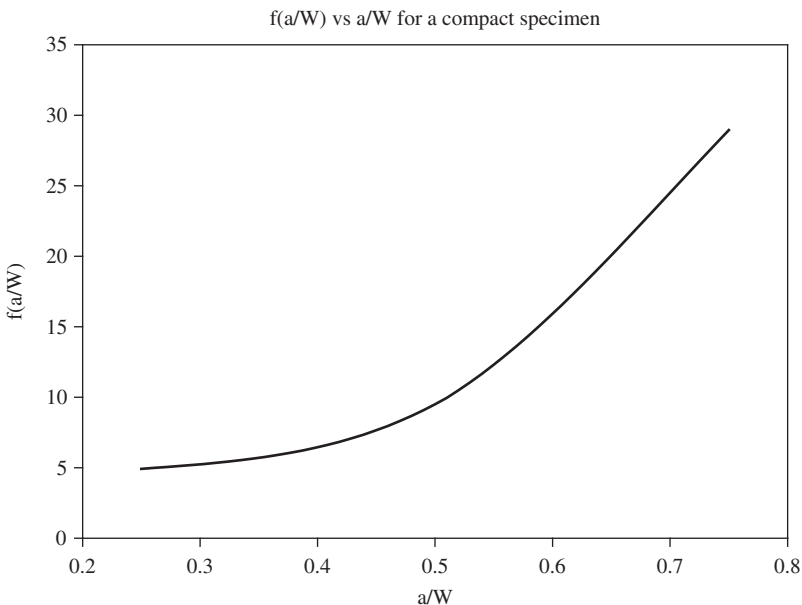
(f) The typical operation of each experiment involves the pressurization of the vessel with a hydrogen pressure of 20 MPa, then an evacuation (down to 0.1 torr), and repetition of these pressurizations and evacuations 1,000 times. If no pretension is applied to the bolts, each bolt will be subjected to a tensile loading ($\sim 33 \text{ MPa}$) and then unloading ($\sim 0 \text{ MPa}$) during each pressurization/evacuation cycle, which results in fatigue loading on the bolts with a stress amplitude of $\sim 16 \text{ MPa}$. A safety factor of 4 would lead to a stress amplitude of 64 MPa ($4 \times 16 \text{ MPa}$). If the fatigue limit is one-third of the yield strength, then the fatigue limit of the bolt would be 133 MPa. Thus, the design is sufficient even when the fatigue loading is considered.

However, the fatigue loading can be further reduced if each bolt is pretightened to a tensile stress of 33 MPa. Under this condition, the stress amplitude

during each pressurization/evacuation cycle is zero, that is, there is no fatigue loading! The principle is as follows. As shown in the figure below, the pretension of 33 MPa in each bolt will compress the cap and flange together with a compressive stress. As the pressurization starts, the cap will be pushed by the hydrogen gas and the stress has to be carried by the bolts. At the end of the pressurization, the pressure inside the vessel is 20 MPa, which generates a 33 MPa tensile stress in each bolt. If this 33 MPa tensile stress generated by the hydrogen pressure were directly added to the pretension of 33 MPa, the tensile stress in each bolt would have been 66 MPa. However, this is not the case at all. When the cap is pushed by the hydrogen gas, the compressive stress between the cap and flange is reduced. At the end of the pressurization, the compressive stress between the cap and flange is actually reduced to zero because in this particular condition, there is no compression between the cap and flange (that is, the precompression due to the pretension in bolts is completely released when the pressure in the vessel reaches 20 MPa). As a result, the tensile stress in each bolt remains 33 MPa during the entire pressurization/evacuation cycle. This way the fatigue loading becomes zero, and the bolts will never fail because of fatigue.

CHAPTER 4

4-1.



- 4-2. For a center-cracked panel, $K_I = \sigma \sqrt{\pi a} \sqrt{\sec \pi a/W}$, $W = 0.2$ m, $a = 0.05$ m

$$K_I = \sigma \sqrt{\pi \times 0.05} \sqrt{\sec \pi \times 0.25} = 0.47\sigma$$

For a compact specimen, $K_I = \left(\frac{P}{BW^{1/2}} \right) f\left(\frac{a}{W}\right)$, where P is the load $f(a/W)$ is given in Problem 3-1 and as Eq. 3-20. For $a/W = 0.5$, $f(a/W) = 9.65$. Then equate the two expressions for K_I ,

$$0.47\sigma = 0.47 \frac{P_{CC}}{BW_{CC}} = 9.65 \frac{P_{CT}}{BW_{CT}^{1/2}}$$

The thickness, B , is the same for each specimen; therefore,

$$\frac{P_{CC}}{P_{CT}} = \frac{9.65}{0.47} \frac{W_{CC}}{W_{CT}^{1/2}} = 20.53 \frac{0.2 \text{ m}}{0.050 \text{ m}^{1/2}} = 18.4$$

The point of the problem is that the use of the compact specimen rather than the center-cracked panel entails much less material and a much lower load, both of which are advantageous in a test program.

- 4-3. Determine a residual strength diagram for a center cracked plate of an aluminum alloy.

$$\sigma_{YS} = 350 \text{ MPa}, K_{IC} = 50 \text{ MPa}\sqrt{\text{m}}, W = 10 \text{ in.} = 0.254 \text{ m}, B = B,$$

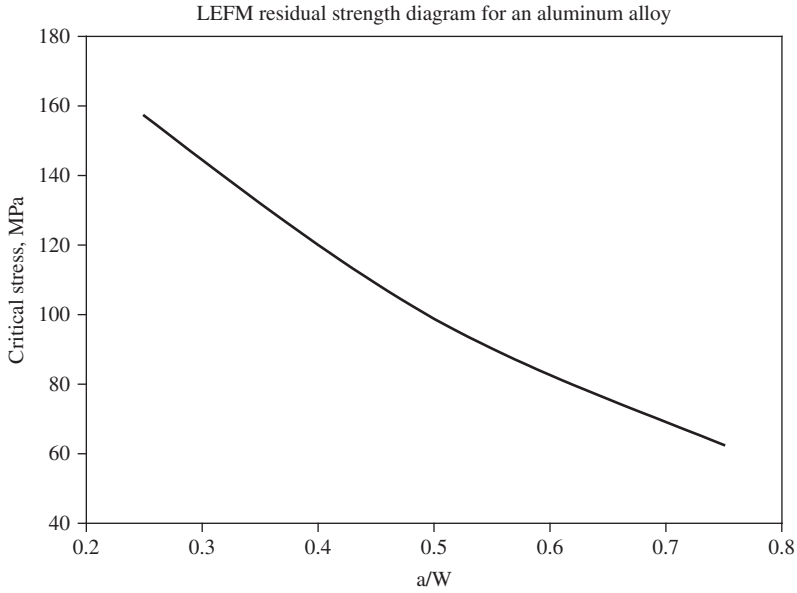
for $0.25 < 2a/W < 0.75$

$$\text{Eq. 3-16, } K_I = \sigma \sqrt{\pi a} \sqrt{\sec \pi a/W}$$

$$\sigma_c = \frac{50}{\sqrt{\pi a} \sqrt{\sec \pi a/0.254}}$$

Crack length = $2a$

a, m	2a/W	σ_c , MPa
0.03	0.25	157.2
0.06	0.50	98.8
0.09	0.75	62.5



4-4.

Steel	Thickness m	σ_{YS} MPa	K_{Ic} MPa \sqrt{m}	$\sigma_{YS}/2$ MPa	$\sigma(K_{Ic})/1.1$ MPa	Dm	Lm	W/ ρ
A	0.08	965	280	<u>482.5</u>	2023	5.15	48.0	65.4
B	0.06	1,310	66	655	<u>477</u>	3.81	87.7	<u>64.4</u>
C	0.04	1,700	40	850	<u>318</u>	1.54	536.9	104.1

σ_w , the working stress, is the lesser of $\frac{\sigma_{YS}}{2}$ or $\frac{\sigma(K_{Ic})}{1.1}$

$$\sigma(K_{Ic}) = \frac{K_{Ic}}{0.71\sqrt{\pi a}}, a = 0.01 \text{ m}, \sigma(K_{Ic}) = 7.95K_{Ic}$$

The working stress for each steel is underlined in the table.

$$D = \frac{2t\sigma_w}{p}, p = 15 \text{ MPa}, D = 0.133 \times t\sigma_w$$

$$\text{Volume} = 1,000 \text{ m}^3 = \pi D^2 L / 4, L = \frac{4,000}{\pi D^2}$$

Weight, $W = \rho(\pi DtL + 2\pi D^2t/4)$, where ρ is the density in Mg/m^3
Select steel B

- 4-5.** For the embedded sharp penny-shaped crack, the fracture toughness (K_{IC}) of this material can be obtained by using $K_{IC} = (2/\pi)\sigma_c\sqrt{\pi a}$.

$$\therefore K_{IC} = (2/\pi)700 \text{ MPa}\sqrt{\pi(0.0125\text{m})} = 88.31 \text{ MPa}\sqrt{\text{m}}$$

Using Eq. (3-33b) to find out whether or not the fracture-toughness value would be a valid number for the thickness of the sheet $B = 0.75 \text{ cm}$:

$$B \geq 0.0635 \frac{K_{IC}^2}{\sigma_Y^2} = 0.0635 \frac{(88.31 \text{ MPa}\sqrt{\text{m}})^2}{(1100 \text{ MPa})^2} = 4.09 \times 10^{-4} \text{ m} = 0.041 \text{ cm}$$

$$\therefore B \geq 0.041 \text{ cm}$$

Here the thickness of the sheet is 0.75 cm , which is larger than the required thickness, 0.041 cm , in order to achieve a plane-strain condition during testing. Thus, the fracture-toughness value will be the valid number.

From the calculation in (b), the minimum thickness for valid K_{IC} measurement is 0.041 cm .

- 4-6.** First, find out the σ_{des} at $T = 100^\circ\text{C}$, which is 40% of the yield strength at $T = 100^\circ\text{C}$. Using the given temperature dependence of the yield strength curve, we can obtain $\sigma_{YS} = 605 \text{ MPa}$. Therefore,

$$\sigma_{des} = 0.4\sigma_{YS} = 0.4 \times 605 \text{ MPa} = 242 \text{ MPa}$$

Then we must calculate the stress intensity in each step for the recommended start-up procedure and the cold start-up procedure.

(a) Recommended start-up procedure

- (i) At the start-up step with the rotor at 50% of the normal rotor design rpm level, the rotor stress is (σ)

$$\frac{\sigma}{\sigma_{des}} = \frac{\omega^2}{\omega_{op}^2} = \frac{(0.5\omega_{op})^2}{\omega_{op}^2} = 0.25 \Rightarrow \therefore \sigma = 242 \text{ MPa}(0.25) = 60.5 \text{ MPa}$$

Thus, the stress intensity factor for the start-up ($K_{(i)}$) is

$$K_{(i)} = \frac{1.12}{A} \sigma \sqrt{\pi a} = \frac{1.12}{\left(\frac{\pi}{2}\right)} (60.5 \text{ MPa}) \sqrt{\pi(2.5 \times 10^{-2} \text{ m})} = 12.09 \text{ MPa}\sqrt{\text{m}}$$

From the temperature dependence of the fracture toughness curve, K_{IC} is about $56 \text{ MPa}\sqrt{m}$ at $T = 20^\circ\text{C}$. Since $K_{(i)} < K_{IC}$, this start-up step is okay.

- (ii) For the proof-test step, which occurs after the rotor temperature = 100°C , the rpm is increased to $1.15 \omega_{op}$ and the rotor stress becomes (σ)

$$\frac{\sigma}{\sigma_{des}} = \frac{\omega^2}{\omega_{op}^2} = \frac{(1.15\omega_{op})^2}{\omega_{op}^2} = 1.3225 \Rightarrow \therefore \sigma = 242 \text{ MPa}(1.3225) = 320.04 \text{ MPa}$$

Therefore, the stress intensity factor for the proof-test step ($K_{(ii)}$) is

$$K_{(ii)} = \frac{1.12}{A} \sigma \sqrt{\pi a} = \frac{1.12}{\left(\frac{\pi}{2}\right)} (320.04 \text{ MPa}) \sqrt{\pi (2.5 \times 10^{-2} m)} = 63.96 \text{ MPa}\sqrt{m}$$

From the temperature dependence of the fracture toughness curve, K_{IC} is about $126 \text{ MPa}\sqrt{m}$ at $T = 100^\circ\text{C}$. Since the $K_{(ii)} < K_{IC}$, this proof-test step is safe.

Thus, the recommended start-up procedure is a safe operation to bring the turbine rotor (with a surface crack) back to the normal service condition.

- (b) Using the cold start-up procedure by introducing the proof-test condition directly at ambient temperature (10°C), the stress intensity factor for the cold start-up procedure ($K_{cold \text{ start-up}}$) is $63.96 \text{ MPa}\sqrt{m}$. However, at this temperature, K_{IC} is $53 \text{ MPa}\sqrt{m}$ from the temperature dependence of the fracture toughness curve. Therefore, the turbine rotor will fail during the cold start-up procedure because $K_{cold \text{ start-up}} > K_{IC}$. Clearly, the supervisor's judgment in this case was very poor and his decision was not an intelligent one.

CHAPTER 5

- 5-1.** The amount of recycled automobile scrap is limited in steelmaking to avoid hot shortness due to too much copper in the charge.

$$\sigma_Y(\text{MPa}) = \sigma_i(\text{MPa}) + k_Y(\text{MPa}\sqrt{m})d(\text{m})^{-1/2}$$

For mild steel, $\sigma_Y = 70.6 + 0.74d^{-1/2}$

For aluminum, $\sigma_Y = 15.69 + 0.07d^{-1/2}$

ASTM No.	AV. Grain Diameter, d , mm	$d(m)^{-1/2}$	σ_Y , Mild Steel $70.6 + 0.74d^{-1/2}$	σ_Y , Aluminum $15.69 + 0.07d^{-1/2}$ v
-3	1.00	31.6	94.0	17.9
-2	0.75	36.5	97.6	18.3
-1	0.50	44.7	103.7	18.8
0	0.35	53.4	110.1	19.4
1	0.25	63.2	117.4	20.1
2	0.18	74.5	125.7	20.9
3	0.125	89.4	136.8	22.0
4	0.091	104.8	148.2	23.0
5	0.062	127.0	164.6	24.6
6	0.044	150.8	182.2	26.3
7	0.032	176.8	201.4	28.1
8	0.022	213.2	228.4	30.6
9	0.016	250.0	255.6	33.2
10	0.011	301.5	293.7	36.8
11	0.008	353.6	332.3	40.5
12	0.006	408.2	372.7	44.3

5-3. Solution: The typical nominal composition of D5 tool steel is:

Composition (wt.%)

C	Mn	Si	Cr	Ni	Mo	V	Co
1.40-1.60	0.6 max	0.6 max	11.00-13.01	0.3 max	0.70-1.23	1.10 max	2.50-3.50

Source: G. Roberts, G. Krauss, and R. Kennedy: "Tool Steels 5th Edition" ASM International, The Materials Information Society, (July 1997).

Yes, this D5 tool steel is suitable for such applications. Because of its high carbon and alloy content, the D5 tool steel has high wear and abrasion resistance. A large volume fraction of alloy carbides and tempered high-carbon martensite play a major role in achieving the wear resistance. The high alloy content provides hardenability and allows martensite formation on air cooling.

D5 tool steel has a carbon concentration of 1.5 wt%. With this carbon concentration it has a large solidification temperature range ($\sim 1000^\circ\text{C}$). Thus, the composition of the solid solidified at the higher temperature is substantially different from that of the solid solidified at the lower temperature ($\sim 1\text{wt}\%$ C difference, see the Fe-C phase diagram for details). Since solid-state diffusion is very slow, D5 tool steel is likely to show the composition variation

from ~ 0.4 wt% C (medium carbon concentration solidified at the higher temperature) to > 1.5 wt% C (high carbon concentration solidified at the lower temperature) as the dendrite grows. Therefore, D5 tool steel is prone to severe carbon segregation.

Two procedures can be suggested to mitigate the carbon segregation problem: Hot forge the workpiece at a temperature between 1000 and 1200°C. Hot forging will deform dendrites from the solidification process. As dendrites are deformed, the composition will become more uniform because plastic deformation will move different parts of the dendrite around and average the composition.

To do a better job, another procedure can be taken. This entails a homogenizing treatment at a high temperature (such as 1250°C) for a sufficient time to allow diffusion to take place and thus homogenize the steel. After the homogenizing treatment, hot forge the workpiece to further decrease the chemical segregation and to reduce grain sizes by severe plastic deformation. Without the follow-on hot forging process, the grain size would be too large and the properties of the steel would be bad.

- 5-4.** Since the coarse bainitic microstructure has a low resistance to shock loading, we can use a Charpy V-notch impact test on lifting fork specimens to measure whether or not its impact energy is low. According to the class lecture, the energy absorption of the specimens is 1.75 kg m/cm^2 , which confirms the suspected low shock resistance. Thus, the premature fracture of the lifting-fork arms is due to brittleness that results from the wrong microstructure. Improper heat treatment or no heat treatment after forging leads to the wrong microstructure. The surface cracks may result from the forging operation or the quenching process and act as stress raisers, assisting in the initiation of fracture. In order to form a fine martensite structure and avoid the formation of bainite, the material must be quenched using a fast cooling rate. Clearly, the manufacturer did not use a sufficiently fast cooling rate in the quenching process. This should be corrected in order to obtain the correct microstructure.

CHAPTER 6

- 6-1.** $E = 200 \text{ GPa}$, $\nu = 0.25$

(511) spacings:

Normal incidence: 0.0550 nm

$\psi = 45^\circ$: 0.0552 nm

$$\begin{aligned}\sigma_\psi &= \frac{E}{(1 + \nu)\sin^2 \psi} \left(\frac{d_i - d_n}{d_n} \right) = \frac{200,000 \text{ MPa}}{(1.25)(0.5)} \left(\frac{0.0552 - 0.0550}{0.0550} \right) \\ &= 1.163.6 \text{ MPa}\end{aligned}$$

CHAPTER 7

7-1. $\dot{\epsilon} = 10^{-4} / \text{sec}$

The local fracture stress is $\sigma_F = 1,380 \text{ MPa}$

From Prob. 2-4, for a Charpy bar the maximum stress ahead of the notch is $2.51\sigma_{YS}$

$$\sigma_{YS} = 1,380 / 2.51 = 549.8 \text{ MPa}$$

From Fig. 6-8, $1.4T \ln \frac{A}{\dot{\epsilon}} = 1.4T \left(\ln \frac{10^8}{10^{-4}} \right) (10^{-3}) = 0.0387T$.

For ABS-C steel, a yield stress of 549.8 MPa corresponds to a parameter value of 5.5.

Therefore, $T = 5.5 / 0.0387 = 142K. (-131^\circ\text{C}) (K = ^\circ\text{C} + 273)$

Note that for an unnotched specimen, the yield stress for brittle fracture would be equal to $\sigma_F = 1,380 \text{ MPa}$. In this case, the value of the parameter as determined by extrapolation in Fig. 6-8 would be about 1.5. So, $0.0387T = 1.5$, and $T = 39K (-254^\circ\text{C})$.

The presence of the notch has brought about a 121°C increase in the brittle transition temperature for the specified strain rate.

7-2. The (yield) strength of a low-carbon steel is 622 MPa at an ASTM grain size of 2.

At a grain size of 8 it is 663 MPa. What will it be at a gain size of 10?

The ASTM grain size number, n , is related to the number of grains per square inch at a magnification of 100, N , by Eq. 6-10:

$$N = 2^{n-1}$$

$$(\text{Note : } \log N = (n - 1) \log 2)$$

$$n - 1 = \log N / \log 2$$

$$n = 1 + \log N / \log 2$$

$$n = \frac{\log 2 + \log N}{\log 2} = \frac{\log 2N}{\log 2} = 3.32 \log 2N,$$

ASTM GS No., n	Yield Strength MPa	N , No. Of Grains/in. ² at 100×	d , in. $\frac{1}{100 \sqrt{N}}$	d , m	$d^{-1/2}$, m ^{-1/2}
2	622	2	0.00707	0.00018	74.53
8	663	128	0.00088	0.00002	223.6
10	?	512	0.00044	0.00001	316.2

Hall-Petch relation: $\sigma_y = \sigma_i + k_y d^{-1/2}$

$$622 = \sigma_i + k_y 74.53 \quad (1)$$

$$663 = \sigma_i + k_y 223.6 \quad (2)$$

Subtract (1) from (2): $41 = 149k_y$, $k_y = 0.27 \text{ MPa}\sqrt{m}$. Therefore, $\sigma_i = 602 \text{ MPa}$.

The yield strength at an ASTM GS No. of 10 is therefore $602 + 0.27 \times 316.2 = 687 \text{ MPa}$.

7-3. The hydrostatic stress, $\sigma_{\theta\theta}$, is given by $\sigma_{\theta\theta} = \bar{\sigma} \ln \left(\frac{a}{2R} + 1 - \frac{r^2}{2aR} \right)$

$$\text{For } a/R = 1/3, \quad \sigma_{\theta\theta} = \bar{\sigma} \ln \left(1.167 - \frac{r^2}{6a^2} \right)$$

$$\text{For } a/R = 1, \quad \sigma_{\theta\theta} = \bar{\sigma} \ln \left(1.500 - \frac{r^2}{2a^2} \right)$$

$$\text{For } a/R = 2, \quad \sigma_{\theta\theta} = \bar{\sigma} \ln \left(2.000 - \frac{r^2}{a^2} \right)$$

r is measured from the centerline, $2a$ is the minimum diameter in neck, and R is the radius of the neck

r/a	$a/R = 1/3$	$a/R = 1$	$a/R = 2$
0	0.15	0.41	0.69
0.25	0.146	0.385	0.662
0.50	0.118	0.318	0.560
0.75	0.070	0.198	0.363
1.0	0	0	0

7-4. (a) At necking, $\sigma_T = 350 \text{ MPa}$, $\varepsilon_T = 0.5$

$$\varepsilon_T = \ln \frac{l}{l_o} = \ln \left(\frac{l_o + \Delta l}{l_o} \right) = \ln(1 + \varepsilon_E)$$

$$1 + \varepsilon_E = e^{\varepsilon_T} = 1.65, \varepsilon_E = 0.65$$

For constant volume, $A_o l_o = Al$

$$l/l_o = A_o/A = 1.65$$

$$\sigma_E = \sigma_T(A/A_o) = 350(1/1.65) = 212 \text{ MPa}$$

(b) Work per unit volume up to the point of necking, W , is

$$W = \int_0^n \sigma d\varepsilon = \int_0^n k\varepsilon^n d\varepsilon = \frac{1}{n+1} k\varepsilon^{n+1}$$

At necking $\varepsilon = n = 0.5$; therefore, $k = \frac{350}{n^n} = 495 \text{ MPa}$.

$$W = 116.7 \text{ Nm/m}^3$$

7-5. (a) In a tensile test the deformation is uniform in the test section, and there is no effect of the gauge length on the calculated strain.

(b) After necking the strain is localized at the neck, and the smaller the gauge length, the higher the calculated elongation.

7-6. $50.8 \text{ mm} : 3.1 = D : 1.16$

$$D = 19 \text{ mm}$$

$$h = 3.175 \text{ mm}$$

$$2h/D = 0.334$$

$$k = 3.04 - 7.236(2h/D) + 9.375(2h/D)^2 - 4.179(2h/D)^3$$

$$k = 3.04 - 2.42 + 1.05 - 0.156 = 1.51$$

7-7. Since the coarse bainitic microstructure has a low resistance to shock loading, we can use a Charpy V-notch impact test on lifting fork specimens to measure whether or not its impact energy is low. According to the class lecture, the energy absorption of the specimens is 1.75 kg m/cm^2 , which confirms the suspected low shock resistance. Thus, the premature fracture of the lifting-fork arms is due to brittleness that results from the wrong microstructure. Improper heat treatment or no heat treatment after forging leads to the wrong microstructure. The surface cracks may result from the forging operation or the quenching process and act as stress raisers, assisting in the initiation of fracture. In order to form a fine martensite structure and avoid the formation of bainite, the material must be quenched using a fast cooling rate. Clearly, the manufacturer did not use a sufficiently fast cooling rate in the quenching process. This should be corrected in order to obtain the correct microstructure. From Eq. 3-17a, $K_{IC} = \frac{1.12}{A} \sigma \sqrt{\pi a}$, we can obtain σ by

$$\sigma = \frac{K_{IC} A}{1.12(\sqrt{\pi a})} = \frac{35 \text{ MPa} \sqrt{m}(1.069)}{1.12(\sqrt{\pi(0.006m)})} = 243.32 \text{ MPa}$$

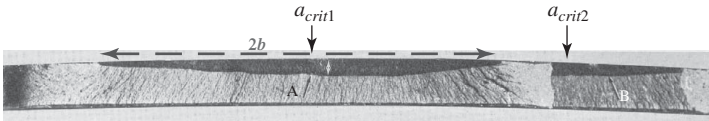
7-8. (a) The morphology of image (a) exhibits a stable crack growth region (an expansion of the semielliptical crack) in a ring shape under a fatigue

condition in which the location of a_{crit} is the crack initiation site, as marked in image (a). The crack grows gradually until it reaches the red line, at which unstable crack propagation takes place. Since the cross-sectional area of the unstable crack propagation region is small, it can be inferred that the applied stress is very small; otherwise, the unstable crack fracture would occur earlier. In contrast, the morphology of image (b) exhibits a radial zone that covers nearly the entire fracture surface. The crack initiation site is at the location of a_{crit} . As shown in image (b), the radial cracks all point back to this a_{crit} location, which proves that this is the crack initiation site. Additionally, since there is no stable crack propagation region, the fracture must occur under high stresses in one single loading. Thus, if we assume that the two materials (a) and (b) have the same fracture toughness, then component (a) must fail under a low stress, whereas component (b) should fail under high stresses.

- (b) If we assume that components (a) and (b) fracture under the same tensile stress load, then component (a) would have a higher fracture toughness than component (b). According to $K_{IC} = \sigma \sqrt{\pi a}$, K_{IC} is proportional to the square root of the a value. Since component (a) has an “ a ” value (the radius of the crack ring) much higher than that of component (b) (only a small spot), K_{IC} of component (a) is much larger than K_{IC} of component (b). In terms of the strength of the material, it is well known that the fracture toughness typically decreases with increasing strength (see the curve below). Therefore, it can be concluded that component (b) has a higher strength than component (a) because of the inverse strength-toughness relationship.

- 7-9. (a) There are two crack initiation sites, as shown by arrows a_{crit1} and a_{crit2} (see the image). These crack initiation sites are on two different fracture planes. Furthermore, the entire dark region is the crack initiation site, which results from quenching followed by oxidation in the subsequent tempering treatment.

- (b) For the top fracture plane in the image, we can find a and b values.



(The image ratio is 1:1 mm) $2b = 94 \text{ mm} \rightarrow b = 47 \text{ mm}$, and $a = 4 \text{ mm}$. This is a semielliptical surface crack. Thus, we choose

$$\therefore \frac{a}{b} = \frac{4}{47} = 0.0851 \text{ and } A = 1.0136$$

For $A = 1.0136$ and $K_{IC} = 50 \text{ MPa}\sqrt{m}$, we can estimate the final fracture stress (σ_c) by using Eq. 3-17a:

$$K_{IC} = \frac{1.12}{A} \sigma_c \sqrt{\pi a} \quad \text{and}$$

$$\sigma_c = \frac{K_{IC} \times A}{1.12(\sqrt{\pi a})} = \frac{50 \text{ MPa}\sqrt{m}(1.0136)}{1.12(\sqrt{\pi(4 \times 10^{-3} m)})} = 404 \text{ MPa}$$

Another, slightly more conservative estimation would be to include two initial cracks in the calculation, as shown below.

Now $2b = 137 \text{ mm} \rightarrow b = 69 \text{ mm}$, and $a = 4 \text{ mm}$.

$$\therefore \frac{a}{b} = \frac{4}{69} = 0.058 \quad \text{and} \quad A = 1.008.$$

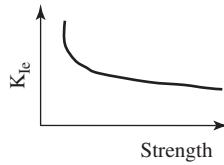
$$\sigma_c = \frac{K_{IC} \times A}{1.12(\sqrt{\pi a})} = \frac{50 \text{ MPa}\sqrt{m}(1.008)}{1.12(\sqrt{\pi(4 \times 10^{-3} m)})} = 402 \text{ MPa}$$

Note that the difference between the two estimations is very small because the critical stress is mainly controlled by a , the depth of the crack. The influence of b is small.

- (c) The characteristics of quench cracks include a flat fracture surface with cracks running toward the center of the mass in a relatively straight line. Since these fracture surfaces are covered with oxides, this could be the result of the tempering process after quenching. Quenching typically does not lead to oxidation because quench cracks form at low temperatures. Another possibility for cracking would result from forging at a low temperature. If this is the case, an examination of the cross section perpendicular to the cracked plane would show a substantial oxidation layer, or even two segments on the cracked plane, with one having more oxidation than the other. The more oxidized region results from oxidation twice or three times during forging, quenching, and tempering, whereas the less oxidized region comes from oxidation during tempering. We should combine these types of evidence with the processing conditions provided by the manufacturer. Thus, we also need to obtain the history (information) of processing of the part from the time of manufacturing, such as how the part was made, what kinds of processes (quenching, tempering) were involved, and at what temperature and what atmosphere the material was processed.

According to $K_{IC} = \sigma \sqrt{\pi a}$, K_{IC} is proportional to the square root of the a value. Since component (a) has an “ a ” value (the radius of the crack ring) much higher than that of component (b) (only a small spot), K_{IC} of component (a) is much larger than K_{IC} of component (b). In terms of the strength of the material, it is well known that the fracture toughness typically decreases with increasing strength (see the curve below). Therefore, it can be concluded that component (b) has a higher

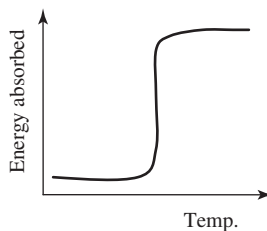
strength than component (a) because of the inverse strength-toughness relationship.



- 7-10. (a)** The known parameters are $E_{steel} = 200 \text{ GPa}$ and $CVN = 30 \text{ J/m}^2$. From the given relationship, we can compute the fracture toughness (K_{IC}):

$$\begin{aligned}\frac{K_{IC}^2}{E} &= 655 CVN \\ K_{IC} &= \sqrt{655 CVN \times E} = \sqrt{655(30 \text{ J/m}^2) \times (200 \times 10^9 \text{ Pa})} \\ &= 62.7 \text{ MPa}\sqrt{m}\end{aligned}$$

- (b)** No. This empirical relationship cannot be used to compute the fracture toughness of the steel in the upper-shelf region because it represents only one data point (when $CVN = 30 \text{ J/m}^2$ and $K_{IC} = 62.7 \text{ MPa}\sqrt{m}$) on the curve, not for the entire curve.
- 7-11. (a)** Yes, this material can exhibit a ductile-to-brittle transition if the two fractographs are from the same material. The fracture surface shown in (a) contains dimples. Therefore, fracture in area (a) was ductile in nature. In contrast, Fig. the fracture surface in (b) is relatively flat and contains transgranular cleavage facets as well as intergranular fracture. Both of these features are indicative of brittle fracture. perty. This ductile-to-brittle transition is due to the temperature dependence of the impact energy in this material (see the curve below).



(a)

- (b)** Material X will likely be a fcc metal with a low to medium yield strength.
- (c)** Material Y will likely be a bcc metal of high yield strength.
- (d)** In one Charpy V-notch specimen, you will most likely find the surface morphology of Fig. (a) at the edge of the specimen (a plane-stress condition), and the morphology seen in Fig. (b) at the center of the specimen (a plane-strain condition).

CHAPTER 8

8-1. Ceramic coating CTE < Metal CTE

CTE = coefficient of thermal expansion

ΔT ceramic > ΔT metal

- (a) If the overall thermal expansion of the ceramic is greater than that of the metal, the ceramic will be in compression, and spalling of the ceramic may occur.
- (b) If the overall thermal expansion of the ceramic is the same as that of the metal, there should be no problem.
- (c) If the overall thermal expansion of the ceramic is less than that of the metal, the ceramic will be in tension and cracking of the ceramic may occur.

8-2. (a) Because of its higher coefficient of expansion, the aluminum will be in compression and the steel will be in tension. The strain in the aluminum is given as $\varepsilon_{Al} = -\frac{\sigma_{Al}}{E_{Al}} + \alpha_{Al}\Delta T$

The strain in the steel is given as $\varepsilon_{St} = \frac{\sigma_{St}}{E_{St}} + \alpha_{St}\Delta T$

Since $A_{Al} = A_{St}$, $\sigma_{St} = -\sigma_{Al} = \sigma$

Further, $\varepsilon_{Al} = \varepsilon_{St}$, so that $-\frac{\sigma}{E_{Al}} + \alpha_{Al}\Delta T = \frac{\sigma}{E_{St}} + \alpha_{St}\Delta T$, and therefore

$$\sigma = \frac{(\alpha_{Al} - \alpha_{St})}{\frac{1}{E_{Al}} + \frac{1}{E_{St}}} \Delta T$$

$$\alpha_{Al} = 0.00001/^{\circ}\text{F} = 0.000018/^{\circ}\text{C}, \quad E_{Al} = 69 \text{ GPa}, \sigma_{YS} = 69 \text{ MPa}$$

$$\alpha_{St} = 0.0000065/^{\circ}\text{F} = 0.000012/^{\circ}\text{C}, E_{St} = 200 \text{ GPa}, \sigma_{YS} = 690 \text{ MPa}$$

(b) For $\sigma = 69 \text{ MPa}$,

$$\begin{aligned} 69 &= \frac{0.000018 - 0.000012}{\frac{1}{69,000} + \frac{1}{200,000}} \Delta T = \frac{0.000006}{1.45 \times 10^{-5} + 0.50 \times 10^{-5}} \Delta T \\ &= 0.31 \Delta T, \Delta T = 223^{\circ}\text{C} \end{aligned}$$

(c) For purposes of discussion, assume that there is no strain hardening and that the yield strength of the aluminum does not change with temperature. At a ΔT of 223°C , the strain in the aluminum is

$$\varepsilon_{Al} = -\frac{69}{69,000} + 0.000018 \times 223 = -0.001 + 0.004 = 0.003$$

$$\varepsilon_{St} = \frac{69}{200,000} + 0.000012 \times 223 = 3.45 \times 10^{-4} + 26.8 \times 10^{-4} = 0.003$$

If the temperature rises further and there is no strain hardening in the aluminum, then the strip will continue to expand, but now at the thermal expansion rate of the steel, since the aluminum offers no further resistance

to the expansion. Note that if the temperature were to rise an additional 223°C , the additional expansion strain would be 0.00268, which is less than in the first temperature interval when the stress in the aluminum was rising. The aluminum, if free to expand, should expand by $0.000018 \times 223 = 0.004$, but being restrained by the steel, it undergoes a plastic compressive strain of $0.0040 - 0.0027 = 0.0013$.

The length of the aluminum is effectively less by this amount per unit length than it was originally. On cooling, a tensile stress will develop in the aluminum that is balanced by an equal compressive stress in the steel. Depending upon the amount of plastic deformation experienced on heating, the stress can vary from zero to 69 MPa.

- (d) The increase in vibration amplitude of the atoms is more easily accommodated in an open (bcc) rather than a closed-packed structure (fcc) due to the asymmetric shape of the atomic potential well.

8-3. When a very hot workpiece is cooled rapidly without phase transformation, the surface of the work piece will cool faster than the interior. As a result, the surface region shrinks more than the interior, thereby inducing tensile stresses at the surface region and compressive stresses in the interior. However, such thermal stresses can be partially released by the interior which is still hot and can deform plastically at this stage to accommodate compression applied by the surface region. As a result, thermal stresses are small at this stage. However, when the interior starts to cool and shrink, the already cooled surface will resist shrinkage. As a result, tensile stresses will develop in the interior and compressive stresses will be created at the surface region.

If martensite formation takes place, the situation changes. Martensite formation leads to volume expansion. Thus, at the early stage of cooling the surface region cools faster and transforms to martensite, leading to volume expansion at the surface region. However, the interior can expand with the surface region at this stage because of the high temperature inside and thus easy deformation of the interior. At the later stage of cooling, when the interior cools and starts to transform to martensite, the surface region has already cooled and will resist expanding with the interior. As a result of this mismatch, compressive stresses are generated in the interior, and tensile stresses are created at the surface region.

8-4. Solution: The temperature change of a turbine blade shown in Fig. 7-2 of the textbook can be used to help illustrate the thermal-mechanical loading. During acceleration the temperature at the surface will increase from 600 to 1100°C within 105 seconds, which leads to compressive strain at the surface because the interior of the blade is still at a lower temperature. The total thermal strain is the sum of the strain due to thermal expansion plus the strain due to the thermal stress developed. However, when the temperature of the interior matches that at the surface, the strain due to thermal stress at the surface will reduce to zero. On deceleration, the temperature of the surface goes down first, leading to tensile strain at the surface which later reduces to zero when the interior cools down. Thus, acceleration and deceleration cycles will result in tensile and compressive

loading cycles at the surface and interior. This phenomenon is termed as the thermal-mechanical loading because of the application of stresses due to heating and cooling. The impact of such a phenomenon is thermal-mechanical fatigue of turbine blades. Therefore, thermal-mechanical fatigue loading is one of the critical design criteria for turbine blades.

- 8-5. Solution:** In order to induce plastic deformation in tension, the tensile stress applied has to be high enough to overcome any residual compressive stress before overall plastic deformation can take place. Since residual compressive and tensile stresses are always present at the same time at different regions, the region with residual tensile stresses will plastically deform first when an external tensile stress is applied. The region with residual compressive stresses will plastically deform later if the applied tensile stress is high enough to overcome the compressive stresses first and then reach the tensile yield strength of the material. Although the region with residual tensile stresses deforms plastically first, the total amount of the plastic strains are nearly the same for different regions regardless of the sign of their residual stresses.

At the early stage of deformation, when the region with the residual tensile stresses deforms plastically, the region with residual compressive stresses only deforms elastically. As a result, the total strain of the cylindrical bar is very, very small because the plastically deformed region is constrained by the elastically deformed region. Only when the region with residual compressive stresses can deform plastically, the total strain of the cylindrical bar can become large. Since usually the elastic strain is very small compared with the plastic strain, all regions regardless the sign of their residual stresses end up with nearly the same plastic strain, and all stress gradients disappear. Upon release of the external tensile stress, all regions recover elastically and uniformly. As a result, residual stresses are eliminated.

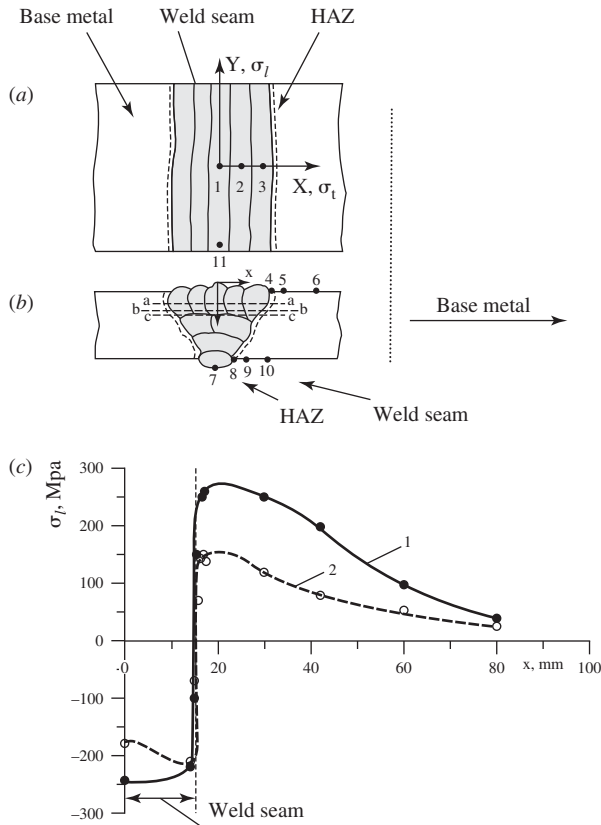
- 8-6. Solution:** Carburizing leads to an increase in the carbon concentration at the surface. During the cooling process a compressive residual stress develops at the surface of a workpiece. This happens because the higher carbon content leads to a decrease of the M_s temperature at the surface. As a result, martensite will form first in the interior because of its lower carbon concentration and thus higher martensite formation temperature. When the surface transforms to martensite at the later cooling stage, the interior will resist expanding with the surface, because the martensite in the interior cannot deform. As such, the interior induces a compressive stress on the surface to prevent it from expanding.

Nitriding will give rise to nitride formation at the surface. The nitride has a relatively low thermal expansion coefficient in comparison with steels. Thus, during cooling, the steel in the interior shrinks more than the surface, leading to compressive stresses at the surface.

In induction hardening, the surface is heated above the transformation temperature and then immediately quenched. When it is quenched, the compressive stress will form on the surface because it transforms from austenite to martensite.

The expansion of the surface due to the formation of martensite is resisted by the interior which does not undergo phase transformation. As a result, compressive stresses develop at the surface. Since the nitriding process is carried out at a temperate below the eutectoid temperature, no phase transformation occurs on cooling. This insures that the dimensions of a part whose dimensions are critical, such as crankshaft, are not altered during the nitriding process.

- 8-7.** The following figures show a linear butt weld between steel plates and the residual stress distribution around the linear weld seam. Provide an explanation as to why the residual stress distribution of Curve 1 in (c) has the shown profile.



(a) Top view of a linear butt weld of steel plates, (b) the cross-section view of the linear butt weld of steel plates, and (c) The distribution of residual stresses as a function of the location measured from the center of the weld seam. 1 — the residual stresses parallel to the weld seam, and 2 — the residual stresses perpendicular to the weld seam along the positions 1, 2, 3, 4, 5, etc. shown in (a) and (b).

Solution: Curve 1 indicates residual compressive stresses in the direction parallel to the weld seam within the weld seam, as well as the residual tensile stresses in the base metal. This stress distribution occurs because of the martensite formation in the weld seam during the cooling process. After solidification the weld seam tends to expand during cooling because of the formation martensite; however, such an expansion tendency is constrained by the surrounding base metal. As a result, the weld seam ends up in compression while the base metal is in tension.

CHAPTER 9

9-1. $\sigma_0 = 70 \text{ MPa}, T = 550^\circ\text{C}, E = 175 \text{ GPa}$

$$\dot{\epsilon} = 5.0 \times 10^{-8} / \text{hr} = A\sigma^4 = A(70)^4$$

$$A = 5.0 \times 10^{-8} / (70)^4 = 5 \times 10^{-8} / 2,401 \times 10^4 = 0.00208 \times 10^{-12}$$

$$A = 2.08 \times 10^{-15} (\text{MPa})^{-4} / \text{hr}$$

Eq. 9-22:

$$\frac{1}{\sigma(t)^{n-1}} = \frac{1}{\sigma_0^{n-1}} + (n-1)AE\Delta t$$

$$\frac{1}{\sigma(t)^3} = \frac{1}{70^3} + 3 \times 2.08 \times 10^{-15} \times 175,000 \text{ MPa} \times 365 \times 24$$

$$= 8.76 \times 10^{-6} + 3.19 \times 10^{-6} = 11.95 \times 10^{-6}$$

$$\sigma(t)^3 = 0.084 \times 10^6$$

$$\sigma(t) = (0.084 \times 10^6)^{1/3} = 43.8 \text{ MPa}$$

9-2. $T = 750^\circ\text{C}, L_0 = 100 \text{ mm}, \sigma = 40 \text{ MPa}, 1.0 \text{ mm clearance}$

$$\text{At } 800^\circ\text{C}, \dot{\epsilon} = 7.5 \times 10^{-8} / \text{sec} = A\sigma^n e^{-\frac{Q}{RT_{1073}}}$$

$$\text{At } 950^\circ\text{C}, \dot{\epsilon} = 1.3 \times 10^{-5} / \text{sec} = A\sigma^n e^{-\frac{Q}{RT_{1223}}}$$

$$1. \ln(7.5 \times 10^{-8}) = \ln A + n \ln 40 - Q/1073R$$

$$2. \ln(1.3 \times 10^{-5}) = \ln A + n \ln 40 - Q/1223R$$

Subtract 1 from 2

$$\ln(173.33) = Q/1,223R + Q/1073R$$

$$5.15520 = -0.00081766Q/R + 0.00093197Q/R = 0.0001131Q/R$$

$$5.15520 = 0.00011Q/R$$

$$Q/R = 46,865 \text{ (K)}$$

At 750°C (1,023 K)

$$\frac{\dot{\epsilon}}{1.3 \times 10^{-5}} = \frac{e^{-46865/1023}}{e^{-46865/1223}} = \frac{e^{-45.81}}{e^{-38.32}} = e^{-7.49} = 0.00056$$

Therefore, $\dot{\epsilon}$ at 750°C = 7.28×10^{-9} , and the time required to reach a strain of 0.01 is $0.01/7.28 \times 10^{-9} = 1.37 \times 10^6$ sec.

Approximately 380 hours = 2.26 weeks = 16 days

9-3. (a) $\dot{\epsilon} = 10 \times 10^{-20} \sigma^3$ per day, where σ is in psi

To convert to SI units and hours, change the units of the coefficient. The original units of the coefficient are $\frac{1}{\text{psi}^3} \frac{1}{\text{day}}$. To convert, use the relations $\frac{(145 \text{ psi})^3}{\text{MPa}}$ and $\frac{\text{day}}{24 \text{ hours}}$.

This leads to $\dot{\epsilon} = 10 \times 10^{-20} \frac{1}{\text{psi}^3 \text{ day}} \frac{(145 \text{ psi})^3}{(\text{MPa})^3} \frac{\text{day}}{24 \text{ hours}} \sigma^3 (\text{MPa})^3$

$\dot{\epsilon} = 1.27 \times 10^{-14}$ per hour with the stress in MPa.

(b)

$$P = 4.48 \times 10^4 \text{ N}, l_0 = 2 \text{ m}, \Delta l = 2.5 \text{ mm},$$

$$\epsilon = \frac{0.0025}{2} = 0.00125, T = 454^\circ\text{C}, t = 10 \text{ years}.$$

$$10 \text{ years} = 10 \times 365 \times 24 = 87,600 \text{ hours}.$$

$$\dot{\epsilon} \times 87,600 = 0.00125 \text{ (the strain)}$$

$$\dot{\epsilon} = 1.43 \times 10^{-8} \text{ per hour}$$

$$\dot{\epsilon} = 1.27 \times 10^{-14} \sigma^3 = 1.43 \times 10^{-8}$$

$$\sigma^3 = 1.13 \times 10^6, \sigma = 104 \text{ MPa}$$

$$\frac{P}{A} = 104 = \frac{0.0448 \text{ MN}}{A}. \quad A = 0.0448/104 = 0.00043 \text{ m}^2$$

$$A = \frac{\pi D^2}{4} = 0.00043, D = 23.4 \text{ mm}$$

(c) After 3 years at 104 MPa, the strain accumulated would be equal to $1.27 \times 10^{-14} (104)^3 \times 3 \times 365 \times 24 = 3.75 \times 10^{-4}$ (or 0.3 of 0.00125)

Total deformation now allowed is 0.0015 m; the new total strain becomes 0.00075.

Total amount of strain allowed in the next 7 years is $0.00075 - 0.000375 = 0.000375$.

$$1.27 \times 10^{-14} \sigma_2^3 \times 7 \times 365 \times 24 = 0.000375$$

$$\sigma_2^3 = 0.4815 \times 10^6$$

$$\sigma_2 = 78.4 \text{ MPa}$$

The load must be reduced by a factor of $78.4/104 = 0.754$.

$$P_2 = 0.754 \times 0.0448 \text{ MN} = 0.0337 \text{ MN}$$

$$A = P/\sigma = 0.0337/78.4 = 0.00043 \text{ m}^2, \text{ as above.}$$

9-4. $273 \text{ K} = 460^\circ\text{R}$ $100^\circ\text{C} = 212^\circ\text{F}$, $9/5^\circ\text{C} + 32 = ^\circ\text{F}$ $273 \text{ K} = 460^\circ\text{R}$

$$1.68 R(C + \log T_R) = C_1, K(C + \log t_R) = C_1/1.68$$

$$R = F + 460, F = R - 460; K = C + 273$$

$$C = 5/9(F - 32) = K - 273, K = C + 273, K = 5/9(F - 32) + 273,$$

$$K = 5/9(R - 460 - 32) + 273 = 5/9R$$

$$9/5K(C + \log t_r) = C_1, K(C + \log t_R) = 5/9C_1$$

$$51 \times 103 \times 5/9 = 28 \times 10^3 = K(C + \log t_R)$$

From Fig. 5-9, for Udimet 700 the stress corresponding to the 100 hour rupture life at 870°C (1,143 K) is 276 MPa. At $1,500^\circ\text{F}$ (816°C , 1,089 K)

Units: t_R in hours, $\dot{\epsilon}$ in $\frac{\text{m}}{\text{hr}}$

At 276 MPa, the value of the Larson-Miller parameter $T(C + \log t_R) = 28 \times 10^3$.

If $T = 1,143\text{K}$ and t_R is 100 hours, what is the value of C ?

Answer: 22.5.

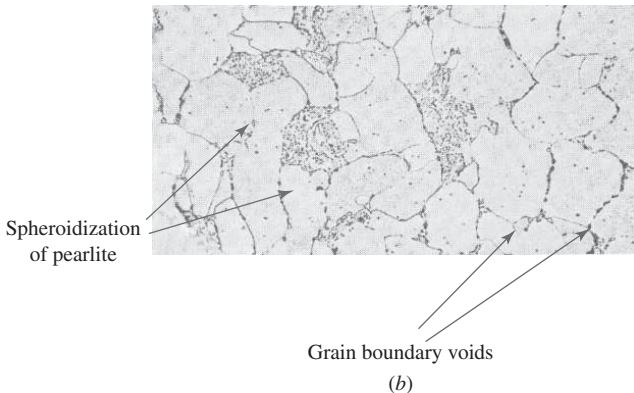
For the same stress, 276 MPa, at 816°C

$$1.4 \times 1,089(20 + \log t_R) = 35,204$$

$$\log t_R = 3.09$$

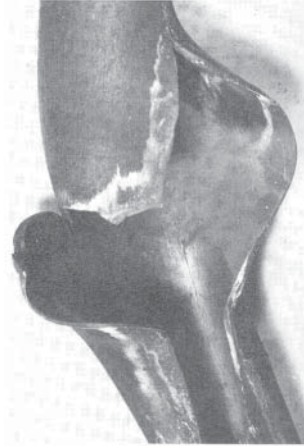
$$t_R = 1,230 \text{ hours}$$

9-5. (a) See the marks below.



- (b) Typically, the temperature at which a pearlite transforms to a spherodite is about 700°C . Thus, based on the formation of spheroidization, we can estimate that this steam boiler tube has been exposed to $650\text{--}720^{\circ}\text{C}$.

9-6. Solution:



- (a) Based on this image, the failure will likely be a thin-walled fracture because the characteristic of the fracture contains a lateral bending at the rupture region and swelling of the tube in the region adjacent to the rupture.
- (b) Due to the characteristic of the fracture in (a), this failure will be a result of substantial overheating. Operation under substantial overheating can lead to substantial softening of the material. As a result, the boiler steel tube is unable to withstand the internal pressure, thereby leading to swelling of the tube, followed by the rapid rupture and lateral bending of the tube.

CHAPTER 10

10-1.

$$K_c = 50 \text{ MN } m^{-3/2} (50 \text{ MPa} \sqrt{\text{m}})$$

$$a_o = 0.2 \text{ mm}, K = 0.73 \Delta \sigma \sqrt{\pi a}$$

$$\frac{da}{dN} = A(\Delta K)^2 = 10^{-10} \times (0.73 \times 200 \sqrt{\pi a})^2$$

$$= 10^{-10} \times 6.7 \times 10^4 \quad a = 6.7 \times 10^{-6} \text{ m}$$

$$\frac{da}{a} = 6.7 \times 10^{-6} dN$$

$$\ln \frac{a_f}{a_o} = 6.7 \times 10^{-6} \Delta N$$

$$K_C = 0.73 \times 200 \times \sqrt{\pi a_f} = 50, a_f = 0.0373 \text{ m}$$

$$\ln \frac{0.0373}{0.0002} = 5.2$$

$$\Delta N = 7.7 \times 10^5 \text{ cycles to failure}$$

10-2. For the [001] orientation, the width of the hysteresis loop at zero stress is $0.8\% = 0.008 = \Delta \varepsilon_p$.

For the [111] orientation, the width of the hysteresis loop at zero stress is $0.25\% = 0.0025 = \Delta \varepsilon_p$.

$$\text{Given } N_f^{1/2} \Delta \varepsilon_p = 0.6$$

For the [001] orientation, $N_f = 5,525$ cycles. (Data for a 0.008 strain range indicates that N_f would be about 5,000 cycles.)

For the [111] orientation, $N_f = 557,600$ cycles. (The data indicate a life of more than 100,000 cycles.)

A better constitutive equation would be $N_f^{0.31} \Delta \varepsilon_p = 0.106$.

10-3.

$$N_f^b \left(\frac{\Delta \sigma}{2} \right) = C$$

$$\Delta \sigma = 300 \text{ MPa}, N_f = 10^5 \text{ cycles}$$

$$\Delta \sigma = 200 \text{ MPa}, N_f = 10^7 \text{ cycles}$$

$$(a) \quad (10^5)^b \times 150 = (10^7)^b \times 100 \quad 100^b = 1.5, \quad b \times 2 = \log 1.5 = 0.176, \quad b = 0.088 \quad (105)^{0.088} \times 150 = C = 413.1$$

$$(b) \quad (N_f)^{0.088} \times 125 = 413.1, \quad N_f = 3.30^{1/0.088} = 780,000 \text{ cycles}$$

$$(c) \quad \frac{5 \times 10^5}{7.8 \times 10^5} = 0.64. \text{ Therefore, } 0.36 \text{ of } N_f \text{ at a stress range of } 200 \text{ MPa remains.}$$

The remaining number of cycles at $\Delta \sigma$ is $0.36 \times 10^7 = 3.6 \times 10^6$ cycles.

10-4. $K_{Ic}, R = 0$. N cycles to failure, $\Delta K = Y \Delta \sigma \sqrt{\pi a}$

$$\frac{da}{dN} = A(\Delta K)^2 = Y^2(\Delta \sigma)^2 \pi a$$

$$\int_{a_0}^{a_f} \frac{da}{a} = AY^2(\Delta \sigma)^2 \pi \Delta N$$

$$\ln \frac{a_f}{a_0} = AY^2(\Delta \sigma)^2 \pi \Delta N$$

$$Y \Delta \sigma \sqrt{\pi a_f} = K_{Ic}, \quad a_f = \frac{1}{\pi} \left(\frac{K_{Ic}}{Y \Delta \sigma} \right)^2$$

$$\ln \frac{1}{\pi a_0} \left(\frac{K_{Ic}}{Y \Delta \sigma} \right)^2 = AY^2(\Delta \sigma)^2 \pi \Delta N$$

$$\frac{1}{\pi a_0} \left(\frac{K_{Ic}}{Y \Delta \sigma} \right)^2 = e^{AY^2(\Delta \sigma)^2 \pi \Delta N}$$

$a_0 = \frac{1}{\pi} \left(\frac{K_{Ic}}{Y \Delta \sigma} \right)^2 e^{-AY^2(\Delta \sigma)^2 \pi \Delta N}$ (all quantities on the right-hand side are known; therefore, a_0 is also known)

$$\frac{a_f}{a_0} = e^{AY^2(\Delta \sigma)^2 \pi \Delta N}$$

$$Y \sigma_{proof} \sqrt{\pi a_0} = K_{Ic}$$

$$\begin{aligned} \sigma_{proof} &= \frac{K_{Ic}}{Y \sqrt{\pi a_0}} = \frac{K_{Ic}}{Y \sqrt{\pi \frac{1}{\pi} \left(\frac{K_{Ic}}{Y \Delta \sigma} \right)^2 e^{-AY^2(\Delta \sigma)^2 \pi \Delta N}}} \\ &= \Delta \sigma e^{\frac{A}{2} Y^2 (\Delta \sigma)^2 \pi \Delta N} \end{aligned}$$

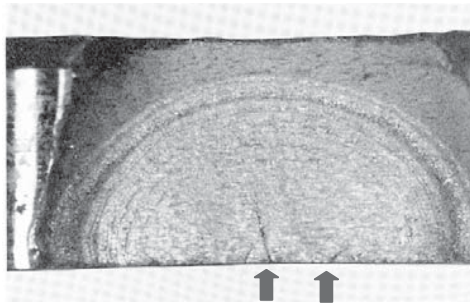
Note that the proof stress is independent of the fracture toughness.

(b) $A = 2 \times 10^{-9}$, $Y = 1$, $\Delta \sigma = 140$ MPa, $N = 10,000$

$$\sigma_{proof} = 140 e^{10^{-9} (140)^2 \pi (10)^4} = 140 e^{0.616} = 259 \text{ MPa}$$

10-5. Solution:

- (a) The visible macrostructure features on the fracture surface are beach marks, ratchet lines, and flatness of the fracture surface. The beach marks are the semicircular rings that develop as the steel experiences periods of cycling load followed by periods of rest or with the changing of the stress amplitude during cyclic loading. There are a few ratchet lines near the crack initiation sites. Also, the fracture surface appears to be flat, which indicates the absence of an appreciable amount of large plastic deformation during fatigue loading.
- (b) There are several crack initiation sites because of the presence of ratchet lines that connect contiguous regions where separate cracks have initiated. Although the precise locations of the crack initiation sites are not clear in this image, we suggest that there are at least three initiation sites based on the presence of two ratchet lines, as indicated by the arrows below.

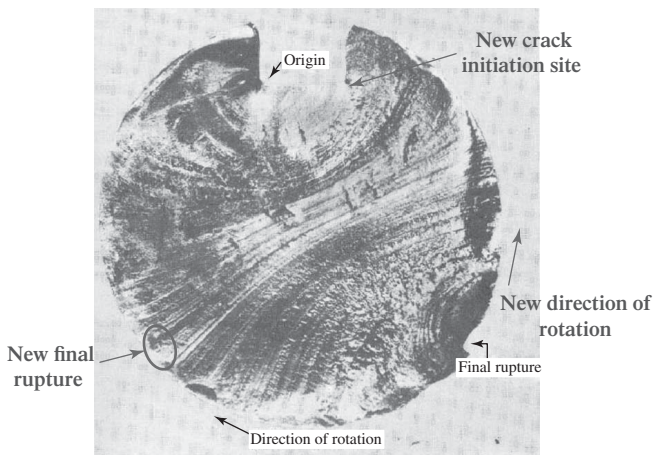


- (c) Determining the stress fracture toughness factor of a semicircular surface crack in a semi-infinite body for σ_{max} and substituting $a = 0.025m$ (the

crack radius measured from the image) and $K_{IC} = 120 \text{ MPa}\cdot\text{m}^{1/2}$ yields

$$\sigma_{\max} = \frac{K_{IC}\sqrt{\pi}}{1.12 \times 2\sqrt{a}} = \frac{120 \text{ MPa}\cdot\text{m}^{1/2}\sqrt{\pi}}{1.12 \times 2\sqrt{0.025\text{m}}} = 600.5 \text{ MPa}$$

- 10-6. (i)** The crack initiation site starts at one of the sharp corners (labeled “Origin” in the image below) where the connection between the shaft and the impeller is provided by a keyway and fillet. This area has a much higher stress concentration than the sharp corner on the other side because of the direction of rotation. As a result, this area is prone to fatigue crack initiation during service. The final fracture region is located at the bottom right (labeled “Final rupture”). It is noted that the final fracture location is on the right side of the shaft. This is attributed to the faster crack propagation on the left-hand side of the shaft than on the right-hand side. The faster crack propagation on the left-hand side, in turn, is due to the direction of the shaft rotation, which leads to a slightly higher stress intensity factor range on the left-hand side than on the right-hand side.
- (j)** The beach markings are present on the fracture surface owing to a loading/unloading cycle. The crack propagates radially during service, but with a larger beach mark spacing on the left-hand side because the left-hand side has a slightly higher stress intensity factor range, as mentioned above.
- (k)** The crack initiation site and the final fracture region are not located symmetrically because of the rotation of the shaft, which leads to a higher stress intensity factor range on the left than on the right.
- (l)** Changing in the direction of rotation will change both the crack initiation site and the final fracture region (see the marks highlighted below with letters and arrows).



CHAPTER 11

11-1. (a) For a Gaussian distribution, the arithmetic mean (μ) can be obtained by

$$\text{using } \mu = \sum_{i=1}^N x_i / N, \text{ and the standard deviation } (\sigma) \text{ can be obtained by}$$

$$\text{using } \sigma = \sqrt{\frac{\sum_{i=1}^N (x_i - \mu)^2}{N-1}}$$

Thus, μ is 129.85 ksi, and σ is 5.88.

(b) The probability function, $f(x)$, = frequency/ $N + 1$.

The cumulative probability function, (Experimental) $F(x)$ = cumulative frequency/ $N + 1$.

Yield Strength, ksi	Frequency	Cumulative Frequency	$f(x)$	Exp $F(x)$
114–115.9	4	4	0.009	0.009
116–117.9	6	10	0.013	0.022
118–119.9	8	18	0.018	0.040
120–121.9	26	44	0.058	0.098
122–123.9	29	73	0.064	0.162
124–125.9	44	117	0.098	0.260
126–127.9	47	164	0.104	0.364
128–129.9	59	223	0.131	0.496
130–131.9	67	290	0.149	0.644
132–133.9	45	335	0.100	0.744
134–135.9	49	384	0.109	0.853
136–137.9	29	413	0.064	0.918
138–139.9	17	430	0.038	0.956
140–141.9	9	439	0.020	0.976
142–143.9	6	445	0.013	0.989
144–145.9	4	449	0.009	0.998

Note: $N = 449$.

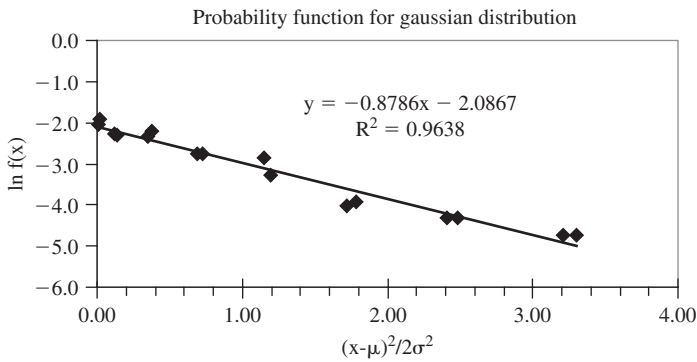
(c) The probability function of a Gaussian distribution can be described as

$$f(x) = \frac{1}{\sigma\sqrt{2\pi}} \exp \left[-\frac{1}{2} \left(\frac{x - \mu}{\sigma} \right)^2 \right] \text{ or}$$

$$\ln f(x) = \ln \frac{1}{\sigma\sqrt{2\pi}} - \frac{1}{2} \left(\frac{x - \mu}{\sigma} \right)^2$$

We need to plot $\ln f(x)$ vs. $\frac{1}{2}\left(\frac{x-\mu}{\sigma}\right)^2$ and examine whether there is a linear relationship between $\ln f(x)$ and $\frac{1}{2}\left(\frac{x-\mu}{\sigma}\right)^2$ with a slope of -1 and the correlation coefficient value, R^2 , close to 1.

Yield Strength, ksi	Average Yield Strength of the Range, ksi	Frequency	Cumulative Frequency	$f(x)$	$1/2[x-\mu/\sigma]^2$	$\ln f(x)$
114–115.9	114.95	4	4	0.009	3.211	–4.723
116–117.9	116.95	6	10	0.013	2.407	–4.317
118–119.9	118.95	8	18	0.018	1.719	–4.030
120–121.9	120.95	26	44	0.058	1.146	–2.851
122–123.9	122.95	29	73	0.064	0.689	–2.742
124–125.9	124.95	44	117	0.098	0.347	–2.325
126–127.9	126.95	47	164	0.104	0.122	–2.259
128–129.9	128.95	59	223	0.131	0.012	–2.032
130–131.9	130.95	67	290	0.149	0.018	–1.905
132–133.9	132.95	45	335	0.100	0.139	–2.303
134–135.9	134.95	49	384	0.109	0.376	–2.217
136–137.9	136.95	29	413	0.064	0.729	–2.742
138–139.9	138.95	17	430	0.038	1.198	–3.276
140–141.9	140.95	9	439	0.020	1.782	–3.912
142–143.9	142.95	6	445	0.013	2.482	–4.317
144–145.9	144.95	4	449	0.009	3.298	–4.723



The R^2 value of the fitting curve is high (0.9638). However, the slope of the fitting curve is (-0.88) instead of (-1.00) .

- (d) The cumulative probability function of a Gaussian distribution can be described as

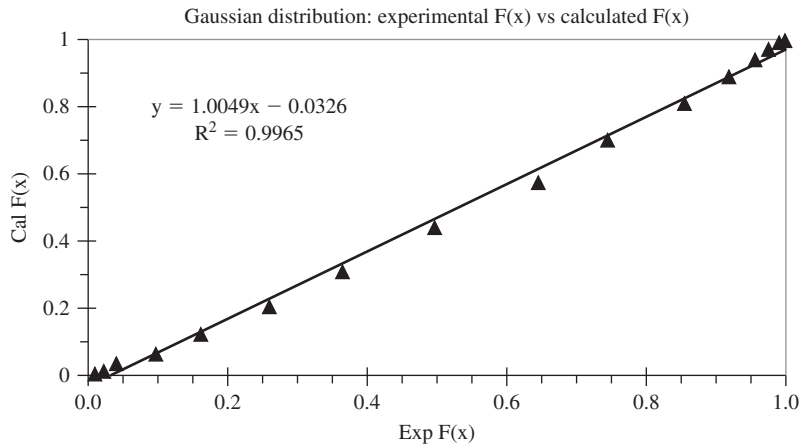
$$F(x) = \frac{1}{2} - \frac{1}{2} \operatorname{erf} \left[- \left(\frac{x - \mu}{\sigma \sqrt{2}} \right) \right] \text{ for } x \leq \mu, \text{ and}$$

$$F(x) = \frac{1}{2} + \frac{1}{2} \operatorname{erf} \left[\left(\frac{x - \mu}{\sigma \sqrt{2}} \right) \right] \text{ for } x \geq \mu.$$

By using the above equations, the calculated $F(x)$ can be obtained. Then the calculated $F(x)$ can be plotted against the experimental $F(x)$ to evaluate their correlations.

Yield Strength, ksi	Average Yield Strength of the Range, ksi	Cumulative		Cal $F(x) = \frac{1}{2} - \frac{1}{2} \operatorname{erf} \left[- \left(\frac{x - \mu}{\sigma \sqrt{2}} \right) \right]; x \leq \mu$	
		Frequency	Frequency	Exp $F(x)$	Cal $F(x) = \frac{1}{2} + \frac{1}{2} \operatorname{erf} \left[\left(\frac{x - \mu}{\sigma \sqrt{2}} \right) \right]; x \geq \mu$
114–115.9	114.95	4	4	0.009	0.006
116–117.9	116.95	6	10	0.022	0.014
118–119.9	118.95	8	18	0.040	0.032
120–121.9	120.95	26	44	0.098	0.065
122–123.9	122.95	29	73	0.162	0.120
124–125.9	124.95	44	117	0.260	0.202
126–127.9	126.95	47	164	0.364	0.311
128–129.9	128.95	59	223	0.496	0.439
130–131.9	130.95	67	290	0.644	0.574
132–133.9	132.95	45	335	0.744	0.701
134–135.9	134.95	49	384	0.853	0.807
136–137.9	136.95	29	413	0.918	0.886
138–139.9	138.95	17	430	0.956	0.939
140–141.9	140.95	9	439	0.976	0.970
142–143.9	142.95	6	445	0.989	0.987
144–145.9	144.95	4	449	0.998	0.995

It is noted that the experimental $F(x)$ and the calculated $F(x)$ have a linear correlation with $R^2 = 0.9965$ and slope = 1.00. Furthermore, the intercept is near zero. Thus, the yield strength data follow the cumulative probability function of a Gaussian distribution quite well.

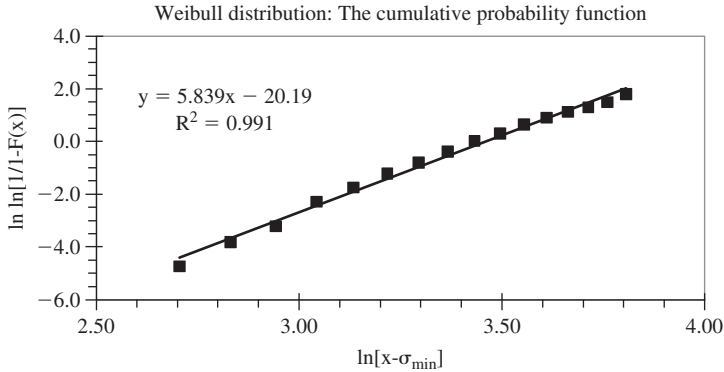


(e) The cumulative probability function of the Weibull distribution can be written as

$$F(x) = 1 - \exp \left[- \left(\frac{x - \sigma_{\min}}{\sigma_o} \right)^m \right] \quad \text{or}$$
$$\ln \ln \left[\frac{1}{1 - F(x)} \right] = m \ln [x - \sigma_{\min}] - m \ln \sigma_o.$$

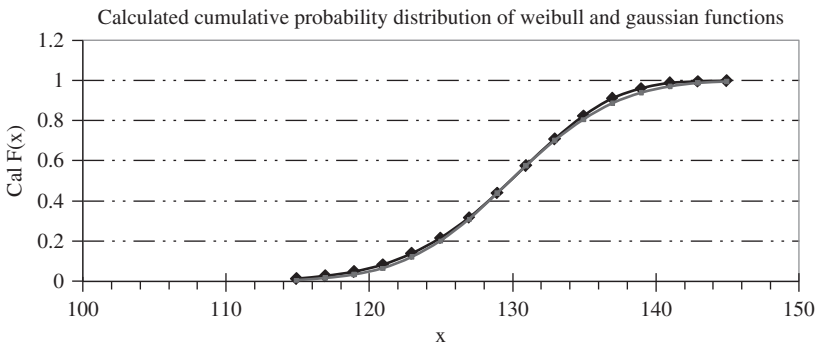
We can evaluate the characteristic of this distribution by plotting $\ln \ln \left[\frac{1}{1 - F(x)} \right]$ vs. $\ln [x - \sigma_{\min}]$ and then examine whether or not there is a linear relationship between them. Here, we choose $\sigma_{\min} = 100$ ksi.

Yield Strength, ksi	Average Yield Strength of the Range, ksi	Frequency	Cumulative Frequency	$F(x)$	$\ln [x - \sigma_{\min}]$	$n \ln [1 / (1 - F(x))]$
114–115.9	114.95	4	4	0.009	2.705	–4.718
116–117.9	116.95	6	10	0.022	2.830	–3.795
118–119.9	118.95	8	18	0.040	2.942	–3.199
120–121.9	120.95	26	44	0.098	3.042	–2.274
122–123.9	122.95	29	73	0.162	3.133	–1.732
124–125.9	124.95	44	117	0.260	3.217	–1.200
126–127.9	126.95	47	164	0.364	3.294	–0.791
128–129.9	128.95	59	223	0.496	3.366	–0.379
130–131.9	130.95	67	290	0.644	3.432	0.034
132–133.9	132.95	45	335	0.744	3.495	0.311
134–135.9	134.95	49	384	0.853	3.554	0.652
136–137.9	136.95	29	413	0.918	3.610	0.916
138–139.9	138.95	17	430	0.956	3.662	1.136
140–141.9	140.95	9	439	0.976	3.712	1.311
142–143.9	142.95	6	445	0.989	3.760	1.504
144–145.9	144.95	4	449	0.998	3.806	1.810

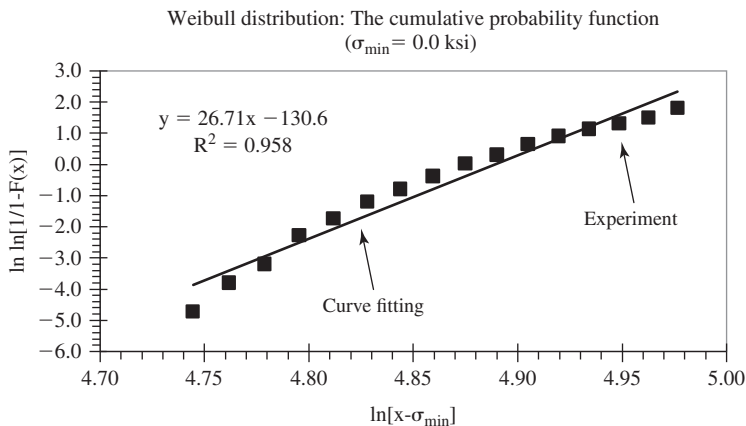


With $R^2 = 0.991$, the data follow the Weibull distribution quite well.

- (f) From (e), the fitting curve is $y = 5.839x - 20.197$. Thus, the Weibull modulus (m) is 5.839 and the scale parameter (σ_o) is 31.78.
- (g) It appears that the yield strength data can be described by both Gaussian and Weibull distributions. The evaluation of the cumulative probability function of the Gaussian distribution (answer (d)) reveals that the experimental $F(x)$ and the calculated $F(x)$ have a linear relation with $R^2 = 0.9965$ and slope = 1.00. The evaluation of the cumulative probability function of the Weibull distribution (answer (e)) also shows a very high R^2 value, 0.9917. Based on these observations, we conclude that this particular set of the yield strength data follows the Gaussian as well as the Weibull distribution. In fact, based on the obtained Gaussian and Weibull distribution functions, we can plot the cumulative probability functions of Gaussian and Weibull distributions in the same figure, as shown below. It can be seen that the difference between them is indeed very small, providing support to the conclusion that the yield strength data follow both Gaussian and Weibull distributions.



- 11-2.** When choosing $\sigma_{\min} = 0.0$ ksi, one obtains the following figure with a lower R^2 value than $\sigma_{\min} = 100.0$ ksi. Thus, $\sigma_{\min} = 100.0$ ksi fits the data better.

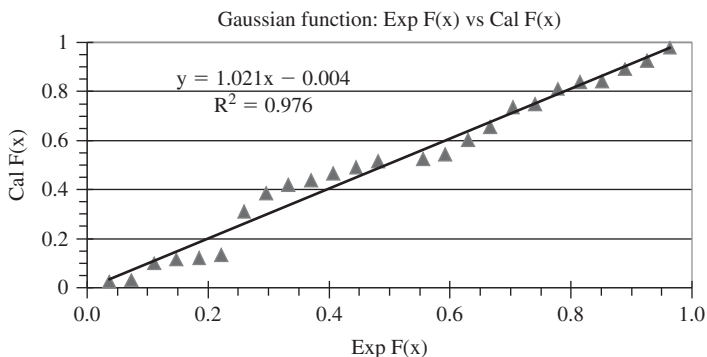


- 11-3. (a)** For a Gaussian distribution, the arithmetic mean (μ) can be obtained by

using $\mu = \sum_{i=1}^N x_i / N$ and the standard deviation (σ) can be obtained by

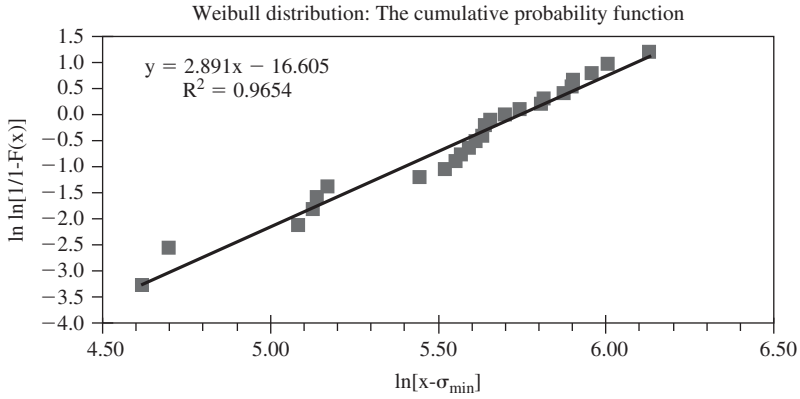
$$\text{using } \sigma = \sqrt{\frac{\sum_{i=1}^N (x_i - \mu)^2}{N-1}}$$

Thus, μ is 976.30 kg/mm², and σ is 89.80.



- (b)** The probability function $f(x) = \text{frequency} / N + 1$.

The cumulative probability function $F(x) = \text{cumulative frequency} / N + 1$.



HV, kg/mm ²	Frequency	Cumulative Frequency	$f(x)$	Exp $F(x)$
801.55	1	1	0.037	0.037
810	1	2	0.037	0.074
861.35	1	3	0.037	0.111
869	1	4	0.037	0.148
870.55	1	5	0.037	0.185
876	1	6	0.037	0.222
931.5	1	7	0.037	0.259
950	1	8	0.037	0.296
957.95	1	9	0.037	0.333
962	1	10	0.037	0.370
968.3	1	11	0.037	0.407
974	1	12	0.037	0.444
979.8	1	13	0.037	0.481
982	2	15	0.074	0.556
986	1	16	0.037	0.593
999.35	1	17	0.037	0.630
1,012	1	18	0.037	0.667
1,033	1	19	0.037	0.704
1,036.15	1	20	0.037	0.741
1,056	1	21	0.037	0.778
1,065	1	22	0.037	0.815
1,066.05	1	23	0.037	0.852
1,087.9	1	24	0.037	0.889
1,106.3	1	25	0.037	0.926
1,160	1	26	0.037	0.963

Note: $N = 26$.

- (c) The cumulative probability function of a Gaussian distribution can be described as

$$F(x) = \frac{1}{2} - \frac{1}{2} \operatorname{erf} \left[- \left(\frac{x - \mu}{\sigma \sqrt{2}} \right) \right] \text{ for } x \leq \mu \text{ and}$$

$$F(x) = \frac{1}{2} + \frac{1}{2} \operatorname{erf} \left[\left(\frac{x - \mu}{\sigma \sqrt{2}} \right) \right] \text{ for } x \geq \mu$$

By using the equations above, the calculated $F(x)$ can be obtained. Then the calculated $F(x)$ can be plotted against the experimental $F(x)$ to evaluate their correlations.

HV, kg/mm ²	Frequency	Cumulative Frequency	$f(x)$	Exp $F(x)$	Cal $F(x)$
801.55	1	1	0.037	0.037	0.026
810	1	2	0.037	0.074	0.032
861.35	1	3	0.037	0.111	0.100
869	1	4	0.037	0.148	0.116
870.55	1	5	0.037	0.185	0.119
876	1	6	0.037	0.222	0.132
931.5	1	7	0.037	0.259	0.309
950	1	8	0.037	0.296	0.385
957.95	1	9	0.037	0.333	0.419
962	1	10	0.037	0.370	0.437
968.3	1	11	0.037	0.407	0.465
974	1	12	0.037	0.444	0.490
979.8	1	13	0.037	0.481	0.516
982	2	15	0.074	0.556	0.525
986	1	16	0.037	0.593	0.543
999.35	1	17	0.037	0.630	0.601
1,012	1	18	0.037	0.667	0.655
1,033	1	19	0.037	0.704	0.736
1,036.15	1	20	0.037	0.741	0.747
1,056	1	21	0.037	0.778	0.813
1,065	1	22	0.037	0.815	0.838
1,066.05	1	23	0.037	0.852	0.841
1,087.9	1	24	0.037	0.889	0.893
1,106.3	1	25	0.037	0.926	0.926
1,160	1	26	0.037	0.963	0.980

With an R^2 value of 0.98, a slope value of 1.02, and an intercept close to zero, the fitting curve is quite linear and matches the Gaussian distribution very well.

- (d) The cumulative probability function of the Weibull distribution can be written as

$$F(x) = 1 - \exp \left[- \left(\frac{x - \sigma_{\min}}{\sigma_o} \right)^m \right] \text{ or}$$

$$\ln \ln \left[\frac{1}{1 - F(x)} \right] = m \ln[x - \sigma_{\min}] - m \ln \sigma_o$$

We can evaluate the characteristic of this distribution by plotting $\ln \ln \left[\frac{1}{1 - F(x)} \right]$ vs. $\ln[x - \sigma_{\min}]$ and then examine whether or not there is a linear relationship between them. Here, we choose $\sigma_{\min} = 700 \text{ kg/mm}^2$.

HV, kg/mm ²	Frequency	Cumulative Frequency	$f(x)$	$F(x)$	$\ln[x - \sigma_{\min}]$	$\ln \ln[1/(1 - F(x))]$
801.55	1	1	0.037	0.037	4.621	-3.277
810	1	2	0.037	0.074	4.700	-2.564
861.35	1	3	0.037	0.111	5.084	-2.139
869	1	4	0.037	0.148	5.130	-1.830
870.55	1	5	0.037	0.185	5.139	-1.586
876	1	6	0.037	0.222	5.170	-1.381
931.5	1	7	0.037	0.259	5.445	-1.204
950	1	8	0.037	0.296	5.521	-1.046
957.95	1	9	0.037	0.333	5.553	-0.903
962	1	10	0.037	0.370	5.568	-0.771
968.3	1	11	0.037	0.407	5.592	-0.648
974	1	12	0.037	0.444	5.613	-0.531
979.8	1	13	0.037	0.481	5.634	-0.420
982	2	15	0.074	0.556	5.642	-0.210
986	1	16	0.037	0.593	5.656	-0.108
999.35	1	17	0.037	0.630	5.702	-0.007
1,012	1	18	0.037	0.667	5.743	0.094
1,033	1	19	0.037	0.704	5.808	0.196
1,036.15	1	20	0.037	0.741	5.818	0.300
1,056	1	21	0.037	0.778	5.875	0.408
1,065	1	22	0.037	0.815	5.900	0.523
1,066.05	1	23	0.037	0.852	5.903	0.647
1,087.9	1	24	0.037	0.889	5.961	0.787
1,106.3	1	25	0.037	0.926	6.007	0.957
1,160	1	26	0.037	0.963	6.131	1.193

The fitting curve gives a straight line with R^2 value of 0.9654. Thus, the data fit the Weibull distribution reasonably well.

- (e) From (d), the fitting curve is $y = 2.891x - 16.605$. Thus, the Weibull modulus (m) is 2.891 and the scale parameter (σ_o) is 312.20.
- (f) The Gaussian distribution can better describe the hardness data listed above than the Weibull distribution because the Gaussian distribution characteristic curve in (c) yields the R^2 value of 0.9768, which is higher than the R^2 value (0.9654) of the Weibull distribution characteristic curve in (d).

11-4. For the 20 tests, $x's = 11$, $o's = 9$, $n_0 = 1$ at 97 MPa, $n_1 = 6$ at 110 MPa, $n_2 = 2$ at 124 MPa; $N = 9$.

$$A = 1 \times 6 + 2 \times 2 = 10 \quad B = 1 \times 6 + 4 \times 2 = 14$$

$$m = y' + d \left(\frac{A}{N} \pm \frac{1}{2} \right)$$

$$m = 96 + 13.8(10/9 + 0.5) = 96 + 14.6 = 118 \text{ MPa (vs. 120 MPa)}$$

$$s = 1.62d \left(\frac{N \cdot B - A^2}{N^2} + 0.029 \right)$$

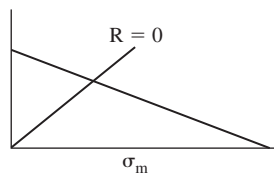
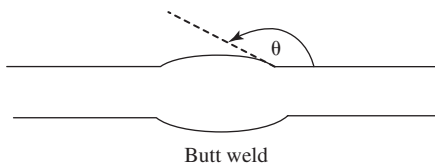
$$= 1.62 \times 13.8(126 - 100/81 + 0.029) = 7.8 \text{ MPa (vs. 7.8 MPa)}$$

CHAPTER 12

12-1. (a) At $R = 0$

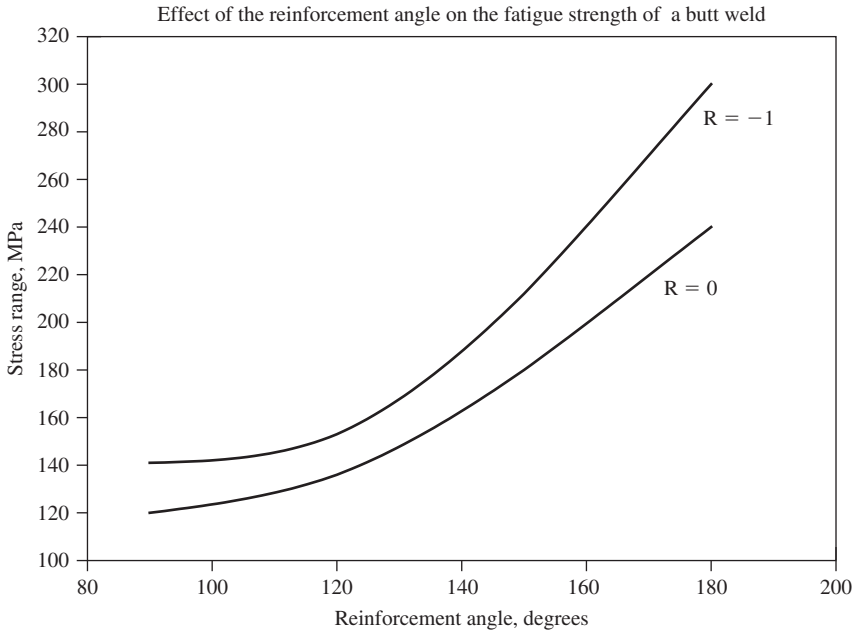
$$\Delta\sigma = 120[2 - \cos(\theta - \pi/2)]$$

θ , radians	$\Delta\sigma_{R=0}$, MPa	$\Delta\sigma_{R=-1}$, MPa
$\pi/2$	120	141
$2\pi/3$	136	153
$5\pi/6$	180	212
π	240	300



(b) $\Delta\sigma = 2\sigma_a$

$$\frac{\sigma_{aR=-1}}{UTS} = \frac{\sigma_{R=0}}{UTS - \sigma_{aR=0}}, \quad \sigma_{aR=-1} = \sigma_{aR=0} \frac{UTS}{UTS - \sigma_{aR=0}}, \quad UTS = 600 \text{ MPa}$$



12-2. 1. The nominal composition of Al 6061 is given in the following table:

Composition (wt %)

Cu	Si	Fe	Mn	Mg	Zn	Cr	Ti	Al
0.15-0.40	0.4-0.8	0.7	0.15	0.8-1.2	0.25	0.04-0.35	0.15	balance

Source: <http://www.elemans.com/2/waa.html>.

- The T6 treatment of an Al 6061 includes solution heat treatment at $\sim 500^\circ\text{C}$ for up to 24 hours, water quenching to obtain a uniform solid solution, and then artificial aging at 155°C for 5–16 hours to attain precipitation hardening.
- The hardness value of Al 6061 at the T6 condition is ~ 95 Bhn (Brinell hardness number).
- The possible cause for the failure of the first elbow is the lack of penetration of the welding metal between the elbow and the tube wall. The lack of penetration resulted in little bonding at the joint. The beach marks on the weld fracture surface indicate that the failure was caused by cyclic

- loading. The hardness value of 102 Bhn taken from the threaded boss and the tube suggest that the proper heat treatment (T6) has been carried out after welding. Otherwise, the hardness near the weld joint would have been lower than 95 Bhn because of the dissolution of precipitates into the Al matrix induced by the exposure to high temperatures during welding. Thus, the separation of the elbow at the weld is attributed to the lack of penetration of the welding material during welding.
5. The possible cause for the failure of the second elbow is due to no or improper heat treatments after the second welding. When the threaded boss was rewelded, the regions near the welding joint were exposed to high temperatures during welding. These regions are normally called the *heat-affected zone* (HAZ). Because of the high-temperature exposure, the precipitate of θ phase in Al 6061 dissolves back into the Al matrix. As a result, the HAZ becomes much softer (~ 50 Bhn, as revealed by the experiment). The tensile strength and fatigue strength of the HAZ decrease as well. Thus, under cyclic loading, the crack initiates and propagates at the HAZ, causing the fracture in the tube near the flange where the material has been affected by high temperatures during welding, and there are stress concentrations due to its complex geometry. Thus, it can be concluded that a proper T6 heat treatment after the second welding would have restored the hardness of the HAZ to ~ 100 Bhn and increased the tensile and fatigue strength of the tube. Therefore, if the heat treatment had been carried out properly after the second welding, the early failure would have been avoided.
 6. As discussed above, the causes for the failure in Case II is the improper or no heat treatment after welding. To provide additional evidence to support this conclusion, the microstructure in the fracture section can be examined by transmission electron microscopy (TEM). TEM can reveal whether or not the microstructure contains the precipitate of the θ phase. If the precipitate is not present, then the T6 heat treatment was not carried out properly or not carried out at all.

CHAPTER 13

13-1. (a)

$$\frac{da}{dt} = 8 \times 10^{-7} K^2 = 8 \times 10^{-7} \sigma^2 \pi a$$

$$K_{Ic} = 30 \text{ MPa}\sqrt{\text{m}}, a_0 = 0.0001 \text{ m}$$

$$\sigma_{hoop} = \frac{pD}{2t} = \frac{6 \text{ MPa} \times 96}{2 \times 12} = 24 \text{ MPa}$$

$a_f = \frac{1}{\pi} \left(\frac{K_{Ic}}{\sigma_{hoop}} \right)^2 = 0.5m$. The wall thickness is 0.012 m. Therefore, the pipe will leak before it bursts.

(Or: $K = 24\sqrt{\pi \cdot 0.012} = 4.66 < 30 \text{ MPa}\sqrt{m}$; pipe will leak)

$$\frac{da}{dt} = 8 \times 10^{-7} (24)^2 \pi a$$

$$\frac{da}{a} = 1.45 \times 10^{-3} dt$$

$$\ln \frac{a_f}{a_0} = \ln \frac{12}{0.1} = 4.79 = 1.45 \times 10^{-3} \Delta t$$

$$\Delta t = 3,300 \text{ hours}$$

(b) For a life of 10,000 hours, determine the maximum pressure.

$$\frac{da}{dt} = 8 \times 10^{-7} \sigma^2 \pi a$$

$$\frac{da}{a} = 8 \times 10^{-7} \sigma^2 \pi dt$$

$$\ln \frac{12}{0.1} = 4.79 = 8 \times 10^{-7} \sigma^2 \pi \times 10,000 \text{ hours}$$

$$\sigma^2 = 191, \sigma = 13.8 \text{ MPa},$$

$$p_{\max} = \frac{\sigma 2t}{D} = \frac{13.8 \times 2 \times 12}{96} = 3.45 \text{ MPa}$$

(c) Proof test pressure to ensure 10,000 hours of service at 1.1 MPa pressure.

$$K_{Ic} = \sigma_H \sqrt{\pi \cdot 0.0001} = 30 \text{ MPa}\sqrt{m}$$

$$\sigma_H = 1,693 \text{ MPa}$$

$$p_{\text{proof}} = \frac{1,693 \times 2 \times 12}{96} = 423 \text{ MPa}$$

(d) System operates at 6 MPa for 2,000 hours.

$$\sigma_{hoop} = \frac{6 \times 96}{2 \times 12} = 24 \text{ MPa}$$

$$\ln \frac{a_{2000}}{0.0001} = 8 \times 10^{-7} (24)^2 \pi \times 2,000$$

$$a_{2000} = 0.0001 \text{ xe}^{8 \times 10^{-7} (24)^2 \pi \times 2000} = 0.0018m$$

$$\ln \frac{12}{1.8} = 8 \times 10^{-7} \left(24 \times \frac{3.5}{6} \right)^2 \times \pi \times \Delta t$$

$$1.79 = 4,926 \times 10^{-7} \Delta t$$

$$\Delta t = 3,600 \text{ hours}$$

CHAPTER 14

14-1. Energy reflected: $IR = \left(\frac{Z_2 - Z_1}{Z_2 + Z_1} \right)^2 = \left(\frac{4.68 - 0.149}{4.68 + 0.149} \right)^2 = 0.88 = .88\%$

Energy transmitted = 0.12 = 12%

14-2. Lucite: $v_L = 0.267 \text{ cm}/\mu \text{ sec}$

Steel: $v_L = 0.594 \text{ cm}/\mu \text{ sec}$

(a) $\sin \theta_{I_1} = \frac{v_{L_1}}{v_{L_2}} = \frac{0.267}{0.594} = 0.45$

$\theta_{I_1} = 26.7^\circ$

(b) $\sin \theta_{I_2} = \frac{0.267}{0.324} = 0.82$

$\theta_{I_2} = 55.5^\circ$

(c) The longitudinal waves are bent toward the normal to the surface, not toward the surface.

14-3. (a) The MT technique will not detect the crack.

(b) The dye penetrant method will not work if the dye is unable to penetrate the crack.

(c) The ET method will not detect the crack since the magnetic permeabilities of the material within the crack and the base material are the same.

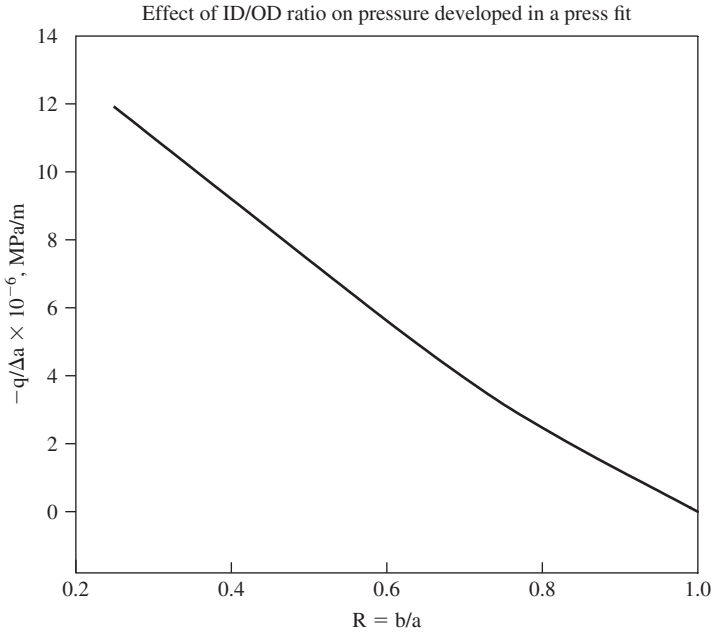
(d) The UT method will detect the crack if the acoustic impedance of the material within the crack differs from that of the base material.

CHAPTER 15

15-1. $OD = 2a = 40 \text{ cm}$, $ID = 2b$, $E = 210 \text{ GPa}$, $\nu = 0.25$

$$\Delta a = \frac{-qa}{E} \left(\frac{a^2 + b^2}{a^2 - b^2} - \nu \right)$$

$$q = -\frac{\Delta a}{a} E \left[\frac{a^2 - b^2}{a^2 (1 - \nu) + b^2 (1 + \nu)} \right]$$



Let $R = b/a$, $b = Ra$

$$q = -\frac{\Delta a}{0.020} 210,000 \left[\frac{0.00040 - 0.00040 R^2}{0.00030 + 0.00050 R^2} \right] = -\Delta a \frac{4,200(1 - R^2)}{0.00030 + 0.00050 R^2}$$

$b, \text{ m}$	R	$-q/\Delta a, \text{ MPa/m}$
0.020	1.0	0
0.015	0.75	3.16×10^6
0.010	0.50	7.4×10^6
0.005	0.25	11.9×10^6

15-2. (a) Life adjustment factor for a bearing reliability of 95%.

From the chart, Fig. 14-7, the percent of rated life is 60%. The life adjustment factor is 0.6.

This corresponds to a life of $0.6 \times 90 \times 10^6$, or 54×10^6 cycles.

Alternatively, from Eq. 14-26, the life adjustment factor, a_i , is related to the % reliability, R , by

$$a_i = 4.48 \left(\ln \frac{100}{R} \right)^{2/3} = 4.48 \left(\ln \frac{100}{95} \right)^{2/3} = 4.48 \times 0.138 = 0.618$$

- (b) Determine L_5 for a system containing four bearings that requires a 5,000-hour life whose rated lives are 12,000, 10,000, 9,000, and 8,000 hours.

Rated Life, hr	L_5 Life, hr*	System Life as % of L_5 Life†	% Reliability Bearing to System Life‡
12,000	7,200	69	94
10,000	6,000	83	92
9,000	5,400	93	91
8,000	4,800	104	88 (est.)

*Determined by multiplying the rated life by a factor of 0.6 obtained from the chart.

†Determined by dividing 5,000 hours by the L_5 life $\times 100$.

‡Determined by using the chart and information from the previous column.

$$\begin{aligned}
 L_{5\text{system}} &= \left[\left(\frac{1}{7,200} \right)^{3/2} + \left(\frac{1}{6,000} \right)^{3/2} + \left(\frac{1}{5,400} \right)^{3/2} + \left(\frac{1}{4,800} \right)^{3/2} \right]^{-2/3} \\
 &= [1.64 \times 10^{-6} + 2.15 \times 10^{-6} + 2.52 \times 10^{-6} + 3.01 \times 10^{-6}]^{-2/3} \\
 &= (7.68 \times 10^{-6})^{-2/3} \\
 &= 2,580 \text{ hours}
 \end{aligned}$$

- 15-3.** What is the reliability of a system containing four bearings that requires a 5,000-hour life when the rated lives of the bearings are 12,000, 10,000, 9,000, and 8,000 hours?

Reliability of the above system at the L_5 level from the chart in the above problem is $0.95 \times 0.92 \times 0.91 \times 0.88 = 0.70$.

That is, the % reliability for 5,000 hours is 70%.

At the L_{10} level:

Rated Life, hr	System Life as % of Rated Life	% Reliability of System to Bearing Life
12,000	42	97
10,000	50	96
9,000	56	95.5
8,000	62	95

% reliability of system is $0.97 \times 0.96 \times 0.955 \times 0.95 = 0.84 = 84\%$ (up from 70 % above)

$$\begin{aligned}
 L_{10\text{system}} &= \left[\left(\frac{1}{12,000} \right)^{3/2} + \left(\frac{1}{10,000} \right)^{3/2} + \left(\frac{1}{9,000} \right)^{3/2} + \left(\frac{1}{8,000} \right)^{3/2} \right]^{-2/3} \\
 &= [0.76 \times 10^{-6} + 1 \times 10^{-6} + 1.17 \times 10^{-6} + 1.40 \times 10^{-6}]^{-2/3} \\
 &= 3,780 \text{ hours (up from 2,325 hours)}
 \end{aligned}$$

Indexes

Name Index

A

Ainsworth, R. A., 102
Alban, L. E., 411, 413, 414
Albrecht, P., 287
Almen, J. O., 288
Anderson, T. L., 102
Archard, J. F., 414
Argon, A. S., 181, 191
Ashby, M. F., 218, 223, 224,
234, 414
Atanmo, P., 288

B

Bagnall, C., 359, 394
Bannantine, J. A., 290
Bao, H., 288
Barsom, J. M., 165, 168, 191
Bennett, P. E., 165, 191
Birnbaum, Z. W., 311
Black, P. H., 288
Boettner, R. C., 247, 287
Bowles, C. Q., 289
Boyce, B. L., 289
Brandon, D., 142, 155
Bressers, J., 130
Bridgman, P. W., 181, 191
Broek, D., 102

Brooks, C. R., 310
Brown, B. F., 341, 342, 344, 345, 346,
347, 359
Brown, C. M., 287
Budiansky, B., 287
Buntin, W. D., 331, 334
Burns, K. W., 163, 191

C

Caddell, R. M., 183, 191, 211, 334
Canonico, D. A., 25
Carter, C. B., 137, 140, 155
Cartwright, D. J., 102
Choudhury, A., 310
Chou, P. C., 46
Clark, N., 26
Clark, P., 288
Colangelo, V. J., 310
Collins, J. A., 234
Comer, J. C., 290
Coudert, E. M., 311
Cowles, B. A., 290
Cox, W. J., 292, 294, 309
Crosby, S., 118
Cross, H. C., 130
Cullity, B. D., 155
Cummings, H. N., 310

D

da Silveira, T. I., 234, 357
 Davies, R. G., 130
 Demers, C. E., 13, 15, 26
 Denhard, E., 343, 359
 Dias da Silva, V., 75
 Dieter, G. E., Jr., 46, 75, 191,
 297, 311
 Differt, K., 287
 Dixon, W. J., 311
 Dolan, T. J., 298, 311
 Donahue, R. J., 288
 Dornheim, M. A., 290
 Dowling, A. R., 102
 Drew, K., 26
 Dudley, D. W., 414
 Dugdale, D. S., 289

E

Ebert, L. J., 209, 211
 Eiber, R. J., 358
 El Haddad, M. H., 290
 Elber, W., 287
 Elices, M., 102
 Endo, M., 269, 270, 272,
 288–290
 Epstein, H. I., 12, 26
 Erdogan, F., 289
 Essmann, U., 287
 Evans, H. E., 234

F

Federson, C. E., 101
 Fikkers, A. T., 358
 Finnie, I., 234
 Fiorino, F., 26
 Fisher, J. W., 13, 15, 26
 Foecke, T., 172, 174, 176, 191
 Forsyth, P. J. E., 288
 French, D. N., 227, 234
 Frost, H. J., 218, 234
 Frost, N. E., 289
 Fuchs, H. O., 256, 288
 Fujihara, M., 275, 290
 Furtado, H. C., 234, 290, 359, 394
 Furukawa, K., 290

G

Gamache, B., 288
 Ghandi, C., 234
 Gonzalez, J., 157, 159, 288
 Griffith, A. A., 80, 101
 Gumbel, E. J., 302, 310
 Gurney, T. R., 210, 211

H

Hadrath, H. F., 289
 Hammitt, F. G., 290
 Hardrock, J. L., 290
 Harlow, D. G., 288
 Harper, R. F., 25
 Hasegawa, T., 288
 Hattori, T., 290
 Heaslip, T. W., 334
 Heiser, F. A., 417
 Heymann, F. J., 290
 Hines, W. A., 380
 Hirst, W., 414
 Holt, J. M., 191
 Hosford, W. F., 183, 191, 211, 334
 Hutchinson, J. W., 287

I

Illg, W., 263, 264, 289
 Irwin, G. R., 80, 84, 88, 89,
 101, 289
 Ishihara, S., 248–252, 287, 288

J

Johnson, H., 358
 Johnston, T. L., 130
 Jones, D. A., 358
 Jones, D. R. H., 9, 25, 130,
 358, 414
 Juvinall, R. C., 255, 288

K

Kanninen, M. F., 102
 Kaplan, W. D., 142, 155
 Kear, B. H., 130
 Kiefner, J. F., 358
 Kitagawa, H., 289

Kobayashi, H., 21, 26
 Kondo, Y., 290
 Korin, F., 334
 Koyasu, Y., 289
 Krauss, G., 209, 211
 Kuhn, P., 289
 Kumble, R., 288
 Kuno, T., 288
 Kunpanichkit, C., 383, 384

L

Laird, C., 288
 Lange, G. A., 417
 Larrainzar, C., 317, 334
 Le May, I., 46, 75, 158, 179, 205,
 234, 290, 350, 357, 358,
 359, 394
 Levan, G., 288
 Lipson, C., 311
 Liu, H. W., 289
 Low, J. R., Jr., 191
 Lutynski, C., 400, 402, 403, 414

M

Mackaldener, M., 413, 414
 Maeda, Y., 212
 Manahan, M. P., 169, 191
 Marsh, F. J., 191
 Matsunaga, H., 290
 Mayr, P., 191
 McClintick, F. A., 181, 191
 McCowan, C. N., 191
 McEvily, A. J., 179, 186–191, 205, 221,
 234, 247, 287–290, 350, 357, 358,
 414
 McMillan, J. C., 254, 288
 Mendelson, A., 75
 Milne, I., 102
 Minakawa, K., 287, 288
 Mood, A. M., 311
 Morlett, J. O., 358
 Morocco, J. D., 26
 Moyer, C., 414
 Mughrabi, H., 130, 287
 Murakami, Y., 102, 258, 259, 263, 264,
 269, 270, 272, 288, 289, 290, 304,
 306, 307, 311

N

Nakamura, R., 290
 Neuber, H., 287
 Newman, J. C., 290, 417
 Nishida, S., 245, 287, 289, 417
 Nowell, D., 218, 399

O

O'Donoghue, P. E., 358
 Oguma, N., 289, 290
 Ohta, A., 212
 Oldersma, A., 279, 290
 Olssen, M., 413, 414
 Orowan, E., 84, 101

P

Pagano, N. J., 46
 Paris, P. C., 289
 Payson, P., 130
 Pelloux, R. M., 253, 288
 Perez Ipiña, J., 334
 Peteves, S., 130
 Pickering, F. B., 163, 191
 Pohl, K., 191
 Popelar, C. H., 102
 Pugh, E. N., 343, 359
 Punter, A., 358

R

Rabinowicz, E., 414
 Reinhold, O., 119, 130
 Remy, L., 198, 199, 211
 Revie, R. W., 358
 Rice, J. R., 102
 Rigney, D. A., 414
 Ritchie, R. O., 289
 Roark, R. J., 414
 Rolfe, S. T., 165, 168, 191
 Rooke, D. P., 102
 Ruth, E. A., 191
 Ryder, D., 288

S

Sakai, T., 289
 Saruki, K., 288

Saunders, S. C., 311
 Savage, C. H., 130
 Schivje, J., 261, 289
 Schulte, W. C., 310
 Sheth, N. J., 311
 Shibata, T., 311
 Shumaker, M. B., 359
 Siewert, T. A., 191
 Sih, G. C., 101
 Simansky, G., 414
 Sinclair, G. M., 165, 191, 298, 311
 Skaar, J., 192
 Smith, E. A., 12, 26
 Smith, G. C., 288
 Smith, K. N., 290
 Sprowls, D. O., 345, 359
 Steen, M., 130
 Stephens, R. I., 256, 288
 Stevick, G. R., 234
 Stewart, A. T., 102
 Stulen, F. B., 310
 Sugai, Y., 287
 Suresh, S., 290
 Suzuki, N., 212

T

Tada, H., 101
 Takahashi, S., 289
 Takai, K., 289
 Takeda, M., 289
 Tanaka, K., 288
 Tanaka, N., 289
 Taplin, D. M. R., 234
 Tetelman, A. S., 191, 221, 234
 Thielsch, H., 234, 334
 Thornton, P. R., 130
 Timoshenko, S., 406, 414

Topper, T. H., 290
 Toriyama, T., 289, 311
 Troiano, A., 358

V

Valiente, A., 102
 Vanstaen, G., 358

W

Wahl, A. M., 283, 284, 290
 Wald, M., 26
 Walsh, J. D., 359
 Wakita, M., 288
 Wanhill, R. J. H., 279, 290
 Wei, R. P., 288
 Weibull, W., 310
 Williams, D. B., 137, 140, 155
 Wilsdorf, H. G. F., 130
 Witherell, C. E., 326, 334
 Wold, G., 191
 Wood, W. A., 287
 Worden, C. O., 253, 288
 Wright, W., 287
 Wulpi, D. J., 417

Y

Yamashita, K., 290
 Yang, Z., 288
 Yokohama, N. N., 289
 Young, W. C., 414

Z

Zahavi, E., 290
 Zapffe, C. A., 253, 288
 Zhuang, Z., 358

Subject Index

A

Acoustic emission testing, 391
Aging aircraft, 17
Air France Concorde Crash, 22
Al-Cu phase diagram, 120
Al-Ni phase diagram, 124
Aloha Airlines Boeing 737, 16
Aluminum alloys, 120
Aluminum-copper system, 120
American Airlines DC-10, 17
Angle beam techniques, 387
Anisotropy, 36
Annealing, 116
API, 5
Arithmetic mean, 293
Arrhenius-type behavior, 220
ASME Boiler and Pressure Vessel Code,
 217
ASME, 4
ASTM Designation E 1351, 143
ASTM Designation E 23, 163
ASTM E 1221, 96
ASTM E 1290, 90
ASTM E 399, 89, 90
ASTM E 561, 91
ASTM E 813, 97
ASTM E 837, 149
ASTM, 4

Austenite, 109, 112
Axisymmetric stress, 180

B

Bainite, 116
Banded microstructure, 330
Banding, 118
Basquin's law, 241
Bearing and system reliability, 407
Bearing failures, 409
Blue brittleness, 118
Bottle cap, 2
Bragg's law, 147
Branch cracking, 344
Brittle fracture, 8, 156
Brittle-to ductile transition
 temperature, 65
Bulk modulus, 37
Burger's vector, 64
Bushings, 403

C

C*, 98
Cannon barrels, 92
Carbon equivalent, 319
Carburizing, 117
Case crushing, 412

Case Studies:

- Airbus 380, 22
- Aircraft crankshaft, 378
- Aircraft gas turbines, 281
- Alexander Kielland, 321
- Aloha Airlines 737, 384
- Backing rings, 356
- Boeing 737-300, 23
- Bushing, 403
- Challenger, 4
- China Airlines Flight 611, 20
- Cigarette lighter, 4
- Citicorp Tower, 7
- Comet Aircraft, 8
- Concorde, 22
- Continuous casting, 329
- Counterfeit part, 332
- Dan Air Boeing 707, 11
- DC 10 crash, Chicago, 17
- F-111 Aircraft, 330
- Fossil-fuel fired boilers, 229
- Golf club shaft, 204
- Hartford Coliseum Roof, 12
- Heat exchanger tube, 226
- Helicopter bolt, 185
- Helicopter tail rotor, 136
- Hydroelectric generator, 276
- Japan Airlines 747 Crash, 20
- Kansas City Hyatt Walkways, 12
- Ladder rung, 349
- Mianus River Bridge, 12
- Molasses tank, 159
- Ovalized tube, 228
- Point Pleasant Bridge, 159
- Railroad car axle, 410
- Sioux City DC-10, 367
- Spring failures, 348
- Stack corrosion, 355
- Steering column component, 134
- Tacoma Narrows Bridge, 8
- Tay bridge, 8
- Titanic, 172
- Three Mile Island, 4
- Train wheel, 149
- USS Thresher, 24
- UTS examination of fuse pins, 389
- Welded pipe, 225
- Welding electrodes, 353
- Zinc die casting, 144
- 747 fuse pin, 277
- Jet engine components, 331
- Casting defects, 328
 - Cavities, 328
 - Centerline piping, 328
 - Defective surface, 328
 - Discontinuities, 328
 - Incomplete casting, 328
 - Incorrect dimensions or shape, 328
 - Metallic projections, 328
 - Nonmetallic inclusions, 328
- Cathodic protection, 346
- Cavitation, 285
- Cementite, 112
- Center-cracked panel, 81
- Chain of custody, 151
- Charpy V-notch test (CVN), 161
- Chemical analysis, 143
- Chevron markings, 158
- Cleavage fracture, 157
- Coatings, 126
- Codes, 4
- Coefficient of variation, 294
- Coffin-Manson law, 241
- Coherent phases, 123
- Coil springs, 283
- Cold working, 116
- Compliance calibration, 92
- Compression, 32
- Concluding remarks, 417
- Constitutive relations, 35
- Corrosion, 336
 - Corrosion fatigue, 337
 - Corrosion fundamentals, 337
 - Corrosion packout, 14
 - Corrosion science, 3
 - Cost of inspections, 393
 - Countersunk rivets, 17
 - Crack arrest, 95
 - Crack arrestor, 352
 - Crack closure, 247
 - Crack opening level, K_{op} , 248
 - Crack tip opening displacement, 90
 - Crack velocity, 158
 - Cracking in oil and gas pipelines, 350
 - Creep characteristics, 217
 - Creep deformation map, 218
 - Creep, 216
 - Creep fracture mechanism map, 224

Creep fracture mechanisms, 222
 Creep parameters, 220
 Critical angles, 386
 Critical strain energy release rate, 84
 Cross-examination, 154
 Crystallographic facets, 156
 Crack tip opening displacement, CTOD,
 90, 91

D

Decomposition of a stress tensor, 29
 Defects, 316
 Delta K_{eff} , ΔK_{eff} , 248
 Depositions, 152
 Depth of field, 141
 Design considerations in fatigue, 240
 Diffusion, 219
 Diffusion Coatings, 129
 Dilatation, 36
 Dimples, 184
 Directionally solidified alloys, 123
 Dislocation, 61
 Dislocation climb, 123, 218
 Dislocation loop, 64
 Distortional energy, 68
 Distortional stress, 29
 Ductile fracture, 177
 Ductile-Brittle transition temperature
 (DBTT), 163
 Dwell-time fatigue, 331

E

Earthquake, 2
 Eddy current inspection, 17
 Eddy current testing, 277
 Edge dislocation, 61
 Elasticity, 3
 Elastic constants, 36
 Elastic constitutive relationships, 36
 Elastic-plastic fracture mechanics, 96
 Electron energy loss spectroscopy (EELS),
 145
 Electron probe microanalysis (EPMA), 145
 Elongated dimples, 184
 Energy dispersive X-ray spectroscopy
 (EDS), 139
 Engineering strain, 32

Engineering stress, 27
 Environmental effects in fatigue, 256
 Environmental effects, 336
 Environmentally assisted cracking, 342
 Epoxy bonding, 16
 Equivalent strain, 69
 Equivalent shear stress, 69
 Eutectic, 114
 Eutectoid, 112
 Everhard-Thornley detector, 140
 Examination and Reporting Procedures,
 132
 Examination in laboratory, 152
 Examination tools (field), 132
 Examples of brittle fracture, 159
 External work, 84

F

Federal Aviation Administration, FAA,
 4, 5
 Fail-safe, 3
 Failure analysis, 1, 2
 Failure Assessment Diagram, 98
 False Brinnelling, 405
 Faraday's law, 339
 Fatigue crack initiation, 246, 254
 Fatigue crack propagation, 252
 Fatigue crack, 8, 11, 92
 Fatigue failure analysis, 273
 Fatigue limit, 238
 Fatigue mechanism, 246
 Fatigue of composite materials, 286
 Fatigue striations, 253, 260
 Fatigue, 237
 Fault trees, 326
 FBI, 4
 Ferrite, 111
 Fillet weld a-measure, 325
 Finite element method (FEM), 3
 Finite fatigue life, 239
 Finite width correction, 85
 Flaw detection, 360
 Foreign object damage (FOD), 240, 282
 Forming defects, 329
 alligatoring, 330
 edge cracking, 329
 flow patterns, 330
 over-under cambering, 329

Forming defects (*cont'd*)
 seams and laps (folds), 330
 residual stresses, 330
 stretcher strains, 330
 Forming limit diagram, 183
 Fourier transform infrared spectroscopy, 145
 Fractography, 3
 Fracture mechanics, 80
 Fracture surface preparation, 133
 Fracture toughness, 82
 Frequency factor, 164
 Fretting fatigue, 399
 Fuel storage tank, 161

G

Galloping Gertie, 8
 Gamma-prime, 123
 Gear design and manufacturing problems, 412, 414
 Gear failures, 410
 Gear material problems, 412
 General yield, 98
 Gerber diagram, 241
 Goodman diagram, 241
 GP zones, 121
 Grain boundaries, 123
 Grain size, 111, 167
 Griffith analysis, 80
 Ground-air-ground cycle (GAG), 243
 Gumbel distribution, 302

H

Hammurabi (laws of), 2
 Hard-alpha, 122, 373
 Hardenability, 116
 High cycle fatigue, 242
 Hole-drilling method, 149
 Homologous temperature, 224
 Hooke's law, 36
 Hot corrosion (sulfidation), 358
 Hot forging, 116
 Hot shortness, 117
 Hot working, 116
 Hydrogen attack, 337, 356
 Hydrogen embrittlement, 337
 Hydrogen-induced cracking (HIC), 337

Hydrostatic pressure, 36
 Hydrostatic stress, 29

I

Incorrect heat treatment, 333
 Infinite fatigue life, 239
 Instability, 91
 Intergranular creep fracture, 223
 Intergranular fracture, 159
 Internal energy, 84
 Iron-carbon equilibrium diagram, 109
 Iron-carbon system, 109
 Iron-nitrogen phase diagram, 379
 Isothermal transformation diagram, 110

J

J integral, J_{IC} , 96

L

Laminar tearing, 320
 Larson-Miller parameter, 220
 Lattice friction, 67
 Leak before burst, 92
 LEFM, 88
 Liberty ships, 159
 Limit of resolution, 134
 Linear elastic fracture mechanics, 88
 Liquid metal embrittlement, 337
 Loading modes, 88
 Localized deformation, 337
 Log normal distribution, 297
 Logarithmic spiral, 73
 Low-cycle fatigue, 242
 Lower shelf, 167
 Lüder's band, 67

M

Magnetic Particle testing, 375
 MAR-M200, 125
 Martensite, 116
 Maximum shear stress criterion, 69
 MCrAlY coatings, 128
 Median, 294
 Miller indices, 65
 Mode I, 88
 Mode II, 88

Mode III, 88
 Mode, (statistics), 294
 Mohr circles, 32, 37,
 Monkman-Grant law, 220
 M_s temperature, 116
 Multiple site damage, 17

N

National Aviation and Space
 Administration, NASA, 4
 Necking in thin strip, 181
 Necking of a bar, 177
 Nelson diagram, 259
 Neuber notch rule, 243
 Neutron irradiation, 168
 Nickel-aluminum system, 124
 Nickel-base superalloys, 122
 Nil-ductility transition temperature
 (NDTT), 170
 Nitriding, 117
 Non-destructive testing, 3
 Non-linear elastic, 96
 Normal beam technique, 386
 Normal distribution, 294
 Normalizing, 116
 Notch, 44
 Notch constraint, 166
 Notch size effect in fatigue, 244
 Nuclear regulatory Commission,
 NRC, 4
 National Transportation Safety Board,
 NTSB, 4
 Nuclear pressure vessel design code, 168

O

Octahedral plane, 65
 Optical examination, 135
 Optical Microscopes, 135
 Occupational Safety and Health
 Administration, OSHA, 4
 Overlay coatings, 129
 Overload, 3
 Oxidation-resistant coatings, 127

P

Palmgren-Miner law, 243
 Paris law, 262

Pb-Zn phase diagram, 144
 Pearlite, 114
 Peirels force, 164
 Penetrameters, 391
 Penetrant testing, 364
 Percent elongation, 65
 Peritectic, 112
 Persistent slip bands, 246
 Phase diagrams, 108
 Pipeline reinforcement, 352
 Pitting corrosion, 356
 Plane strain, 44
 Plane strain fracture toughness,
 K_{Ic} , 84
 Plane stress, 38
 Plastic deformation, 59
 Plastic-zone size, 88
 Plating problems, 353
 Point rupture fracture, 224
 Poisson's ratio, 36
 Polycrystalline alloys, 122
 Polymers, 84
 Potential-current diagram, 340
 Pourbaix diagram, 341
 Power law creep, 219
 Preheating, 117
 Pretrial preparation, 152
 Principal stress, 30
 Problem Solutions, 419
 Product liability, 4
 Pure shear, 33

Q

Quench cracking, 119, 204

R

Radiographic testing, 389
 R-curve, 91
 Record keeping and testimony, 151
 Recrystallization, 116
 Redundancy, 3
 Redundant, 3
 Reference stress intensity
 factor, 114
 Reference temperature, 168
 Renitriding, 378
 Replicas, 142

Residual life assessment, 230
 Residual stress toughening, 208
 Residual Stress, 132, 146, 196
 carburizing, 117
 induction hardening, 207
 measurement, 211
 nitriding, 208
 non-uniform plastic deformation, 200
 quenching, 204
 welding, 210
 Resolved shear stress, 66
 Retained austenite, 116
 Return period, 303
 River patterns, 158
 Robinson's life fraction rule, 222
 Roller bearings, 404
 Rolling contact fatigue, 406

S

S/N curve, 238
 Safe-life, 3
 Safety factor, 3
 Scanning atomic force microscopy
 (AFM), 146
 Scanning Auger microanalysis
 (SAM), 145
 Scanning Electron Microscope
 (SEM), 138
 Scatter in fatigue, 297
 Screw dislocation, 61
 Secondary ion mass spectrometry, 145
 Semicircular surface flaw, 86
 Shear modulus, 36
 Shear strain, 34
 Shear stress, 28
 Short crack limitation, 92
 Shot peening, 256
 Single crystal, 66
 SI units, 5, 6
 Slip direction, 65
 Slip plane, 65
 Small spot electron spectroscopy (EPS),
 145
 Sour gas, 253
 Spectrographic analysis, 143
 Spheroidizing, 117
 Springback, 200
 Stage I, 257

Stage II, 257
 Standard deviation, 294
 Statistical distributions, 294
 Statistics of fatigue, 296
 Steels, 109
 Stereo-pair, 142
 Storage of evidence, 152
 Stored elastic energy, 42
 Strain, 32
 Strain energy, 45
 Strain energy density, 42
 Strain localization, 179
 Strain rate, 91
 Strain-rate sensitivity, 164
 Strength of materials, 3
 Stress analysis, 3
 Stress deviator tensor, 29
 Stress intensity factor, 85
 Stress measurement by X-rays, 147
 Stress relaxation, 232
 Stress relieving, 117
 Stress tensor, 29
 Stress-corrosion cracking, 237
 Stress-strain relations, 38
 Sulfide print, 144
 Surface energy, 80
 Surface finish in fatigue, 255

T

Technical Report, 150
 Temper embrittlement, 118
 Tempering, 117
 Tension, 30
 Theoretical strength, 59
 Thermal shock, 196, 198
 Thermal strain, 196
 Thermal Stress, 196
 Thermal-barrier coatings, 127
 Thermal-mechanical cyclic
 strain, 198
 Thermal-mechanical fatigue, 243, 285
 Thickness and fracture toughness, 89
 Three-point bend specimen, 87
 Threshold for SCC, K_{Isc} , 338
 Titanium alloys, 121
 (Ti-6Al)-V phase diagram, 122
 Torsion, 43
 Torsional failure, 185

Transformation range, 114
Transgranular creep fracture, 223
Transgranular fracture, 156
Transmission Electron Microscope
(TEM), 136
Tresca criterion, 69
Trial testimony, 153
True strain, 34
True stress, 27

U

Ultimate tensile strength, 67
Ultra-long life fatigue, 271
Ultrasonic testing, 384
Upper shelf, 167

V

Vacuum remelting, 374
Viscoelasticity, 3
Viscous creep, 218
Visual examination, 133, 364
Von Mises criterion, 68

W

Wear, 396
Weibull distribution, 298, 406
Weld cooling rate, 319
Weld defects, 159, 316, 318
 weld mismatch, 319
 weld porosity, 318
 weld reinforcement, 318
 weld shrinkage, 319
 weld slag inclusions, 319
 weld spatter, 319
Weld toe, 317
Wöhler curves, 318
Wrong alloys, 333

X

X-ray analysis, 146

Y

Yield criteria, 68
Yield stress, strength, 69
Young's modulus, 36

